Transactions of the ASME®

Transactions of the ASME, Journal of Turbomachinery (ISSN 0889-504X) is published quarterly (Jan., Apr., July, Oct.) by The American Society of Mechanical Engineers, Three Park Avenue, New York, NY 10016. Periodicals postage paid at New York, NY and additional mailing offices. POSTMASTER: Send address changes to Transactions of the ASME, Journal of Turbomachinery, c/o THE AMERICAN SOCIETY OF MECHANICAL ENGINEERS, 22 Law Drive, Box 2300, Fairfield, NJ 07007-2300.
CHANGES OF ADDRESS must be received at Society headquarters seven weeks before they are to be effective. Please send old label and new address.
STATEMENT from By-Laws. The Society shall not be responsible for statements or opinions advanced in papers or ... printed in its publications (B7.1, Par. 3).

INDEXED by Applied Mechanics Reviews and Engineering Information, Inc. Canadian Goods & Services Tax Registration #126148048

Journal of Turbomachinery

Published Quarterly by The American Society of Mechanical Engineers

VOLUME 125 • NUMBER 2 • APRIL 2003

TECHNICAL PAPERS

(**Contents continued on inside back cover**)

This journal is printed on acid-free paper, which exceeds the ANSI Z39.48-1992 specification for permanence of paper and library materials. ♾™
♻ 85% recycled content, including 10% post-consumer fibers.

Journal of Turbomachinery **Volume 125, Number 2** **APRIL 2003**

The ASME Journal of Turbomachinery is abstracted and indexed in the following:

Aluminum Industry Abstracts, Aquatic Science and Fisheries Abstracts, AMR Abstracts Database, Ceramics Abstracts, Chemical Abstracts, Civil Engineering Abstracts, Compendex (The electronic equivalent of Engineering Index), Corrosion Abstracts, Current Contents, Ei EncompassLit, Electronics & Communications Abstracts, Energy Information Abstracts, Engineered Materials Abstracts, Engineering Index, Environmental Science and Pollution Management, Excerpta Medica, Fluidex, Fuel and Energy Abstracts, INSPEC, Index to Scientific Reviews, Materials Science Citation Index, Mechanical & Transportation Engineering Abstracts, Mechanical Engineering Abstracts, METADEX (The electronic equivalent of Metals Abstracts and Alloys Index), Metals Abstracts, Oceanic Abstracts, Pollution Abstracts, Referativnyi Zhurnal, Shock & Vibration Digest, Steels Alert

Combustor Turbine Interface Studies—Part 1: Endwall Effectiveness Measurements

W. F. Colban

K. A. Thole

Mechanical Engineering Department,
Virginia Polytechnic Institute and State University,
Blacksburg, VA 24061

G. Zess

Pratt and Whitney,
East Hartford, CT 06108

Improved durability of gas turbine engines is an objective for both military and commercial aeroengines as well as for power generation engines. One region susceptible to degradation in an engine is the junction between the combustor and first vane given that the main gas path temperatures at this location are the highest. The platform at this junction is quite complex in that secondary flow effects, such as the leading edge vortex, are dominant. Past computational studies have shown that the total pressure profile exiting the combustor dictates the development of the secondary flows that are formed. This study examines the effect of varying the combustor liner film-cooling and junction slot flows on the adiabatic wall temperatures measured on the platform of the first vane. The experiments were performed using large-scale models of a combustor and nozzle guide vane in a wind tunnel facility. The results show that varying the coolant injection from the upstream combustor liner leads to differing total pressure profiles entering the turbine vane passage. Endwall adiabatic effectiveness measurements indicate that the coolant does not exit the upstream combustor slot uniformly, but instead accumulates along the suction side of the vane and endwall. Increasing the liner cooling continued to reduce endwall temperatures, which was not found to be true with increasing the film-cooling from the liner. [DOI: 10.1115/1.1561811]

Introduction

Today's world heavily depends on gas turbine engines for military and commercial propulsion as well as for industrial applications. This dependence demands engines that are both durable and produce large amounts of power-two requirements that are somewhat conflicting. The reason for this conflict is that high temperatures are needed at the entrance to the rotor, which in turn cause reduced component life. One critical region in an engine is the combustor-turbine junction. Combustor designs, particularly for aeroengines, typically have film holes or slots that provide cooling along the liner of the combustor. The coolant that is injected out of the liner produces highly nonuniform temperature and pressure radial profiles as it exits the combustor and enters into the turbine. These nonuniformities typically span 10–15% of the inner and outer radii at the platforms of the first vane. In addition, most combustor-turbine interfaces include, depending on the design, a backward-facing slot, a forward-facing slot, or a flush slot through which coolant leaks into the main gas path. The interaction between the liner and slot flows as well as interaction with the highly turbulent mainstream, which is produced from combustor dilution holes, dictates the total pressure profile coming in to the passage of the first vane. In turn, this total pressure profile in the near-platform region dictates the development of the secondary flow through the vane passage. Moreover, these secondary flows dictate the heat transfer to the platform of the first vane and the exit flow angles for the rotor.

To improve the understanding of this complex flow, highly-resolved measurements were taken using a combined large-scale combustor simulator and first vane. The combustor simulator includes large dilution holes, film-cooling holes along the approaching liner, and a backward-facing slot at the combustor-turbine interface. Although this simulator does not include the effects of combustion, these studies were directed at understanding the effects of representative combustor flow fields on the secondary flow development in the first vane passage. The combustor simulator produces non-uniformities in both the span (radial) and pitch (circumferential) directions through the use of the liner film-cooling, insuring representative near-platform flows, and dilution jets, insuring the appropriate levels of mainstream turbulence.

This paper is the first of a two-part series that investigates the effects of different combustor liner flows on adiabatic effectiveness levels on the downstream vane platform. Part 1 presents a discussion of the inlet conditions that were simulated as well as measured adiabatic wall temperatures along the vane platform. Part 2 presents flow and thermal field measurements for selected cases of interest. In general, the objectives for the work presented in this paper were the following: i) to evaluate the effect of various liner flows on the exit total pressure profiles and ii) to quantify adiabatic wall temperatures as a function of different liner cooling flows and different slot flows.

Summary of Past Literature

Many past studies have led to a range of secondary flow models in turbine airfoil passages. Secondary flows refer to velocity components not aligned with the inviscid flow through the passage. Driving the secondary flows are two pressure gradients: the inherent pressure gradient from turning the flow and the pressure gradient resulting from nonuniform inlet conditions along the radial span of the airfoil passage. Langston [1] proposed an accurate representation of the secondary flows for a vane with an approaching two-dimensional turbulent boundary layer along the endwall. A horseshoe vortex is formed by a downturning of the flow as it approaches the vane leading edge. The pressure side leg of the horseshoe vortex turns into the passage vortex while the suction side leg of the horseshoe vortex is suppressed by the passage vortex as it convects through the passage. It is questionable whether or not the secondary flows in today's engines behave in this manner because the inlet conditions to the first vane are much different than the turbulent boundary layer assumption made by Langston and others.

While there are no studies that have accounted for multiple rows of inclined film-cooling holes placed in a combustor liner upstream of a backward-facing slot, there have been a few studies

Contributed by the International Gas Turbine Institute and presented at the International Gas Turbine and Aeroengine Congress and Exhibition, Amsterdam, The Netherlands, June 3–6, 2002. Manuscript received by the IGTI January 16, 2002. Paper No. 2002-GT-30526. Review Chair: E. Benvenuti.

that have measured endwall heat transfer as a result of injection from a two-dimensional, flush slot just upstream of the vane. Blair [2] measured adiabatic effectiveness levels and heat transfer coefficients for a range of blowing ratios through a slot placed just upstream of the leading edges of his single passage flow channel. One of the key findings was that the endwall adiabatic effectiveness distributions showed extreme variations across the vane pitch. Much of the coolant was swept across the slot toward the suction side corner resulting in reduced coolant near the pressure side. As the blowing ratio was increased, he found that the extent of the coolant also increased. Measured heat transfer coefficients were similar between no slot and slot injection cases. In a later study by Granser and Schulenberg [3], similar adiabatic effectiveness results were reported with higher values occurring near the suction side of the vane.

A series of experiments have been reported for various injection schemes upstream of a nozzle guide vane with a contoured endwall by Burd and Simon [4], Burd et al. [5], Oke et al. [6,7]. In the studies in [4,5,7] coolant was injected from an interrupted, flush slot that was inclined at 45 deg just upstream of their vane. Similar to others, they found that most of the slot coolant was directed toward the suction side at low slot flow conditions. As they increased the percentage of slot flow to 3.2% of the exit flow, however, their measurements indicated better coverage occurred across the pitch of the airfoil endwall. Their flow field measurements indicated that as the bleed flow was increased the secondary flow structure moved from the pressure surface toward the suction surface for the contoured endwall. Above 3.2% their results indicated no increased thermal benefit. In contrast, the study by Oke et al. [6] used a double row of film-cooling holes that were aligned with the flow direction and inclined at 45 deg with respect to the surface while maintaining nearly the same optimum 3% bleed flow of their previously described studies. They found that the jets lifted off the surface producing more mixing thereby resulting in a poorer thermal performance than the single slot.

Similarly, Zhang and Jaiswal [8] made comparisons between the thermal performance of a slot and two rows of film-cooling holes upstream of a vane along the endwall. They also report a migration of the coolant towards the suction side of the vane. Their results indicated uniform coverage was achieved at high slot flows (rather than film-cooling jet flows), while higher effectiveness levels at the trailing edge were achieved at high film-cooling flows.

Roy et al. [9] compared their experimental measurements and computational predictions for a flush cooling slot that extended over only a portion of the pitch directly in front of the vane stagnation. Contrary to the previously discussed studies, their adiabatic effectiveness measurements indicated that the coolant migrated toward the pressure side of the vane. Their measurements indicated reduced values of local heat transfer coefficients at the leading edge when slot cooling was present relative to no slot cooling.

Kost and Nicklas [10] and Nicklas [11] combined an upstream slot with film-cooling holes in the downstream vane passage to examine the effects of each on the secondary flow field and platform heat transfer at transonic conditions. One of the most interesting results from this study was that they found for the slot flow alone, which was 1.3% of the passage mass flow, the horseshoe vortex became more intense. This increase in intensity resulted in the slot coolant being moved off of the endwall surface and heat transfer coefficients that were over three times that measured for no slot flow injection. They attributed the strengthening of the horseshoe vortex to the fact that for the no slot injection the boundary layer was already separated with fluid being turned away from the endwall at the injection location. Given that the slot had a normal component of velocity, injection at this location promoted the separation and enhanced the vortex. Their adiabatic effectiveness measurements indicated higher values near the suction side of the vane due to the slot coolant migration.

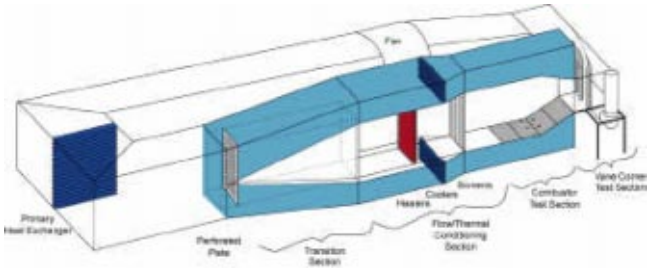

Fig. 1 Schematic of the wind tunnel facility

All of the studies involving interface slot coolant flows previously discussed used a slot that was flush with the endwall surface. In many modern engine designs, a step exists at the combustor-vane interface that provides a flow path for coolant leakage. In addition, these past studies have not considered the effects of coolant injection from the multiple rows of cooling holes from the upstream combustor liners. The combined effects of upstream film-cooling holes and slot flow from a backward facing step make this study unique as well as necessary for an improved understanding of the combustor-turbine interface.

Experimental Facilities and Instrumentation

The experiments for this study were performed in a low speed, closed-loop wind tunnel. The development of the vane test section was previously described by Radomsky and Thole [12] while the development of the combustor simulator was previously described by Barringer et al. [13]. The geometric scaling factor for the vane and combustor was 9X, which allows for good measurement resolution in the experiments. Measurements that are presented in this paper include adiabatic endwall temperatures, total pressure profiles, and mean and turbulent velocities.

Experimental Facilities. Figure 1 illustrates the wind tunnel containing the combustor simulator and vane test section. Downstream of a primary heat exchanger is a transition section that divides the flow into three channels that include a heated primary channel, representing the main gas path, and two symmetric secondary channels, representing the coolant flow paths. Within the transition section of the primary channel, the flow immediately passes through a perforated plate that provides the necessary pressure drop to control the flow splits between the primary and secondary passages. At a distance 3.5 m downstream of the perforated plate, the flow passes through a thermal and flow conditioning section containing a bank of heaters followed by a series of screens and flow straighteners. The heater section comprises three individually controlled banks of electrically powered, finned bars supplying a maximum total heat addition of 55 kW. Downstream of the flow straighteners, the heated primary flow enters the combustor simulator. In the combustor simulator, secondary coolant flow is injected into the primary flow passage through liner panels and dilution holes. In addition, the flow is accelerated prior to entering the turbine section. The contraction was designed to match the flow acceleration through that of an aeroengine combustor.

The flow in the secondary passages, also shown in Fig. 1, is first directed through heat exchangers. In addition to heat being rejected from the primary heat exchanger, the heat exchangers in the secondary passages provide additional heat rejection for the coolant flow. The experiments generally required 3–4 h for steady state conditions to be achieved. Throughout the experiments, which took nominally 1 h, all of the temperatures were constantly monitored. Room conditions were maintained throughout the experiment through the use of an air conditioning system, which insured thermal equilibrium with the environment. The flow in the secondary passages is then directed into a large plenum that supplies combustor liner coolant, dilution hole flow, and exit slot

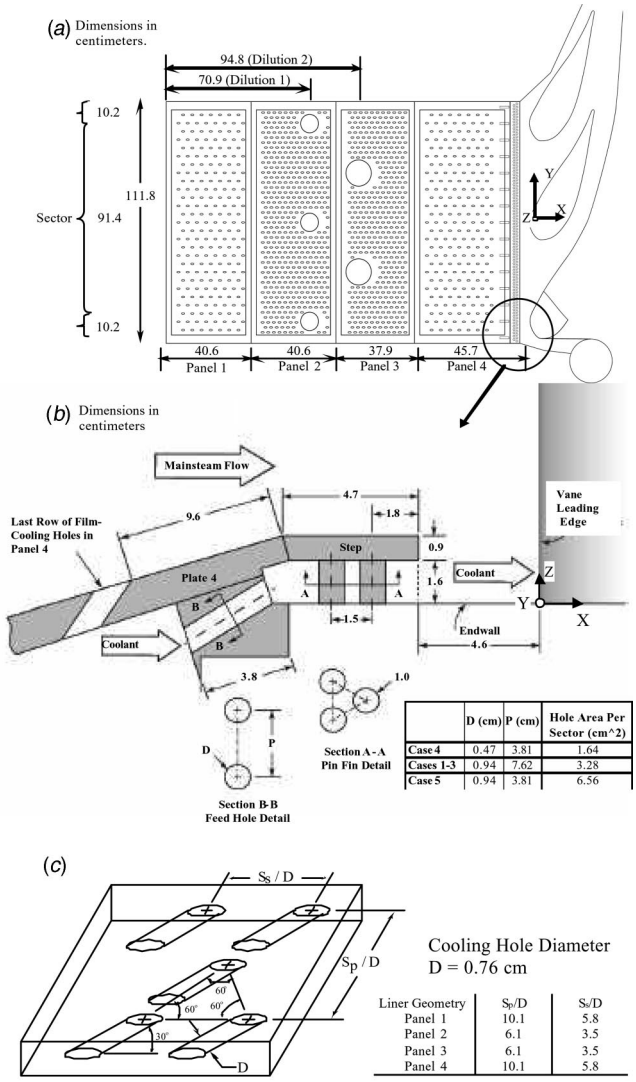

Fig. 2 Illustration of the film-cooling holes relative to the vane location (*a*); slot geometry (*b*), and film cooling-hole configuration (*c*)

coolant. The cooling hole pattern in the liners, the dilution holes, and the slot exit are illustrated in Figs. 2(*a*) and (*b*). To insure the correct coolant flow splits among the liner panels and dilution rows, separate supply chambers with adjustable shutters were constructed for each liner panel and row of dilution jets. The coolant flow for the exit slot at the end of the combustor panels was maintained by providing the required pressure in the large supply chamber. The mass flow exiting the film-cooling holes was set by applying the appropriate pressure ratio between the supply plenum and the exit static pressure. Using measured discharge coefficients [13], the mass flows through the panels were determined. The mass flows exiting the dilution holes were set by measuring the velocity across the dilution holes. The geometry for the combustor-turbine interface slot, shown in Fig. 2(*b*) includes feeder holes, two rows of staggered pin fins, followed by the backward facing slot. As will be discussed in the next section of this paper, a range of slot flow conditions were studied. The slot flows were controlled by changing the diameter and spacing of the feeder holes. Figure 2(*c*) shows the film-cooling hole configuration for the liner panels, while the callout below gives the film-cooling hole geometry for each of the four liner panels. The film-cooling hole diameter for the liners was 0.76 cm, while the liner thickness was 0.9 cm. The diameters of the dilution holes were 8.5 cm and 12.1 cm for the first and second rows, respectively.

The vane test section was designed to model a sector of the turbine. The correct inlet Reynolds number based on chord was set at 2.3×10^5 for the vane by insuring that the correct mass flow exited the combustor simulator. Exit tailboards were used to insure periodicity for the two passages, which was verified through flow field measurements and static pressure measurements at the vane mid-span. Setting these tailboards required an iterative process during which measurements of the static pressure distribution were compared with computational, inviscid flow predictions using pitchwise periodic boundary conditions. The upstream liner, endwall platform, and vane itself were constructed from urethane foam that had a low thermal conductivity (0.037 W/mK) to allow for measurements of adiabatic surface temperatures. Note that calculations were done to determine whether any heat would be transferred by the warmer fluid above the step to the coolant flow below the step. These calculations indicated a negligible temperature rise ($\sim10^{-4}$ K) for the coolant fluid.

Instrumentation and Measurement Uncertainty. An infrared camera was used to measure adiabatic wall temperatures on the endwall surface. Measurements were taken at thirteen different viewing locations to insure that the entire endwall surface was mapped. Each picture covered an area that was 19.4 cm by 15.7 cm with the area being divided into 255 by 206 pixel locations. The spatial integration for the camera was 0.37 cm (0.0062 chords). At each viewing location five images were averaged with each image being averaged over 16 frames, which provided a total of 80 data points that were averaged at each pixel location. Overlapping images were also averaged as the complete picture was assembled. Small shiny thumbtacks were embedded in the endwall as location markers to determine the orientation of the picture in a global coordinate system. Each picture was transformed into the global coordinate system and meshed together to obtain the complete temperature representation of the endwall.

Calibration of the infrared camera was made using thermocouples embedded in the endwall along the passage. Thermocouples were also used to monitor freestream, coolant, and endwall temperatures. The coolant temperature and the temperature downstream of the heater were monitored with thermocouples to transform endwall adiabatic temperatures into adiabatic effectiveness levels according to the following equation:

$$\eta=(T_{aw}-T_{ave})/(T_{cool}-T_{ave}) \tag{1}$$

where T_{ave} is the mass-averaged temperature exiting the combustor simulator. This mass-averaged temperature was calculated using the coolant temperature weighted with the flow rate in the secondary channels and the heated air temperature weighted by the primary flow rate. The heated air temperature was measured with several thermocouples upstream of the combustor simulator.

Total pressure measurements were taken with a small Kiel probe having a head diameter of 1.6 mm. A small probe diameter was used to insure good measurement resolution for the exit slot, which had a height of 16 mm. The Kiel probe reduced the effect of probe orientation relative to the velocity angles for a yaw angle range between ±52 deg and pitch angle range between ±45 deg. A 0.64 mm H_2O pressure transducer converted the pressure difference to a voltage which was digitized with an a/d board housed in a personal computer.

Velocities were measured using a two-component laser Doppler velocimeter (LDV). The LDV was a fiber optic system whereby the probe volume was set by the focusing lens (350 mm) to be 1.3 mm in length and 90 microns in diameter. The flow was seeded with 1 micron diameter olive oil particles. Measured velocities were corrected for bias errors using the residence time weighting correction scheme.

The partial derivative and sequential perturbation methods, described by Moffat [14], were used to estimate the uncertainties of the measured values. Precision uncertainties were calculated

based on a 95% confidence interval. The velocity measurements that were made to quantify the inlet flow conditions were made using a laser Doppler velocimeter. These measurements included a sample size of 15,000 data points. The precision uncertainty for the streamwise rms velocities was ±2.6%, while the bias uncertainty for the mean velocity measurements was ±1%. Each total pressure measurement used 60,000 data points to compute the mean values. The estimate of bias and precision uncertainties for the mean pressures, which were presented in non-dimensional form was ±1.6%. The bias and precision uncertainties on the adiabatic effectiveness values, using the five-averaged pictures, was ±0.04 giving an uncertainty of ±4.5% at $\eta=0.9$ and ±12.6% at $\eta=0.3$.

Influences of Panel and Dilution Flows on Combustor Exit Conditions

Prior to making endwall adiabatic effectiveness measurements on the vane platform, a number of measurements were made to determine the sensitivity of the liner and slot panel flows on the exiting total pressure profiles of the combustor simulator. After analyzing these results, a test matrix was designed to determine the sensitivity of the endwall adiabatic effectiveness levels to the panel and slot flows.

The total pressure profiles along the span were measured above the top of the step just upstream of the vane at a pitchwise location in line with the vane stagnation. These total pressure profiles were measured for a range of flow rates exiting the first panel of the combustor liner and are shown in Fig. 3(*a*). For these tests, the per cent flows exiting the three downstream panels remained the same as the design conditions, which were 3.5%, 2.2%, and 1.5%, respectively. The measured total pressures are presented relative to that occurring at the centerline and are normalized by the local dynamic pressure. Figure 3(*a*) shows that the pressure is peaked near the top of the slot, becomes a minimum at 20% of the span, and then increases near midspan. The peak near the liner is a result of the film-cooling from the liner panels while the increase near the midspan is a result of the added dilution flow. The measured total pressure results indicate that there is no effect of the increased liner flow on the exit total pressure profile of the combustor simulator. Conversely, Fig. 3(*b*) shows that the exit total pressure profile is highly dependent on the flow from the fourth panel. As the mass flow from the fourth panel is increased from 1.5 to 3.5% the peak nondimensional total pressure increases from 0.25 to 1.25. Although these results are not shown here, the total pressure was also found to be quite sensitive to the flow rate exiting the third panel.

Experiments were conducted to determine the sensitivity to the dilution flows by measuring the total pressure profiles at the exit of the combustor above the step on the bottom half of the combustor simulator. Figure 3(*c*) shows total pressure measurements as a function of only the top dilution row as compared with injection from both the top and bottom dilution holes. Note that the mass flows exiting both the third and fourth panels were increased for these experiments as compared with that shown in Fig. 3(*b*). The peak in the near wall region exists for both dilution flow cases even though the dilution injection was changed. Further away from the endwall, the data in Fig. 3(*c*) indicates that there are higher total pressure values for the top dilution only case as compared with the top and bottom dilution case. These higher total pressures may be attributed to the penetration of the higher total pressure dilution jet closer to the bottom endwall without the resistance of the opposing jet.

Given that there are nearly an infinite number of test cases that could be identified using the combustor simulator, it was imperative to identify a select number that would provide the most information on the effects of the liner cooling and slot cooling. Five different test cases were chosen for the endwall adiabatic effectiveness measurements as indicated in Table 1. Note that the percentage flows are given for the bottom set of liner panels only.

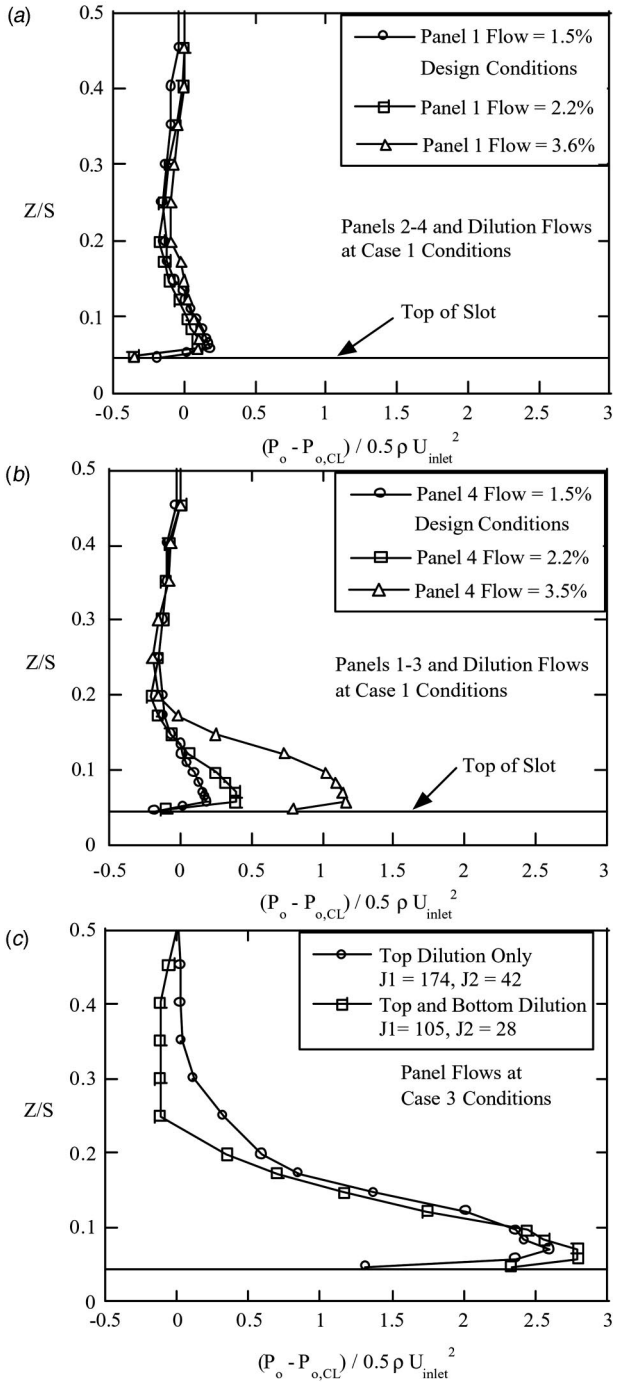

Fig. 3 Total pressure profiles measured on top of the step at the exit of the combustor indicating the relative effect of the panel flows (*a* and *b*) and the dilution holes (*c*)

The top set of liner panels were set at the same conditions. Also note that the momentum flux ratios for each of the panels are given. Given that the density ratios are nominally 0.97, the mass flux ratios can be calculated by taking the square root of the momentum flux ratios. These five cases were identified based on the total pressure profiles previously described. For the first three cases, the panel flows alone were varied to include a relatively uniform total pressure field, a nominally peaked profile, and a very peaked profile. The total pressure fields above the slot are shown in Figs. 4(*a*, *b*, and *c*) for these three cases. For the last two cases, the film-cooling flow through the panels remained the same

Table 1 Percentage of coolant based on exit mass flow (jet momentum flux ratios are in parentheses)

Case	1	2	3	4	5
Panel 1	1.5 (15.6)	1.5 (17.3)	1.5 (19.7)	1.5 (16.8)	1.5 (18.4)
Panel 2	3.5 (12.3)	3.5 (13.7)	3.4 (15.1)	3.5 (13.3)	3.5 (14.5)
Panel 3	3.4 (7.7)	4.5 (13.9)	5.4 (21.6)	4.5 (13.6)	4.5 (14.4)
Panel 4	1.6 (2)	2.7 (5.5)	3.7 (10.3)	2.7 (5.4)	2.7 (5.6)
Dilution 1	8.8 (130)	8.3 (128)	7.9 (128)	8.3 (125)	8.3 (136)
Dilution 2	8.8 (33)	8.5 (33)	8.2 (33)	8.5 (32)	8.5 (34)
Slot	0.63	0.63	0.63	0.315	1.26

as that for the nominally peaked pressure profile while the flowrate from the slot was either halved (half-slot case) or doubled (double slot case).

Figures 4(*a*, *b*, and *c*) show the effect of increased liner flow on the total pressure exiting the combustor. There is a large effect up to $Z/S=0.15$. There is also a noticeable difference in the mainstream that can be related to the influence of the dilution flow. In order to keep the same mass flow rate exiting the combustor while increasing the panel flow, the dilution jets are slightly decreased in the total mass injected (Table 1). This reduced dilution mass flow and momentum flux ratio results in less overall mixing thereby giving a total pressure footprint in the mainstream. The lower total pressure areas are aligned with the second row of dilution jets because these jets act as a flow resistance due to the jets being placed in the contraction section injecting in the upstream direction.

The total pressure profiles measured in the slot were highly non-uniform due to the interaction of the flow from the feed holes and the pin fins. To determine the total pressure in the slot downstream of the pin fins, profiles were measured across the height and pitch directions of the slot and spatially averaged with respect to the pitch. Pitchwise-averaged profiles measured at the combustor exit below and above the slot are shown in Fig. 5 for all five cases. Figure 5 shows the flat (case 1), nominally peaked (case 2), and highly peaked (case 3) profiles above the slot while the total pressure inside the slot remained the same for each of the these three cases. For the variation in slot flows, the data for the low slot flow (case 4) indicates lower total pressures in the slot than for the case for the high slot flow (case 5).

Turbine Inlet Flow Field Conditions

To insure that periodic flow fields occurred for both turbine vane passages, two-component laser Doppler velocimeter measurements were made across the two vane passages (inside and outside passages in Fig. 2(*a*)) at an axial location of the vane stagnation and at a spanwise location at the midspan. Both mean and turbulent velocity fluctuations were analyzed. Figure 6(*a*) shows the mean velocity measurements made for the inside and outside passages with and without the simulator [12] as compared with a two-dimensional, inviscid computation assuming periodicity. Note that $Y/P=0$ refers to the stagnation location and as Y/P decreases to -1 one is moving toward the pressure surface of the vane. The computation was made using FLUENT (1998) [12] using periodic boundary conditions. The measurements indicate that equal flow rates exist between the inside and outside passages for the case with the combustor simulator.

Figure 6(*b*) compares the turbulence levels exiting the combustor simulator as compared with those measured using an active grid turbulence generator [12]. The turbulence values were nominally the same for the inside and outside passages with the combustor simulator. In comparing these measurements to those for the active grid case, similar profiles were obtained with only

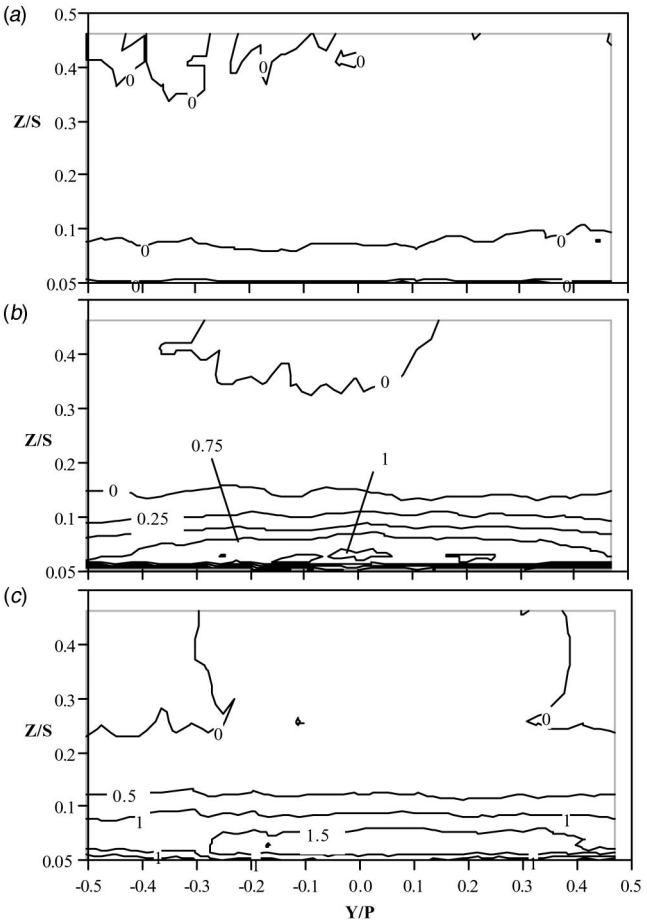

Fig. 4 Total pressure contours across the vane passage (midpitch to midpitch) measured at combustor exit

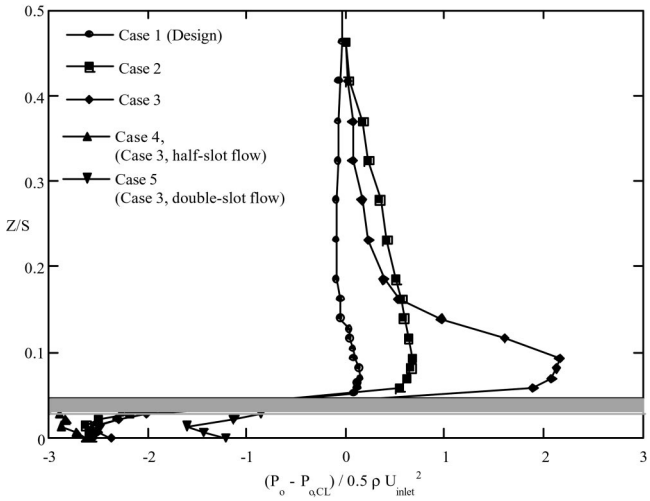

Fig. 5 Total pressure profiles measured at the combustor exit for the five cases investigated in this study

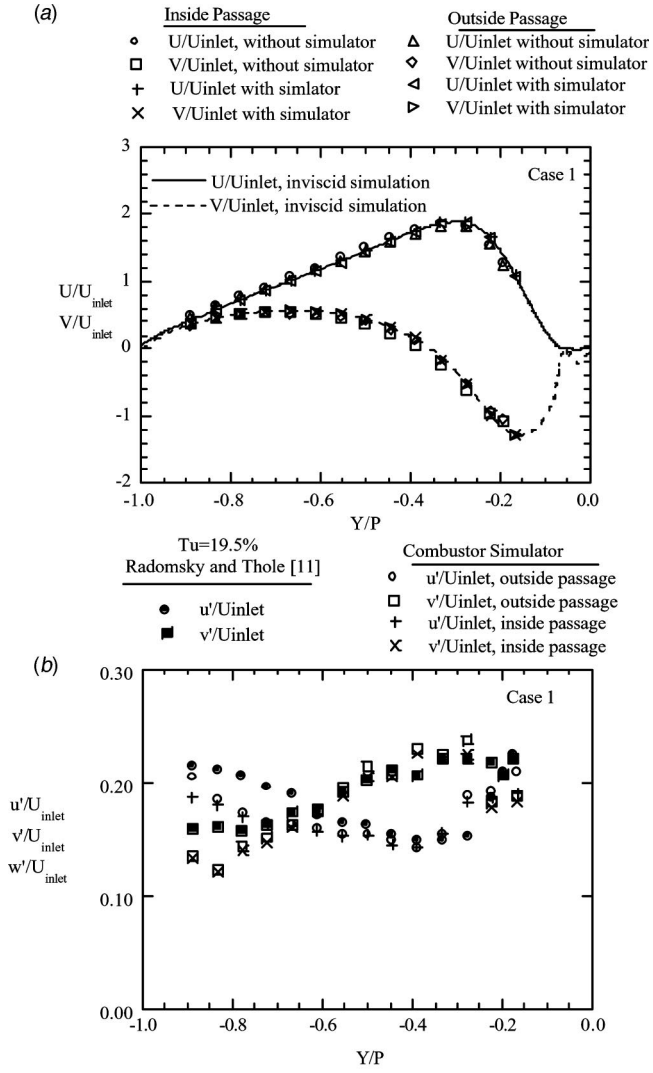

Fig. 6 Flow uniformity of the mean and turbulent velocities measured at the midspan across both the inside and outside vane passages

slightly higher values near the pressure side. These results indicate the effect of the dilution jets in generating high levels of turbulence at the entrance to the vane. The pitchwise average turbulence level at this location was 25% based on the inlet, incident velocity of 6.3 m/s.

Pressure distributions at the vane midspan were also recorded for all of the five cases and are shown in Fig. 7 as compared with the two-dimensional, inviscid computation. As seen by the figure, the pressure distribution remained nearly the same for all of the five cases that were tested.

Endwall Adiabatic Effectiveness Measurements

The endwall adiabatic effectiveness levels for the five cases that were previously discussed are shown in Figs. 8–12. The straight vertical lines on these plots indicate the downstream edge of the backward-facing step. Upstream of this line, the adiabatic wall temperatures were measured on top of the step for the combustor liner. Figure 8 shows the endwall effectiveness measurements for case 1, which was the design flow for the slot and film-cooling panels. Figure 8 indicates that a large portion of the slot flow is exiting near the suction side of the vane, thereby providing most of the cooling in this region. As the flow progresses through the passage, the coolant continues to be swept towards the suction

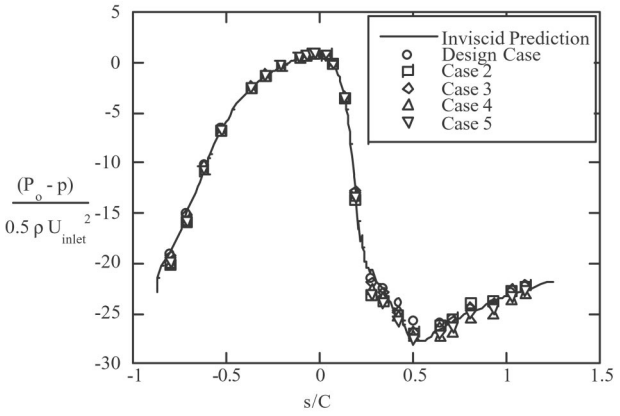

Fig. 7 Static pressure distribution along the vane midspan for the five cases investigated

side of the vane by the cross passage flow. It is clear that the combined liner and slot coolant is not effective at the leading edge region. A warm ring (low effectiveness) is present around the vane particularly at the vane stagnation. The endwall region near the pressure side of the vane sees very little effect from the slot flow. Note that the effectiveness levels are between 0.2 and 0.3 in the downstream passage as a result of the film-cooling from the combustor liner.

In determining the effect of increased film-cooling from the liner, comparisons of Fig. 8 can be made with Figs. 9 and 10. As would be expected, there is a slight increase in adiabatic effectiveness on top of the step as the combustor liner film cooling increases. This effect is important because the top of the step is a critical area where there are often durability issues. It is important to keep in mind that not only is the amount of available coolant increasing from 10 to 14% for cases 1 to 3, the total pressure profile has been altered. While the overall effectiveness pattern remains quite similar between these cases, there are several apparent differences. As the peak total pressure increases in the near-wall region, the driving pressure between the flow above the slot

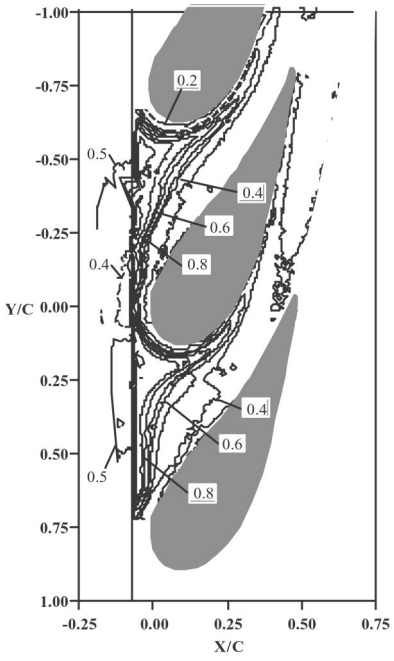

Fig. 8 Adiabatic effectiveness contours for case 1

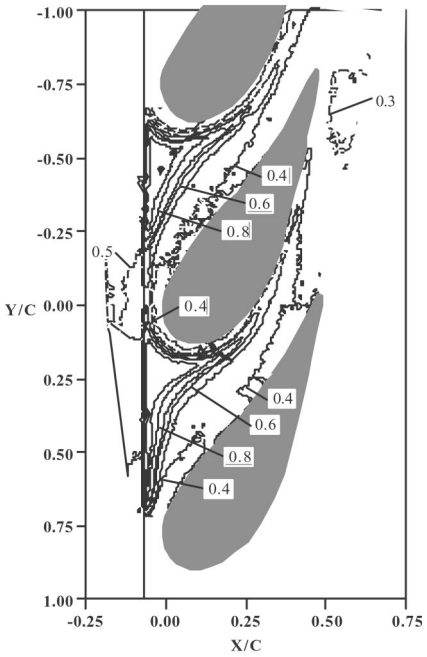

Fig. 9 Adiabatic effectiveness contours for case 2

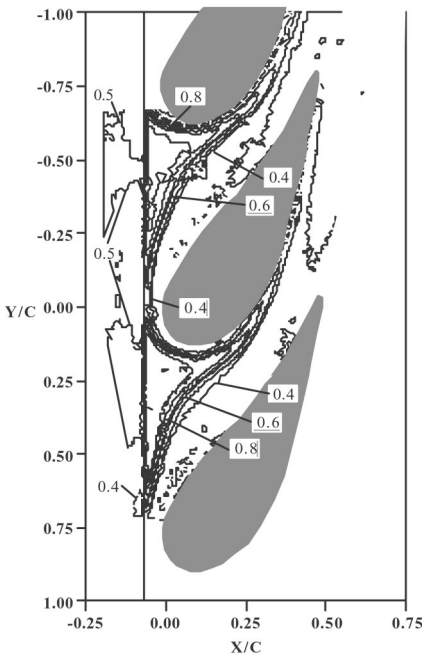

Fig. 11 Adiabatic effectiveness contours for case 5

and below the slot also increases (Fig. 5). As a result of this increase in driving pressure, a larger portion of the liner cooling flow on top of the slot is pulled toward the endwall at the vane stagnation region. In comparing Fig. 8 with Fig. 10, it can be seen that the region just upstream of the vane stagnation for case 3 with the higher panel flows has slightly cooler adiabatic wall temperatures. This can be attributed to two effects. First, there is a larger driving potential between the flow above the step and flow in the slot. Second, there is cooler fluid on top of the step with the higher panel flow (case 3) as compared with the design panel flow (case 1).

The effect of the larger driving potential is not only evident in the stagnation region of the vane, but is also evident for the slot flow in general. Even though the same slot flow is exiting for cases 1 and 3, the coverage of the coolant flow from the slot has been reduced for case 3. This reduction occurs due to the fact that there is ingestion of flow from above the step into the slot that mixes with the slot coolant prior to the coolant exiting the slot. Although the ingested flow is relatively cool, it is still warmer than the slot flow itself. The ingestion of the flow from above the step into the slot itself was predicted by a CFD simulation (FLUENT) done by Stitzel [15]. The results of this CFD simulation are

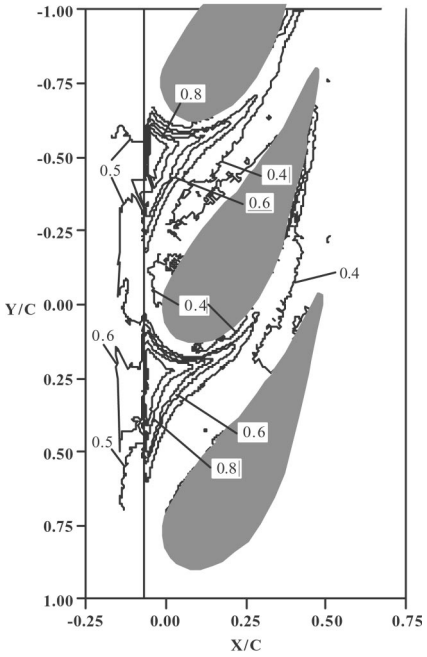

Fig. 10 Adiabatic effectiveness contours for case 3

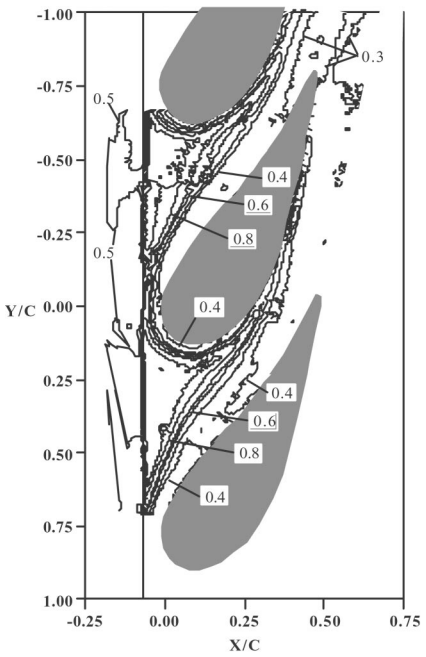

Fig. 12 Adiabatic effectiveness contours for case 5

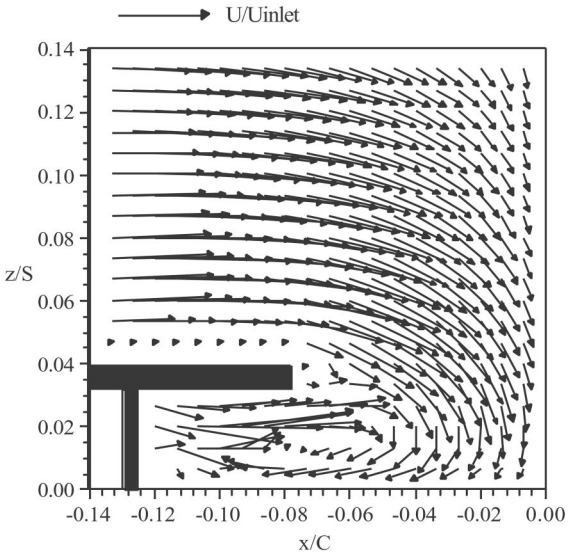

Fig. 13 Flow field prediction for case 1 indicating injestion of flow above the step into the slot [13]

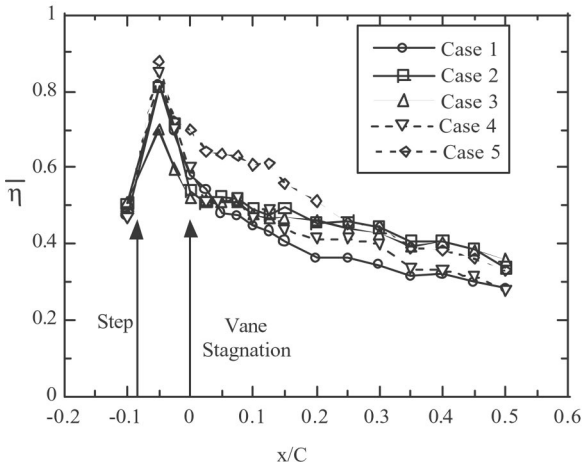

Fig. 14 Pitchwise-averaged adiabatic effectiveness levels

shown in Fig. 13 for case 1 flow conditions. The strong ingestion into the slot will be illustrated in Part 2 of this paper through flow and thermal field measurements.

The larger amount of film-cooling flow present for case 3 gives only slightly increased effectiveness levels on the downstream endwall surface as compared with case 2. These results suggest that there is an optimal amount of combustor liner film cooling that will benefit the downstream vane platform. One plausible reason for this limit in improvement is that by increasing the liner flow, the inlet total pressure profile is also changed. With increased liner coolant, there is an increase in the peak total pressure resulting in stronger secondary flows. A peak in total pressure will cause a flow split along the vane span above which flow will be transported up the vane and below which flow will be transported toward the endwall (similar to that shown in Fig. 13). Even though more cooling is available, much of it will be transported up the vane span.

The effect of increasing the slot flow may be determined by comparing Figs. 11, 9, and 12 (in order of increasing slot flow). Note that the effectiveness levels on top of the step were nominally the same for each case. Adiabatic effectiveness levels for the design and half slot flow cases (Figs. 11 and 9) are similar near the vane leading edge and along the suction side. The two cases show similar wedge-shaped slot-cooled regions. However, near the pressure side and in the passage the effectiveness levels for the half slot flow are noticeably lower than the design slot flow case. As the amount of slot flow is doubled (Fig. 12), the effectiveness levels near the leading edge are as much as 0.15 higher than the design slot flow case. The wedge shaped region that is cooled by the slot is clearly larger for case 5. The double slot flow case is also more effective near the stagnation region as well. At a distance of $X/C=0.25$ down the passage, the effectiveness levels are nearly the same for both the double and design slot flow cases.

The measured effectiveness values were pitchwise-averaged at a number of axial locations along the vane. Figure 14 shows the pitchwise averages for each of the five cases. Effectiveness levels are initially high, due to the injection of coolant onto the endwall by the slot. The first location presented is on top of the step and is a result of the liner cooling. The highest value occurs for case 3 given that this condition is the highest liner cooling. Just downstream of the slot, the highest value occurs for the highest slot flow. The values drop off sharply near the leading edge and then decline uniformly throughout the passage for all cases. It is interesting to note that the case with the most combustor panel flow has the lowest pitchwise effectiveness level at the leading edge. This is because of the effect that the increased panel flow has on the slot flow by increasing endwall secondary flow.

Figure 15 shows the area-averaged effectiveness values ($\bar{\bar{\eta}}$) for each of the flow cases that have been presented. Note that the percentage mass flow only includes the film and slot flows from one side of the combustor panels and does not include the dilution flow. The percentages of the mass flow shown in Fig. 15 are based on the total exit mass flow of the combustor simulator (inlet flow to the vane section). The data on this figure shows the trade-offs between increased film-cooling flow relative to increased slot cooling flow. The area-averaged effectiveness slightly increases with increased film-cooling flow before leveling off to a value that is 0.45 for film-cooling flows of more than 12.5% of the total exit flow.

In contrast to increased film-cooling flow, Fig. 15 indicates that there is a continual increase (over the small range investigated) in endwall effectiveness levels associated with increasing the slot flow. These results suggest that it is more beneficial for endwall heat transfer to increase the slot flow rather than the combustor panel flow. One plausible reason for the larger increase in effectiveness for increased slot flow is because of the reduced ingestion into the slot. The near-slot region dictates the relative differences between the slot flow cases.

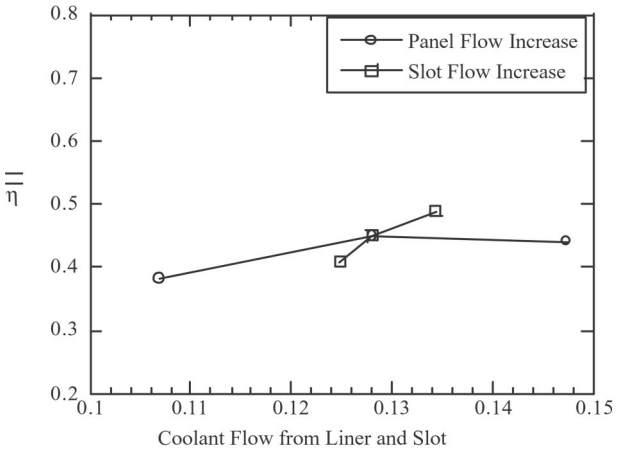

Fig. 15 Area-averaged adiabatic effectiveness levels

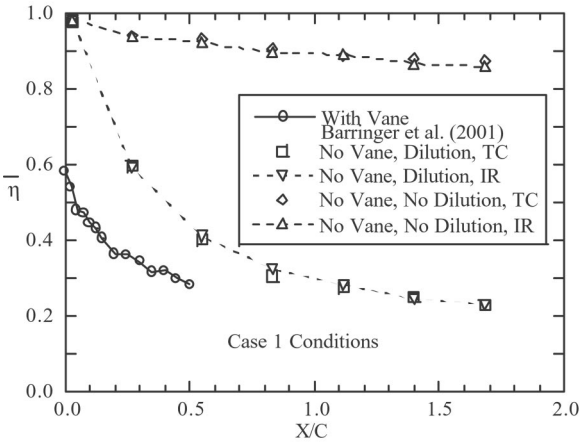

Fig. 16 Comparison of pitchwise-averaged effectiveness

Figure 16 addresses the effects of dilution flow and secondary flows on the degradation of the cooling from the backward facing slot and from the film-cooling holes. Plotted in Fig. 16 are adiabatic effectiveness values downstream of the same combustor geometry operating at the same conditions for cases with and without the turbine vane. Without a turbine vane or dilution flow, the effectiveness levels are extremely high downstream of the combustor. Adding dilution flow considerably reduces the effectiveness levels downstream of the combustor. In the case where the turbine vane is present, the secondary flows significantly reduce the pitchwise-averaged effectiveness values as compared to the case when the turbine vane is not present. These results indicate a large thermal benefit is achieved by eliminating the secondary flows in the first vane.

Conclusions

The experimental results that were presented in this paper indicate the importance of understanding the inlet total pressure profile upstream of the first vane. The difference in total pressure between the fluid above the backward-facing step and below the backward-facing step caused ingestion into the slot that ultimately reduces the coolant temperature as it exited the slot. As the slot flow was increased, the total pressure of the fluid in the slot also increased thereby decreasing the driving potential between the main gas path and slot fluid. This reduction in driving potential was indicated by the adiabatic effectiveness values measured on the downstream vane endwall. Increasing the slot flow over the range that was investigated increased the area-averaged effectiveness values on the downstream endwall. Alternatively, measured effectiveness values indicated that increased film-cooling flow from the liner did not result in a continual increase in area-averaged effectiveness values.

The nonuniformities that occur at the inner and outer diameter regions of the combustor exit in a gas turbine engine have a large impact on the durability of vane and endwall. Much of the combustor liner coolant is swept toward the vane suction-endwall juncture. Secondary flows that occur in the vane stagnation region as well as those that develop in the vane passage further deteriorate an effective usage of the coolant.

Acknowledgments

The authors are grateful to Pratt and Whitney and the US Air Force Research Lab for their support of this project. In particular, the authors thank Joel Wagner and Matthew Meininger for their contributions.

Nomenclature

A_{hole} = area of film-cooling hole
C = true chord of stator vane
C_d = discharge coefficient, $C_d = \dot{m}/A_{\text{hole}}\sqrt{2\rho(P_{o,c}-p_\infty)}$
J = momentum flux ratio, $J=\rho_c U_c^2/\rho_\infty U_\infty^2$
k_{cond} = thermal conductivity
$\dot{m}$ = mass flow rate
P = pitch of stator vane
P_o, p = total and static pressures
Re = Reynolds defined as $\text{Re}=CU_\infty/\nu$
s = surface distance along vane measured from flow stagnation
S = span of stator vane
T_{ave} = mass-averaged freestream temperature
Tu = turbulence level defined as u_{rms}/U
u', v', w' = root mean square of velocity fluctuations
U = local, mean streamwise velocity component
X,Y,Z = global coordinates defined at combustor exit and endwall
η = adiabatic effectiveness, $\eta=(T_{\text{ave}}-T_{\text{aw}})/(T_{\text{ave}}-T_{\text{cool}})$
ΔP = nondimensional pressure, $\Delta P=(P_o-P_{o,\text{ms}})/(0.5\rho U_{\text{ave}}^2)$
ρ = density
ν = kinematic viscosity

Subscripts

1,2 = dilution rows 1 and 2
— = pitchwise average at given axial location
= = area average over entire endwall
aw = adiabatic wall
cool = coolant conditions
ms = midspan conditions
ave = mass-averaged freestream conditions (primary flow)
inlet = inlet incident velocity

References

[1] Langston, L. S., 1980, "Crossflows in a Turbine Cascade Passage," ASME J. Eng. Power, **102**, pp. 866–874.
[2] Blair, M. F., 1974, "An Experimental Study of Heat Transfer and Film Cooling on Large-Scale Turbine Endwalls," ASME J. Heat Transfer, **Nov.**, pp. 524–529.
[3] Granser, D., and Schulenberg, T., 1990, "Prediction and Measurement of Film Cooling Effectiveness for a First-Stage Turbine Vane Shroud," 90-GT-95.
[4] Burd, S. W., and Simon, T. W., "Effects of Slot Bleed Injection over a Contoured Endwall on Nozzle Guide Vane Cooling Performance: Part I: Flow Field Measurements," ASME Paper No. 2000-GT-199.
[5] Burd, S. W., Satterness, C. J., and Simon, T. W., "Effects of Slot Bleed Injection over a Contoured Endwall on Nozzle Guide Vane Cooling Performance: Part II: Thermal Measurements," 2000-GT-200.
[6] Oke, R., Simon, T., Burd, S. W., Vahlberg, R., "Measurements in a Turbine Cascade Over a Contoured Endwall: Discrete Hole Injection of Bleed Flow," 2000-GT-214.
[7] Oke, R., Simon, T., Shih, T. Zhu, B., Lin, Y. L., Chyu, M. "Measurements Over a Film-Cooled, Contoured Endwall with Various Coolant Injection Rates," 2001-GT-140.
[8] Zhang, L. J., and Jaiswal, R. S., 2001, "Turbine Nozzle Endwall Film Cooling Study Using Pressure-Sensitive Paint," ASME J. Turbomach., **123**, pp. 730–738.
[9] Roy, R. P., Squires, K. D., Gerendas, M., Song, S., Howe, W. J., and Ansari, A., "Flow and Heat Transfer at the Hub Endwall of Inlet Vane Passages-Experiments and Simulations," 2000-GT-198.
[10] Kost, F., and Nicklas, M., 2001, "Film-Cooled Turbine Endwall in a Transonic Flow Field: Part I-Aerodynamic Measurements," ASME J. Turbomach., **123**, pp. 709–719.
[11] Nicklas, M., 2001, "Film-Cooled Turbine Endwall in a Transonic Flow Field: Part II-Heat Transfer and Film-Cooling Effectiveness Measurements," ASME J. Turbomach., **123**, pp. 720–729.
[12] Radomsky, R. W., and Thole, K. A., 2000, "Flowfield Measurements for a

Highly Turbine Flow in a Stator Vane Passage,'' ASME J. Turbomach., **122**, pp. 255–262.
[13] M. D. Barringer, O. T. Richard, J. P. Walter, S. M. Stitzel, and K. A. Thole, 2001, ''Flow Field Simulations of a Gas Turbine Combustor,'' 2001-GT-0170; to appear in J. Turbomach.
[14] Moffat, R. J., 1988, ''Describing the Uncertainties in Experimental Results,'' Exp. Therm. Fluid Sci., **1**, pp. 3–17.
[15] Stitzel, S. (2001), ''Flow Field Computations of Combustor-Turbine Interactions in a Gas Turbine Engine,'' MSME thesis, Mechanical Engineering Department, Virginia Tech.

Combustor Turbine Interface Studies—Part 2: Flow and Thermal Field Measurements

W. F. Colban

A. T. Lethander

K. A. Thole

Mechanical Engineering Department,
Virginia Polytechnic Institute and State University,
Blacksburg, VA 24061

G. Zess

Pratt and Whitney,
East Hartford, CT 06108

Most turbine inlet flows resulting from the combustor exit are nonuniform in the near-platform region as a result of cooling methods used for the combustor liner. These cooling methods include injection through film-cooling holes and injection through a slot that connects the combustor and turbine. This paper presents thermal and flow field measurements in the turbine vane passage for a combustor exit flow representative of what occurs in a gas turbine engine. The experiments were performed in a large-scale wind tunnel facility that incorporates combustor and turbine vane models. The measured results for the thermal and flow fields indicate a secondary flow pattern in the vane passage that can be explained by the total pressure profile exiting the combustor. This secondary flow field is quite different than that presented for past studies with an approaching flat plate turbulent boundary layer along the upstream platform. A counter-rotating vortex that is positioned above the passage vortex was identified from the measurements. Highly turbulent and highly unsteady flow velocities occur at flow impingement locations along the stagnation line. [DOI: 10.1115/1.1561812]

Introduction

The flow and thermal fields at the combustor-turbine junction in a gas turbine engine are highly complex and cannot be idealized by a uniform mean field superimposed with high turbulence levels. This is particularly true in the turbine platform region, which has been generally assumed to have an approaching two-dimensional, flat plate, turbulent boundary layer exiting the combustor. These idealized conditions are generally not possible given the nature of the combustor design that often contains large dilution holes, film-cooling holes along the approaching liner, and some type of leakage juncture at the combustor-turbine interface. This type of combustor design produces nonuniformities near the platform in both the span (radial) and pitch (circumferential) directions with large levels of turbulence in the mainstream.

This paper is the second of a two-part series (Colban et al. [1]) that investigates the effects of a range of combustor liner flows on the first vane heat transfer, flow fields, and thermal fields. Part 1 presented a discussion of the inlet conditions that were simulated as well as the adiabatic wall temperatures measured along the platform. Part 2 presents flow and thermal field measurements for selected cases of interest. In general, the objectives for the work presented in this paper were the following: i) to evaluate the effect of non-uniform inlet conditions on the formation of what has been commonly known as the leading edge horseshoe vortex, ii) to evaluate the effect of increasing the liner coolant flow at the vane stagnation, and iii) to evaluate the effect of increasing the slot flows on the secondary flow development. These effects will be presented in terms of measured flow and thermal fields. While the relevant past literature and test facility were discussed in Part 1, some details will be presented on how the velocity and temperature fields were measured. Finally, measured results are presented.

Experimental Facilities and Instrumentation

As discussed in Part 1, the experiments for this study were performed in a low-speed, closed-loop wind tunnel that housed a combustor simulator and a downstream turbine vane. The data was acquired for large-scale models of the combustor and vane to allow for good measurement resolution. The test cases that were investigated for this study are repeated from Part 1 in Table 1 for clarity.

Flowfields were measured for two planes that included a stagnation plane (SP) and one suction side plane (SS2). The suction side plane was orthogonal to the vane surface, as shown in Fig. 1, to discern the secondary flows. Note that Kang and Thole [2] previously presented flow field results for the same vane geometry in a number of planes, including SP and SS2, for an approaching turbulent boundary layer along the platform. This previous study will be used for comparisons to the data presented in our paper. Two-component measurements (u and w) were measured for the SP plane while three-component measurements were made for the SS2 plane. The three-component measurements were made by positioning the two-component fiber optic probe of the laser Doppler velocimeter (LDV) system in two different orientations.

The back-scatter fiber optic LDV system used in this study consisted of a 5-W laser used in conjunction with a TSI model 9201 Colorburst beam separator. Velocity data was processed using TSI model IFA 755 Digital Burst Correlator controlled using TSI's FIND software. Two different focusing lenses were used for these measurements. For the SP plane, a 750-mm focusing lens with a beam expander was used. For the SS2 plane a 350-mm focusing lens without a beam expander was used to make measurements of the streamwise (u) and pitchwise (v) components through the top endwall. The spanwise component (w) was measured from the side also using a 350-mm focusing lens. The probe volume length and diameter for the 350-mm lens were 1.3 mm and 90 microns whereas the probe volume length and diameter for the 750-mm lens with the beam expander were 0.85 mm and 46 microns. For each component of velocity 20,000 data points were used to compute the mean and turbulent quantities. The flow was seeded using 1 micron diameter olive oil particles. The data were corrected for velocity bias effects by applying the residence time weighting. The thermal field measurements were made using a Type E thermocouple that was placed on a traversing unit.

Uncertainty Estimates. The partial derivative and sequential perturbation methods, described by Moffat [3], were used to estimate the uncertainties of the measured values. Uncertainties were calculated based on a 95% confidence interval. The estimates of uncertainties on each of the values presented in this paper are

Contributed by the International Gas Turbine Institute and presented at the International Gas Turbine and Aeroengine Congress and Exhibition, Amsterdam, The Netherlands, June 3–6, 2002. Manuscript received by the IGTI January 16, 2002. Paper No. 2002-GT-30527. Review Chair: E. Benvenuti.

Table 1 Percentage of coolant based on exit mass flow (jet momentum flux ratios are in parentheses)

Case	1	2	3	4	5
Panel 1	1.5 (15.6)	1.5 (17.3)	1.5 (19.7)	1.5 (16.8)	1.5 (18.4)
Panel 2	3.5 (12.3)	3.5 (13.7)	3.4 (15.1)	3.5 (13.3)	3.5 (14.5)
Panel 3	3.4 (7.7)	4.5 (13.9)	5.4 (21.6)	4.5 (13.6)	4.5 (14.4)
Panel 4	1.6 (2)	2.7 (5.5)	3.7 (10.3)	2.7 (5.4)	2.7 (5.6)
Dilution 1	8.8 (130)	8.3 (128)	7.9 (128)	8.3 (125)	8.3 (136)
Dilution 2	8.8 (33)	8.5 (33)	8.2 (33)	8.5 (32)	8.5 (34)
Slot	0.63	0.63	0.63	0.315	1.26

given in Table 2. Note that the uncertainty estimates were made for the near endwall region where the highest uncertainties arise. Also note that the definitions of these variables will be provided later in the text (refer to Fig. 3). The uncertainty for the normal velocity (V_n) was significantly higher than the other velocity components and primarily arose from the uncertainty in the flow angle at the midspan location. For V_n, both u and v velocity components contributed with neither dominating. In comparison for V_s, the term $u \cos \psi_{ms}$ is quite large with the u -component dominating. While for V_s the uncertainty was dictated by the uncertainty in the u-component, the uncertainty for V_n was dictated by the uncertainty in ψ_{ms}

Flow Quality and Analysis for the SS2 Plane

As a check on the flow quality in the spanwise direction, total pressure profiles were measured downstream of the step at the vane midpitch and just off the suction side surface of the vane in the SS2 plane. These total pressures were measured for case 2 using a Kiel probe and were normalized as shown in Fig. 2. For both planes, the flow is quite symmetric with only slightly different values occurring near the wall. The reason for the differences in magnitude near the wall is because the flow exiting the slot is highly sensitive to the interaction between the feed holes and pin fins. This sensitivity of the total pressure profile on the interaction between the feed holes and pin fins was previously reported by Barringer et al. [4]. These profiles indicated a very non-periodic pattern. Any slight differences between the feed hole alignment and the downstream pin fins will cause a range of differences in the total pressure exiting the slot.

In general, the total pressure measurements taken at the midpitch inlet plane (between the two vanes), shown in Fig. 2, indicate very low total pressure values near the platform with a peak in total pressure at nominally 10% span. The high values correspond to the higher total pressure of the film-cooling flow while the low total pressure values correspond to the slot flow in this region. Very little flow is exiting the slot at the mid-pitch region, as was shown in Part 1 from the adiabatic effectiveness measurements.

As the flow progresses through the vane passage, a strong passage vortex develops that is able to sweep high pressure film-coolant fluid down towards the endwall. This vortex will be shown later in this paper. As a result of this sweeping motion, the total pressure in the near-wall region is higher than the slot exit flow (shown in Fig. 2). Moving away from the endwall the total pressure decreases whereby the minimum level corresponds to the center of the passage vortex. Above the minimum level, there is again an increase in total pressure as a result of the film-cooling as indicated in Fig. 2. Most of the midregion is nearly uniform at a total pressure level less than the peak value.

The primary interest of this study was to discern the secondary flows convecting through the turbine vane passage in the SS2 plane. The velocity vectors of these vortices, which will be referred to as the secondary flow vectors, were determined by transforming the measured local velocities (u, v, and w) into the mean flow direction based on that occurring at the midspan (V_s, V_n, and V_z). These velocity components are illustrated in Fig. 3. For this transformation the inviscid turning angle was calculated based on the measured velocities at the vane midspan (u_{ms} and v_{ms}) using the following relation:

$$\psi_{ms} = \tan^{-1}(v_{ms}/u_{ms}) \tag{1}$$

The local transformed velocities are then calculated from the following:

$$V_s = u \cos \psi_{ms} + v \sin \psi_{ms} \tag{2}$$

$$V_n = -u \sin \psi_{ms} + v \cos \psi_{ms} \tag{3}$$

$$V_z = w \tag{4}$$

where u and v are the locally measured velocities. The secondary flow vectors are plotted using the components normal to the mean flow direction (V_n, V_z).

Stagnation Plane Flow Field

Langston's [5] depiction of the secondary flows is comprised of a leading edge horseshoe vortex and passage vortex. This depic-

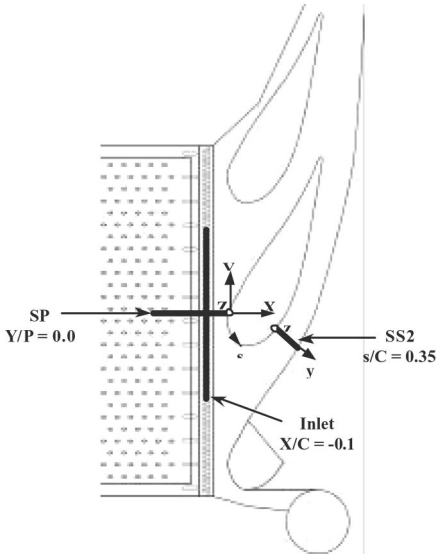

Fig. 1 Locations of flow and thermal field measurements

Table 2 Uncertainty estimates for measurements

θ	$\pm$4.4% at $\theta = 0.9$ $\pm$12.3% at $\theta = 0.3$
V_s	$\pm$1% near vane-endwall
V_n	$\pm$7.5% near vane-endwall
V_z	$\pm$1.5% near vane-endwall
Tu	$\pm$2.4% near vane-endwall
ϕ	$\pm$1% near vane-endwall
$\frac{P_o - P_{o,ms}}{0.5\rho U_{in}^2}$	$\pm$1.6%

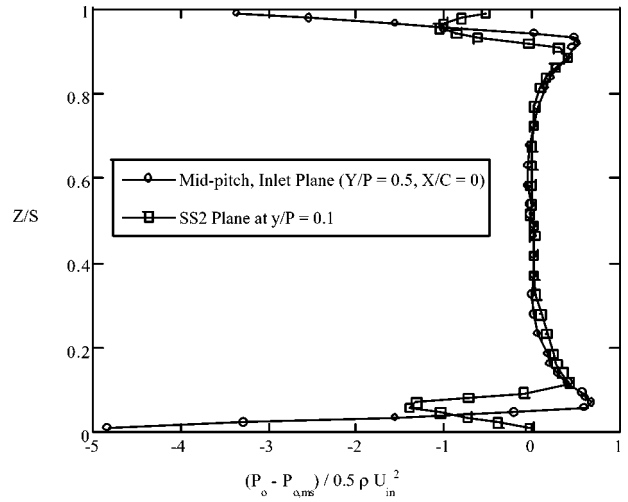

Fig. 2 Total pressure measurements at two locations indicating the midspan symmetry

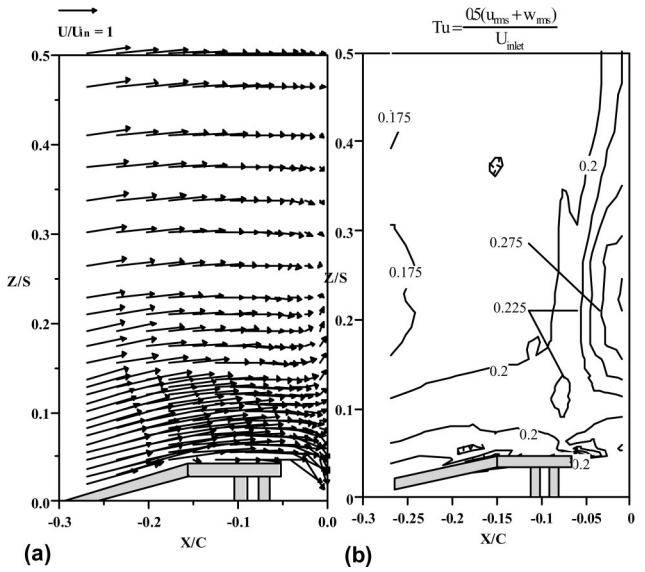

Fig. 4 Measured mean (*a*) and turbulent (*b*) velocities at the stagnation plane for case 2 with a nominal total pressure peak and nominal slot flow conditions

tion was in agreement with his own measurements as well as those reported by Kang et al. [6] and Kang and Thole [2] for the same vane geometry reported in this paper. Note, however, his model and those measurements were for an approaching turbulent boundary layer along the upstream platform. For the geometry of a backward-facing slot reported in our paper, the incoming total pressure profile produced is quite different than that of a flat plate, turbulent boundary layer.

The measured mean and turbulent velocity fields in the SP plane for case 2, as described in Part 1 (nominally peaked total pressure profile above the slot and nominal slot flow), are shown in Figs. 4(*a*, *b*). The velocity vectors indicate flow moving up the combustor liner wall with no indication of any type of separation on the top of the step. Unlike that for an approaching turbulent boundary layer along the endwall, there is no roll-up of a leading edge horseshoe vortex on top of the combustor liner. It was not possible to acquire flow field measurements below the step because of optical accessibility, but based on the CFD predictions shown in Part 1 there is a confined vortical roll-up under the slot area.

The vectors shown in Fig. 4(*a*) also indicate slightly slower velocities in the 15–30% span region than at the wall or platform. The larger velocities near the wall are a result of the film-cooling injection and the acceleration along the liner wall. At the end of the step, there are strong downward velocities indicated as the mainstream fluid is pulled into the slot region. This ingestion into the slot was also previously predicted using CFD, as shown in Part 1 of this paper. Note, however, the CFD analysis was conducted for case 1 in which the total pressure profile above the step was relatively flat. For the data shown in Fig. 4(*a*), there was a slightly higher peak in the total pressure profile due to the film-cooling (case 2).

Another important feature of the flow as it approaches the stagnation location is that there are a number of flow splits that occur. These flow splits occur where the *w*-component of the velocity changes direction from a positive value (indicating flow toward the midspan) to a negative value (flow toward the endwall). These flow splits can more easily be shown by examining profiles of the *w*-component of the velocity as shown in Fig. 5. At the location farthest from the vane ($X/C=-0.06$), most of the velocities are nearly zero except near the wall. Approaching the wall from the midspan indicates slightly negative velocities followed by an inflection point with a tendency toward positive velocities. The negative velocities are a result of the fluid being pulled into the slot whereas the positive, near-wall velocities are a remnant of the flow following the liner wall.

Moving closer to the vane, the *w*-component profiles shown in Fig. 5 indicate several inflection points at locations of $Z/S=0.1$ and 0.23. Moving toward the midspan near the $Z/S=0.1$ location, the *w*-component indicates the flow is switching sign from negative to positive values. This results in a flow split. Moving toward the midspan near the $Z/S=0.026$ location, the *w*-component indicates the flow is switching sign from positive to negative values. This results in a flow impingement, as also seen by the vector plot in Fig. 4(*a*). The total pressure profile above the slot as in Part 1 for case 2, can be used to explain the flow splits.

In general, the turbulence levels in the stagnation plane, presented in Fig. 4(*b*) are quite high as a result of the dilution flow. The levels are 17.5% in a majority of the midspan region. The highest turbulence levels, of nearly 30%, occur in the region of the previously described flow impingement location. The turbulence in this region is even higher than that near the wall due to the film-cooling flow.

Because the flow in the stagnation region, particularly in the 10–30% span region had such high turbulence levels, the probability density functions (PDFs), also known as histograms, were analyzed. PDFs indicate the number of occurrences of a particular velocity level in a given bin size. The equation for the PDFs is given by

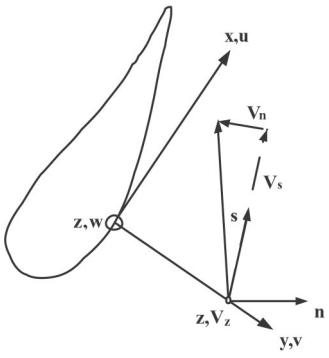

Fig. 3 Measured and transformed velocity components

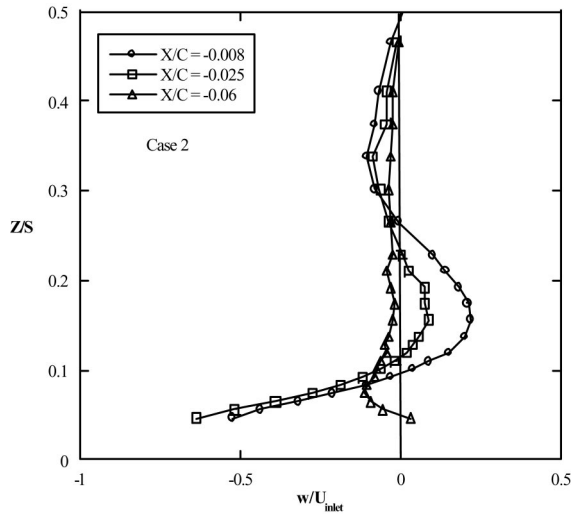

Fig. 5 Measured *w*-component velocities at the stagnation plane (SP) for case 2 with a nominal total pressure peak and nominal slot flow conditions

$$\mathrm{PDF}(w/U_{\mathrm{inlet}}) = \frac{N_i}{N}\frac{1}{\Delta w/U_{\mathrm{inlet}}} \tag{6}$$

where N is the total number of data points and N_i is the number of occurrences in a given $\Delta w/U_{\mathrm{inlet}}$ bin size. For most turbulent flows, the PDFs indicate a Gaussian distribution of the velocities whereby the range of velocities is $\pm 3w_{\mathrm{rms}}$.

As discussed, there were two different flow field phenomena occurring along the stagnation location. First, there is a flow split that happens when the velocity vectors are directed away from the same location. This split occurs at $Z/S=0.1$ as shown in Fig. 4 as the *w*-component changes from negative to positive (moving away from the endwall). Second, there is a flow impingement when the velocity vectors are directed toward the same location. This impingement occurs at $Z/S=0.26$ as the *w*-component changes from positive to negative. The PDFs for several positions along the span of the vane are shown in Fig. 6. The velocity PDFs reveal that the turbulence in the region of the flow split has a single peak with a nearly Gaussian distribution. In the region of a flow impingement, however, the PDFs indicate a bi-modal distribution. This bi-modal distribution is an indication that the flow is very unstable in this region. It is quite plausible that a flow impingement at low velocities is very unstable. These results also lead us to believe that the high levels of turbulence in the 20% span region are because of the flow instability that occurs. The flow instability, in turn, can be promoted by the high levels of turbulence as well.

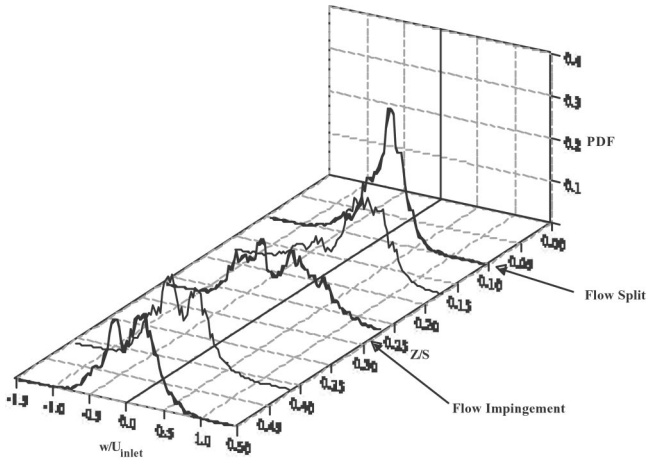

Fig. 6 PDFs of w/U_{in} component of the velocity along the vane stagnation location ($X/C=-0.008$) for case 2

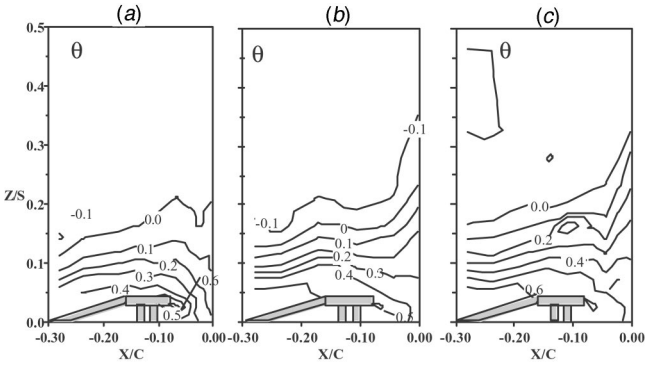

Fig. 7 Contours of normalized temperatures (θ) in the stagnation plane for case 1 (*a*), case 2 (*b*), and case 3 (*c*)

Stagnation Plane Thermal Fields

The thermal fields were measured for three different flow cases to illustrate the effect of increasing the film-cooling liner flow (cases 1–3) while maintaining the same nominal slot flow conditions. The measured thermal fields for these cases are shown in Figs. 7(*a-c*). The temperatures were normalized using the mass-averaged inlet temperature at the vane entrance. In some instances, the θ values are negative in the midspan. The reason for these negative values is because of the large amount of coolant that is injected into the main gas path. As a result of the added coolant, the mass-averaged temperature is cooler than the heated midspan fluid.

The thermal fields illustrated in Figs. 7(*a-c*) show that the film-cooling flow has significantly increased from case 1 to case 3 as indicated by lower temperatures (higher nondimensional temperatures) on top of the liner. Two detrimental effects are apparent from these thermal field measurements with regards to the vane endwall. First, with an increase in liner coolant there is also an increase in the amount of the cooling flow that is being transported along the vane span. Much of the coolant is being transported along the vane span away from the endwall. It is apparent that the $\theta=0.1$ contour moves from being pulled into the slot for case 1 to being pushed up the vane span to a location of $Z/S=0.17$ for case 3. These contour plots contradict the desired result of cooling the endwall surface by adding more coolant from the liner holes. Second, as the liner cooling is increased the coolant ingested by the slot becomes relatively cooler.

As the film-cooling jet injection increases, the driving pressure between the jets and the mid-span flow increases, as well as the driving pressure between the jets and the slot flow. Based on the thermal field measurements at the vane stagnation, however, there is a larger increase in the transport of the film-cooling flow up the vane stagnation as the liner film-cooling flow is increased. The thermal field results, along with the adiabatic effectiveness results in Part 1 do indicate that the flow inside the slot is mixed with the film-cooling flow before exiting the slot. This results in overall higher temperatures (lower θ values) exiting the slot

Passage Flows as Affected by the Slot Flow

As previously discussed, the flow fields were mapped in the SS2 plane for the nominal slot flow (case 2) as well as the double slot flow (case 5) cases. Prior to making the velocity transformations, the flow field at the mid-span was compared with a three-dimensional, viscous CFD prediction for the design slot flow con-

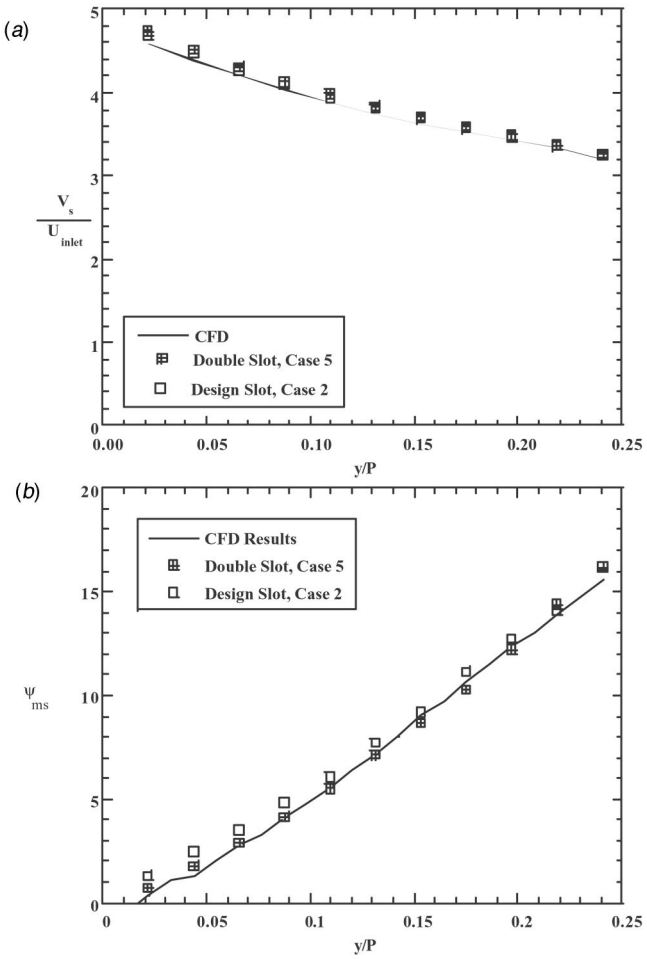

Fig. 8 Comparison of the measured and predicted streamwise velocity component (*a*) and flow turning angle (*b*) at the midspan SS2 location for case 2

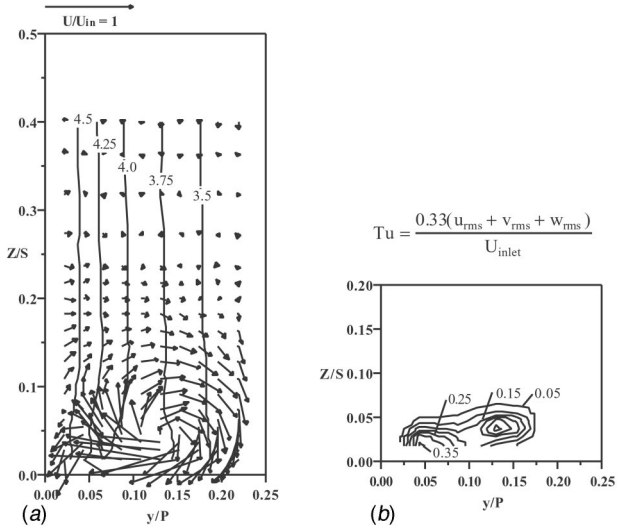

Fig. 9 Measured streamwise velocity contours (V_s / U_{inlet}) along with secondary velocity vectors (*a*) and turbulence level contours (*b*) for an inlet turbulent boundary layer [2] for the SS2 plane

ditions (case 1). Note the CFD prediction will be presented in a later publication. Figures 8(*a*, *b*) show the predicted and measured streamwise velocity component and flow turning angle at the midspan location for the SS2 plane. Good agreement was found between the prediction and measurements across the pitch for both the slightly peaked total pressure profile with the nominal slot flow (case 2) as well as the double slot flow (case 5).

As a point of reference, it is important to show the resulting secondary flow field for a case with an inlet turbulent boundary layer along the upstream endwall for this same vane geometry as reported by Kang and Thole [2]. Note that the boundary layer thickness just upstream of the vane was $\delta/S = 0.1$ for their study. The secondary flow field for the inlet condition of a turbulent boundary layer is shown in Fig. 9(*a*). Superimposed on the secondary flow vectors are contours of the streamwise velocity component. At the SS2 location, the maximum streamwise velocity has accelerated by a factor of 4.75 over that of the inlet velocity. The secondary velocity vectors show remnants of the suction side leg of the horseshoe vortex at the suction side-endwall corner (near $y/P = 0$) and the dominant passage vortex. Downward turning flow is apparent as high as 20% of the vane span as a result of the passage vortex. The center of the vortex is located at approximately $y/P = 0.12$. The turbulence levels for the SS2 plane are shown in Fig. 9(*b*) for the inlet turbulent boundary layer. These turbulence levels are quite high near the endwall and show two peak levels that correspond with the suction side leg and passage vortices.

In contrast to the case with a turbulent boundary layer, Fig. 10(*a*) shows the measured secondary flows for the case with the nominal slot and film-cooling flows (case 2). The streamwise velocity contours indicate a slightly larger effect of the secondary flows on the streamwise velocities for case 2 as compared with the turbulent boundary layer conditions (shown in Fig. 9(*a*)). The secondary flow fields shown in Figs. 9(*a*) and 10(*a*) are clearly different. Any remnants of a suction side leg of a horseshoe vortex are essentially very small at this location for case 2 as compared with the turbulent boundary layer case. While the passage vortex is still present for both cases, the location of this vortex has shifted toward the suction side of the vane with the center being located closer to $y/P = 0.08$. The overall strength of the passage vortex has increased in Fig. 10(*a*) relative to the data shown in Fig. 9(*a*) while the extent in the span direction was reduced to be below $Z/S = 0.12$.

The most noticeable difference between Figs. 9(*a*) and 10(*a*) is the appearance of a counterclockwise vortex located off of the endwall surface that is driving flow up the pressure side of the

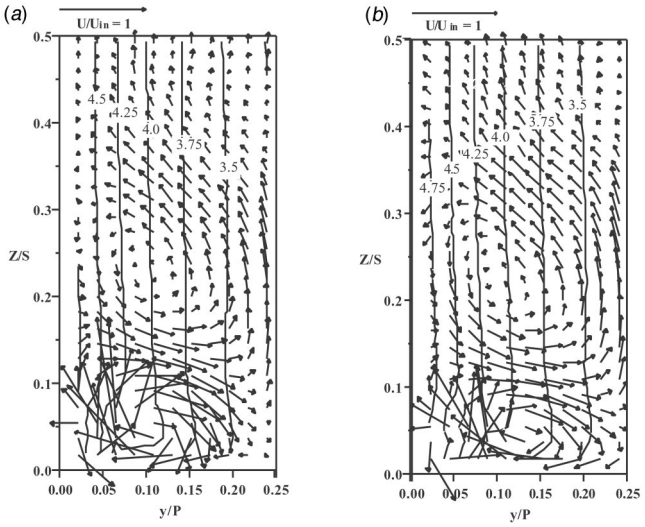

Fig. 10 Measured streamwise velocity contours (V_s / U_{inlet}) along with secondary velocity vectors for case 2 inlet conditions (*a*) and case 5 inlet conditions (*b*)

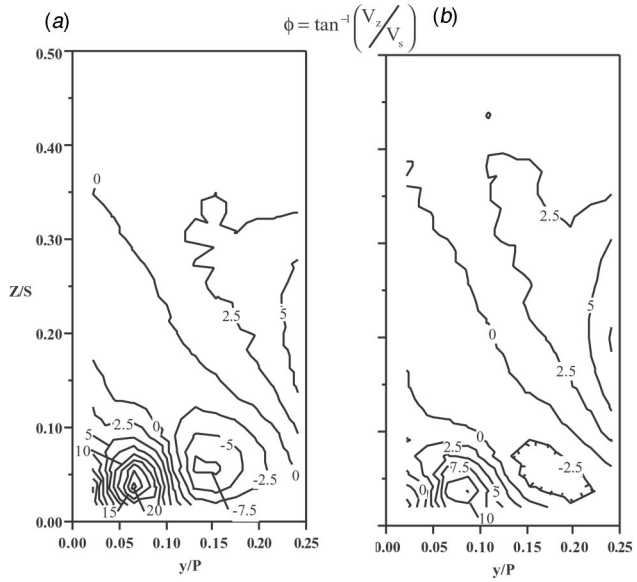

Fig. 11 Contours of the pitch angle(ϕ) in the SS2 plane for cases 2 (*a*) and 5 (*b*)

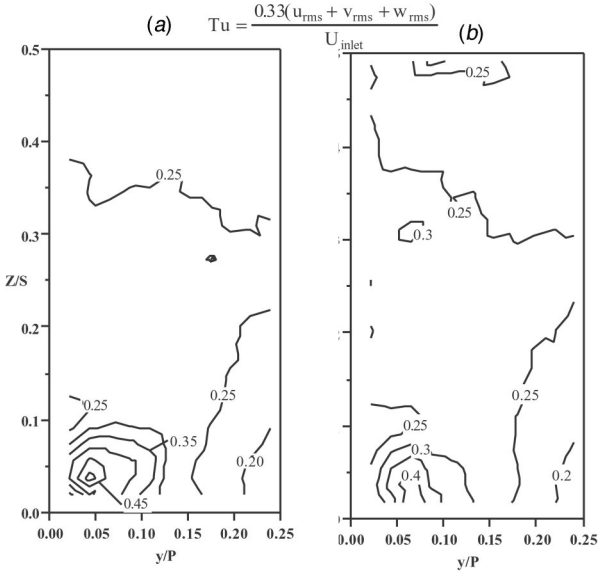

Fig. 12 Contours of turbulence in the SS2 plane for cases 2 (*a*) and 5 (*b*)

adjacent vane and down the suction side of the vane. The center of this counter-rotating vortex is only slightly closer to the pressure surface than the passage vortex. The flow split along the suction side is located at $Z/S=0.17$ while the flow split along the pressure side is located at $Z/S=0.05$. The formation of the counter-rotating vortex shown in Fig. 10(*a*) is a result of the total pressure profile previously discussed. The higher total pressure from the film-cooling jets on top of the liner step along with the slightly lower total pressure in the mainstream results in a driving pressure difference. This pressure difference results in a counter-rotating vortex pattern. Although this counter-rotating vortex was computationally predicted by Hermanson and Thole [7] for an inlet condition of a peaked total pressure near the platform, there have been no experimental studies to validate its existence.

Figure 10(*b*) shows the effect of doubling the slot flow on the secondary flow field. While the streamwise velocity contours are almost the same as the nominal slot flow condition (case 2), there are some effects on the secondary flow field. The strength, size, and position of the passage vortex have been altered for the double slot flow case. The strength and size are reduced as a result of the higher total pressure exiting the slot for the double slot flow case. Alternatively, the counter-rotating vortex strength has increased in magnitude. This increase in the counter-rotating vortex is because of a reduced competing effect to drive the flow towards the platform due to the higher slot flow pressure.

To illustrate the stronger turning for the nominal slot flow case (case 2) relative to the double slot flow case (case 5), contours of the pitchwise angle are presented in Figs. 11(*a*,*b*). These contours represent the upward turning angle of the secondary flow vectors. The contours of the pitch angles in Fig. 11(*a*) indicate much larger turning angles on both legs of the passage vortex for case 2 as compared with Fig. 11(*b*) for the double slot flow case 5.

The turbulence level contours for the nominal and double slot flow cases are shown in Fig. 12(*a, b*), respectively. The characteristics of the turbulence overall are much higher than the turbulent boundary layer approach shown in Fig. 9(*b*). The freestream turbulence level, due to the dilution jets, for the flow fields given in Figs. 12(*a*) and (*b*) indicate levels between 25 and 30%. Recall that the velocity has also increased by over 3.25 to 4.75 times that of the inlet velocity meaning that the turbulence level based on the local velocity is closer to 5.5%.

The peak turbulence levels in Figs. 12(*a*) and (*b*) correspond to the upward leg of the vortex in all of the cases including that shown in Fig. 9(*b*). There are two noticeable differences, however, in comparing the turbulent inlet profile case to the cooled liner/slot cases. First, the turbulence levels are as much higher for the cooled liner/slot cases. Second, there is just a single-peaked contour level for the cooled liner/slot cases as compared with a double-peaked contour for the approaching turbulent boundary layer case. Only a single-peaked contour level for the cooled liner/slot cases occurs because the turbulence level of the flow outside the vortices is nearly at the same level of what occurs due to the vortex interaction itself. This fact is illustrated by considering that the turbulence level for the turbulent boundary layer case (Fig. 9(*b*)) has a peak level of $Tu=0.35$. The combustor simulated profiles have turbulence levels above the endwall of $Tu\sim 0.25-0.3$. Since these turbulence levels are nearly the same, we believe that the contour levels would not show a local peak.

Conclusions

The results presented in this paper show the importance of quantifying the proper inlet conditions to the turbine, particularly in the near platform region. Although the secondary flow models that have been proposed previously in the literature are quite helpful in understanding how the flow develops through a first vane passage, these models all have assumed a simple two-dimensional, flat plate, turbulent boundary layer along the endwall. The measurements discussed in this paper provide the first experimental measurements for the effects of a more realistic combustor exit profile on the secondary flow field that develops in the downstream nozzle guide vane.

The flow field measurements at the vane stagnation location indicate no presence of a horseshoe vortex on top of the combustor liner. The flow pattern under the lip of the liner, however, is expected to contain a vortex confined by the lip of the liner and the upstream pin fins. The film-cooling from above the liner is ingested into the slot thereby mixing with the slot coolant. The ingestion ultimately provides a higher exit coolant temperature (lower θ value) resulting in higher adiabatic wall platform temperatures. A number of flow splits and flow impingement points were identified from the flow field measurements as the spanwise velocity component changed direction along the span. The flow impingement location was correlated with a region having relatively low total pressure levels, causing very high turbulence levels. With an increase in the film-cooling flow, there is also an

increase in the local total pressure. The thermal field measurements at the vane stagnation location indicate that there is a significant transport of this coolant away from the endwall and towards the midspan. This results in little thermal benefit to the endwall.

The flow field measurements in the passage for an upstream film-cooled liner/cooling slot configuration indicate a secondary flow pattern much different than that of an approaching two-dimensional turbulent boundary layer. While the suction side leg of the horseshoe vortex is smaller than it is for a turbulent boundary layer, the passage vortex becomes stronger for the liner/slot configuration. In addition, a counter-rotating vortex above the passage vortex was identified. Both of these vortices can be explained by the total pressure variation exiting the combustor. As the liner cooling is increased, the strength and size of the passage vortex were reduced as a result of the higher total pressure exiting the slot. Alternatively, the counter-rotating vortex above the passage vortex increased in strength.

Clearly, the importance of considering the nonuniformities exiting the combustor is critical to predicting the resulting secondary flow field in the nozzle guide vane. The flow angles exiting the nozzle guide vane are an important consideration in designing the rotor. Moreover, in designing the endwall film-cooling hole pattern the secondary flow and thermal fields need to be quantified for the correct combustor exit conditions. The results indicated in this paper also show that coolant exiting a stepped slot upstream of the vane needs to have a high momentum to insure coolant injection rather than hot gas ingestion.

Acknowledgments

The authors are grateful to Pratt and Whitney and the US Air Force Research Lab for their support of this project. In particular, the authors thank Joel Wagner and Matthew Meininger for their contributions of this work.

Nomenclature

C = true chord of stator vane
N = number of data points
p = pitch of stator vane
P_o = total pressure
PDF = probability density function
S = span of stator vane
T = temperature
Tu = turbulence level defined in figures
U, u = mean velocities as defined in Fig. 3
V, v = mean velocities as defined in Fig. 3
V_n, V_s, V_z = secondary velocity components to inviscid flow direction
W, w = mean velocities as defined in Fig. 3
X, x = global and local streamwise coordinate as defined in Fig. 3
Y, y = global and local normal coordinate as defined in Fig. 3
Z, z = global and local spanwise coordinate as defined in Fig. 3
δ = boundary layer thickness (99% edge)
Δw = bin size for PDF
θ = nondimensional temperature, $(T_{\text{ave}}-T)/(T_{\text{ave}}-T_{\text{cool}})$
ϕ = pitch angle, $\tan^{-1}(V_z/V_s)$
ρ = density
ν = kinematic viscosity
ψ = yaw turning angle at midspan, $\tan^{-1}(v/u)$

Subscripts

ave = mass-averaged
cool = coolant conditions
ms = midspan
inlet = inlet incident velocity
rms = root mean square

References

[1] Colban, W. F., Thole, K. A., and Zess, G., 2002, "Combustor-Turbine Interface Studies—Part 1: Endwall Effectiveness Measurements," ASME J. Turbomach., **125**, pp. 193–202.
[2] Kang, M., and Thole, K. A., 2000, "Flowfield Measurements in the Endwall Region of a Stator Vane," ASME J. Turbomach., **122**, pp. 458–466.
[3] Moffat, R. J., 1988, "Describing the Uncertainties in Experimental Results," Exp. Therm. Fluid Sci., **1**, pp. 3–17.
[4] Barringer, M. D., Richard, O. T., Walter, J. P., Stitzel, S. M., and Thole, K. A., 2001, "Flow Field Simulations of a Gas Turbine Combustor," 2001-GT-0170 to appear in ASME J. Turbomach.
[5] Langston, L. S., 1980, "Crossflows in a Turbine Cascade Passage," ASME J. Eng. Power, **102**, pp. 866–874.
[6] Kang, M., Kohli, A., and Thole, K. A., 1999, "Heat Transfer And Flowfield Measurements In The Leading Edge Region of A Stator Vane Endwall," ASME J. Turbomach., **121**(3), pp. 558–568.
[7] Hermanson, K., and Thole, K. A., 1999, "Effect of Inlet Profiles on Endwall Secondary Flows," J. Propul. Power, **16**(2), pp. 286–296.

Effects of Aeroderivative Combustor Turbulence on Endwall Heat Transfer Distributions Acquired in a Linear Vane Cascade

Forrest E. Ames
Mem. ASME

Pierre A. Barbot

Chao Wang

Mechanical Engineering Department,
University of North Dakota,
Grand Forks, ND 58202

Vane endwall heat transfer distributions are documented for a mock aeroderivative combustion system and for a low turbulence condition in a large-scale low speed linear cascade facility. Inlet turbulence levels range from below 0.7% for the low turbulence condition to 14% for the mock combustor system. Stanton number contours are presented at both turbulence conditions for Reynolds numbers based on true chord length and exit conditions ranging from 500,000 to 2,000,000. Low turbulence endwall heat transfer shows the influence of the complex three-dimensional flow field, while the effects of individual vortex systems are less evident for the high turbulence cases. Turbulent scale has been documented for the high turbulence case. Inlet boundary layers are relatively thin for the low turbulence case, while inlet flow approximates a nonequilibrium or high turbulence channel flow for the mock combustor case. Inlet boundary layer parameters are presented across the inlet passage for the three Reynolds numbers and both the low turbulence and mock combustor inlet cases. Both midspan and 95% span pressure contours are included. This research provides a well-documented database taken across a range of Reynolds numbers and turbulence conditions for assessment of endwall heat transfer predictive capabilities. [DOI: 10.1115/1.1559897]

Introduction

New low-emission combustion systems are designed to have limited peak temperatures using lean combustion mixtures to produce low levels of NO_x. A consequence of these lower peak temperatures is flatter temperature profiles leaving the combustion system. Another consequence of low NO_x strategies is that any cooling air added after the combustion system reduces average rotor inlet temperature and the resulting performance of the engine. Older systems often burned fuel/air mixtures at higher equivalence ratios for better operability ranges producing higher peak temperatures. Endwall surfaces were often insulated from higher peak gas temperatures by supplying a plentiful flow of colder air near these surfaces. Consequently, new combustion strategies have the effect of reducing midspan heat loads to vanes and significantly increasing endwall heat loads. Cooling engineers no longer have the option of adding more cooling air and compensating by increasing the combustion temperature. Designers must provide reliable component cooling using a minimum amount of air. As a result, they need better tools to predict endwall heat transfer.

The present research has been designed to develop of comprehensive database of endwall heat transfer measurements across a range of relevant turbulence conditions. This current paper presents results taken at a low level of turbulence and at a high level of turbulence generated with a mock aeroderivative combustor. These heat transfer measurements have been taken at true chord exit Reynolds numbers ranging from 500,000 to 2,000,000 and inlet turbulence characteristics and inlet boundary layer integral parameters have been comprehensively documented for all cases. Rolls Royce of Indianapolis is currently conducting an analytical effort with a goal of grounding and improving predictive methods for endwall heat transfer using the results of the current experimental study.

Contributed by the International Gas Turbine Institute and presented at the International Gas Turbine and Aeroengine Congress and Exhibition, Amsterdam, The Netherlands, June 3–6, 2002. Manuscript received by the IGTI December 4, 2001. Paper No. 2002-GT-30525. Review Chair: E. Benvenuti.

Background

Secondary Flows. Sieverding [1] presented a noteworthy review of secondary flows in turbine blade passages collecting information from various sources and presenting models of secondary flows from Klein [2] and Langston [3]. Sieverding gives Klein credit for first recognizing the complex secondary flows developing on the endwall of a blade row. He indicates that the importance of work on secondary flows became evident as heat transfer and aerodynamic loss investigations began to show their impact on heat transfer rates and secondary losses. Langston's model denotes the main vortex systems including the suction and pressure side leg of the horseshoe vortex as well as the passage vortex. Additionally, Langston indicates the existence of corner vortices in the stagnation region and along the pressure and suction surfaces of the blade. Marchal and Sieverding [4] suggest that secondary losses grow more rapidly in the region of the flow downstream from the maximum velocity. Unpublished work by Ames et al. [5] at Allison Gas Turbine Division of General Motors showed that secondary losses increased with increasing thickness of the endwall inlet boundary layer and the position of the passage vortex core rose above the endwall in the exit region of the vane cascade. Recent vane cascade investigations show that leading edge fillets (Zess and Thole [6]) and inlet endwall contouring (Burd and Simon [7]) can reduce the impact of secondary flows.

Endwall Heat Transfer. Experimental studies on vane endwall heat transfer include studies by York et al. [8], Harasgama and Wedlake [9], Spencer et al. [10], Arts and Heider [11], and Radomsky and Thole [12]. Experimental studies on blade endwall heat transfer include studies by Goldstein and Spores [13] and

Giel et al. [14]. Generally, similar results are achieved showing increased heat transfer in the stagnation region of the airfoil and downstream of or adjacent to the pressure surface of the airfoil. Location of the hotspot off the pressure surface seems to depend on cascade geometry, Reynolds number, and Mach number. Harasgama and Wedlake conducted heat transfer tests in a compressible annular cascade and found that heat transfer in the hub differed somewhat from heat transfer in the tip region. Spencer et al. added the influence of high turbulence with similar results. Radomsky and Thole compared the influence of high to low turbulence on endwall heat transfer in an incompressible linear cascade. They found the largest augmentation (~40%) in the low velocity inlet regions and a reduced level of augmentation (~10%) in the higher velocity regions. CFD computations can at times produce reasonable predictions of endwall heat transfer cases but can also produce inaccurate results. Boyle and Lucci [15] found that endwall heat transfer predictions are dependent on the turbulence model and agreement between predictions and experiment can vary from case to case for a given model. This suggests that endwall heat transfer data taken over a relevant range of parameters is needed to adequately test the relevancy of turbulence models for endwall heat transfer and secondary flow prediction.

Experimental Approach

This heat transfer research has been conducted in the University of North Dakota's large-scale low speed cascade facility. This facility is configured in a steady state blow down arrangement and is documented to a further extent in GT-2002-30524. The wind tunnel is powered by a 45 kW blower capable of providing 6.6 m^3/s of air at a static pressure rise of 5000 Pa. The blower outlet flow is directed through a two stage multivane diffuser section to distribute and diffuse the flow prior to entering a heat exchanger. The heat exchanger system, which uses a cooling water recirculation system, helps to provide a steady and controllable inlet air temperature. The flow is further conditioned downstream of the heat exchanger in a four section screen box. The low turbulence baseline configuration uses a 3.6:1 area ratio two-dimensional nozzle to further accelerate the air prior to entrance into the linear vane cascade test section.

The cascade test section used in this study is shown schematically in Fig. 1. The cascade is based on an eleven times scale mid span vane profile representative of a modern mid-sized industrial gas turbine. The vane profile was designed for incompressible flow and has a velocity distribution, which is consistent with current conventionally or fully loaded vanes in industrial engines. The test section is designed to produce accurate two-dimensional aerodynamics at the midspan of the cascade using a four-vane three-passage configuration. The cascade has inlet bleeds and exit tailboards to allow inlet flow uniformity and exit flow periodicity. The inlet bleed flows were designed along two-dimensional streamlines predicted by FLUENT [16] and the flexible exit tailboards can be shaped to account for streamline curvature. The cascade has a row of inlet static taps one-quarter axial chord upstream from the vane leading edge and a row of exit taps one-quarter axial chord downstream to monitor the cascade setup. Ten probe access ports are provided along the row of inlet static pressure taps to measure inlet temperature and total pressure and to survey inlet turbulence characteristics.

The vane has a true chord of 47.8 cm and an axial chord of 25.0 cm. The vanes have a 38.4 cm spacing and a height of 25.4 cm. The diameter of the leading edge is 5.59 cm and the diameter of the trailing edge is 0.98 cm. The stagger angle of the vane is 55.1 deg and the calculated air exit angle is 73.4 deg. The span to chord length aspect ratio of the present cascade geometry is 0.53, comparing reasonably well with the 0.68 aspect ratio of the engine vane geometry.

This study investigated endwall heat transfer at exit Reynolds numbers based on true chord length of 500,000, 1,000,000, and 2,000,000. This range of first vane chord exit Reynolds numbers is consistent with a range of small to medium industrial or propulsion gas turbine engines.

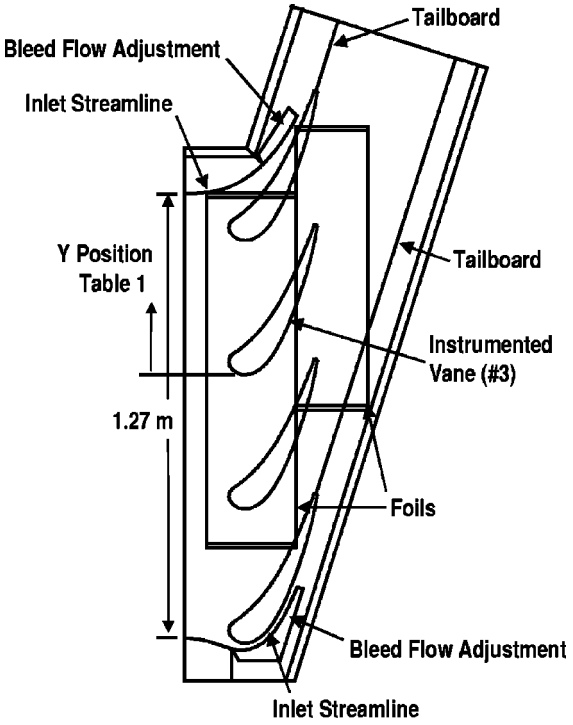

Fig. 1 Schematic of UND linear cascade facility

Turbulence Generator. This study was designed to investigate turbulence characteristics representative of modern combustion systems and their influence on endwall heat transfer. A mock aeroderivative combustion system was developed to provide turbulence with characteristics, which are representative of many current engines and have been documented in the literature. The mock combustor configuration is shown schematically in Fig. 2. Looking at the cross-sectional view, flow enters from the right and is forced through the slots in the back panel and the two rows of holes in the side panels simulating a recirculation zone and a dilution zone. The flow then leaves the mock combustor through the 2 to 1 area ratio contraction nozzle on the left of the cross-sectional view and immediately enters the cascade. This mock combustor replaces the 3.6:1 area ratio nozzle for the high turbulence test case.

Vane Pressure Distribution. Heat transfer and pressure distributions were acquired on the third vane from the bottom. This

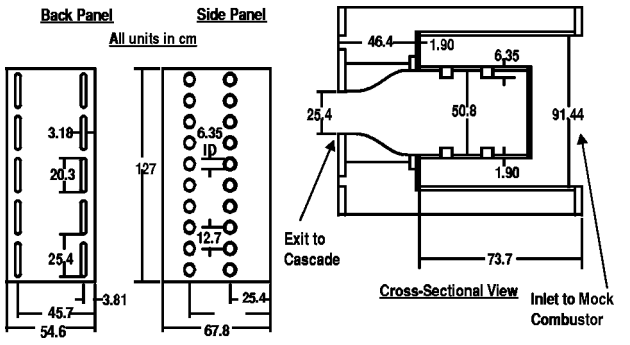

Fig. 2 Schematic of mock aeroderivative combustor turbulence generator

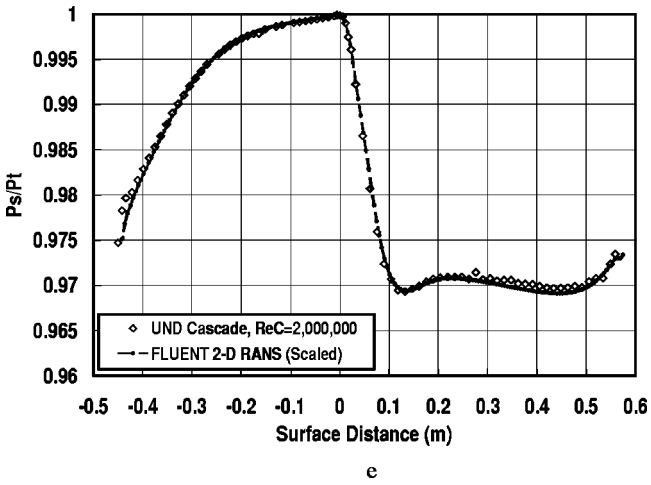

e

Fig. 3 Comparison between measured and predicted vane midspan pressure distribution

"instrumented" vane can be inserted through a machined hole in the acrylic endwall where it is held in place using a flange. The pressure vane was cast from epoxy over a structure of 82 pressure tubes incrementally spaced along and adjacent to its surface. Static pressure taps were fabricated by drilling through the epoxy surface into the brass tube with a 0.8-mm-dia drill bit. The baseline pressure distribution for the low turbulence case is shown in Fig. 3 where it is compared to a 2-D prediction using FLUENT. On this figure negative surface distance is taken from the calculated stagnation point (0 cm) along the pressure surface toward the trailing edge and positive surface distance is determined along the suction surface. The viscous prediction calculates the data with precision. Overall, the comparison is excellent and gives confidence in the quality of the midspan aerodynamics produced by the cascade. Developing accurate aerodynamics is critical to producing a heat transfer database, which is valuable for understanding the impact of new combustion systems and for grounding predictive methods.

The 2-D FLUENT computations were made to support the design of the present facility and for comparison with the measured midline pressure distributions. The Spalart-Allmaras one-equation eddy viscosity transport model was selected since the model is computationally efficient and considered quite capable of producing accurate pressure distributions on the surface of a vane. For the computation, 220 grid points were placed along the surface of the vane with concentrations in the leading and trailing edges. A boundary layer mesh was applied to the vane to ensure an orthogonal grid was adjacent to the flow surface and to resolve the boundary layer into the laminar sublayer.

Endwall Heat Transfer Measurements. Endwall surface heat transfer measurements have been acquired using a constant heat flux boundary condition generated by a 0.023 mm. Inconel foil and narrow band thermochromic liquid crystal thermometry. On the third vane from the bottom, a commercially fabricated foil was wrapped from the suction surface trailing edge around the leading edge to the pressure surface trailing edge to generate a constant surface heat flux. Two foils were applied to the endwall to develop a constant surface heat flux in that region. All three foils were incrementally heated at consistent heat flux levels to paint isotherms over the endwall at different Stanton number levels. Backup instrumentation for the endwall heat transfer test was fabricated by placing fine wire thermocouples under the surface of the endwall to determine the midpassage surface temperatures. These temperature measurements served to check the narrow band liquid crystal paint temperatures.

Application of narrow band microencapsulated thermochromic liquid crystal (TLC) paints have resulted in uncertainty bands for driving temperature difference of +/−1% for a 25°C temperature difference (Hippensteele, Russell, and Torres, [17]; Hippensteele, Russell, and Torres, [18]; Hippensteele and Russell, [19]; Jones and Hippensteele, [20]. Camci et al. [21] report the ability to resolve surface temperature using narrow band liquid crystal paints to within +/−0.1°C when using a single color such as green. Giel et al. [14] indicate microencapsulated liquid crystals are less sensitive to viewing and illumination angles. The liquid crystal paint selected for the present experiment has a 1°C bandwidth with a 37°C start. The microencapsulated liquid crystal paint was calibrated using an aluminum test surface, which was first heated then allowed to cool. Temperatures were recorded as a function of time during the cooling process while digital photos of the test surface were acquired periodically. The camera was set to a fully manual mode to allow the highest reproducibility of color and intensity. The results show a sensitivity of 229 deg/°C around 37°C. This sensitivity of hue angle to temperature for the highest green intensity is very high and accuracy of the 37°C color change was estimated to be within 0.2°C over the span of the tests.

A constant heat flux boundary condition was generated on one of the endwalls using a rectangular constant heat flux foil. The foil was adhered to a thin epoxy board, which in turn was secured to a one-inch layer of polyisocyanurate foam insulation. Under the footprint of the vane, an aluminum vane shaped heat exchanger was placed to conduct away the thermal energy generated in this region by the foil. In this way, both the endwall and the vane could be run at a constant heat flux that was matched. Many full surface vane and endwall heat transfer experiments do not have matched boundary conditions between at the vane and endwall interface. This condition produces an unheated starting length condition when flow approaches from an inactive surface.

The surface Stanton number data were acquired by first increasing the heat flux rate on all the plates until the first green color appeared on the surface. At that point, the surface heat flux was increased until the next incremental Stanton number was achieved based on exit conditions and surface to total temperature difference.

$$\mathrm{St} = \frac{(q'' - q''_{\mathrm{rad}})}{(T_{\mathrm{green}} - T_{T,IN})\rho U_\infty Cp}$$

The radiative heat loss was estimated to be

$$q''_{\mathrm{rad}} = \varepsilon\sigma(T^4_{\mathrm{green}} - T^4_{T,IN})$$

The conduction loss was ignored because the radiative loss estimate was slightly overestimated and the conduction loss was within the uncertainty band of that estimate. When the test surface had reached steady state, pictures were acquired using a digital camera in the manual mode for all endwall locations where color appeared. The heat flux rate of the foils surface was then adjusted to produce the next incremental iso-Stanton number. The procedure to change the heat flux, wait for steady state, and then acquire digital images was repeated until the last incremental iso-Stanton number was achieved. Uncertainties were highest for the lowest Stanton numbers at the lowest Reynolds number where the overall uncertainty was estimated to be +/−10% at 20 to 1 odds. At this condition the estimated radiative loss less the 1-D conduction loss was 21% of the net surface heat flux. At the highest Reynolds number the maximum uncertainty in Stanton number was estimated to be +/−5% at 20 to 1 odds. The largest source of error was due to the uncertainty in the radiative loss.

Data Acquisition. Pressures were acquired using two Rosemount Smart Pressure Transmitters scaled to ranges of 250 and 5000 Pa full scale with 0.1% of scale accuracy. Voltage outputs for both the pressure transmitters and for the chromel-alumel thermocouples were scanned and read using an HP 3497A data acquisition system. The data acquisition unit has an integral voltmeter with 1μV sensitivity. Thermocouples were all connected through

Table 1(a) Endwall inlet boundary layer parameters, low turbulence condition

Low turbulence					
Reynolds	Tu	U (m/s)	Lx (cm)	Lu (cm)	ε (m^2/s^3)
500,000	0.0069	4.96	8.12	127.0	0.00005
1,000,000	0.0076	10.43	5.02	154.5	0.00035
2,000,000	0.0060	18.71	3.58	15.5	0.0144

Low turbulence (LT) Re_c=500,000							
Y (cm)	U_∞ (m/s)	δ_2 (cm)	δ_1 (cm)	H	$Cf/2$	Tu_∞	Re δ_2
16.90	4.55	0.076	0.195	2.560	0.00099	0.0081	222
9.22	4.09	0.094	0.223	2.370	0.00097	0.0086	247
1.54	4.63	0.102	0.243	2.390	0.00087	0.0070	301
−6.14	5.82	0.098	0.228	2.320	0.00080	0.0067	362
−13.82	5.26	0.091	0.235	2.580	0.00075	0.0076	300

Low turbulence (LT) Re_c=1,000,000							
Y (cm)	U_∞ (m/s)	δ_2 (cm)	δ_1 (cm)	H	$Cf/2$	Tu_∞	Re δ_2
16.90	8.63	0.054	0.095	1.770	0.00270	0.0079	297
9.22	7.59	0.062	0.105	1.700	0.00280	0.0087	302
1.54	9.80	0.058	0.093	1.590	0.00297	0.0043	370
−6.14	11.83	0.064	0.122	1.930	0.00165	0.0036	486
−13.82	10.65	0.070	0.148	2.110	0.00130	0.0050	484

Low turbulence (LT) Re_c=2,000,000							
Y (cm)	U_∞ (m/s)	δ_2 (cm)	δ_1 (cm)	H	$Cf/2$	Tu_∞	Re δ_2
16.90	16.03	0.063	0.095	1.520	0.00245	0.0080	647
9.22	15.70	0.074	0.127	1.530	0.00230	0.0087	743
1.54	19.52	0.071	0.102	1.440	0.00243	0.0057	874
−6.14	22.92	0.057	0.081	1.430	0.00253	0.0046	821
−13.82	19.94	0.053	0.082	1.530	0.00234	0.0050	671

a passive constant temperature junction and were referenced using an ice bath junction. Hot wires were powered, low-pass filtered, bucked and gained using a two channel TSI ISA 300 hot wire anemometry bridge. Raw signals were read with a PC based high-speed data acquisition card with 12 bits of resolution. Mean velocities were acquired at a data acquisition rate equivalent to about three integral time scales. Velocity time records for spectral analysis were acquired in 40 sets of 8192 samples and post-processed.

Data Uncertainties. Estimates for the uncertainty in heat transfer, pressure, velocity, and turbulence measurements were determined using the root sum square method described by Moffat [22]. Uncertainty in the local vane surface static pressure was estimated at a maximum of 2.5%. Exit velocity was determined at a precision of 2%. The uncertainty in turbulence level for the single wire was estimated to be 3% of the reported value. The experimental error in turbulent scale is estimated to be 11%. All uncertainty estimates are quoted for a 95% confidence interval.

Inlet Conditions and Turbulence Characteristics. Two turbulence conditions are reported in this endwall heat transfer paper. Heat transfer data, inlet velocity profiles, and turbulence measurements were taken for both turbulence conditions and all three Reynolds numbers. Span averaged turbulence data (Tu, Lx, Lu, and ε) are reported in the initial section of the tables while parameters for the inlet velocity profiles are reported for five circumferential positions in the remainder of the tables. These measurements were acquired seven cm upstream from the leading edge plane of the vanes. Midspan or peak velocity (U_∞), integral thicknesses (δ_2 and δ_1), shape factor (H) skin friction coefficient ($Cf/2$), turbulence level (Tu), and momentum thickness Reynolds number ($Re_{\delta 2}$) were determined for each condition and are presented in Tables 1(*a*) and (*b*).

Experimental Results

The experimental results documented in this paper include comprehensive inlet boundary layer parameters and turbulence conditions, 95% span pressure distributions for the six conditions, and endwall heat transfer distributions for the six conditions. The inlet boundary layers have been documented using a single-wire probe for all six conditions at five inlet locations. These inlet locations are equally spaced at 1/5th of the vane circumferential spacing. For the low turbulence inlet conditions the boundary layers are very thin and the lower Reynolds number inlet boundary layers show laminar behavior. The six 95% span pressure distributions provide an indication of the pressure gradients present on the endwall surface, which are drivers for secondary flows. A lampblack and oil flow visualization photo taken on a similar cascade provides an indication of the location of the separation saddle point and suction and pressure surface separation lines due to endwall pressure gradients. The six endwall surface heat transfer distributions provide a well-resolved picture of influence of turbulence level and Reynolds number on the Stanton number distributions and are expected to useful for grounding computational models.

Inlet Boundary Layer Parameters and Turbulence Conditions. Inlet boundary layer measurements were taken at the inlet to the cascade at five circumferential positions and are documented in Tables 1(*a*) and (*b*) for both turbulence conditions and all Reynolds numbers. The circumferential position (Y) is taken from the bottom most Y location of the suction surface of the instrumented vane as shown in Fig. 1. For the low turbulence condition at the low Reynolds number, the inlet boundary layers are all laminar as indicated by the skin friction coefficient, $Cf/2$, and the shape factor. The entering boundary layer is very thin due to the entrance contraction just upstream of the cascade test section. At the 1,000,000 chord Reynolds number, the boundary layers at the top three positions are turbulent, while the lower two stations show transitional flow. Inlet boundary layers for the low turbulence, high Reynolds number condition, are all turbulent. Determining the skin friction coefficients for the laminar and transitional boundary layers was quite uncertain, perhaps as much as 20% or more due to the lack of near wall velocity measurements.

Inlet boundary layer measurements for the aero-combustor simulator are presented in Table 1(*b*) for three Reynolds numbers.

Table 1(b) Endwall inlet boundary layer parameters, aero-combustor condition

Aero-combustor						
Reynolds	Tu	U (m/s)	Lx (cm)	Lu (cm)	ε (m^2/s^3)	
500,000	0.1313	5.24	3.68	7.24	6.67	
1,000,000	0.1402	9.32	3.52	6.36	51.5	
2,000,000	0.1339	18.39	3.58	7.35	302.0	
Aero-combustor (AC) Re_c=500,000						
Y (cm)	U_∞ (m/s)	δ_2 (cm)	δ_1 (cm)	H	$Cf/2$	Tu_∞	Re δ_2
16.90	4.83	0.726	0.889	1.226	0.00250	0.1567	2238
9.22	4.41	0.786	0.988	1.261	0.00220	0.1732	2184
1.54	5.40	0.411	0.500	1.217	0.00275	0.1321	1409
−6.14	6.09	0.360	0.428	1.189	0.00298	0.1097	1408
−13.82	5.48	0.456	0.544	1.195	0.00280	0.1270	1599
Aero-combustor (AC) Re_c=1,000,000						
Y (cm)	U_∞ (m/s)	δ_2 (cm)	δ_1 (cm)	H	$Cf/2$	Tu_∞	Re δ_2
16.90	8.43	0.706	0.860	1.217	0.00225	0.1625	3774
9.22	7.88	0.806	0.997	1.245	0.00191	0.1720	3890
1.54	9.51	0.382	0.456	1.201	0.00248	0.1350	2235
−6.14	11.10	0.278	0.322	1.160	0.00295	0.1073	1928
−13.82	9.90	0.311	0.368	1.181	0.00278	0.1255	1953
Aero-combustor (AC) Re_c=2,000,000						
Y (cm)	U_∞ (m/s)	δ_2 (cm)	δ_1 (cm)	H	$Cf/2$	Tu_∞	Re δ_2
16.90	16.96	0.575	0.860	1.193	0.00190	0.1557	6217
9.22	15.33	0.627	0.767	1.223	0.00151	0.1741	6121
1.54	18.60	0.306	0.359	1.178	0.00221	0.1287	3557
−6.14	21.47	0.237	0.269	1.136	0.00265	0.1034	3247
−13.82	19.37	0.268	0.312	1.165	0.00232	0.1197	3311

Generally, peak velocities occurred at the midspan of the channel so perhaps the term nonequilibrium channel flow would be a better term. These profiles are nonequilibrium in the sense they are strongly influenced by the freestream turbulence, which is convected downstream from the turbulence generator. The profiles exhibit no wake due to the turbulence interaction but are affected by the pressure gradients at the inlet plane of the cascade. Momentum thickness at a given position scales inversely with the local peak velocity. Velocity profiles suggest that the large-scale high intensity turbulence is very effective at redistributing low momentum flow. Figure 4 shows the measured velocity distribution at the highest measuring station for the highest Reynolds number compared with a fully developed nonequilibrium channel flow calculation assuming a linear shear stress distribution $[\tau/\tau_w = 1-(2y)/H]$ and the ATM model of Ames et al. [23]. This calculated profile is strongly influenced by the nonequilibrium turbulence generated in the mock combustor and is substantially different than a typical equilibrium channel flow. However, the calculated profile has significant similarities to the measured inlet velocity profile and may be of utility as a baseline inlet profile for a combustor.

Ninety-Five Percent Span Pressure Distributions. Ninety-five percent span pressure profiles for the low and aero-combustor turbulence cases are shown in Figs. 5 through 7 compared with midspan profiles. The profiles are plotted in terms of *Ps/Pt* versus surface arc for the low through high Reynolds numbers respectively. The 95% span profiles show a reduction in minimum pressure on the near suction surface (positive surface distance) due to the secondary flows, which first move away from the suction surface and then are pushed toward and up onto the surface. The high turbulence case with the largest momentum thickness shows the biggest variation between the midspan and 95% span distributions. However, the difference between the midchord and 95%

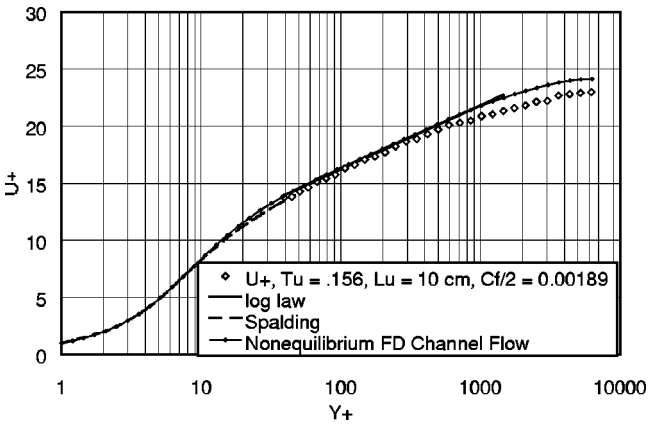

Fig. 4 Cascade Inlet Velocity Profile Compared with nonequilibrium FD channel flow, ATM, top position, Re_c=2,000,000

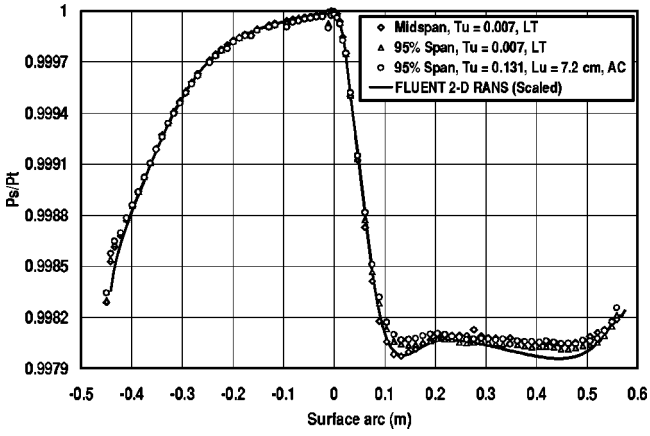

Fig. 5 Comparison of 95% span pressure distributions with midspan values, Re_c=500,000

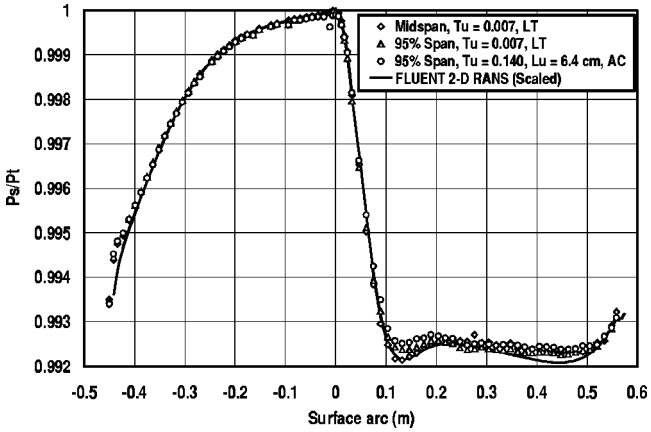

Fig. 6 Comparison of 95% span pressure distributions with midspan values, Re_c=1,000,000

pressure distributions is not large indicating that the secondary flows have only a modest effect. Generally similar trends appear at the three Reynolds numbers but influence of the secondary flows on the highest Reynolds number is the most significant.

Endwall Flow Visualization. A lampblack and oil endwall flow visualization is presented in Fig. 8 taken from [5]. This figure shows the separation saddle point upstream from the vane along with the pressure surface and suction surface separation lines. The pressure side of the horseshoe vortex and the passage vortex form above the separation saddle point and are sweep upward toward the adjacent vane suction surface. The suction side of the horseshoe vortex moves downward around the suction surface and is swept up onto the surface. These flow visualization measurements were taken in a five-vane cascade at an exit Reynolds number based on chord length of 2,000,000 and an exit Mach number of 0.6. The inlet momentum thickness was about 3800, comparable to the present high turbulence case, and the inlet turbulence level was 6.5%. The geometry of the cascade used by Ames et al. has similarities to the present cascade and the flow visualization provides some insight for the heat transfer patterns seen on the present endwall.

Endwall Stanton Number Distributions. Endwall Stanton number contours are shown in Figs. 9 through 14 for Reynolds numbers ranging from 500,000 to 2,000,000 with low and high turbulence levels. All Stanton numbers are based on exit conditions. Comparisons between the low freestream Stanton numbers

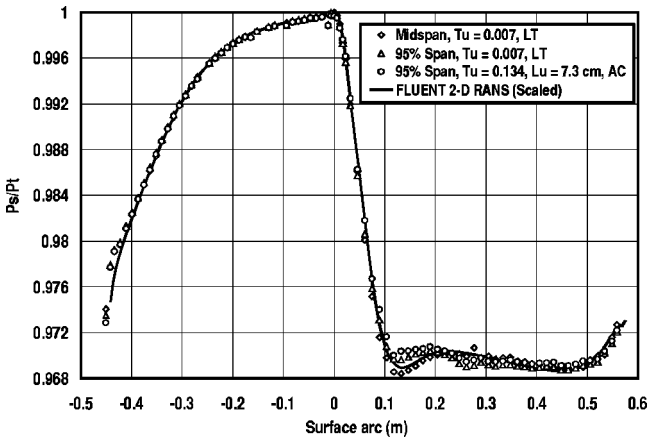

Fig. 7 Comparison of 95% span pressure distributions with midspan values, Re_c=2,000,000

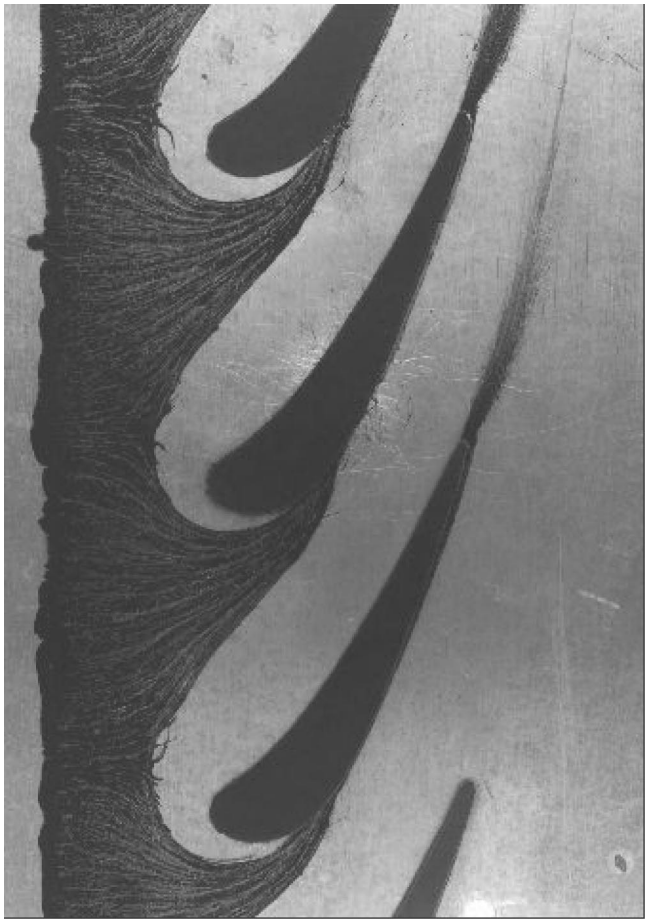

Fig. 8 Endwall flow visualization using lampblack and oil showing the separation saddle point and pressure and suction surface separation lines [5]

and the mock aerocombustor Stanton number distributions have been shown on one page at a single Reynolds number. In the first comparison, Stanton number contours are shown for an exit chord Reynolds number of 500,000 for the low turbulence condition in Fig. 9 and for the aerocombustor in Fig. 10. In these figures, the middle vane has a consistent heat flux boundary condition with the black endwall surface, while the upper and lower vanes have no heating. Around the leading edge of the middle vane, Stanton number levels decrease as the thermal boundary layer thickens and then increase as the stagnation region is approached. The high heat transfer rates in this region are consistent with the horseshoe vortex with forms in this region and Stanton number levels in this regions are as high as any shown on the surface. The favorable static pressure gradient, which moves away from the stagnation region and the pressure surface tends to drive the separation line for the inlet boundary layer toward the suction surface of the adjacent vane. The results of this separation line can be seen in the jagged contour lines for the 0.0013 Stanton number and the low heat transfer island shown for the 0.0011 Stanton number. This lowest heat transfer region is consistent with the convergence of the separation streamline from the suction surface leg of the horseshoe vortex and the separation streamline due to the roll up of the pressure surface leg of the horseshoe vortex by the passage vortex. The influence of the convergence of these vortices and their lift off onto the suction surface can be seen in the Stanton number contours along the suction surfaces of the upper and middle vanes. Heat transfer levels are generally highest downstream from the trailing edge region of the vanes due to the intense generation of turbulence, which occurs in the wakes due to

Fig. 9 Endwall Stanton number contours, LT, Tu=0.007, Re_c =500,000

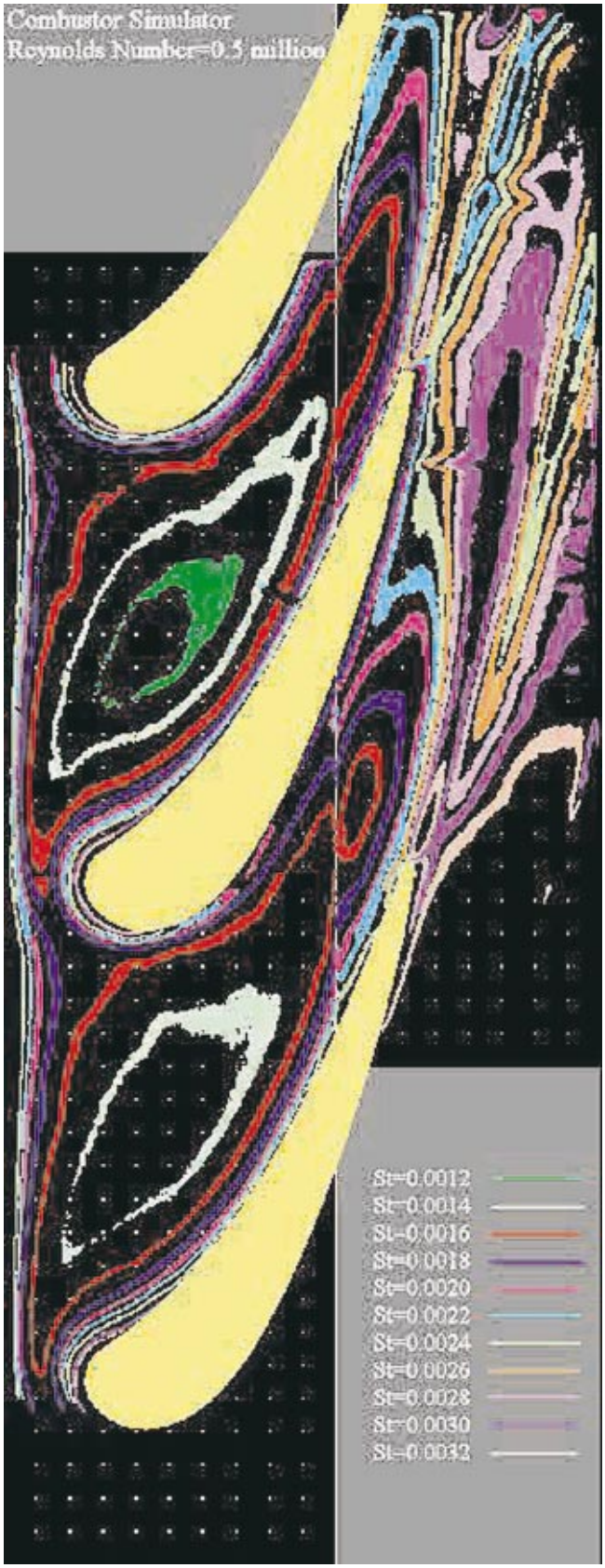

Fig. 10 Endwall Stanton number contours, AC, Tu=0.131, Lu =7.2 cm, Re_c=500,000

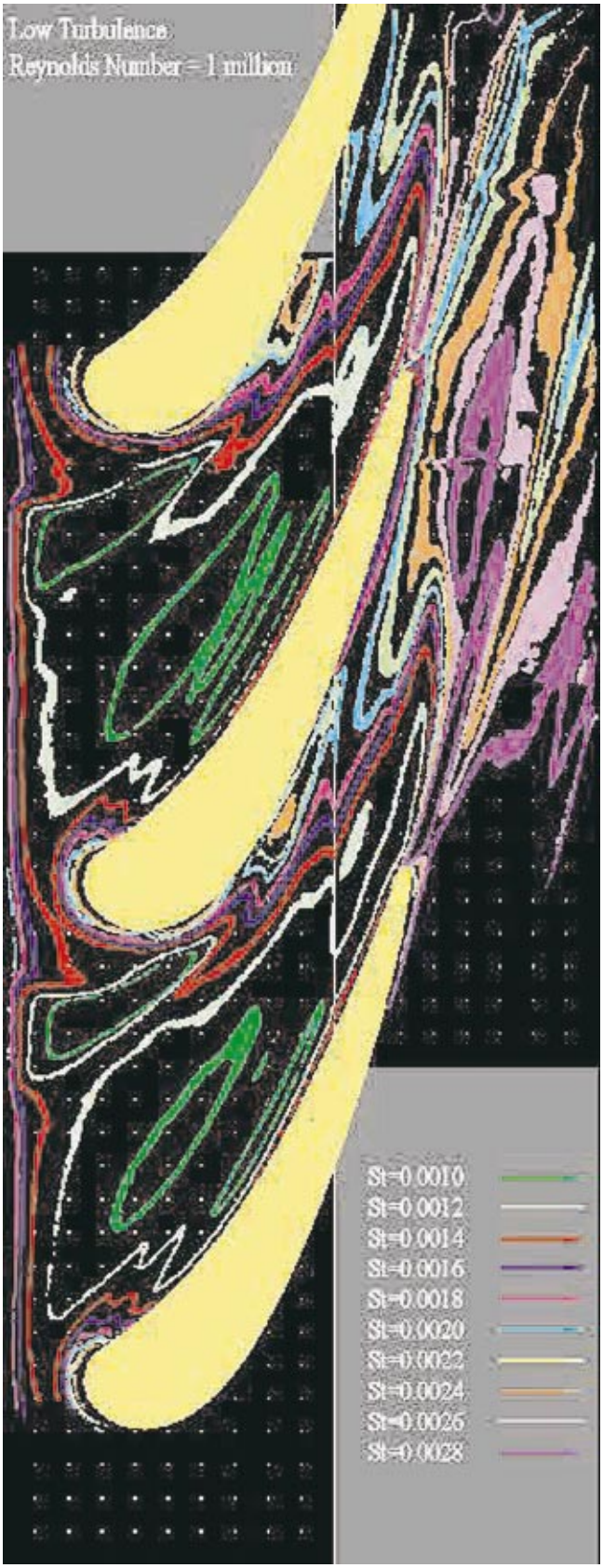

Fig. 11 Endwall Stanton number contours, LT, Tu=0.007, Re_c =1,000,000

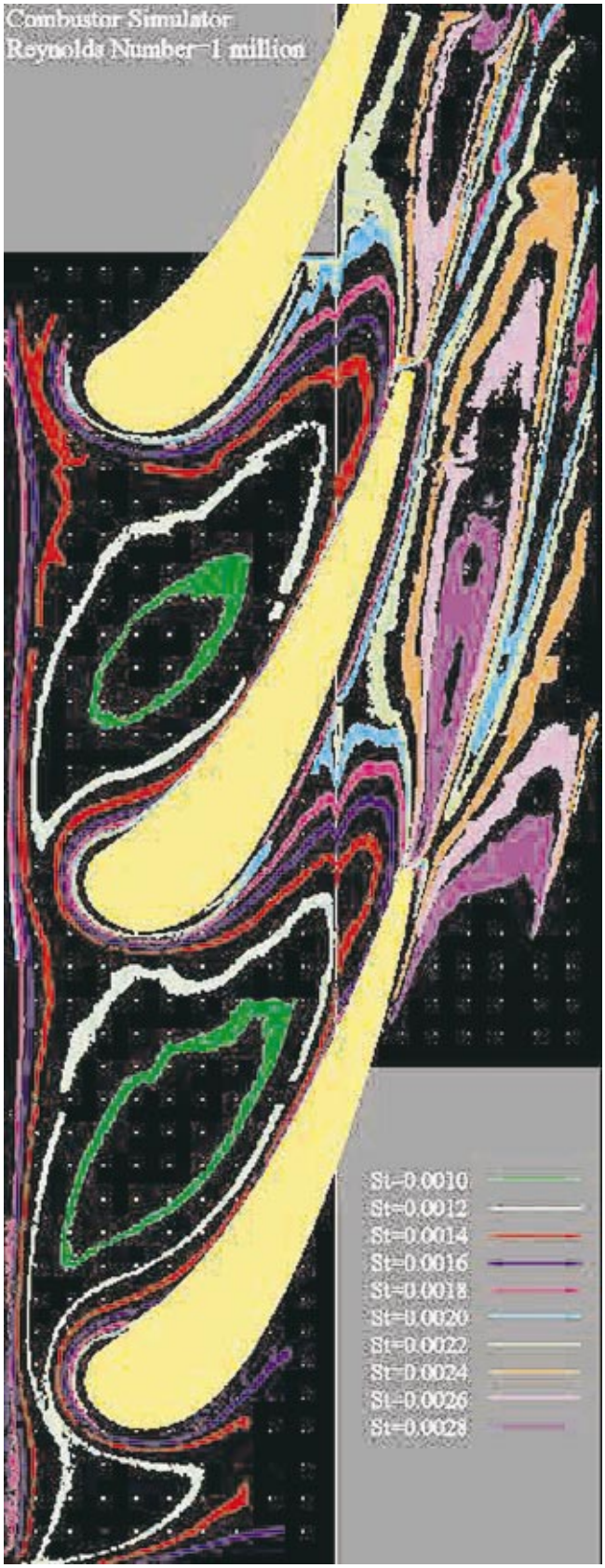

Fig. 12 Endwall Stanton number contours, AC, Tu=0.140, Lu =6.4 cm, Re_c=1,000,000

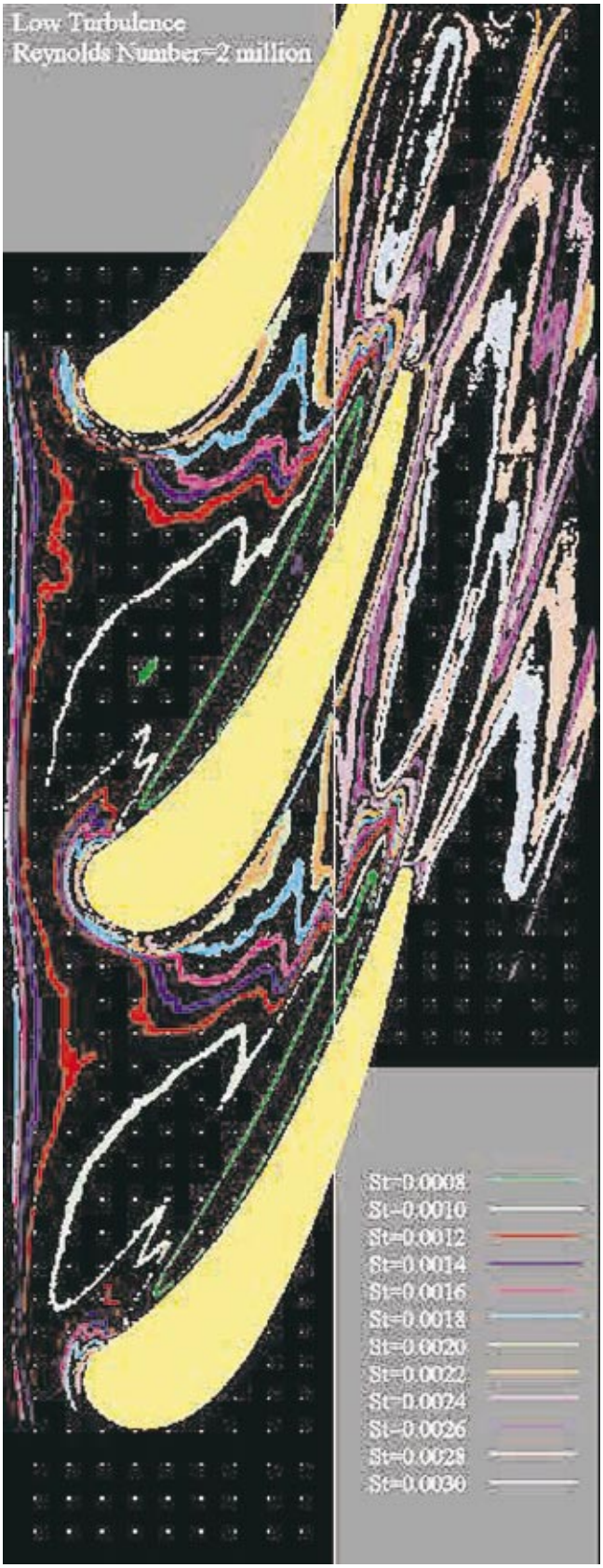

Fig. 13 Endwall Stanton number contours, LT, Tu=0.007, Re_c =2,000,000

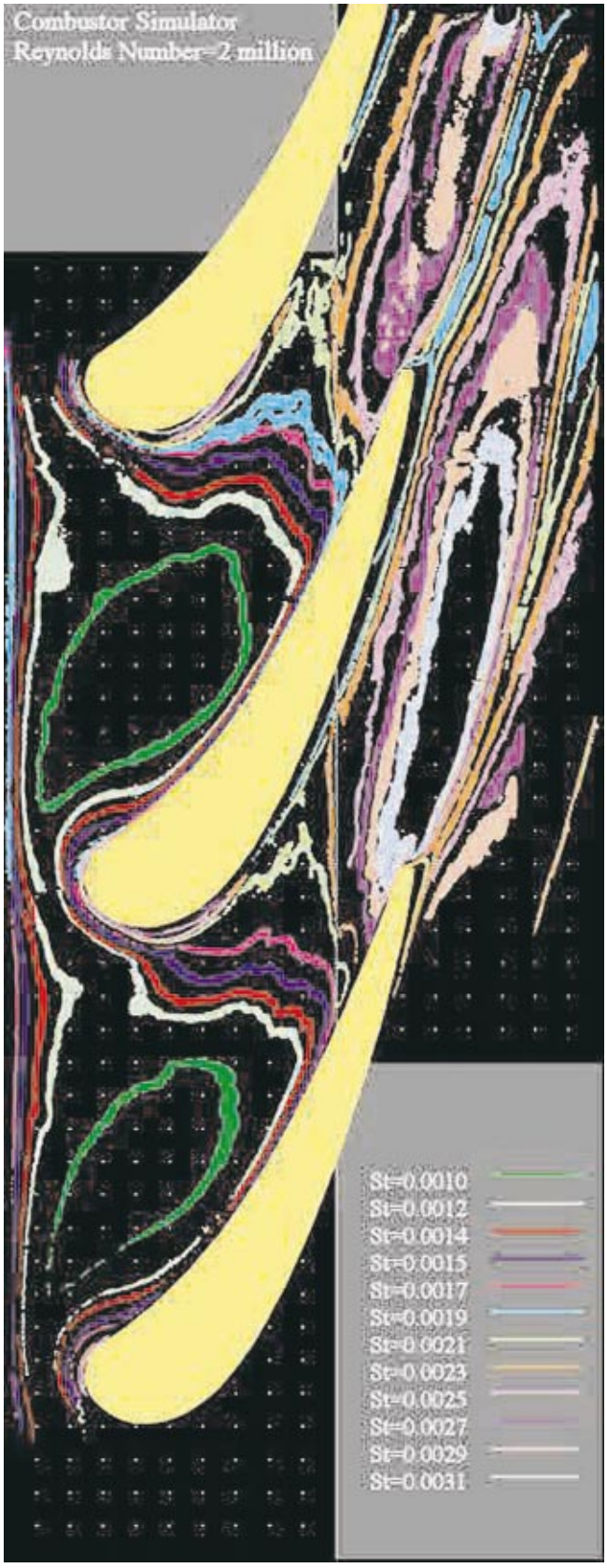

Fig. 14 Endwall Stanton number contours, AC, Tu=0.134, Lu =7.3 cm, Re_c=2,000,000

the velocity deficit. The trajectory of this high heat transfer island curves toward the circumferential direction. This path is consistent with the characteristic over turning near the endwall, which is typically present due the combination of endwall pressure gradients and an accumulation of low momentum fluid in the endwall region. Additionally, the presence of corner vortices along the suction surface appears to affect heat transfer in the aft region of the surface. The combination of high convective velocity and pressure gradient off the pressure surface produces a relatively high Stanton number (0.0015) in the region downstream from that surface. However, this Stanton number is significantly lower than levels in the same region for the highest Reynolds number flow. For the 500,000 Reynolds number this level of Stanton number is more consistent with laminar or transitional flow than turbulent flow for this high velocity region. The presence of the heated vane does not appear to have a strong influence for this condition. However, some significant differences are apparent downstream from the trailing edges of the vane.

The Stanton number patterns on Fig. 10 for the high turbulence case appear to be less affected by the secondary flows than the lower turbulence case. Other than outside of the stagnation region and downstream from the trailing edge, few patterns can be correlated with the expected secondary flow structures. This difference is likely due to the large-scale turbulence. Large-scale turbulence is very effective at mixing away gradients in the flow. Mixing is not only enhanced in the wall normal direction, but the large-scale motions present in the streamwise and lateral components of turbulence are effective at both moving around flow structures and to a lesser extent mixing them away. Generally, the heat transfer appears to be about 10 to 20% higher in most locations for the higher turbulence case and the isotherms seem to have a pattern which is smoother and more aligned with the geometry of the passage. This augmentation level is lower than the level found by Radomsky and Thole and is due in part to the difference in the inlet boundary layers between low and high turbulence cases. High heat transfer rates are still present in the stagnation region and downstream from the trailing edge of the vane but the effect of the separation streamline is not apparent. In this high turbulence case the heated middle vane appears to affect the level of heat transfer in the middle of the passage. This is evident by the appearance of a 0.0012 iso-Stanton number in the upper passage with no similar feature in the lower passage. Additionally, the heat transfer level in the heated vane wake is lower than the unheated vane wake.

Figure 11 presents the Stanton number patterns for the 1,000,000 exit chord Reynolds number for the low free-stream turbulence case. The patterns show many similarities to the 500,000 Reynolds number case for the low turbulence condition. However, for this higher Reynolds number the effect of the leading edge corner vortex appears to be much more evident. A low heat transfer region adjacent to midarc on the pressure surface ($St=0.001$) appears to be due to the downwash of laminar flow from the pressure surface. Again the convergence and lift-off of the suction leg of the horseshoe vortex with the passage/pressure leg of the horseshoe vortex shows a noticeable influence on heat transfer at mid arc along the suction surface. Downstream from the trailing edge of the vanes, the influence of the wake is apparent on the endwall heat transfer. In addition, the highest velocities occur just downstream from the trailing edge and cause a high heat transfer location in between the lower wake and upper suction surface.

Figure 12 shows a psuedo picture of iso-Stanton numbers for the high turbulence, 1,000,000 Reynolds number case. The overall level of heat transfer is similar to that for the low turbulence case. This augmentation level is lower than the level found by Radomsky and Thole and is due in part to the relatively thin inlet boundary layers of the low turbulence case. However, similar to the lower Reynolds number comparison the iso-Stanton numbers have a pattern, which is smoother and has a weaker connection to typical secondary flow patterns. Again, the leading edge and wake footprint are regions of high heat transfer. The footprint of the wake is much wider than compared to the low turbulence case. This spreading is consistent with effects of turbulence on wake development documented by Ames and Plesniak [24]. However, this widening of the wake footprint may also be associated with the high heat transfer area seen for the low turbulence case.

Figure 13 shows the endwall Stanton number contours for the 2,000,000 exit chord Reynolds number with the low turbulence condition. Patterns for this condition show the influence of the vortex system in the leading edge region, downstream from the trailing edge and off the suction surface where the two vortex systems merge and are swept off the endwall. The high heat transfer, which was evident off the trailing edge of the pressure surface and between the wakes, has now expanded. The endwall region just off the pressure surface shows a region of low heat transfer likely due to laminar fluid sweeping down off the surface due the cross passage pressure gradient. Downstream of this region, steep Stanton number contours correspond to significant changes in velocity occurring on the endwall in a region where the boundary layer is expected to be thin, leading to the high heat transfer region between the wake of the lower airfoil and the suction surface of the upper one. Heat transfer off the heated vane pressure surface is noticeably lower in this figure suggesting that the consistent thermal boundary condition in this case has a significant effect.

Figure 14 presents the Stanton number contours for the higher turbulence condition at a chord exit Reynolds number of 2,000,000. The patterns are much smoother than the low turbulence condition at a 2,000,000 Reynolds number but the overall level does not appear to be significantly higher. Stanton number contours through the passage seem to be tied to the local convective velocity indicating turbulent flow on the surface. The high heat transfer footprint downstream from the pressure surface trailing edge has expanded. However, unlike the low turbulence case, which shows two distinct regions, one wake generated, and one likely generated by high velocities and thin boundary layers, the high turbulence condition shows only one high heat transfer region.

Conclusions

The present endwall heat transfer data document surface heat transfer for a low inlet turbulence with relatively thin boundary layers and for a turbulence condition generated using a mock combustor, which produces peak velocities at mid channel. The data were taken at exit chord Reynolds numbers of 500,000, 1,000,000, and 2,000,000. The data have well documented inlet boundary layers and turbulence conditions and are expected to have significant merit for use in grounding predictive methods for endwall heat transfer.

The low turbulence heat transfer contours show strong evidence of the impact of secondary flows on heat transfer patterns. Not only do the leading edge horseshoe vortex and trailing edge wake show the impact of these secondary flows on raising surface heat transfer, but the impact of the passage vortex and suction surface leg of the horseshoe vortex can be seen as well.

The inlet laminar boundary layers, which occurred at the lowest Reynolds number and turbulence condition, generally produced a lower average passage Stanton number by 10 to 20%. The overall influence of turbulence on endwall heat transfer was less dramatic for the higher Reynolds number cases. This small difference is likely due to the thin inlet boundary layers developed for the low turbulence case compared to the relatively large inlet momentum deficit of the higher turbulence case.

The high-turbulence heat transfer contours show weaker evidence of the impact of secondary flows on heat transfer patterns due to the enhanced turbulent mixing and because the larger

scales tend to push around the flow structures. High heat transfer rates in the leading edge and wake regions are still present due to the influence of the horseshoe vortex and wake.

The heated constant heat flux boundary condition on the vane generally had a noticeable influence on the heat transfer level in the passage and downstream in the wake region. However, the influence of the active vane surface was not shown to be dramatic.

Acknowledgments

The authors gratefully acknowledge the support from DOE's National Energy Technology Laboratory's Advanced Gas Turbine System Research Program, which funded this research and to Rolls Royce of Indianapolis for providing the vane geometry used in this study. Additionally, the authors would like to acknowledge the seed grant from the North Dakota EPSCoR program, which supported the development of the large-scale low speed cascade facility used in this study. In addition, the authors are indebted to the University of North Dakota for providing additional support and laboratory space and to Jay Evenstad for machine shop support. Finally, the authors would like to acknowledge the work of Dan Pelarski, Robert Stengel, Scott Ciocetto, Jeremy Stocke, and Bobby Shimpa who helped design and fabricate the original test section as a senior design project and to Troy Lassle, Mark Hettwer, Brad Wall, and Scott Lindfors who worked as summer research assistants on this project.

Nomenclature

C = vane true chord length, m
$Cf/2$ = skin friction coefficient, $Cf/2=\tau_w/\rho U_\infty^2$
Cp = specific heat at constant pressure, J/kg K
h = heat transfer coefficient, W/m^2/K, based on T_{green} and T_∞
H = shape factor, $H=\delta_1/\delta_2$
Lu = energy scale, $Lu=1.5|u'|^3/\varepsilon$
Lx = longitudinal integral scale of u' fluctuation
P = pressure, Pa
q'' = surface heat flux
Re_c = Reynolds no. based on true chord and exit conditions
$\text{Re}_{\delta 2}$ = momentum thickness Reynolds no., $\text{Re}_{\delta 2}=U_\infty\delta_2/\nu$
St = Stanton no., $\text{St}=h/(\rho Cp U_{\text{exit},\infty})$
T = temperature, K
Tu = turbulence level, $\text{Tu}=|u'|/U_\infty$
U_∞ = freestream velocity, m/s
$U+$ = velocity nondimensionalized on inner variables, $U+=U(y)/[U_\infty\cdot(Cf/2)^{1/2}]$
u', $|u'|$ = streamwise component rms fluctuation velocity, m/s
Y = normal distance from test surface, m
$Y+$ = wall normal distance nondimensionalized on inner variables, $Y+=y\cdot[U_\infty\cdot(Cf/2)^{1/2}]/\nu$
δ_1 = displacement thickness, Eq. (6.5) [25]
δ_2 = momentum thickness, Eq. (6.6) [25]
ε = emissivity
ε = turbulent dissipation rate, m^2/s^3
ν = kinematic viscosity, m^2/s
ρ = fluid density, mass per unit of volume, kg/m^3
σ = Stefan-Boltzman's constant
τ = shear stress, N/m^2

Subscripts

exit = conditions at nozzle exit plane
green = peak in green intensity condition
rad = radiative mode of heat transfer
s = static condition
t = total or stagnation condition
∞ = evaluated in free stream

References

[1] Sieverding, C. H., 1985, "Recent Progress in the Understanding of Basic Aspects of Secondary Flow in Turbine Blade Passages," ASME J. Eng. Gas Turbines Power, **107**, pp. 248–257.
[2] Klein, A., 1966, "Investigation of the Entry Boundary Layer on the Secondary Flows in the Blading of Axial Turbines," BHRA T 1004.
[3] Langston, L. S., Nice, M. L., and Hooper, R. M., 1977, "Three-Dimensional Flow Within a Turbine Cascade Passage," ASME J. Eng. Power, pp. 21–28.
[4] Marchal, P., and Sieverding, C. H., 1977, "Secondary Flows Within Turbomachinery Bladings," AGARD Conf. Proc., AGARD CP 214.
[5] Ames, F. E., Hylton, L. D., and York, R. E., 1986, unpublished work on the impact of the inlet endwall boundary layer on secondary losses and velocity vectors in a compressible turbine cascade, Allison Gas Turbine Division of General Motors.
[6] Zess, G. A., and Thole, K. A., 2001, "Computational Design and Experimental Evaluation of Using an Inlet Fillet on a Gas Turbine Vane," ASME Paper No. 2001-GT-404.
[7] Burd, S. W., and Simon, T. W., 2000, "Flow Measurements in a Nozzle Guide Vane Passage With a Low Aspect Ratio and Endwall Contouring," ASME J. Turbomach., **122**, pp. 659–666.
[8] York, R. E., Hylton, L. D., and Milelc, M. S., 1984, "An Experimental Investigation of Endwall Heat Transfer and Aerodynamics in a Linear Vane Cascade," ASME J. Eng. Gas Turbines Power, **106**, p. 159.
[9] Harasgama, S. P., and Wedlake, E. T., 1989, "Heat Transfer and Aerodynamics of a High Rim Speed Turbine Nozzle Guide Vane Tested in the RAE Isentropic Light Piston Cascade," ASME J. Turbomach., **113**, pp. 384–391.
[10] Spencer, M. C., Jones, T. V., Lock, G. D., 1996, "Endwall Heat Transfer Measurements in an Annular Cascade of Nozzle Guide Vanes at Engine Representative Reynolds and Mach Numbers," Int. J. Heat Fluid Flow, **17**, pp. 139–147.
[11] Arts, T., and Heider, R., 1994, "Aerodynamic and Thermal Performance of a Three Dimensional Annular Transonic Nozzle Guide Vane, Part-I Experimental Investigation," Paper No. 1994-31, 30th AIAA/ASME/SAE/ASEE Joint propulsion conference.
[12] Radomsky, R., and Thole, K. A., 2000, "High Freestream Turbulence Effects in the Endwall Leading Edge Region," ASME J. Turbomach., **122**, pp. 699–708.
[13] Goldstein, R. J., and Spores, R. A., 1988, "Turbulent Transport on the Endwall in the Region Between Adjacent Turbine Blades," ASME J. Heat Transfer, **110**, pp. 862–869.
[14] Giel, P. W., Thurman, D. R., Van Fossen, G. J., Hippensteele, A. A., and Boyle, R. J., 1996, "Endwall Heat Transfer Measurements in a Transonic Turbine Cascade," ASME Paper No. 96-GT-180.
[15] Boyle, R. J., and Lucci, B. L., 1996, "Predicted Turbine Heat Transfer for a Range of Test Conditions," ASME Paper No. 96-GT-304.
[16] FLUENT 5.5, 2000, FLUENT 5.5 User's Guide, Fluent, Inc., Lebanon, N.H.
[17] Hippensteele, S. A., Russell, L. M., and Torres, F. J., 1985, "Local Heat-Transfer Measurements on a Large, Scale-Model Turbine Blade Airfoil Using a Composite of a Heater Element and Liquid Crystals," MASA Technical Memo. 86900.
[18] Hippensteele, S. A., Russell, L. M., and Torres, F. J., 1986, "Use of a Liquid-Crystal, Heater-Element Composite for Quantitative High-Resolution Heat Transfer Coefficients on a Turbine Airfoil, Including Turbulence and Surface Roughness Effects," NASA Tech. Memo., 87355.
[19] Hippensteele, S. A., 1988, "High-Resolution Liquid-Crystal Heat-Transfer Measurements on the End Wall of a Turbine Passage with Variations in Reynolds Number," NASA Tech. Memo., 100827.
[20] Jones, T. V., and Hippensteele, S. A., 1988, "High-Resolution Heat-Transfer-Coefficient Maps Applicable to Compound-Curve Surface Using Liquid Crystals in a transient wind tunnel," NASA Tech. Memo., 89855.
[21] Camci, C., Glezer, B., Owen, J. M., Pilbrow, R. G., and Syson, B. J., 1998, "Application of Thermochromic Liquid Crystal to Rotating Surfaces," ASME J. Turbomach., **120**, pp. 100–103.
[22] Moffat, R. J., 1988, "Describing the Uncertainties in Experimental Results," Exp. Therm. Fluid Sci., **1**, pp. 3–17.
[23] Ames, F. E., Kwon, O., and Moffat, R. J., 1999, "An Algebratic Model for High Intensity Large Scale Turbulence," ASME Paper No. 99-GT-160.
[24] Ames, F. E., and Plesniak, M. W., 1997, "The Influence of Large Scale, High Intensity Turbulence on Vane Aerodynamic Losses, Wake Growth, and Exit Turbulence Parameters," ASME J. Turbomach., **119**, pp. 182.
[25] Kays, W. M., and Crawford, M. E., 1993, *Convective Heat and Mass Transfer*, 3rd Edition, McGraw-Hill, New York.

Measurement and Prediction of the Influence of Catalytic and Dry Low NO_x Combustor Turbulence on Vane Surface Heat Transfer

Forrest E. Ames
Mem. ASME

Chao Wang

Pierre A. Barbot

Mechanical Engineering Department,
University of North Dakota,
Grand Forks, ND 58202

New combustion systems developed for low emissions have produced substantial changes to the characteristics of inlet turbulence entering nozzle guide vanes. This paper documents the characteristics of turbulence generated by mock combustion system configurations representative of recently developed catalytic and dry low NO_x combustors. Additionally, heat transfer rates are determined on the surface of a vane subjected to inlet turbulence generated by these mock combustor configurations. Six different inlet turbulence conditions with levels ranging up to 14% are documented in this study and vane heat transfer rates are acquired at exit chord Reynolds numbers ranging from 500,000 to 2,000,000. Heat transfer distributions show the influence of turbulence level and scale on heat transfer augmentation and transition. Cascade aerodynamics are well documented and match pressure distributions predicted by a commercial CFD code for this large-scale low-speed facility. The vane pressure distribution could be characterized as a conventional or fully loaded distribution. This comprehensive data set is expected to represent an excellent test case for vane heat transfer predictive methods. Predictive comparisons are shown based on a two-dimensional boundary layer code using an algebraic turbulence model for augmentation as well as a transition model. [DOI: 10.1115/1.1559898]

Introduction

Turbulence from combustion systems has a very large influence on heat transfer distributions of first stage vanes. New strategies for achieving very low NO_x levels have produced a variety of new combustor technologies, which have a significant influence on the turbulence levels at the entrance of high-pressure turbines. Consequently, gas turbine engineers are being challenged with developing component cooling schemes, which match the heat load requirements for these new systems. In order to achieve reliable yet efficient cooling schemes for first vanes, gas turbine engineers must be equipped with knowledge of the turbulence characteristics produced by these new low NO_x combustion systems. They also need an understanding of the impact that turbulence with these characteristics has on heat transfer distributions.

The objective of this research has been to investigate the characteristics of turbulence generated by new low NO_x combustion systems and to acquire heat transfer distributions on the surface of a vane and endwall in a linear cascade facility. Consequently, a mock dry low NO_x (DLN) combustion system was designed and fabricated based on two industrial representative configurations. A mock catalytic combustion system (CC) was also developed based on an industry representative catalytic surface. In addition, for comparison purposes turbulence was generated with a low turbulence (LT) configuration, a mock aero-derivative combustion (AC) system at two upstream positions (ACS), and a biplanar square-mesh square bar grid (grid). Turbulence levels and scales have been comprehensively documented for the six turbulence configurations. Vane heat transfer distributions were taken over a four to one range of chord exit Reynolds numbers and provide a comprehensive test case to ground heat transfer predictive capabilities.

Contributed by the International Gas Turbine Institute and presented at the International Gas Turbine and Aeroengine Congress and Exhibition, Amsterdam, The Netherlands, June 3–6, 2002. Manuscript received by the IGTI November 8, 2001. Paper No. 2002-GT-30524. Review Chair: E. Benvenuti.

Background

Heat transfer on the central portion of a turbine vane is predominately two-dimensional. Consequently, heat transfer on a vane surface can be discussed in terms of the different regimes of flow. In addition to the specific velocity distribution on the surface of a vane, inlet turbulence boundary conditions are the major driver of heat transfer augmentation and transition on smooth airfoils. Therefore, this background section will discuss typical inlet turbulence conditions from combustion systems, stagnation region heat transfer augmentation, heat transfer augmentation to the laminar region on the pressure surface, transition, and augmentation to the turbulence boundary layer.

Combustor Turbulence. Values of turbulence intensity at the exit of gas turbine combustion systems reported in the literature have ranged from about 7% to nearly 30% (see Dils and Follansbee [1], Zimmerman [2], Bicen and Jones [3], Ames and Moffat [4], Moss and Oldfield [5], Goebel et al. [6], Zhang and Glezer [7], Ames [8], and Van Fossen and Bunker [9]. Ames [8] measured turbulence downstream from a mock aeroderivative combustor and suggested that turbulence scale, *Lu*, was typically 1/3 to 1/2 of the inlet passage. For most conventional combustion systems, which depend on large-scale recirculation to stabilize flames, turbulence level seems to depend on length to height ratio of the combustor and on the main flow to turbine inlet contraction ratio. For example in this present paper, the turbulence intensity downstream from the mock dry low NO_x (DLN) combustor is about 14.3% for the two to one combustor area to inlet flow contraction ratio. Van Fossen and Bunker [9] report turbulence levels of 27% downstream from their DLN combustion system with its 1

to 0.9 combustor flow to inlet area contraction. Since the local fluctuation velocity and scale are the main drivers for heat transfer augmentation and transition, understanding turbulence conditions in turbine passages is critical for accurate predictions.

Stagnation Region Heat Transfer Augmentation. Stagnation regions often have the highest heat transfer rates on a turbine airfoil. Relative heat transfer rates in stagnation regions tend to increase with lower chord Reynolds numbers and higher inlet to exit velocity ratios. Inlet turbulence can produce augmentation levels more than 50% greater than the low turbulence baseline level. Recent research (Ames and Moffat [4] and Van Fossen et al. [10]) has shown that both scale and turbulence intensity have a significant impact on stagnation region heat transfer. Hunt [11] predicted that relatively small-scale turbulence is amplified by vortex stretching resulting from the strain field applied by a stagnation region flow. Britter et al. [12] later corroborated this theory. Ames and Moffat applied Hunt's work to the development of an algebraic eddy viscosity model and a correlating parameter, which are used to predict and correlate the results of this experimental investigation.

Laminar Region Heat Transfer Augmentation. In spite of significant disturbances due to free-stream turbulence, the pressure surface of a vane is typically laminar when exit chord Reynolds numbers are below one million due to the high flow field acceleration. However, a significant level of heat transfer augmentation can take place due to mixing caused by the external turbulence. For example, Arts et al. [13] found augmentation levels of up to 100% on the laminar portion of a vane subjected to 6% grid turbulence. Ames [8] found laminar augmentation scaled on turbulence intensity, chord to length-scale ratio to the 1/3rd power, and Reynolds number to the 1/3rd power. He suggested that this 1/3rd power Reynolds number scaling was consistent with no noticeable amplification of turbulence occurring. However, his Reynolds numbers range was limited. Wang, Goldstein, and Olson [14] looked at the effect of high turbulence levels with large scale on turbine blade mass transfer. The suction surface of their blade had a favorable pressure gradient to midchord and they found increasing mass transfer augmentation and earlier transition with increasing turbulence level and Reynolds number. The pressure surface of their blade had an overspeed region, which made comparative assessment of parametric affects more difficult.

Transition. Mayle [15] presented a relatively comprehensive account of transition on the surface of a turbine airfoil. He suggests onset of transition is largely affected by the momentum thickness Reynolds number and turbulence level. However, he indicates that turbulent scale likely impacts transition onset as well. In addition, transition is suppressed on surfaces with high acceleration rates, where K is greater than 3E-6, even at high levels of turbulence. Zhang and Han [16] looked at the effect of grid generated turbulence on heat transfer augmentation and transition on a turbine blade. Their results showed that at roughly equivalent turbulence levels, their finer grid produced earlier transition on the suction surface. This study indicates that turbulent length scale may have an impact on transition onset. In addition, Boyle and Simon [17] suggest that Mach number significantly influences transition length.

Turbulent Boundary Layer Augmentation. Ames and Moffat [4] and Thole and Bogard [18] have shown that relatively large-scale turbulence has a reduced influence on turbulent boundary layer heat transfer augmentation. Consequently, thin turbulent boundary layers on first vane suction surfaces are typically not strongly influenced by the relatively large-scale turbulence produced by combustion systems.

Experimental Approach

This heat transfer research has been conducted in the University of North Dakota's large-scale low-speed cascade facility. This facility is configured in a steady state blow down arrangement. The cascade test section is shown schematically in Fig. 1. Air enters the facility through a large inlet filter, which protects the hot wires from fouling. The wind tunnel is powered by a 45-kW blower capable of providing 6.6 m^3/s of air at a static pressure rise of 5000 Pa. The blower outlet flow is directed through a two stage multivane diffuser section to distribute and diffuse the flow prior to entering a heat exchanger. The heat exchanger system, which uses a cooling water recirculation system, helps to provide a steady and controllable inlet air temperature. The flow is further conditioned downstream of the heat exchanger in a four section screen box. The low turbulence baseline configuration uses a 3.6:1 area ratio two-dimensional nozzle to further accelerate the air prior to entrance into the linear vane cascade test section.

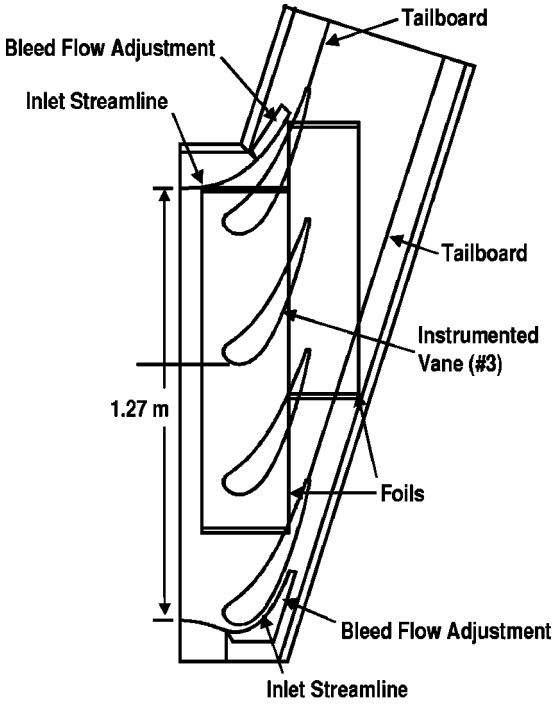

Fig. 1 Schematic of cascade test section for large-scale low-speed wind tunnel

The cascade test section used in this study is based on an eleven times scale midspan vane profile representative of a modern mid-sized industrial gas turbine and is displayed in Fig. 2. The vane profile was designed specifically for incompressible flow and has a velocity distribution, which is consistent with current conventionally or fully loaded vanes in industrial engines. The cascade test section, shown in Fig. 1, was designed to produce accurate two-dimensional aerodynamics with a four-vane three-passage configuration. The cascade has inlet bleeds designed along 2-D streamlines to allow for the proper flow around the top and bottom vanes. These inlet bleed sections were calculated using a 2-D FLUENT [19] simulation. These inlet bleeds provide control of the inlet flow uniformity, which is verified by a row of 30 static pressure taps placed 7 cm upstream from the vane leading edge plane. The cascade also has flexible exit tailboards, which can be shaped along exit streamlines to control the exit flow periodicity. The cascade has a row of exit taps one-quarter axial chord downstream of the trailing edge plane to monitor the exit flow periodicity. Ten probe access ports are provided along the row of inlet static pressure taps to measure inlet temperature and total pressure and to survey inlet turbulence characteristics.

The eleven times scale vane has a true chord of 47.8 cm and an axial chord of 25.0 cm. The vanes have a 38.4 cm spacing and a height of 25.4 cm. The diameter of the leading edge is 5.59 cm

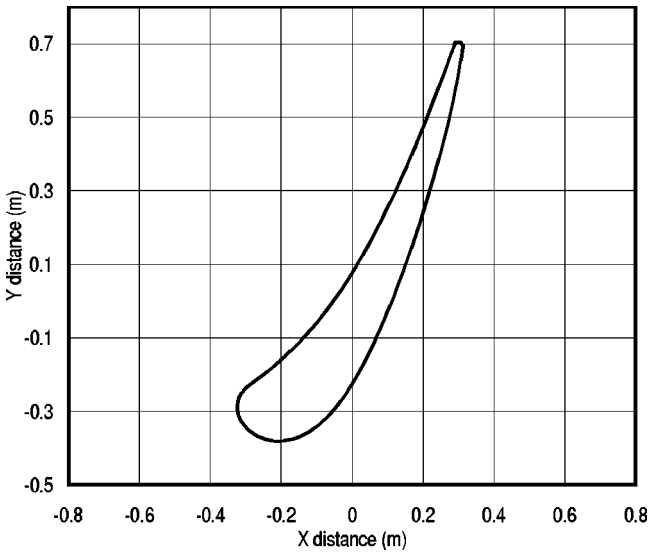

Fig. 2 Cross-sectional view of large-scale conventionally loaded vane used in this study

and the diameter of the trailing edge is 0.98 cm. The stagger angle of the vane is 55.1 deg and the calculated air exit angle is 73.4 deg.

The cascade was run at exit Reynolds numbers based on true chord of 500,000, 1,000,000, and 2,000,000. Exit velocity and pressure were calculated based on inlet total pressure and temperature and the average exit static pressure at the row of exit static pressure ports. This range of Reynolds numbers is consistent with values for small to medium industrial or propulsion gas turbine engines.

Turbulence Generators. This study was designed to investigate turbulence characteristics representative of modern low NO_x combustion systems and their influence on vane heat transfer. Two separate low NO_x configurations were developed. One configuration represented a conventional dry low NO_x combustion system and the other a catalytic combustion system. In addition, an aeroderivative combustion system was developed to provide turbulence with characteristics, which are representative of many current engines and has been documented in the literature. All three mock combustion systems used the same combustor liner and nozzle configuration, which is shown with the aeroderivative geometry in Fig. 3. This liner geometry replaces the 3.6:1 area ratio nozzle for the high turbulence test cases. For the low NO_x combustor configurations the side panels of the mock combustor system are replaced with solid panels and either the swirler arrangement or the catalytic surface are attached at the back panel position. The swirler arrangement for the conventional DLN is shown in Fig. 4, while the mock catalytic surface is shown in Fig. 5.

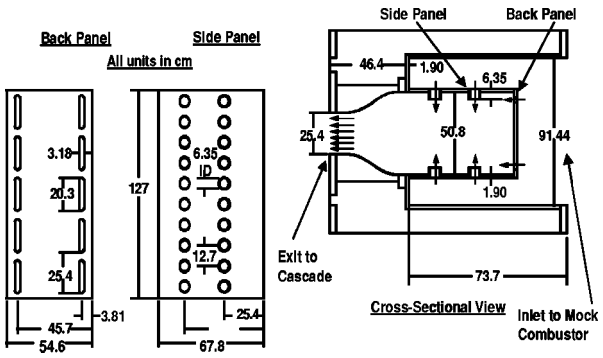

Fig. 3 Schematic of mock aeroderivative combustor turbulence generator

Fig. 4 Digital photo of dry low NO_x swirlers installed in mock combustor liner

The back panel for the mock DLN combustor consists of ten swirlers. Each swirler is fabricated from a 20.3-cm schedule 40 PVC pipe and has a 5.1-cm centerbody. Each swirler has 12 vanes, which are essentially a 36-deg projection of a 45-deg slice through the pipe. The design of the low NO_x combustion system is a compromise between the model dry low NO_x system published by Van Fossen and Bunker [9] and a green thumb combustor system of Rolls Royce [20]. The Van Fossen mock combustor had a swirler flow to combustor liner flow area ratio of 33% and a vane inlet flow to combustor liner flow area ratio of 90%. The swirlers used by Van Fossen had 45 deg vanes. The Rolls Royce green thumb combustor has a swirler to combustor flow area ratio of 40% and a vane inlet area to combustor flow area ratio of 33%. The swirler vane angles range from 45 to 60 deg. The current design has a swirler flow to combustor flow ratio of 46% and an inlet to liner flow ratio of 50%.

The mock catalytic combustion system was crafted after the system used by Catalytica. Catalyica's foil has a serpentine groves running across it. These grooves are spaced 2.2 mm apart. As the foils are folded back across each other and rolled together to form a round porous structure, grooves from one side of the foil cross with grooves from the adjacent foil helping to promote mixing. UND's mock catalytic combustor is made from evaporative cooling pads, which contain the same type of crossing grooved channels. The evaporative cooling pads are 12 times the size of the actual catalytic combustor surface. This scaling is very similar to the vane scaling, which is 11 times the actual size.

Turbulence was also generated using a square bar square mesh biplanar grid. The grid used 1.27 cm square bars, which were spaced on 6.35 cm centers producing a 64% open area grid. The grid was held 63.5 cm or ten mesh lengths upstream of the vane leading edges for the heat transfer tests. The grid was held in a

Fig. 5 Digital photo of catalytic combustor surface installed in mock combustor liner

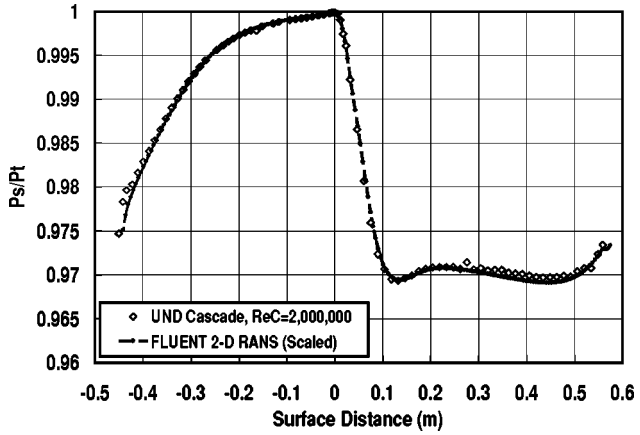

Fig. 6 Comparison between measured and predicted vane midspan pressure distribution

25.4 cm by 127 cm rectangular spool section, which was 91.5 cm long and attached between the 3.6:1 area ratio nozzle and the cascade test section.

In addition, a second level of turbulence was generated with the mock aero-combustor turbulence generator using the 91.5 cm long, 25.4 cm wide, and 127 cm high rectangular spool as an extended development length. For this condition the spool section was placed between the mock combustor and the inlet to the cascade to allow for the decay of turbulence.

Vane Pressure Distribution. The third vane from the bottom was used to acquire the heat transfer and pressure distributions. This ''instrumented'' vane can be inserted through a machined hole in the acrylic endwall where it is held in place using a flange. The pressure vane was cast out of epoxy with 82 pressure tubes incrementally spaced along and cast adjacent to its surface. Static pressure taps were fabricated by drilling through the epoxy surface into the brass tube with a 0.8-mm-dia drill bit. The baseline pressure distribution for the low turbulence case is shown in Fig. 6 where it is compared to a prediction using FLUENT. On this figure negative surface distance is taken from the calculated stagnation point (0 cm) along the pressure surface toward the trailing edge and positive surface distance is determined along the suction surface. The viscous prediction matches the data with precision. Overall, the comparison is excellent and provides confidence in the quality of the midspan aerodynamics produced by the cascade. Developing accurate aerodynamics is critical to producing a heat transfer database, which is valuable for understanding the impact of new combustion systems and for grounding predictive methods.

Heat Transfer Vane Description. The heat transfer vane has a polyurethane foam core with a 1.6-mm epoxy shell cast around it. The present heat transfer data were acquired using the 52 fine wire chromel-alumel thermocouples cast around the surface. The vane was covered with a 0.023-mm Inconel foil bonded to a 0.127-mm sheet of Kapton and backed with 0.05 mm of high temperature acrylic adhesive. The 101.6 cm by 25.4 cm foil has 6.35 mm by 0.5 mm copper bus bars soft soldered to its ends to evenly distribute the large DC current used to produce the constant surface heat flux. These copper bus bars are recessed into the surface of the epoxy near the trailing edge on both the pressure and suction surfaces. The resulting Inconel foil, as adhered to the epoxy surface, produces an aerodynamically smooth visually attractive heat transfer surface. The heating ends 1.3 cm from the trailing edge on both the pressure and suction surfaces.

Heat transfer baselining tests were conducted for the low turbulence condition over the four to one range in Reynolds numbers. Prior to heating the foil, the recovery temperature distribution was acquired for each Reynolds number. Subsequently, the midline surface temperature distribution was acquired at the desired surface heat flux condition. Surface heat flux was determined by measuring the voltage across and the current through the heater. The heater current was determined using a precision shunt resistor. Only radiation losses were accounted for. Due to the relatively thick and very low conductivity polyurethane core, conduction through the vane was ignored. Conduction along the surface of the foil was also ignored due to the thin Inconel foil. Radiation losses were estimated using the local surface temperature radiating to the inlet total temperature using a foil emissivity of 0.21 and assuming a blackbody background. As a consistency check heat transfer data were acquired at one-half and full power. The resulting root mean square difference was only 0.5% with a maximum variation of 1.7%.

A comparison between the experimentally determined Stanton number distribution and a finite difference boundary layer calculation (STAN7 Kays [21]) using the predicted pressure distribution is shown in Fig. 7 for the three low turbulence cases. Notice that all three distributions are laminar. The comparisons between the predicted and experimental Stanton number distributions are generally better than 10% and give confidence in the experimental technique.

Data Acquisition. Pressures were acquired using two Rosemount Smart Pressure Transmitters scaled to ranges of 250 and 5000 Pa full scale with 0.1% of scale accuracy. Both transmitters were read for each pressure and the most sensitive reading was kept. Pressures were scanned using a homemade miniature solenoid valve system and were referenced to the inlet total pressure. Transmitters were zeroed at the beginning of each use to minimize uncertainties due to drift. Voltage outputs for both the pressure transmitters and for the chromel-alumel thermocouples were scanned and read using an HP 3497A data acquisition system. The data acquisition unit has an integral voltmeter with 1 μV sensitivity. Thermocouples were all connected through a passive constant

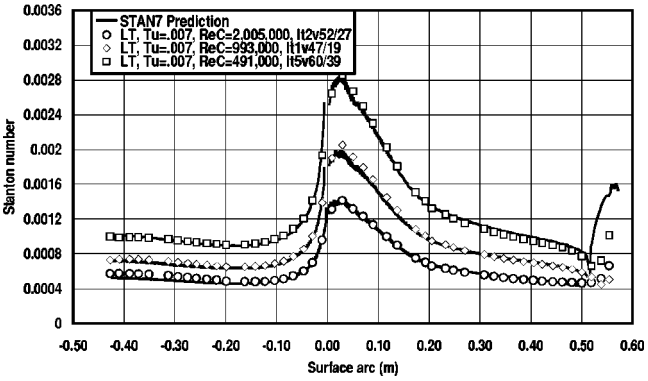

Fig. 7 Low-turbulence vane Stanton number distributions with STAN7 predictions

temperature junction and were referenced using an ice bath. Hot wires were powered, low-pass filtered, bucked and gained using a two-channel TSI ISA 300 hot wire anemometry bridge. Raw signals were read with a PC based high-speed data acquisition card with 12 bits of resolution. Mean velocities were acquired at a data acquisition rate equivalent to about three integral time scales. Velocity time records for spectral analysis were acquired in 40 sets of 8192 samples and post processed.

Data Uncertainties. Estimates for the uncertainty in heat transfer, pressure, velocity, and turbulence measurements were determined using the root sum square method described by Moffat [22]. Based on a data reduction program perturbation method, *N*th-order uncertainty in reported local Stanton number ranged to plus or minus 5% at a 95% confidence interval. The uncertainty estimate for run-to-run comparisons was estimated at plus or minus 3%. Uncertainty in the local vane surface static pressure was estimated at a maximum of 2.5%. Exit velocity was determined at a precision of 2%. The uncertainty in turbulence level for the single wire was estimated to be 3% of the reported value. The experimental error in turbulent scale is estimated to be 11%. All uncertainty estimates are quoted for a 95% confidence interval.

Inlet Conditions and Turbulence Characteristics. A total of six different turbulence conditions were developed for this midspan heat transfer investigation. Both heat transfer data and turbulence measurements were taken for all turbulence conditions and Reynolds numbers. Velocity and turbulence data were acquired at the midspan of the inlet at five positions distributed evenly across one passage 7-cm upstream from the leading edge plane of the vanes. The turbulence level (Tu), average midspan velocity (U), integral scale (Lx), energy scale (Lu), and dissipation (ε) were determined for each condition and averages are presented in Table 1. Mean velocity and turbulence intensity were determined from 8192 data samples acquired at a time increment equal to about two or three integral time scales. Turbulent scales and dissipation rates were determined from 40 records of 8192 points taken at 10 to 35 kHz depending on the cascade inlet velocity. This allows for better statistical resolution of the power spectrum at the lower wavenumbers. The longitudinal integral scale was determined using Taylor's hypothesis by multiplying the integral time scale by the local convective velocity. The integral time scale was determined by integrating the autocorrelation in time to the first zero crossing. The autocorrelation was calculated using an inverse FFT of the average power spectral density function of the velocity time records.

The energy scale (or dissipation scale of Hancock and Bradshaw [23]), Lu is a macroscale of turbulence estimated from 1.5 times the cube of the rms value of u' divided by the dissipation rate.

$$Lu = 1.5|u'|^3/\varepsilon \tag{1}$$

The dissipation rate is determined from the inertial subrange of the u' power spectrum. Hinze [24] suggests that in the inertial subrange of a turbulent spectrum for u' the spectrum function can be related to the dissipation rate and the wavenumber.

$$E_1(k_1) = 18/55A\varepsilon^{2/3}k_1^{-5/3} \tag{2}$$

Ames and Moffat [25] suggest that the constant A be taken as 1.62. The energy scale is quite useful because as Hinze [24] suggests, the dissipation rate alone determines the spectrum from the start of the inertial subrange to the end of the dissipation range. Also, since the integral of the one-dimensional spectrum of u' is equal to $|u'|^2$, the turbulence intensity, local velocity, and energy scale provide a quantitative description of an energy spectrum. A typical one-dimensional spectrum of u' is shown in Fig. 8 as taken downstream from the mock aeroderivative turbulence generator.

The circumferential uniformity of the streamwise fluctuation velocity, $|u'|$, and the dissipation level were quite good across the inlet of the cascade for the four highest turbulence levels generated. The grid turbulence dissipation level and $|u'|$ varied by less than 5% across the survey plane. The dissipation level and $|u'|$ for the mock aeroderivative combustor varied by no more than 10%. The mock DLN combustor produced a dissipation level which was uniform within 11% and a $|u'|$ level which was uniform within 15%.

Table 1 Characteristics of inlet velocities, turbulence level and scale, and dissipation for various turbulence generators

	Reynolds	Tu	U (m/s)	Lx (cm)	Lu (cm)	ε (m^2/s^2)
low turbulence	500,000	0.0069	4.96	8.12	127.0	0.00005
[LT]	1,000,000	0.0076	10.43	5.02	154.5	0.00035
	2,000,000	0.0060	18.71	3.58	15.5	0.0144
aeroderivative	500,000	0.1313	5.24	3.68	7.24	6.67
combustor	1,000,000	0.1402	9.32	3.52	6.36	51.5
[AC]	2,000,000	0.1339	18.39	3.58	7.35	302.0
grid	500,000	0.0821	4.77	2.00	3.27	2.70
[grid]	1,000,000	0.0861	10.19	2.04	3.35	29.8
	2,000,000	0.0884	19.27	2.35	3.53	206.8
catalytic	500,000	0.0103	4.95	5.26	3.83	0.0052
combustor	1,000,000	0.0153	9.46	0.62	5.15	0.093
[CC]	2,000,000	0.0102	19.63	0.89	1.75	0.680
combustor	500,000	0.0915	5.11	5.08	9.03	1.67
with spool	1,000,000	0.0950	9.74	4.61	8.81	13.23
[ACS]	2,000,000	0.0928	18.19	4.44	9.49	75.17
dry low NO_x	500,000	0.1342	5.17	4.57	8.78	5.60
[DLN]	1,000,000	0.1433	9.65	4.34	8.95	43.73
	2,000,000	0.1417	19.11	4.47	10.77	274.5

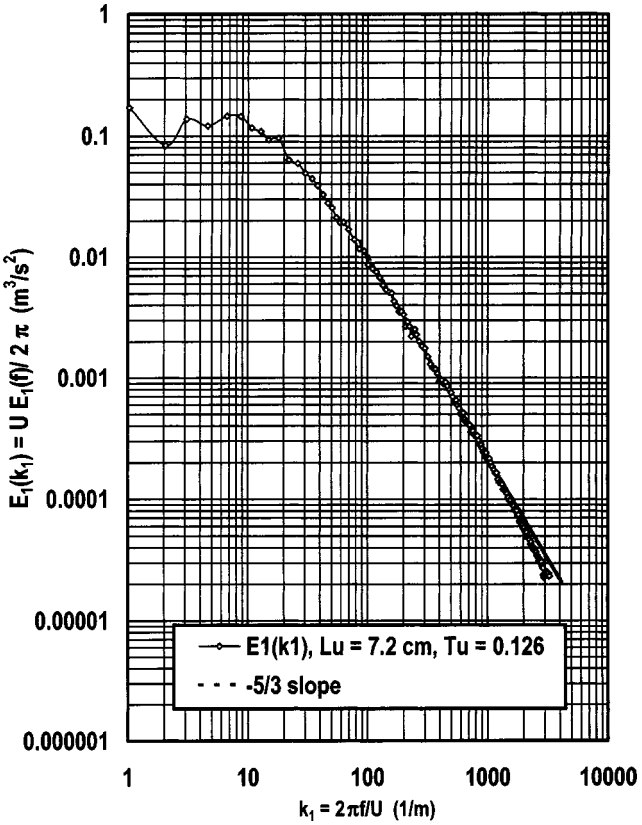

Fig. 8 One-dimensional spectra of u' for aero-derivative combustor

Heat Transfer Results

This section examines the vane surface heat transfer results both qualitatively and quantitatively for the influence of turbulence, scale, and Reynolds number on heat transfer augmentation and location of transition. First, the qualitative effects of the turbulence on augmentation and location of transition will be observed. Next, the level of augmentation in the laminar regions of the flow will be examined quantitatively in terms of turbulence level, scale and Reynolds number. Finally, heat transfer predictions will be made using STAN7 [21], the augmentation model of [25], and the transition model of [15].

Stanton Number Results. Stanton number distributions are presented in Figs. 9 through 11 for all six turbulence conditions for exit chord Reynolds numbers of 500,000, 1,000,000, and 2,000,000. The figures plot Stanton number versus surface distance with negative surface distance taken over the pressure surface and positive surface distance taken over the suction surface. The turbulence intensities quoted in the figures have been adjusted to account for the decay, where $\mathrm{Tu}(x)=1/[1/\mathrm{Tu}(0)+x/(2\,Lu)]$. Figure 9 presents the distributions of the six turbulence conditions for the 500,000 Reynolds number case. Here the low turbulence (LT) case shows laminar flow over the entire surface. The catalytic combustor produces a turbulence level of only 1.0% with about a 2-cm energy scale (Lu) and shows little effect from the turbulence. This low turbulence level produced by the catalytic combustor has significance for heat transfer designs as flow over the majority of the vane surface will be laminar. Turbulence produced by the grid and the aero-combustor with spool (ACS) significantly augments laminar heat transfer on the pressure surface and stagnation region and leads to transition on the suction surface. Notice that the grid condition transitions earlier than the aero-combustor with spool in spite of the latter's higher turbulence level. This slightly earlier transition is likely the result of the

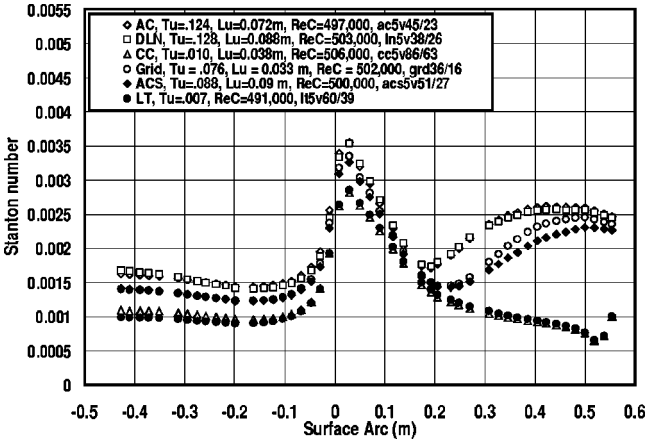

Fig. 9 Effects of mock combustor turbulence characteristics on vane Stanton number distributions, Re_c=500,000

grid turbulence's smaller scale and occurs at all three Reynolds numbers. This observation is consistent with the expectations of Mayle [15]. Results for the mock dry low NO_x (DLN) and aero-combustor (AC) show similar trends but higher heat transfer augmentation in the laminar flow regions and earlier transition on the suction surface. Notice that the smaller scale turbulence of the

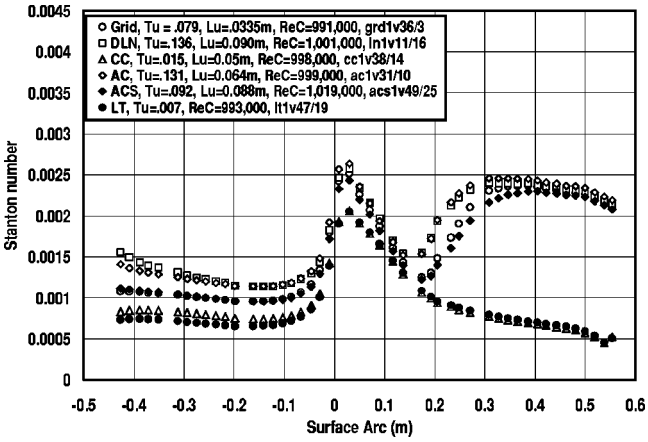

Fig. 10 Effects of mock combustor turbulence characteristics on vane Stanton number distributions, Re_c=1,000,000

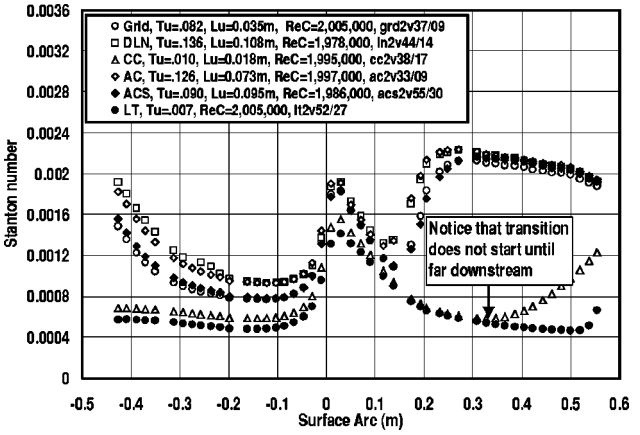

Fig. 11 Effects of mock combustor turbulence characteristics on vane Stanton number distributions, Re_c=2,000,000

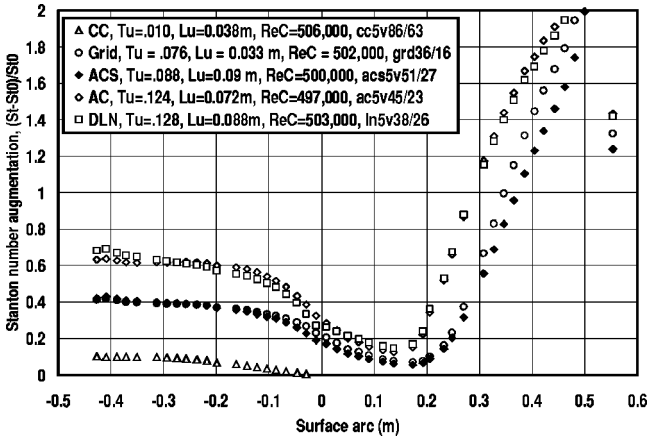

Fig. 12 Effects of mock combustor turbulence characteristics on Stanton number augmentation and location of transition, Re_c=500,000

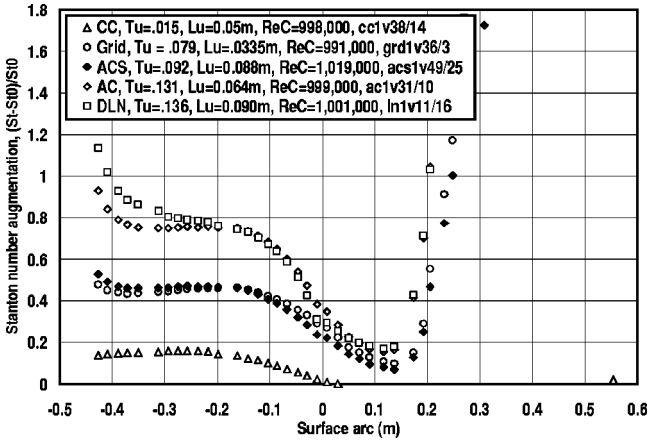

Fig. 13 Effects of mock combustor turbulence characteristics on Stanton number augmentation and location of transition, Re_c=1,000,000

mock AC compensates for the slightly higher turbulence level of the mock DLN combustor in terms of laminar augmentation and transition location.

Figure 10 presents Stanton number distributions for six turbulence conditions for the 1,000,000 chord Reynolds number case. Qualitatively the trends for the six turbulence cases are very similar to the lower Reynolds number data. However, laminar region augmentation levels are higher, suction surface transition occurs at an earlier location, and the AC and DLN cases show signs of the initiation of transition at a surface distance of about −0.3 m. Additionally, at this higher Reynolds number the turbulent boundary layer Stanton numbers on the suction surface now approach the level of heat transfer in the stagnation region. Figure 11 presents Stanton number distributions for the 2,000,000 chord Reynolds number case. Again the trends are qualitatively similar but laminar augmentation levels are higher and suction surface transition occurs even earlier. Also, the four higher turbulence cases (DLN, AC, ACS, and Grid) show signs of transition on the pressure surface at a surface location of about −0.22 m. For this higher Reynolds number case the catalytic combustor now shows some laminar augmentation on the pressure surface and the start of transition on the suction surface at a surface arc of 0.31 m. At this Reynolds number the turbulent boundary layer Stanton numbers on the suction surface exceed those of the laminar stagnation region.

Pressure Surface Heat Transfer Augmentation. Heat transfer augmentation to the pressure surface is presented as $(St\text{-}St_0)/St_0$ versus surface distance in Figs. 12 through 14. Figure 12 presents the 500,000 chord Reynolds number case. The pressure surface or negative surface arc shows a rising increase past the stagnation region and a relatively steady value further downstream past a surface arc of −0.1 m. This behavior indicates laminar augmentation due to turbulence. The augmentation levels at −0.2 m are about 6% for the mock catalytic system, 36% for the grid and aerocombustor with spool, and about 58% for the aerocombustor and DLN combustor. The increase on the suction surface is of course due to transition. Figure 13 shows the fractional increase in Stanton number for the 1,000,000 Reynolds number case. The majority of the pressure surface shows laminar behavior. However, these augmentation curves show a change in behavior toward the aft end of the surface with upturn in augmentation rate. This behavior is consistent with the start of transition on the pressure surface and it occurs for the four highest turbulence levels. The laminar augmentation levels at −0.2 m are about 14% for the mock catalytic combustor, 46% for the grid and aero-combustor with spool, and 75% for the aero and DLN combustors. Figure 14 shows Stanton number augmentation for the 2,000,000 Reynolds number case. The augmentation curves suggest transition starts at about −0.3 m for the grid and aero-combustor with spool and at −0.2 m for the aero and DLN combustors. Since the onset of transition is similar for the grid and aero-combustor with spool, while the scale and turbulence level is somewhat different, these heat transfer data sets may be useful for testing transition models. Further, the laminar augmentation levels at −0.2 m are about 22% for the catalytic combustor, 64% for the grid and aero-combustor with spool and about 98% for the aero and DLN combustors. Augmentation noticeably increases with Reynolds number and turbulence intensity. Comparisons between the grid and aero-combustor with spool suggest that given similar turbulence levels and Reynolds number, augmentation increases with decreasing scale.

Ames [8] suggested that heat transfer augmentation to a laminar boundary layer should scale on turbulence intensity (Tu), Reynolds number to the 1/3rd power and energy scale (Lu) to the negative 1/3rd power. That is $(St\text{-}St_0)/St_0 \propto Tu\,Re_C^{1/3}(C/Lu)^{1/3}$. This implies that the dissipation of the turbulence adjacent to a pressure surface boundary layer is unaltered by the boundary layer velocity gradient or the streamwise acceleration. Further, as indicated in [25] this $Tu^*Lu^{-1/3}$ dependency implies that the relatively larger turbulent eddies in the v' spectrum are blocked by the presence of the wall leaving only the smaller eddies to penetrate into the thin pressure surface boundary layer and augment

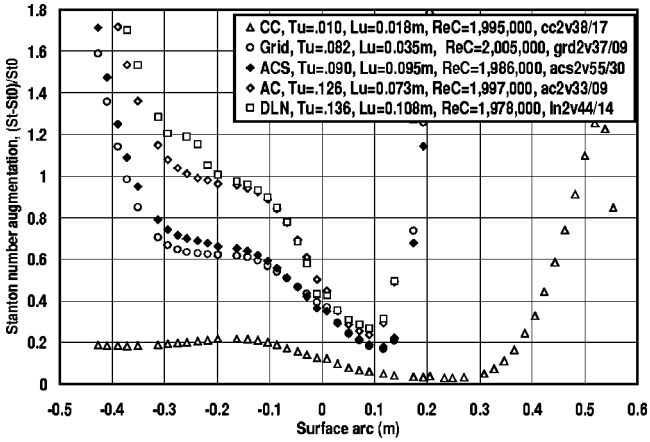

Fig. 14 Effects of mock combustor turbulence characteristics on Stanton number augmentation and location of transition, Re_c=2,000,000

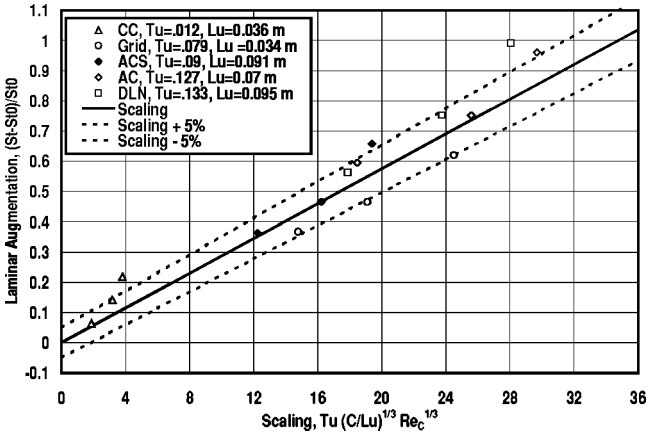

Fig. 15 Correlation of pressure surface Stanton number augmentation with turbulence intensity, energy scale, and chord Reynolds number

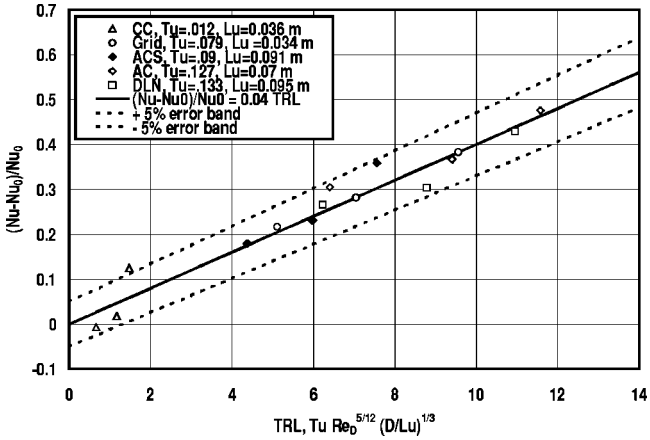

Fig. 16 Correlation of stagnation region Nusselt number augmentation with TRL parameter

mixing. Ames [8] studied heat transfer on a vane pressure surface at chord Reynolds numbers of 800,000 and 500,000. He concluded that the data supported a Reynolds number dependence of a 1/3rd power for laminar heat transfer augmentation of the pressure surface boundary layer. He suggested that this dependence was also supported by a simple asymptotic analysis of a laminar boundary after Ames and Moffat [4]. The present data represent an opportunity to test this physical model across a much wider (4 to 1) range in Reynolds numbers. Figure 15 presents augmentation levels $(\mathrm{St}\text{-}\mathrm{St}_0)/\mathrm{St}_0$ on the pressure surface versus the heat transfer dependence parameter, $\mathrm{Tu}\,(C/Lu)^{1/3}\,\mathrm{Re}_C^{1/3}$ for average augmentation levels at -0.162 and -0.199 m. A best-fit line through the data is shown along with plus and minus 5% error bands with very good results. These data provide support of the above augmentation dependence.

Stagnation Region Augmentation. At lower chord Reynolds numbers heat transfer levels in the stagnation region of a vane or blade are often higher than any other location as shown in Figs. 9 and 10. Consequently, predicting heat transfer accurately in this region is critical to designing cooling methods, which are reliable and efficient. Heat transfer through the laminar boundary layer in a stagnation region is different than on a pressure surface due to the rate of strain, which is present there. Hunt [11] first predicted the response of small and large scale turbulent eddies to the straining, which occurs in the stagnation region of a cylinder using rapid distortion theory. He concluded that the relatively small scale eddies are amplified as they are stretched around the stagnation region of a cylinder by the approaching flow and the large scale eddies are largely blocked by the cylinders presence. Britter et al. [12] later experimentally verified this conclusion. Ames and Moffat [4] used the results of Hunt to develop a simple model spectrum for turbulence approaching a cylinder stagnation point. They used the spectrum model in a simple asymptotic analysis to develop a correlating parameter for stagnation region heat transfer, which included the effect of scale. Based on this analysis heat transfer augmentation $[(\mathrm{Nu}\text{-}\mathrm{Nu}_0)/\mathrm{Nu}_0]$ in a stagnation region is expected to increase as a function of turbulence intensity, Reynolds number to the 5/12th power, and diameter to energy scale to the 1/3rd power. That is $(\mathrm{Nu}\text{-}\mathrm{Nu}_0)/\mathrm{Nu}_0 \propto \mathrm{Tu}\,\mathrm{Re}_D^{5/12}(D/Lu)^{1/3}$. The different Reynolds number dependence compared to the pressure surface is due to the amplification of the turbulence from the straining effect. Since the present data represents a relatively wide range of turbulence levels and Reynolds numbers, it provides a good test to this correlation. Ames [8] suggests a good engineering approximation for this correlation is $(\mathrm{Nu}\text{-}\mathrm{Nu}_0)/\mathrm{Nu}_0 = 0.04\,\mathrm{Tu}\,\mathrm{Re}_D^{5/12}(D/Lu)^{1/3}$. Figure 16 presents stagnation region heat transfer augmentation data in terms of $(\mathrm{Nu}\text{-}\mathrm{Nu}_0)/\mathrm{Nu}_0$ versus the $\mathrm{Tu}\,\mathrm{Re}_D^{5/12}(D/Lu)^{1/3}$ for the two data points on either side of the predicted stagnation point (-0.01 and $+0.0088$ m). The solid line represents the above correlation, while data for the three Reynolds numbers are presented for each of the five higher turbulence conditions. The data are well correlated by this turbulence parameter and all data fall within $+/-7.4\%$ of the line. Considering the collective uncertainty of the turbulence parameter is $+/-5\%$ and the repeatability of the heat transfer data is $+/-3\%$, the correlation fits the data with very good accuracy.

Finite Difference Boundary Layer Predictions. These data provide an excellent test for vane heat transfer predictive capabilities due to the range of turbulence conditions and Reynolds numbers present as well as the relevant fully loaded vane design. Two-dimensional finite difference boundary layer predictions were made for this complete data set using the algebraic turbulence model [ATM] of [25], the transition model of Mayle [15], and STAN7 [21], a finite difference boundary layer code. The ATM is a simple spectral model of v' turbulence accounting for the attenuation of large eddies in the proximity of the wall due to the wall's blocking effect. It was originally developed to predict the augmentation to a turbulent boundary layer [4] and was shown to produce the correct near wall eddy viscosity distributions in a laminar boundary layer developing on the pressure surface of a vane by Ames, Kwon, and Moffat [25]. The basic model is given as follows:

$$\nu_{M,0} = 1.5 C_\mu \mathrm{Tu}_\infty U_\infty L u_\infty [1 - \exp(-2.9Y/Lu_\infty)]^{4/3} D_\nu \qquad (3)$$

The near wall damping function, D_ν, accounts for the effect of viscous action on the turbulent spectrum and is presented below:

$$D_\nu = (1 - \exp(-y/[\eta C_\eta])) \qquad (4)$$

η is the Kolmogorov length scale and C_η is a constant set equal to 6.7. Note that the constant, C_η was erroneously given in the numerator rather than the denominator of the exponential in [25]. STAN7 uses the inlet approach velocity, turbulence level, and energy scale for the inlet turbulence boundary conditions and predicts the decay of turbulence using the freestream turbulent kinetic energy equation. For these heat transfer predictions, the turbulent Prandtl number is taken as 0.85. This value is an estimate and data are needed to determine the actual turbulent Prandtl number across an accelerating laminar boundary layer subjected to high levels of flow field turbulence.

Heat transfer predictions are shown for the three Reynolds numbers in Figs. 17, 18, and 19. Largely, the level of augmentation predicted by the ATM matches the experimental augmentation on the laminar region of the pressure surface well. On the

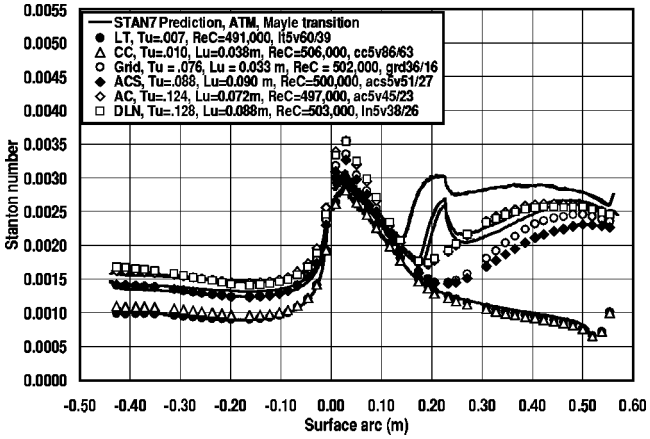

Fig. 17 Prediction of turbulence effects on vane Stanton number distributions using STAN7 with ATM and Mayle [15], Re_c =500,000

pressure surface for the lower Reynolds number shown in Fig. 17, the data are as much as 12% below the predictions midway along the pressure surface but improve toward the trailing edge. This represents the largest discrepancy found in the laminar region of the pressure surface for all data sets. On the suction surface near the stagnation region, the calculations underpredict the level of augmentation because the ATM does not account for the action the rapid strain has on the turbulence in the stagnation region. This underprediction for the stagnation region is consistent across all three Reynolds numbers. The pressure surface data of Figs. 18 and 19 for chord exit Reynolds numbers of one and two million show the start of transition. For the one million Reynolds number, Mayle's [15] transition model begins to predict transition when the acceleration parameter, *K*, drops below 3E-6 on the pressure surface at a surface arc of −0.35 m. Augmentation data in Fig. 13 suggest that this location is appropriate for the grid, aero-combustor with spool, and aero-combustor. However, the data for the DLN combustor indicate that transition may start before −0.3 m. For the highest Reynolds number the acceleration constraint allows transition to proceed after a surface arc of −0.25 m. However, the DLN combustor data indicate transition starts at around −0.2 m. In spite of slight discrepancies in the location of transition, Mayle's transition model performs very well on the pressure surface for these data.

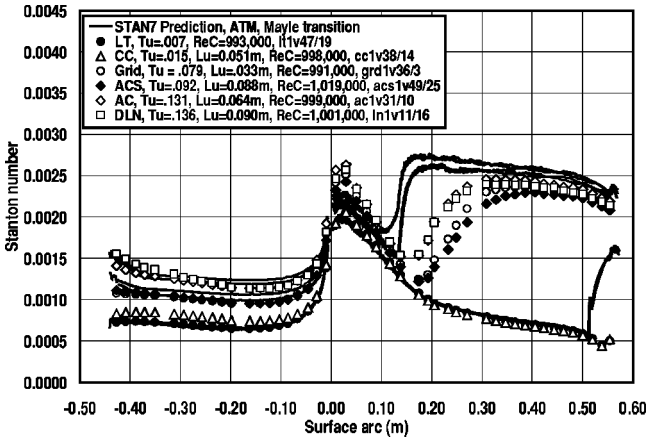

Fig. 18 Prediction of turbulence effects on vane Stanton number distributions using STAN7 with ATM and Mayle [15], Re_c =1,000,000

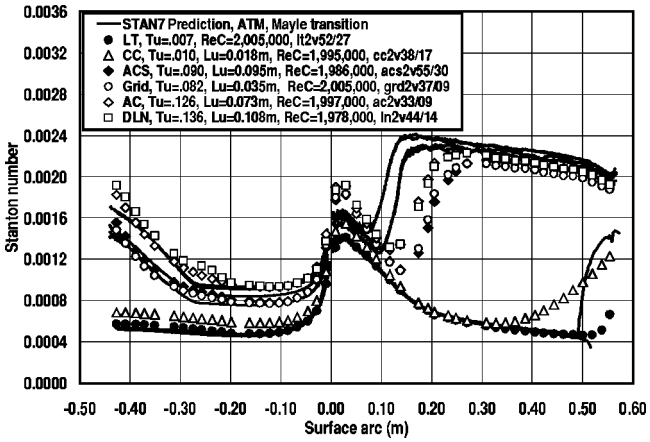

Fig. 19 Prediction of turbulence effects on vane Stanton number distributions using STAN7 with ATM and Mayle [15], Re_c =2,000,000

The transition model is shown to predict transition early on the suction surface for all Reynolds numbers at the higher levels of turbulence. For the lowest Reynolds number case, Fig. 17, transition is predicted to proceed after the adverse pressure gradient on the suction surface begins. However, after a favorable pressure gradient commences, the spot production rate model drops rapidly producing the wiggle in the prediction.

Stagnation Region Prediction. The ATM given in equation (3) underpredicts the stagnation region heat transfer data as shown in Figs. 17 through 19. However, stagnation region heat transfer correlates well on the TRL parameter of Ames and Moffat [4] as shown in Fig. 16. This suggests that the ATM model could be improved if we could account for the effect of the rapid strain in the stagnation region of an airfoil by predicting this turbulence amplification similar to the TRL correlation. Hunt [11] used rapid distortion theory to account for the amplification of small-scale turbulence in the presence of a cylindrical stagnation region. The spectrum function in the inertial subrange can be related to the dissipation rate. By applying Hunt's results to the edge of the stagnation region boundary layer, the increase in the dissipation rate can be correlated by the stagnation region's diameter Reynolds number.

$$\varepsilon/\varepsilon_0 = (\mathrm{Re}_D/4)^{1/4} \tag{5}$$

The stagnation region diameter Reynolds number can be estimated using the local streamwise velocity gradient at the stagnation region.

$$\mathrm{Re}_D \cong \rho_\infty U_\infty^2 3.62/(dU_{\mathrm{App}^2}(X=0)/dx)/\mu_\infty \tag{6}$$

The change in the dissipation can be related to an increase in the near wall eddy viscosity through the length scale term, Lu_∞ in equation (3). This turbulence amplification is observed to be present around the stagnation region where high strain rates occur but is not noticeably present on the pressure surface as shown by the Reynolds number dependence in the present data as well as by the eddy diffusivity data [25]. Other turbulence models have previously been tied to the local strain rates. For example, Forest [26] used the Pohlhausen parameter to correlate a constant in his eddy viscosity model. In the calculations shown in Fig. 20, the following function was used to ''turn on'' and ''turn off'' the amplification of turbulence:

$$f_{\mathrm{amp}} = [1 - \exp\{-2.5[(dU_\infty(X)/dx)/(dU_\infty(X=0)/dx)]^2\}] \tag{7}$$

The increase in eddy viscosity can be estimated as shown

$$\nu_M/\nu_{M,o} = 1 + [(\mathrm{Re}_D/4)^{1/12} - 1]^* f_{\mathrm{amp}} \tag{8}$$

This function works well in the stagnation region, where the function f_{amp} is close to 1.0. The accuracy of these predictions in the

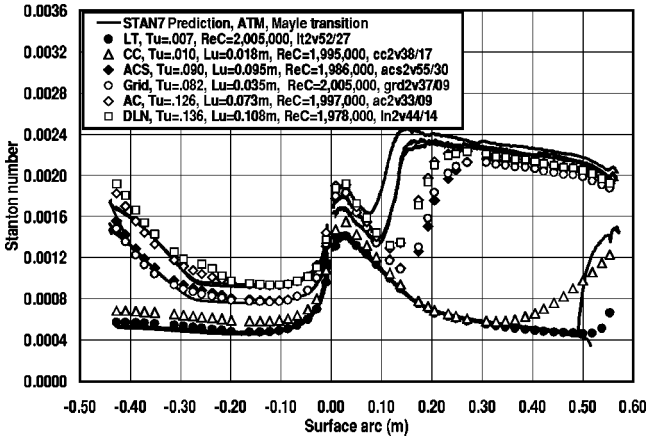

Fig. 20 Prediction of turbulence effects on vane Stanton number distributions with stagnation region model, Re_c=2,000,000

stagnation region support the appropriateness of the Ames and Moffat [4] stagnation region turbulence model. The function also works well over the pressure surface where the f_{amp} is close to zero. However, the accuracy of the function in estimating the amplification of turbulence as the acceleration changes from the high levels found in the stagnation region to more moderate levels found on the pressure surface has not been determined.

Summary and Conclusions

The present vane heat transfer data document the influence of mock DLN and catalytic combustion systems on a conventionally loaded vane over a four-to-one range in Reynolds numbers. These data should help reduce the risk of integrating these new technology combustors into industrial gas turbine systems. Additionally, heat transfer data have been acquired for low turbulence, grid turbulence, and two levels of aero-derivative combustor turbulence over the same Reynolds number range. These data offer turbine designers heat transfer comparisons between known and new inlet configurations providing information on the likely response of turbine heat transfer to these new systems.

These data provide quantitative information on turbulence characteristics developed in DLN and catalytic combustion systems, which previously have had little documentation in the open literature. Additionally, these data suggest that in clean environments laminar flow is predominately present on first vanes in small to medium sized gas turbine systems with catalytic combustion systems. This knowledge has significant potential for simplifying first vane designs for gas turbine systems with catalytic combustion.

These data help demonstrate the impact of flow field straining on the turbulence in the stagnation region of a vane and the corresponding impact on heat transfer. The resulting difference in the effect of Reynolds number scaling was shown for the pressure surface and the stagnation region. Further, a simple method to account for this leading edge effect has been added to the ATM of [25] based on eddy diffusivity scaling ideas developed by Ames and Moffat [4].

Comparative predictions have been made using the STAN7 [21] finite difference boundary layer code with the ATM model of Ames et al. [25] and the Mayle [15] transition model. Results showing laminar augmentation in the stagnation region and pressure surface were very good. The location and length of transition were captured well on the pressure surface, but appeared slightly conservative on the suction surface. These present midline heat transfer data are expected to provide a useful database for the grounding of vane heat transfer predictive methods.

Acknowledgments

The authors would like to gratefully acknowledge support for this work from the Advanced Gas Turbine System Research program, which is funded by a consortium including the National Energy Technology Laboratory of the Department of Energy and participating industrial members. Additionally, this project was initially funded through a seed grant from the North Dakota EPSCoR program, the University of North Dakota, and the Mechanical Engineering Laboratory endowment fund. The authors would like to acknowledge the turbine aero group at Rolls Royce of Indianapolis for developing a special incompressible vane design in a conventionally loaded configuration for this project. Additionally, the authors would like to thank UND student's Dan Pelarski, Troy Lassle, and Mark Hettwer as well as the senior design team, which helped with this project.

Nomenclature

C = vane true chord length, m
Cp = specific heat at constant pressure, J/(kg K)
C_μ = a $k-\varepsilon$ model constant, $C_\mu = 0.09$
D = vane leading edge diameter or effective diameter based on $D = 3.62\, U_{App}/(dU_{App}/dx)$
D_ν = near-wall viscous damping function
$E_1(f)$ = one-dimensional spectrum as function of frequency, f, of streamwise fluctuation velocity, u', m^2/s
$E_1(k_1)$ = one-dimensional energy spectrum function, $E_1(k_1) = UE_1(f)/2/\pi$, m^3/s^2
f = frequency, 1/s
h = heat transfer coefficient, $W/m^2/K$, based on T_r and T_w
k = thermal conductivity, W/m/K
K = free stream acceleration parameter, $K = \nu/U_\infty^2 \cdot (dU_\infty/dx)$
k_1 = wavenumber, $k_1 = 2\pi f/U$, m^{-1}
Lu = energy scale, $Lu = 1.5|u'|^3/\varepsilon$, m
Lx = longitudinal integral scale of u' fluctuation, m
Nu = Nusselt no., hD/k
P = pressure, Pa
Pr = Prandtl no., $\mathrm{Pr} = \rho Cp\,\nu/k$
Pr_t = turbulent Prandtl no., see Eq. (13)
Re_C = true chord Reynolds no., based on exit conditions
St = Stanton no., $\mathrm{St} = h/(\rho Cp U_\infty)$
Tu = turbulence level, $\mathrm{Tu} = |u'|/U_\infty$
TRL = turbulence, Reynolds no., length-scale parameter for correlating stagnation region heat transfer, $\mathrm{TRL} = \mathrm{Tu} \cdot \mathrm{Re}_D^{5/12} \cdot (D/Lu)^{1/3}$
u' = streamwise fluctuation velocity, m/s
$|u'|$ = rms streamwise fluctuation velocity, m/s
Y = normal distance from test surface, m
ε = turbulent dissipation rate, m^2/s^3
η = Kolmogoroff microlength scale, $\eta = (\nu^3/\varepsilon)^{1/4}$, m
ν = kinematic viscosity, m^2/s
ν_M = eddy diffusivity for momentum, m^2/s
ρ = fluid density, mass per unit of volume, kg/m^3

Subscripts

0 = value at same position for low turbulence condition
App = upstream approach or inlet velocity
i = "inner region" of boundary layer
o = "outer region" of boundary layer
s = static condition
t = total or stagnation condition
∞ = evaluated in the free stream

References

[1] Dils, R. R., and Follansbee, P. S., 1977, "Heat Transfer Coefficients Around Cylinders in Crossflow in Combustor Exhaust Gases," ASME J. Eng. Power, **99**, p. 497.

[2] Zimmerman, D. R., 1979, ''Laser Anemometer Measurements at the Exit of a T63-C20 Combustor,'' NASA Conf. Publ., CR-159623.
[3] Bicen, A. F., and Jones, W. P., 1986, ''Velocity Characteristics of Isothermal and Combusting Flows in a Model Combustor,'' Combust. Sci. Technol., **49**, p. 1.
[4] Ames, F. E., and Moffat, R. J., 1990, ''Heat Transfer With High Intensity, Large Scale Turbulence: The Flat Plate Turbulent Boundary Layer and the Cylindrical Stagnation Point,'' Report No. HMT-44, Thermosciences Division of Mechanical Engineering, Stanford University.
[5] Moss, R. W., and Oldfield, M. L. G., 1991, ''Measurements of Hot Combustor Turbulence Spectra,'' ASME Paper No. 91-GT-351.
[6] Goebel, S. B., Abuaf, W., Lovette, T. A., and Lee, C.-P., ''Measurement of Combustor Velocity and Turbulence Profiles,'' ASME Paper 93-GT-228.
[7] Zhang, L. J., and Gleazer, B., 1995, ''Indirect Turbulence Measurement in Gas Turbine Stages Using Heat Flux Probe,'' ASME Paper No. 95-GT-153.
[8] Ames, F. E., 1997, ''The Influence of Large-Scale High-Intensity Turbulence on Vane Heat Transfer,'' ASME J. Turbomach., **199**, pp. 23–30.
[9] Van Fossen, G. J., and Bunker, R. S., ''Augmentation of Stagnation Heat Transfer Due to Turbulence From a DLN Can Combustor,'' ASME Paper No. 2000-GT-215.
[10] Van Fossen, G. J., Simoneau, R. J., and Ching, C. Y., 1995, ''The Influence of Turbulence Parameters, Reynolds Number, and Body Shape on Stagnation Region Heat Transfer,'' ASME J. Heat Transfer, **117**, pp. 597–603.
[11] Hunt, J. C. R., 1973, ''A Theory of Turbulent Flow Round Two-Dimensional Bluff Bodies,'' J. Fluid Mech., **61**(4), p. 625.
[12] Britter, R. E., Hunt, J. C. R., and Mumford, J. C., 1979, ''The Distortion of Turbulence by a Circular Cylinder,'' J. Fluid Mech., **92**.
[13] Arts, T., Lambert de Rouvroit, M., and Rutherford, A. W., 1990, ''Aero-thermal Investigation of a Highly Loaded Transonic Linear Turbine Guide Vane Cascade,'' Technical Note 174, von Karman Institute for Fluid Dynamics, Belgium.
[14] Wang, H. P., Goldstein, R. J., and Olson, S. J., ''Effect of Freestream Turbulence With Large Length Scale on Blade Heat/Mass Transfer,'' ASME J. Turbomach., **121**, pp. 217–224.
[15] Mayle, R. E., 1991, ''The Role of Laminar-Turbulent Transition in Gas Turbine Engines,'' ASME J. Turbomach., **113**, pp. 509–537.
[16] Zhang, L., and Han, J.-C., 1994, ''Influence of Mainstream Turbulence on Heat Transfer Coefficients From a Gas Turbine Blade,'' ASME J. Heat Transfer, **116**, pp. 896–903.
[17] Boyle, R. J., and Simon, F. F., 1999, ''Mach Number Effects on Turbine Blade Transition Length Prediction,'' ASME J. Turbomach., **121**, pp. 694–701.
[18] Thole, K. A., and Bogard, D. G., 1995, ''Enhanced Heat Transfer and Skin Friction Due to High Freestream Turbulence,'' ASME J. Turbomach., **117**, p. 418.
[19] FLUENT 5.3, 1999, FLUENT 5.3 User's Guide, Fluent, Inc., Lebanon, NH.
[20] Smith, D., 2000, private communication, Rolls-Royce, Indianapolis.
[21] Kays, W. M., 1987, ''STAN7, a Finite Difference Boundary Layer Code.''
[22] Moffat, R. J., 1988, ''Describing the Uncertainties in Experimental Results,'' Exp. Therm. Fluid Sci., **1**, pp. 3–17.
[23] Hancock, P. E., and Bradshaw, P., 1983, ''The Effect of Free Stream Turbulence on Turbulent Boundary Layers,'' ASME J. Fluids Eng., **105**, pp. 284.
[24] Hinze, J., 1975, *Turbulence*, 2nd Ed., McGraw-Hill, New York.
[25] Ames, F. E., Kwon, K., and Moffat, R. J., 1999, ''An Algebraic Model for High Intensity Large Scale Turbulence,'' ASME Paper No. 99-GT-160.
[26] Forest, A. E., 1977, ''Engineering Predictions of Transitional Boundary Layers,'' AGARD-CP-224.

Heat Transfer in Turbulent Boundary Layers Subjected to Free-Stream Turbulence—Part I: Experimental Results

Michael J. Barrett
Mem. ASME,
Valparaiso University,
Mechanical Engineering Department,
Valparaiso, IN 46383
e-mail: barrettm@asme.org

D. Keith Hollingsworth
Mem. ASME,
University of Houston,
Department of Mechanical Engineering,
Houston, TX 77204
e-mail: Hollingsworth@uh.edu

Turbulent boundary layers were subjected to grid-generated free-stream turbulence to study the effects of length scale and intensity on heat transfer. Relative to conventional boundary layer thickness measures, test conditions included very small-scale free-stream turbulence. The boundary layers studied ranged from 400–2700 in momentum-thickness Reynolds number and from 450–1900 in enthalpy-thickness Reynolds number. Free-stream turbulence intensities varied from 0.1–8.0%. Ratios of free-stream length scale to boundary-layer momentum thickness ranged from 4.4–32.5. The turbulent-to-viscous length-scale ratios presented are the smallest found in the heat-transfer literature; the ratios spanned from 115–1020. The turbulent-to-thermal ratios (using enthalpy thickness as the thermal scale) are also the smallest reported; the ratios ranged from 3.2–12.3. Relative to clean-free-stream expectations based on the momentum- and enthalpy-thickness Reynolds numbers, the skin friction coefficient increased by up to 16%, and the Stanton number increased by up to 46%. [DOI: 10.1115/1.1538622]

Introduction

We know that wall fluxes are augmented when a boundary layer is subjected to free-stream turbulence. However, our knowledge of the complex mechanisms that drive the augmentation remains incomplete even for the basic flat-plate flow. This paper presents a new elevated-turbulence data set for the flat-plate turbulent boundary layer flow. The experiments were designed to extend the free-stream length scale range to which a heated boundary layer has been subjected. Observations of the effects of very small-scale free-stream turbulence can provide insight into scale-related effects in blade-wake flow interactions. The experimental apparatus and methods are presented first. Particular attention is paid to the characteristics of the small-scale turbulence and to the grid designs used to generate these scales. Comparing clean-free-stream data to widely accepted correlations and DNS results then provides evidence for validation of the facility. Experimental uncertainty estimates for relevant parameters are given. Next, experimental results for the elevated-turbulence cases are displayed. Results include free-stream length scales, boundary layer profiles and wall flux information. A detailed tabular summary is given for archival purposes. Analysis and correlation of the data are the subjects of the Part II companion of this work.

Experimental Facility and Techniques

Wind Tunnel. The wind tunnel is located in the Turbulent Shear Flow Lab of the Department of Mechanical Engineering at the University of Houston. A schematic of the flow loop is given in Fig. 1. The two-stream tunnel was constructed to study mixing-layer behavior in the first test bay immediately downstream of the splitter wall (Anwer [1]).

In the current work both streams were set at the same velocity so that the device acted as a standard single-stream tunnel. The free-stream velocities examined ranged from 2–12 m/s. Boundary-layer suction was used to remove the boundary layers that developed on the splitter wall. The second test bay was used in the present study; the bay begins 2.35 m downstream of the trailing edge of the splitter wall and its cross section is approximately 1.05 m (width) by 1.70 m (height). One wall of the test bay is constructed of acrylic plastic sheeting to provide visibility into the test section and aid in probe placement. Test bay walls are adjustable to essentially eliminate the average streamwise pressure gradient in the test section.

Flat Plate Apparatus. The flat-plate test surface is positioned at mid-height in the second bay of the tunnel test section (Belbas [2]). The test surface is 2.45 m long and 0.95 m wide. Leading and trailing edges are installed to reduce localized flow separation and pressure gradients. A 2.3-mm-dia trip wire is located at the start of the test surface on the top and bottom of the plate to promote transition to a fully turbulent boundary layer. In the discussion that follows, the streamwise (x) coordinate is defined from the boundary layer trip, the vertical (y) coordinate is measured from the upper surface of the plate, and the spanwise (z) coordinate is measured from the centerline of the plate.

Inconel foil sheets are adhered to the top and bottom surfaces of the plate as resistance heaters to produce a constant flux surface for the heat transfer measurements. The sheets are 0.051 mm thick and are applied in successive 0.24 m by 0.89 m strips. Twenty sheets in total (ten on the top surface and ten on the bottom) are installed. The resistance heaters are powered by a variable 12 V,

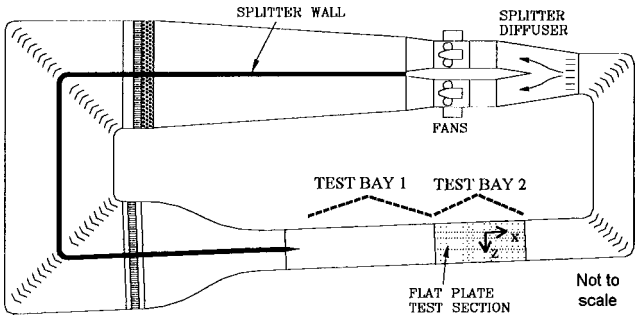

Fig. 1 Wind tunnel flow loop

Contributed by the International Gas Turbine Institute and presented at the National Heat Transfer Conference, Albuquerque, New Mexico, August 14–17, 1999, of THE AMERICAN SOCIETY OF MECHANICAL ENGINEERS. Manuscript received by the IGTI, October 29, 2002. Associate Editor: R. Bunker.

Table 1 Summary of reference information for grid installations

Grid Identifier	Mesh thickness (mm)	Bar width (mm)	M_h (cm)	M_v (cm)	Ribbons	Tu_∞	Measurement locations (x/M_v)
W	0.75	3.2	3.3	5.0	none	6%	10
WR	0.75	3.2	3.3	5.0	1120 randomly oriented	7-8%	20
YR	0.75	3.2	3.3	5.0	560 uniformly oriented	4%	29
O	0.64	hor: 9.0, ver: 3.5	10.5	6.0	none	4%	10

200 A DC power supply. Conduction losses from the surface to the fiberglass-laminate substructure are minimized by symmetrically heating the upper and lower surfaces. The plate surface temperature is measured at 140 locations using 1.5 mm by 2.5 mm resistance temperature devices (RTDs) that are attached directly to the underside of the foil surface. Five of the 140 RTDs are located on the bottom surface to verify upper and lower surface similarity. With an automated channel selector and desktop PC, the resistance of each RTD is measured using a digital multimeter controlled via an IEEE-488 interface bus. The free-stream reference temperature is also measured using an RTD and one channel of the mechanical selector.

Turbulence-Generation Grids. Four different turbulence-generating grids were used to produce varying turbulence intensities and scales at different locations on the test surface. The grids were ''passive;'' i.e., the turbulence was generated by a uniform flow passing through the mesh. This limited the free-stream intensities to a maximum of 8%, but it afforded the generation of very small scales relative to the boundary-layer thickness. The grids were given the following configuration reference identifiers: W, WR, YR, and O. The details of their construction are summarized in Table 1.

A component common to each grid design was a monoplanar thin plastic mesh. The mesh was cut to fit the tunnel cross-section and was secured using spring-loaded tension rods placed adjacent to the vertical tunnel walls. This system allowed simple installation at different locations in the tunnel. The W, WR, and YR grids used a 0.75-mm-thick rectangular mesh with smallest bar dimension of 3.2 mm and horizontal and vertical mesh spacings, M_h and M_v, of 3.3 and 5.0 cm, respectively. To generate higher-intensity turbulence while keeping the scales small, ribbons were added to the downstream side of the mesh to produce the WR and YR grids. The flexibility of the ribbons reduced the blockage effects (Roach [3]) typically encountered when generating very small-scale turbulence with a rigid, biplanar mesh. The ribbons, 7 mm wide and 14 cm long, were secured to the mesh at the ribbon midpoint. The high-density ribboned mesh (WR) was made using 1120 randomly oriented ribbons—one attached to the center of each vertical and horizontal element. The low-density ribboned mesh (YR) had 560 uniformly oriented ribbons added to only the vertical elements of the baseline mesh. Images of the baseline (W) and low-density (YR) grids are shown in Fig. 2.

The O grid was made using a 0.64-mm-thick rectangular mesh. The horizontal bars were 9.0 mm wide and the vertical bars were 3.5 mm wide. The horizontal and vertical mesh spacings were 10.5 and 6.0 cm, respectively. No ribbons were present on the O grid.

Grids were installed in the tunnel in configurations that mimicked the installation of Johnson and Johnston [4]. The grid was located such that the boundary layer had developed on the test surface upstream of the grid. This allowed very small scales to be introduced at a point in the flow where the boundary-layer thickness was nonzero. The first horizontal element is located within the boundary layer at one-half the vertical mesh spacing above the plate. The ''one-half'' spacing of the first horizontal element was used for each grid installation in this study. Following conventional grid usage guidelines [3], no measurements were taken within 10 mesh spacings downstream of the grid. For the W mesh, the largest of the two mesh spacings, M_v, was used as the reference. Because of the asymmetry of the O mesh, M_v was chosen as the characteristic mesh spacing based on actual length scale measurements recorded downstream. (The horizontal bars of the O grid, being wider and more densely spaced than the vertical bars, dominated the turbulence production.) The downstream buffer distance allowed inhomogeneities in the turbulence to mix out prior to the measurement station.

Grid-Generated Turbulence Characteristics. An ''ideal'' wind-tunnel grid would generate isotropic free-stream turbulence. In reality, with a ''very good'' grid we hope to produce homogeneous turbulence that is axisymmetric with small-scale isotropy. To assess the free-stream turbulence generated by the grids, we

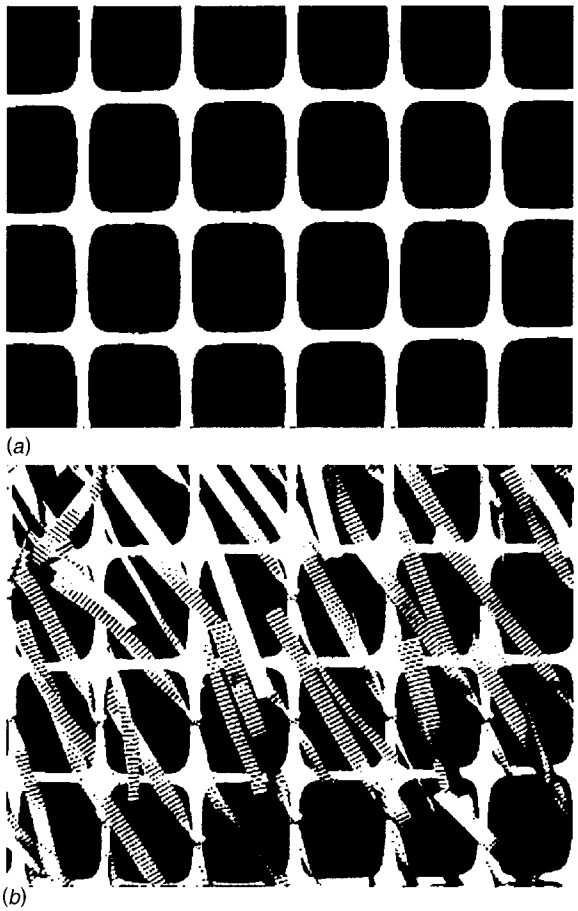

Fig. 2 Passive grids: (*a*) W grid, (*b*) YR grid

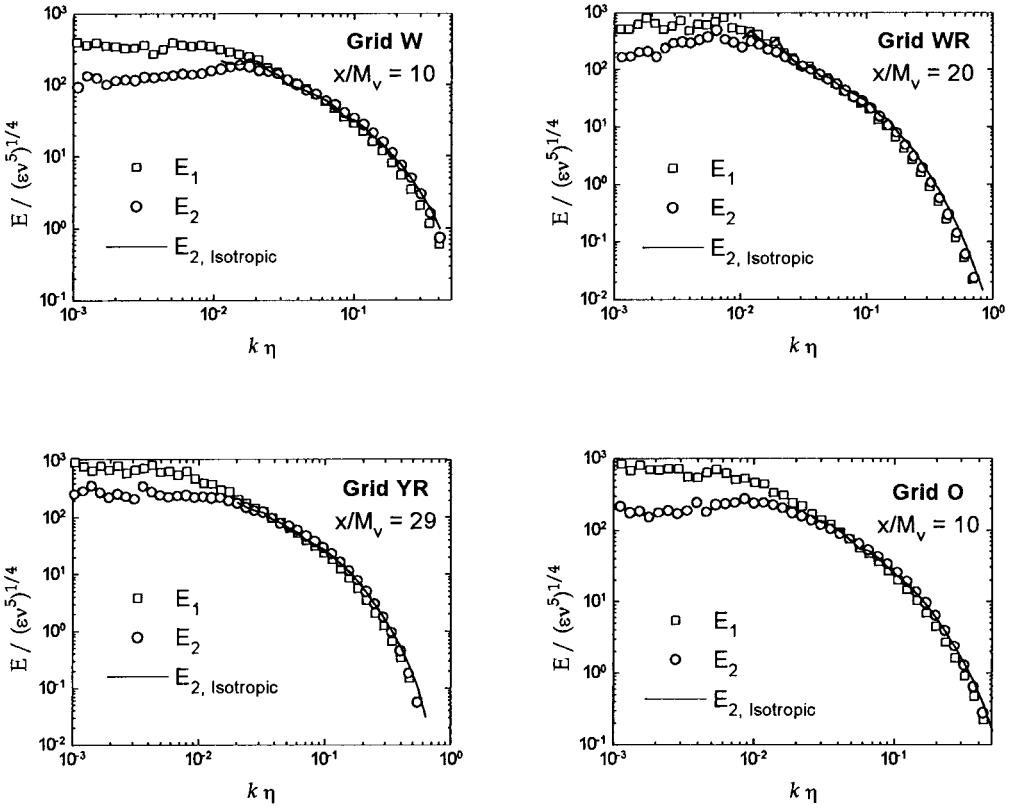

Fig. 3 Small-scale isotropy verification

use isotropic theory to predict the spectral relationship between the energy contained in the normal, v'^2, and streamwise, u'^2, fluctuating components. The relationship is given by Townsend [5] as

$$E_2 = \frac{1}{2}\left(E_1 - k_1 \frac{dE_1}{dk_1}\right) \tag{1}$$

where E_2 and E_1 are the spectral distributions for the normal and streamwise components respectively. Using the E_1 spectrum calculated from a measured u'^2 signal, the isotropic prediction for E_2 can be computed. The prediction can then be compared to the spectrum calculated from the measured v'^2 signal to evaluate the isotropic behavior at different wave numbers. Figure 3 shows that the free-stream turbulence produced by each grid trended towards small-scale isotropy at the *x*-station where boundary-layer measurements were acquired.

To examine cross-stream uniformity, Fig. 4 shows the worst-case measurements (over all cases) of the mean velocity and streamwise intensity plotted versus *z*. The uniformity checks were made at the streamwise locations used in Fig. 3 and at two *y*-positions: the edge of the boundary layer (the free-stream condition, $y=\delta$) and at $y^+=150$. A measurement was also made at $y^+=150$ in a clean-free-stream (CFS) boundary layer for comparison over the same *z* distance. The worst-case variation occurred using the WR grid and was approximately $\pm 10\%$ of the spatially averaged time-mean velocity and ± 0.02 in intensity over

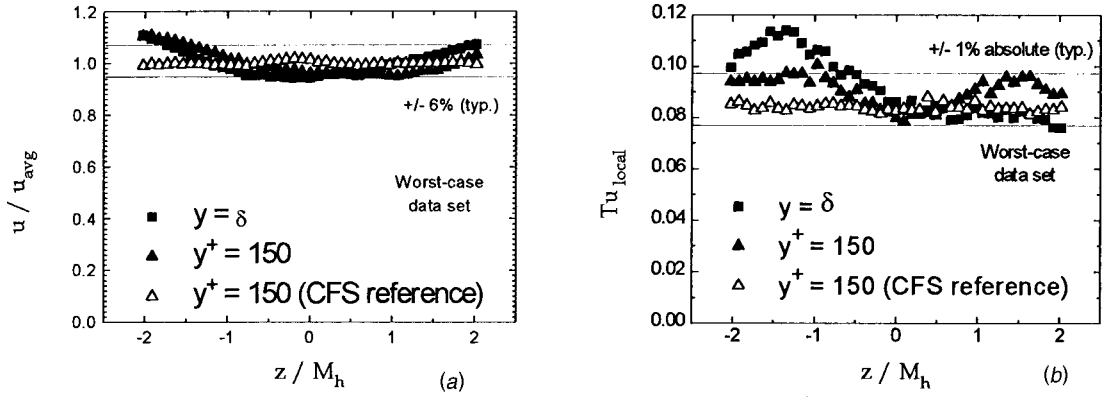

Fig. 4 Worst-case cross-stream variation in (*a*) mean velocity, and (*b*) intensity

four mesh widths. Typically, mean variations were 3–6% of the average; the intensity usually varied less than ± 0.01. These ranges are typical of other grid-generated turbulence studies in the heat transfer literature. Table 1 summarizes this information for each grid installation.

Hot-Wire Anemometry. Mean and fluctuating velocities were measured using constant-temperature hot-wire anemometry. Single-wire and two-wire (x-wire) sensors were used with a TSI model IFA 100 flow analyzer. The IFA 100 housed the bridge circuitry, amplifiers, and analog filters that were used to condition the analog signal prior to digitalization by an IOtech model ADC488 A-to-D converter. Under typical flow conditions the dynamic range of the signal spanned 70% of the available input. The A-to-D converter was controlled using a desktop PC via an IEEE-488 interface bus. Data acquisition software was written in Microsoft® Visual Basic®.

The single-wire sensor was an Auspex miniature surface probe fabricated with an uncoated tungsten wire of length 0.5 mm and diameter 2.5 μm. The x-wire was also an Auspex miniature probe that used two 2.5-μm-uncoated tungsten wires with support-prong separations of 0.5 mm. Standard King's Law calibration curves were generated for each wire by comparing the conditioned output signal with the velocity measured using a pitot-static tube and a ± 1 torr differential pressure transducer in a uniform, CFS flow. For the x-wire, the yaw-calibration technique of Browne et al. [6] was used to determine the effective angle of each wire.

The hot-wire probes were mounted on a two-axis traverse that was controlled with a desktop PC and IEEE-488 bus interface. At 20 threads/in., the vertical lead screw attached to a 200 pulse/rotation stepper-motor gave a vertical-step resolution of 6.35 μm (1/4000 in.).

The only hot-wire measurement correction that was applied is that of Maniam [7]. For measurements at $y^+ = 15$, Maniam found that the inability of a finite-length wire to resolve the smallest scales called for a correction to the measured u'/u_τ involving a ratio of the hot-wire length to the viscous length scale

$$u'_{15}/u_\tau|_{\text{actual}} = u'_{15}/u_\tau|_{\text{measured}}/(1 - l^+/200) \tag{2}$$

where l is the length of the hot wire. Herein, data displayed in a boundary layer profile is uncorrected; tabular u'_{15} values are corrected. In the present work, application of Eq. (2) yielded increases in u'_{15} of 2–8%.

Cold-Wire Thermometry. Mean fluid temperatures through the boundary layer were measured using cold-wire thermometry. The system used a hot-wire probe as one resistor of a standard Wheatstone bridge circuit that produced a voltage signal proportional to the wire resistance. Amplifiers and filters integral to the system provided signal conditioning for the bridge output. For convenience, the same Auspex single-wire used to make velocity measurements was used as the sensor in the cold-wire circuit. The traverse and A-to-D systems described in the foregoing were also used for cold-wire measurements.

General Data Acquisition and Analysis Techniques. Velocity measurements were made with the plate unheated. To record a velocity profile the probe was initially positioned near the plate and incrementally moved in the positive y direction. Measurement locations in the profile were referenced to the initial y location; determination of the initial y-offset is addressed in the forthcoming. After the velocity data was acquired, without changing the tunnel settings, the plate heaters were activated. The plate and free-stream temperatures were monitored during the warm-up period (typically one hour) to ensure that a steady-state condition was reached before temperatures were recorded. For temperature profiles across the boundary layer, the probe was positioned in the manner described in the foregoing; the process used to obtain the initial y-offset is also explained in the forthcoming. The heater settings were selected such that the maximum plate-to-free-stream temperature difference was no less than 9 K and no greater than 15 K. The largest property variation over this range was found in the kinematic viscosity of the fluid in contact with the wall which, at the 15 K setting, increased 8% from the unheated to the heated conditions. The data analysis was conducted assuming constant properties, so this variation contributed to the uncertainty in the results.

The friction velocity, u_τ, and the initial y-offset, y_{initial}, for the velocity profiles were determined by fitting each measured velocity profile to the dimensionless DNS results of Spalart [8] for $y^+ \leqslant 100$ at $\text{Re}_\theta = 1410$. Spalart's results at $\text{Re}_\theta = 1410$ match the traditional linear and log-law relationships

$$u^+ = y^+ \quad \text{for} \quad y^+ < 5 \tag{3}$$

and

$$u^+ = 2.44 \ln(y^+) + 5.0 \quad \text{for} \quad 50 < y^+ < \text{wake region} \tag{4}$$

that are frequently used to determine y_{initial} and u_τ in boundary layer measurements. By using the DNS results, we gain additional guidance from the region $5 < y^+ < 50$. Numerous authors have shown that u^+ deviates from Eq. (4) at low Re_θ; however, the lowest Re_θ at which Eq. (4) remains applicable is not clear (Fernholz and Finley [9]). Spalart's results indicate that Eq. (4) is still applicable over a discernible range of y^+ at $\text{Re}_\theta = 670$. Only one CFS data set was recorded below $\text{Re}_\theta = 670$ in the current study, so a fit to Spalart's dimensionless profile was used for all CFS cases. Elevated free-stream turbulence data were recorded for many cases with $\text{Re}_\theta < 670$. However, several authors (for example, Fernholz and Finley [9]; Thole and Bogard, [10]; Maniam [7]) have noted that in the presence of free-stream turbulence, fewer "low-Re_θ" effects are observed, and the applicability of Eq. (4) and the consistency of the buffer layer are more robust in elevated-turbulence situations. As a result, all y_{initial} and u_τ estimates for velocity profiles in the current work were based on agreement with Spalart's dimensionless profile for $y^+ \leqslant 100$.

The convective heat transfer coefficient, $h(\equiv q_{w,\text{convective}}/(\overline{t}_w - \overline{t}_\infty))$, was found by subtracting the estimated radiative heat flux from the measured total heat flux to arrive at the value for $q_{w,\text{convective}}$. The radiative flux was calculated using an emittance of 0.15 for the Inconel surface [2].

The initial y-offset for the temperature profiles was calculated by fitting the near-wall region of a measured temperature profile to

$$\frac{\overline{t}_w - \overline{t}(y)}{\overline{t}_w - \overline{t}_\infty} = \frac{hy}{k_{\text{air}}} \tag{5}$$

which is derived from a simplified near-wall energy balance. Because of consistency in the traverse control system, it was possible to position the probe at nearly the same y-offset as that for the companion velocity profile. The temperature profile was obtained using identical step increments as those used for the velocity profile. This practice helped reduce uncertainties in the calculation of the enthalpy-thickness Reynolds number, Re_{Δ_2}, which required velocity and temperature information at the same y location.

Spectral distributions of the energy associated with the fluctuating velocity signals were calculated from discrete time series using standard fast Fourier transform (FFT) routines. In acquiring time series for most of the spectra, the IFA 100 filter cut-offs were set at 2000 Hz and a sample rate of 5000 samples/s was used with a record size of 16,384 samples. For flows with significant energy at high wave numbers, the filters were set at 5000 Hz and a sample rate of 10,000 samples/s was used. Spectra from 16 records were ensemble-averaged and smoothed (based on local bin values) to generate the distribution curves. The appropriate filter settings and sample rates were determined based on assessments of preliminary spectra calculated from a single record at 5000 samples/s.

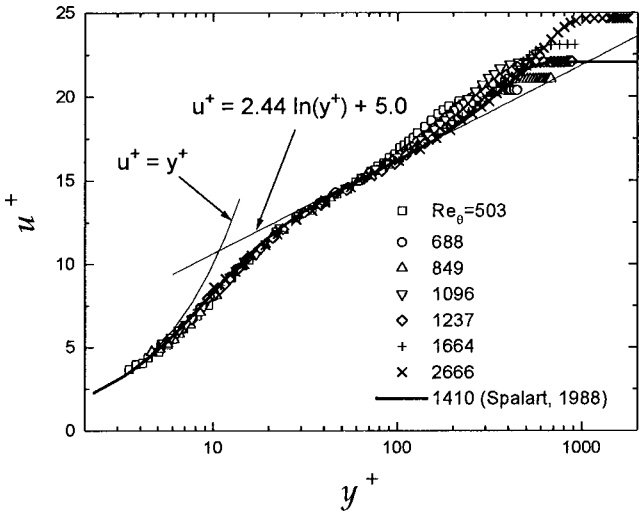

Fig. 5 CFS mean velocity profiles

Using the method of Barrett and Hollingsworth [11], the energy-based turbulent length scale, $L_e = 1.5(u'^2)^{3/2}/\epsilon$, was estimated from spectral energy dissipation curves.

Clean Free-Stream (CFS) Validation Data

In the following examination, mean and fluctuating streamwise velocity measurements are always taken from single-wire data. Figure 5 displays mean velocity profiles measured at various Reynolds numbers and compares them with Eq. (3), Eq. (4) and the DNS results of Spalart [8]. The profile at the smallest Reynolds number, $\mathrm{Re}_\theta \cong 500$, still exhibits a small logarithmic region. Figures 6 and 7 show profiles of streamwise (u') and normal (v') fluctuating velocity profiles. At similar Re_θ, the streamwise and normal fluctuations generally compare well with Spalart's results.

Figure 8 shows experimental values of the skin friction coefficient, $C_f/2$, plotted against Re_θ with the correlation of Kays and Crawford [12]

$$C_f/2 = 0.0125\ \mathrm{Re}_\theta^{-1/4} \tag{6}$$

included for comparison. While the current values tend to be slightly below the correlation, they are within a typical experimental uncertainty of 5% on C_f for this type of CFS analysis.

Mean temperature profiles are presented in Fig. 9. Linear and logarithmic equations given by Kays and Crawford [12] for the sublayer and core region of a fully turbulent air boundary layer ($\kappa = 0.41$, $\mathrm{Pr} = 0.7$, $\mathrm{Pr}_t = 0.86$) are also plotted for comparison.

For turbulent boundary layers with constant wall temperature, Kays and Crawford [12] give a correlation for St in terms of Re_{Δ_2},

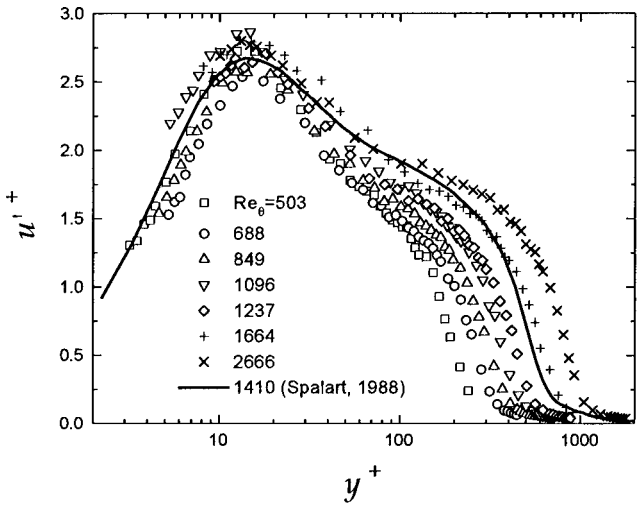

Fig. 6 CFS streamwise fluctuation profiles

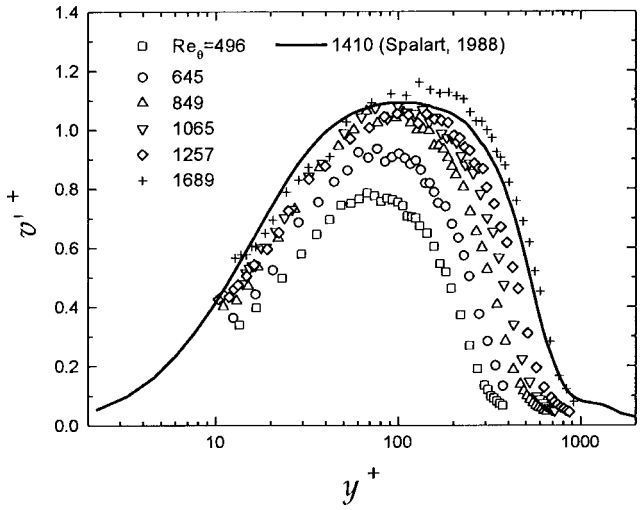

Fig. 7 CFS normal fluctuation profiles

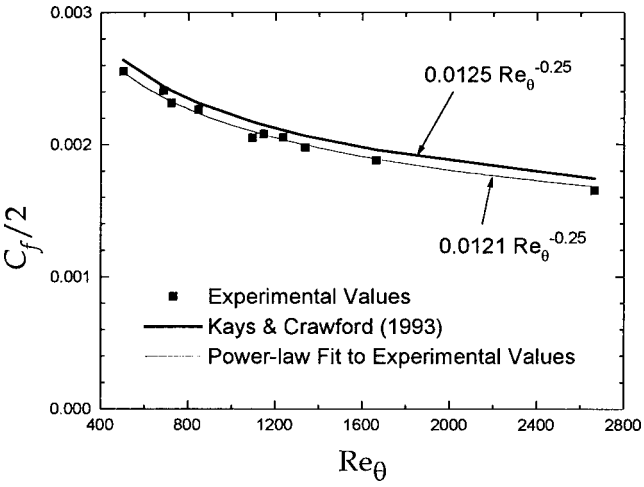

Fig. 8 CFS skin friction coefficient versus Re_θ

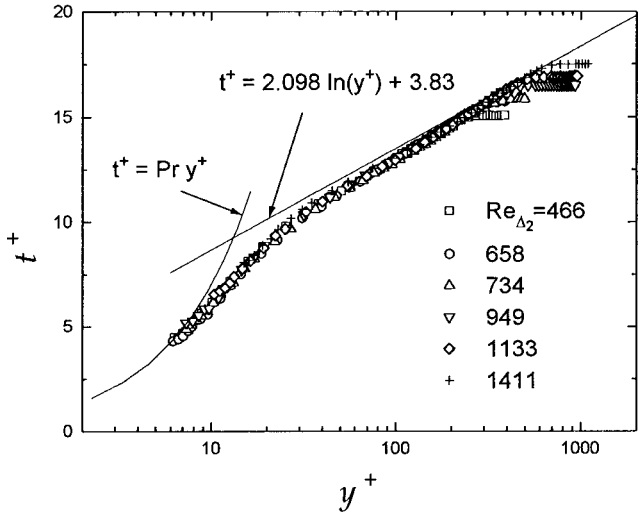

Fig. 9 CFS mean temperature profiles

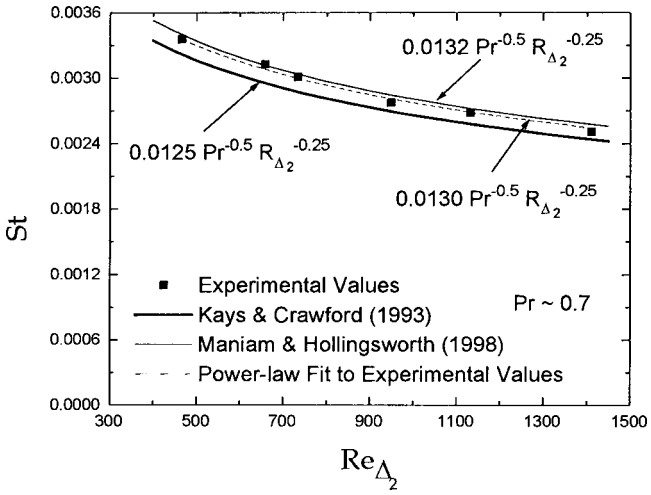

Fig. 10 CFS Stanton number versus Re_{Δ_2}

$$St = 0.0125\ Pr^{-1/2}\ Re_{\Delta_2}^{-1/4}. \quad (7)$$

Figure 10 shows that the present CFS data lie approximately 4% above the correlation. Kays and Crawford [12] show that a uniform heat flux surface, as used in the present study, produces approximately 4% higher St compared to an Re_x-based correlation for a constant surface temperature. Maniam and Hollingsworth [13] expect a similar increase when compared to Eq. (7). Although uniform flux surfaces are common in studies of elevated free-stream turbulence (for example, Thole and Bogard [10,14], Maniam and Hollingsworth [13], Ames and Moffat [15]), Eq. (7) is often used to represent the baseline levels when developing correlations of St. Since Eq. (7) falls within the present experimental uncertainty in St (approximately 6%), it is used as the reference St value for the remainder of the current work.

Experimental Uncertainty Estimates

The method of Kline and McClintock [16] was used to estimate uncertainties for calculated quantities based on uncertainties in the relevant measured quantities. Table 2 presents the typical uncertainties for standard parameters. Values in square brackets are worst-case situations that occurred when the radiative heat flux was approximately 10% of the total flux. Uncertainties for other parameters are presented in the text as these parameters are discussed.

Table 2 Summary of uncertainty information for some standard parameters

Parameter	Uncertainty estimate
Time-mean streamwise velocity, $\overline{u}$	2% | $\overline{u}>2$ m/s 3% | $\overline{u}<2$ m/s
Streamwise velocity fluctuation, u'	3%
Normal velocity fluctuation, v'	5%
Friction velocity, u_τ (unheated plate)	3%
Friction velocity, u_τ (heated plate)	5%
Distance from the wall, y	3% of $5\nu/u_\tau$ for the profile (0.15 dimensionless y^+)
Momentum-thickness Reynolds number, Re_θ	7%
Energy-based turbulent length scale, L_e	11%
Time-mean temperature, $\overline{t}$ (cold wire)	0.25°C
Temperature difference, $t_w-\overline{t}_\infty$ (RTDs)	1.1%
Foil emittance	0.05
Wall convective heat flux, $q_{w,\text{convective}}$	5% [10% worst-case]
Convective heat transfer coefficient, h	5.1% [10.1% worst-case]
Stanton number, St	5.5% [10.5% worst-case]
Fluctuation Stanton number, St′	6% [10.5% worst-case]
Enthalpy-thickness Reynolds number, Re_{Δ_2}	9%

Experimental Results

Turbulent Length Scales. Most of the previous heat transfer studies examined flows with free-stream length scales that were larger than the scales in the core of the accompanying boundary layer. However, a significant portion of the current data represent flows with free-stream scales that are as small or smaller than those in the boundary-layer core. To illustrate this point, two boundary-layer profiles of L_e^+ (L_e divided by the viscous length scale, ν/u_τ) are displayed in Fig. 11. The filled symbols show a typical profile with free-stream L_e larger than scales in the core of the boundary layer. The open symbols present a typical length-scale profile when free-stream L_e is as small or smaller than scales that naturally occur in the boundary layer.

Figure 12 compares the θ/L_e values in the current work to previous studies. Length scales were measured at $y^+=150$ for the CFS case. The current investigation examines length scales that are as small (relative to the momentum thickness) as those obtained by Johnson and Johnston [4] and an order of magnitude smaller than many studies. Since Johnson and Johnston did not measure heat transfer, the current data are unique for the heat transfer literature. Figure 13 shows that in comparison to the viscous length scale, the current scales are the smallest examined.

Figure 12 also exhibits the Tu_∞ and Re_θ ranges included in the

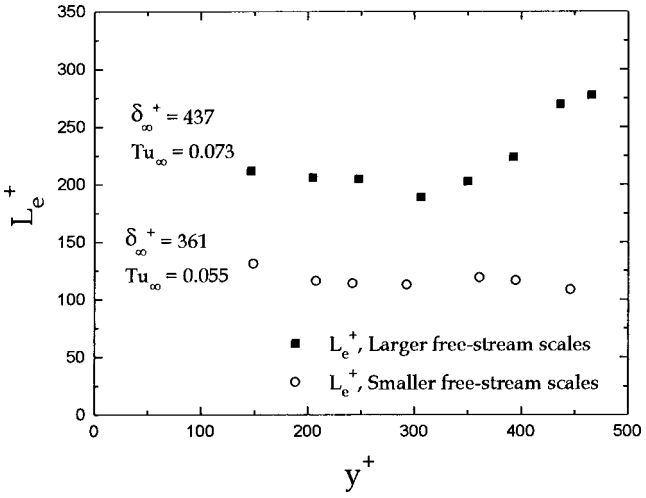

Fig. 11 L_e^+ length-scale profiles

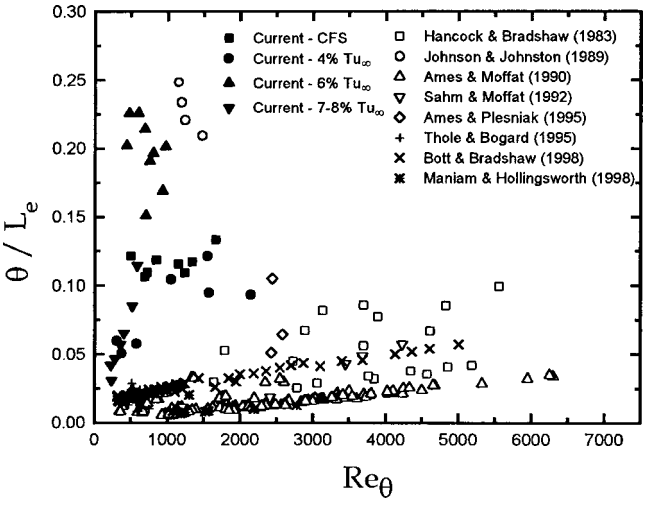

Fig. 12 Length-scale ratios in current and previous studies (θ/L_e versus Re_θ)

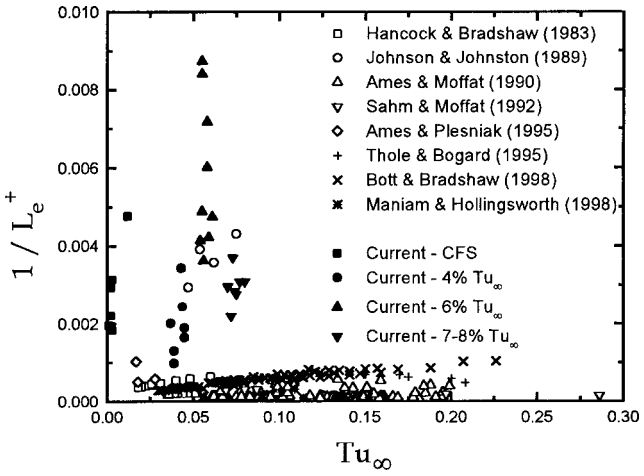

Fig. 13 Length-scale ratios in current and previous studies ($1/L_e^+$ versus Tu_∞)

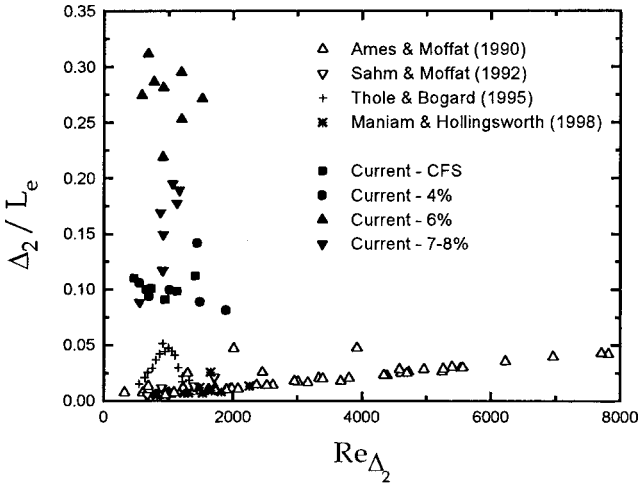

Fig. 14 Length-scale ratios in current and previous studies (Δ_2/L_e versus Re_{Δ_2})

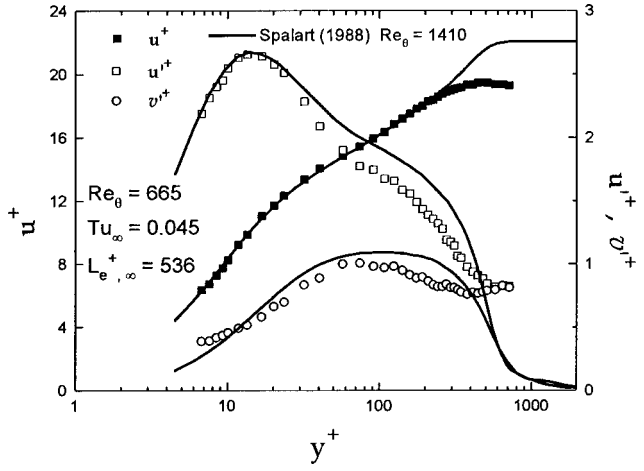

Fig. 15 Dimensionless velocity profiles with elevated Tu_∞

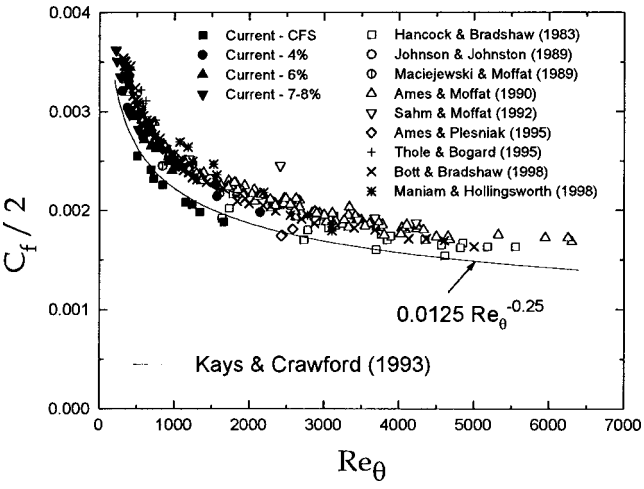

Fig. 16 Skin-friction coefficient versus Re_θ

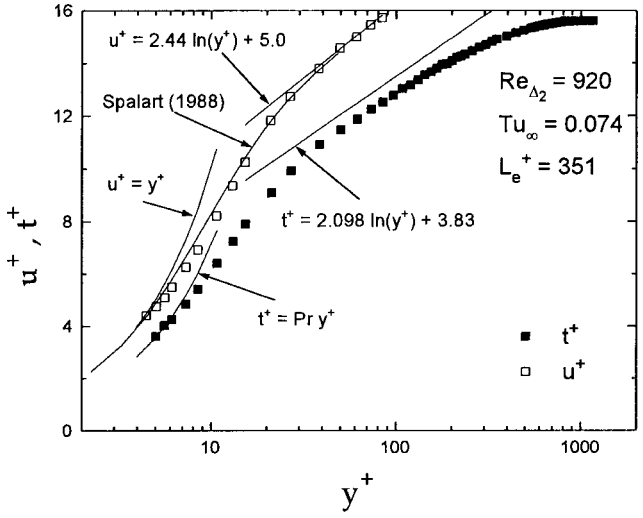

Fig. 17 Dimensionless mean temperature profile with elevated Tu_∞

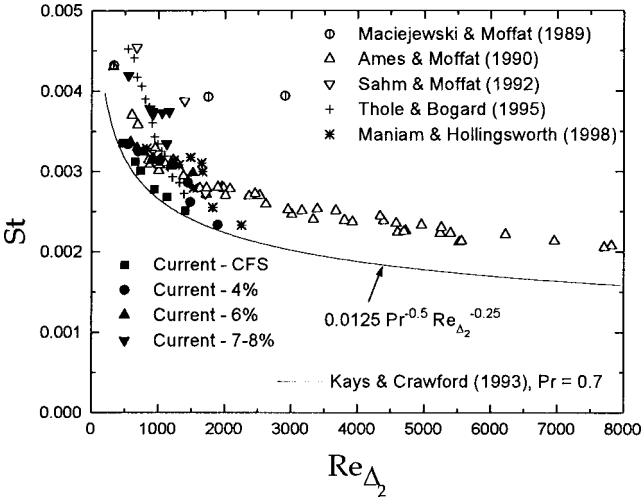

Fig. 18 Stanton number versus Re_{Δ_2}

current study: $0.1\% < Tu_\infty < 8.0\%$, $400 < Re_\theta < 2700$. The ranges are applicable to heat transfer in multistage low-pressure gas turbines as identified by Halstead et al. [17]. Uncertainties on Tu_∞ and Re_θ were 3.6% and 7%, respectively.

Figure 14 compares thermal length scale ratios, Δ_2/L_e, with those from other studies. The small size of the present free-stream length scales is even more pronounced when compared to the thickness of the thermal boundary layer. The ratios (inversely proportional to L_e) obtained in the current work are the largest reported. Figure 14 also displays the Re_{Δ_2} range covered by the present study: $450 < Re_{\Delta_2} < 1900$; uncertainty in Re_{Δ_2} was 9%.

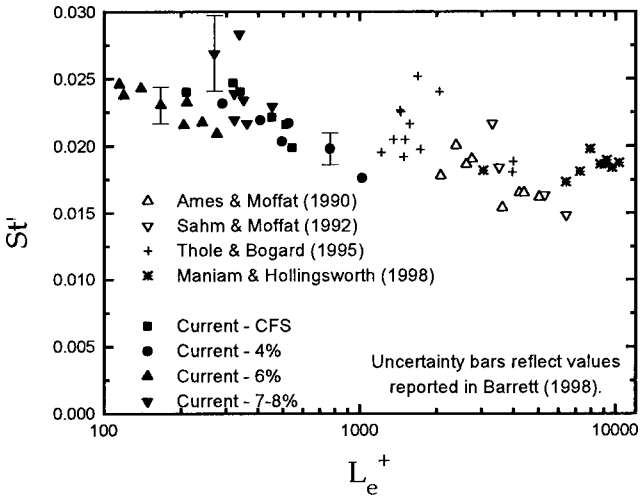

Fig. 19 St′ versus L_e^+

Velocity Profiles. A set of typical velocity profiles for elevated Tu_∞ is given in Fig. 15. Comparison is again made with Spalart's DNS results (CFS, Re_θ=1410). As necessitated by the technique used to determine u_τ, the mean profile shows strong agreement with the DNS results through the buffer layer and a portion of the log layer. The experimental u'^+ and v'^+ profiles do, of course, differ from the DNS results in the outer portion of the profile due to the free-stream turbulence.

Skin Friction Coefficient. Skin friction coefficient data from the current work are displayed with those from earlier studies in Fig. 16. Enhancements in C_f characteristic of elevated Tu_∞ are apparent. When compared to Eq. (6), the CFS Re_θ-based correlation, enhancements between 6 and 16% are observed in the present data.

Temperature Profiles. A t^+ profile with nonzero Tu_∞ is shown in Fig. 17. The data exhibit linear near-wall characteristics and a logarithmic behavior at the outer edge of the buffer layer. The generality of the thermal law of the wall has been questioned

Table 3 Summary of data ($\nu \approx 15.5E-6\ m^2/s$ used for all cases)

Case	Grid	$\bar{u}_\infty$ (m/s)	Tu_∞ (%)	$L_{e,\infty}$ (cm)	u'15 (cm/s)	$\bar{t}_w$ (°C)	$\bar{t}_\infty$ (°C)	$\bar{t}_{L_e}$ (°C)	Re_θ	$C_f/2$	Re_{Δ_2}	St
1	None	1.92	1.2%	-	26.8	38.15	24.50	-	503	0.00255	466	0.00336
2	None	2.59	0.3%	-	32.7	36.99	24.44	-	688	0.00241	658	0.00312
3	None	2.49	0.2%	-	32.8	-	-	-	724	0.00232	-	-
4	None	3.15	0.2%	-	39.4	35.86	24.37	-	849	0.00226	734	0.00301
5	None	4.04	0.2%	-	50.5	34.70	24.24	-	1148	0.00208	949	0.00277
6	None	5.01	0.2%	-	62.1	36.29	24.34	-	1237	0.00206	1133	0.00268
7	None	5.06	0.1%	-	62.9	-	-	-	1339	0.00198	-	-
8	None	7.08	0.3%	-	89.3	34.55	24.33	-	1664	0.00188	1411	0.00251
9	None	11.69	0.2%	-	142.3	-	-	-	2666	0.00165	-	-
10	YR	2.81	4.3%	2.84	40.4	35.93	24.62	-	306	0.00321	551	0.00334
11	YR	3.68	4.4%	3.13	54.6	35.95	24.86	-	374	0.00304	705	0.00325
12	YR	4.68	4.5%	3.35	67.5	36.09	25.07	-	581	0.00274	1019	0.00313
13	YR	5.62	3.7%	2.78	79.1	36.64	25.48	-	1050	0.00245	1445	0.00286
14	YR	6.00	4.5%	3.32	82.8	-	-	-	1554	0.00226	-	-
15	O	6.75	3.9%	3.82	89.2	37.07	27.09	-	1570	0.00214	1488	0.00262
16	O	9.09	3.9%	3.93	120.3	36.11	27.04	-	2147	0.00198	1897	0.00233
17	W	3.73	6.1%	1.71	50.3	39.53	24.62	26.00	808	0.00262	914	0.00314
18	W	4.02	5.9%	1.87	52.4	-	-	-	972	0.00240	-	-
19	W	2.41	5.5%	1.40	33.4	38.56	24.17	26.15	440	0.00299	688	0.00329
20	W	2.34	5.5%	1.40	32.0	37.58	24.30	25.94	476	0.00295	588	0.00336
21	W	3.00	5.8%	1.39	40.0	36.58	24.48	26.03	604	0.00271	778	0.00324
22	W	3.63	5.8%	1.38	49.9	37.24	24.55	26.12	692	0.00265	922	0.00317
23	W	4.46	5.4%	1.60	63.6	36.50	24.14	25.47	706	0.00278	1200	0.00310
24	W	4.83	5.5%	1.29	68.6	36.31	24.48	25.94	760	0.00262	1198	0.00306
25	W	6.02	5.6%	1.43	85.6	34.80	24.76	25.82	932	0.00249	1522	0.00298
26	WR	3.08	7.4%	3.06	48.7	35.12	24.53	25.02	283	0.00335	921	0.00371
27	WR	2.50	7.0%	3.85	36.9	34.79	24.52	24.74	404	0.00297	556	0.00419
28	WR	2.14	7.3%	3.72	30.0	37.47	24.47	25.34	586	0.00278	880	0.00378
29	WR	3.62	7.7%	2.30	61.6	33.46	24.46	25.18	225	0.00362	1064	0.00373
30	WR	4.48	7.2%	2.66	72.9	35.13	24.57	24.90	235	0.00351	912	0.00374
31	WR	2.84	7.5%	3.42	43.9	36.79	24.47	25.30	357	0.00333	1133	0.00334
32	WR	3.26	8.0%	2.90	51.0	34.53	24.54	25.30	519	0.00282	1169	0.00374

by numerous authors (e.g., Bradshaw and Huang [18]) and our data indicates that, in the core region, the dimensionless temperature profile given by Kays and Crawford [12]

$$t^+ = \frac{\mathrm{Pr}_t}{\kappa}\ln(y^+) - 2.58\frac{\mathrm{Pr}_t}{\kappa} + 13.2\mathrm{Pr} \tag{8}$$

is not adequate if universally constant values of $\kappa = 0.41$ and $\mathrm{Pr}_t = 0.86$ are assumed. The companion near-wall velocity profile is included in Fig. 17 for u_τ verification.

Stanton Numbers. Conventional Stanton number versus Re_{Δ_2} behavior is displayed in Fig. 18. Compared to Eq. (7), enhancements as high as 46% were observed in the current study. Figure 19 shows the near-wall Stanton number, St′, of Maciejewski and Moffat [19,20] plotted versus dimensionless length scale L_e^+. The L_e-dependence of St′ (easily identifiable due to the presence of the new small-scale data in Fig. 19) is more thoroughly analyzed in Part II of this work.

Data Summary. Table 3 is given as a detailed summary of key results for archival purposes. Complete profile data for each test case and additional parameter values are available in Barrett [21].

Conclusions

Free-stream turbulence with intensity of up to 8% and small-scale (high wave number) isotropy can be generated using passive grids. Using the placement technique of Johnson and Johnston [4], integral-to-boundary-layer thickness ratios as low as $3.2(L_e/\Delta_2)$, $4.4(L_e/\theta)$, and $115(L_e^+)$ can be achieved.

Subjecting turbulent boundary layers to moderate intensity, small-scale free-stream turbulence generates significant enhancements in wall fluxes relative to CFS flows at the same Reynolds number. With free-stream intensities equal to or less than 8%, maximum observed increases in skin-friction coefficient and Stanton number were 16 and 46%, respectively.

In Part II of this work, the present data are used to evaluate length-scale dependence in heat transfer coefficients such as St′ and in established heat transfer correlations. The small scales produced here allow such evaluations to be made over a much larger length-scale range than has been possible previously. Part II also introduces new skin friction and heat transfer correlations built on turbulence length scales instead of boundary layer thickness measures.

Acknowledgments

The authors thank Dr. S. J. Kleis for his consultation and the use of his wind tunnel facility. Support was received from the Texas Higher Education Coordinating Board (ATP Grant No. 003652-944), the UH Institute for Space Systems Operations and the UH Energy Lab. Dr. Barrett received additional support from the NASA/Texas Space Grant Consortium and the SAE Doctoral Scholars Program.

While not specifically referenced in the text, the data of Hancock and Bradshaw [22], Sahm and Moffat [23], Ames and Plesniak [24], Thole and Bogard [25], and Bott and Bradshaw [26,27] were also used for result comparisons; their data appear in appropriate figures.

Nomenclature

C_f = skin friction coefficient ($=2\tau_w/\rho u_\infty^2$)
C_{f_0} = skin friction coefficient from Kays and Crawford correlation
ΔC_f = increase in skin friction coefficient
c_p = specific heat
E = power spectral density of fluctuating velocity (also referred to as "energy spectrum")
h = heat transfer coefficient
k = wave no.
L = experimentally determined length scale related to ϵ
Pr = Prandtl no. ($=\nu/\alpha$)
Pr_t = turbulent Prandtl no. ($=\varepsilon_M/\varepsilon_H$)
q = heat flux
Re = Reynolds no.
Re_{Δ_2} = enthalpy-thickness Reynolds no. ($=\overline{u}_\infty\Delta_2/\nu$)
Re_θ = momentum-thickness Reynolds no. ($=\overline{u}_\infty\theta/\nu$)
St = Stanton no. ($=h/\rho c_p\overline{u}_\infty$)
St_o = Stanton no. from Kays and Crawford correlation
ΔSt = increase in Stanton no.
St_τ = Stanton no. based on u_τ ($=h/\rho c_p u_\tau$)
$\mathrm{St}_{\tau,t15}$ = Stanton no. based on u_τ and t_{15} ($=q_w/[\rho c_p u_\tau(\overline{t}_w - \overline{t}_{15})]$)
St′ = Stanton no. based on u' at y^+ of 15 ($=h/\rho c_p u'_{15}$)
St'_τ = Stanton no. based on u' at y^+ of 15 and u_τ ($=h/\rho c_p\sqrt{u'_{15}u_\tau}$)
t = temperature
t^+ = dimensionless temperature ($=(\overline{t}_w - \overline{t})u_\tau/(q_w/\rho c_p)$)
Tu = turbulence intensity ($=u'/\overline{u}$)
u = streamwise velocity
u_τ = boundary-layer friction velocity ($=\sqrt{\tau_w/\rho}$)
u^+ = dimensionless velocity ($=\overline{u}/u_\tau$)
uv^+ = dimensionless Reynolds stress ($=-\overline{uv}/u_\tau^2$)
v = velocity in direction normal to surface
x = streamwise coordinate
y = coordinate in direction normal to surface
y^+ = dimensionless distance from wall ($=yu_\tau/\nu$)
z = cross-stream coordinate
α = thermal diffusivity
β = empirical-fit constant
γ = empirical-fit constant
δ = boundary-layer thickness or shear-layer width
Δ_2 = boundary-layer enthalpy thickness
ϵ = dissipation of turbulent kinetic energy
η = Kolmogorov length scale [$=(\nu^3/\epsilon)^{1/4}$]
θ = boundary-layer momentum thickness
κ = von Kármán constant (= 0.41)
ν = kinematic viscosity
ρ = density
σ = standard deviation
τ_w = wall shear stress

Subscripts

1 = x-component related
15 = located at $y^+ = 15$
∞ = free-stream
e = energy-based
w = wall
Δ_2 = based on enthalpy thickness
θ = based on momentum thickness

Superscripts

$\overline{\ }$ = Reynolds-averaged mean
′ = fluctuating (RMS value)
+ = nondimensionalized using wall variables

References

[1] Anwer, M. N., 1985, "Design, Construction, and Testing of a Two-Stream Mixing Layer Wind Tunnel Facility," M.S. thesis, Dept. of Mech. Eng., University of Houston.
[2] Belbas, C. A., 1993, "Design and Qualification of a Heat Transfer Surface for Studies of High Turbulence," M.S. thesis, Dept. of Mech. Eng., University of Houston.
[3] Roach, P. E., 1987, "The Generation of Nearly Isotropic Turbulence by Means of Grids," Int. J. Heat Fluid Flow, **8**(2), pp. 82–92.
[4] Johnson, P. L., and Johnston, J. P., 1989, "The Effects of Grid-Generated Turbulence on Flat and Concave Turbulent Boundary Layers," Report No. MD-53, Dept. of Mech. Eng., Stanford University.

[5] Townsend, A. A., 1976, *The Structure of Turbulent Shear Flow*, Cambridge University Press.
[6] Browne, L. W. B., Antonia, R. A., and Chua, L. P., 1989, ''Calibration of x-Probe for Turbulent Flow Measurements,'' Exp. Fluids, **7**, pp. 201–208.
[7] Maniam, B. M., 1997, ''An Experimental Study of the Turbulent Momentum and Thermal Boundary Layers Beneath a Two-Stream Mixing Layer,'' Ph.D. dissertation, Dept. of Mech. Eng., University of Houston.
[8] Spalart, P. R., 1988, ''Direct Simulation of a Turbulent Boundary Layer up to $R_\theta = 1410$,'' J. Fluid Mech., **187**, pp. 61–98.
[9] Fernholz, H. H., and Finley, P. J., 1996, ''The Incompressible Zero-Pressure-Gradient Turbulent Boundary Layer: An Assessment of the Data,'' Prog. Aerosp. Sci., **32**, pp. 245–311.
[10] Thole, K. A., and Bogard, D. G., 1996, ''High Freestream Turbulence Effects on Turbulent Boundary Layers,'' ASME J. Fluids Eng., **118**, pp. 276–284.
[11] Barrett, M. J., and Hollingsworth, D. K., 2001, ''On the Calculation of Length Scales for Turbulent Heat Transfer Correlation,'' ASME J. Heat Transfer, **123**, pp. 878–883.
[12] Kays, W. M., and Crawford, M. E., 1980, *Convective Heat Transfer*, 2nd Edition, Mc-Graw Hill.
[13] Maniam, B. M., and Hollingsworth, D. K., 1998, ''Experimental Investigation of Heat Transfer in a Three-Dimensional Boundary Layer Beneath a Mixing Layer,'' *Proc., 7th AIAA/ASME Joint Thermophysics and Heat Transfer Conference*, Albuquerque, NM, **2**, pp. 123–130.
[14] Thole, K. A., and Bogard, D. G., 1995, ''Enhanced Heat Transfer and Shear Stress Due to High Free-Stream Turbulence,'' ASME J. Turbomach., **117**, pp. 418–424.
[15] Ames, F. E., and Moffat, R. J., 1990, ''Heat Transfer with High Intensity, Large Scale Turbulence: The Flat Plate Turbulent Boundary Layer and the Cylindrical Stagnation Point,'' Report No. HMT-44, Dept. of Mech. Eng., Stanford University.
[16] Kline, S. J., and McClintock, F. A., 1953, ''Describing Uncertainties in Single Sample Experiments,'' Mech. Eng. (Am. Soc. Mech. Eng.), **75**, pp. 3–8.
[17] Halstead, D. E., Wisler, D. C., Okiishi, T. H., Walker, G. J., Hodson, H. P., and Shin, H.-W., 1997, ''Boundary Layer Development in Axial Compressors and Turbines: Part 3 of 4—LP Turbines,'' ASME J. Turbomach., **119**, pp. 225–237.
[18] Bradshaw, P., and Huang, G. P., 1995, ''The Law of the Wall in Turbulent Flow,'' *Proc., Royal Society of London A*, **451**, pp. 165–188.
[19] Maciejewski, P. K., and Moffat, R. J., 1989, ''Heat Transfer with Very High Free-Stream Turbulence,'' Report No. HMT-42, Dept. of Mech. Eng., Stanford University.
[20] Maciejewski, P. K., and Moffat, R. J., 1992, ''Heat Transfer with Very High Free-Stream Turbulence,'' ASME J. Heat Transfer, Part I-Experimental data. **114**, 827–833; Part II-Analysis of results, **114**, 834–839.
[21] Barrett, M. J., 1998, ''Skin Friction and Heat Transfer in Turbulent Boundary Layers Subjected to Small-Scale Free-Stream Turbulence,'' Ph.D. dissertation, Dept. of Mech. Eng., University of Houston.
[22] Hancock, P. E., and Bradshaw, P., 1983, ''The Effect of Free-Stream Turbulence on Turbulent Boundary Layers,'' ASME J. Fluids Eng., **105**, pp. 284–289.
[23] Sahm, M. K., and Moffat, R. J., 1992, ''Turbulent Boundary Layers with High Turbulence: Experimental Heat Transfer and Structure on Flat and Convex Walls,'' Report No. HMT-45, Dept. of Mech. Eng., Stanford University.
[24] Ames, F. E., and Plesniak, M. W., 1995, ''The Influence of Large Scale, High Intensity Turbulence on Vane Aerodynamic Losses, Wake Growth, and the Exit Turbulence Parameters,'' *Proc., International Gas Turbine and Aeroengine Congress and Exposition*, Houston, TX, ASME Paper 95-GT-290.
[25] Thole, K. A., 1992, ''High Free-Stream Turbulence Effects on the Transport of Heat and Momentum,'' Ph.D. dissertation, The University of Texas at Austin.
[26] Bott, D. M., and Bradshaw, P., 1997, ''Effect of High Levels of Free-Stream Turbulence on Boundary Layer Skin Friction and Heat Transfer,'' Report No. MD-75, Dept. of Mech. Eng., Stanford University.
[27] Bott, D. M., and Bradshaw, P., 1998, ''Effect of High Free-Stream Turbulence on Boundary Layer Skin Friction and Heat Transfer,'' *Proc., 36th Aerospace Sciences Meeting & Exhibit*, Reno, NV, AIAA Paper 98-0531.

Heat Transfer In Turbulent Boundary Layers Subjected to Free-Stream Turbulence—Part II: Analysis and Correlation

Michael J. Barrett
Mem. ASME,
Mechanical Engineering Department,
Valparaiso University,
Valparaiso, IN 46383
e-mail: barrettm@asme.org

D. Keith Hollingsworth
Mem. ASME,
Department of Mechanical Engineering,
University of Houston,
Houston, TX 77204
e-mail: Hollingsworth@uh.edu

A new heat transfer correlation for turbulent boundary layers subjected to free-stream turbulence was developed. The new correlation estimates dimensionless heat transfer coefficients without the use of conventional boundary-layer thickness measures and the associated Reynolds numbers. Using only free-stream parameters (mean velocity, turbulence intensity and length scale), the new correlation collected many authors' elevated-turbulence, flat-plate Stanton number data to within ±11%. The level of scatter around the new correlation compared well to previous correlations that require additional flow information as input parameters. For a common subset of data, scatter using earlier correlation methods ranged from 5–10%; scatter around the new correlation varied from 6–9% over the same data subset. A length-scale dependence was identified in a Stanton number previously defined using a near-wall streamwise velocity fluctuation, St′. A new near-wall Stanton number was introduced; this parameter was regarded as a constant in a two-region boundary layer model on which the new correlation is based.
[DOI: 10.1115/1.1538623]

Introduction

The turbulent flow of a fluid bounded by a heated surface is a wonderfully complex yet derisively mundane phenomenon. Despite its commonness in natural and man-made environments, we struggle to accurately predict its behavior in many simple situations. A complexity encountered in a number of flows is the presence of free-stream turbulence. A turbulent free-stream typically yields increased surface friction and heat transfer. Turbulent boundary layers with turbulent free-streams are encountered in gas-turbine engines, rocket nozzles, electronic-cooling passages, geophysical flows, and numerous other dynamic systems. Regardless of the setting, the essence of the problem is the same—to account for the free-stream turbulence so that skin friction and heat transfer can be accurately predicted.

The companion article, Part I, introduced a new data set that expands the turbulence length-scale range of high free-stream turbulence studies. This paper presents a new method of correlating turbulent-boundary-layer heat transfer for flows with elevated free-stream turbulence. First, prior elevated-turbulence heat-transfer research is briefly summarized. Based on the summary, representative correlations are reviewed using the data set from Part I and data from the literature. A previously unidentified length-scale dependence in an existing correlation is established. Next, the new heat transfer correlation is developed and compared with established correlations in terms of accuracy and requisite information. Finally, limitations of the new correlation are discussed and conclusions are presented.

Literature Review

The work that defined the contemporary approach to evaluating free-stream turbulence effects on flat-plate boundary-layer skin friction and heat transfer was presented by Simonich and Bradshaw [1]. They examined the effects of both turbulence intensity, Tu_∞, and turbulent-to-boundary-layer length scale ratio, L/δ. (The length scale, L, is representative of the largest, energy-containing turbulent eddies.) The data indicated that both C_f and Stanton number, St, increased as the intensity increased and the length-scale ratio decreased. Their work also included an extension of the scaling analysis presented by Kader and Yaglom [2]. Simonich and Bradshaw commented that the viscous length scale, ν/u_τ, was the appropriate reference length scale (relative to the shear-layer thickness) to ensure compatibility with the similarity analysis. However, they adopted a characterization using the momentum-thickness, θ, based on the belief that, in practice, it was more convenient to compare boundary layers at similar momentum-thickness Reynolds numbers, Re_θ. The use of Re_θ as the basis for enhancement comparison was an improvement over x-based Reynolds number comparisons for correlative purposes; however, its introduction masked the importance of viscous-length scaling and limited the predictive usefulness of the resulting correlations.

The first systematic evaluation of the effect of free-stream turbulent length scale on C_f was conducted by Hancock and Bradshaw [3]. Based on their observations, they offered

$$\Delta C_f/C_{f_0} \propto \mathrm{Tu}_\infty/(2+L/\delta) \tag{1}$$

where C_{f_0} is the skin friction coefficient at the same Re_θ (measured) for a zero-intensity ($\mathrm{Tu}_\infty=0$) free-stream flow. The grouping, $\mathrm{Tu}_\infty/(2+L/\delta)$, is known as the HB parameter.

Blair [4] examined C_f and St enhancement in terms of the HB parameter. From low-Re_θ data, he modified the HB parameter with a "damping-term"

$$\text{Modified HB}=\mathrm{Tu}_\infty/[(2+L/\delta)(1+3\exp(-\mathrm{Re}_\theta/400))] \tag{2}$$

to which he stated that both $\Delta C_f/C_{f_0}$ and $\Delta \mathrm{St}/\mathrm{St}_0$ were proportional. While others have offered similar modifications (e.g., Castro [5]), Eq. (2) will be used to represent this type of enhancement analysis.

Using a biplanar grid in a water tunnel, Johnson and Johnston [6] obtained some of the smallest length-scale ratios recorded. The free-stream intensity ranged from 4.7–7.5%; the L/δ ratios varied from 0.27 to 0.4. For a variation in Re_θ of 1150–1475 over a

Contributed by the International Gas Turbine Institute and presented at the National Heat Transfer Conference, Albuquerque, New Mexico, August 14–17, 1999, of THE AMERICAN SOCIETY OF MECHANICAL ENGINEERS. Manuscript received by the IGTI, October 29, 2002. Associate Editor: R. Bunker.

significant range in HB, they showed C_f enhancement at fixed Re_θ of 15–18%. No heat transfer data were taken in their study.

Maciejewski and Moffat [7,8] used a free jet to generate free-stream turbulence. A significant contribution of this work was the introduction of a near-wall fluctuation Stanton number, St′, defined as

$$\mathrm{St}' \equiv q_w / \rho c_p u'_{\max}(\overline{t}_w - \overline{t}_\infty) \tag{3}$$

The fluctuating velocity, $u'_{\max}$, is the maximum streamwise velocity fluctuation observed along a line drawn normal to the surface at the point where the heat transfer was measured. For flows of air with Tu_∞ from 20–60%, Maciejewski and Moffat suggested that St′ was essentially a constant. They showed a substantial variation in St′ for Tu_∞ near 10%, but a return to the constant value of approximately 0.023 at lower intensities.

Ames and Moffat [9] studied the effects of large-scale, high-intensity free-stream turbulence. To correlate St enhancement, they introduced the parameter

$$\Delta \mathrm{St}/\mathrm{St}_0 \propto \mathrm{Tu}_\infty (\Delta_2 / L)^{1/3} (\mathrm{Re}_{\Delta_2}/1000)^{1/4} \tag{4}$$

The grouping on the right-hand side is known as TLR. Equation (4) was derived using the distortion-theory results of Hunt and Graham [10]. Ames and Moffat chose to evaluate St enhancement at fixed enthalpy-thickness Reynolds number, Re_{Δ_2}. While providing an excellent correlative tool, it is difficult to anticipate Re_{Δ_2}, so the predictive usefulness of the resulting correlation suffers.

Thole [11], Thole et al. [12], and Thole and Bogard [13,14] used wall-injection jets to study free-stream turbulence effects. This work affirmed the constancy of St′ even for Tu_∞ near 10%. It also built on the work of Ames and Moffat by suggesting an empirical fit for Eq. (4) that captured most of the data to within ±10%.

Maniam and Hollingsworth [15] measured wall shear stress and heat transfer in the shear-layer/boundary-layer flow combination of Hollingsworth and Bourgogne [16]. They observed a Re_{Δ_2} variation in St′ that was given by

$$\mathrm{St}'(\Delta_2/\theta)^{1/2}\mathrm{Pr}^{1/2} = 0.0573\,\mathrm{Re}_{\Delta_2}^{-1/6} \tag{5}$$

They also introduced a different near-wall fluctuation Stanton number, St'_τ, defined using the geometric mean of a near-wall streamwise fluctuation and the friction velocity, u_τ

$$\mathrm{St}'_\tau = \frac{q_w}{\rho c_p (u'_{y^+=15} \cdot u_\tau)^{1/2} (\overline{t}_w - \overline{t}_\infty)} \tag{6}$$

The associated correlation

$$\mathrm{St}'_\tau(\Delta_2/\theta)^{1/10}\mathrm{Pr}^{1/2} = 0.08224\,\mathrm{Re}_{\Delta_2}^{-1/7} \tag{7}$$

collected their own data to within approximately ±5%. When those of Ames and Moffat [9] and Sahm and Moffat [17] were added, the scatter increased to approximately ±8%.

Although Sahm and Moffat [17] focused on free-stream turbulence effects in flows with curvature, they also provided flat-plate results that confirmed the ability of the TLR parameter to correlate heat-transfer data. They used passive and jet grids to examine flows with intensities from 7–29% and L/Δ_2 ratios from 47–190. Though the data showed a significant amount of scatter, they reported values for St′ in the neighborhood of 0.023. The most serious problem with their flat-plate data, as they acknowledged, was the likelihood that the free-stream flow was not fully developed in the flat-plate region behind the grid. Still recovering from grid disturbances, the data indicated that the boundary layer thinned as it progressed downstream.

Questioning the generality of results from works using other than passive grid-generated turbulence, Bott and Bradshaw [18,19] used a passive grid in a wind tunnel that had a rotating belt for one wall. By varying the belt speed, the maximum free-stream intensity relative to the differential velocity, $u'_\infty/(\overline{u}_\infty - \overline{u}_{\mathrm{wall}})$, was increased from that obtained in earlier passive-grid studies. This apparatus achieved intensities from 5–23% with L/θ ratios from 17–66. Near-wall velocities were not measured due to complications from belt vibration. No temperature profiles were measured; however, a center strip of the belt was coated with thermochromic liquid crystals to measure surface temperatures. The belt was heated near its leading edge with a high-intensity light source. The measured downstream decay of the surface temperature was smoothed and used as input to a complex computational model of the thermal response of the belt. The model calculated Stanton numbers and enthalpy-thickness Reynolds numbers along the belt surface. Enhancements were presented in terms of the Blair-modified HB and the Castro parameter.

Three other recent pieces of work provide additional reference information for the present study. All three include flow measurements downstream of blade rows in either a compressor or turbine stage that was scaled to simulate an aircraft engine environment. Camp and Shin [20] showed that distinct wakes from compressor blades coherently propagated into downstream blade passages and, in some cases, generated regions that were characterized by turbulent length scales as small as 4% of mean chord. Ames and Plesniak [21] (also Ames [22]) measured L/θ ratios as small as 9.5 in a blade passage that simulated the first stator row downstream of a combustor. Even though no wakes from upstream blades were present, the scales in the blade passage were still significantly smaller than those generated by the combustor. In the blade passage they measured Tu from 2–3% and Re_θ from 2400–2600. Probably the most extensive measurements to date taken in a rotating, multistage turbine test apparatus were provided by Halstead et al. [23]. The measurements showed that the peak turbulence intensities encountered in the downstream stages of a low-pressure turbine coincided with the passage of the coherent wakes from upstream blades. The wakes, likely characterized by small scales as in the compressor study of Camp and Shin, carried peak Tu of less than 5%. The suction-surface Re_θ measured in the rotating, multistage rig ranged from 100–1000; the highest values were measured while simulating engine start-up conditions.

Present Objectives

The literature indicates that there are currently two principal methods used to account for free-stream turbulence effects. The first uses free-stream turbulence properties to correlate enhancement in C_f and St at fixed Re_θ or Re_{Δ_2}. The HB and TLR methods are both of this type. The second makes use of a near-wall Stanton number, St′ or St'_τ, that is assumed to be constant or is related to Re_{Δ_2} and a boundary-layer thickness ratio. The predictive usefulness of either method is limited by the requisite Reynolds number and/or fluctuating velocity information.

Recognizing the design engineer's dilemma and considering the recent experimental data for gas-turbine flows, three objectives for the present work are as follows:

1. Over a range of Reynolds numbers and Tu_∞ representative of flows around aircraft turbine blades, investigate the effect of small-scale free-stream turbulence on heat transfer using the data presented in Part I of this work [24].
2. By extending the range of length-scale ratios examined, explore the possibility of length-scale dependence in the fluctuation Stanton numbers, St′ and St'_τ.
3. For flows with elevated Tu_∞, correlate the heat transfer at the wall to the characteristics of the turbulence without reference to Re_θ or Re_{Δ_2}.

Momentum Boundary Layer: Skin Friction Correlation

This paper focuses on heat transfer correlation. Therefore, from the momentum-layer analysis of Barrett and Hollingsworth [25]

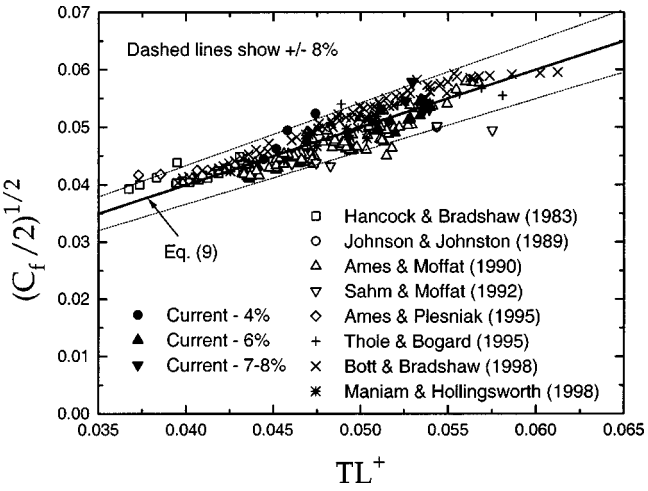

Fig. 1 Skin friction correlated on free-stream intensity and length scale

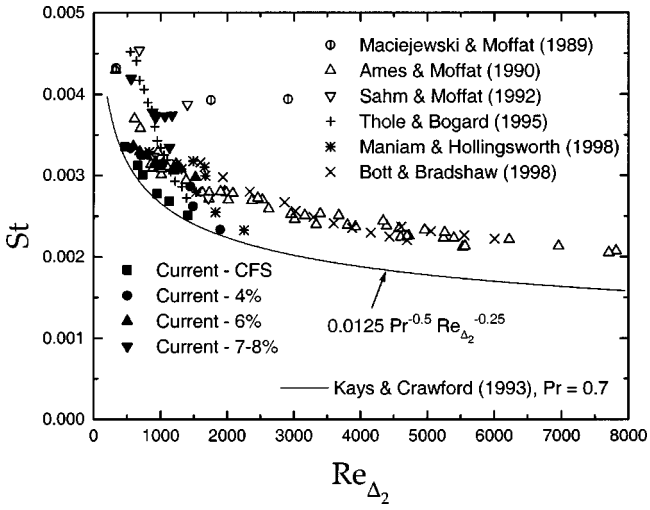

Fig. 2 Stanton number behavior in current and previous studies (St versus Re_{Δ_2})

(also Barrett [26]), only elements essential to the heat transfer analysis are summarized in the forthcoming. The momentum analysis abandons like-Re_θ comparisons and evaluates velocity profiles with similar dimensionless friction velocities. This approach produces the relationships

$$u'_{15}/u_\tau = 1.97(L_e^+)^{1/18} \tag{8}$$

and

$$\sqrt{C_f/2} = TL^+ \tag{9}$$

where TL^+ is given by

$$TL^+ \equiv 0.117(L_e^+)^{-1/18}\mathrm{Tu}_\infty^{0.18}. \tag{10}$$

The subscript 15 indicates that the measurement was made at the location $y^+ = 15$. Figure 1 compares Eq. (9) with data from numerous authors. For a prediction in terms of only Tu_∞ and free-stream length scale (but not Re_θ), the agreement is encouraging. Equation (9) correlates C_f to within $\pm 16\%$ ($\pm 2\sigma$ of data shown). Figure 1 is cast in terms of $(C_f/2)^{1/2}$ because, as we will show, the friction velocity, $u_\tau = \overline{u_\infty}(C_f/2)^{1/2}$, is useful for heat transfer correlation. The data shown in Fig. 1 represent intensities (Tu_∞) from 2 to 30%, length scale ratios (L_e^+) from 100 to 11,000 and Re_θ from 300 to 6300. To predict C_f from Eq. (9), we need only the free-stream mean and fluctuating velocities, $\overline{u_\infty}$ and u'_∞, the length scale, $L_{e,\infty}$ and the fluid properties. We emphasize that a-priori knowledge of Re_θ is unnecessary using this C_f estimator.

Thermal Boundary Layer

Established Heat-Transfer Comparisons. The St behavior observed in the current work is displayed with data from earlier studies in Fig. 2. Figure 3 shows the heat transfer enhancement results from this and other studies using the Blair-modified HB parameter. The reference value, St_0, is taken from Kays and Crawford [27], $St = 0.0125 Pr^{0.5} Re_{\Delta_2}^{0.25}$. The data collapse in Fig. 3 is not very convincing. The highest-intensity small-scale data of the current work is consistently above the upper 40% bound. However, because this graph is of St enhancement, the poor collapse is somewhat misleading. For the data shown, St is actually predicted to within $\pm 10\%$ (as shown in Fig. 4) using the relationship, $\Delta St/St_0 = 0.167\ HB_{mod}$, from Fig. 3. Figure 5 presents St enhancement in terms of the TLR parameter of Ames and Moffat [9]. Using the equation given by Thole and Bogard [13], the TLR parameter yields St predictions to within $\pm 5\%$ (as shown in Fig. 6). Despite the artificial attenuation predicted for the CFS case

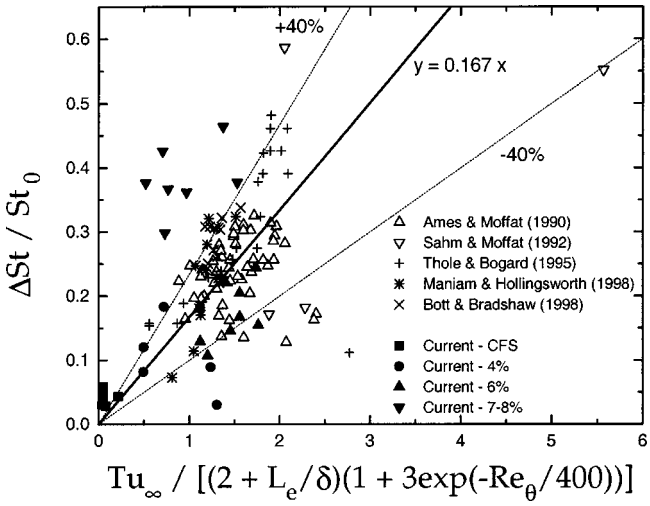

Fig. 3 Stanton number enhancement versus the modified HB parameter

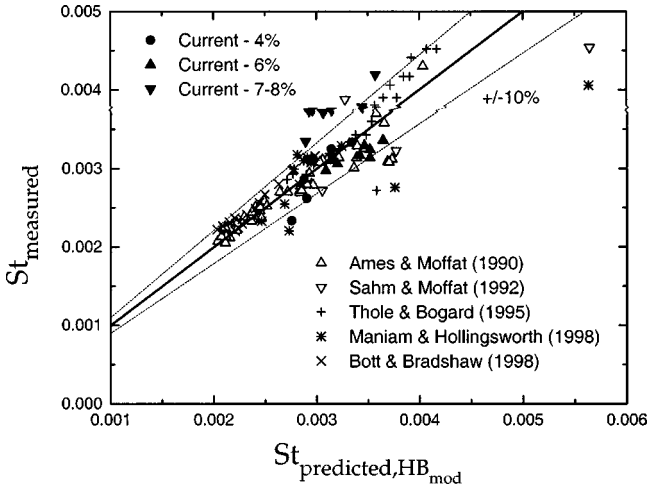

Fig. 4 Measured St versus predicted St using modified HB

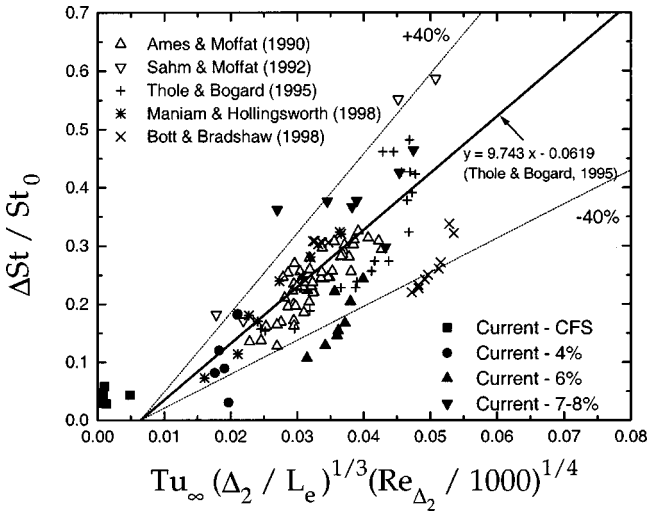

Fig. 5 Stanton number enhancement versus the TLR parameter

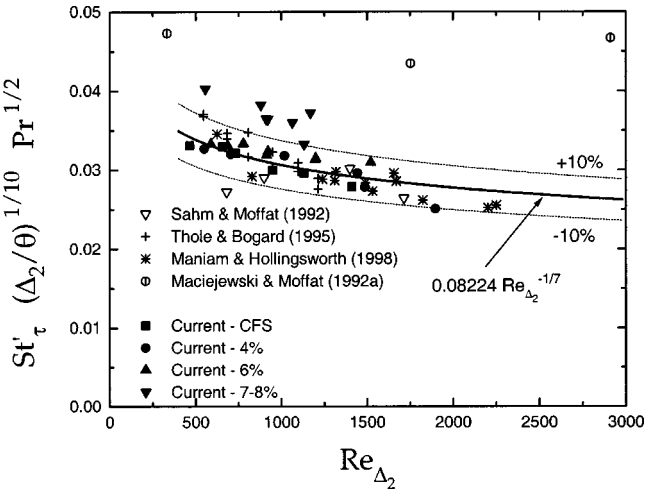

Fig. 7 Near-wall Stanton number of Maniam and Hollingsworth [15] versus Re_{Δ_2}

($\Delta St/St_0 < 0$ when $Tu_\infty = 0$), their equation limits the scatter to approximately the experimental uncertainty in the measurement. The data of Bott and Bradshaw separate into two distinct groups when examined using TLR. Those data associated with the lowest belt-to-free-stream velocity ratio, $\overline{u}_{wall}/\overline{u}_\infty = 0.25$, fall within the 5% scatter. However, for $\overline{u}_{wall}/\overline{u}_\infty = 0.55$, their data fall below the lower 5% bound. Furthermore, since the data outside the scatter band appears to have deterministic trends, Bott and Bradshaw's data is not included in the 2σ random scatter estimate. (To provide meaningful comparisons, their data is also excluded from the $\pm 10\%$ calculation for HB and, unless otherwise noted, all subsequent random error estimates.) Since neither near-wall velocities nor temperature profiles were measured in their study, it is impossible to examine the near-wall structure of the momentum or thermal boundary layers. As a result, it is difficult to conclusively determine why the 0.55 data appears ''out-of-family.'' The systematic trend of the current $Tu_\infty = 6\%$ data (characterized by the smallest L_e^+ values observed) is explained later in the paper.

Figure 7 shows the St'_τ values for the current work as compared with other data and the correlation of Maniam and Hollingsworth [15]. The St'_τ correlation collects most of the data to within $\pm 10\%$. The data of Maciejewski and Moffat [8] and the 7–8% case of the current small-scale data are notable exceptions. Unfortunately, Maciejewski and Moffat did not measure free-stream length scales, so their data cannot be evaluated in the other comparisons.

Length-Scale Dependence in St′. The Reynolds-number dependence in St has been established by Maniam and Hollingsworth [15]. However, an explicit dependence of St′ on turbulent length scale has not been demonstrated until now. Some studies have suggested that there was no consistent connection between turbulent length scale and St′. The following two factors concealed the functional relationship in previous results: first, the observed length-scale-ratio range was not broad enough to detect a trend; second, the length ratio used to analyze the data, either L/θ or L/Δ_2, introduced an unnecessary measurement uncertainty. When the current small-scale data are combined with earlier observations as shown in Fig. 8, a trend is obvious. Over the length-scale range shown, the value of St′ drops approximately 23%. Since the measurement uncertainty on St′ is typically less than 6% in both the current work and that of Maniam and Hollingsworth [15], we can say with confidence that the observed decrease is real. A log-linear regression analysis yields odds of less than 1:10,000,000 ($p < 0.0000001$) that St′ and L_e are not correlated.

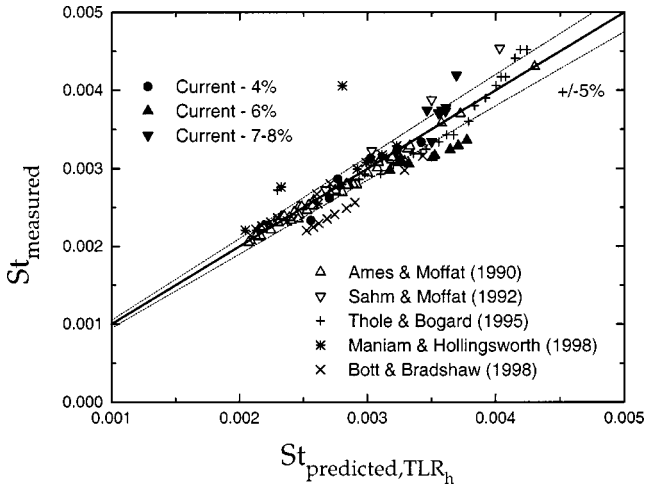

Fig. 6 Measured St versus predicted St using TLR

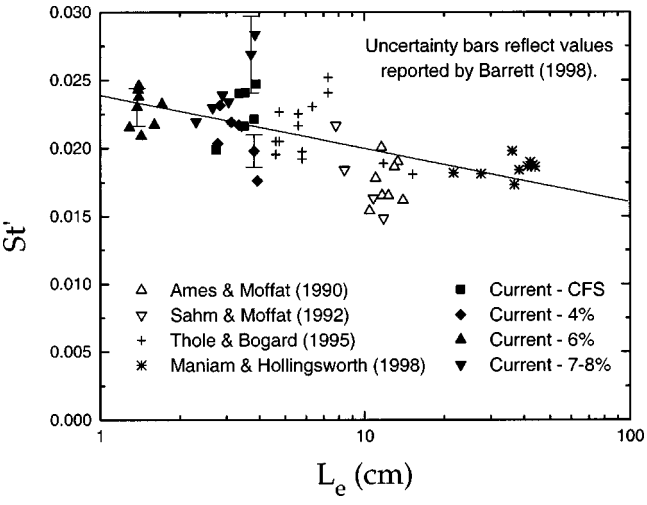

Fig. 8 St′ dependence on L_e

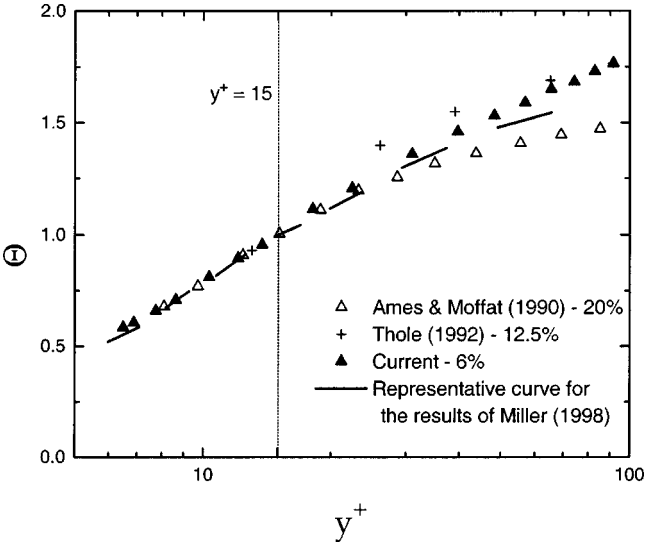

Fig. 9 Profiles of Θ in selected experiments

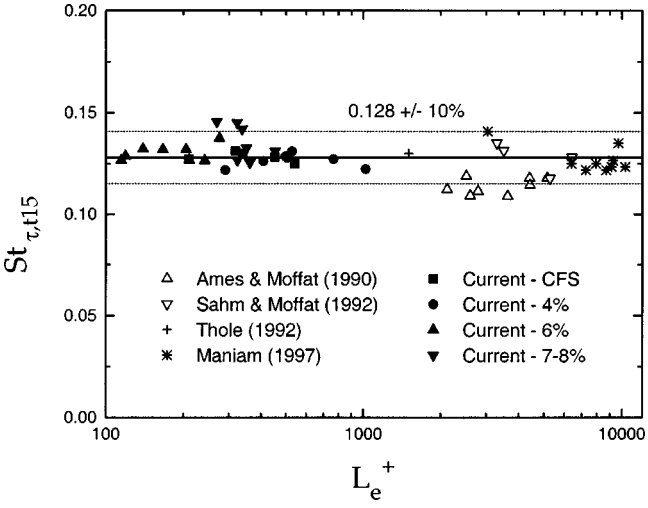

Fig. 10 $St_{\tau,t15}$ versus L_e^+

Re-Evaluating Near-Wall Heat Transfer. Since Maciejewski and Moffat [7] first introduced St′, an advantageous property anticipated by hopeful investigators was that St′, was a universal constant. Because we have uncovered a length-scale dependence in St′, we search for a different dimensionless heat transfer coefficient that can provide a near-wall reference in a boundary-layer heat transfer model.

We begin by invoking the boundary-layer and Couette heat flux assumptions and write the Reynolds-averaged thermal energy equation nondimensionalized using the friction velocity and viscous length scale

$$\frac{q\{y\}}{u_\tau} = -\rho c_p \left(\frac{1}{\mathrm{Pr}} \frac{\partial \overline{t}}{\partial y^+} - \frac{\overline{v't'}}{u_\tau} \right) = \frac{q_w}{u_\tau} \tag{11}$$

We introduce a dimensionless temperature Θ

$$\Theta \equiv \frac{\overline{t}_w - \overline{t}}{\Delta t} \tag{12}$$

where the wall temperature, $\overline{t}_w$, and a yet undetermined characteristic temperature difference, Δt, are used. At a specified x-location, Δt does not vary in the y-direction. The dimensionless equation follows as

$$\frac{q_w}{\rho c_p u_\tau \Delta t} = \frac{1}{\mathrm{Pr}} \frac{\partial \Theta}{\partial y^+} + \frac{\overline{v't'}}{u_\tau \Delta t} \tag{13}$$

For our near-wall analysis, we define the characteristic temperature difference using the value at $y^+ = 15$

$$\Delta t \equiv \overline{t}_w - \overline{t}_{15} \tag{14}$$

The temperature data of Maniam and Hollingsworth [15] were recast by Miller [28] using this characteristic temperature difference and the resulting profiles inside $y^+ = 15$ are easily represented by a single curve. Figure 9 compares the results of Miller to other experiments in air; these comparisons suggest that selecting a universal near-wall profile for Θ is practicable when unheated starting lengths are not significant. If we evaluate Eq. (13) at our near-wall outer boundary ($y^+ = 15$), a universal Θ profile indicates that, for a specified fluid, the first term on the right-hand-side of the equation is a constant. Using the current CFS measurements, the expected value of the constant is 0.051 ($\mathrm{Pr} = 0.7, \partial\Theta/\partial y^+|_{15} = 0.036$).

To examine the last term in Eq. (13), we invoke a gradient-diffusion model along with the turbulent Prandtl number and write

$$\frac{-\overline{v't'}}{u_\tau \Delta t} = \frac{uv^+}{\mathrm{Pr}_t} \frac{\partial \Theta / \partial y^+}{\partial u^+ / \partial y^+} \tag{15}$$

The DNS results of Spalart [29] definitely indicate that uv_{15}^+ is not a universal constant. However, from $\mathrm{Re}_\theta = 300$ to $\mathrm{Re}_\theta = 1410$ the variation is within roughly 5% of an average value. Spalart does show that the turbulent production term, $uv^+ \partial u^+/\partial y^+$ at $y^+ = 15$ is constant over the same Re_θ range. These observations are representative of traditional CFS "low-Reynolds number" behavior. Other authors (Fernholz and Finley [30], Thole and Bogard [14], Maniam [31]) have indicated that in the presence of free-stream turbulence, fewer "low-Re_θ" effects are observed. We expect the elevated turbulence cases to exhibit fewer traditional boundary layer variations at low Reynolds numbers. As we have assumed a universal dimensionless near-wall profile (and therefore a constant du^+/dy_{15}^+), to within the measurement uncertainty, treating uv_{15}^+ as a constant may yield useful results. For a constant turbulent Prandtl number, $\mathrm{Pr}_{t,15}$, the net result of assuming universal Θ and u^+ profiles and a constant uv_{15}^+ is that the dimensionless turbulent heat flux is also constant

$$\left. \frac{-\overline{v't'}}{u_\tau \Delta t} \right|_{15} = \text{constant} \tag{16}$$

For universal profiles, Eq. (16) is true even if the Reynolds stress and turbulent Prandtl number at $y^+ = 15$ vary with downstream development as long as the ratio of the two is constant. If in our near-wall region we have universal dimensionless profiles and Eq. (16) holds, then Eq. (13) allows us to state that

$$\mathrm{St}_{\tau,t15} \equiv \frac{q_w}{\rho c_p u_\tau (\overline{t}_w - \overline{t}_{15})} = \text{constant} \tag{17}$$

We present Eq. (17) as the definition of a near-wall Stanton number based on the friction velocity and the characteristic near-wall temperature difference, $\Delta t = \overline{t}_w - \overline{t}_{15}$. Figure 10 shows values of $\mathrm{St}_{\tau,t15}$ versus L_e^+ for various data sets. The data shown encompass Tu_∞ from 0 to 30% and Re_{Δ_2}, from 300 to 4000. The solid line in the graphs represents a value of 0.128 which is the average value obtained from the current CFS measurements. (From the data set of Thole [11], only the $\mathrm{Tu}_\infty = 12.5\%$ case is presented in the figures because of concerns regarding the $\mathrm{Tu}_\infty = 20\%$ temperature profile.) To within approximately ± 10%, the CFS and most of the

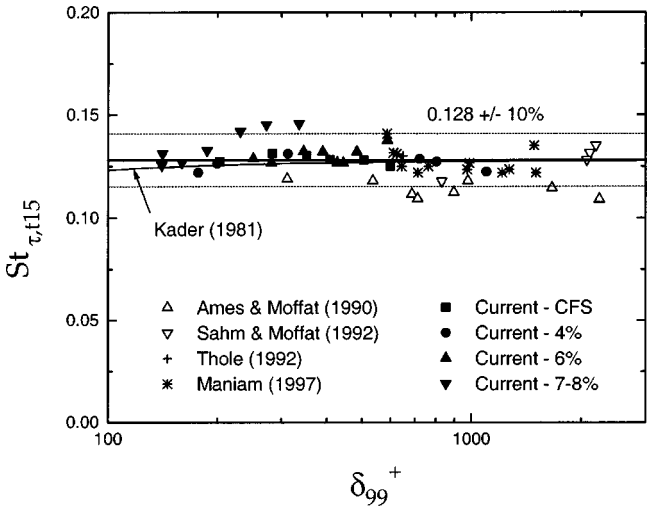

Fig. 11 $St_{\tau,t15}$ **versus** δ_{99}^{+}

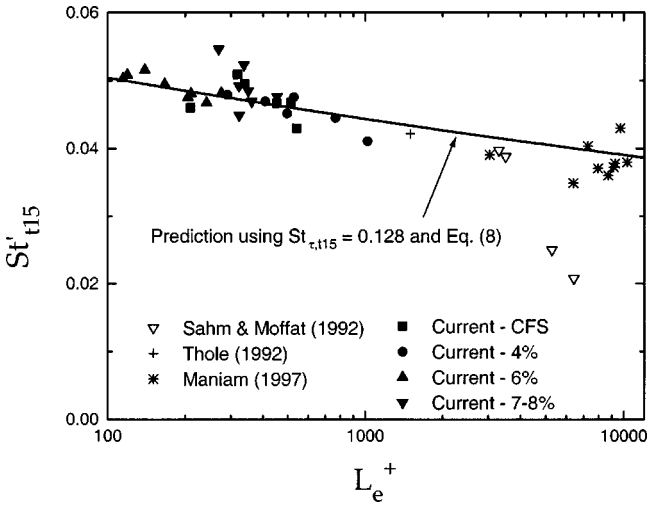

Fig. 12 **Length-scale variation in** St'_{t15}

elevated-intensity data support the constant-value claim. Notice that $St_{\tau,t15}$ is equivalent to $1/t^+$ at $y^+=15$. While we agree with the many authors that state that the thermal law-of-the-wall is not universal in the core region, to within the uncertainty of the measurement, it appears that the value of t^+ at $y^+=15$ does not vary. A detailed analysis of the experimental uncertainty in the measurement of $St_{\tau,t15}$ is presented by Barrett [26]. The results of the analysis indicate that the uncertainty is most likely between 10 and 13% with an upper limit of approximately 16%. The scatter observed in Fig. 10 is reasonable according to these results.

For an additional comparison we consult the DNS results of Kim and Moin [32]. In a simulation of passive scalar transport in a turbulent channel flow, they found that the temperature profiles, t^+, agreed remarkably well with the empirical formulas of Kader [33]. Using Kader's formulas to represent the DNS data, Fig. 11 shows that the DNS results agree with the current CFS average value of 0.128.

We return to the data of Spalart [29] for a quantitative consistency check of the analysis. Using $St_{\tau,t15}=0.128$, Eqs. (13) and (15) are combined to provide an equation for $Pr_{t,15}$

$$Pr_{t,15}=\left[\frac{uv^+}{(0.128+Pr^{-1}\partial\Theta/\partial y^+)}\frac{\partial\Theta/\partial y^+}{\partial u^+/\partial y^+}\right]\Bigg|_{y^+=15} \tag{18}$$

In Eq. (18) we use Spalart's uv_{15}^+ and du^+/dy_{15}^+ values ($Re_\theta=1410$) with our CFS average value for $\partial\Theta/\partial y_{15}^+$ to calculate a $Pr_{t,15}$ of 1.0. This result is in excellent agreement with the experimental results of Blackwell et al. [34] and Hollingsworth et al. [35] and the summary (Antonia [36]) of the DNS results of Kim and Moin [32], Lyons et al. [37] and Kasagi et al. [38].

Assuming a constant value for $St_{\tau,t15}$ allows us to re-evaluate the length-scale dependence of St′ and St'_τ. When St′ is referenced to the characteristic temperature difference $\overline{t}_w-\overline{t}_{15}$, i.e., St'_{t15}, the u'_{15}/u_τ behavior noted earlier convincingly accounts for the variation as noted in Fig. 12. Similar length-scale accountability in $St'_{\tau,t15}$ has been confirmed by Barrett [26].

Development of St Correlation. To evaluate thermal energy transfer within the boundary layer, we divide the boundary layer into a near-wall and a core region. Having constructed a universal near-wall, dimensionless heat transfer coefficient, $St_{\tau,t15}$, we now formulate a correlation for the conventional Stanton number, St. We accomplish this by linking the free-stream boundary conditions to the near-wall result via a turbulent heat flux model that uses rapid distortion theory (RDT) to predict the characteristic fluctuating velocity.

Evaluating the Turbulent Heat Flux Using RDT. In the derivation of the TLR correlation, Ames and Moffat [9] used the RDT results of Hunt and Graham [10] to model the effect that a solid boundary (the wall) has on the fluctuating velocity profile, $v'\{y\}$, when the far-field fluctuating value is nonzero. To estimate the damping of v' by the wall, Ames and Moffat used a limiting form of Hunt and Graham's results that was applicable only for large-scale turbulence. The use of the limiting form is unnecessarily restrictive because the general relationship developed by Hunt and Graham is valid for both large and small-scale far-field turbulence. To make use of the general form, we fit a curve through the results of Hunt and Graham [10] that represents the wall damping of v' in terms of the far-field fluctuation, v'_∞, and the length scale associated with the v' fluctuation, $L_{v'}$

$$v'^2=[(1-e^{-Y})+1.4e^{-1.7Y}Y^{2/3}]v'^2_\infty \tag{19}$$

where $Y=y/L_{v'}$. Assuming isotropic far-field turbulence ($v'_\infty=\overline{u}_\infty Tu_\infty$), a one-velocity, one-length-scale gradient diffusion model coupled with Eq. (19) gives us

$$-\overline{v't'}\propto\frac{[(1-e^{-Y})+1.4e^{-1.7Y}Y^{2/3}]^{1/2}\overline{u}_\infty Tu_\infty y}{Pr_t}\frac{\partial\overline{t}}{\partial y} \tag{20}$$

Equation (20) represents our revision to the Ames and Moffat analysis.

At the boundary between the near-wall and core region ($y^+=15$), we use Eq. (20) to model the increase in v'_{15} due to wall-damped free-stream turbulence. Because the local shear-related production of turbulent kinetic energy approaches a maximum near $y^+=10$, one cannot expect RDT alone to yield the correct value of v'_{15}. For example, Fig. 13 shows measured v'/v'_∞ compared with predicted values from Eq. (19). A value of unity on the ordinate indicates exact agreement. Present data are supplemented with measurements from LDV studies [6,11]; flows represented encompass a range of Tu_∞ and L_e. In addition to the seven profiles shown, the filled diamonds identify v'_{15}/v'_∞ measurements in a total of 13 data sets. The data indicate that for $Tu_\infty\approx5\%$ or less, wall-damped external turbulence is not of adequate scale and intensity to be the dominate contributor at $y^+=15$. For higher Tu_∞, the data are generally well-predicted by Eq. (19). However, some of the data indicate that RDT *under*predicts the wall damping effect; that is, in some data sets, the measured v' at $y^+=15$ are smaller than predicted. However, measurement uncertainty using either a two-wire probe or an LDV at $y^+=15$ must be acknowledged here. For example, the hotwire data shown from the current

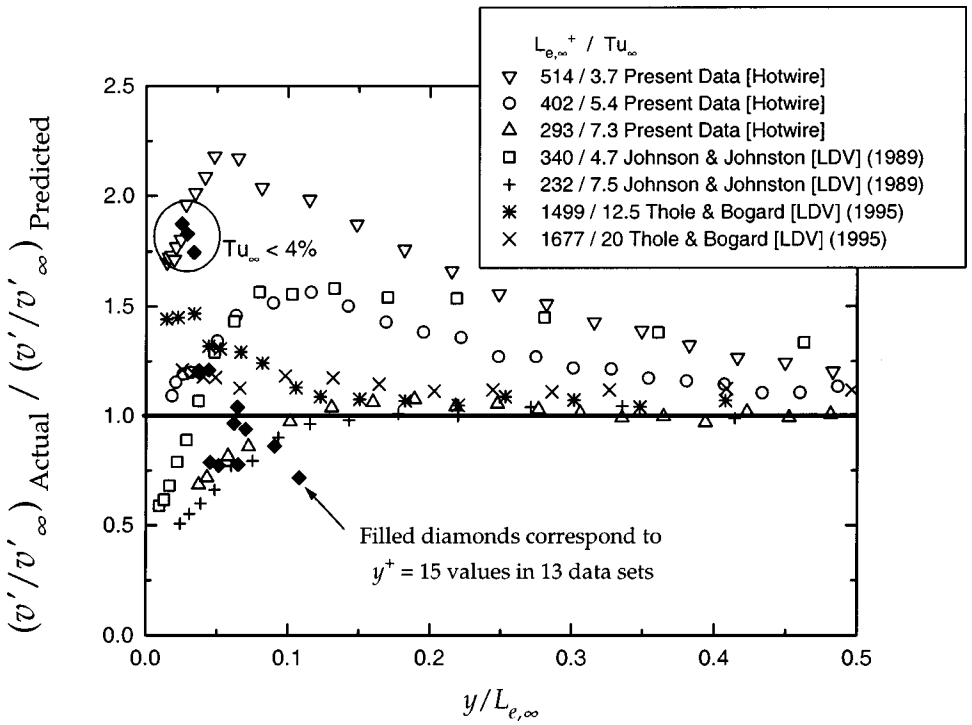

Fig. 13 Comparison of actual and predicted fluctuating velocity ratios

experiments have at least ±9% uncertainty in the ordinate ratio. Figure 13 does not include profiles from Ames and Moffat as they report no measurements of v' below $y^+ \approx 400$. However, their St data are convincingly captured by the predictor that results from this analysis, as will be shown presently.

We reiterate that RDT is used here to develop the form of the increase in v'_{15} due to wall-damped free-stream turbulence—not the absolute value for v'_{15}. At a later step in the analysis, we will empirically scale the contribution of Eq. (20) to the resulting St predictor by comparing that predictor to the available data. With the background of Eq. (20) established, we apply it at $y^+ = 15$ and nondimensionalize as earlier

$$\left.\frac{-\overline{v't'}}{u_\tau \Delta t}\right|_{15} \propto \frac{[(1-e^{-Y_{15}}) + 1.4e^{-1.7Y_{15}} Y_{15}^{2/3}]^{1/2} \overline{u}_\infty \mathrm{Tu}_\infty y_{15}}{\mathrm{Pr}_t u_\tau \Delta t} \left.\frac{\partial \overline{t}}{\partial y}\right|_{15} \tag{21}$$

At this point we introduce the following relationship to estimate the temperature gradient:

$$\left.\frac{\partial \overline{t}}{\partial y}\right|_{15} \propto \frac{(\overline{t}_w - \overline{t}_{15})}{y_{15}} \approx \frac{(\overline{t}_{15} - \overline{t}_\infty)}{y_{15}} \tag{22}$$

Equation (22) is probably the weakest element in our analysis, but its use is driven by the necessity to incorporate the far-field temperature reference into the approximation. In general, the temperature drop from the wall to $y^+ = 15$ is roughly the same magnitude as the remaining drop across the core. So, as an admittedly coarse estimate, the temperature difference across the core is used to approximate the near-wall drop.

Substituting Eq. (22) into Eq. (21), applying Eq. (16) and assuming that L_e appropriately represents $L_{v'}$ yields

$$\frac{(\overline{t}_{15} - \overline{t}_\infty)}{\Delta t} \propto \frac{\mathrm{Pr}_t}{\mathrm{Tu}_\infty} [(1-e^{-15/L_e^+}) + 1.4e^{-1.7(15/L_e^+)} (15/L_e^+)^{2/3}]^{-1/2} \frac{u_\tau}{\overline{u}_\infty} \tag{23}$$

which provides the desired temperature difference across the core. From this, we elicit an expression that relates the temperature difference across the entire boundary layer to only far-field parameters. In terms of Θ and C_f, we have

$$\Theta_\infty - 1 \propto \frac{\mathrm{Pr}_t}{\mathrm{Tu}_\infty} [(1-e^{-15/L_e^+}) + 1.4e^{-1.7(15/L_e^+)} (15/L_e^+)^{2/3}]^{-1/2} \sqrt{C_f/2} \tag{24}$$

Since it is an integral scale, L_e can be interpreted as a measure of the longest correlation distance between two points in the flow field (Hinze [39]). So, when estimating the temperature gradient in the gradient-diffusion model, we should not select characteristic temperatures from points in the flow field that are separated by a distance greater than L_e. For the approximation in Eq. (22) to have merit, the far-field reference location must be within one correlation distance from the wall. In other words, if the reference temperatures in Eq. (22) are to be related in a meaningful way, they must be in correlative proximity. As such, we redefine our core as the section of the boundary layer from $y^+ = 15$ to a distance of "one-L_e" from the wall, i.e., $15 \leqslant y^+ \leqslant L_e^+$. For large scales, $L_e > \Delta$, the free-stream temperature, $\overline{t}_\infty$, and the temperature at a distance of "one-L_e" from the wall, $\overline{t}_{L_e^+}$, are the same, $\overline{t}_\infty = \overline{t}_{L_e^+}$. However, when the scales are small relative to the thermal boundary-layer thickness, $L_e < \Delta$, the $\overline{t}_{L_e^+}$ value must be used as the far-field temperature reference for the gradient-diffusion model to be accurate. For a uniform temperature free-stream, this modification affects only the small-scale data sets.

We define Θ_{ref} as

$$\Theta_{\mathrm{ref}} \equiv \frac{\overline{t}_w - \overline{t}_{L_e^+}}{\overline{t}_w - \overline{t}_{15}} \tag{25}$$

and write the refined-core parallel to Eq. (24)

$$\Theta_{\text{ref}}-1\propto\frac{\text{Pr}_t}{\text{Tu}_\infty}[(1-e^{-15/L_e^+})+1.4e^{-1.7(15/L_e^+)}(15/L_e^+)^{2/3}]^{-1/2}\sqrt{\frac{C_f}{2}} \quad (26)$$

which is equivalent to Eq. (24) when the free-stream is characterized by large-scale turbulence.

Combining the Near-wall and Core Models. To develop a general Stanton number correlation, we begin by defining a Stanton number using the refined-core reference temperature

$$\text{St}_{\text{ref}}\equiv\frac{q_w}{\rho c_p(\overline{t}_w-\overline{t}_{L_e^+})\overline{u}_\infty}=\text{St}_{\tau,t15}\left(\frac{\overline{t}_w-\overline{t}_{15}}{\overline{t}_w-\overline{t}_{L_e^+}}\right)\frac{u_\tau}{\overline{u}_\infty}=\text{St}_{\tau,t15}\Theta_{\text{ref}}^{-1}\sqrt{\frac{C_f}{2}} \quad (27)$$

We introduce a linear expression for Θ_{ref} and define the resulting parameter as TL^+

$$\text{TL}_t^+\equiv\frac{\text{St}_{\tau,t15}\sqrt{C_f/2}}{1+\gamma+\dfrac{\beta\text{Pr}_t}{\text{Tu}_\infty}\sqrt{\dfrac{C_f}{2}}\left[(1-e^{-15/L_e^+})+1.4e^{-1.7(15/L_e^+)}\left(\dfrac{15}{L_e^+}\right)^{2/3}\right]^{-1/2}} \quad (28)$$

where γ and β are constants. To determine γ and β, we fit the available experimental data to the equation,

$$\text{St}_{\text{ref}}=\text{TL}_t^+ \quad (29)$$

Using measured values of C_f and assuming $\text{Pr}_t=1$, values of $\gamma=0.38$ and $\beta=0.28$ allow Eq. (29) to collect the data to within $\pm10\%$ as shown in Fig. 14. (The 2σ scatter increases to $\pm11\%$ if Bott and Bradshaw's data is included.) These γ and β values are used in the remainder of the work.

Using a predicted St_{ref} from Eq. (29), the conventional Stanton number, St, is calculated by

$$\text{St}=\text{St}_{\text{ref}}\left(\frac{\overline{t}_w-\overline{t}_{L_e^+}}{\overline{t}_w-\overline{t}_\infty}\right) \quad (30)$$

If, as designers, we do not know how L_e compares with the boundary-layer thickness, Δ, or if we do not know the value for $\overline{t}_{L_e^+}$, we can assume large-scale turbulence and set the reference temperature equal to the free-stream temperature giving $\text{St}=\text{St}_{\text{ref}}$. (This is actually valid only for the large-scale cases.) Figure 15 compares the measured St to that predicted when large scales are assumed for all test cases (assume $\overline{t}_\infty=\overline{t}_{L_e^+}$); the correlation collects the data to within $\pm11\%$ ($\pm12\%$ including Bott and Bradshaw). Note that, as expected, the variance is slightly increased due to the presence of the small-scale data. This same length-scale phenomenon causes the current 6% data to fall below the lower scatter band in Fig. 6 because the TLR predictor uses the traditional free-stream temperature reference ($\overline{t}_\infty$ not $\overline{t}_{L_e^+}$) for St.

Estimates for St and St_{ref} can be obtained from only far-field information when the value of $(C_f/2)^{1/2}$ is predicted using Eq. (9). Using only $\overline{u}_\infty$, Tu_∞ and $L_{e,\infty}$, both St and St_{ref} data are captured to within 11% ($\pm12\%$ including Bott and Bradshaw). The St agreement is shown in Fig. 16. Just as Eq. (9) gives a prediction for C_f without reference to Re_θ, Eqs. (29) and (30) eliminate Re_θ and Re_{Δ_2} from the information needed to predict St. As a result, the value of the equations as predictive thermal analysis tools is enhanced.

To compare the Stanton number predictive capability of the foregoing TL^+ correlations to that of the HB, TLR, or St'_τ methods, we can only use data for which the measured Re_θ and Re_{Δ_2} are available. Using this subset of data for the comparison, Table 1 summarizes the scatter and information requirements of the various methods. Figure 17 further examines error similarity between TL^+ predictions and those obtained using TLR over all data

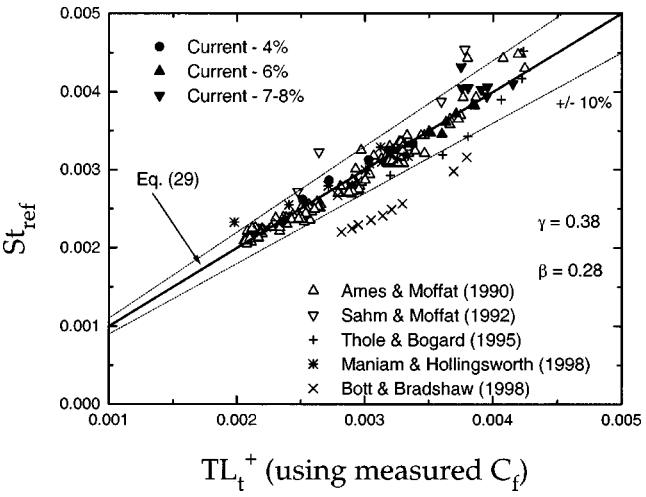

Fig. 14 Predicting St_{ref} using Eq. (29) and measured C_f

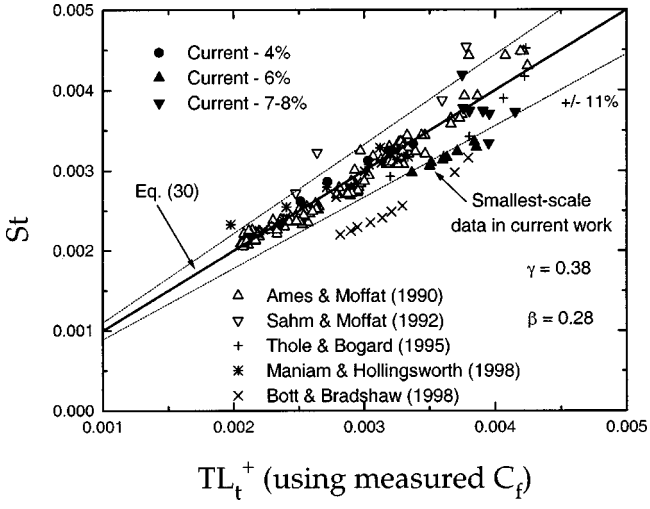

Fig. 15 Predicting St using Eq. (30) and measured C_f (assuming large-scale turbulence)

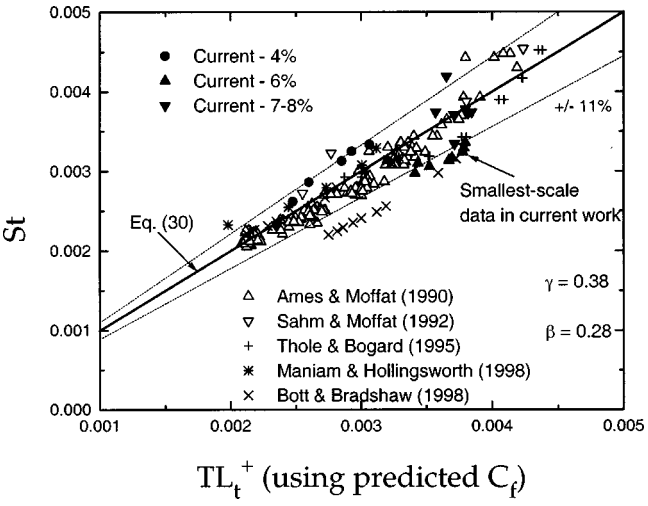

Fig. 16 Predicting St using Eq. (30) and predicted C_f (assuming large-scale turbulence)

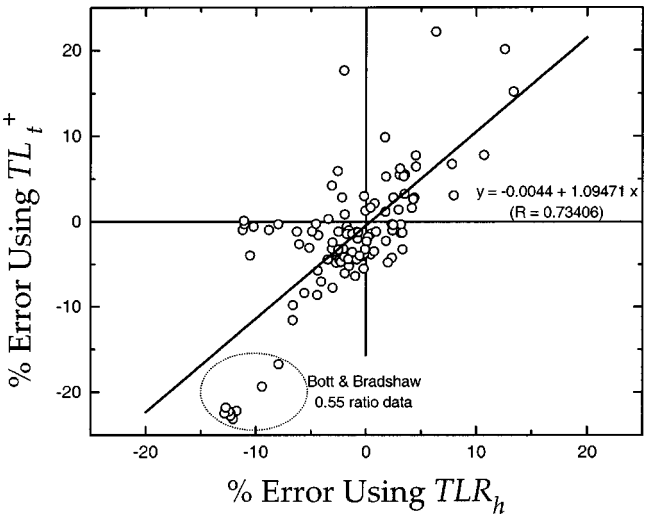

Fig. 17 Error in predictions: TL^+ versus TLR

sets. Since TL^+ and TLR share elements of RDT and neither model uses momentum-thickness information, the statistical correlation observed in Fig. 17 is not surprising.

Limitations and Weaknesses

As were the HB, TLR, and St'_τ correlations, the new TL^+ correlation was developed based on flat-plate turbulent-boundary-layer theory and data. In its present state, the correlation does not account for surface roughness, curvature, streamwise pressure gradient, unheated starting length or the presence of a laminar boundary layer beneath a turbulent free-stream. These conditions are certainly important to many flows of interest. However, just as the baseline correlation of Kays and Crawford has been adapted to address some of these conditions, the hope is that the TL^+ correlations can also be modified to include the stated effects.

In attempts to adapt the TL^+ correlations to more challenging flows, weaknesses in the current formulation will require particular attention. As noted earlier, the weakest element is likely the equating of the temperature drop across the near-wall region, $\overline{t}_w - t_{15}$, to the temperature drop across the refined core, $t_{15} - t_{L_e^+}$. This equality was assumed solely to introduce the far-field temperature, which led to a prediction for the conventional Stanton number. If the structure of the temperature profile changes (as for flows with curvature and streamwise pressure gradient), an alternate approach should be investigated.

An additional vulnerability of the TL^+ correlation is that the Hunt and Graham RDT results were applied at $y^+ = 15$, where RDT alone is not expected to yield the correct value of v'_{15}. The subsequent introduction of empirical constants γ and β essentially reduces the RDT contribution to a prediction of the functional form of wall-damped free-stream enhancement in the near-wall characteristic velocity. It appears that RDT reasonably captures that form for the purpose of predicting Stanton number in flat-plate boundary layers subjected to the levels of free-stream turbulence seen in the experimental studies to date.

The value of the constant near-wall Stanton number, $St_{\tau,t15}$, should be evaluated in more complex flows. The near-wall t^+ profile must differ significantly from that shown in Fig. 9 for the value of $St_{\tau,t15}$ to change. A roughened wall can alter the near-wall profile, so $St_{\tau,t15}$ is expected to vary with surface roughness. Finally, any effort to predict heat transfer through a laminar boundary layer exposed to a turbulent free-stream must redefine an appropriate near-wall Stanton number for the TL^+ approach to be fruitful.

The momentum and enthalpy-thickness Reynolds numbers hold enormous amounts of information about the flow conditions; this is one reason their prediction is not a simple task. Correlations based on Re_θ and Re_{Δ_2} benefit from that wealth of information. While the TL^+ correlations require less flow information for use, because Re_θ and Re_{Δ_2} information is not included, they may require more extensive modifications to address complex flows.

Table 1 Summary of data scatter and requisite inputs for the correlations (uses data subset for which both Re_θ and Re_{Δ_2} are available)

				New Correlation			
	HB_{mod}	TLR	$St'_\tau w$/ Eq. (8)	Eq. (30) (measured C_f)	Eq. (30) (predicted C_f)	Eq. (30) ($L_e > \Delta$ assumed) (measured C_f)	Eq. (30) ($L_e > \Delta$ assumed) (predicted C_f)
2σ scatter on St prediction	10%	5%	9%	6%	8%	8%	9%
Tu_∞	Req'd	Req'd		Req'd	Req'd	Req'd	Req'd
$L_{e,\infty}$	Req'd	Req'd	Req'd	Req'd	Req'd	Req'd	Req'd
$t_{L_e^+}$				Req'd	Req'd		
C_f			Req'd	Req'd		Req'd	
u_∞	Req'd	Req'd	Req'd	Req'd	Req'd	Req'd	Req'd
θ	Req'd		Req'd				
Δ_2	Req'd	Req'd	Req'd				

Conclusions

The new TL^+ correlations are able to predict the flat-plate dimensionless heat transfer coefficient to within $\pm 11\%$ using only free-stream information. This suggests that the boundary layer is responding to the free-stream flow in a locally self-similar manner. That is, at any x location, a systematic near-wall flow ''response'' is driven primarily by inputs from the outer-region flow. This is not a new idea; local similarity is a key assumption in correlations that use Reynolds numbers based on boundary-layer integral length scales as well. In this light, the choice of L_e^+ to characterize the differences in the outer-region (L_e) and near-wall (or viscous, ν/u_τ) scales seems intuitive.

The TL^+ correlations compare well in accuracy to earlier correlation methods; the scatter ranges from 6–9%, while the HB TLR, and St'_τ methods ranged from 5–10% over the same data subset. Since the TL^+ correlations do not require conventional boundary-layer Reynolds number information, they hold promise as predictive tools.

Acknowledgments

The authors thank Dr. S. J. Kleis for his consultation and the use of his wind tunnel facility. Support was received from the Texas Higher Education Coordinating Board (ATP Grant #003652-944), the UH Institute for Space Systems Operations and the UH Energy Lab. Dr. Barrett received additional support from the NASA/Texas Space Grant Consortium and the SAE Doctoral Scholars Program.

References

[1] Simonich, J. C., and Bradshaw, P., 1978, ''Effect of Free-Stream Turbulence on Heat Transfer Through a Turbulent Boundary Layer,'' ASME J. Heat Transfer, **100**, pp. 671–677.
[2] Kader, B. A., and Yaglom, A. M., 1972, ''Heat and Mass Transfer Laws for Fully Turbulent Wall Flows,'' Int. J. Heat Mass Transf., **15**, p. 2329.
[3] Hancock, P. E., and Bradshaw, P., 1983, ''The Effect of Free-Stream Turbulence on Turbulent Boundary Layers,'' ASME J. Fluids Eng., **105**, pp. 284–289.
[4] Blair, M. F., 1983, ''Influence of Free-Stream Turbulence on Turbulent Boundary Layer Heat Transfer and Mean Profile Development,'' ASME J. Heat Transfer, ''Part I—Experimental Data,'' **105**, pp. 33–40. ''Part II—Analysis of Results,'' **105**, pp. 41–47.
[5] Castro, I. P., 1984, ''Effect of Free Stream Turbulence on Low Reynolds Number Boundary Layers,'' ASME J. Fluids Eng., **106**, pp. 298–306.
[6] Johnson, P. L., and Johnston, J. P., 1989, ''The Effects of Grid-Generated Turbulence on Flat and Concave Turbulent Boundary Layers,'' Report No. MD-53, Dept. of Mech. Eng., Stanford University.
[7] Maciejewski, P. K., and Moffat, R. J., 1989, ''Heat Transfer with Very High Free-Stream Turbulence,'' Report No. HMT-42, Dept. of Mech. Eng., Stanford University.
[8] Maciejewski, P. K., and Moffat, R. J., 1992, ''Heat Transfer with Very High Free-Stream Turbulence,'' ASME J. Heat Transfer, ''Part I—Experimental Data.'' **114**, 827–833; ''Part II—Analysis of Results,'' **114**, pp. 834–839.
[9] Ames, F. E., and Moffat, R. J. 1990, ''Heat Transfer with High Intensity, Large Scale Turbulence: The Flat Plate Turbulent Boundary Layer and the Cylindrical Stagnation Point,'' Report No. HMT-44, Dept. of Mech. Eng., Stanford University.
[10] Hunt, J. C. R., and Graham, J. M. R., 1978, ''Free-Stream Turbulence Near Plane Boundaries,'' J. Fluid Mech., **84**(2), pp. 209–235.
[11] Thole, K. A., 1992, ''High Free-Stream Turbulence Effects on the Transport of Heat and Momentum,'' Ph.D. dissertation, The University of Texas at Austin.
[12] Thole, K. A., Bogard, D. G., and Whan-Tong, J. L., 1994, ''Generating High Freestream Turbulence Levels,'' Exp. Fluids, **17**, pp. 375–380.
[13] Thole, K. A., and Bogard, D. G., 1995, ''Enhanced Heat Transfer and Shear Stress Due to High Free-Stream Turbulence,'' ASME J. Turbomach., **117**, pp. 418–424.
[14] Thole, K. A., and Bogard, D. G., 1996, ''High Freestream Turbulence Effects on Turbulent Boundary Layers,'' ASME J. Fluids Eng., **118**, pp. 276–284.
[15] Maniam, B. M., and Hollingsworth, D. K., 1998, ''Experimental Investigation of Heat Transfer in a Three-Dimensional Boundary Layer Beneath a Mixing Layer,'' *Proc., 7th AIAA/ASME Joint Thermophysics and Heat Transfer Conference*, Albuquerque, NM, **2**, pp. 123–130.
[16] Hollingsworth, D. K., and Bourgogne, H.-A., 1995, ''The Development of a Turbulent Boundary Layer in High Free-Stream Turbulence Produced by a Two-Stream Mixing Layer,'' Exp. Therm. Fluid Sci., **11**, pp. 210–222.
[17] Sahm, M. K., and Moffat, R. J., 1992, ''Turbulent Boundary Layers with High Turbulence: Experimental Heat Transfer and Structure on Flat and Convex Walls,'' Report No. HMT-45, Dept. of Mech. Eng., Stanford University.
[18] Bott, D. M., and Bradshaw, P., 1997, ''Effect of High Levels of Free-Stream Turbulence on Boundary Layer Skin Friction and Heat Transfer,'' Report No. MD-75, Dept. of Mech. Eng., Stanford University.
[19] Bott, D. M., and Bradshaw, P., 1998, ''Effect of High Free-Stream Turbulence on Boundary Layer Skin Friction and Heat Transfer,'' *Proc., 36th Aerospace Sciences Meeting & Exhibit*, Reno, NV, AIAA Paper 98-0531.
[20] Camp, T. R., and Shin, H.-W., 1995, ''Turbulence Intensity and Length Scale Measurements in Multistage Compressors,'' ASME J. Turbomach., **117**, pp. 38–46.
[21] Ames, F. E., and Plesniak, M. W., 1995, ''The Influence of Large Scale, High Intensity Turbulence on Vane Aerodynamic Losses, Wake Growth, and the Exit Turbulence Parameters,'' *Proc., International Gas Turbine and Aeroengine Congress and Exposition*, Houston, TX, ASME Paper 95-GT-290.
[22] Ames, F. E., 1997, ''The Influence of Large-Scale High-Intensity Turbulence on Vane Heat Transfer,'' ASME J. Turbomach., **119**, pp. 23–30.
[23] Halstead, D. E., Wisler, D. C., Okiishi, T. H., Walker, G. J., Hodson, H. P., and Shin, H.-W., 1997, ''Boundary Layer Development in Axial Compressors and Turbines: Part 3 of 4-LP Turbines,'' ASME J. Turbomach., **119**, pp. 225–237.
[24] Barrett, M. J., and Hollingsworth, D. K., 2003, ''Heat Transfer in Turbulent Boundary Layers Subjected to Free-Stream Turbulence—Part I: Experimental Results,'' ASME J. Turbomach., **125**, pp. 232–241.
[25] Barrett M. J., and Hollingsworth D. K., 2002, ''Correlating Friction Velocity in Turbulent Boundary Layers Subjected to Free-Stream Turbulence,'' *Proc., 32nd AIAA Fluid Dynamics Conference and Exhibit*, St. Louis, Missouri, Paper No. AIAA-2002-2863.
[26] Barrett, M. J., 1998, ''Skin Friction and Heat Transfer in Turbulent Boundary Layers Subjected to Small-Scale Free-Stream Turbulence,'' Ph.D. dissertation, Dept. of Mech. Eng., University of Houston.
[27] Kays, W. M., and Crawford, M. E., 1993, Convective Heat Transfer, Mc-Graw Hill.
[28] Miller, S., 1999, ''Correlating Turbulent Boundary Layer Heat Transfer in the Presence of Free-Stream Turbulence,'' M. S. thesis, Dept. of Mech. Eng., University of Houston.
[29] Spalart, P. R., 1988, ''Direct Simulation of a Turbulent Boundary Layer up to $R_\theta = 1410$,'' J. Fluid Mech., **187**, pp. 61–98.
[30] Fernholz, H. H., and Finley, P. J., 1996, ''The Incompressible Zero-Pressure-Gradient Turbulent Boundary Layer: An Assessment of the Data,'' Prog. Aerosp. Sci., **32**, pp. 245–311.
[31] Maniam, B. M., 1997, ''An Experimental Study of the Turbulent Momentum and Thermal Boundary Layers Beneath a Two-Stream Mixing Layer,'' Ph.D. dissertation, Dept. of Mech. Eng., University of Houston.
[32] Kim, J., and Moin, P., 1989, ''Transport of Passive Scalars in a Turbulent Channel Flow,'' *Turbulent Shear Flows 6*, J.-C. André, et al., eds., Springer-Verlag.
[33] Kader, B. A., 1981, ''Temperature and Concentration Profiles in Fully Turbulent Boundary Layers,'' Int. J. Heat Mass Transf., **24**(9), pp. 1541–1544.
[34] Blackwell, B. F., Kays, W. M., and Moffat, R. J., 1972, ''The Turbulent Boundary Layer on a Porous Plate: An Experimental Study of the Heat Transfer Behavior with Adverse Pressure Gradients,'' Report No. HMT-16, Dept. of Mech. Eng., Stanford University.
[35] Hollingsworth, D. K., Moffat, R. J., and Kays, W. M., 1992, ''The effect of Concave Surface Curvature on the Turbulent Prandtl Number and the Thermal Law of the Wall,'' Exp. Therm. Fluid Sci., **5**, pp. 299–306.
[36] Antonia, R. A., 1993, ''Direct Numerical Simulations and Hot Wire Experiments: A Possible Way Ahead?'' *New Approaches and Concepts in Turbulence*, Dracos, Th., and Tsinober, A., eds., Birkhauser Verlag.
[37] Lyons, S. L., Hanratty, T. J., and McLaughlin, J. B., 1991, ''Direct Numerical Simulation of Passive Heat Transfer in a Turbulent Channel Flow,'' Int. J. Heat Mass Transf., **34**, pp. 1149–1162.
[38] Kasagi, N., Tomita, Y., and Kuroda, A., 1991, ''Direct Numerical Simulation of the Passive Scalar Field in a Two-Dimensional Channel Flow,'' *Proc., Third ASME-JSME Thermal Engineering Joint Conference*, Reno, NV.
[39] Hinze, J. O., 1975, *Turbulence*, McGraw-Hill.

Leading-Edge Film-Cooling Physics—Part III: Diffused Hole Effectiveness

William D. York

James H. Leylek

Department of Mechanical Engineering,
Clemson University,
Clemson, SC 29634

A proven computational methodology was applied to investigate film cooling from diffused holes on the simulated leading edge of a turbine airfoil. The short film-hole diffuser section was conical in shape with a shallow half-angle, and was joined to a plenum by a cylindrical metering section. The diffusion resulted in a film-hole breakout area of 2.5 times that of a cylindrical hole. In the present paper, predictions of adiabatic effectiveness for the cases with diffused holes are compared to results for standard cylindrical holes, and performance is analyzed in the context of extensive flowfield data. The leading edge surface was elliptic in shape to accurately model a turbine airfoil. The geometry consisted of one row of holes centered on the stagnation line, and two additional rows located 3.5 hole (metering section) diameters downstream on either side of the stagnation line. Film holes in the downstream rows were centered laterally between holes in the stagnation row. All holes were angled at 20 deg with the leading edge surface, and were turned 90 deg with respect to the streamwise direction (radial injection). The average blowing ratio was varied from 1.0 to 2.5, and the coolant-to-mainstream density ratio was equal to 1.8. The steady Reynolds-averaged Navier-Stokes equations were solved with a pressure-correction algorithm on an unstructured, multi-block grid containing 4.6 million finite-volumes. A realizable k-ε turbulence model was employed to close the equations. Convergence and grid-independence was verified using strict criteria. Based on the laterally averaged effectiveness over the leading edge, the diffused holes showed a marked advantage over standard holes through the range of blowing ratios. However, ingestion of hot crossflow and thermal diffusion into the second row of film holes was observed to cause significant, and potentially detrimental, heating of the film-hole walls.
[DOI: 10.1115/1.1559899]

1 Introduction

To achieve high cycle efficiency in modern gas turbine engines, the temperature of combustion gases entering the turbine is typically at a temperature greater than the metal airfoils could withstand without a carefully designed cooling scheme. One of the most effective and often used methods for cooling the airfoils is film cooling. Air is bled from the compressor, sent directly to channels inside the blades and vanes, and then injected to the exterior surface through an array of small holes. Film cooling is especially critical at the leading edge of the turbine blades, since the largest thermal load occurs here and the cooling flow effects the aerodynamics and heat transfer of the entire airfoil. The problem is complicated by difficult mechanisms, including a stagnating freestream, strong acceleration and curvature, and interactions between the required multiple rows of coolant jets.

The gas turbine industry currently relies on a database of one and two-dimensional empirical correlations and engine performance data to design film-cooling schemes. A three-dimensional, predictive tool could potentially revolutionize cooling design and provide quick turn-around and relatively low cost. Computational fluid dynamics (CFD) can fill this role, but only if it is proven to give consistently accurate results. Toward that goal, the present study applies a systematic computational methodology to the leading-edge film-cooling problem. Validation of the methodology in the prediction of adiabatic effectiveness was achieved in Part I of this series of papers by York and Leylek [1].

This portion of the research program is an excellent case study in using CFD effectively in the actual design process. Currently, film-cooling holes on the leading edge of turbine blades are almost exclusively cylindrical in shape. Numerous numerical and experimental research has shown that exit-diffused film holes can provide far better cooling performance over cylindrical holes when used in the suction and pressure-side hole rows. The shaped hole may also provide increased performance on the leading edge, but little data is available to the designer on this configuration. On the request of an industry sponsor, film holes with a conical diffuser at their exits were simulated using the computational methodology, which was previously validated with experimental data on the standard holes. The sponsor received fast and reliable information on the conical diffuser hole design to help determine feasibility for use in current engine programs.

2 Literature Review

In the past two decades, there has been a fair amount of research, both experimental and numerical, on the leading-edge film-cooling problem. Notable experimental studies include the work of Mick and Mayle [2], Mehendale and Han [3], Ekkad et al. [4], and Salcudean et al. [5]. These researchers measured the adiabatic effectiveness and heat transfer coefficients on film-cooled leading edge models. All of these authors employed cylindrical holes in their tests. A more detailed explanation of the papers listed in the foregoing may be found in Part I of this series [1].

Cruse [6] used an infrared imaging technique to acquire detailed adiabatic effectiveness data on a film-cooled leading edge that was elliptical in shape, similar to an actual turbine airfoil. Again, the film holes were cylindrical in shape. The conditions of Cruse [6] were simulated in Part I of the present set of papers [1], and the computations were validated against this data.

The only known study in the open literature that examines the use of shaped holes on the leading edge is that of Reiss and Bölcs

Contributed by the International Gas Turbine Institute and presented at the International Gas Turbine and Aeroengine Congress and Exhibition, Amsterdam, The Netherlands, June 3–6, 2002. Manuscript received by the IGTI October 10, 2001. Paper No. 2002-GT-30520. Review Chair: E. Benvenuti.

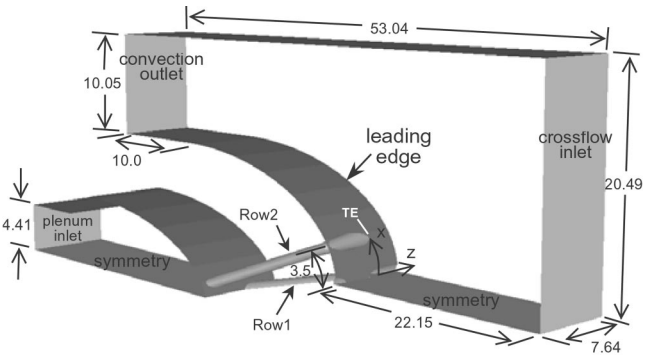

Fig. 1 View of the computational domain with dimensions in film-hole diameters ($D=6.32$ mm). The transparent side boundaries are periodic planes.

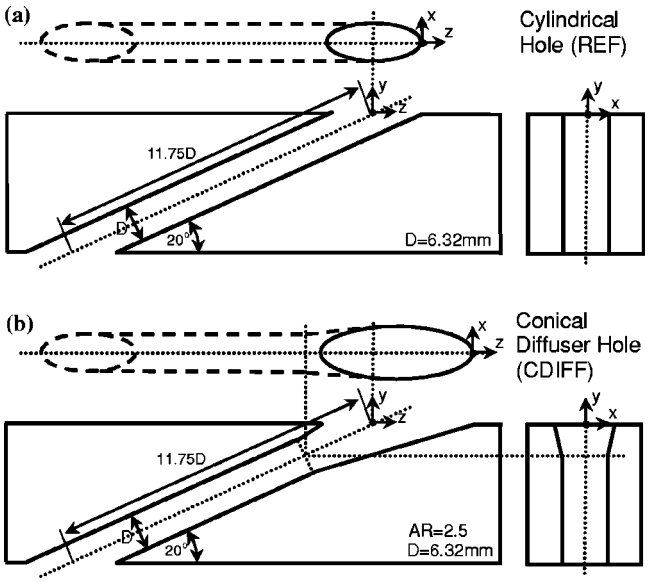

Fig. 2 Schematic of (*a*) the cylindrical (REF) film-hole, and (*b*) the conical diffuser (CDIFF) hole in the three orthogonal planes

[7]. The authors used a transient liquid crystal technique to make detailed measurements of the adiabatic effectiveness and heat transfer coefficient on a cylindrical leading edge. Five staggered rows of cooling holes were located at 0, ±20, and ±40 deg with respect to the stagnation line. In addition to standard cylindrical holes, the authors investigated holes with exits expanded in the flow direction and in the lateral direction. The holes with the forward expansion performed the best, generally exhibiting the highest spanwise averaged effectiveness and lowest heat transfer at all blowing ratios. The laterally diffused holes gave a small improvement in effectiveness over the standard cylindrical holes, but showed large increases in heat transfer downstream of the holes at high blowing ratios.

On the numerical side, a blind test was organized to assess the ability of CFD in predicting leading edge film cooling. Chernobrovkin and Lakshminarayana [8], Lin et al. [9], Martin and Thole [10], and Thakur et al. [11] each ran simulations following the experimental conditions of Cruse [6] with a cylindrical leading edge model. Only a single blowing ratio was examined ($M=2.0$). The different authors applied varied grid types, discretization schemes, and turbulence models to the problem. The agreement with the experimental effectiveness data was mixed. There are no known numerical studies of shaped or diffused holes on the leading edge in the literature. The present paper aims to add significantly to the knowledge base in this area by providing surface data for conical diffuser holes and explaining the physics involved.

3 Methodology

3.1 Computational Model. The computational model employed in the present work is identical to that described in Part I [1], with the only exception being the addition of a diffuser section to the film holes. The numerical domain is shown in Fig. 1. The model developed and validated in Part I [1] was derived from the experimental setup of Cruse [6]. The leading edge was elliptical in shape, with a major axis of 132 mm and a minor axis of 66.0 mm, and the thickness of the leading-edge wall (separating the freestream from the plenum) was 25.4 mm. A symmetry plane was used to impose the freestream stagnation condition and was normal to the elliptic leading edge at it widest part. One row of cooling holes was located along the stagnation line (Row1), and a second row of holes was located $3.5D$ downstream (Row2) and was staggered such that holes in this row were centered laterally between holes in the Row1. All film holes had an injection angle of $\alpha=20$ deg and a compound angle of $\phi=90$ deg (spanwise injection). The holes had a lateral spacing (within each row) of $S=7.64D$ between their centerlines.

The conical diffuser (CDIFF) hole geometry was specified by a gas turbine engine manufacturer from design considerations, and is shown schematically in Fig. 2 with a comparison to the standard cylindrical hole. The CDIFF geometry would result from driving a cone-shaped cutting tool into the end of the cylindrical film hole, such that expansion is identical in all directions. The diffuser section had a shallow half-angle and it began only a short distance upstream of the exit plane (on the hole centerline). This resulted in an area ratio of AR=2.5, meaning that the CDIFF breakout area was 2.5 times greater than the standard (REF) holes. The cylindrical "metering" section at the upstream side of the holes had a diameter of $D=6.32$ mm to match the REF holes, as did the total hole length of $11.75D$.

Periodic planes served as the lateral bounds of the domain and were located halfway between the midpoints of two adjacent holes (in different rows), and were spaced apart by the film-hole pitch (S). Because of the significantly wider breakout of the CDIFF holes, the periodic plane had to pass through the Row1 diffuser section, and thus the Row1 hole breakout is actually split with a portion located on each side of the computational domain, as seen in Fig. 1. When the periodic and the symmetry conditions are imposed, the domain simulates a leading edge with three rows of cooling holes and infinite span that is identical to the configuration with the REF holes in Part I [1].

Mainstream air at a temperature of 300 K entered the domain through a uniform velocity inlet with $U_\infty=10$ m/s located 140 mm upstream of the stagnation point. The turbulence intensity at the mainstream inlet was set at 0.2%, and the length scale of turbulence was specified as one-tenth of the inlet height to match the simulations from Part I [1]. Coolant air entered the plenum through a uniform velocity inlet at a temperature of 166.5 K, which produced a density ratio of DR=1.8. The plenum inlet velocity was varied to achieve specific blowing ratios. The blowing ratios discussed in this study are calculated from the mean velocity in the cylindrical metering section averaged over all holes. Thus, for a specific blowing ratio, the CDIFF and REF cases have the same overall mass flux of coolant. All fluid exited the domain well downstream of the leading-edge model through a convection outlet. A flat wall joined the curved leading edge surface to the outlet, and the upper boundary of the domain was a solid wall. All walls were specified as adiabatic (zero heat transfer).

3.2 Grid. To allow a fair comparison with the validated results for the standard holes from Part I [1], the finite-volume mesh employed was virtually identical to that used the REF simulations.

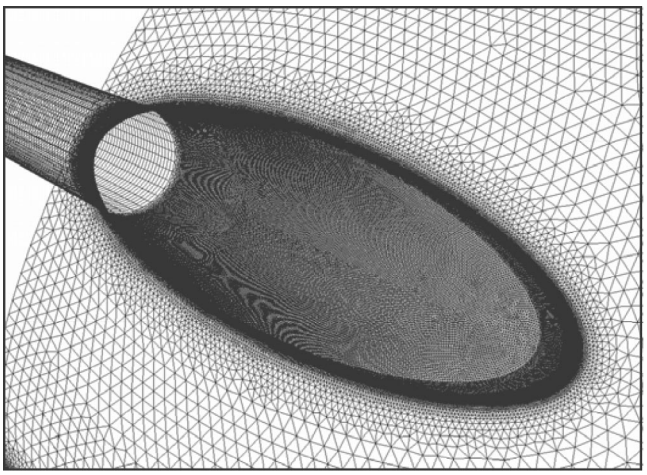

Fig. 3 View of the film-hole and leading edge surface mesh at the Row2 hole breakout. The extremely dense grid in this region was necessary to achieve a y^+ of unity or less along the walls while maintaining high quality cells.

A superblock, unstructured approach was used to maximize overall grid quality, and the mesh was comprised of hexahedra, triangular prism, and tetrahedra cells. To fully resolve the viscous sublayers, all cells along walls were sized such that the first grid point was located at a maximum wall distance of $y^+=1$. Due to the larger volume of the film holes with the diffuser, the CDIFF cases contained 4.8 million total cells, approximately 30% more cells than the REF cases. A view of the surface mesh on the leading edge and film-hole wall at the Row2 breakout is shown in Fig. 3. Grid generation was accomplished with GAMBIT and T-Grid software from Fluent, Inc.

3.3 Simulation Details. The steady Reynolds-averaged Navier-Stokes equations were solved with the aid of a pressure-correction algorithm and a multi-grid convergence accelerator in Fluent 5 software from Fluent, Inc. Discretization of the governing equations was second-order accurate. The realizable k-ε (RKE) turbulence model of Shih et al. [12] was used to close the set of equations. The satisfaction of the realizability constraints in the k-ε model eliminates the spurious production of turbulent kinetic energy in regions of large fluid strain. The RKE model is therefore expected to give superior results to the standard k-ε model for the flowfield of the present study, while retaining the economic advantage of the two-equation model. A two-layer near wall treatment, in which the k-equation was solved in the wall-adjacent region, was used to resolve the turbulent boundary layers down to the walls.

The solution was declared as converged only when strict criteria were satisfied. First, residuals of the governing equations, normalized by their respective inlet fluxes, dropped below 0.1%. Second, the global mass and energy imbalances dropped below 0.01%. Lastly, profiles of flowfield variables (U, T, P, k, and ε) and surface temperature showed negligible change with further iterations. To verify grid-independence, the background mesh was refined in regions of large gradients of the flowfield variables, such that there was a 20% increase in the total number of cells. A hanging-node adaption technique was employed to retain the high quality of the original grid. Due to the extremely high density of the background grid, changes of less than 2% for all flowfield variables and the adiabatic effectiveness were observed when switching to the refined grid. The simulation was therefore declared to be grid-independent with the original grid.

The simulations were run on 20 parallel processors on a Sun Microsystems Ultra 6500 computer with 10 gigabytes of RAM. A single iteration took approximately 40 s, and about 3000 to 4000 iterations were required for convergence at each simulated blowing ratio.

4 Results and Discussion

This section details the performance of the conical diffuser holes by first examining the adiabatic effectiveness and then looking at the flowfield characteristics. Again, note that since the blowing ratio is defined with the velocity in the metering section, the CDIFF holes have the same coolant mass flow rate as the REF holes at a specific value of M. The basic principle behind the CDIFF hole is simple. As the cross-sectional area is gradually increased toward the film-hole exit plane (FHEP), the average velocity of the coolant decreases due to the diffusion. The breakout area of the CDIFF hole is 2.5 times greater than the REF breakout area. Velocity is inversely proportional to the area, so the average velocity across the FHEP is 40% smaller for the CDIFF hole. If the diffuser works well and a uniform velocity exists over the FHEP, the momentum of the coolant will be only 16% of the value in the REF case, since momentum varies with the square of the velocity. Theoretically, the reduction in coolant y-momentum should keep it closer to the surface, giving better thermal protection of the leading edge as compared to film holes without diffusers.

4.1 Surface Results. Contours of adiabatic effectiveness on the ''unwrapped'' leading edge with CDIFF holes for the blowing ratios $M=1.0$ and $M=2.0$ are given in Fig. 4. At the low blowing ratio, a region of high effectiveness trails directly aft of the Row1 hole. Because of the reduced momentum due to the diffuser, the coolant does not travel laterally and therefore does not protect the region between holes on the stagnation line. Another area of relatively high effectiveness is seen to lie directly downstream of the Row2 hole, and again the lack of lateral motion of the coolant is observed. At the higher blowing ratio of $M=2.0$, a region of effectiveness approaching unity lies just aft and to the TE side on the Row1 hole. The coolant generally protects the stagnation line, before traveling downstream and directly into the Row2 jet. A fairly wide region of elevated effectiveness is seen aft of Row2. The coolant footprint is significantly wider than for the REF holes, for which contours are given in Part I of the paper [1]. While there is still a ''hot streak'' for the CDIFF holes aft of Row2, this unprotected region is far reduced in size as compared to the REF case.

Plots of the laterally averaged effectiveness versus streamwise distance from the stagnation line are given in Fig. 5, along with the curves from the REF simulations. At the lowest blowing ratio of $M=1.0$, the effectiveness was observed to be zero over most of the area between Row1 holes (Fig. 4(a)). This translates to a very low laterally averaged effectiveness of $\overline{\eta}=0.2$ at the stagnation line (Fig. 5(a)). At the downstream edge of Row1, $\overline{\eta}$ increases to a local maximum of about 0.55, which is over 20% greater than the REF case. With decent coolant coverage between holes in Row2, there is a spike in $\overline{\eta}$ at the streamwise location of Row2 ($x/D=3.5$). The wide coolant footprint aft of Row2 results in a nearly constant 20% advantage in $\overline{\eta}$ over the REF case on the remaining portion of the leading edge surface.

As M increases, the effectiveness increases in region between adjacent holes in Row1, and at $M=2.0$, the value of $\overline{\eta}$ at the stagnation line reaches the REF value of 0.8. For all blowing ratios, the CDIFF holes give values of $\overline{\eta}$ that are 0.05 to 0.10 greater than the REF holes in the region between the two rows. At the blowing ratio $M=1.5$ and above, the Row1 coolant flows over the Row2 hole and merges completely with this jet. This leaves most of the area between the Row2 holes unprotected, causing the laterally averaged effectiveness to significantly fall at $x/D=3.5$. The most severe case is at $M=2.0$, where the Row1 jet flows directly over the Row2 hole, and the local value of $\overline{\eta}$ drops from 0.4 to under 0.2 (Fig. 5(c)).

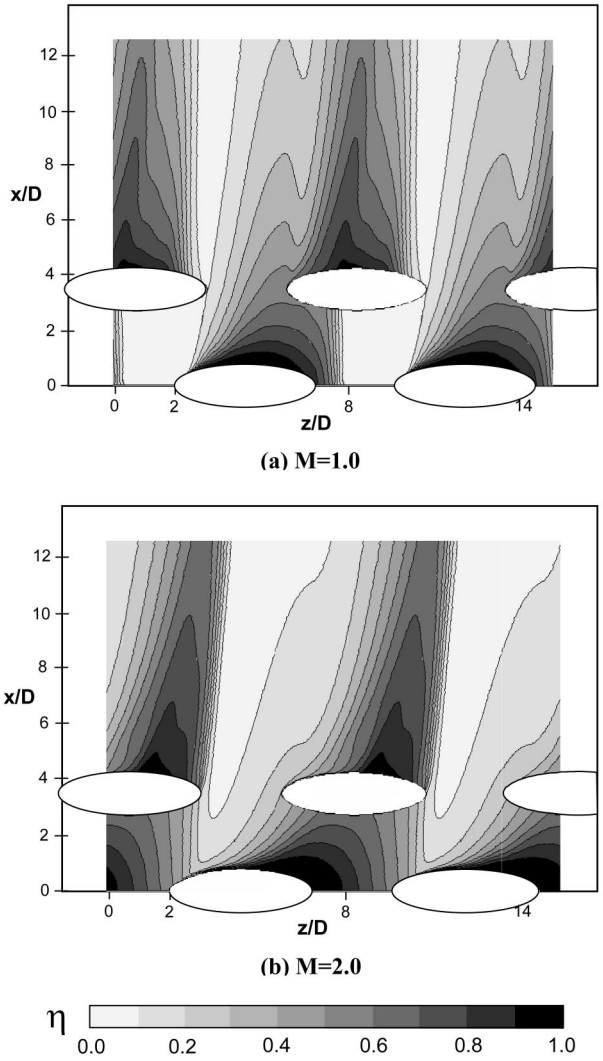

Fig. 4 Contours of adiabatic effectiveness on the leading edge with CDIFF holes for (*a*) *M*=1.0, and (*b*) *M*=2.0

Also, as the blowing ratio increases, the region of high effectiveness aft of Row2 decreases in width and migrates from the LE side of the hole to the TE side. For all M, however, the coolant footprint downstream of the Row2 hole is spread over a greater lateral distance than in the REF case. Because of this behavior, $\overline{\eta}$ is up to 40% greater downstream of Row2 for the CDIFF holes. Overall, in terms of surface results, the CDIFF holes perform superior to the standard cylindrical holes. With a couple of exceptions at the location of a row of holes, the conical diffuser holes give a significantly higher laterally averaged effectiveness over the entire leading edge through the range of blowing ratios.

4.2 Flowfield Physics. This section analyzes the leading edge film-cooling flowfield with the conical diffuser holes in place. Comparisons are made to the REF cases, which are described in Part I of this series [1]. Since the blowing ratio was defined with the average coolant velocity in the long cylindrical metering section, which has the same diameter as the REF holes, coolant flow rates through the two hole geometries are equal. Thus, the CDIFF case exhibits the same fluid mechanics as found in the REF configuration from the film-hole inlet to the beginning of the short diffuser section. The coolant was observed to enter the diffuser section with a nearly uniform velocity profile and negligible secondary flow.

Because of a nearly uniform pressure field along the stagnation line and over the Row1 FHEP, the diffuser works well for this hole row. Figure 6 shows contours of the normalized y-velocity at the FHEP of the Row1 hole. The velocity is nearly constant across this plane, with V_y values of 0.4 to 0.5 (40 to 50% of the value in the REF case). Because of the small normal component of momentum, the Row1 jet has a much shallower trajectory than the REF case. This is seen in contours of normalized temperature on three planes of constant z-coordinate in Fig. 7. In the first two planes to the right of the hole centerline, the contour lines are much more flat and spread out in the streamwise direction than in the REF case. Since the coolant does not have as much lateral momentum, it is turned in the streamwise direction quickly. By the third plane (at $z/D=5.7$), the low temperature contours at the surface have disappeared as the coolant has turned downstream already. Though the coolant does not travel as far laterally as the REF case, the expanded breakout of the diffusers greatly reduce the metal distance between adjacent film holes and coverage along the stagnation line is excellent.

At Row2, the flow in the diffuser section is strongly influenced by the interaction of the crossflow with the emerging jet. The physics are largely the same as in the REF case. A high-pressure region develops at the upstream half of the hole where the crossflow slows as it meets the dense coolant jet. As a result, coolant migrates toward the downstream edge of the diffuser section. The development of this jetting region is clearly seen in the case of $M=2.0$ in Fig. 8, lines on constant normalized y-velocity on a plane cutting through the Row2 film hole from upstream edge to downstream edge. Views of the normalized velocity contours on the Row2 FHEP for $M=1.0$ and 2.0 are given in Fig. 9. The highly non-uniform momentum across the exit plane is evident. At the low blowing ratio, the full upstream half of the hole breakout is occupied by a region of zero normal velocity, meaning that essentially no coolant leaves the hole on this side. In fact, there is an area near the upstream edge where the value of V_y is actually negative, the implication of which are discussed later. Velocities rapidly increase toward the downstream edge of the hole near the LE point, where V_y exceeds a value of 3.0. At $M=2.0$, a similar pattern develops, although the jetting is not as severe, with a maximum V_y of near 2.1 along the downstream edge. This maximum value of the velocity is slightly less than in the REF case (where V_y was locally above 2.7) since the coolant jetting region extends across the significantly wider breakout of the diffuser section. The diffuser does not work optimally for Row2, but the momentum of the coolant is reduced slightly from the REF case as it exits the hole.

In Fig. 10, contours of normalized temperature are displayed on three planes of constant x-coordinate downstream of the Row2 hole. The dashed lines in this figure bound the region on the leading-edge surface that sees a temperature of less than or equal to $\theta=0.3$. In At $x/D=4.5$, just downstream of the edge of the diffuser breakout, the jet core is observed to be spread out over a distance roughly equal to the lateral dimension of the FHEP (LE to TE). As in the REF simulation, the coolant has penetrated farther into the mainstream on the LE side of the hole (right side in this view). However, due to the smaller velocity in the jetting region along the downstream film-hole wall, the coolant does not lift off the surface as far as in the REF case. A fairly strong streamwise vortex lies near aft of the LE side of the hole, as seen in Fig. 11, in-plane velocity vectors at $x/D=4.5$. But since coolant lift-off is not as great for the CDIFF hole, the vortex does not bring hot crossflow under the jet core to the extent of the REF case. Secondary flow is clearly visible in the velocity vectors in this plane. Despite some movement of hot crossflow underneath the coolant jet core on the right side, a large portion of the jet is in contact with the surface on the left side, and the CDIFF hole gives

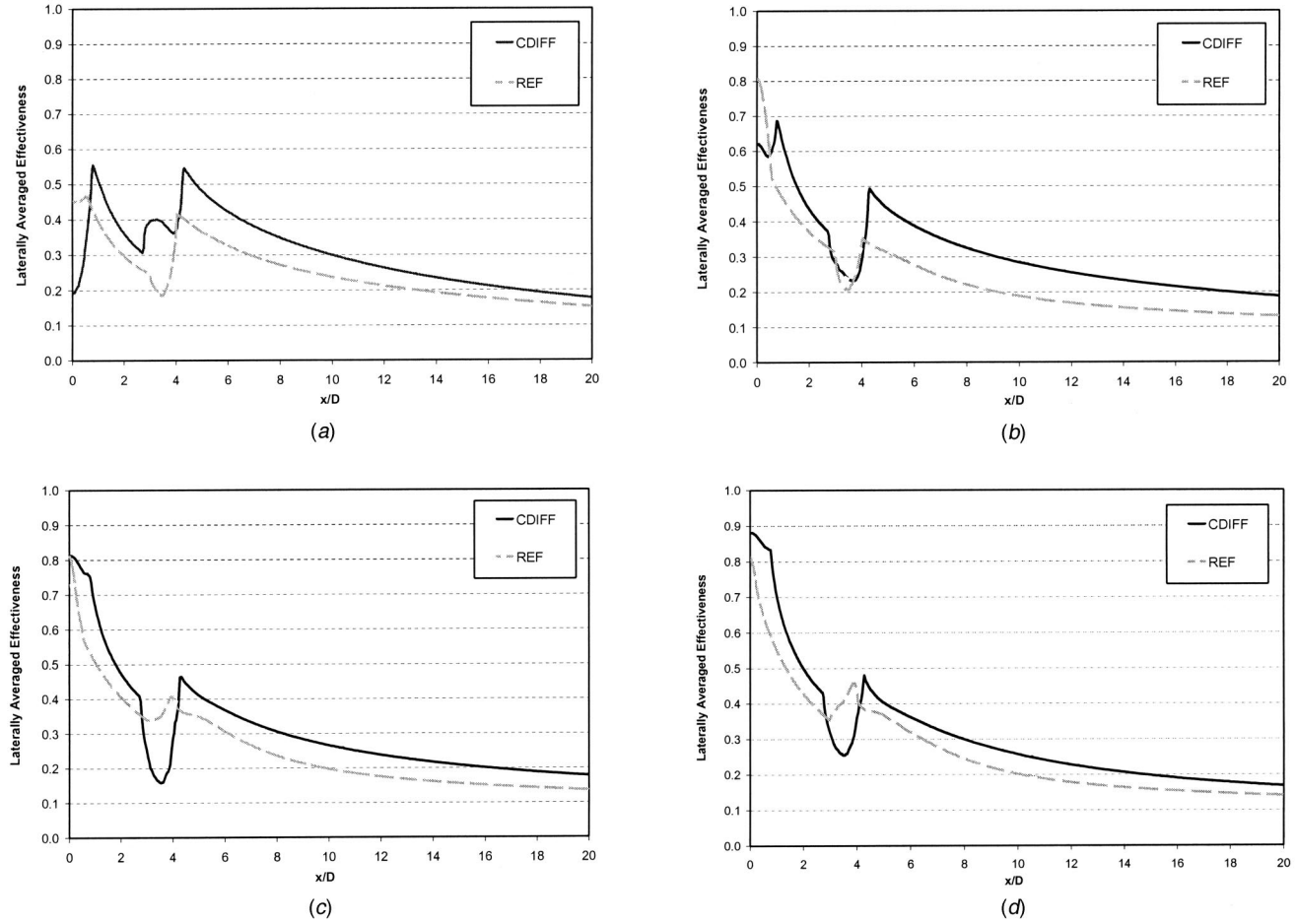

Fig. 5 Plots of predicted laterally averaged effectiveness for the CD, FF, and REF geometries of blowing ratios of (*a*) $M=1.0$, (*b*) $M=1.5$, (*c*) $M=2.0$, and (*d*) $M=2.5$

better lateral coverage than the REF hole. This trend continues downstream, and at $x/D=6.5$ and $x/D=8.5$ the coolant is located closer to the surface and is exhibits a greater lateral spread than the REF case (Fig. 10).

Interaction between the two rows of coolant jets from the CDIFF holes is impossible to avoid since the breakout planes of the film holes are so wide. At $M=2.0$, the Row1 coolant, which has less lateral momentum than the REF case, travels directly over the Row2 hole. This is illustrated in Fig. 12 by coolant pathlines from both rows of holes. The pathlines merge into a single stream, which becomes narrower with downstream distance because of the strong acceleration. Thus, as in the case of the REF configuration, there is a wide region directly aft of the Row1 hole that

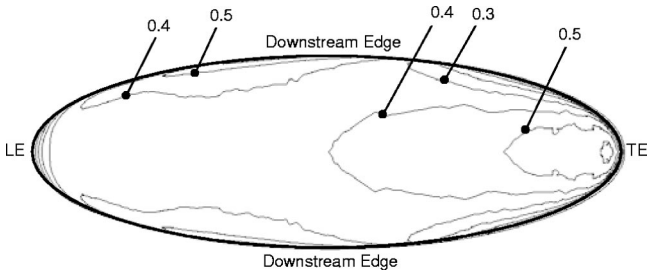

Fig. 6 Contours of V_y on the FHEP of the Row1 conical diffuser hole at $M=2.0$ show a fairly low, uniform coolant flow

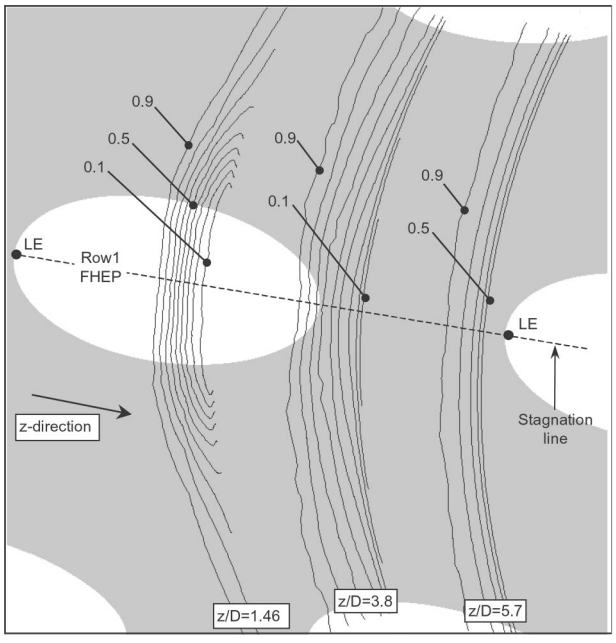

Fig. 7 Lines of constant θ on three planes of constant z-coordinate between Row1 hole centerlines at the blowing ratio $M=2.0$. Note the extremely low trajectory of the coolant jet.

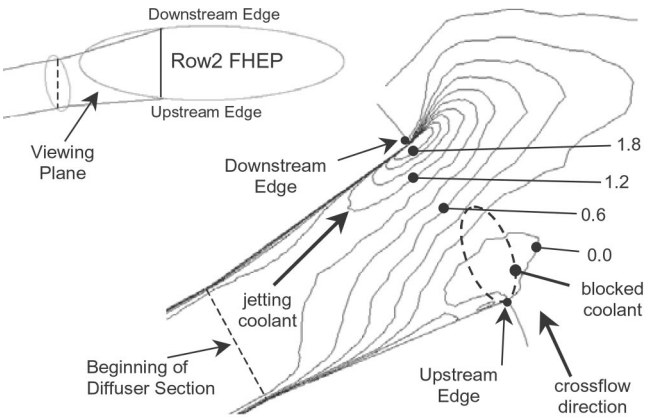

Fig. 8 Contours of V_y on a plane through the centerline of the Row2 film hole (from upstream to downstream edge) at $M=2.0$ shows the development of a jetting region

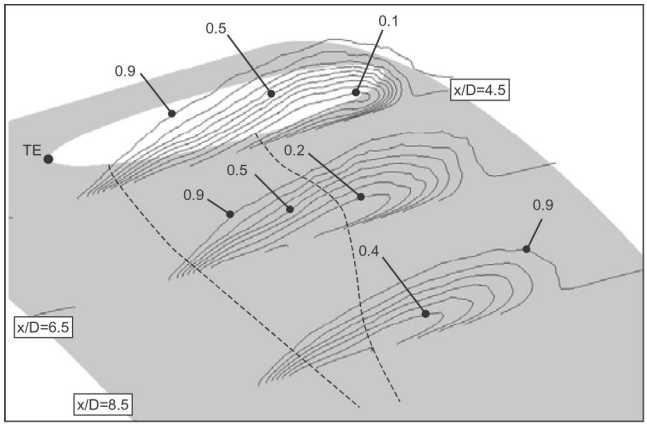

Fig. 10 Contours of θ on three planes of constant x-coordinate aft of the Row2 film hole for the blowing ratio $M=2.0$. The dashed lines mark the extent of the region on the surface in which $\theta \leq 0.3$.

sees no coolant, and this fact was evident in the contours of effectiveness. Merging of the Row1 and Row2 coolant jets was present to some degree throughout the range of simulated blowing ratios.

4.2.1 Heating Within the Film Hole. From the contours of normalized y-velocity in Fig. 9, it was observed that crossflow blockage results in a large ''dead'' region at the upstream side of the Row2 FHEP where almost no coolant exits the hole. This is a prime condition for two phenomena that may cause thermal problems inside the film hole: crossflow ingestion and thermal diffusion. McGrath and Leylek [13] highlighted the potential risk of these mechanisms in simulations of film cooling from diffused holes at large compound angles. Crossflow ingestion arises from the action of a vortex that directs hot fluid below the FHEP in a region where coolant momentum is minimal. The typical ingestion vortex results when the vorticity in the crossflow boundary layer becomes oriented in the local direction of flow as flow wraps around the emerging jet (the ''horseshoe'' vortex). A clue that minor crossflow ingestion is present in the Row2 CDIFF film hole is the region of negative normal velocity near the LE side of the hole at $M=2.0$ (Fig. 9). The horseshoe vortex can be identified in Fig. 13 by the coalescence and roll-up of the paths of zero-mass particles released in the crossflow boundary layer (0.1 mm above the surface) just upstream of Row2. The fluid is clearly observed

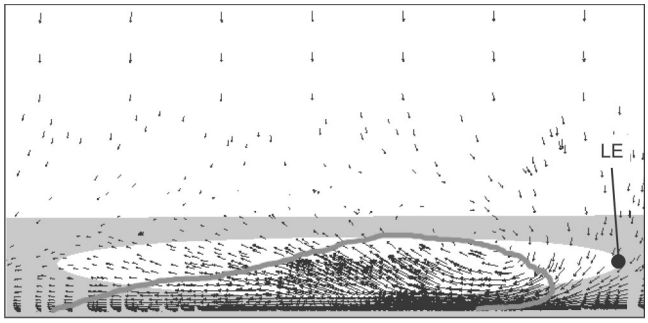

Fig. 11 Velocity vectors sized by in-plane velocity magnitude on the $x/D=4.5$ plane (just aft of the Row2 hole) at $M=2.0$ showing a relatively strong secondary flow. The gray line marks the $\theta=0.5$ isotherm.

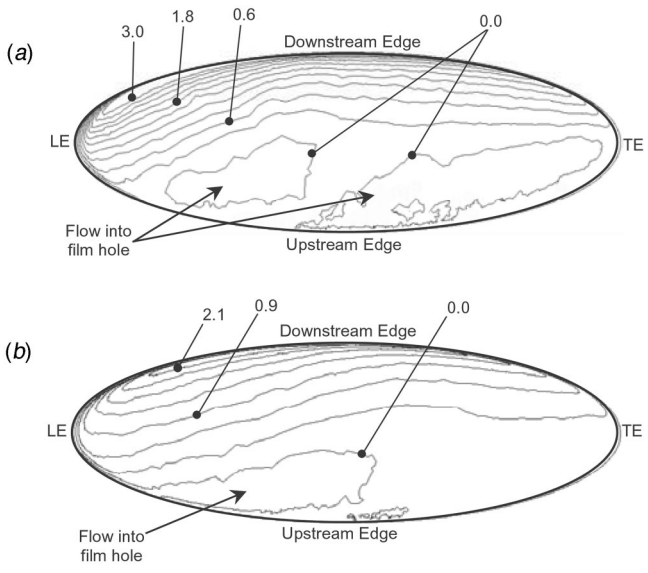

Fig. 9 Lines of constant V_y on the Row2 FHEP for (*a*) $M=1.0$, and (*b*) $M=2.0$ show the highly nonuniform velocity field at the diffuser exit

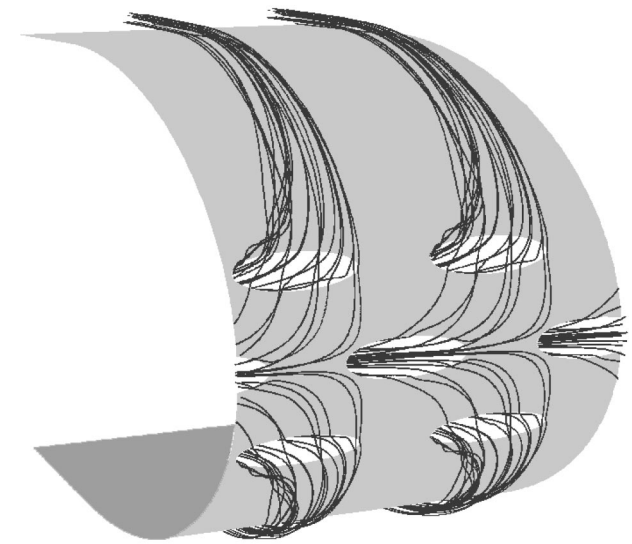

Fig. 12 Pathlines of the coolant from Row1 and Row2 for the case of $M=2.0$ show the strong interaction between rows

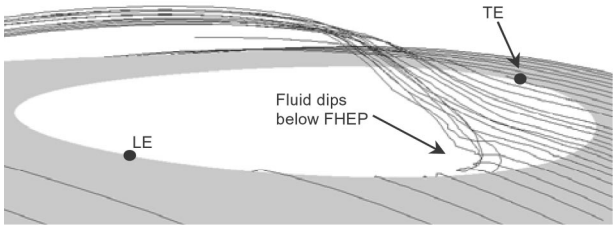

Fig. 13 Paths of massless particles released in the crossflow boundary layer just upstream of Row2 for $M=2.0$ show the vortex that brings crossflow below the FHEP

to dip below the FHEP. Throughout the range of blowing ratios simulated, crossflow ingestion was very mild and the fluid that travels into the hole is at a moderately low temperature because it contains coolant from Row1. Also, the ingestion is located away from the film-hole wall, so it does not cause significant heating of the metal.

Diffusion of thermal energy from the crossflow into the coolant is a more important mechanism than secondary flow under the present conditions. This phenomenon occurs in areas where hot crossflow moves over stagnant coolant at the FHEP, and it is greatly aided by the high turbulence levels observed in the vicinity of the jet-mainstream interaction. In the case of $M=2.0$, most of the crossflow traveling over the hole is relatively cool from the Row1 coolant, and only near the TE the crossflow approaches $\theta=1$. However, at $M=1.0$ most of the Row2 hole sees the maximum crossflow temperature. Additionally, at this blowing ratio the coolant is blocked over a larger portion of the FHEP, creating more surface area for diffusion to take place.

Figure 14 shows contours of temperature on the FHEP of Row2 for $M=1.0$ and $M=2.0$. At the low blowing ratio, the temperature increases toward the TE to a maximum of greater than $\theta=0.8$, almost at the mainstream temperature. The heating is not as severe in the case of $M=2.0$, in which the normalized temperature exceeds 0.4 near the TE. The film-hole wall is located very close to the FHEP on this side of the hole, since the shallow injection angle and the diffusion combine to give a quite small film-hole wall angle at the TE. Thus, diffusion of thermal energy occurs right down to the wall inside of the hole. Contours of normalized temperature on the film-hole wall are shown in Fig. 15 for $M=1.0$ and 2.0. At $M=1.0$, wall heating is severe, with θ increasing rapidly to a value of about 0.9 at the TE. The effect is less severe

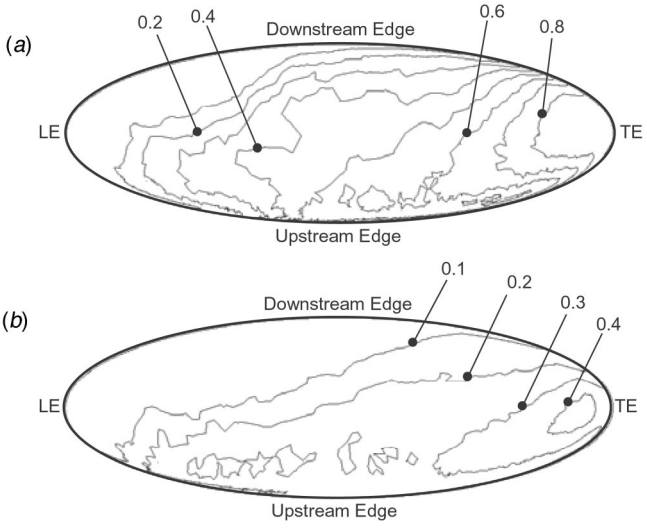

Fig. 14 Contours of θ on the FHEP of the Row2 conical diffuser hole for the cases of (*a*) $M=1.0$, and (*b*) $M=2.0$

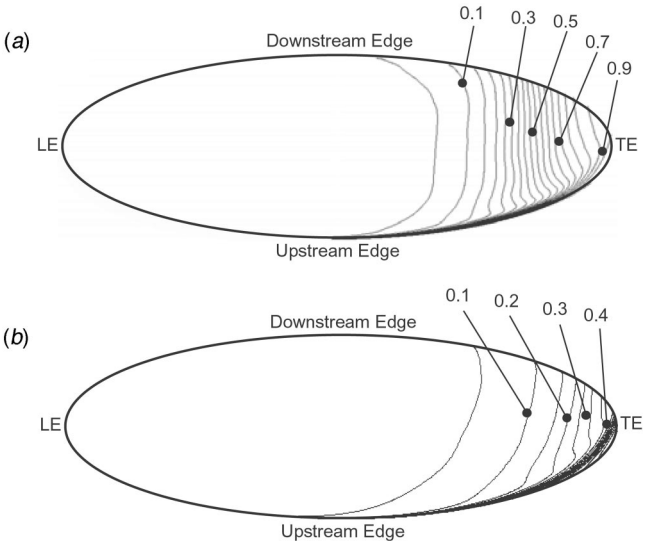

Fig. 15 Lines of constant θ on the film-hole walls inside the Row2 CDIFF hole at blowing ratios of (*a*) $M=1.0$, and (*b*) $M=2.0$ reveal the severe heating of the metal surface near the TE

at the higher blowing ratio. The heating of the metal may result in detrimental thermal stresses in this area of complex geometry and is likely an important design consideration.

5 Conclusions

A previously validated computational methodology was extended to evaluate the performance of exit-diffused holes in film cooling of a turbine airfoil leading edge. The conical diffuser holes gave a 10 to 40% increase in laterally averaged effectiveness as compared to the cylindrical holes over the complete leading edge, with the only exception being right at the location of the hole rows. This trend was observed through the range of simulated blowing ratios. The advantage in effectiveness was due to the shallower trajectory of the coolant exiting the holes, causing it to stay closer to the surface than in the case of nondiffused holes. However, the increased effectiveness comes at the expense of a tendency for heating of the Row2 film-hole wall near the TE, where the metal is very near the FHEP due to the small injection angle. The heating within the hole is due primarily to thermal diffusion in a low-momentum region that develops near the upwind side of the FHEP, and it could be problematic if not accounted for in the overall design. Finally, this work illustrates how a carefully designed computational program may be effectively used to conduct design iterations, in this case the analysis of an innovative film-hole geometry.

Acknowledgments

This research was supported by General Electric Aircraft Engines (GEAE) as part of the University Strategic Alliance (USA) program. The authors appreciate the assistance of D.C. Wisler, F.A. Buck, and M.L. Shelton at GEAE. The first author is grateful for funding from a National Science Foundation Graduate Research Fellowship. Appreciation also goes to Sun Microsystems for a grant of computer hardware and to Fluent, Inc. for software support.

Nomenclature

AR = film-hole exit area ratio (CDIFF to REF)
CDIFF = referring to the *c*onical *diff*user film holes
D = film-cooling hole diameter [m]
DR = coolant-to-mainstream density ratio $=\rho_j/\rho_\infty$
FHEP = film-hole exit plane

k = turbulent kinetic energy [m^2/s^2]
L = film-cooling hole length [m]
LE = film-hole leading edge
M = global coolant to mainstream mass flux (blowing) ratio = $\rho_j U_j / \rho_\infty U_\infty$
P = static pressure [N/m^2]
REF = referring to standard cylindrical film holes
RKE = realizable k-ε turbulence model
Row1 = pertaining to row of film holes on stagnation line
Row2 = pertaining the downstream row of film holes
S = film-cooling hole lateral spacing (within each row) [m]
T = static temperature [K]
TE = film-hole trailing edge surface
U = local velocity [m/s]
V_y = normalized y-velocity = U_y / U_{yj}
x = streamwise coordinate originating at stagnation line
y = coordinate normal to leading edge surface
y^+ = nondimensional distance from wall
z = spanwise coordinate
α = injection angle with respect to leading-edge surface
ϕ = compound angle
ε = dissipation rate of turbulent kinetic energy [m^2/s^3]
η = adiabatic effectiveness = $(T_{aw} - T_\infty)/(T_j - T_\infty)$
$\overline{\eta}$ = laterally averaged adiabatic effectiveness
ν = kinematic viscosity [m^2/s]
ρ = density [kg/m^3]
θ = dimensionless temperature = $(T - T_j)/(T_\infty - T_j)$

Subscripts

∞ = mainstream conditions at crossflow inlet plane
aw = adiabatic wall
j = coolant jet (average) conditions
y = y direction component (normal to leading edge and FHEP)

References

[1] York, W. D., and Leylek, J. H., 2002, "Leading-Edge Film-Cooling Physics: Part I—Adiabatic Effectiveness," ASME Paper No. GT-2002-30166.
[2] Mick, W. J., and Mayle, R. E., 1988, "Stagnation Film Cooling and Heat Transfer, Including Its Effect Within the Hole Pattern," ASME J. Turbomach., **110**, pp. 66–72.
[3] Mehendale, A. B., and Han, J. C., 1992, "Influence of High Main-stream Turbulence on Leading Edge Film Cooling Heat Transfer," ASME J. Turbomach., **114**, pp. 707–715.
[4] Ekkad, S. V., Han, J. C., and Du, H., 1997, "Detailed Film Cooling Measurements on a Cylindrical Leading Edge Model: Effect of Free-Stream Turbulence and Coolant Density," ASME Paper No. 97-GT-181.
[5] Salcudean, M., Gartshore, I., Zhang, K., and McLean, I., 1994, "An Experimental Study of Film Cooling Effectiveness Near the Leading Edge of a Turbine Blade," ASME J. Turbomach., **116**, pp. 71–79.
[6] Cruse, M. W., 1997, "A Study of Film Cooling Adiabatic Effectiveness for Turbine Blade Leading Edges," M.S. thesis, University of Texas at Austin.
[7] Reiss, H., and Bölcs, A., 1999, "Experimental Study of Showerhead Cooling on a Cylinder Comparing Several Configurations Using Cylindrical and Shaped Holes," ASME Paper No. 99-GT-123.
[8] Chernobrovkin, A., and Lakshminarayana, B., 1998, "Numerical Simulation and Aerothermal Physics of Leading Edge Film Cooling," ASME Paper No. 98-GT-504.
[9] Lin, Y.-L., Stephens, M. A., and Shih, T.I.-P., 1997, "Computation of Leading-Edge Film Cooling with Injection Through Rows of Compound-Angle Holes," ASME Paper No. 97-GT-298.
[10] Martin, C. A., and Thole, K. A., 1997, "A CFD Benchmark Study: Leading Edge Film-Cooling With Compound Angle Injection," ASME Paper No. 97-GT-297.
[11] Thakur, S., Wright, J., and Shyy, W., 1997, "Computation of Leading-Edge Film Cooling Flow Over an Experimental Geometry," ASME Paper No. 97-GT-381.
[12] Shih, T.-H., Liou, W. W., Shabbir, A., and Zhu, J., 1995, "A New k-ε Eddy-Viscosity Model for High Reynolds Number Turbulent Flows: Model Development and Validation," Comput. Fluids, **24**(3), pp. 227–238.
[13] McGrath, E. L., and Leylek, J. H., 1999, "Physics of Hot Crossflow Ingestion in Film Cooling," ASME J. Turbomach., **121**, pp. 532–541.

Numerical Investigation of Heat Transfer in Turbine Cascades With Separated Flows

P. de la Calzada
e-mail: pedro.delacalzada@itp.es

A. Alonso
e-mail: alfredo.alonso@itp.es

ITP, Industria de Turbo Propulsores S.A.,
Madrid, Spain

Modern design of turbine blades usually requires highly loaded, very thin profiles in order to save weight and cost. If local leading edge incidence is kept close to zero, then flow separation might occur on the pressure side. Although it is known that flow separation, flow reattachment, and the associated zones of recirculation have a major impact on the heat transfer to the wall, the turbomachinery community needs an understanding of the heat transfer mechanisms in separated flows as well as models and correlations to predict them. The aim of the present investigation is a detailed study by means of an in-house CFD code, MU^2S^2T, of the heat transfer mechanisms in separated flows, in particular in separation and reattachment point regions. Furthermore, an attempt is made to identify a limited number of parameters (i.e., Re, M, inlet flow angle, etc.) whose influence on the heat flux would be critical. The identification of these parameters would be the starting point to develop special correlations to estimate the heat transfer in separated flow regions. [DOI: 10.1115/1.1556014]

Keywords: Heat Transfer, Flow Separation, Turbine Cascades

Introduction

Nowadays, in the aeroengine and gas turbine industries, there is an increasing demand for more efficient gas turbine engines, a reduction in weight, cost, and design time scales, while meeting the even increasing environmental, safety, and reliability requirements. In order to achieve these targets, turbine peak cycle temperature increased rapidly in the last decade enabled by the extensive use of cooling technology. Additionally, driven by the opportunity of weight reduction, low-pressure turbine (LPT) airfoils are usually thin, and therefore flow separation might occur on the pressure side. These two factors require a reliable and accurate prediction of the heat transfer in blades with complex or separated flow.

The use of numerical prediction methods (i.e., CFD), which have acquired an acceptable level of maturity, becomes essential for the aerothermal design of turbomachinery components. Traditionally, these tools have been validated for heat transfer in high-pressure turbines (HPT) featuring high Reynolds number and attached flow on the airfoil sections. In the last years, the capability of different CFD codes to predict the heat transfer on these configurations has been investigated, where especial attention has been paid mainly to mesh sensitivity and turbulent effects.

Very little attention has been paid to the heat transfer in separated flows in turbine representative conditions. Bassi et al. [1] present CFD results on the separated flow region of an HPT airfoil with cut trailing edge and no cooling ejection; but only a short discussion about the separated flow physics is included. Regarding experimental investigations, Rivir et al. [2] have measured the flat plate heat transfer in a region of turbulent separation, and Bellows and Mayle [3] have measured the heat transfer on a blunt body leading edge separation bubble. However, very little attention has been paid to low Reynolds, large separated flow regions on turbines representative geometry. Only recently, Wolff et al. [4] have performed an experimental investigation on the LPT highly loaded airfoil T106-300 with a large region of separated flow at the pressure side. However, there are several concerns about the validity of the measurement technique used. The main reason is that the behavior of a thermal boundary layer, fully developed from the blade leading edge, is different than that of a local thermal boundary layer developed when isolated heat sources (hot films) are placed on the blade surface.

Qualitatively, from experimental investigations, it is known that separated flow regions are characterized by large and rapid variations of the heat transfer. Furthermore, the heat transfer presents a local minimum and a local maximum in the vicinity of separation and reattachment points, respectively, with regions where the heat transfer coefficient is much larger than that in attached flows (Merzkirch et al. [5], Rivir et al. [2]). Taking into account that separated flow regions are usually characterized by high turbulence levels and large-scale unsteadiness, there is a tendency in the heat transfer community to explain the heat transfer phenomenon in separated flows in terms of the generation of turbulence and the behavior of the skin-friction coefficient.

The present investigation is part of the Brite Euram project *Aerothermal Investigation on Turbine Endwalls and Blades* (AITEB), where both an experimental and a numerical investigation of heat transfer under separated flow is performed. The aim of the present investigation is a detailed numerical study of the heat transfer phenomenon in separated flows at flow conditions representative of LPT airfoils. Based on these numerical results, an attempt is made to understand and explain the flow physics in the vicinity of separation and reattachment points that might influence the heat flux. Finally, inlet flow angle, Reynolds number, and Mach number effects on the heat transfer mechanisms are investigated.

CFD Simulations

Description of the T106-300 Model. The T106-300 blade section has been used as a generic geometry representative of a typical LPT highly loaded airfoil (Hoheisel [6]); see Fig. 1. In this investigation, the T106 blade profile is subjected to extremely large incidences in order to have a long separated bubble. Mach and Reynolds number are varied around typical LPT values.

Computational Grid. All grids were generated with G2D, an in-house tool for unstructured mesh generation on turbomachinery. The generated grids are hybrid in nature with higher definition

Contributed by the International Gas Turbine Institute and presented at the International Gas Turbine and Aeroengine Congress and Exhibition, Amsterdam, The Netherlands, June 3–6, 2002. Manuscript received by the IGTI September 27, 2001. Paper No. 2002-GT-30225. Review Chair: E. Benvenuti.

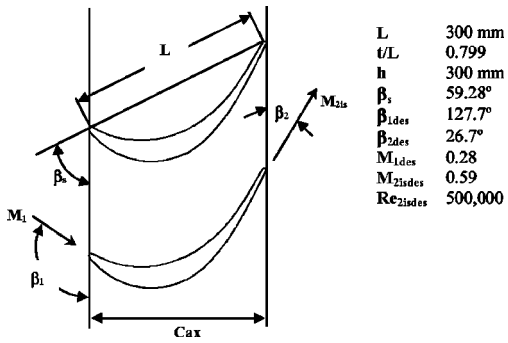

Fig. 1 T106-300 cascade geometry and aerodynamic design conditions

in regions adjacent to the wall, trailing edge and leading edge. A typical grid is divided in two regions; see Fig. 2.

Region 1, adjacent to the wall, is a viscous anisotropic mesh with large thickness to enclose the separated flow region and with a given grid stretching towards the wall. With such high definition in blade wall adjacent regions, temperature gradients at the wall can be accurately computed. Furthermore, a set of CFD studies were done on the VKI-LS89 highly loaded transonic turbine blade (Arts and Lambert de Rouvroit [7]) to validate MU^2S^2T for heat transfer calculations and to estimate an optimum y^+ range in cells adjacent to the wall. As a result of this study, the optimum range for heat transfer calculations was found to be $y^+<3$, even in laminar regions.

Region 2, outside the strong temperature gradient region, is an isotropic triangular mesh obtained by Steiner triangulation (Corral and Fernandez-Castañeda [8]) and grid smoothing.

A grid sensitivity study was done for the T106-300 LPT airfoil and similar conclusions than those obtained for the VKI-LS89 airfoil were obtained. In all the CFD simulations, a grid with 8623 nodes was kept unchanged with y^+ values at the pressure side in the order of $y^+<3$.

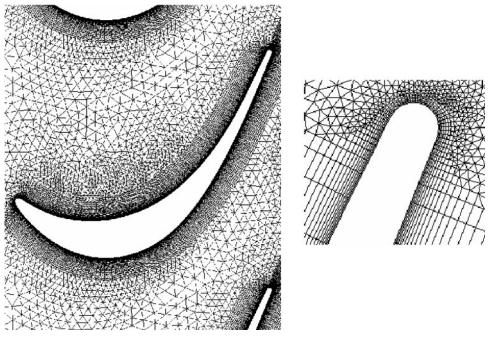

Fig. 2 2-D hybrid mesh around the T106 blade—left: mesh on linear cascade; right: hybrid mesh around trailing edge

CFD Modeling. In the present investigation, an in-house CFD code, MU^2S^2T, was used for calculations. This code solves the RANS equations written in conservative form in an absolute frame of reference coupled with the two equations $k-\omega$ turbulence model (Wilcox [9], Corral and Contreras [10]). The scheme used is based upon Jameson et al. [11]. Convective terms are discretized using a cell vertex scheme and the viscous terms are computed by means of the Hessian matrix. Integration in time is performed using an explicit five-stage Runge-Kutta scheme where the viscous and artificial dissipation terms are evaluated in the first, third, and fifth stages. Once the velocity and temperature fields are computed, their gradients at the wall are post-processed so that the local Stanton number, skin friction and heat transfer coefficients can be calculated.

The main nondimensional coefficient used for result comparison purposes is the local Stanton number based on the local free-stream velocity (Eq. (1)). The local Stanton number is the equivalent for the temperature to the local skin friction coefficient (Eq. (2)) for the velocity. Although local Stanton number variations do not represent variations in heat transfer alone, it is the most adequate parameter to describe the thermal boundary layer behavior and to develop special correlations for heat transfer estimation (i.e., Reynolds analogy).

Regarding the local convective heat transfer coefficient used in this study, it is defined as the ratio of the computed wall heat flux and the difference between the total temperature and the local wall temperature. Note that the inlet total temperature (303 K) is used in the HTC definition since it is equal to the adiabatic wall temperature as shown in Fig. 12 where adiabatic wall cases are presented.

$$Ch_x=\frac{\mathrm{HTC}}{\rho_e c_p u_e}=\frac{-k\left(\frac{\partial T}{\partial n}\right)_w}{(T_o-T_w)\rho_e c_p u_e} \tag{1}$$

$$Cf_x=\frac{\tau_w}{\frac{1}{2}\rho_e u_e^2}=\frac{\mu\left(\frac{\partial u}{\partial n}\right)_w}{\frac{1}{2}\rho_e u_e^2} \tag{2}$$

The T106 CFD turbulent simulations are carried out for different flow conditions, a stagnation temperature of 303 K, a fixed wall temperature of 325 K and different inlet flow angles. A summary of the flow conditions is listed in Table 1. Upstream the cascade inlet plane, a free-stream turbulence level of 3.7% was used in all CFD simulations.

MU^2S^2T Validation. MU^2S^2T was validated for heat transfer in attached flows against a highly loaded transonic turbine guide vane named LS89 [7] widely used for validation purposes. The T106-300 grid philosophy was adopted.

Firstly, a CFD model with a Reynolds number equal to 10^6, an isentropic exit Mach number of 0.875, a constant stagnation temperature of 420 K and a constant wall temperature of 450 K was

Table 1 T106 CFD simulations[a]

β_1	127.7 deg	105 deg	100 deg	95 deg	90 deg
$Re_{2is}=150{,}000;\ M_{2is}=0.1$		√			
$Re_{2is}=150{,}000;\ M_{2is}=0.2$		√			
$Re_{2is}=150{,}000;\ M_{2is}=0.3$		√			
$Re_{2is}=150{,}000;\ M_{2is}=0.5$	√	√	√	√	√
$Re_{2is}=150{,}000,\ M_{2is}=0.7$		√			
$Re_{2is}=200{,}000;\ M_{2is}=0.1$		√			
$Re_{2is}=300{,}000,\ M_{2is}=0.1$		√			
$Re_{2is}=400{,}000;\ M_{2is}=0.1$		√			

[a]90° inlet flow angle results only used for CFD profile pressure coefficient validation purposes (see Fig. 8).

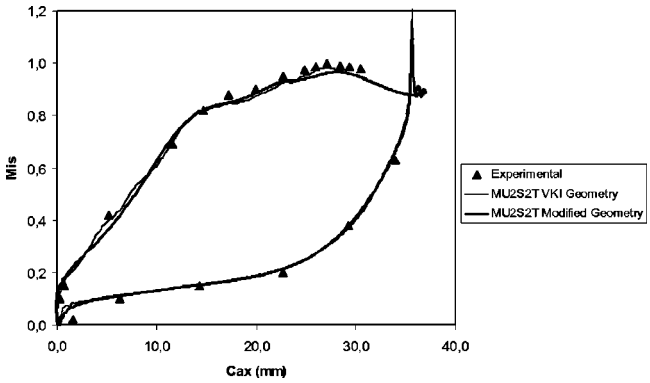

Fig. 3 LS89 blade isentropic Mach number distribution ($Re_{2is}=10^6$, $M_{2is}=0.875$)

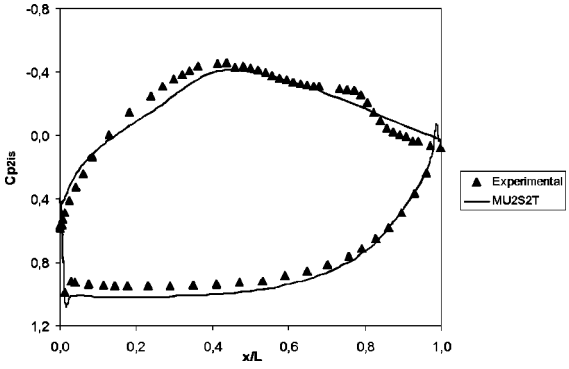

Fig. 6 T106 profile pressure coefficient-No separation ($Re_{2is}=1.5\times10^5$, $M_{2is}=0.5$, $\beta_1=127.7$ deg, $T_w=325$ K)

run to validate the obtained pressure distribution around the blade. Excellent agreement with the experimental results was achieved as shown in Fig. 3.

Secondly, for heat transfer validation purposes, only laminar simulations were performed since we are not especially concerned about turbulent effects here. As plotted in Figs. 4 and 5, a good agreement with experimental results is obtained in both sides with the exception of the leading edge and the suction side flow accelerated regions.

Note that two different numerical solutions have been included; one with the original VKI geometry, which presented some oscillations in the solution, reported by other authors (Gehrer and Jericha [12], Boyle and Ameri [13]), and a second one with a slightly modified geometry to ensure continuity in the curvature while keeping the same aerodynamics. As shown in the aforementioned plots, both solutions are aerothermodynamically equivalent but the modified geometry suppresses the oscillations completely.

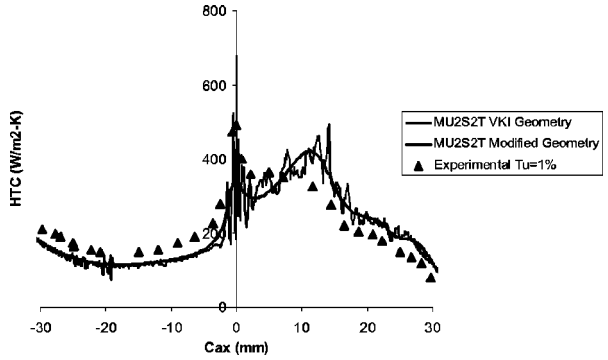

Fig. 4 LS89 blade heat transfer distribution ($Re_{2is}=5.0\times10^5$, $M_{2is}=0.92$, $T_w=450$ K)

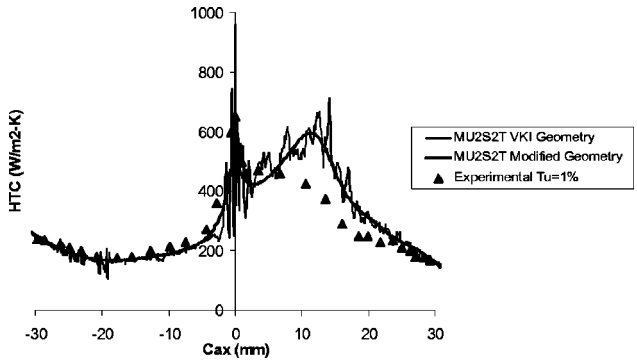

Fig. 5 LS89 blade heat transfer distribution ($Re_{2is}=10^6$, $M_{2is}=0.70$, $T_w=450$ K)

Results

In order to get an understanding of the flow physics associated with separated flows, inlet flow angle, Mach number and Reynolds number effects on heat flux are investigated. The local Stanton number, heat transfer and skin friction coefficients are used for comparison of results.

Inlet Flow Angle Effects. Inlet flow angles of 90, 95, 100, 105, and 127.7 deg (attached flow) have been simulated for a nominal isentropic exit Reynolds number of 1.5×10^5 and an isentropic exit Mach number of 0.5. The obtained profile pressure coefficient distributions, as used in [4], are compared with measurements from [4] in Figs. 6–8. Since the main point of interest is the airfoil pressure side, no attention will be paid to the separation bubble at the back surface diffusion that the code does not predict at all, probably due to a too soon turbulence generation. Nevertheless, the pressure side bubble is well predicted although the reattachment point is located slightly downstream with a steeper pressure recovery. In the present investigation, the reattachment point (RP) on the blade pressure side is defined as the point where the profile pressure coefficient presents a local maximum.

The observed pressure recovery is a typical phenomenon of a reattaching boundary layer due to accelerating flows. In the first part of the bubble (denoted in Figs. 7 and 8 by a constant pressure coefficient region), the static pressure on the wall is approximately uniform and equal to the static pressure on the limiting streamline enclosing the bubble. In this region, downstream of the separation point, following the bubble limiting streamline, the flow acceler-

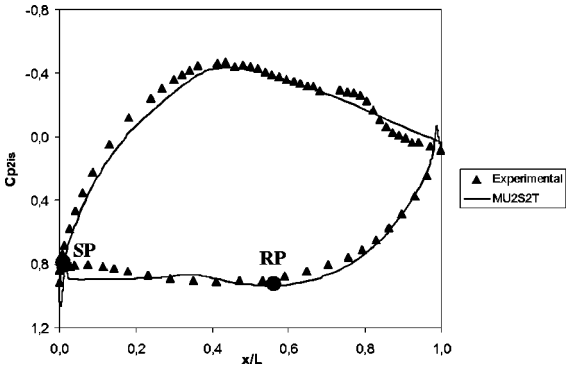

Fig. 7 T106 profile pressure coefficient ($Re_{2is}=1.5\times10^5$, $M_{2is}=0.5$, $\beta_1=105$ deg, $T_w=325$ K)

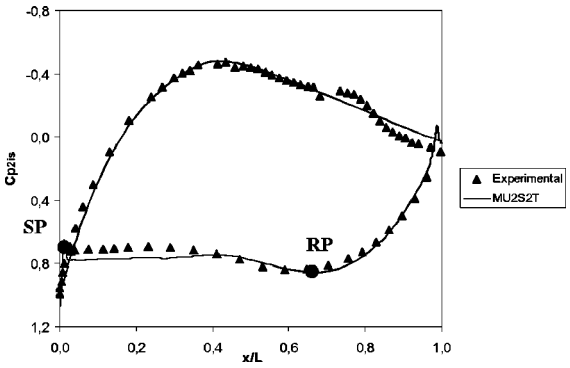

Fig. 8 T106 profile pressure coefficient ($Re_{2is}=1.5\times10^5$, $M_{2is}=0.5$, $\beta_1=90$ deg, $T_w=325$ K)

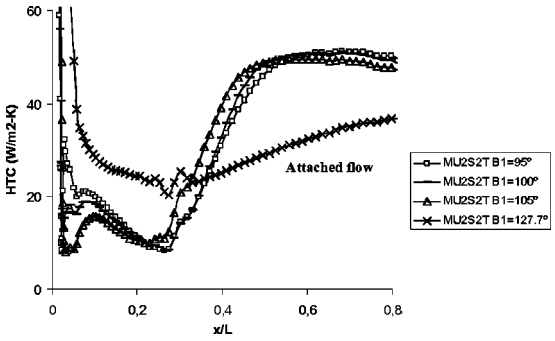

Fig. 10 T106 pressure side local HTC ($Re_{2is}=1.5\times10^5$, $\beta_1=95$, 100, 105, 127.7 deg, $M_{2is}=0.5$, $T_w=325$ K)

ates increasing its total pressure up to a certain value corresponding to that of a point of the shear layer developed at the outer edge of the bubble. This value is lower than the inlet total pressure and is isentropically recovered at the stagnation reattachment point, hence increasing the static pressure in the flow reattachment region. Although the pressure is not uniform in the bubble aft section (pressure recovery region), it only changes in the streamline direction, being essentially constant in the normal direction to the velocity.

The pressure recovery within the bubble can be expressed in terms of a reduction in the available dynamic pressure outside of the bubble. Independently of inlet flow angle, Reynolds number and Mach number, it was found that the decrease in dynamic pressure is constant and represents a 25% of the available dynamic pressure (Eq. (3))

$$\frac{q_{\text{reattachment}}}{q_{P=\text{constant}}} \cong k_1 = 0.75 \tag{3}$$

Although not shown here, the numerical results for 90 and 95-deg inlet flow angles present a high turbulent region with the generating core located in the center of the main vortex from where the turbulent kinetic energy is convected downstream. This turbulent region is always kept relatively far from the wall. On the other hand, for a 105-deg inlet flow angle no significant turbulence generation appears at the pressure side, while the observed flow physics is similar in both cases. Consequently, turbulence is not thought to have a prime role on the observed physics in these cases as will be explained later.

Heat transfer results for different inlet flow angles (see Figs. 9 and 10) showed a rapid decrease in both the HTC and the local Stanton number as the flow approaches the separation point. At the separation point a local minimum in the Stanton number is reached, followed by a continuous increase up to the reattachment point region, where a local maximum is reached. The flow configuration in this case presents multiple bubbles within the separation region, as shown in the friction coefficient distribution in Fig. 11, which in turn significantly affects the heat transfer if compared with results in separated flows with just one single bubble. In configurations with just one large bubble as the one described in the Reynolds number effects section, it is clear the existence of a single local minimum and a single local maximum located in the flow separation point and reattachment point regions, respectively.

In flow configurations with multiple bubbles, there are two additional stagnation points due to bubble interactions. This type of configuration is the same as the one presented in Fig. 16 (bottom picture). The two main bubbles are easily identifiable because of the large core sizes. The third bubble is a small one, stretched against the wall, located below the other two, and it is the responsible for the heat transfer variation aforementioned. The local maximum in the Stanton number just after the first local minimum is due to the stagnation point generated by the reattachment of the small bubble while the local minimum downstream this local maximum is due to its separation. Downstream, the local Stanton number increases up to a point located slightly downstream of the main bubble reattachment point due to the effect of the main bubble vortex.

The observed reduction in the local HTC and local Stanton number in the vicinity of a separation point region is in line with previous findings and it is generally explained to be due to the reduction of the skin friction coefficient. However, in the vicinity of a reattachment point, the local skin friction coefficient also tends to zero, but a local peak in the local Stanton number is observed. This is it is commonly explained as a turbulent effect. Although the results for 90 and 95 deg inlet flow angles showed a

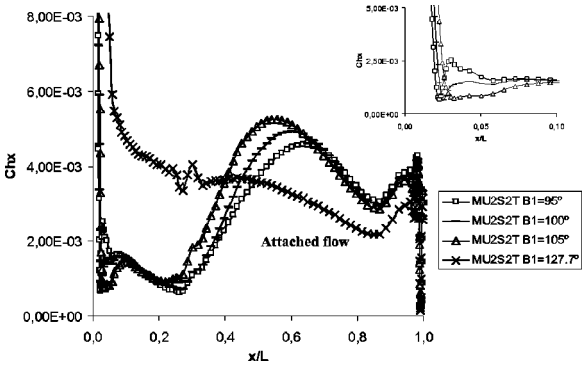

Fig. 9 T106 pressure side local Stanton number—leading edge region enlarged ($Re_{2is}=1.5\times10^5$, $\beta_1=95$, 100, 105, 127.7 deg, $M_{2is}=0.5$, $T_w=325$ K)

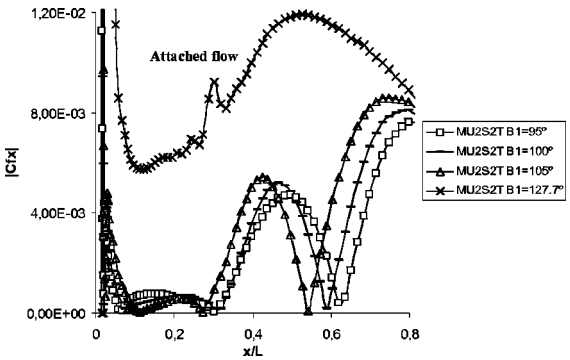

Fig. 11 T106 pressure side local Cf_x—absolute value ($Re_{2is}=1.5\times10^5$, $\beta_1=95$, 100, 105, 127.7 deg, $M_{2is}=0.5$, $T_w=325$ K)

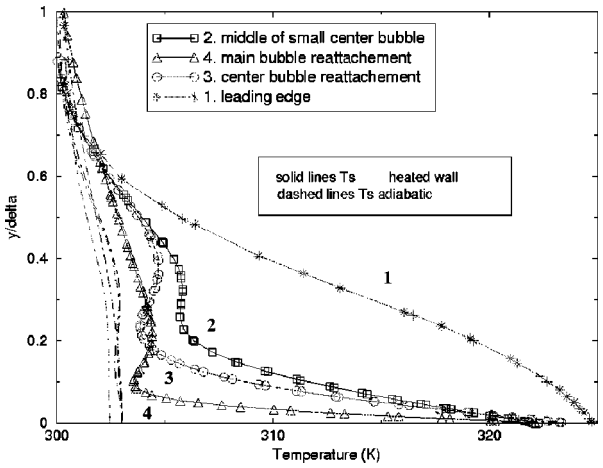

Fig. 12 T106 pressure side thermal boundary layer-heated wall and adiabatic wall ($Re_{2is}=1.5\times10^5$, $\beta_1=105$ deg, $M_{2is}=0.5$, $T_w=325$ K)

high turbulent region, for a 105 deg inlet flow angle no significant turbulence appears while the achieved Stanton number at the local maximum is about 45% higher than that for the attached flow; see Fig. 9. Same effects are observed for the HTC behavior.

Therefore, although both the turbulence and the reduction in the local skin-friction coefficient must have an effect in the heat transfer mechanisms in separated flows, other flow features associated with stagnated flow regions dominate the heat transfer phenomenon. More specifically, the existence of an ejection or an impingement stagnation point will determine the presence of a local minimum or maximum in the Stanton number. An ejection stagnation point is defined as a point where the velocity direction takes wall boundary layer mass flow away, and the impingement stagnation point as the point where external mass flow is taken to the wall.

For the sake of clarity, the temperature distribution within the separated flow region in a multiple bubble configuration is shown in Fig. 12. Dotted lines represent the temperature distribution for an adiabatic wall case, while solid lines show the temperature distribution within the recirculation region at different locations for a heated wall. Line 1 shows a typical temperature distribution within the bubble close to the separation point. The low temperature gradient at the wall is quite significant and it is due to the high total temperature in the region obtained by the convection of hot fluid from the wall by the ejection stagnation point configuration.

Lines 2 and 3 show a typical temperature distribution in the mid-region of a bubble. Starting at the limiting streamline enclosing the recirculating flow and going towards the wall, the temperature shows a slow variation followed by a recovery towards the adiabatic-wall case values. This peak in temperature is attained in the vortex core region where velocity tends to zero and the temperature tends to its total value. Through this region, the temperature is not significantly different to the adiabatic case, but from here to the wall, the largest temperature gradients occur, hence creating the genuine thermal boundary layer.

In Line 4, at the reattachment point, an impingement stagnation region is created. Along this line, cold fluid from the freestream is brought to the heated wall, hence generating high temperature gradients at the wall and a local maximum in the local Stanton number. It is believed that the mechanism of convective transport of fluid from or towards the wall together with the conduction is the main responsible of the total temperature distribution within the bubble, and therefore of the large heat transfer variation observed in the separated regions.

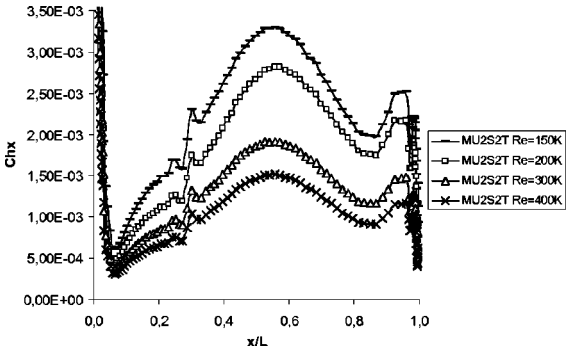

Fig. 13 T106 pressure side local Stanton number ($Re_{2is}=1.5$, 2, 3 and 4×10^5, $\beta_1=105$ deg, $M_{2is}=0.1$, $T_w=325$ K)

Reynolds Number Effects. Relating the Stanton number with other nondimensional parameters, it can be expressed as

$$Ch_x=\left(\frac{\mathrm{Nu}_x}{\mathrm{Re}_x\mathrm{Pr}}\right) \tag{4}$$

where the local Nusselt number is defined as

$$\mathrm{Nu}_x=\frac{\mathrm{HTC}_x X}{k}=\frac{(\partial T/\partial n)X}{(T_o-T_w)} \tag{5}$$

Taking into account that (T_o-T_w) is constant, the main parameters influencing the Stanton number are the local Reynolds number, Prandtl number and the temperature gradient at the wall. Furthermore, for air and current flow conditions, the Prandtl number is almost constant with a value very close to 0.71. Local Stanton number and HTC results for different isentropic exit Reynolds number and a constant isentropic exit Mach number of 0.1 are shown in Figs. 13 and 14. Note that for a $M_{2is}=0.1$ only one bubble is formed when the flow separates.

Again, a local minimum in the Stanton number is observed at separation (ejection stagnation point) followed by a continuous increase up to the reattachment region (impingement stagnation point) where a local maximum is reached slightly downstream of the reattachment point. In all these cases, the length of the separated flow region does not vary with the Reynolds number; see Fig. 15. However, it is expected a strong Reynolds number effect on the bubble thickness and on the thermal stresses.

As the Reynolds number increases, the local Stanton number decreases showing a similar behavior than that of the local skin-friction coefficient. On the other hand, the local HTC, and so the local Nusselt number, increases with the Reynolds number showing what it is intuitively expected, namely that an increase in

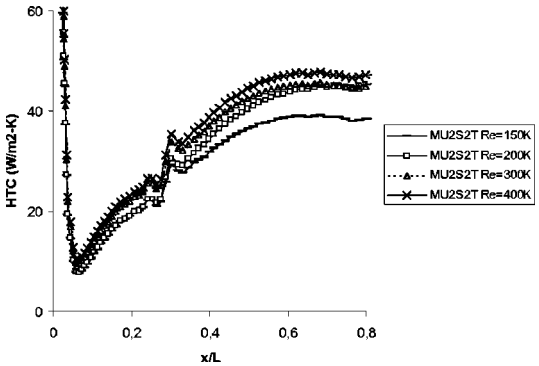

Fig. 14 T106 pressure side local HTC ($Re_{2is}=1.5$, 2, 3, and 4×10^5, $\beta_1=105$ deg, $M_{2is}=0.1$, $T_w=325$ K)

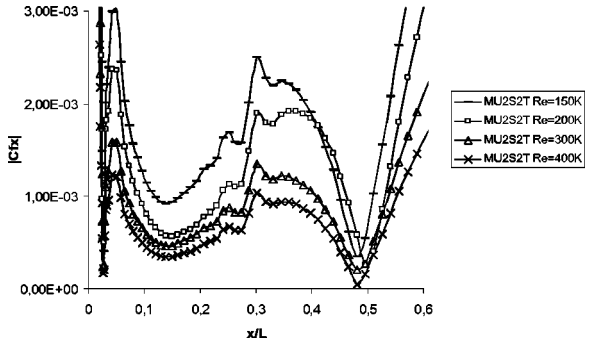

Fig. 15 T106 pressure side local Cf_x—absolute value (Re_{2is} = 1.5, 2, 3, and 4×10^5, β_1 = 105 deg, M_{2is} = 0.1, T_w = 325 K)

Reynolds number reduces the boundary layer thickness and increases the thermal stresses hence increasing the temperature gradient at the wall.

It is widely accepted that the Reynolds-Colburn analogy is only reliable in attached flows only for modest, near-zero pressure gradients and with a constant wall temperature (Hall and Pletcher [14]). The computed local skin-friction coefficient (absolute value) is shown in Fig. 15 to demonstrate that the Reynolds-Colburn analogy relating the Stanton number and skin-friction coefficient is not valid for separated flows even when no pressure gradient exists. Furthermore, it is not only at the reattachment point where skin friction falls to zero but also all along the separated flow region (negative skin friction) where the Reynolds-Colburn analogy is not applicable. This is a clear proof that there is a very weak coupling between velocity and thermal boundary layers in separated flows. It is the convective transport of fluid in a normal direction to the wall and the conduction effects in low velocity regions what drive the heat transfer phenomenon, hence supporting once again the prime role of the stagnation point configurations on the heat transfer mechanisms.

Mach Number Effects. Mach number effects are investigated for an isentropic exit Reynolds number of 1.5×10^5, an inlet flow angle of 105 deg and an isentropic exit Mach number varying from 0.2 up to 0.7. The main effect of an increasing Mach number is on the flow field configuration. As the Mach number increases, the small bubble located below the two main bubbles, becomes bigger and moves its vortex core away from the wall. For very low Mach numbers, less than 0.2 at the cascade exit, a single long bubble is formed when the flow separates (see Fig. 16, top). However, it is thought that the observed change in the flow configuration as the Mach number increases is a numerical effect, probably due to a non proper scaling of the artificial viscosity at very low Mach numbers.

Regarding Mach number effects on heat transfer, they are not as critical as those from Reynolds number (see Figs. 17 and 18), and it is not expected to have a prime role on the flow physics in separated flow regions. In Fig. 17, the local Stanton number is plotted for different Mach numbers and associated Prandtl numbers. Due to the very small variation of the Prandtl number, no influence on the Stanton number is ensured. As expected for low subsonic cases, as we have at the cascade inlet, the results show a small influence of the Mach number on both the local Stanton number and the local HTC. However, some effects are expected for high subsonic and transonic cases.

Conclusions

A better understanding of the flow physics and the heat transfer mechanisms in separated flow regions have been acquired by means of a numerical investigation of the heat transfer on the T106-300 LPT airfoil. Both the local Stanton number and the local HTC drop approaching the separation point reaching a local minimum and rise rapidly up to the region where the flow reattaches presenting a local maximum slightly downstream of the reattachment point. Although turbulence and low skin friction coefficient in stagnated flow regions must have an effect on the heat transfer mechanisms in separated flows, the presence of an ejection or and impingement stagnation point determines the presence of local peaks in the Stanton number and large heat transfer variations observed under separated flows. The attempt to define the parameters whose influence on heat transfer is critical showed that

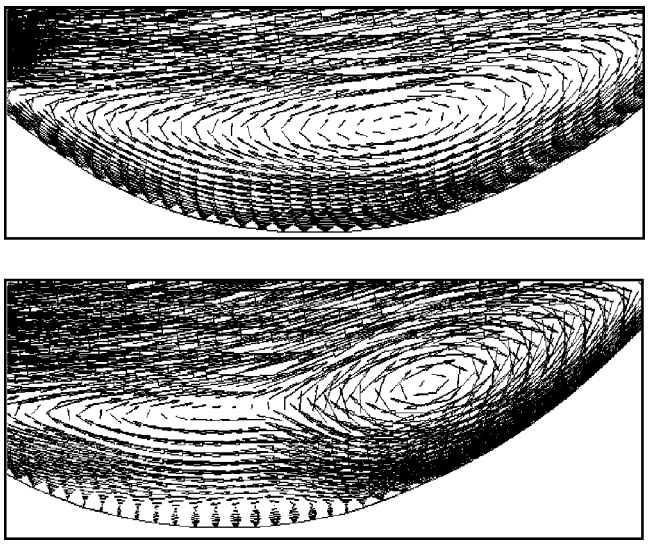

Fig. 16 T106 CFD flow pattern-velocity vectors—top: single vortex at M_{2is} = 0.1; bottom: two vortices at M_{2is} = 0.5 (Re_{2is} = 1.5×10^5, β_1 = 105 deg, T_w = 325 K)

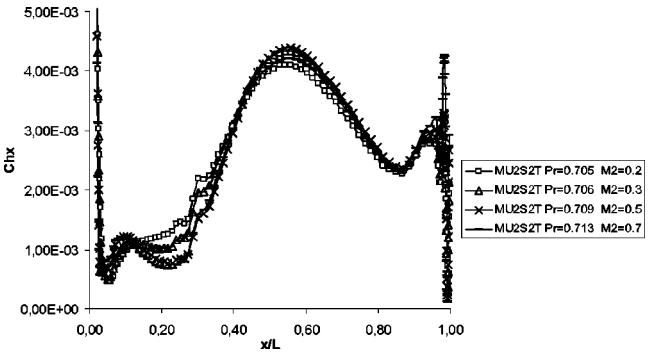

Fig. 17 T106 pressure side local Stanton number (Re_{2is} = 1.5×10^5, β_1 = 105 deg, M_{2is} = 0.2, 0.3, 0.5, 0.7, T_w = 325 K)

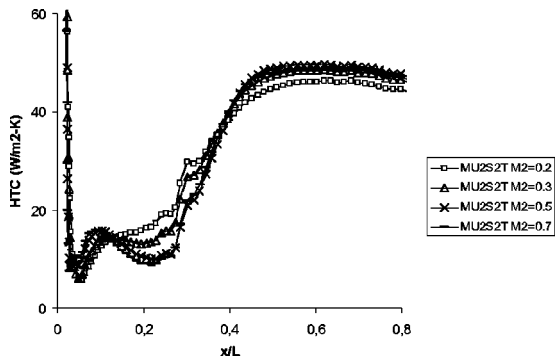

Fig. 18 T106 pressure side local HTC (Re_{2is} = 1.5×10^5, β_1 = 105 deg, M_{2is} = 0.2, 0.3, 0.5, 0.7, T_w = 325 K)

Reynolds number is the dominant parameter, and in a less manner the Mach number and the inlet flow angle. When the Reynolds number is increased, the separated flow region does not change its size, but the local Stanton number decreases.

Recognizing the complexity of the heat transfer mechanisms in separated flows, accurate experimental data is required in LPT turbine blades to validate the presented findings and based on that, to develop special correlations for heat transfer in separated flows.

Acknowledgments

This material is based upon work funded by the Commission of the European Communities under contract G4RD-CT-1999-00055.

Nomenclature

2-D = two-dimensional
Cax = axial chord (m)
Cf = skin friction coefficient
Ch = Stanton no.
Cp = pressure coefficient $2(P-P_\infty)/\rho_\infty u_\infty$
HTC = convective heat transfer coefficient (W/m^2-K)
L = real chord (m)
LPT = low-pressure turbine
M = Mach no.
MU^2S^2T = multirow unsteady unstructured specific solver for turbomachinery
Nu = Nusselt no.
P = pressure (N/m^2)
Pr = Prandtl no.
RANS = Reynolds-averaged Navier Stokes equations
Re = Reynolds no.
RP = reattachment point
SP = separation point
T = temperature (°K)
Tu = turbulence level (%)
VKI = von Karman Institute
X = real chord axis coordinate (m)
c_p = specific heat at constant pressure
h = blade height (m)
k = thermal conductivity of fluid (W/m-K)
q = dynamic pressure (N/m^2)
t/L = pitch ratio
u = free-stream velocity (m/s)
$\partial T/\partial n$ = temperature gradient normal to wall (K/m)
k = turbulent kinetic energy (m^2/s^2)
ω = specific dissipation rate
β_s = stagger angle (deg.)
β = flow angle (deg)
ρ = density (kg/m^3)
τ = shear stress
μ = viscosity (kg/m-s)

Subscripts

∞ = free-stream conditions
o = stagnation conditions
des = design conditions
e = boundary layer edge conditions
1 = inlet conditions
2 = exit conditions
is = isentropic conditions
s = static conditions
w = wall conditions
x = local conditions

References

[1] Bassi, F., Rebay, S., Savini, M., Colantuoni, S., and Santoriello, G. ''A Navier-Stokes Solver With Different Turbulence Models Applied to Film-Cooled Turbine Cascades,'' Heat Transfer and Cooling in Gas Turbines, AGARD-CP-527, 1993.

[2] Rivir, R. B., Johnston, J. P., and Eaton, J. K., 1997, ''Heat Transfer on a Flat Surface Under a Region of Turbulent Separation,'' ASME J. Turbomach., **116**(1), pp. 57–62.

[3] Bellows, R. J., and Mayle, R. E., 1986, ''Heat Transfer Downstream of a Leading Edge Separation Bubble,'' ASME J. Turbomach., **108**(3), pp. 131–136.

[4] Wolf, S., Homeier, L., and Fottner, L., 2001, ''Experimental Investigation of Heat Transfer in Separated Flow on a Highly Loaded LP Turbine Cascade,'' Proc. RTO/AVT Symposium and Specialists Meeting Heat Transfer and Cooling in Propulsion and Power Systems, Loen, Norway, May 7–11.

[5] Merzkirch, W., Page, R. H., and Fletcher, L. S., 1988, ''A Survey of Heat Transfer in Compressible Separated and Reattached Flows,'' AIAA J., **26**(2), pp. 144–150.

[6] Hoheisel, H., 1990, ''Test Case E/CA-6, Subsonic Turbine Cascade T106,'' Test Cases for Computation of Internal Flows in Aero Engine Components, AGARD-AR-275, July.

[7] Arts, T., and Lambert de Rouvroit, M., 1990, ''Aero-Thermal Performance of a Two Dimensional Highly Loaded Transonic Turbine Nozzle Guide Vane,'' Gas Turbine and Aeroengine Congress and Exposition, Brussels, Belgium, June 11–14.

[8] Corral, R., and Fernandez-Castañeda, J., 1998, ''Surface Mesh Generation by Means of Steiner Triangulation,'' AIAA-98-3013, presented at 29th AIAA Fluid Dynamics Conference, Albuquerque, NM, June 15–18.

[9] Wilcox, D. C., 1988, ''Reassessment of the Scale Determining Equation for Advanced Turbulence Models,'' AIAA J., **26**, pp. 1299–1310.

[10] Corral, R., and Contreras, J., 2000, ''Quantitative Influence of the Steady Non-Reflecting Boundary Conditions on Blade-to-Blade Computations,'' presented at 45th ASME Gas Turbine and Aeroengine Congress, Exposition and Users Symposium, Munich, May 8–11.

[11] Jameson, A., Schmidt, W., and Turkel, E., 1981, ''Numerical Solution of the Euler Equations by Finite Volume Method using Runge-Kutta Time Stepping Schemes,'' AIAA Pap., 81–1259.

[12] Gehrer, A., and Jericha, H., 1999, ''External Heat Transfer Predictions in a Highly Loaded Transonic Linear Turbine Guide Vane Cascade Using and Upwind Biased Navier-Stokes Solver,'' ASME J. Turbomach., **121**(3).

[13] Boyle, R. J., and Ameri, A. A., 1997, ''Grid Orthogonality Effects on Predicted Turbine Midspan Heat Transfer and Performance,'' ASME J. Turbomach., **119**(1).

[14] Hall, E. J., and Pletcher, J. D., 1985, ''Application of a Viscous-Inviscid Procedure to Predict Separated Flows with Heat Transfer,'' ASME J. Heat Transfer, **107(3)**, pp. 557–563.

Effect of Endwall Motion on Blade Tip Heat Transfer

V. Srinivasan

R. J. Goldstein

Heat Transfer Laboratory,
Department of Mechanical Engineering,
University of Minnesota,
Minneapolis, MN 55455

Local mass transfer measurements were conducted on the tip of a turbine blade in a five-blade linear cascade with a blade-centered configuration. The tip clearance levels ranged from 0.6 to 6.9% of blade chord. The effect of relative motion between the casing and the blade tip was simulated using a moving endwall made of neoprene mounted on the top of the wind tunnel. Data were obtained for a single Reynolds number of 2.7 $\times 10^5$ *based on cascade exit velocity and blade chord. Pressure measurements indicate that the effect of endwall motion on blade loading at a clearance of 0.6% of blade chord is to reduce the pressure gradients driving the tip leakage flow. With the introduction of endwall motion, there is a reduction of about 9% in mass transfer levels at a clearance of 0.6% of chord. This is presumably due to the tip leakage vortex coming closer to the suction side of the blade and 'blocking the flow,' leading to reduced tip gap velocities and hence lower mass transfer.* [DOI: 10.1115/1.1554411]

1 Introduction

In a gas turbine engine, the difference in pressure between the pressure and suction surfaces of the blade drives some flow through the gap between the end of a rotating blade and the surrounding casing. This is usually called the tip clearance flow, or tip leakage flow. The deleterious effects of this leakage flow have been known for several years and have been the subject of much study. In addition to the reduction in the work extracted from the hot gas by the blades due to escape of the flow to the suction side without being utilized, the leakage flow also mixes with the oncoming flow on the suction side, causing entropy losses. Booth et al. [1] estimate that a clearance of 1% of blade span can cause losses of about 1–3% in stage efficiency. Another effect that has been studied only in the last two decades is the deterioration of the blade tip surface due to constant wear and abrasion by the hot gas. The high velocity of the gas flowing through the tip gap causes high convection coefficients. The blade tip is difficult to cool since it is surrounded by the hot gas on three sides, and cooling it imposes a further thermodynamic penalty on system efficiency, since the air used for cooling the turbine blade is extracted at the exit of the last compressor stage and would otherwise have been used for doing work.

The basic feature of the flow in the tip area can be summarized as follows: the flow is driven through the clearance by the pressure difference on the pressure and suction sides of the blade. The flow separates and reattaches at the pressure side edge. At the exit of the clearance, the mixed-out flow meets the oncoming flow on the suction side and rolls up into a vortex.

Considerable effort has been expended over the past few years in quantifying the losses and the heat transfer parameters associated with the tip clearance flow, and are summarized in the review by Bunker [2]. Graham [3] studied the tip leakage flow in a water tunnel cascade and observed that the size of the separation bubble at the pressure edge drastically decreases as the clearance is reduced. Sjölander and Amrud [4] show that the tip leakage flow inhibits the formation of the passage vortex that is found for the case of no clearance, since the pressure leg of the horseshoe vortex at the leading edge is swept away into the clearance very near the leading edge. Therefore, the flow approaching the tip pressure surface at downstream chordwise locations is composed mainly of mainstream fluid. Moore and Tilton [5] verified the existence of a narrow region of very low pressure on the pressure edge of the tip that may cause tip burnout.

Studies by Morphis and Bindon [6] on an annular turbine cascade showed that introduction of a corner radius at the pressure edge of the blade prevents separation. The flow stays attached on the tip; however, this also leads to increased leakage since the flow is no longer blocked by the separation bubble. The LDA measurements of Metzger and Rued [7] show that on the pressure side of the blade near the tip clearance, the flow is highly accelerated, with apparent relaminarization of the turbulent layer close to the tip. The gap flow velocity measurements of Yaras and Sjölander [8,9] indicate that with the introduction of endwall relative motion, the mass flow rate decreases by 50% over that with a stationary endwall. The boundary layers on the endwall and on the tip were shown to be very thin, implying that the clearance flow is essentially inviscid.

Mayle and Metzger [10] were the first to study the thermal effects of tip leakage flow. Modeling the clearance flow as a duct flow, they found that their data agreed with the Colburn equation. A later paper [11] suggested the use of the Dittus-Boelter equation with a correction to account for the entrance effect. Chyu et al. [12] used a mass transfer technique to investigate the heat transfer on rectangular cavities simulating grooved turbine blade tips including the effect of shroud motion. Metzger and Rued [7,13] found very high rates of acceleration on the pressure side very close to the tip that caused the formation of thin boundary layers, relaminarization, and an enhancement in heat transfer of up to 200% of that for the case of no clearance. They also found that the leakage vortex significantly affects the heat transfer on the suction side. Extensive studies on film cooled blade tip heat transfer and effectiveness were performed by Kim and others [14,15].

In the last two years, considerable data have emerged on blade tip heat transfer using linear cascades instead of idealized models as was the case earlier. Bunker et al. [16] provide full surface information on heat transfer coefficients with pressure distribution on blade tips of a power generation turbine for sharp- and radiused-edge blades for different clearance levels. The flow and heat transfer data on the blade tips of an aeroengine turbine stage obtained by the liquid crystal technique are reported by J.-C Han's research group [17–19]. Jin [20] used the naphthalene technique to determine the effects of clearance level, turbulence intensity and Reynolds number on the mass/heat transfer from the tip and near-tip surfaces of the blade.

The effect of endwall relative motion has never been determined in a linear cascade. Mayle and Metzger [10] argue, using a

Contributed by the International Gas Turbine Institute for publication in the JOURNAL OF TURBOMACHINERY. Manuscript received by the IGTI August 15, 2002. Associate Editor: S. Bunker.

duct-flow model, that the heat transfer from the tip should increase over that without rotation when the flow path length in the clearance is more than 20 times the clearance. The data presented in [12] and Chyu et al. [21] are in agreement with the model. Recent data of Jin [20] show that the Sherwood number data at several chordwise locations on the tip surface for different tip clearance levels collapse to the same curve when normalized with the 0.8th power of a Reynolds number based on the cascade inlet velocity and the tip clearance. This points to the nominally duct-like character of the flow, as suggested by Mayle and Metzger [10]. However, it has been shown by investigators that the passage vortex is dragged closer to the suction side with the introduction of rotation. Yaras and Sjölander [8,9] report a reduction in leakage flow with endwall relative motion, leading one to expect a reduction in flow velocities, and therefore, heat transfer. The current experiment was designed to test the hypothesis presented in [10].

Admittedly, endwall motion is not a substitute for simulating rotation, since it does not simulate some real engine effects, such as centrifugal forces leading to radial flows in the blade passage. However, in and around the tip gap region, endwall motion can be expected to be the dominant factor compared to other effects of rotation.

Experimental Method and Apparatus

The napthalene sublimation technique is based on the mass/heat transfer analogy and is a well-established method of measuring the mass/heat transfer from complex geometric surfaces. A review of the method can be found in the review by Goldstein and Cho [22]. To summarize, the technique can be used to determine the convective component of heat transfer with the absence of conduction or radiation errors. A heat transfer problem can be converted to that of mass transfer using the heat/mass transfer analogy. The analogy uses the equivalence of the Prandtl number and the Schmidt number in heat and mass transfer, respectively. The mass transfer coefficient is analogous to the heat transfer coefficient and is defined as

$$h_m = \frac{\dot{m}}{\rho_{v,w} - \rho_{v,\infty}} = \frac{\dot{m}}{\rho_{v,w}} \tag{1}$$

since $\rho_{v,\infty} = 0$

$$\text{where } \dot{m} = \rho_s \frac{\delta y}{\delta \tau} \tag{2}$$

A dimensionless mass transfer coefficient, the Sherwood number (Sh), similar to the Nusselt number is used to describe the results. A low-turbulence (intensity $<0.2\%$) blowing-type wind tunnel in the Heat Transfer Laboratory of the University of Minnesota is used.

Air at room temperature drawn through a filter by a 22.4-kW blower passes through a diffuser and heat exchanger before flowing through settling chambers with screens inside. The air is then blown through a square cross-sectional contraction nozzle with an area contraction ratio of 6.25:1 and an exit area of 45.7 $\times$45.7 cm^2 into the test section.

The test section is connected to the exit of the contraction of the wind tunnel. The linear cascade consists of five (aluminum) simulated high performance turbine rotor blades placed in a blade-centered configuration. The blades have a high turning angle, 107.5 deg, and a chord of 18.41 cm. The gap between the top of the blades and the top wall of the test section simulates the clearance. This gap can be varied by adding or removing spacers at the base of the blades. The blade profile is shown in Fig. 1. The tip clearances employed in this study are 0.6, 0.86, 1.72, 3.45, and 6.9% of chord. Due to the high aspect ratio of the blades (2.48) this translates to 0.24, 0.35, 0.69, 1.38, and 2.77% of span. During the experiments, the change in tip clearance due to sublimation was at most 4.6% of the nominal clearance value at the smallest clearance level.

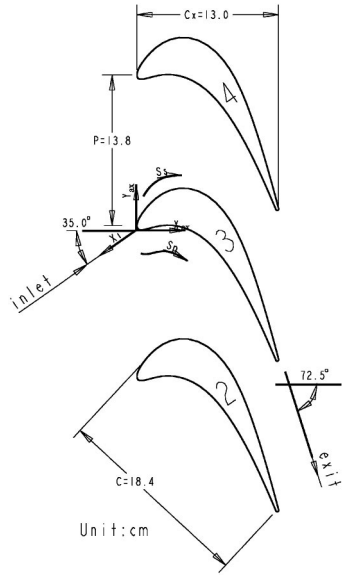

Fig. 1 Cascade coordinates and parameters

The moving wall apparatus used for simulating rotation of the blades against the stationary casing in a turbine consists of a 2-kW three-phase induction motor, a rubber belt, three rollers on which the moving wall rotates, and two pitch pulleys which transmit power from the motor to the belt. The whole apparatus rests on an aluminum base that fits on to the top wall of the linear cascade section. A schematic diagram of the moving wall apparatus is shown in Fig. 2.

The moving wall uses a belt made of N-8 Sampla synthetic rubber that is placed flush with the inner top wall of the test section. The belt moves from the direction of the suction side of the stationary blades to the pressure side on three aluminum rollers of diameter 75 mm supported on bearings housed in an aluminum frame. There are two primary rollers and a tertiary roller; one of the two primary rollers is driven by a 2-kW three-phase induction motor (also bolted to the frame) through a system of pitch pulleys. It was experimentally verified that the ''flapping''

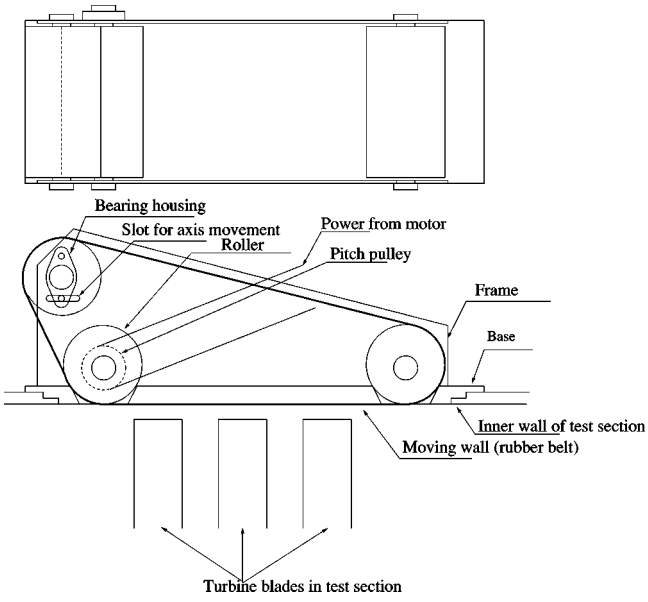

Fig. 2 Schematic diagram of the moving wall apparatus

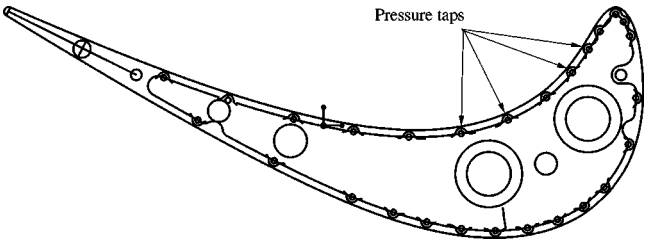

Fig. 3 Part drawing of tip surface of hollow blade with location of pressure taps

effect of the belt due to vibrations during operation resulted in a variation of tip clearance of not more than 0.1% of chord.

To reduce ''flapping'' motions of the belt, the belt was operated at 25 m/s. In order to attain an engine-representative Reynolds number, however, the wind tunnel was operated at a cascade inlet speed of 12.5 m/s, i.e., half the speed of the moving wall. We recognize that this is not consistent with the design velocity triangles; however, the effects of relative motion should still make themselves felt at this ratio of velocities.

The degree to which the magnitude of relative motion in an actual turbine is simulated by the endwall motion is measured in terms of the engineering equivalent speed (EES) defined as

$$\mathrm{EES} = V_{\mathrm{ew}}/(2 \times U_{\mathrm{inlet}}) \tag{3}$$

where the constant of 2 was chosen from the constraint mentioned above. Here U_{inlet} refers to the inlet velocity relative to the blade cascade. The endwall velocity V_{ew} represents the velocity of the blade tip relative to the casing.

Detailed pressure measurements were made on the tip using a row of holes on a hollow blade. Holes were located both on the pressure and suction surface 22 mm ($z/C = 0.12$) away from the tip, and on the tip surface itself. Figure 3 shows a part drawing of the tip surface including the pressure taps located 2 mm from the metal rim. For mass transfer measurements, a specially designed mold and casting procedures were used to coat an aluminum blade with naphthalene to produce a smooth surface. The T-type thermocouples were calibrated and integrated with a GPIB-enabled Linux workstation for data acquisition.

The dynamic and static pressure were measured with a micro manometer and a manometer, respectively. Pressure profiles on the blade are measured with a water manometer. Naphthalene sublimation thickness is measured with a dedicated four-axis table developed in the Heat Transfer Laboratory of the University of Minnesota.

The absolute uncertainty in the static pressure coefficient C_p is 0.02, which is small compared to the values of C_p. The uncertainty in sublimation depth measurement is less than 0.8%, while the uncertainty in measurement of Sherwood number is 7.6%; 97% of the error is due to the uncertainty in properties of naphthalene. The sublimation due to natural convection is accounted for in the calculation of Sherwood number. The experimental procedure is described in detail in Srinivasan [23].

Experimental Results and Discussion

Before the runs, the test section's tailboards and bleed plates were adjusted till the midspan distribution matched the inviscid flow solution. Figure 4 shows the effect of endwall motion on the pressure distribution on the near-tip pressure and suction surfaces for a clearance of $t/C = 0.6\%$. Also shown are similar data for $t/C = 0.86\%$ from Jin [20] for comparison. It is seen that at $z/C = 0.12$, i.e., about 14 gap heights below the tip surface, there is very little difference between the cases with and without endwall motion, indicating a highly localized effect, if any. The pressure profiles are shown relative to the midspan inviscid solution (solid line). It can be seen from the curve marked ''near-tip profile, zero clearance'' that deviations from the midspan solution are not only due to the presence of the clearance, but also due to the presence of the endwall. Figure 5 shows the pressure profile on the tip surface itself, using taps drilled 2 mm away from the rim. Note that the figure may be misleading, since the low pressures observed are on the pressure side of the blade, where separation of the flow entering the tip gap causes a sharp drop in pressure right at the pressure edge. The separation bubble can be clearly seen in the flow visualization presented in a subsequent section. The pressure then rises as the flow reattaches and the flow attains a more uniform velocity profile before reaching the suction side. This low pressure indicates that the largest leakage flow occurs at a location corresponding to the region of highest turning of the blade profile. With the introduction of endwall motion, the overall pressure rises. For $t/C = 0.86\%$, the pressure rises by about 10%, but there is no observable change in the pressure differential across the tip gap. For $t/C = 0.6\%$, the pressure rises by about 15%, accompanied by a 12% decrease in the pressure differential on an average.

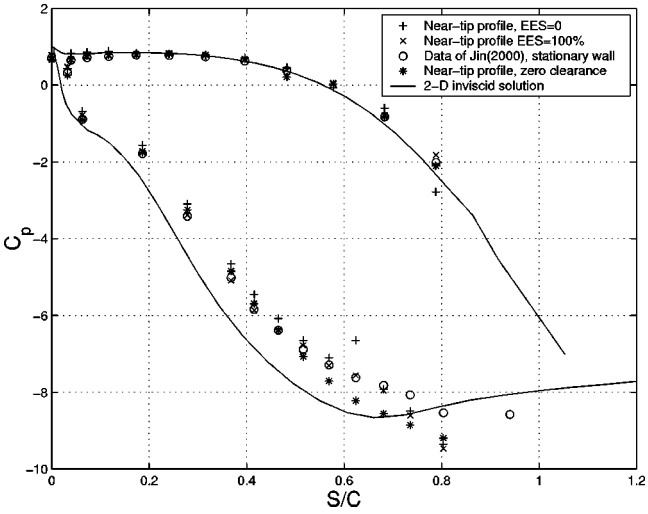

Fig. 4 Blade loading near the tip at $z/C = 0.12$ for $t/C = 0.6\%$

The mass transfer results from the present study are first compared with the data of [20]. Then, the effect of endwall relative motion is shown. Measurements were conducted in blade chord coordinates (shown in Fig. 6) using a linear variable differential transformer (LVDT) gage. The Reynolds number based on blade chord and exit velocity is 2.72×10^5. Local mass transfer data to

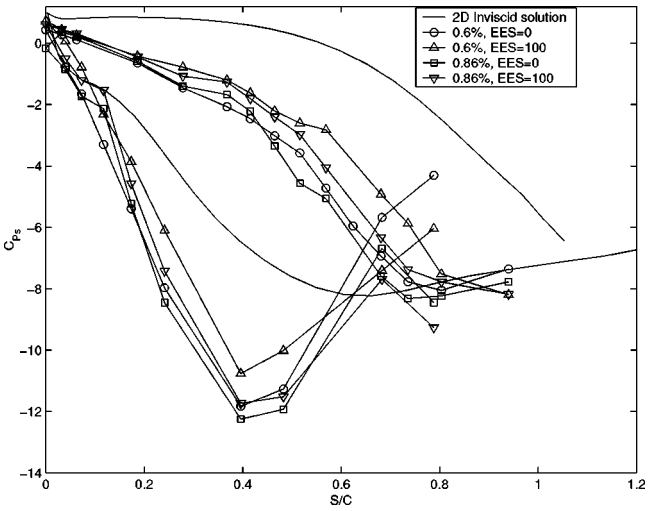

Fig. 5 Pressure profile on tip for $t/C = 0.6$, 0.86%

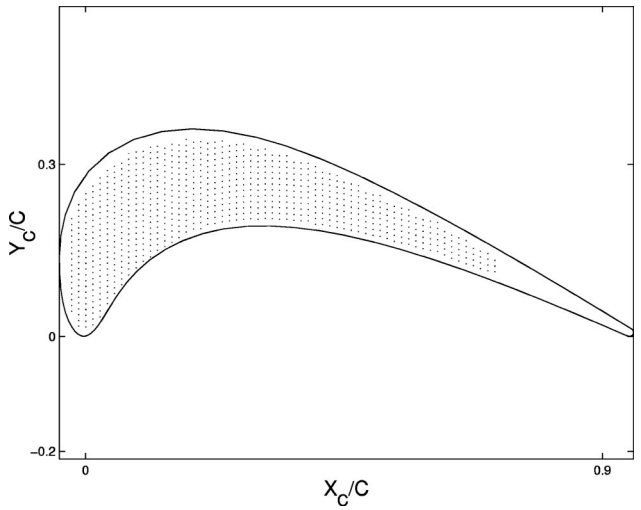

Fig. 6 Coordinate system used for measurement

be shown are plotted in blade true chord coordinates. The dots on the tip surface in Fig. 6 show the 631 locations of measurement using the LVDT probe.

For mass transfer tests, in order to ensure that the moving wall apparatus itself did not alter the flow in any way, a baseline test was conducted at the conditions $t/C=6.9\%$, $\mathrm{Re}_{ex}=5.5\times10^5$, EES=0, corresponding to the test conditions of Jin [20]. No significant difference was found in the results, which are not shown here. All further tests were conducted at the lower Reynolds number of 2.72×10^5.

Results

Figure 7 shows the contour plot of the Sherwood number for a clearance of 0.6% of chord, with no endwall motion. An area of relatively low Sh is seen in the forward half of the blade, corresponding to the 'sweet spot' observed by Bunker et al. [16]. This corresponds to low-pressure gradients driving the tip flow in this region. Near the pressure edge, separation and reattachment of the flow causes a narrow region of high mass transfer. Mass transfer levels are elevated on the aft half of the blade due to the greater pressure differentials, and presumably, greater leakage velocities at these *X*-locations.

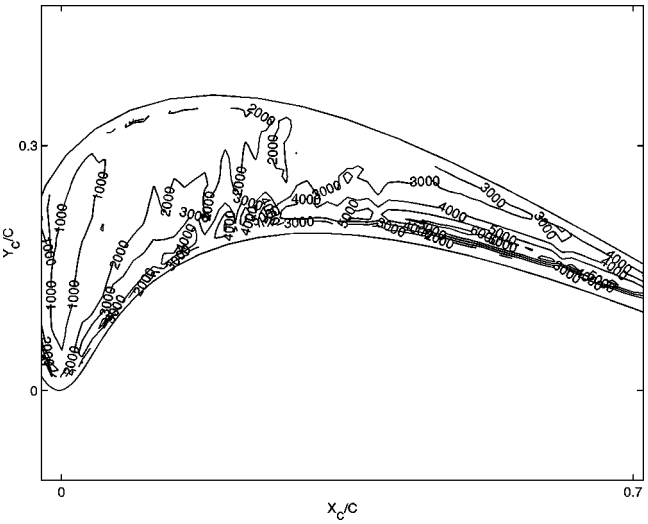

Fig. 7 Contour plot of Sh for $t/C=0.6\%$, EES=0

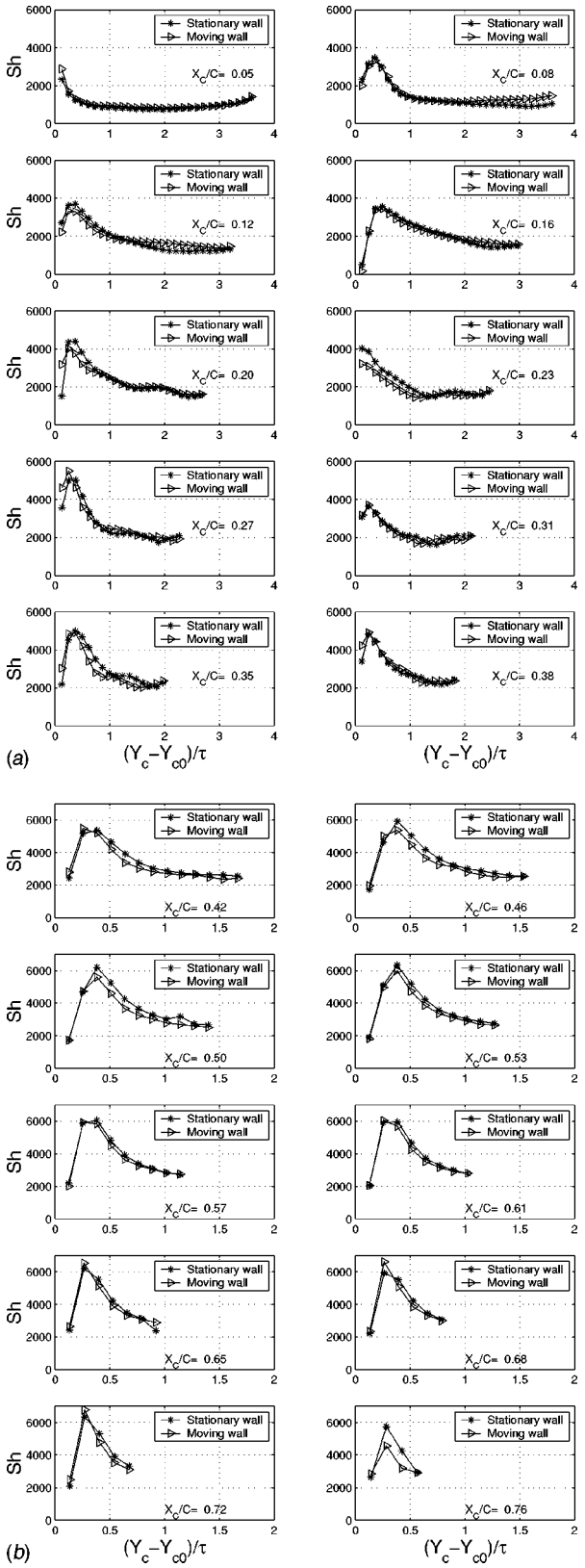

Fig. 8 (*a*) Sh on fore half of blade, $t/C=0.6\%$; (*b*) Sh on aft half of blade, $t/C=0.6\%$

Figures 8–10 show the local Sherwood number plotted against the measurement path expressed in terms of tip clearance lengths, $(Y_c-Y_{c0})/t$, for different chordwise locations. Here Y_{c0} is the Y_c-coordinate of the pressure edge at a particular chordwise loca-

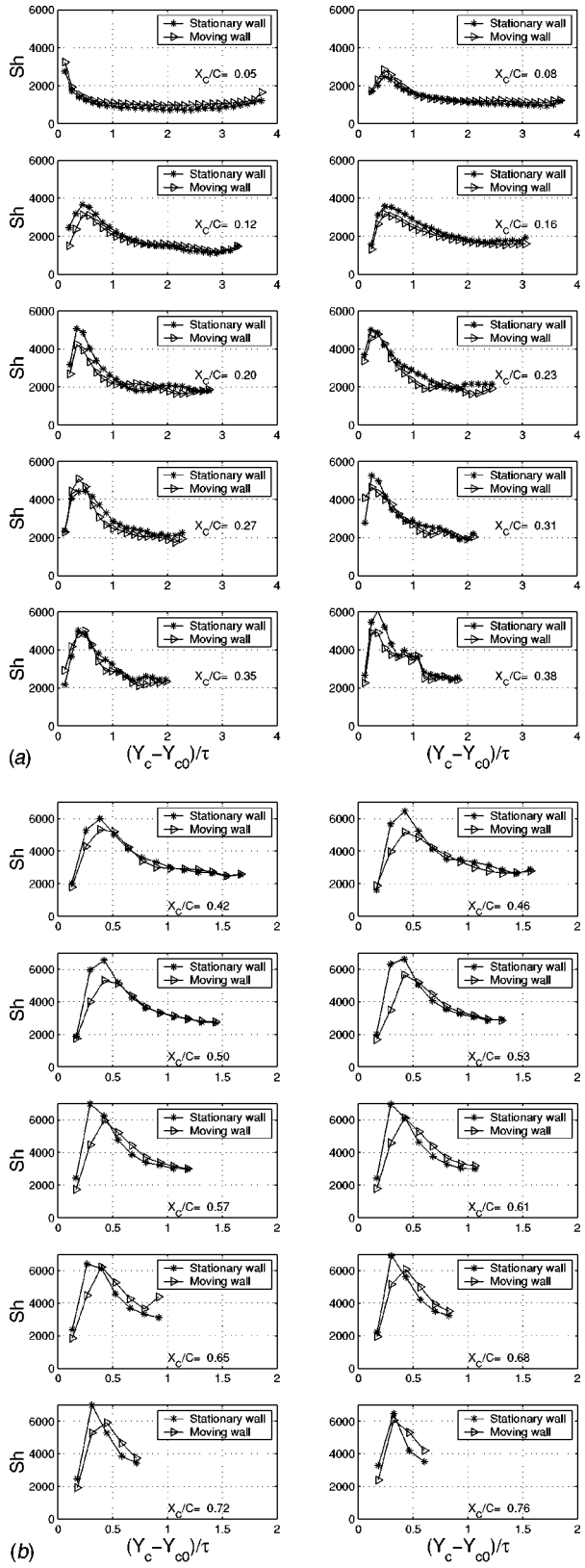

Fig. 9 (*a*) **Sh on fore half of blade, $t/C=0.86\%$; (*b*) aft half of blade, $t/C=0.86\%$**

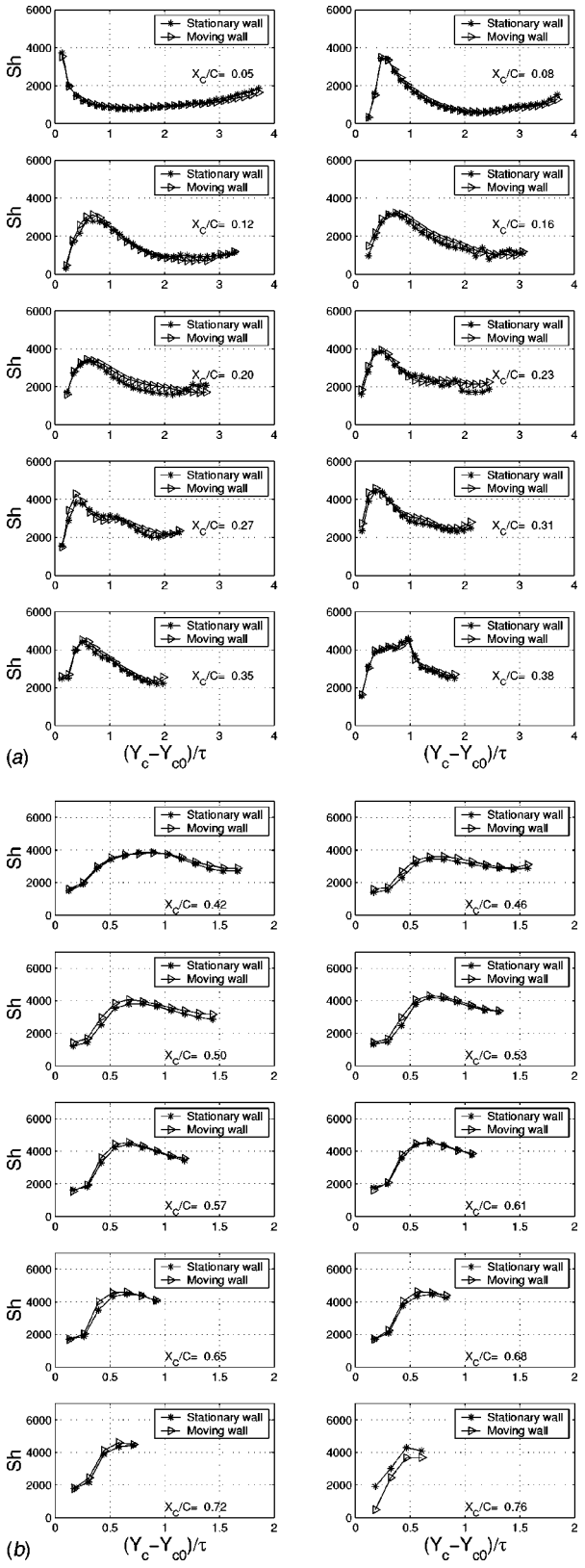

Fig. 10 (*a*) **Fore half of blade, $t/C=1.72\%$; (*b*) aft half of blade, $t/C=1.72\%$**

tion. It must be noted that the measurement grid is not aligned with the flow direction of the fluid at most locations on the tip.

For $t/C=0.6\%$, very close to the leading edge, the Sherwood number decreases monotonically as y increases, indicating reattachment at the edge, outside the naphthalene surface. Figure 8(*a*) shows that for downstream chordwise locations, up to $X_c/C=0.2$, reattachment, as inferred from the maximum in Sh, occurs at roughly 4 clearance heights. At $X_c/C=0.23$ there is a reduction

in the Sherwood number, from values of about 5000 to nearly 4000. However, towards the trailing edge (Fig. 8(*b*)), there is very little effect of wall motion on the Sherwood number. In the fore half of the blade, for a large path length $(Y-Y_{c0})/t>30$, there is some increase in Sh, as predicted by Mayle and Metzger, but this is not consistent for all values of x/C. Their predictions are for a two-dimensional flow; however, both the pressure profile on the tip and the Sherwood number contours show that the flow field is strongly three-dimensional, with large transverse pressure gradients. In addition, the leakage and passage vortices located in the adjacent blade passage at the exit of the clearance detract from the ductlike character of the flow, especially in the aft half of the blade.

Sherwood numbers with a moving endwall were consistently lower than those with no motion, indicating that there does exist a slight effect of endwall motion that acts to reduce Sh. The area-averaged reduction in Sherwood numbers for the entire tip surface was 9, 3.2, and 5.5% for tip clearances of 0.6, 0.86, and 1.72% of chord, respectively.

However, the uncertainty estimate for Sherwood numbers obtained in this experiment is 7.6%, indicating that the effects of endwall motion alone are small. A possible explanation for this reduction is that at small clearances, viscous effects become sufficiently strong as to slightly drag the leakage vortex towards the suction side and alter the driving pressure gradients. The leakage flow may be slightly reduced in magnitude, resulting in smaller velocities and smaller mass transfer coefficients. The movement of the reattachment point towards the pressure edge corroborates this.

At $t/C=0.86\%$, the picture is similar to that for $t/C=0.6\%$ on the first half of the blade, as seen in Fig. 9(*a*). Reattachment occurs at roughly the same Y_c-position as for $t/C=0.6\%$. However, there is virtually no effect of endwall motion on the Sherwood numbers on the first half of the blade. Sherwood numbers are lower for the case of endwall motion, as with the smallest clearance, with the difference lying within the experimental error limits of this study. However, Fig. 9(*b*) shows that there is a larger effect on the second half of the blade, with the Sherwood numbers slightly increasing with the introduction of wall motion. This is somewhat difficult to explain, since both the flow visualization and the pressure measurements point to a reduced flow velocity near the trailing edge at this clearance level as compared to $t/C=0.86\%$. However, the data were repeatable. The reattachment point seems to shift towards the suction side, indicating a slight increase in the size of the separation bubble, which is not observed from the flow visualization. As the clearance is increased to $t/C=1.72\%$ (Figs. 10(*a*) and (*b*)), the trend of reduced Sherwood numbers continues. As the flow moves downstream towards the trailing edge, the point of maximum Sherwood number shifts towards the suction side, indicating an increase in the size of the separation bubble near the trailing edge. At the very last X_c/C location shown, there is no maximum of Sh, indicating that the bubble covers the entire width of the tip. There is no discernable effect of endwall motion at this clearance level.

The data for the two largest clearance levels of 3.45 and 6.9% of chord are not shown. As expected from the foregoing discussion, the effect of relative motion was negligible at such large clearances.

The conclusions were also verified qualitatively by flow visualization, which was performed by coating the tip surface with a mixture of oil and lamp-black (Fig. 11). The oil pattern shows all the features observed by previous investigators, such as the separation bubble at the pressure edge, and the narrow region of high shear stress caused by flow reattachment immediately behind the bubble. Discrete oil streaks are observed at midchord locations which are thought to be due to several small leakage vortices, observed earlier. However, no difference in the oil distribution was found for runs with and without endwall motion, indicating that the shear stress distribution remains the same, within the limits of visual observation.

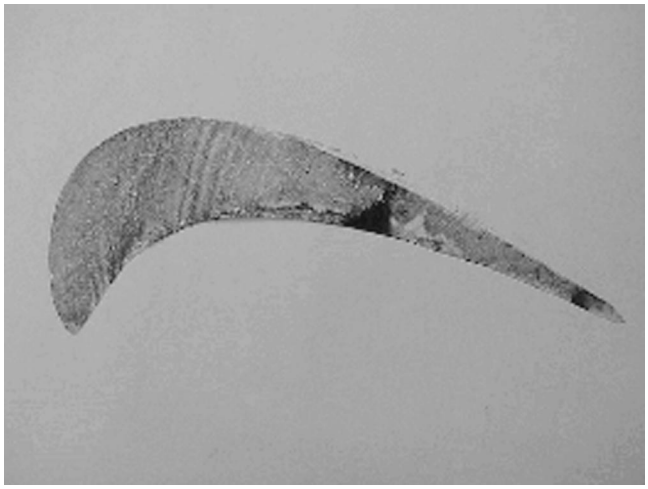

Fig. 11 Oil-lampblack flow visualization on tip

Conclusions

The effects of relative endwall motion at 100% EES can be summarized as follows:

1. The pressure and mass transfer measurements indicate that at a clearance of $t/C=0.6\%$, there is a small but definite reduction of 9% on the heat/mass transfer due to wall motion at certain midchord locations. This may be caused by the leakage vortex moving closer to the suction surface. This would cause reduced pressure gradients across the tip compared to the case of no wall motion, and lead to lower leakage velocities. While this is a possible explanation, the magnitude of the effect is too small to draw definite conclusions.
2. The increase in Sh predicted by Mayle and Metzger for large path length is observed at three chordwise locations on the fore half-blade, and is not consistent at all locations. The deviation may be due to the strong three-dimensionality of the flow that is ignored in the model.
3. At a clearance of $t/C=0.86\%$, there appears to be little effect of wall motion on the Sherwood number, except very near the trailing edge where Sh increases.
4. At all higher clearances, there is no measurable effect of relative motion on Sh, indicating that at such clearances the flow is essentially pressure-driven and viscous effects are negligible.

Acknowledgments

This research was supported by the U.S. Department of Energy-Federal Energy Technology Center through the AGTSR program.

Nomenclature

$\dot{m}$ = mass flux
C = blade chord, 18.4 cm
C_{ps} = static pressure coefficient
C_x = blade axial chord, 13.0 cm
D = diffusion coefficient of naphthalene in air
EES = engineering equivalent speed, Eq. (3)
h_m = local mass transfer coefficient
Re_{ex} = Reynolds no. based on cascade exit velocity and blade chord
Sh = Sherwood no., h_m/D
t = tip clearance
U = cascade inlet velocity

V_{ew} = endwall (belt) velocity
X_c = blade local Cartesian coordinates, Fig. 5
Y_c = blade local Cartesian coordinates, Fig. 5
z = spanwise direction (measured from tip surface)
δt = exposure time in wind tunnel (s)
δy = local sublimation loss for naphthalene (m)
ρ = freestream density
ρ_s = solid density of naphthalene
ρ_v = naphthalene vapor density
τ = time

Subscripts

c0 = pressure edge of blade at x location
∞ = mainstream parameter
w = property at wall
0 = stationary endwall (EES=0)
1 = moving endwall (EES=100)

References

[1] Booth, T. C., Dodge, P. R., and Hepworth, H. K., 1982. ''Rotor-tip Leakage: Part I- Basic Methodology,'' ASME J. Eng. Power, **104**, pp. 154–161.
[2] Bunker, R. S., 2001. ''A Review of Turbine Blade Tip Heat Transfer,'' *Proceedings, International Symposium on Heat Transfer in Gas Turbine Systems*, ed., R. J. Goldstein, Annals of the New York Academy of Sciences, New York, Vol. 934, pp. 64–79.
[3] Graham, J. A. H., 1986. ''Investigation of a Tip Clearance Cascade in a Water Analogy Rig,'' ASME J. Eng. Gas Turbines Power, **108**, pp. 38–46.
[4] Sjölander, S. A., and Amrud, K. K., 1987. ''Effects of Tip Clearance on Blade Loading in a Planar Cascade of Turbine Blades,'' ASME J. Turbomach, **109**, pp. 237–244.
[5] Moore, J., and Tilton, J. S., 1988. ''Tip Leakage Flow in a Linear Turbine Cascade,'' ASME J. Turbomach., **110**, pp. 18–26.
[6] Morphis, G., and Bindon, J. P., 1988. ''The Effects of Relative Motion, Blade Edge Radius and Gap Size on the Blade Tip Pressure Distribution in an Annular Turbine Cascade With Clearance,'' ASME Paper 88-GT-256.
[7] Metzger, D. E., and Rued, K., 1989. ''Influence of Turbine Clearance Gap Leakage on Passage Velocity and Heat Transfer Near Blade Tips. Part I: Sink Flow Effects on Blade Pressure Sides,'' ASME J. Turbomach., **111**, pp. 284–292.
[8] Yaras, M. I., and Sjölander, S. A., 1992. ''Effects of Simulated Rotation on Tip Leakage in a Planar Cascade of Turbine Blades: Part I—Tip Gap Flow,'' ASME J. Turbomach., **114**, pp. 652–659.
[9] Yaras, M. I., and Sjölander, S. A., 1992. ''Effects of Simulated Rotation on Tip Leakage in a Planar Cascade of Turbine Blades: Part II- Downstream Flow Field and Blade Loading,'' ASME J. Turbomach., **114**, pp. 660–667.
[10] Mayle, R. E., and Metzger, D. E., 1982. ''Heat Transfer at the Tip of an Unshrouded Turbine Blade,'' *Proc. Seventh Int. Heat Transfer Conference*, **3**, pp. 87–92.
[11] Metzger, D. E., Dunn, M. G., and Hah, C., 1991. ''Turbine Tip and Shroud Heat Transfer,'' ASME J. Turbomach., **113**, pp. 502–507.
[12] Chyu, M.-K., Moon, H. K., and Metzger, D. E., 1989. ''Heat Transfer in the Tip Region of Grooved Turbine Blades,'' ASME J. Turbomach., **111**, pp. 131–138.
[13] Rued, K., and Metzger, D. E., 1989. ''Influence of Turbine Clearance Gap Leakage on Passage Velocity and Heat Transfer Near Blade Tips. Part II: Source Flow Effects on Blade Suction Sides,'' ASME J. Turbomach., **111**, pp. 293–300.
[14] Kim, Y. W., Downs, J. P., Soechting, F. O., Abdel-Messeh, W., Steuber, G. D., and Tanrikut, S., 1995. ''A Summary of the Cooled Turbine-Blade Tip Heat Transfer and Film Cooling Effectiveness Investigations Performed by Dr. D. E. Metzger,'' ASME J. Turbomach., **117**, pp. 1–11.
[15] Kim, Y. W., and Metzger, D. E., 1995. ''Heat Transfer and Film Cooling Effectiveness on Film Cooled Turbine Blade Tip Models,'' ASME J. Turbomach., **117**, pp. 12–21.
[16] Bunker, R. S., Bailey, J. C., and Ameri, A. A., 1999. ''Heat Transfer and Flow on the First Stage Blade Tip of a Power Generation Gas Turbine. Part I: Experimental Results.'' *ASME Paper 99-GT-169*.
[17] Teng, S., Han, J.-C., and Azad, G. S., 2001. ''Detailed Heat Transfer Coefficient Distributions on a Large-Scale Gas Turbine Blade Tip,'' ASME J. Heat Transfer, **123**(4), pp. 803–809.
[18] Azad, G., Han, J.-C., and Boyle, R. J., 2000, ''Heat Transfer and Flow on the Squealer Tip of a Gas Turbine Blade,'' *ASME Paper 2000-GT-195*.
[19] Azad, G., Han, J.-C., and Teng, S., 2000 ''Heat Transfer and Pressure Distribution on a Gas Turbine Blade Tip,'' *ASME Paper 2000-GT-194*.
[20] Jin, P., and Goldstein, R. J., 2002. ''Local, Mass/Heat Transfer on a Turbine Blade Tip,'' Proc., 9th Intl. Symposium on Transport Phenomena and Dynamics of Rotating Machinery, Honolulu, Hawaii, February 10–14.
[21] Chyu, M.-K., Metzger, D. E., and Hwan, C. L., 1987. ''Heat Transfer in Shrouded Rectangular Cavities,'' J. Thermophys. Heat Transfer, **1**, pp. 247–252.
[22] Goldstein, R. J., and Cho, H. H., 1995. ''A Review of Mass Transfer Measurements Using Naphthalene Sublimation,'' Exp. Thermo Fluid Sci. **10**, pp. 416–434.
[23] Srinivasan, V., 2000. ''Effect of Simulated Rotation on the Mass/Heat Transfer From the Tip of a Turbine Blade,'' Master's thesis, University of Minnesota, Minneapolis, Minnesota.

Heat Transfer Enhancement Using a Convex-Patterned Surface

H. K. Moon
Mem. ASME

T. O'Connell

R. Sharma
Mem. ASME

Solar Turbines Incorporated,
San Diego, CA 92186

The heat transfer rate from a smooth wall in an internal cooling passage can be significantly enhanced by using a convex patterned surface on the opposite wall of the passage. This design is particularly effective for a design that requires the heat transfer surface to be free of any augmenting features (smooth). Heat transfer coefficients on the smooth wall in a rectangular channel, which had convexities on the opposite wall were experimentally investigated. Friction factors were also measured to assess the thermal performance. Relative clearances (δ/d) between the convexities and the smooth wall of 0, 0.024, and 0.055 were investigated in a Reynolds number (Re_{HD}) range from 15,000 to 35,000. The heat transfer coefficients were measured in the thermally developed region using a transient thermochromic liquid crystal technique. The clearance gap between the convexities and the smooth wall adversely affected the heat transfer enhancement (Nu_{HD}). The friction factors (f), measured in the aerodynamically developed region, were largest for the cases of no clearance ($\delta/d=0$). The average heat transfer enhancement ($\overline{Nu}_{HD}$) was also largest for the cases of no clearance ($\delta/d=0$), as high as 3.08 times at a Reynolds number of 11,456 in relative to that (Nu_o) of an entirely smooth channel. The normalized Nusselt numbers ($\overline{Nu}_{HD}/Nu_o$), as well as the normalized friction factors (f/f_o), for all three cases, decreased with Reynolds numbers. However, the decay rate of the friction factor ratios (f/f_o) with Reynolds numbers was lower than that of the normalized Nusselt numbers. For all three cases investigated, the thermal performance ($(\overline{Nu}_{HD}/Nu_o)/(f/f_o)^{1/3}$) values were within 5% to each other. The heat transfer enhancement using a convex patterned surface was thermally more effective at a relative low Reynolds numbers (less than 20,000 for $\delta/d=0$) than that of a smooth channel.
[DOI: 10.1115/1.1556404]

Background

Advanced cooling techniques are essential for further improvement of the gas turbine durability and efficiency. Sophisticated cooling designs are commonly found throughout engine hot sections such as combustor liners, turbine vanes, and blades. The type of heat transfer augmentor is selected by considering enhancement level, available pressure ratio, cost, and complexity. For an uprated (higher firing temperature) engine, a cooling design improvement of the initially smooth cooling passage without any casting changes may be a crucial factor for economical viability. Any heat transfer augmenting features on the casting will result in an expensive new casting-die or change. The present study investigates such a cooling design experimentally for turbine vane applications where the heat transfer from a smooth wall (casting side) is significantly augmented by a contacting convex patterned surface on the opposite wall (insert side). The limited convex-patterned surface, often found on the insert, is merely for the mechanical support to maintain a certain gap. Neither heat transfer nor frictional data for this type of cooling design is currently available in the open literature although a concavity-patterned surface has been studied by a number of investigators. Kesarev and Kozlov [1] conducted a test with a single concavity inside surface. Schukin et al. [2], Chyu et al. [3], Moon et al. [4], and Mahmood et al. [5] experimentally studied the friction and heat transfer in a dimpled channel and mentioned potential gas turbine applications. The flow and heat transfer induced by rows of concavities were also numerically investigated by Lin and Shih [6]. To further enhance the heat transfer in a dimpled channel, Mahmood et al. [7] and Ligrani et al. [8] added concavities (protrusions) on opposite wall and reported higher heat transfer rate and pressure loss. But these investigators did not study the heat transfer from a smooth wall augmented by a contacting convex-patterned opposite wall.

Impingement cooling arrays are often designed on the inserts to cool the smooth casting walls in the nozzle vanes because of their simplicity as well as their ability to cool local hot areas. However, narrow channel gaps in the cooling passages can result as much as 40% heat transfer degradation at downstream region due to the cross-flow effect of the ''spent air.'' The array of round jets impinging perpendicular to a flat surface was studied extensively by a number of investigators in the past. Kercher and Tabakoff [9] studied the average surface heat transfer coefficients under a perforated plate of multiple, square array, round impinging air jets and provided the correlation that included the effects of the ''spent air'' flowing perpendicular to the jets. The downstream cooling is further degraded by the effects of crossflow temperature within an array of impingement jets as discussed by Florschuetz and Su [10]. Narrow gaps between the casting and insert can result in an impingement array design with a high hole-density to avoid localized cooling. This is not desirable according to Hollworth and Cole [11] for a thermally optimized design. Another adverse aspect of the impingement array is its inability to adjust to the external heat load distribution in streamwise direction due to the crossflow effect at the downstream. The present cooling scheme overcomes this adverse aspects, which are resulted from a relatively low coolant flow and narrow passage gap. These conditions are often found in the low-pressure (LP) nozzle vane of a midsize industrial gas turbine engine with a low heat load distribution. The coolant Reynolds number (Re_{HD}), based on the passage hydraulic diameter, is typically less than 15,000 and the spacing between the casting and insert can be as narrow as 0.5 mm.

Three different clearance gaps with a fixed convex-patterned on one side were experimentally investigated. Local heat transfer coefficients in the thermally developed region were measured with a transient thermochromic liquid crystal imaging system, and the equivalent friction factors in the aerodynamically developed re-

Contributed by the International Gas Turbine Institute and presented at the International Gas Turbine and Aeroengine Congress and Exhibition, Amsterdam, The Netherlands, June 3–6, 2002. Manuscript received by the IGTI October 23, 2001. Paper No. 2002-GT-30476. Review Chair: E. Benvenuti.

gion were measured using static taps. The thermal performance $((\overline{Nu}_{HD}/Nu_o)/(f/f_o)^{1/3})$ results were compared at different Reynolds numbers.

Experimental Apparatus and Procedures

The local heat transfer coefficient was measured with a Thermochromic Liquid Crystal (TLC) technique. The present TLC technique, which is based on a transient heat transfer solution of the semi-infinite medium suddenly exposed to a convective boundary condition, has been previously used by a number of different investigators (Ireland and Jones [12], Vedula and Metzger [13], Camci et al. [14], Yu and Chyu [15], Ekkad et al. [16], etc.). The basic methodology of a transient technique was demonstrated earlier with use of melting paint surface coatings (Larson [17], Larson and Metzger [18]).

Figure 1 shows a schematic of the test apparatus. Compressed air was filtered, dried, before monitored with a turbine flow meter. The plenum was equipped with a flow deflector to avert the incoming jet from the supply line reaching the channel inlet. The plenum is wedge-shaped in streamwise direction to avoid a sudden contraction at the inlet. The wedge-shaped plenum was chosen for ease of fabrication. The air is preheated with a 6-kw electric circulation heater to the desired temperature (typically 58°C) and diverted away from the test section until it reaches steady state. A thermal transient is initiated by using a pneumatic three-way valve to suddenly route the heated airflow through the test section. The pneumatic 3-way valve also triggered a ''time zero'' light on the test section for the image processing system. The image processing system, which included a Y-C camera (Cohu 82100) and a Silicon Graphics workstation (R4000SC), digitally recorded the images of the surface pixels as they experienced a color transition during the test. The composite signal was decomposed into red, green, and blue components. The time of color change to green at each point on the test surface was the measured quantity. Green color was chosen for its signal strength and sharpness. As the wall surface does not experience a pure step change in air temperature, the actual air temperature rise is represented by a superposed set of elemental steps in T_m, and the fundamental solution is modified accordingly.

$$T_s - T_i = \sum_{i=1}^{N} U(\theta - \tau_i)\Delta T_m \tag{1}$$

where

$$U(\theta - \tau_i) = 1 - \exp\left[\frac{h^2\alpha(\theta - \tau_i)}{k^2}\right]\mathrm{erfc}\left[\frac{h\sqrt{\alpha(\theta - \tau_i)}}{k}\right] \tag{2}$$

In the present experiments, separate air temperature profile measurements were conducted in a transient mode before heat transfer experiments. Using this air temperature profile data along with six thermocouples (five upstream and one downstream of the test area (see Fig. 2)), a mixed mean air temperature (T_m) was obtained.

The entire test section was constructed from a transparent acrylic material. The convex-patterned surface, which had a total of 15 rows of convexities, as shown in Fig. 2 was produced from 3.2-mm-thick plate. The staggered arrays of convexities were produced (fabricated) by thermal setting (heating) on a machined base-plate. The test surface was smooth and 12.7 mm thick. All the convexities had the same imprint diameter, height and were equally spaced. Heat transfer coefficients were measured beneath the thirteenth and fourteenth rows of convexities to ensure a fully developed thermal boundary layer ($x_o/D_h > 21$). Three different clearance gaps (0, 2.3, and 3.6 mm) were tested while its channel width and length were kept at 24 and 83 cm, respectively. Only one side of the channel was equipped with convexities during the

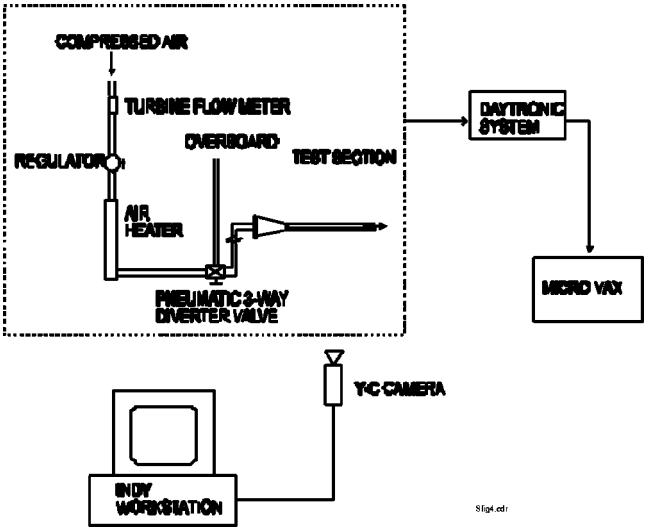

Fig. 1 Schematic view of test apparatus

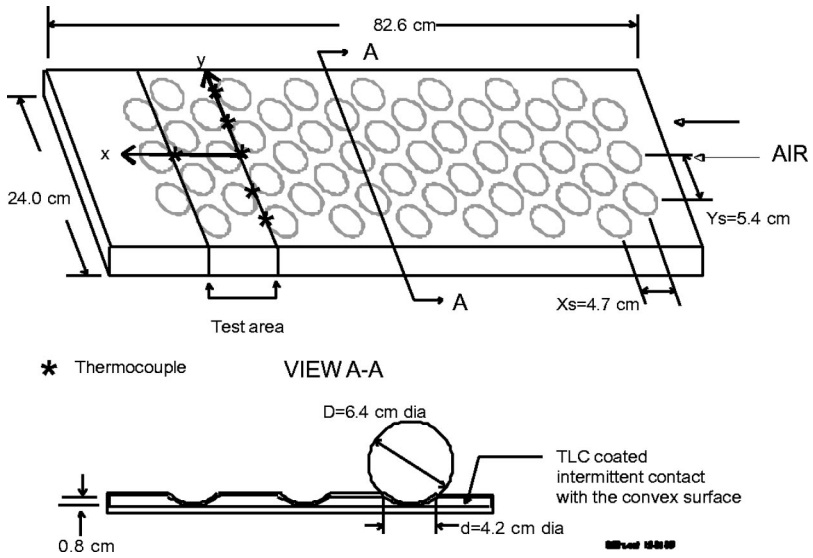

Fig. 2 Schematic view of convex-patterned surface, $\delta/d = 0$

entire investigation. The test surface (smooth side) first was coated with a TLC (Hallcrest, R35C1W) and then sprayed with black paint (Hallcrest, BB-G1) to provide an optimum contrasting visual background for the TLC color display. For the pressure loss experiments, the same test sections were used and instrumented with static taps at 4.7-cm streamwise intervals. The static taps, therefore, were placed on the channel sidewall, not in particular locations relative to the convexity rows.

A diffuse-light source was mounted on the camera to eliminate view-angle dependency of the TLC color transition, as discussed by Herrold and Wiegel [19]. Transition temperature calibration of green color was done on a copper coupon with TLC coating at the representative view angle at the beginning of each test.

The experimental uncertainty for the present measurement of the average Nusselt number was within $\pm 10\%$ and was largest with the no clearance gap experiment, due to their relatively high heat transfer coefficients (up to 482 W/m^2-°K). Although it is possible to have thermal conduction from the convexities to the smooth surface for the no clearance gap experiments, it was neglected. However, its impact to overall accuracy is expected to be minimal since it is intermittent contact in reality and affects a very small area. The heat transfer level (transient time) is directly related to the experimental uncertainty, as described by Höcker [20], who investigated the optimization of the transient TLC technique on error estimation in detail. Considering the air supply system stability and pressure transducer accuracy, the uncertainty in friction factors was estimated to be within $\pm 10\%$. Uncertainties were calculated using the single sample methods of Kline and McClintock [21] and Moffat [22].

Results and Discussion

Figure 3 shows typical air temperature profiles within the channel at the middle of the 12th and 13th row of convexities, for the contacting case. The normalized air temperature $((T_p - T_a)/(T_p - T_i))$ is higher toward the convex side as expected. The air cool down as it travels through the channel during transient process. Although the convex side heat transfer was not investigated in the present study, the air temperature (T_a) is expected to be cooler near the convex side due to its larger surface area compared to the smooth side and possibly due to higher heat transfer coefficients.

For comparison, the Nusselt number distributions on the smooth wall, which were reduced based on a local mixed mean temperature, are plotted in Figs. 4–6 for the three relative clearances at a relatively similar Reynolds number range (15,500–15,800). In order to understand the relative positions, the convexities on the opposite wall were overlaid on the same plot. As shown in Fig. 4 for the case of $\delta/d=0$, the relatively high heat transfer enhancement occurs under the front half of the convexities, in contrast to the low heat transfer region following the contact point. This heat transfer pattern is attributed to the flow accelerating and separating around the convexities. The higher enhancements under the front parts of the convexities are due to greater streamwise advection. A recirculating, secondary-flow-type phenomenon is expected after the flow separation. Beneath the outmost convexities at the 14th row (second row from the top in Fig. 4), the heat transfer patterns are skewed diagonally to the middle as the high-momentum flow stream close to the sidewall deflects the separated flow. The aft area underneath the middle convexity (13th row) shows an exceptionally high heat transfer enhancement, which may have been caused by unintended clearance gap (test fixture limitation). The heat transfer coefficient distribution for the contacting case exhibited a similar pattern for all the Reynolds numbers that were studied ($15{,}000 < \mathrm{Re_{HD}} < 35{,}000$).

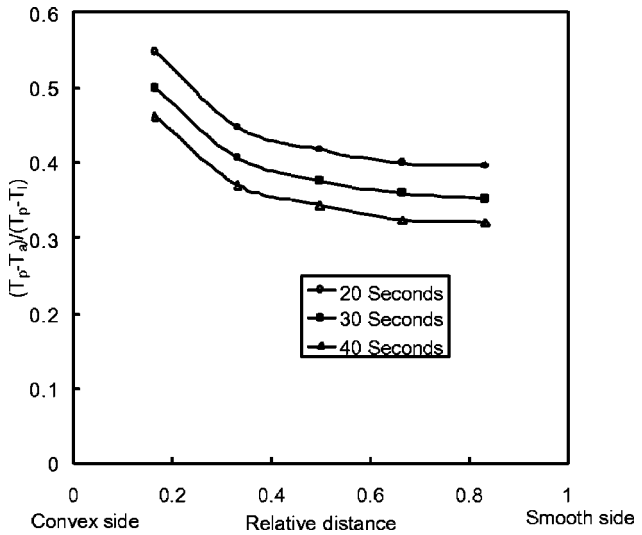

Fig. 3 Normalized air temperature profile, $\delta/d=0$, $\mathrm{Re_{HD}}=19{,}555$

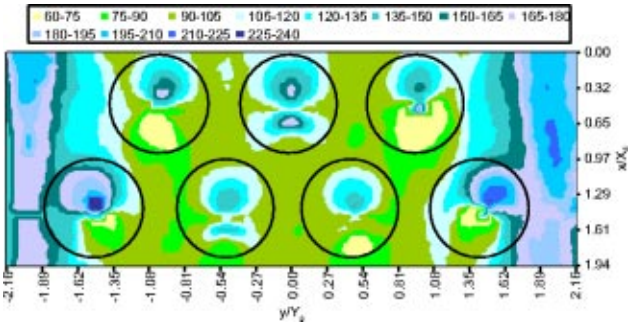

Fig. 4 Local Nusselt number $(\mathrm{Nu_{HD}})$ distribution, $\delta/d=0$, $\mathrm{Re_{HD}}=15{,}403$

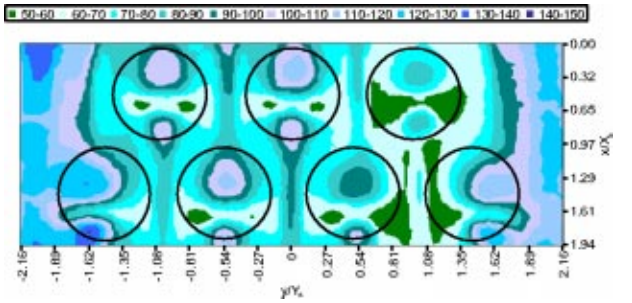

Fig. 5 Local Nusselt number $(\mathrm{Nu_{HD}})$ distribution, $\delta/d=0.24$, $\mathrm{Re_{HD}}=15{,}713$

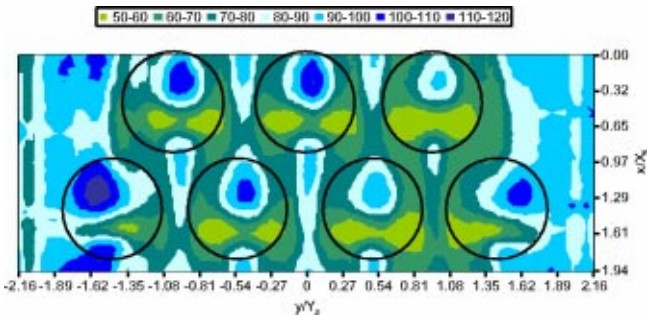

Fig. 6 Local Nusselt number $(\mathrm{Nu_{HD}})$ distribution, $\delta/d=0.055$, $\mathrm{Re_{HD}}=15{,}558$

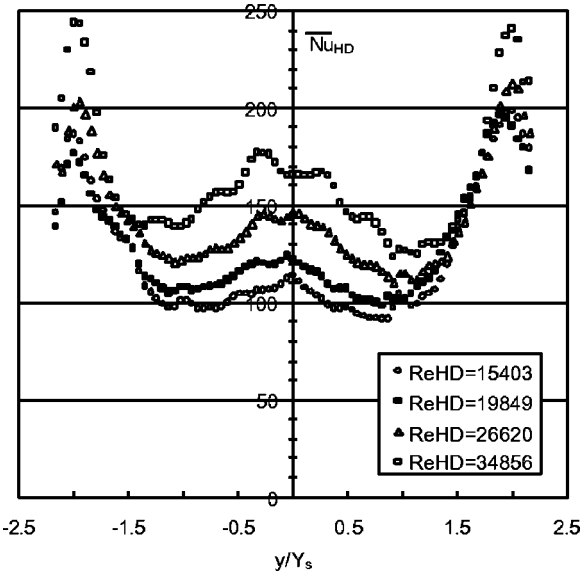

Fig. 7 Streamwise-averaged Nusselt number distribution, $\delta/d=0$

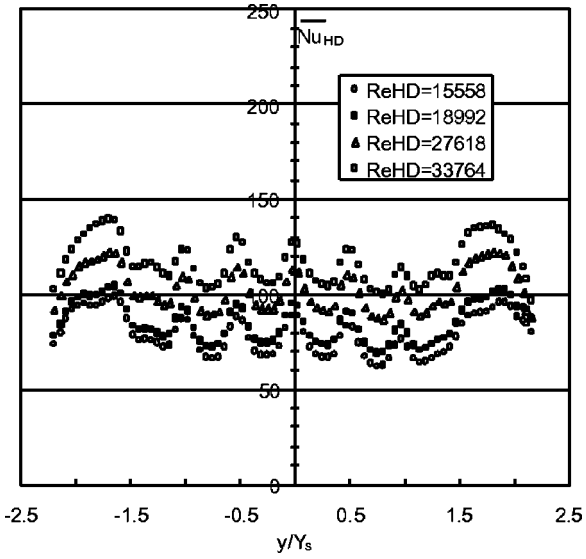

Fig. 9 Streamwise-averaged Nusselt number distribution, $\delta/d=0.055$

The heat transfer pattern changes significantly as the clearance gap opens under the convexities as shown in Figs. 5 and 6. There is no longer a low heat transfer region under the second half of the convexities. The low heat transfer region appears in a butterfly pattern as the flow accelerates and diffuses under the concavities. The secondary high heat transfer enhancement area follows immediately the convexity and extends till the region between the downstream concavities. This pattern of heat transfer coefficient distribution becomes more apparent with larger clearance gaps, as it can be seen by comparing Figs. 6 to 5. Without flow visualizations, it is speculated that the flow merging process between concavities caused this secondary high heat transfer region. Beneath the outmost convexities at the fourteenth row (second row from the top in Figs. 5 and 6), the heat transfer patterns were again influenced by the high-momentum flow close to the sidewall as for the contacting case.

Figures 7–9 show the streamwise-averaged Nusselt numbers over $0<x<2X_s$, plotted in the spanwise direction. For the case of $\delta/d=0$, the streamwise-averaged Nusselt number distribution is similar to the velocity profile shown in Fig. 10, where the velocity distribution was measured at the test section exit plane using a Kiel probe. This suggests that Nusselt number augmentations are tied to levels of streamwise advection, as well as to the strengths of the vortices which also increase as the mainstream velocity becomes larger. The two highest points of the streamwise-averaged Nusselt number distribution in Fig. 7 correspond to the velocity peaks near the side walls, where fewer convexities (less flow resistance) exist in the streamwise direction. As the Reynolds number increases for the case of $\delta/d=0$, the distribution of heat transfer enhancement changes at the middle as shown in Fig. 7. As the clearance gap increases, the two highest points of the streamwise-averaged Nusselt number distribution near the sidewalls become less pronounced and the overall profiles become flat. The local highest points of the streamwise-averaged Nusselt number distribution as shown in Figs. 8 and 9 are aligned with a row of convexities and are due to the high heat transfer regions which occur under the fore and aft convexity

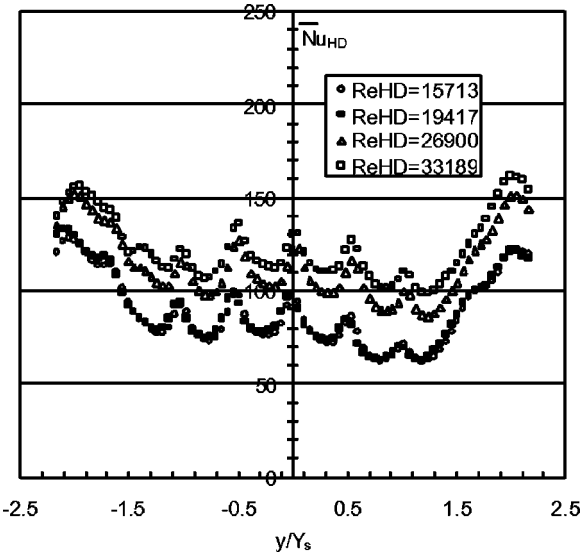

Fig. 8 Streamwise-averaged Nusselt number distribution, $\delta/d=0.024$

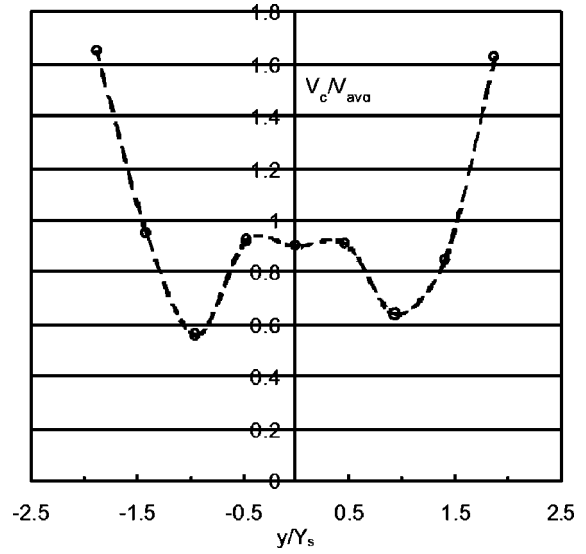

Fig. 10 Centerline velocity distribution, $Re_{HD}=19{,}879$, $\delta/d=0$

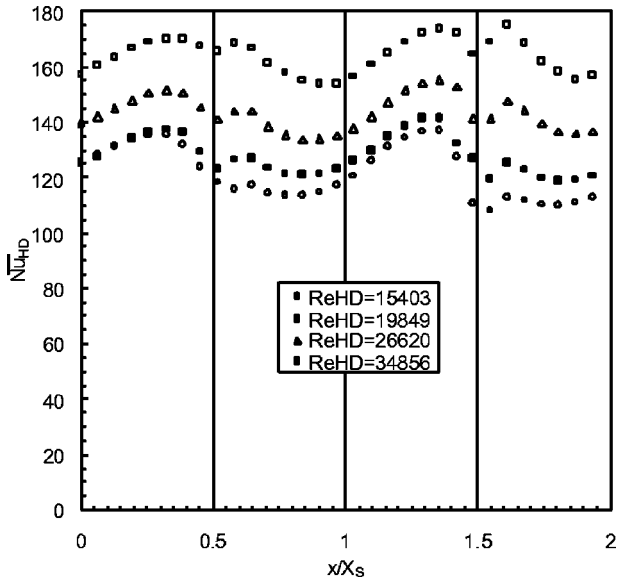

Fig. 11 Spanwise-averaged Nusselt number distribution, $\delta/d=0$

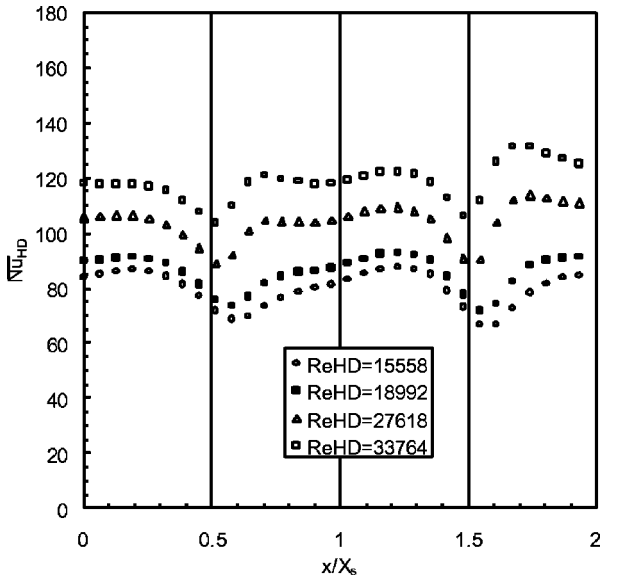

Fig. 13 Spanwise-averaged Nusselt number distribution, $\delta/d=0.055$

center. Although there are seven rows of convexities, the data show only five distinct local peaks, due to a wash-off effect of the aforementioned high-speed flow near the sidewall.

The spanwise-averaged Nusselt numbers over $-2.2Y_s<y<2.2Y_s$, plotted in Figs. 11–13, show a local minimum value immediately following the convexity center location (approximately $x/X_s=0.5$ and 1.5). This results from the low heat transfer locations directly beneath the convexity centers and immediately downstream locations where a flow separation might have occurred. These low points are less noticeable for the case of $\delta/d=0$ as the regions are smaller compared to those for the cases with a clearance gap. The clearance gap elongates the lowest heat transfer regions and results in more pronounced secondary peaks as shown in Figs. 12 and 13. The second $\overline{Nu}_{HD}$ peak following the fourteenth row of the convexities is higher due to the number of convexities (four convexities at this location compared to three at the 13th row).

The overall average Nusselt numbers are normalized to that of a smooth channel and are plotted as a function of Reynolds numbers in Fig. 14. The heat transfer from a smooth surface is significantly enhanced by contacting convex-pattern surface ($\delta/d=0$), especially at low Reynolds numbers. As shown in Fig. 14, the normalized Nusselt number ($\overline{Nu}_{HD}/Nu_o$) and therefore, the heat transfer enhancement decreases noticeably with increasing clearance gap. At a Reynolds number of 15,500, the normalized Nusselt number for the case of $\delta/d=0$ is approximately 37% higher than the noncontacting cases. It is clear from Fig. 14 that Nu_o increases much faster with the Reynolds number than the average Nusselt number of the current cooling scheme for all three cases. The normalized Nusselt number for the contacting case ($\delta/d=0$) is approximately doubled as the Reynolds number decreases

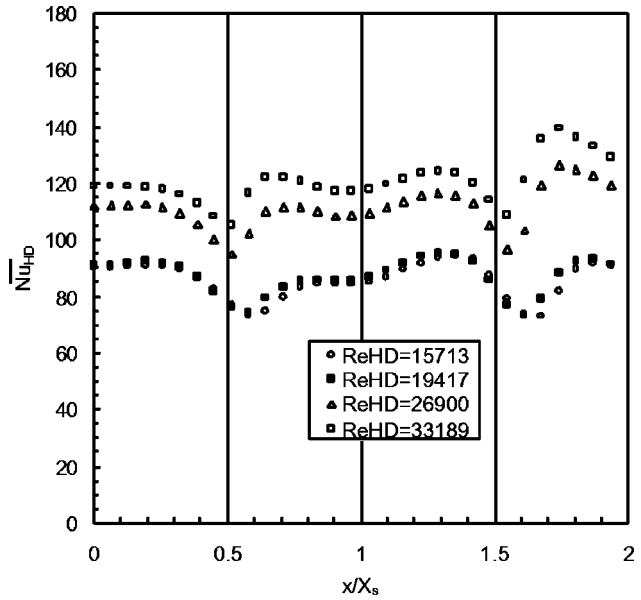

Fig. 12 Spanwise-averaged Nusselt number distribution, $\delta/d=0.024$

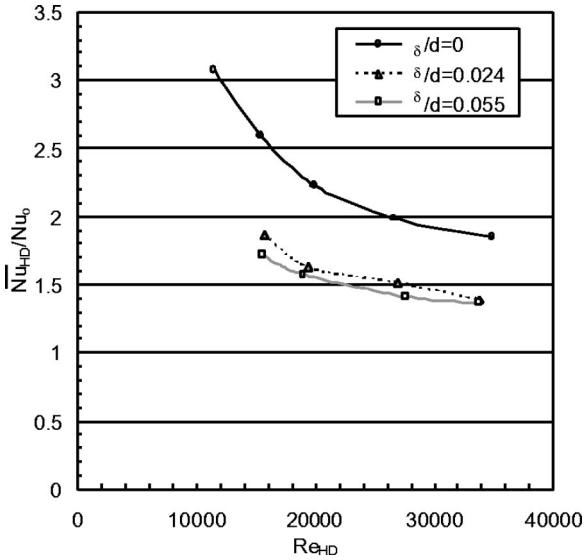

Fig. 14 Overall heat transfer enhancement with different Reynolds numbers

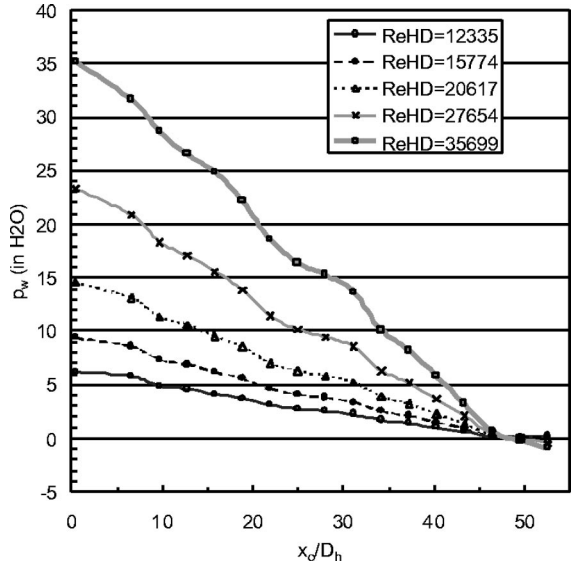

Fig. 15 Wall static pressure distribution, $\delta/d=0$

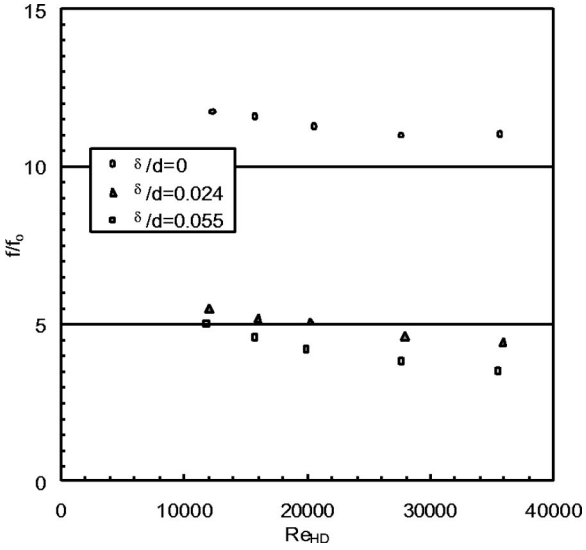

Fig. 17 Normalized friction factors

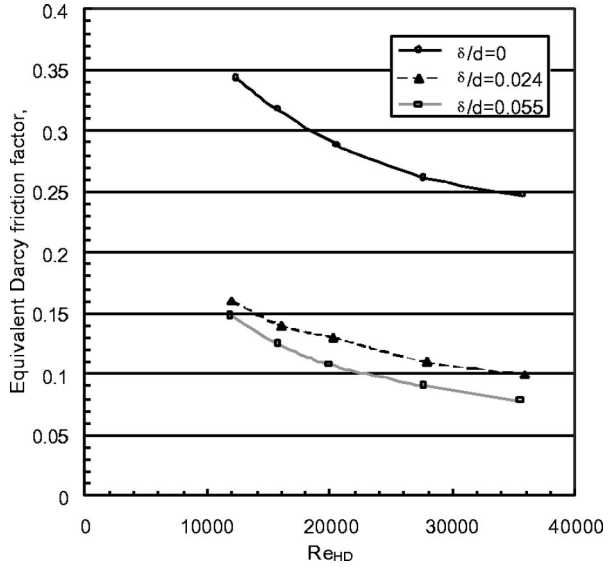

Fig. 16 Friction factors

from 34,856 to 15,403. Since the normalized Nusselt numbers of all three cases behave similar with Reynolds number change, the dominant heat transfer mechanism is expected to be also similar. It is speculated that at a low Reynolds number the flow is unsteady and vortexlike, whereas at higher Reynolds number it becomes somewhat close to a typical turbulence flow. The changes at higher Reynolds numbers also occur because the vortices which form become more diffuse.

Figure 15 shows a static pressure distribution along the channel for the case of $\delta/d=0$. The uneven distributions, especially more noticeable at higher Reynolds numbers, were caused by the static tap placement locations relative to the convexity rows as it consistently occurred at the same locations regardless of the flow rates (Reynolds numbers). More detailed measurements of static pressure distribution are beyond the current scope of work. A least-square-fitted line was drawn through the data points and equivalent Darcy friction factors (f) were calculated. The equivalent Darcy friction factors for the fully developed region (asymptotic values), which consistently occurred at a x_o/D_h of about 20, are plotted in Fig. 16. This ($x_o/D_h \approx 20$) demonstrates that the aerodynamic entrance length is comparable to that of a typical turbulent smooth channel flow. The friction factors (f) decrease with the Reynolds numbers. The friction factors of the contacting case ($\delta/d=0$) are significantly higher than those of noncontacting cases. The friction factors were normalized to that (Moody Chart) of a smooth channel and plotted in Fig. 17. The normalized friction factors decrease with increasing Reynolds numbers, indicating that the friction factors of the rectangular channel with a convex-patterned surface on one side decrease at a faster rate than that of a smooth channel.

The thermal performance ($(\overline{\mathrm{Nu}}_{\mathrm{HD}}/\mathrm{Nu}_o)/(f/f_o)^{1/3}$) values were calculated as suggested by Webb and Eckert [23] and plotted in Fig. 18. Note one additional data point at $\mathrm{Re}_{\mathrm{HD}}=11456$ for the case of $\delta/d=0$, which was tested to ensure the thermal performance trend at a low Reynolds number range. The thermal performance value increases exponentially with a decrease in Reynolds numbers for all cases. For the contacting case ($\delta/d=0$), the rectangular channel with a smooth wall on one side and convexities on the other thermally performed better than a completely smooth channel for the Reynolds numbers below 20,000.

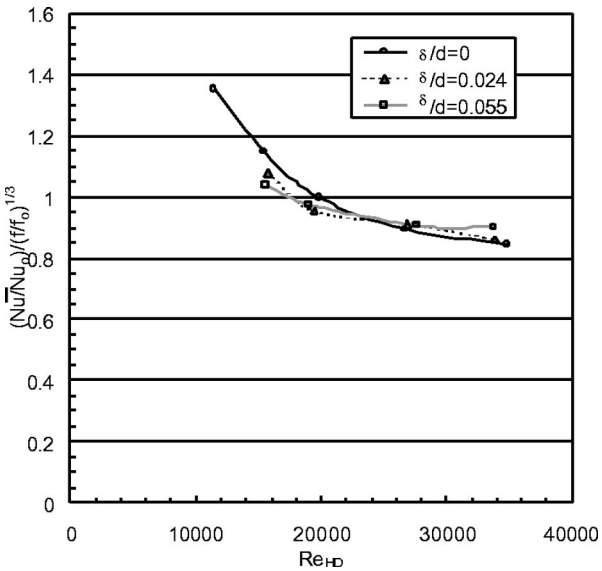

Fig. 18 Thermal performance comparison

Summary and Conclusions

The heat transfer augmentation using a convex-patterned surface was experimentally investigated using a transient Thermochromic Liquid Crystal technique. Only one side of the rectangular channel had convexities (staggered arrays) during the study, and the heat transfer rates were measured from the smooth wall side. The clearance gaps of $\delta/d=0$, 0.024, 0.055 and the Reynolds number range of $15{,}400<\mathrm{Re_{HD}}<34{,}900$ were studied. The heat transfer coefficients were measured in the thermally fully developed region and the friction factors were measured in the aerodynamically fully developed region. The principal conclusions of the present study are summarized as follows:

- The heat transfer enhancement is significantly higher in the region immediately upstream of convexities than the rest of region, for all three clearance cases studied.
- The heat transfer enhancement is lowest in the regions directly beneath and immediately downstream of the convexities, for all three clearance cases.
- The heat transfer coefficient distribution for the contacting case ($\delta/d=0$) exhibited a different pattern compared to those for the noncontacting cases ($\delta/d=0.024$ and 0.055).
- The normalized Nusselt numbers ($\overline{\mathrm{Nu}}_{\mathrm{HD}}/\mathrm{Nu}_o$) for all three cases decrease with the Reynolds number, and the contacting case resulted in the highest heat transfer enhancement for a given Reynolds number (ex. $\overline{\mathrm{Nu}}_{\mathrm{HD}}/\mathrm{Nu}_o=3.08$ for the contacting case at $\mathrm{Re_{HD}}=11{,}456$).
- The heat transfer enhancement difference between different clearance gaps is small except for the contacting case.
- The equivalent Darcy friction factor decreases with Reynolds number and is highest for the contacting case.
- The equivalent Darcy friction factors decrease at a higher rate than those of a smooth channel, for all three clearances.
- For all three cases investigated, the thermal performance $((\overline{\mathrm{Nu}}_{\mathrm{HD}}/\mathrm{Nu}_o)/(f/f_o)^{1/3})$ values were relatively close to each other (within 5%).
- For the contacting case ($\delta/d=0$), the rectangular channel with a smooth wall on one side and convexities on the other thermally performed better than a completely smooth channel for the Reynolds numbers below 20,000.

Nomenclature

d = convexity diameter (see Fig. 2)
D = ball diameter (see Fig. 2)
D_h = hydraulic diameter
f = Darcy friction factor, $2\,D_h\Delta\mathrm{p}/L\rho U^2$
f_o = Darcy friction factor of smooth channel (Moody chart)
h = heat transfer coefficient
H = channel height
K = thermal conductivity
L = channel length
P_w = wall static pressure
Δp = pressure drop
x = streamwise coordinate (see Fig. 2)
x_o = streamwise distance from inlet
y = spanwise coordinate (see Fig. 2)
T = temperature
U = mean velocity in channel
X_s = streamwise distance between convexities
Y_s = spanwise distance between concavities
$\mathrm{Nu_{HD}}$ = local Nusselt no., hD_h/k
$\overline{\mathrm{Nu}}_{\mathrm{HD}}$ = average Nusselt no., $\overline{h}D_h/k$
Nu_o = smooth channel Nusselt no.
$\mathrm{Re_{HD}}$ = Reynolds no., $\rho UD_h/\mu$
α = thermal diffusivity
δ = clearance gap under concavities
ρ = air density
μ = dynamic viscosity
θ = time
τ = time step

Subscripts

a = air
c = centerline
i = initial
m = mixed mean
p = plenum
s = surface

References

[1] Kesarev, V. S., and Kozlov, A. P., 1993, "Convective Heat Transfer in Turbulized Flow Past a Hemispherical Cavity," Heat Transfer-Sov. Res., **25**(2), Scripta Technica Inc, pp. 156–160.
[2] Schukin, A. V., Kozlov, A. P., and Agachev, R. S., 1995, "Study and Application of Hemispherical Cavities for Surface Heat Transfer Augmentation," ASME Paper 95-GT-59.
[3] Chyu, M. K., Yu, Y., and Ding, H., 1997, "Concavity Enhanced Heat Transfer in an Internal Cooling Passage," ASME Paper 97-GT-437.
[4] Moon, H. K., Moon, H. K., and Glezer, B., 2000, "Channel Height Effect on Heat Transfer and Friction in a Dimpled Passage," ASME J. Eng. Gas Turbines Power, **122**, pp. 307–313.
[5] Mahmood, G. I., Hill, M. L., Nelson, D. L., Ligrani, P. M., Moon, H. K., and Glezer, B., 2001, "Local Heat Transfer and Flow Structure on and Above a Dimpled Surface in a Channel," ASME J. Turbomach., **123**, pp. 115–123.
[6] Lin, Y. L., and Shih, T. I-P, 2001, "Flow and Heat Transfer Induced Rows of Hemispherical Cavities," Int. J. Transport Phenomena, **3**, pp. 1–11.
[7] Mahmood, G. I., Sabbagh, M. G., and Ligrani, P. M., 2001, "Heat Transfer in a Channel With Dimples and Protrusions on Opposite Walls," J. Thermophys. Heat Transfer, **15**(3), pp. 275–283.
[8] Ligrani, P. M., Mahmood, G. I., Harrison, J. L., Harrison, J. L., Clayton, C. M., and Nelson, D. L., 2001, "Flow Structure and Local Nusselt Number Variations in a Channel With Dimples and Protrusions on Opposite Walls," Int. J. Heat Mass Transf., **44**(23), pp. 4413–4425.
[9] Kercher, D. E., and Tabakoff, W., 1970, "Heat Transfer by a Square Array of Round Jets Impinging Perpendicular to a Flat Surface Including the Effect of Spent Air," ASME J. Eng. Power, **92**, pp. 73–82.
[10] Florschuetz, L. W., and Su, C. C., 1987, "Effects of Crossflow Temperature on Heat Transfer Within an Array of Impinging Jets," ASME J. Heat Transfer, **109**, pp. 74–82.
[11] Hollworth, B. R., and Cole, G. H., 1987, "Heat Transfer to Arrays of Impinging Jets in a Crossflow," ASME Paper No. 87-GT-198, Turbo Expo Anaheim, CA.
[12] Ireland, P. T., and Jones, T. V., 1985, "The measurement of Local Heat Transfer Coefficients in blade cooling passages," AGARD Conf. Proc., CP. 390 Paper 28, Bergen.
[13] Vedula, R. I., and Metzger, D. E., 1991, "A Method for Simultaneous Determination of Local Effectiveness and Heat Transfer Distributions in Three Temperature Convection Situations," ASME Paper 91-GT-345.
[14] Camci, C., Kim, K., Hippensteele, S. A., and Poinsatte, P. E., 1993, "Evaluation of Hue Capturing Based Transient Liquid Crystal Method for High Resolution Mapping of Convective Heat Transfer on Curved Surfaces," ASME J. Heat Transfer, **115**, pp. 311–318.
[15] Yu, Y., and Chyu, M. K., 1996, "Influence of a Leaking Gap Downstream of the Injection Holes on Film Cooling Performance," ASME Paper 96-GT-175.
[16] Ekkad, S. V., Zapata, D., and Han, J. C., 1995, "Heat Transfer Coefficients Over a Flat Surface With Air and CO_2 Injection Through Compound Angle Holes Using a Liquid Crystal Image Method," ASME Paper 95-GT-10.
[17] Larson, D. E., 1983, "Transient Heat Transfer Measurements in 90-deg Bends Using Surface Coatings Having Prescribed Melting Points," M.S. thesis, Arizona State University, Tempe AZ.
[18] Larson, D. E., and Metzger, D. E., 1986, "Use of Melting Point Surface Coatings for Local Convection Heat Transfer Measurements in Rectangular Channel Flows With 90-deg Turns," Trans. ASME, **108**, pp. 48–54.
[19] Herold, W., and Wiegel, D., 1980, "Problems of Photographic Documentation of Liquid Crystalline Thermographs," *Advances in Liquid Crystal Research and Applications*, ed., L. Bata, Pergamon Press, Oxford, pp. 1255–1259.
[20] Höcker, R., 1996, "Optimization of Transient Heat Transfer Measurements Using Thermochromic Liquid Crystals Based on Error Estimation," ASME Paper 96-GT-235.
[21] Kline, S. J., and McClintock, F. A., 1953, "Describing Uncertainties in Single Sample Experiments," Mech. Eng. (Am. Soc. Mech. Eng.), **75**, pp. 3–8.
[22] Moffat, R. J., 1988, "Describing the Uncertainties in Experimental Results," Exp. Therm. Fluid Sci., **1**, pp. 3–17.
[23] Webb, R. L., and Eckert, E. R. G., 1972, "Application of Rough Surfaces to Heat Exchanger Design," Int. J. Heat Mass Transf., **15**, pp. 1647–1658.

Thomas Coton
e-mail: coton@vki.ac.be

Tony Arts

Turbomachinery and Propulsion Department,
von Karman Institute for Fluids Dynamics,
1640 Rhode-Saint-Genèse, Belgium

Michaël Lefebvre

Nicolas Liamis

Snecma Moteurs—Turbine
Aero-Cooling Department,
Center de Villaroche,
77550 Moissy Cramayel, France

Unsteady and Calming Effects Investigation on a Very High-Lift LP Turbine Blade—Part I: Experimental Analysis

An experimental and numerical study was performed about the influence of incoming wakes and the calming effect on a very high-lift low-pressure turbine rotor blade. The first part of the paper describes the experimental determination of the pressure loss coefficient and the heat transfer around the blade mounted in a high-speed linear cascade. The cascade is exposed to incoming wakes generated by high-speed rotating bars. Their aim is to act upon the transition/separation phenomena. The measurements were conducted at a constant exit Mach number equal to 0.8 and at three Reynolds number values; namely, 190,000, 350,000, and 650,000. The inlet turbulence level was fixed at 0.8%. An additional feature of this work is to identify the boundary layer status through heat transfer measurements. Compared to the traditionally used hot films, thin film heat flux gages provide fully quantitative data required for code validation. Numerical computations are presented in the second part of the paper. [DOI: 10.1115/1.1556013]

Introduction

The continuous effort to lower the operating cost of civil aircraft engines has led, among other options, to blade count reduction within the low-pressure (LP) turbine stages. On the other hand, very high efficiencies are required for these components, as the LP turbine drives the fan which delivers the largest part of the thrust. The reduction of blade number therefore implies an increase of the aerodynamic load of each individual airfoil, leading to the concept of *high-lift* design. Increasing the suction side peak Mach number and/or moving its location more upstream to increase the front loading are two possibilities to fulfill this requirement. This approach is however limited as shock losses or large diffusions promoting a laminar boundary layer separation in this low Reynolds number environment (Re~130,000 typically) have to be avoided to maintain high efficiencies.

Zweifel [1] was the first to link aerodynamic load and efficiency for a cascade, with the aim of determining the optimal pitch to chord ratio. His well known coefficient is mainly based on geometrical characteristics; no attention was paid to the working conditions (Reynolds and Mach numbers, turbulence level, . . .) and to their influence on the boundary layer status. Fortunately, the work of Emmons [2] on transition and the discovery by Schubauer and Klebanoff [3] of the calmed regions following the turbulent spots have recently found a new interest to prevent a laminar separation in LP turbines. Because of their high level of turbulence, the wakes shed by the upstream blade row promote bypass transition. Curtis et al. [4] showed that this passage from the laminar to the turbulent state is beneficial to increase the loading of LP turbine blades, as separation can be avoided.

The reliability of the high lift concept has been demonstrated in the literature over the last years. Among other authors, Howell et al. [5], Brunner et al. [6], and Solomon [7] have illustrated the reliability of the wake induced transition for the high lift design in LP turbines. Mayle [8], Gostelow et al. [9,10], Halstead et al. [11] and Schulte and Hodson [12] have contributed to a better description and simulation of the mechanisms of the unsteady transition phenomena by providing turbulent spot and calmed region characteristics (production rate, spreading angle, . . .) as a function of flow conditions (pressure gradient, freestream turbulence level, Reynolds number, . . .). In spite of the huge efforts made, a full comprehension does not seem to be reached yet. As a consequence, correct predictions of the boundary layer transition in a real LP turbine environment are too rarely achieved. This prevents designers to consider the wake induced transition features in a very practical way.

These limits are still principally coming from the lack of information about the operating conditions influence upon the unsteady bypass transition. All these conditions are usually not simultaneously simulated in the experiments. The main ones, namely Reynolds number and turbulence intensity, are generally correctly reproduced, but the compressibility effects and a correct velocity triangulation of the incoming wakes are often considered of second-order importance. Recently, Schultz and Volino [13] have shown that concave curvature has a significant effect on transition at high free stream turbulence.

The aim of the present contribution is therefore to provide new insight into the subject by a more complete experimental simulation. The investigation is based upon wall heat flux measurements to qualify the boundary layer status. A similar approach was already used in the past in the domain of transition in turbines. Lagraff et al. [14] and Ashworth et al. [15] studied the unsteady interactions produced by rotating bars in front of a transonic high-pressure turbine cascade and their impact on transition by means of heat flux gages; but it is the first time, from the authors knowledge, that this technique is used to study the unsteady wake induced transition in LP turbines. The status of the boundary layer was assessed and quantitative data were produced to be used, in addition, for code validation.

Experimental Apparatus

The experiments were performed in the CT-2 Compression Tube facility of the von Karman Institute (laboratory ''Jacques Chauvin''). A complete description of this wind tunnel and of the associated measurement techniques was presented by Arts et al. [16]. The exit Mach and Reynolds numbers as well as the freestream to wall temperature ratio can be adjusted independently in order to correctly simulate realistic operating conditions.

Contributed by the International Gas Turbine Institute and presented at the International Gas Turbine and Aeroengine Congress and Exhibition, Amsterdam, The Netherlands, June 3–6, 2002. Manuscript received by the IGTI December 21, 2001. Paper No. 2002-GT-30227. Review Chair: E. Benvenuti.

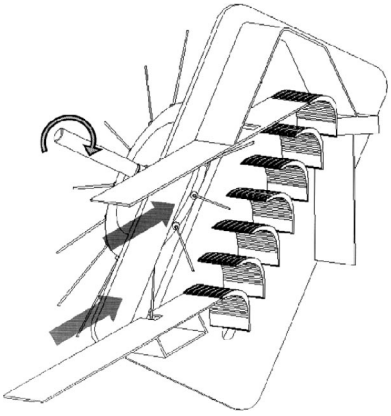

Fig. 1 Sketch of the wake generator

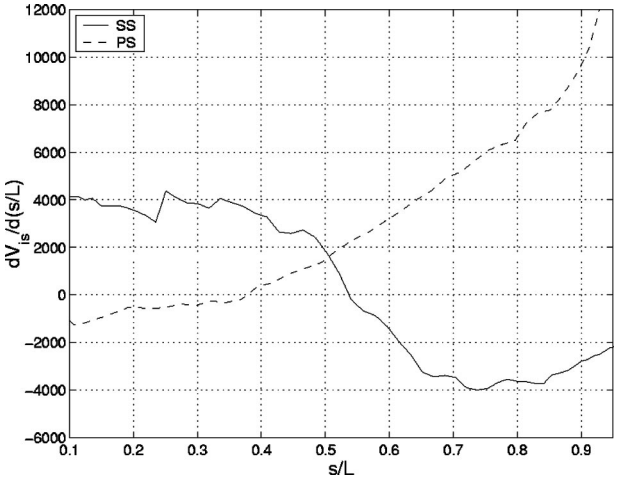

Fig. 2 Distribution of the acceleration around the blade (based on fully turbulent NS computation)

The exit isentropic Mach number was maintained at 0.8 for all tests. Three Reynolds number values based on chord and isentropic exit velocity were investigated, namely 190,000, 350,000, and 650,000. The inlet freestream turbulence intensity was fixed at 0.8%, which is the natural turbulence level of the facility.

To simulate the effect of the upstream wakes, a wake generator was installed in front of the test section (Fig. 1). It consists of a rotating disk carrying on its perimeter bars of 2 mm diameter (of the order of the trailing edge diameter). The disk is driven by a small air turbine and allows the high bar velocity required to match the correct velocity triangle of the incoming wakes. The wake frequency can be adjusted both by changing the bar number or the disk rotational speed. To match correctly the inlet velocity triangle, a fixed rotational speed should be imposed. It was however decided, for the present tests, to operate at different rotational speeds (including the nominal one) with a constant bar number. The bar pitch to blade chord ratio at midspan of the blade was superior to unity.

The peripheral velocity varies along the bar length; its evolution from midspan to the lateral wall represents a variation of ~ 1 deg in the incidence angle at the maximum rotational speed of the wake generator. It will affect the incidence of the airfoil and the relative angle of the wake with the cascade. Nevertheless, most of the measurements were taken at 50% span, on the central blade where the bars are parallel to the airfoil height. The bars were rotating at 0.5 c_{ax} upstream of the leading edge plane. As shown on Fig. 1, boards were placed around the slits milled in the endwalls to accommodate the wake generator. The volumes of the two enclosures containing the wake generator and the downstream probe traversing system were isolated from each other and from the atmosphere, and were minimized to avoid lateral leaks through the upstream and downstream slits.

The cascade is made of six blades. These profiles are characterized by a loading about 30% higher than conventional LP blades. Based on fully turbulent NS computations (see Roux et al. [17]), the suction side peak Mach number is located at 0.54 L. The suction side boundary layer is then subjected to an important deceleration (Fig. 2). The calculations also indicate that the flow along the pressure side strongly decelerates just downstream of the leading edge (not shown on Fig. 2). Considering these velocity gradients, important losses due to boundary layer separation can be expected.

The impact on the blade performance is quantified by means of the pressure loss coefficient. Inlet total pressure profiles have shown that the boundary layer developing on the tunnel walls reaches 15% of the span at low Re. The upstream pressure is measured with a Pitot tube located in the leading edge plane of the cascade and at 30% span. The pitchwise distribution of the downstream total pressure is obtained by a three-hole probe mounted on a pneumatic traversing system at 0.3 c_{ax} from the cascade exit plane. For each test, the probe covers at least two pitches. During the experiment, the probe sees successively the pressure side and the suction side of the blades. To determine the profile loss coefficient, the downstream pressure probe was maintained at midspan. In addition, the secondary flow pattern was quantified for selected operating conditions by repeating the traverses at different blade heights. The static pressure P_2 was measured by means of 22 wall pressure taps placed in a plane parallel to the trailing edge plane at 0.3 c_{ax} downstream of it.

Heat flux measurements were performed by means of platinum thin film gages, painted at midspan along the spanwise direction on a MACOR ceramic substrate. Their typical dimensions are $10\times 0.5\times 0.3\ 10^{-3}$ mm. The central blade of the cascade is instrumented with 21 films on the suction side and 14 on the pressure side. A detailed description of this measurement technique was presented by Schultz and Jones [18].

All pneumatic measurements were sampled at 4 kHz (2048 samples). The pressure measurements present an uncertainty of ± 1 mbar (20:1). The loss coefficient uncertainty depends on the Reynolds number. A value of 0.5 points can be quoted for the absolute uncertainty on the profile loss coefficient, decreasing when $\mathrm{Re}_{is,2}$ increases. The heat flux signals were acquired at 30 kHz (16,000 samples) and low-pass filtered at 12 kHz. The heat flux uncertainty is $\pm 5\%$. The wake generator rotational speed was measured by means of an optical cell.

Results

Profile Losses. LP turbine blades are characterized by a large aspect ratio; the profile losses can therefore represent up to 80% of the total losses, the suction side representing the main contribution [4]. The determination of the cascade performance for different operating conditions is based upon the kinematic loss coefficient (Eq. (1)). The bar superscript means that the quantity has been pitch area averaged. All loss coefficient results are nondimensionalized with the value measured at $\mathrm{Re}_{is,2}=190{,}000$ and no upstream wakes.

$$\xi = 1 - \frac{1-\left(\dfrac{\overline{P_2}}{\overline{P_{02}}}\right)^{\gamma-1/\gamma}}{1-\left(\dfrac{\overline{P_2}}{\overline{P_{01}}}\right)^{\gamma-1/\gamma}} \tag{1}$$

The loss coefficient versus Strouhal number evolution is plotted in Fig. 3. At the lowest Reynolds number, the passage from zero to the maximum bar frequency represents a loss reduction of

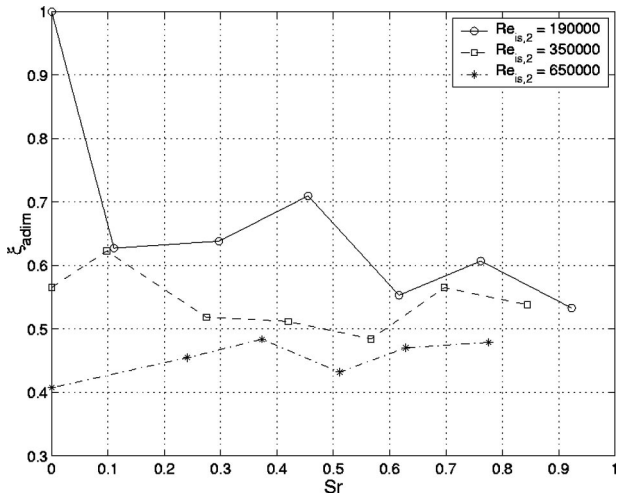

Fig. 3 Profile loss evolution with wake frequency

46.7%. The largest wake impact is observed between the absence (Sr=0) and the first presence of wakes (Sr=0.11) with a loss decrease of 37.2%; the further increase of Sr up to 0.92 shows an additional gain of 9.5%. This behavior is physically explained by the temporary suppression of the suction side boundary layer separation under the influence of the passing wakes. The fact that the benefit for increasing frequencies is smaller than the step between the steady and the lowest Sr case has two complementary explanations. Firstly, the time-averaged value of the loss coefficient intrinsically results from a compromise between the suppression of the separation and additional turbulent losses brought by the wakes. Secondly, as seen by several researchers (e.g., Bons et al. [19]), a separation bubble takes time to reappear once its suppression mechanism is turned off. It means that another wake does not need to arrive directly after the previous one to permanently avoid separation.

The spot production rate increases with Re; transition is therefore promoted. When Re increases, the separation is delayed and can even be cancelled. As shown by Coton et al. [20] for cascades subjected to flow separation, this results in a strong reduction of ξ for increasing Re at Sr=0 (Fig. 3). When $Re_{is,2}$ rises to 350,000, the loss difference between the steady case and the maximum Sr value is restricted to 4.9%. At $Re_{is,2}$=650,000, the tendency is reversed with a total loss increase of 17.6%. Research on LP turbines usually focuses on very low Reynolds number prevailing at cruise conditions. Nevertheless, take-off conditions should not be forgotten as they represent a critical period of the flight where maximum power is requested. Any efficiency reduction at this moment must be carefully considered as well.

Secondary Flows. The secondary flow distribution was measured 0.3 a_{ax} downstream of the cascade exit plane at $Re_{is,2}$ =190,000 and for three values of the Strouhal number (0, 0.44, 0.88). The traversing planes were all located on the same half of the test section which is the most distant from the slits allowing the passage of the bars and of the probe (Fig. 1). For clarity, the data were mirrored to present a full exit plane. The displacement of the measurement planes from the blade midspan towards the endwall means that the local wake generator radius varies. This leads to different peripheral bar velocities, and hence different inlet triangulations, as commented before; the same wake frequency is however maintained. The results are presented under the form of (*Z*, *Y*) maps of the adimensional loss coefficient (Fig. 4); *Z* and *Y* are aligned the with spanwise and pitchwise directions, respectively.

At Sr=0, important loss cores exist at midspan and at $Z/c \sim 0.65$. This indicates most probably the existence of a nonuniform boundary layer status along the blade height. Under the wake action, the lateral cores move towards the endwalls and their intensity is strongly reduced. The wakes have therefore also a consequent positive impact on the secondary flow structures. A similar phenomenon was put in evidence by Brear et al. [21]. They showed that the dead flow inside a separation bubble migrates along the spanwise direction and reinforces the secondary flows. If the size of the bubble decreases, the secondary flow magnitude drops. This bubble size reduction is put in evidence in the time-averaged heat transfer section.

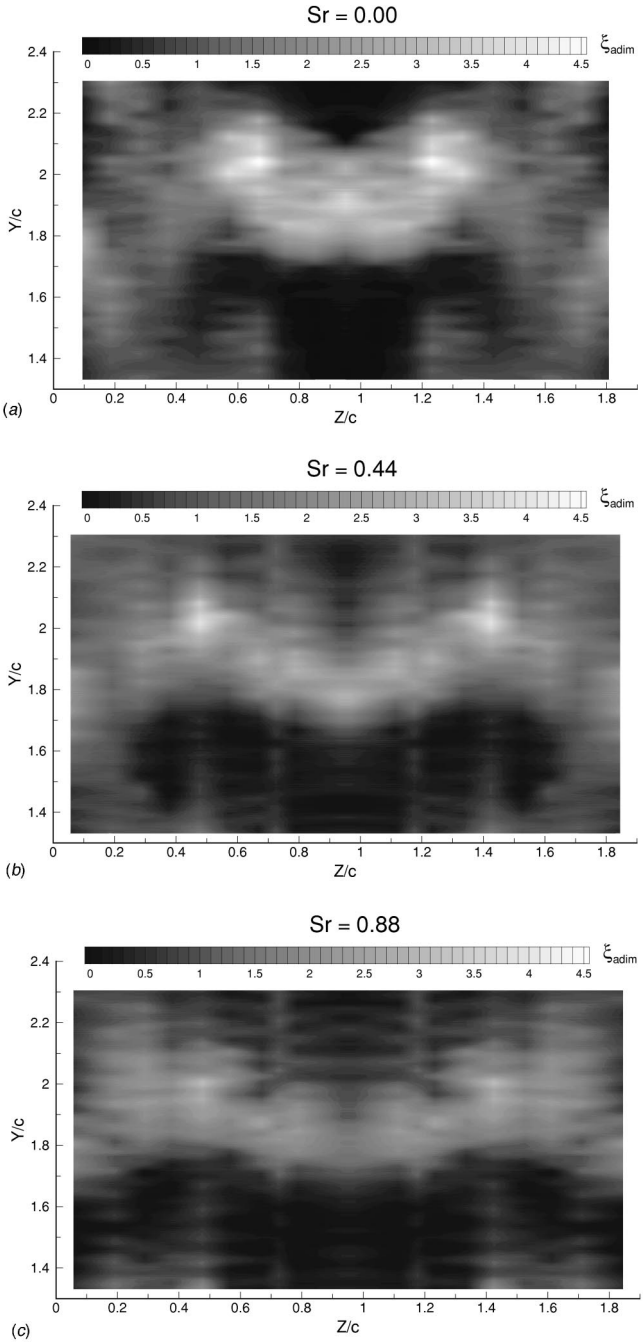

Fig. 4 Loss coefficient maps ($Re_{is,2}$=190,000)

Heat Transfer. The imposed gas to wall temperature difference is about 100 K. For the present study, the heat transfer coefficient, labeled $h(t)$, is defined as the ratio between the heat flux $q(t)$ and the initial value of this temperature potential. This simple

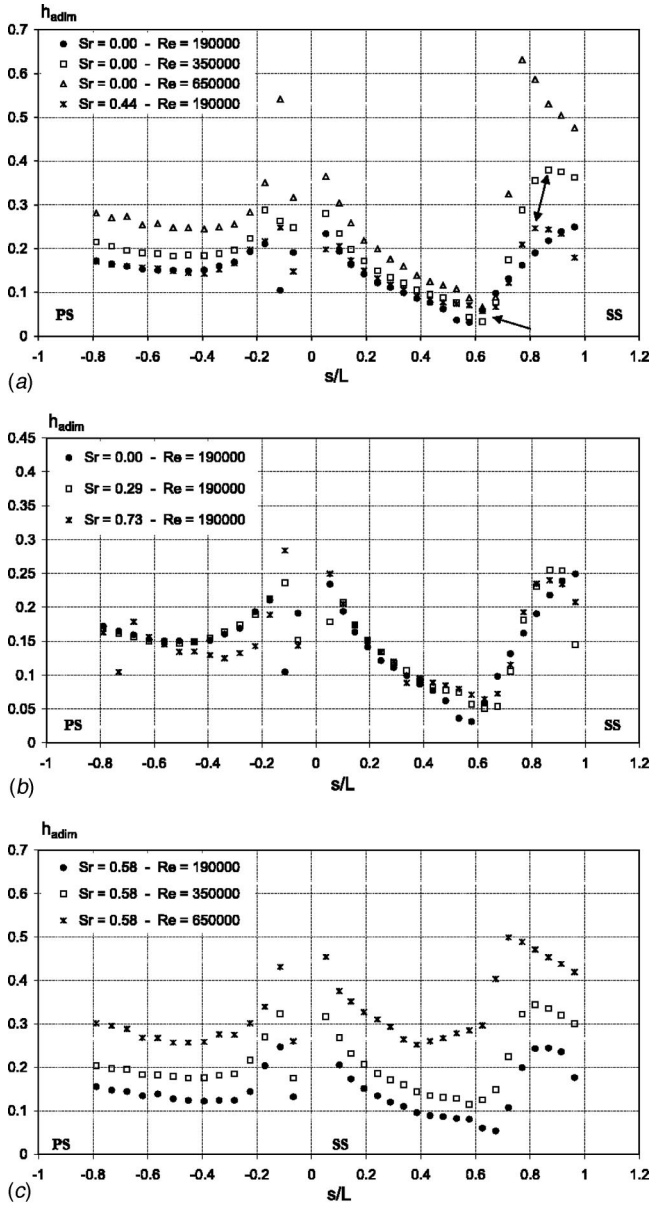

Fig. 5 Heat transfer coefficient distributions ($g_b/c=1.235$)

division by a constant particular to each experiment allows the comparison between different tests. All heat transfer results are nondimensionalized by the stagnation point heat transfer coefficient at $Re_{is,2}=190{,}000$ and $Sr=0$. The measurements are performed at midspan. Considering the relative sizes of the gages and the loss distributions presented in Fig. 4, the effects of lateral nonuniformity is expected to be small.

Time-Averaged Heat Transfer. The onset, separation and reattachment points are determined from the mean heat transfer distributions looking at local abrupt variations of heat flux. Figure 5(*a*) shows the time averaged heat transfer coefficient distributions for the different Reynolds numbers at $Sr=0$ (no bars). The stagnation point results are not plotted for clarity. At $Re_{is,2}=190{,}000$, a separation is observed at 0.55 L on the suction side and at -0.1 L on the pressure side. As $Re_{is,2}$ increases to 650,000, the separation (sharp drop in heat flux) disappears on the suction surface and the transition length decreases. This confirms the assumption made during the profile loss coefficient analysis. The transition onset location is more or less invariant, its end varies a lot and moves upstream, leading to a shorter bubble or transition length. With increasing Reynolds numbers, the pressure surface separation bubble gradually disappears and the global heat transfer level increases.

The impact of the upstream wakes on the mean heat transfer is also observed on Fig. 5(*a*). Their effect at $Re_{is,2}=190{,}000$ to avoid separation is as efficient as what was observed at the highest Re at $Sr=0$. However, this last operating condition is characterized by a generally higher heat transfer load. Compared to the steady case at $Re_{is,2}=350{,}000$, the wakes at $Sr=0.44$ and $Re_{is,2}=190{,}000$ suppress more effectively the separation and the end of transition occurs sooner (arrows on Fig. 5(*a*)). It is finally worthwhile to note that all these distributions more or less converge along the front, accelerating part of the suction side; the differences appear in the adverse pressure gradient area. It shows, for this kind of very highly loaded blade, the importance of transition and of the parameters influencing it.

Figure 5(*b*) shows the heat transfer distribution at $Re_{is,2}=190{,}000$ for three different Sr values. The transition onset on the suction side moves upstream when wakes are shed on the blades. This is clearly seen, from 0.4 L, when comparing with the heat transfer distribution for $Sr=0$. From this point, the acceleration decreases (Fig. 2). It means that the transition onset is not only sensitive to dV/ds, but also to the gradient of dV/ds. This remark seems to be confirmed by very recent complementary measurements.

Considering now only the variation of Re for a given Sr, Fig. 5(*c*) shows the general increase of heat transfer level and the upstream displacement of the transition end with increasing Reynolds number. At $Re_{is1,2}=650{,}000$, the suction side heat transfer distribution is characterized by two inflections along its evolution, demonstrating a clear departure from a laminarlike behavior. The most obvious one appears at 0.63 L and leads to the conclusion of the transition process (0.71 L). Why it occurs so late and not at the velocity peak is not yet explained. The second one, located at 0.4 L, was discussed hereabove and indicates the transition onset location. Transition clearly starts at 0.71 L for the lowest Re, and slightly sooner for the intermediate Re value. The size of the separation bubble on the pressure surface reduces when Sr increases. This is clearly demonstrated when looking at the heat transfer coefficient levels (Figs. 5(*a*), (*b*)) and supports the discussion presented in the section on secondary flows.

As most of the principal changes take place on the suction surface and as the largest contribution to the profile losses comes from this side, the following analysis will focus on this surface.

Time-Resolved Heat Transfer. Figure 6 shows a number of time resolved heat flux traces along the suction side at $Re_{is,2}=190{,}000$. The graph on the left illustrates the $Sr=0$ case where separation occurs at 0.55 L as shown in Fig. 5(*a*). The first turbulent activity is detected close to the reattachment point at about 0.65 L; it develops rapidly as the flow decelerates.

The graph in the middle corresponds to $Sr=0.44$. At the leading edge, the wakes are marked by deep valleys. This is due to the wake velocity deficit affecting the forced convection, but also to a lower temperature level present in the wakes as the bars are not initially at the flow temperature. As the flow moves downstream, the boundary layer grows and it is the turbulent behavior of the wakes which is mostly perceived, namely heat transfer peaks. However, the strong acceleration along the front part of the suction side damps these heat flux peaks and brings the flow back close to the $Sr=0$ level between 0.34 and 0.4 L. Turbulent activity is then redetected as the flow acceleration decreases. It is worth to note that it is not necessary from the previous heat transfer peaks that the turbulent characteristics develop. A small spike can become very huge as illustrated between 0.58 and 0.72 L (see labels A). The level of these peaks increases first, and afterwards they become flatter and larger (covering more time). Finally they merge together (label B). All these features are similarly reproduced when doubling the wake passing frequency (Fig. 6(*c*), $Sr=0.88$). The difference is that the number of turbulent patches is

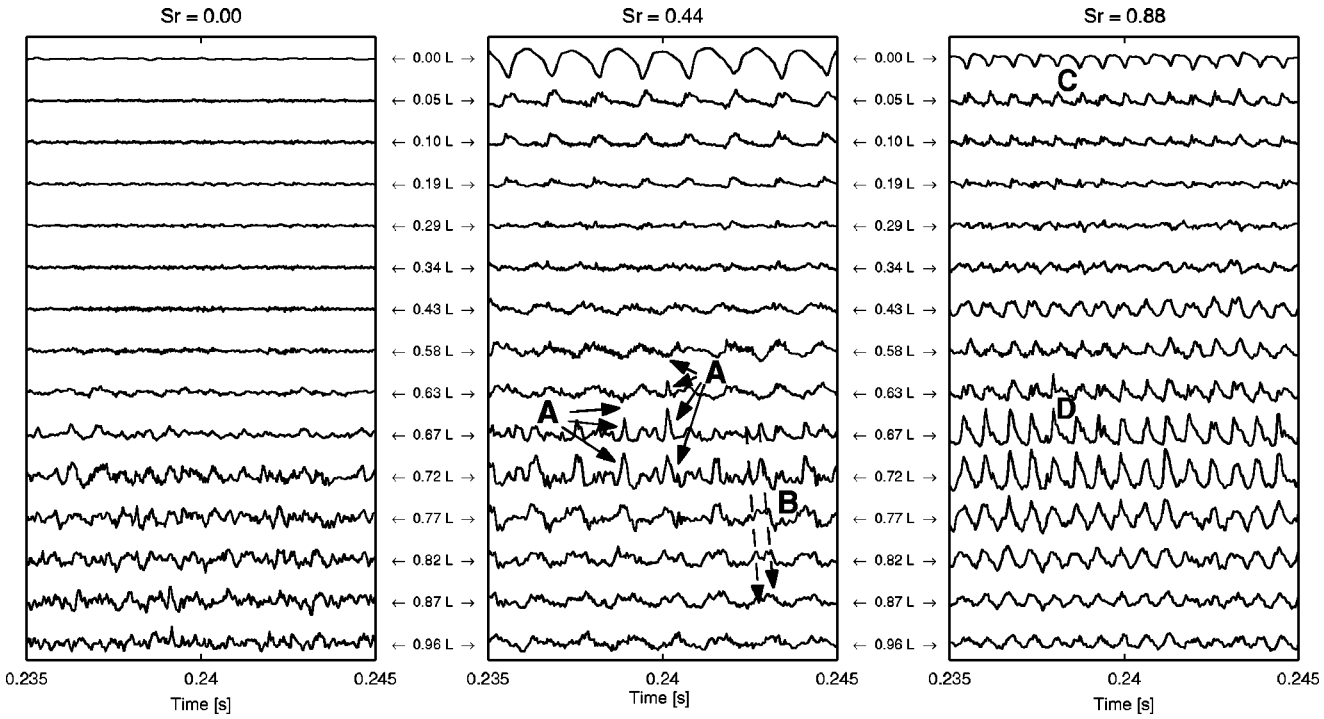

Fig. 6 Simultaneous raw heat transfer coefficient traces at $Re_{is,2}=190,000$ (suction side)

doubled and so cover more time. Calming phenomena are hardly observable from these raw traces. At the three first stations after the leading edge, there are some weak relaxation tendencies (label C) from the heat transfer peaks; but they completely collapse downstream. They do not reappear for Sr=0.44, but, at Sr=0.88, the characteristic heat flux relaxation of a calmed region (label D) follows the peaks at 0.63 and 0.67 L. Contrary to other investigations (e.g., Gostelow et al. [9]), where the calmed regions were the remaining proof of the turbulent spot existence in a turbulent flow environment, there is no trace of them further downstream. A variable other than the raw heat transfer coefficient would probably have more chances to lift the veil on the calmed regions.

A better representation of the unsteady phenomena can be provided by space-time diagrams of the phase-locked-averaged signals. This phase-locked averaging procedure was applied for 20 wake passing periods. The variables represented in Figs. 7 to 9 are the non dimensional heat transfer coefficient, its standard deviation (STD) and the heat transfer fluctuation intensity (HTFI), defined as follows:

$$\mathrm{STD}=\sqrt{\langle h'^2(t)\rangle}=\sqrt{\frac{1}{N}\sum_{i=1}^{N}\left(h_i(t)-\langle h(t)\rangle\right)^2} \tag{2}$$

$$\mathrm{HTFI}=100\cdot\frac{\mathrm{STD}}{\langle h(t)\rangle} \tag{3}$$

Figure 7 corresponds to the nominal case ($Re_{is,2}=190,000$,Sr $=0$) but the signals are not phase-locked-averaged, even if the time is considered as for the Sr=0.29 case of Fig. 8. The stagnation point measurements have been omitted to enhance the color scale. Starting from the leading edge, the heat transfer decreases as the laminar boundary layer develops. The very low heat transfer region at 0.55 L corresponds to the separation bubble. Afterwards, the flow reattaches, resulting in a strong increase of the heat transfer. The STD evolution clearly shows the passage between these two different states and the HTFI especially highlights the separation and transition areas.

An increase of the Reynolds number (Fig. 8(*b*)) results in an overall higher heat transfer level. Looking at the wake impact at

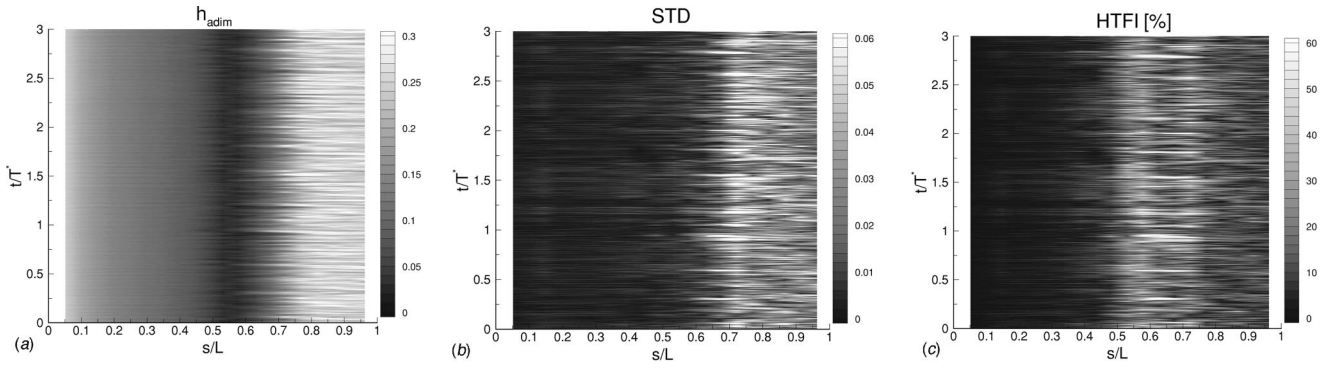

Fig. 7 Space-time diagrams of h_{adim} (*a*), STD (*b*), and HTFI (*c*) at $Re_{is,2}=190,000$, Sr=0

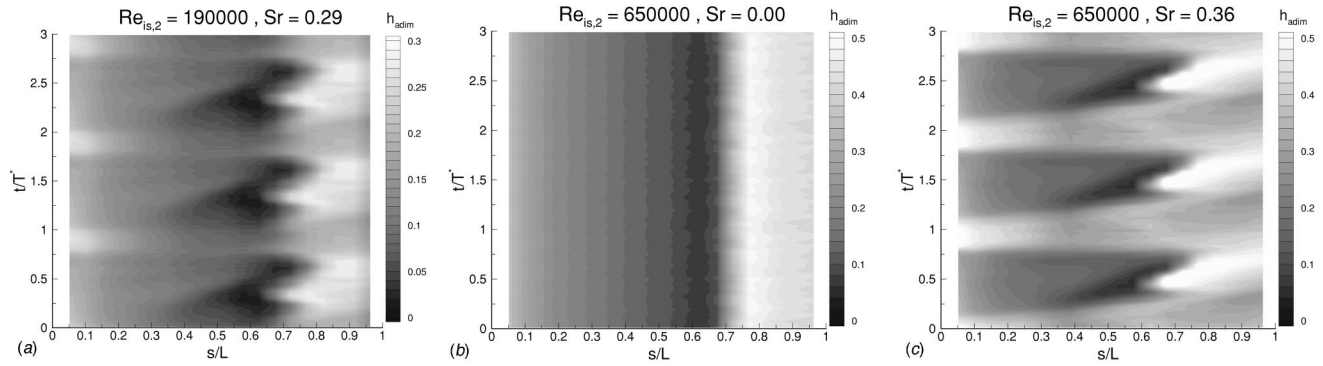

Fig. 8 Phase-locked-averaged h_{adim}: $Re_{is,2}=190{,}000$, Sr=0.29 (*a*); $Re_{is,2}=650{,}000$, Sr=0, (*b*); $Re_{is,2}=650{,}000$, Sr=0.36 (*c*)

low Re (Fig. 8(*a*)), it is clearly visible that the separation still exists, but is periodically suppressed in the wake streets. It is interesting to note that the separation is avoided almost directly at the wake arrival ($t/T^*\sim 0.75$), but that it reappears a certain time after the wake departure ($t/T^*\sim 1.05$ and $s/L\sim 0.67$). The steep heat transfer gradient at reattachment and the separation zone move upstream ($s/L\sim 0.6$ for separation), going back to the status of the Sr=0 case around $t/T^*=1.3$. Afterwards, these zones move backwards ($s/L\sim 0.7$ for separation) until the next wake. This last motion is not clearly understood. The heat puff appearing at $t/T^*\sim 1.3$ (between $s/L=0.2$ and 0.3) can be an explanation but its origin is not explained. Figure 8(*c*) shows the cumulative effect of both parameters at $Re_{is,2}=650{,}000$ and Sr=0.36. The wake impact on transition is reinforced by the Reynolds number increase.

Finally, Fig. 9 presents the evolution of STD and HTFI with passing wakes (Sr=0.29 and $Re_{is,2}=350{,}000$). The standard deviation shows a transition fluctuating line around 0.7 L, which accounts for transition at reattachment and in the wake. The wake street is also visible since the leading edge. The separation evolution is well seen from the heat transfer fluctuation intensity. It still presents the non explained behavior of displacement towards the trailing edge in the second half of the wake period. When the wake frequency is increased (not shown here) the time covered by the separation bubble is reduced. The wakes seem more and more to merge at the leading edge, but the phenomena taking place along the rest of the blade portion can still be well distinguished from each other. Let us finally note that the presence of calmed regions was not clear from these variables.

A number of other variables were built to emphasize any calmed region effect. This detection is usually grounded on the RMS of the wall shear stress signal. Considering the huge amount of research done with hot films gages, it seems that an efficient choice should take into account the fluctuating component of the signal. A new variable Δ' was defined from the phase locked averaged fluctuating heat transfer coefficient (Eq. (4)). It represents the variation of the absolute fluctuation $|h'(t)|$ with respect to its time mean value. Consequently, a region representing a strong transitional activity would be associated with high values of Δ'. On the contrary, low levels would correspond to a well-established flow regime.

$$\langle \Delta' \rangle = \frac{\langle |h'(t)| \rangle - \overline{\langle |h'(t)| \rangle}}{\overline{\langle h(t) \rangle}} \tag{4}$$

The variable Δ' is plotted in an (s,t) diagram, (Fig. 10) for Sr=0.29 at $Re_{is,2}=350{,}000$. The light color zones correspond to high transition activity, specially well marked as transition process via the separation bubble (arrow shape between 0.6 and 0.7 L). The wake-induced transition is also clearly visible from the leading edge up to fully turbulent flow around 0.8 L where Δ' starts to be more uniform and lower. The previously mentioned, heat puffs between two wake passages appear actually to be without effect on the transition process.

Finally, the presence of calmed regions was addressed, but no obvious evidence of them was found. They seem to correspond to regions where Δ' relaxes from its high values in the spots. As the standard deviation is believed to be lower in the calmed region than in the turbulent spot, Δ' was multiplied by STD to enhance the distinction between the two regions. However, the calmed regions were still hardly detected. At this stage, two possible conclusions can be drawn.

1. Calming phenomena, if they exist, have a very limited impact, at least in the present flow conditions. For example, if the zones following the two turbulent spots observed at 0.75 and 1.1 T^* in Fig. 12 are considered as calmed regions, it could explain the temporal evolution of h_{adim} in Fig. 8

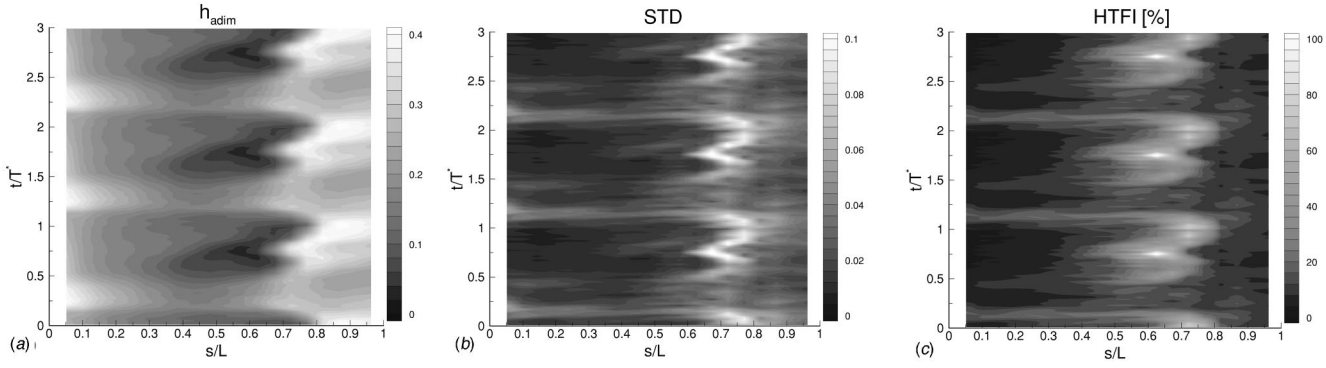

Fig. 9 Phase-locked-averaged h_{adim} (*a*), STD (*b*), and HTFI (*c*) at $Re_{is,2}=350{,}000$, Sr=0.29

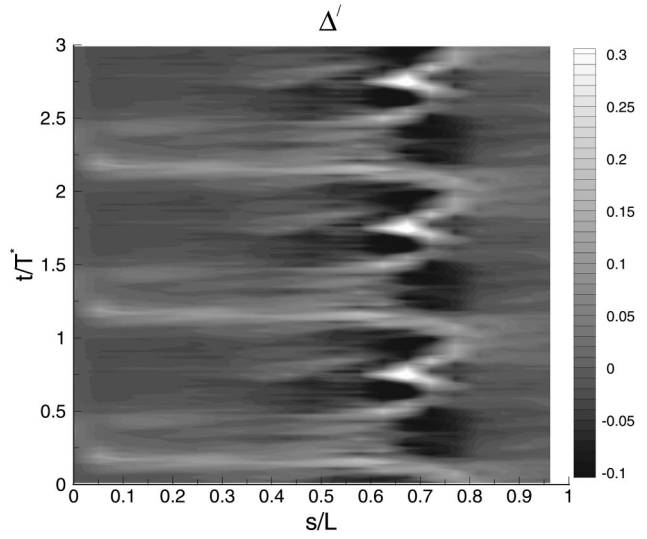

Fig. 10 Phase-locked-averaged Δ′ ($Re_{is,2}$=350,000,Sr=0.29)

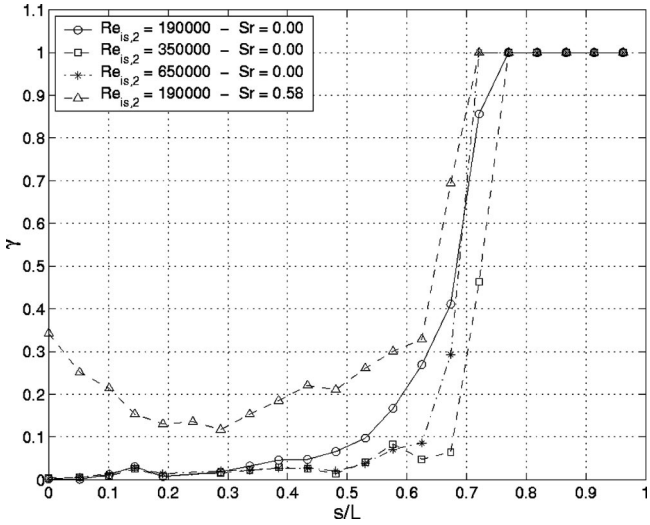

Fig. 11 Time-averaged intermittency factor evolution

around 0.7 and 0.75 L. Nevertheless, this influence is extremely local on the (*s*,*t*) diagrams. On the contrary, other researchers have presented results where the calmed region is clearly visible, as D'Ovidio et al. [22] with an integrated rms disturbance level. The transition process was however operating very differently. The flow was established on a flat plate at very low turbulence level and speed. The spot was generated inside the boundary layer, as opposed to the present case where the instability source of the turbulent spot comes from outside the boundary layer. As demonstrated by the DNS computations of Wu et al. [23], this can deeply modify the spot structure. A second difference could be found in the compressibility effects, even if those were not isolated in the present study.

2. The chosen way of investigation highlights scarcely the calmed region. The boundary layer investigation by measuring the heat flux instead of the wall shear stress is not in doubt. Indeed, the nondimensional heat transfer coefficient is most of the time strongly linked to the skin friction coefficient. Moreover, Zhong et al. [24] have obtained quantitative data about the turbulent spots by means of the thermochromic liquid crystal technique. However, the fact that the measurements are performed at the wall can affect the perception of the transition mechanism as it is well known that the intermittency factor varies across the boundary layer height (e.g., [13]).

Intermittency Factor. The intermittency factor γ will be presented in two forms. The first consists in the evolution along the blade suction surface of its time averaged value. The second considers its temporal variation.

Time-Averaged Value. The computation of the time-averaged intermittency factor is based on conditional sampling (e.g., Schobeiri et al. [25]). From the authors knowledge, this technique has never been applied to heat flux signals. As shown by Hedley and Keffer [26] the common variables used for this purpose are derived from velocities. However, the signal from a thin film gage in a laminar boundary layer presents enough differences from the one in a transitional, and possibly turbulent, flow to reach at least qualitatively the intermittency factor evolution. However, it has to be kept in mind that γ computed from heat transfer measurements at the wall can be quite different from the intermittency factor determined from boundary layer recorded signals.

The time mean value of γ in a given location is equal to the ratio between the number of samples corresponding to a turbulent flow state and the total number of samples. The conditional sampling technique is used to classify the points as laminar or not. A given detector function $S(t)$, built from the heat transfer signal, is then compared with a threshold level C to make a distinction between the two flow regimes. This threshold has been obtained from a study based on signals known as perfectly laminar or turbulent. The time mean value of the intermittency factor is finally defined by the following equations:

$$I(t)=\begin{cases}1 & \text{if } S(t)\geqslant C\\ 0 & \text{if } S(t)<C\end{cases} \tag{5}$$

$$\gamma=\frac{1}{Ns}\sum_{k=1}^{Ns} I(t_k) \tag{6}$$

The variables used as detector function $S(t)$ must present discriminatory capabilities between laminar and non laminar parts of the signal. As the absolute heat transfer level intrinsically varies along the blade surface, h could not be considered because it requires the accurate knowledge of the local laminar and turbulent state values (see Funazaki et al. [27]). However the way it fluctuates in time seemed promising. Four variables were tested: the absolute value of the variation of h, the previously defined $|h'|$ divided by $\overline{h}$, the first time derivative of $|h'|$ and the second time derivative of h.

From the present measurements, it appears that the energy spectrum of the flow evolves with transition, showing a higher frequency content. The present authors therefore suggest an additional, original, definition of the intermittency factor based on the integral of the power spectral density (PSDI) of the heat transfer coefficient signal. It compares the actual PSDI of a given gage signal with the typical values found in laminar and fully turbulent flow conditions (Eq. (7)). This coefficient has the advantage to present a more stable and logical evolution along the blade. Nevertheless, as the previously calculated γ represents the basic physics of the flow, it was decided to take both into account and to weigh γ with γ_{PSDI} (Eq. (8)). The final value of intermittency results from the average of the different spectrally weighted factors. Looking at the values of γ_{PSDI}, it is clear that the point following $\gamma_{\mathrm{PSDI}(s)}=1$ can be considered as fully turbulent and the final value of the intermittency factor was forced to unity from this point.

$$\gamma_{\mathrm{PSDI}(s)}=\frac{\mathrm{PSDI}(s)-\mathrm{PSDI}_L}{\mathrm{PSDI}_T-\mathrm{PSDI}_L} \tag{7}$$

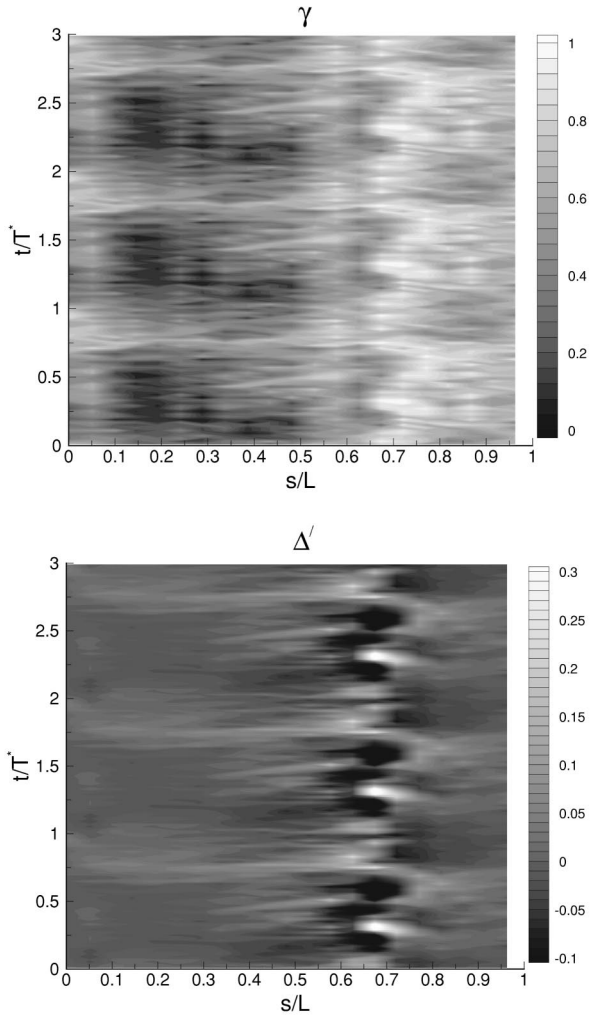

Fig. 12 Space-time evolutions of γ and Δ' ($Re_{is,2}=190{,}000$,Sr $=0.29$)

$$\gamma \rightarrow \sqrt{\gamma \cdot \gamma_{PSDI}} \tag{8}$$

Figure 11 shows typical intermittency factor evolutions resulting from the present approach. As shown previously at Sr=0, the transition onset is delayed and its length is shorter for the two higher Reynolds numbers. The computed evolution of γ shows that a fully turbulent state is reached around 0.75 L for $Re_{is,2}=190{,}000$. However, the heat transfer coefficient still increases downstream of this location (Fig. 5(*a*)). This apparent contradiction is most probably related to the frequency response of the heat flux gages and their inability to completely detect all turbulent features at very high frequency. This means that the highest values of γ have to be considered with caution. As the transition onset features, occurring at much lower frequency, are much better detected, the lower values of γ, typically below 0.5 . . . 0.6, are much more reliable. Anyway, the interpretation of γ should always be supported by the mean heat transfer coefficient distribution. The last curve of Fig. 11 is related to the wake impact (Sr $=0.58$) at low Reynolds number. The turbulent behavior of the flow at the leading edge is deeply promoted by the wakes. The subsequent strong acceleration damps this feature until 0.3 L. Close to this location, the acceleration begins to reduce and at 0.54 L, where the maximum Mach number is reached, γ starts to rise more quickly. The final steepest increase is computed from 0.6 L, earlier than the Sr=0 configurations.

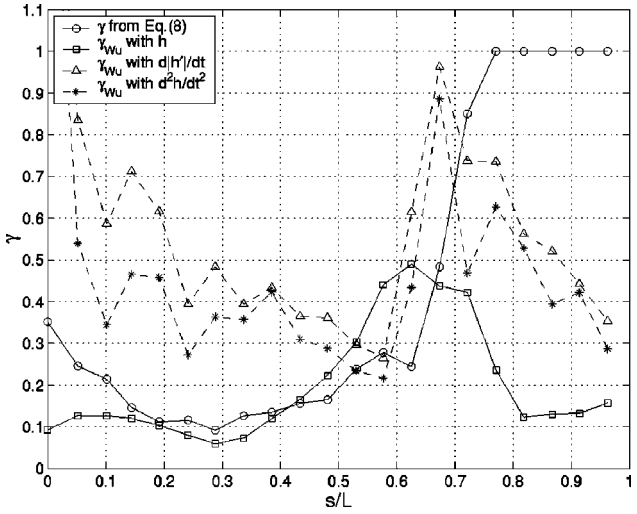

Fig. 13 Distribution of the intermittency factor based on Wu's formulation ($Re_{is,2}=190{,}000$,Sr$=0.29$)

Space-Time Evolution. The evolution in time of the intermittency factor is obtained by looking at the phase-locked-average of the different detector functions $S(t)$. The computation of γ is realized in the same way as presented before. However, the average of the identification $I(t)$ is computed over the number N of periods rather than over the number *Ns* of samples (Eq. (9)).

$$\langle \gamma(t_k) \rangle = \frac{1}{N} \sum_{i=1}^{N} I_i(t_k) \tag{9}$$

Among the various detector functions, $S(t)=|h'(t)|$ provides the most meaningful results, presented in Fig. 12 ($Re_{is,2}=190{,}000$,Sr$=0.29$). They support the previously mentioned impact of the wakes. As they hit the leading edge, the wakes induce a very turbulent strip (γ close to 1) almost instantaneously. When the flow decelerates, this strip starts to spread over the time axis. Finally, the boundary layer appears to be fully turbulent around 0.7 L (as seen in Fig. 11). The representation of Δ' for these working conditions is also provided in Fig. 12. Strong similarities exist between the (s,t) diagrams of $\langle \Delta' \rangle$ and $\langle \gamma \rangle$, e.g., the relatively low intermittency patches between 0.6 and 0.7 L. The regions of important transition activity (high values of Δ') correspond to high intermittency level as the patch at $t/T^*=1.5$ between 0.5 and 0.6 L. This undoubtedly establishes the link between the turbulent spot/patch and the transition process. Calmed regions are hardly seen.

To conclude this section about the different representations of the intermittency factor, a final attempt was made to characterize the boundary layer transitional state. This ''new version'' of γ is built from the formulation proposed by Wu et al. [23] (Eq. (10)). This coefficient is equal to 0 in a laminar flow and tends to 0 after the completion of transition. As stated by Wu, if a global maximum occurs somewhere, it indicates that the boundary layer is in its strongest transitional state at this location (its properties are the most distant from those in either laminar or turbulent regime). The great advantage of this definition is mainly that it does not involve the use of threshold values. Initially, Wu computed his coefficient using the friction coefficient or the Stanton number. In the present study, it is based on the different detector functions and on the heat transfer coefficient.

$$\gamma_{Wu} = \frac{\sqrt{\overline{(\langle S \rangle - \overline{S})^2}}}{\overline{S}} \tag{10}$$

The results of this formulation are compared in Fig. 13 with the

intermittency factor distribution found from Eq. (8). This last definition of γ results in a value almost equal to 0.5 at 0.67 L. The distributions from Wu's formulation exhibit a maximum at almost the same location, supporting the previous intermittency factor definition. The use of STD and HTFI as detector function provided much lower quality results.

Conclusions

A very high-lift high-subsonic LP turbine blade exposed to passing wakes has been investigated in a linear cascade at various Reynolds numbers and wake passing frequencies. The benefits of this configuration are put in evidence when the wake-induced transition phenomena are taken into consideration. The main conclusions of this contribution are the following:

1. The passing wakes have a positive impact on the profile loss coefficient at $\mathrm{Re}_{is,2}=190{,}000$. As the Reynolds number increases, the transition is promoted and the effect of the wakes is reduced. At high Reynolds numbers, the profile losses with wakes become even larger than without. The relative impact between wake frequencies seems to decrease with increasing Sr.
2. The wakes also have a positive effect on the secondary flows. By reducing the pressure side separation bubble, they decrease the amount of flow feeding the vortex core. The secondary flow pattern spreads out over the entire blade passage, reducing the spanwise nonuniformities.
3. The mean heat transfer coefficient distributions show the suction side separation bubble reduction due to the incoming wakes. Some phenomena such as (time mean) separation delay, upstream motion of the onset and end of transition have been detected as a function of Reynolds and Strouhal number. It should however be stressed that those measurements were only performed at midspan; additional data are required to quantify the spanwise variations.
4. Phase locked averaging of different variables was performed. The standard deviation of the heat transfer coefficient highlights the transition area, while the heat transfer fluctuation intensity enhances more the separation zone. A new variable $\langle \Delta' \rangle$ based on the temporal variation of the fluctuating component with respect to its time-averaged value was built to improve the analysis. Nevertheless, the presence of calmed regions is hardly detected. This could be linked to the operating conditions as the compressibility effects, but further investigations are needed to confirm.
5. The intermittency factor was computed both in a time-mean and in a time-resolved form. Both approaches show logical evolutions with respect to the time averaged and (s,t) diagrams of the heat transfer coefficient. γ has been also calculated following Wu's formulations. It has confirmed the method of computing the time-averaged intermittency factor, at least for the first half of the transition process.

Acknowledgment

The authors thank Snecma-Moteurs for the appreciated financial support and the permission to publish this paper. The first author also acknowledges F.R.I.A. (Fonds pour la Formation à la Recherche dans l'Industrie et dans l'Agriculture, Belgium) for the attribution of the Ph.D. fellowship.

Nomenclature

c = blade chord
f_b = bar frequency
g = pitch
h = heat transfer coefficient $= q/(T_g - T_w)$
q = heat flux
s = curvilinear coordinate
C = threshold level of detection function
H = blade height
L = blade surface length
P = pressure
Re = isentropic Reynolds no. $= (Vc)/\nu$
S = detection function
T = temperature
T^* = period duration
Sr = Strouhal no. $= f_b \cdot c/V_{ax}$
U = tangential velocity
V = velocity
Y = pitchwise coordinate
Z = spanwise coordinate
α = flow angle referring to the axial direction
γ = intermittency factor
ξ = loss coefficient

Subscript, Superscript, Symbol

0 = total condition
1 = inlet condition
2 = exit condition
adim = referred to the case ($\mathrm{Re}_{is,2}=190{,}000$, Sr $=0$)
ax = axial component
is = isentropic
b = bar
g = gas
w = wall
$'$ = fluctuating component
$|\ldots|$ = absolute value
$\langle \ldots \rangle$ = phase locked-averaged value
$\overline{\ldots}$ = time or pitch-area-averaged value

References

[1] Zweifel, O., 1945, "The Spacing of Turbo-Machine Blading, Especially with Large Angular Deflection," Brown Boveri Rev., **32**(12), pp. 436–444.
[2] Emmons, H. W., 1951, "The Laminar-Turbulent Transition in a Boundary Layer—Part I," J. Aerosp. Sci., **18**, pp. 490–498.
[3] Schubauer, G. B., and Klebanoff, P. S., 1955, "Contributions on the Mechanics of Boundary Layer Transition," NACA TN 3489; and 1289, 1956 NACA Rep.
[4] Curtis, E. M., Hodson, H. P., Banieghbal, M. R., Denton, J. D., Howell, R. J., and Harvey, N. W., 1997, "Development of Blade Profiles for Low-Pressure Turbine Applications," ASME J. Turbomach., **119**, pp. 531–538.
[5] Howell, R. J., Ramesh, O. N., Hodson, H. P., Harvey, N. W., and Schulte, V., 2001, "High Lift and Aft-Loaded Profiles for Low-Pressure Turbines," ASME J. Turbomach., **123**, pp. 181–188.
[6] Brunner, S., Fottner, L., and Schiffer, H.-P., 2000, "Comparison of Two Highly Loaded Low Pressure Turbine Cascades under the Influence of Wake-Induced Transition," ASME Paper 2000-GT-268.
[7] Solomon, W. J., 2000, "Effects of Turbulence and Solidity on the Boundary Layer Development in a Low Pressure Turbine," ASME Paper 2000-GT-273.
[8] Mayle, R. E., 1991, "Fundamental Aspects of Boundary Layers and Transition in Turbomachines," VKI Lecture Series on "Boundary Layers in Turbomachines," LS 1991-06.
[9] Gostelow, J. P., Melwani, N., and Walker, G. J., 1996, "Effects of Streamwise Pressure Gradient on Turbulent Spot Development," ASME J. Turbomach., **118**, pp. 737–743.
[10] Gostelow, J. P., Walker, G. J., Solomon, W. J., Hong, G., and Melwani, N., 1997, "Investigation of the Calmed Region Behind a Turbulent Spot," ASME J. Turbomach., **119**, pp. 802–809.
[11] Halstead, D. E., Wisler, D. C., Okiishi, T. H., Walker, G. J., Hodson, H. P., and Shin, H., 1997, "Boundary Layer Development in Axial Compressors and Turbines: Part 1—Composite Picture; Part 2—Compressors; Part 3—LP Turbines; Part 4—Computations and Analyses," ASME J. Turbomach., **119**, pp. 114–127, 426–444, 225–237, 128–139.
[12] Schulte, V., and Hodson, H. P., 1998, "Prediction of the Becalmed Region for LP Turbine Profile Design," ASME J. Turbomach., **120**, pp. 839–846.
[13] Schultz, M. P., and Volino, R. J., 2001, "Effects of Concave Curvature on Boundary Layer Transition under High Free-Stream Turbulence Conditions," ASME Paper 2001-GT-0191.
[14] LaGraff, J. E., Ashworth, D. A., and Schultz, D. L., 1989, "Measurement and Modeling of the Gas Turbine Blade Transition Process as Disturbed by Wakes," ASME J. Turbomach., **111**, pp. 315–322.
[15] Ashworth, D. A., LaGraff, J. E., and Schultz, D. L., 1989, "Unsteady Interaction Effects on a Transitinal Turbine Blade Boundary Layer," ASME J. Turbomach., **111**, pp. 162–168.
[16] Arts, T., and Lambert de Rouvroit, M., January 1992, "Aero-Thermal Performance of a 2-D Highly Loaded Transonic Turbine Nozzle Guide Vane: A Test

Case for Inviscid and Viscous Flow computations,'' ASME J. Turbomach., **114**, pp. 147–154.
[17] Roux, J.-M., Lefebvre, M., and Liamis, N., 2002, ''Unsteady and Calming Effects Investigation on a Very High Lift LP Turbine Blade—Part II: Numerical Analysis,'' ASME Paper GT-2002-30228.
[18] Schultz, D. L., and Jones, T. V., 1973, ''Heat Transfer Measurements in Short-Duration Facility,'' AGARDograph No. 165.
[19] Bons, J. P., Sondergaard, R., and Rivir, R. B., 2001, ''Turbine Separation Control Using Pulsed Vortex Generator Jets,'' ASME J. Turbomach., **123**, pp. 198–206.
[20] Coton, T., Arts, T., and Lefebvre, M., 2001, ''Effects of Reynolds and Mach Number on the Profile Losses of a Conventional Low Pressure Turbine Rotor Cascade with Increasing Pitch to Chord Ratio,'' 4th European Conference on Turbomachinery, ATI-CST-011/01, pp. 139–150.
[21] Brear, M. J., Hodson, H. P., Gonzalez, P., and Harvey, N. W., 2001, ''Pressure Surface Separations in Low Pressure Turbines: Part 2—Interactions With the Secondary Flow,'' ASME Paper 2001-GT-0438.
[22] D'Ovidio, A., Harkins, J. A., and Gostelow, J. P., 2001, ''Turbulent Spots in Strong Adverse Pressure Gradients. Part 2—Spot Propagation and Spreading Rates,'' ASME Paper 2001-GT-0406.
[23] Wu, X., Jacobs, R. G., Hunt, J. C. R., and Durbin, P. A., 1999, ''Simulation of Boundary Layer Transition Induced by Periodically Passing Wakes,'' J. Fluid Mech., **398**, pp. 109–153.
[24] Zhong, S., Kittichaikan, C., Hodson, H. P., and Ireland, P. T., 2000, ''Visualization of Turbulent Spots under the Influence of Adverse Pressure Gradients,'' Exp. Fluids, **28**(5), pp. 385–293.
[25] Schobeiri, M. T., Chakka, P., and Pappu, K., 1998, ''Unsteady Wake Effects on Boundary Layer Transition and Heat Transfer Characteristics of a Turbine Blade,'' ASME Paper 98-GT-291.
[26] Hedley, T. B., and Keffer, J. F., 1974, ''Turbulent/Non-Turbulent Decisions in an Intermittent Flow,'' J. Fluid Mech., **64**, pp. 625–644.
[27] Funazaki, k., Kitazawa, T., Koizumi, K., and Tanuma, T., 1997, ''Studies on Wake-Disturbed Boundary Layer under the Influences of Favorable Pressure Gradient and Free-Stream Turbulence—Part I—Experimental Setup and Discussion on Transition Model,'' ASME 1997-GT-451.

An Experimental and Computational Study of the Formation of a Streamwise Shed Vortex in a Turbine Stage

Graham Pullan
e-mail: gp10006@eng.cam.ac.uk

John Denton

Michael Dunkley[1]

Whittle Laboratory,
University of Cambridge,
Cambridge, CB3 0DY United Kingdom

Shear layers shed by aircraft wings roll up into vortices. A similar, though far less common, phenomenon can occur in the wake of a turbomachine blade. This paper presents experimental data from a new single-stage turbine that has been commissioned at the Whittle Laboratory. Two low-aspect ratio stators have been tested with the same rotor row. Surface flow visualization illustrates the extremely strong secondary flows present in both NGV designs. These secondary flows lead to conventional passage vortices, but also to an intense vortex sheet which is shed from the trailing edge of the blades. Pneumatic probe traverses show how this sheet rolls up into a concentrated vortex in the second stator design, but not in the first. A simple numerical experiment is used to model the shear layer instability and the effects of trailing edge shape and exit yaw angle distribution are investigated. It is found that the latter has a strong influence on shear layer rollup: inhibiting the formation of a vortex downstream of NGV 1 but encouraging it behind NGV 2. [DOI: 10.1115/1.1545766]

Introduction

Results from two stators which have been designed to perform the same duty in a new low-speed axial flow research turbine are presented. Notwithstanding the large body of research devoted to secondary flows within turbomachines (see Horlock and Lakshminarayana [1], Sieverding [2], Langston [3]), the second stator design, NGV 2, produced an entirely unexpected strong vortex—a feature not generated by NGV 1. This feature had been poorly predicted by the three-dimensional steady-flow CFD used to model the stage in the design process. The turbine fitted with NGV 2 stators had a measured brake isentropic efficiency 1.1% points lower than that obtained when NGV 1 stators were employed, and a significant fraction of this decrement was attributed by Dunkley [4] to the new vortex. This paper examines the mechanism by which the vortex forms and seeks an explanation as to why NGV 2 produces the feature when NGV 1 does not; such information is required by designers of similar blading who wish to avoid such vortices in the future.

Hawthorne [5] found that three components of secondary circulation are present downstream of a blade row: distributed secondary circulation, which forms in the blade passages; and trailing filament and trailing shed vorticity, which occur in the wakes of the blades. The last of these three is caused by a variation in lift with span and would occur even if the aerofoils were immersed in a stream of uniform stagnation pressure. The former two components result from the deformation of the vortex filaments present in the inlet flow. Figure 1 illustrates the distortion of a filament convecting through a blade row with zero inlet swirl. The filament becomes caught around the leading edge and the differing velocities on the suction and pressure surfaces lead to the distributed secondary circulation, ab, and the trailing filament circulation, $b'c$.

The distributed secondary circulation described by Hawthorne [5] manifests itself as the passage vortices observed by many subsequent authors; for example, Langston et al. [6], Goldstein and Spores [7], and Wang et al. [8]. Many investigators, for example, Binder and Romey [9], Gregory-Smith et al. [10], and Zaccaria and Lakshminarayana [11], have also found additional vortices, of a reduced strength and rotating in the opposite direction to the passage vortices, located in the wake adjacent to the passage vortices. These features are consistent with a combination of the trailing filament and trailing shed circulations identified by Hawthorne [5].

Figure 1 shows that distributed secondary circulation and trailing filament circulation are related—one does not occur without the other. This is apparent from a consideration of the spanwise velocities at the trailing edge. Near the casing, for example, flow moves outwards on the pressure-surface and across the end-wall before pitching inwards down the suction-surface. Downstream of the trailing edge, these two opposing streams graze against each other forming a shear layer. Such interfaces have long been studied by fluid mechanicists and are known to be susceptible to the Kelvin-Helmholtz instability if perturbed by wavelengths greater than the order of the layer thickness, see, for example, Sherman [12], or Drazin and Reid [13]. Excellent visualization of the resultant ''roller'' vortices has been provided, for the case of a two-dimensional stratified shear layer, by Thorpe [14] and Atsavapranee and Gharib [15].

The three-dimensional instability of the interface between two nonparallel grazing streams, which is of greater relevance to the shear layers shed by turbomachine blades, has also been studied, both experimentally (Hackett and Cox [16], Gründel and Fiedler [17], Schröder et al. [18], Fric [19]), and computationally (Lu and Lele [20], Schröder et al. [18]). Gründel and Fiedler [17] present smoke flow visualization illustrating both the formation of streamwise structures and also the pairing of adjacent vortices reminiscent of the ''winding rope'' model suggested by Lanchester [21] for wing-tip vortices. Lu and Lele [20] used a finite difference Navier-Stokes solver to study the three-dimensional shear layer between grazing streams. They observed the rollup of the interface into vortices and also found that vortex breakdown was predicted to occur if the convergence angle of the two streams was large (≈90 deg).

[1]Present address: Cambridge Consultants Ltd, Cambridge Science Park, U.K.

Contributed by the International Gas Turbine Institute and presented at the International Gas Turbine and Aeroengine Congress and Exhibition, Amsterdam, The Netherlands, June 3–6, 2002. Manuscript received by the IGTI October 11, 2001. Paper No. 2002-GT-30331. Review Chair: E. Benvenuti.

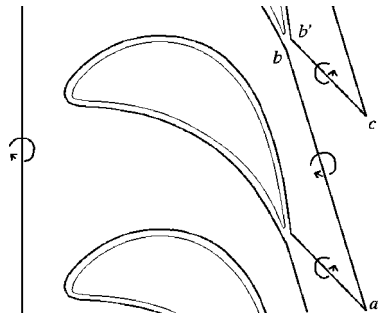

Fig. 1 Schematic of vortex filament convection through a blade row, after Hawthorne [5]

Experimental Method

The experimental results presented in this paper were collected from a previously unreported low speed axial flow turbine. The machine is characterized by a significant radius change through the NGV row, Fig. 2, and by the small number of low-aspect ratio NGVs in comparison to the more conventional rotor design.

Air is drawn through the turbine by a fan driven by a 200 kW motor. An electromagnetic dynamometer holds the rotational speed constant to within ± 0.5 rpm. Area traverses with five-hole pneumatic probes may be performed at each of the locations shown in Fig. 2, and time-accurate hot-wire and fast response pressure transducer traverses are also available at plane 3. In this paper, results are presented from planes in the stator-rotor gap region, together with oil and dye surface flow visualization within the NGV passage itself.

Data from two stator designs are presented in this paper, Fig. 3. NGV 1 may be considered a datum blade. NGV 2 was designed to mitigate the effects of the secondary flows which dominate highly loaded low aspect ratio blades. The over-turning at the endwalls and underturning toward 30% span measured in NGV 1 was countered by reducing the NGV 2 exit metal angles at the hub and casing, and increasing it at 30% span. The centroidal stack of NGV 2 then results in the highly three-dimensional trailing edge shown in Fig. 3.

Computational Method

Extensive computational simulations of the turbine stage have been performed using the three-dimensional steady/unsteady multi-row solver, UNSTREST. The code is widely used in both industry and research institutions and features a new algorithm, the ''Scree'' scheme, see Denton [22], which has low inherent viscosity and requires low levels of artificial smoothing to maintain stability. UNSTREST resolves the vortex shed by NGV 2 far more clearly than the calculations used in the design process of the stator which were performed using the opposed-difference scheme, Denton [23]. It was also found that the vortex developed more slowly in steady-state calculations of the complete stage than in simulations of the NGV 2 row alone. It seems that the mixing-plane used in steady-state stage calculations inhibits the development of the vortex, but the reasons for this are not clear. Despite the features under investigation in this paper being steady, the accuracy of the UNSTREST predictions of the vortex formation was found to improve when a time-accurate dual time stepping scheme was employed and so all computational results presented in this paper were obtained using this method.

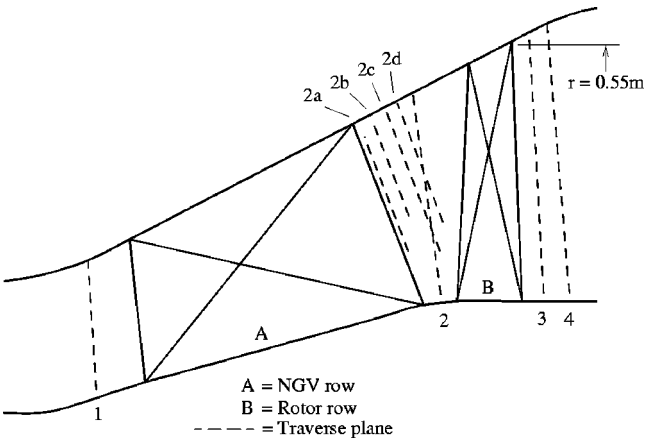

Fig. 2 Meridional view of research turbine

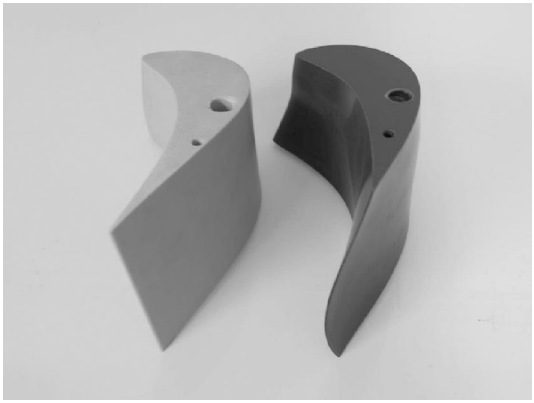

Fig. 3 Photograph of NGV 1 (left) and NGV 2

Experimental Results

Surface Flow Visualization. Figure 4 shows the results of an oil and dye surface flow visualisation experiment performed on NGV 2; NGV 1 exhibits very similar features but is not included here. Prior to running the turbine, the blade surfaces were painted red and the endwalls green. Figure 4 depicts a view from downstream of the NGV trailing edge, looking back up the passage. The companion line drawing illustrates the direction of the flow next to the surfaces in the central passage, and also identifies the locations of lift-off lines.

The severity of the secondary flows in Fig. 4 is immediately apparent. The cross-passage pressure gradient drives end-wall fluid from the pressure-surface to the suction-surface of the adjacent blade. These flows then pitch down the suction-surface from the casing and ascend it from the hub. The radial pressure gradient and three-dimensional blade design ensure that the spanwise penetrations of the hub and casing secondary flows are asymmetric. The suction-surface boundary layer growing from the leading edge (red) is confined to an ever smaller zone on the surface as it is squeezed away from the blade by the counter-rotating passage vortices.

The lift-off lines associated with the hub and casing horseshoe vortices can be traced from the leading edge of the NGV to the locations shown in Fig. 4. The pressure-side legs of the horseshoe vortices, which form lines A and D, are driven across the endwalls from the adjacent blade. The suction-side leg at the casing, labeled B, is seen to travel below the pressure-side leg in the manner described, for example, by Goldstein and Spores [7]. The corresponding lift-off line at the hub, C, does not remain distinct up to the trailing edge and it is possible that the suction-side leg of the hub horseshoe vortex leaves the surface of the blade, see Wang et al. [8].

The feature of Fig. 4 most relevant to this paper is, however, the opposing spanwise velocities on either side of the blade in the upper passage at the trailing edge. In the wake of the blade, these flows lead to a shear layer of concentrated streamwise vorticity

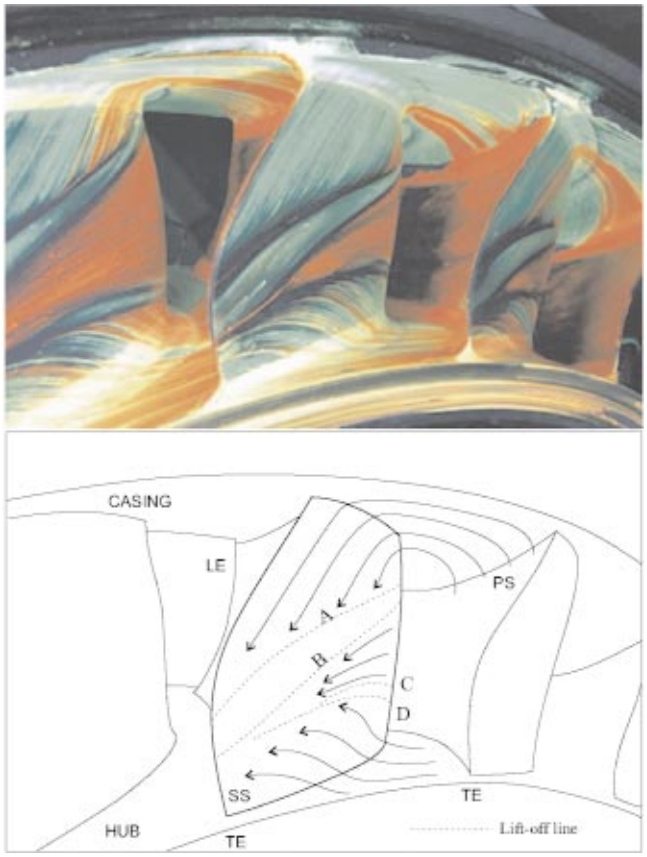

Fig. 4 NGV 2 surface flow visualization

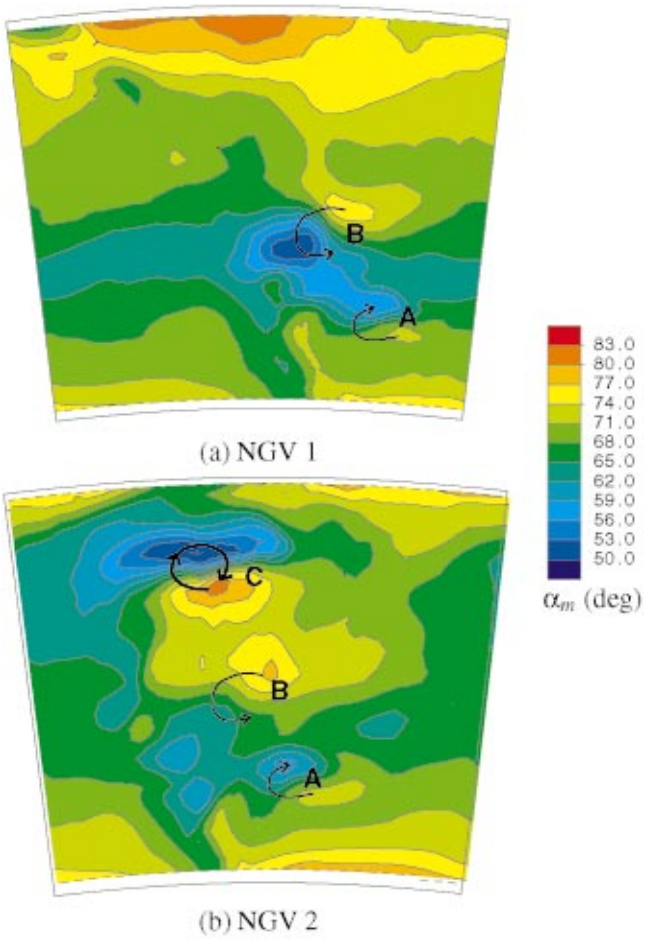

Fig. 5 NGV exit meridional yaw, α_m, (traverse plane 2)—(*a*) NGV 1, (*b*) NGV 2

which extends from 30% span to the casing, as the numerical simulation result in Fig. 7 shows. The behavior of this interface is now discussed.

Pneumatic Probe Traverses. Contours of NGV exit meridional yaw angle, as measured by a five-hole probe at traverse plane 2, are presented for both stator designs in Fig. 5. The measurement window covers one NGV pitch from 2.5 to 97.5% span and a grid of 41×41 uniformly spaced points was employed. The wake is approximately central, with the suction-surface to the right. Binder and Romey [9] noted that vortices are distinctive in plots of yaw angle, appearing as a series of parallel circumferential contours (solid-body core) sandwiched above and below by concentric elliptical contours (free vortex outer). Using this technique, the hub and casing passage vortices can be identified for both NGV 1 and NGV 2 (labeled "A" and "B" in Fig. 5). A third vortex, 'C,' dominates the exit flowfield of NGV 2. It has formed at 75% span and has a meridional yaw angle change of more than 30 deg across it. The sense of rotation, opposite to that of the upper passage vortex, is consistent with the streamwise vorticity in the shear layer forming downstream of the NGV. In the remainder of the paper, this feature will be referred to as the "shed vortex."

To investigate the evolution of the shed vortex, a series of four five-hole probe traverses were performed in the stator-rotor gap of the turbine. Geometric constraints prevent the measurement window from extending across the whole span, but the behavior of the shear layer was clearly captured. Figure 6 shows plots of measured streamwise vorticity and meridional yaw angle, as well as the meridional yaw angle predicted by an UNSTREST simulation. The streamwise vorticity was evaluated from traverse data using the equation $\nabla p_0/\rho=\mathbf{v}\times\boldsymbol{\omega}$ and by obtaining a streamwise direction from a "least squares" linear fit of pitchwise averaged yaw and pitch angles. This approach is similar to that adopted by Gregory-Smith et al. [10]. The streamwise vorticity is nondimensionalized using:

$$\omega'_{SW}=\omega_{SW}\frac{\Delta x_{m75}}{4\pi V_{m75}} \tag{1}$$

where Δx_{m75} is the meridional distance between stator and rotor and V_{m75} is the approximate meridional velocity, both at 75% height. This method for producing a reduced streamwise vorticity is intended to indicate the number of rotations that a lump of fluid with such a vorticity would make as it traveled between the blade rows at 75% height.

In Fig. 6(*a*) at plane 2a, the wake is identified by a narrow region of negative streamwise vorticity running across the measurement window inclined at approximately 45 deg to the radial direction. The unusual wake shape is caused by the curved geometry of the NGV 2 trailing edge, Fig. 3. The greatest magnitude of streamwise vorticity occurs at 75% of the passage height and indicates that fluid in this region will rotate of the order of five times before entering the rotor. At plane 2b, an island of vorticity has formed and the contours of meridional yaw angle, Fig. 6(*b*), show that the shed vortex is forming at this point. The vortex remains distinct at the remaining two measurement planes with additional, weaker, vortical features forming at lower radii.

The calculated meridional yaw angle plots, Fig. 6(*c*), do not show complete agreement with the measurements. Although the code does predict the formation of the shed vortex, it shows a more gradual rollup of the trailing shear layer. The simulation suggests that the vortex forms 15% of span inboard of the location

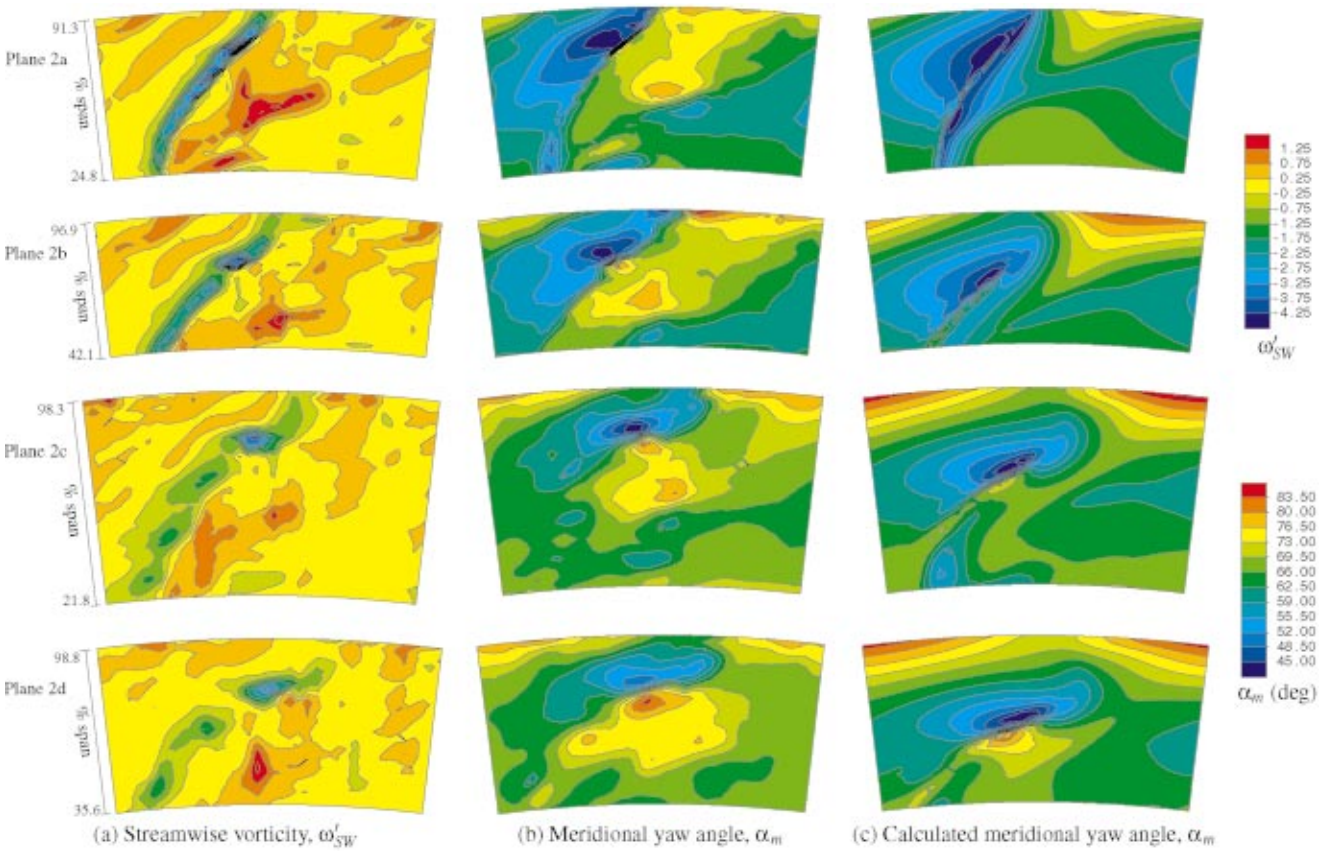

Fig. 6 The development of a "shed vortex" downstream of NGV 2—(*a*) streamwise vorticity, ω'_{SW}, (*b*) meridional yaw angle, α_m, (*c*) calculated meridional yaw angle, α_m

observed experimentally and also exaggerates the over-turning of the flow toward the casing.

Shear Layer Simulation

The secondary flows within the stator passage lead to similar shear layers downstream of the trailing edges of NGV 1 and NGV 2, Fig. 7. The shape of the wake is different in each design, being approximately radial in NGV 1 but circumferentially inclined in NGV 2, due to the geometry of the blades. However, the region of maximum streamwise vorticity lies between 50% span and 75% span in both cases. The question as to why only NGV 2 forms a shed vortex is now addressed. A series of numerical simulations of idealised shear layers was performed in order to qualitatively assess the affect of two factors on vortex formation: first, the trailing edge shape and second, the NGV exit yaw angle distribution.

Simulation Results. In general, the computational domain was a cuboid with an inlet face, an exit face, two periodic faces and two solid faces, Fig. 8. The orientation of the periodic faces eliminates end-wall effects and results in the simulation of an infinite shear layer. The distance between the periodic boundaries is λ_v. The grid comprised $73\times100\times73$ nodes in the spanwise, axial and pitchwise directions respectively. A shear layer was created at the inlet boundary by superimposing a discontinuous radial velocity on to a uniform axial velocity. The resultant pitch angles on either side of the domain centerline were equal in magnitude, but opposite in direction. To simulate the nonuniform nature of the shear-layer shed from the NGVs of the research turbine, the pitch angles varied smoothly from $\pm10°$ at the top and bottom of the domain to ±30 deg at midspan. Visualisation of the rollup was aided by a passive scalar technique, similar to that used by Lu and

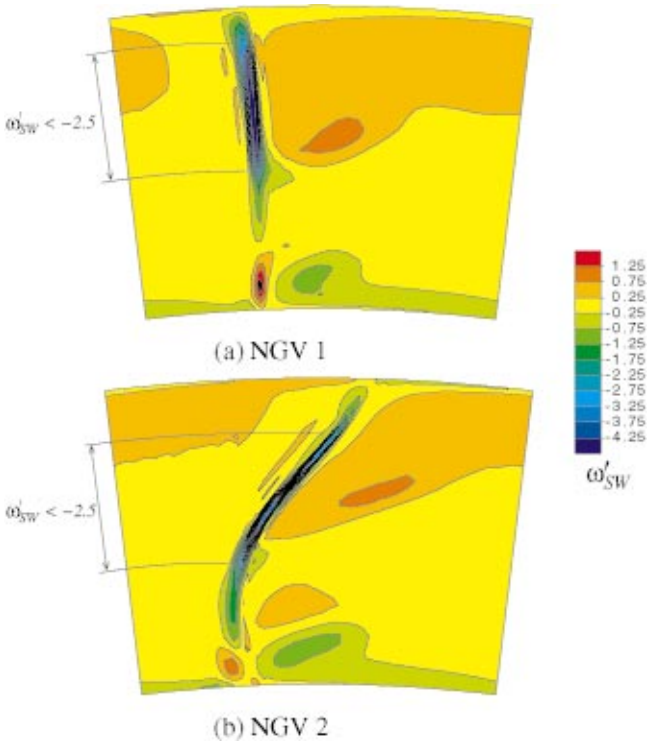

Fig. 7 Calculated streamwise vorticity, ω'_{SW}, downstream of stator trailing edge (plane 2*a*)—(*a*) NGV 1, (*b*) NGV 2

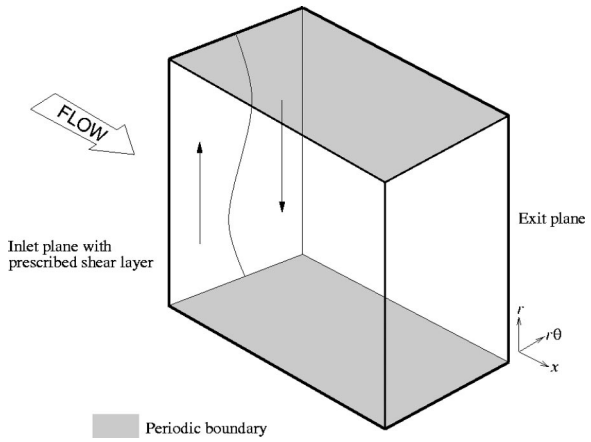

Fig. 8 Schematic of domain used for shear layer simulations

Lele [20], so that nodes on one side of the inlet pitch angle discontinuity were assigned a value of the convecting scalar different to those on the other.

Figure 9 shows passive scalar contour plots at three axial locations for five different simulations. In Fig. 9(*a*), the shear layer is initially straight, but the high concentration of vorticity in the center of the domain soon causes a clockwise rotation of the interface about that point. By the time the flow reaches the $x/\lambda_v = 0.72$ plane, this instability has resulted in the formation of a streamwise vortex.

Figures 9(*b*) and (*c*) differ from the previous calculation only in that the shear layer is not straight at the inlet to the domain, but it is perturbed by a sinusoid of wavelength λ_v. The perturbation in Fig. 9(*c*) is opposite to that of Fig. 9(*b*). As was the case in the datum simulation, the interface starts to rotate clockwise about the center of the domain. In Fig. 9(*b*), the initial displacement is in the same direction as that caused by the shear layer instability with the result that the rollup process is more advanced at subsequent axial locations than the first calculation. Conversely, the perturbation in Fig. 9(*c*) hinders the formation of a vortex so that none is visible at $x/\lambda_v = 0.72$.

The simulations in Figs. 9(*d*) and (*e*) both start from an initially straight shear layer. In contrast to the datum calculation of Fig. 9(*a*), however, a spanwise varying tangential velocity component has been added. The resultant yaw angle distribution for Fig. 9(*d*) is shown in Fig. 10, while a mirror-image yaw profile was used in Fig. 9(*e*). To maintain compatibility, each stream-surface of the simulation was sheared according to the inlet yaw angle at that radial location so that the side walls of the domain became curved.

The yaw angle distribution in Fig. 9(*d*), with flow moving to the right above the domain centerline and to the left below it, is in a direction so as to encourage the clockwise rollup of the vortex sheet. As a consequence, the formation of the central vortex occurs more rapidly than the datum simulation of Fig. 9(*a*). The opposite yaw angle profile of Fig. 9(*e*) has a dramatic stabilising effect on the rollup process with the shear layer remaining approximately straight throughout the calculation domain.

Application to NGV 1 and NGV 2. The qualitative data provided by the shear layer simulations are now applied to the sheet of vorticity shed from the trailing edges of the two stators tested in the research turbine. Despite the significant differences in blade design, Fig. 7 shows that the distribution of streamwise vorticity behind each NGV is similar. In terms of the classical secondary flow theory of Hawthorne [5], this indicates that the contribu-

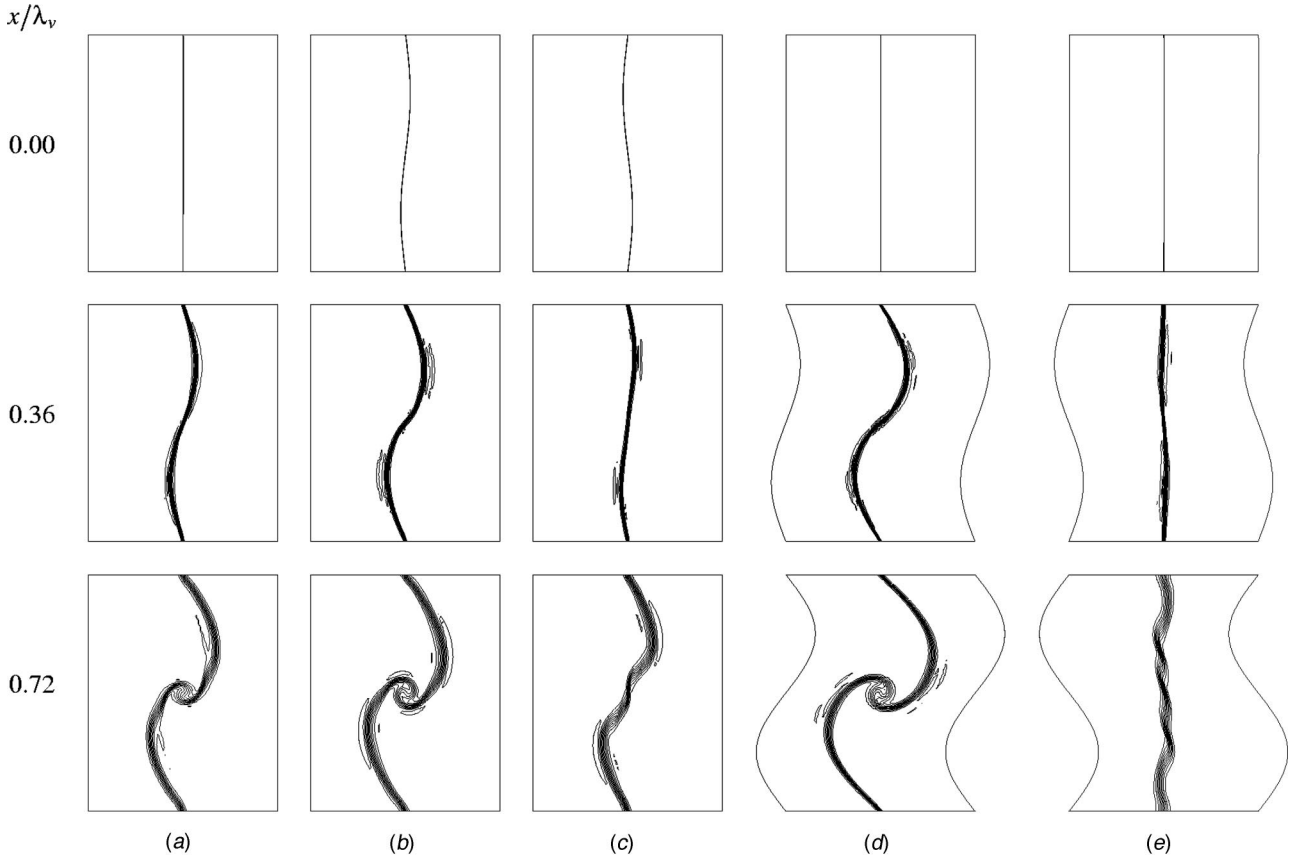

Fig. 9 The effect of initial shape, (*a*)–(*c*), and yaw angle distribution, (*d*) and (*e*), on the instability of a simulated vortex sheet-passive scalar contours

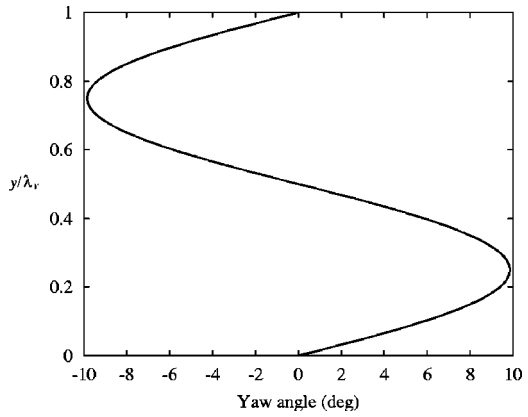

Fig. 10 Distribution of inlet yaw angle for shear layer simulation

tion of trailing shed circulation caused by a variation in blade loading with span is small compared to the trailing filament circulation resulting from the vorticity of the boundary layers at inlet to the blade row. In both designs, the greatest magnitude of streamwise vorticity is predicted to occur between 50 and 75% of the passage height and vortex formation is anticipated at the point of peak shear at approximately 65% span.

Figure 11 shows the trailing edge geometry when viewed along the mean exit camberline. The NGV 1 trailing edge is straight whereas that of NGV 2 is curved slightly. In fact, the direction of the radial velocities on either side of the wake mean that the shape of the NGV 2 trailing edge at 65% span will tend to *promote* vortex formation. However, the shape of NGV 1 will not inhibit wake rollup and so this does not provide an explanation as to why no vortex is observed downstream of the first design.

The calculated distributions of pitchwise averaged meridional yaw angle for both NGV designs at plane 2a is shown in Fig. 12. The area of greatest wake shear is also indicated. It can be seen that yaw angle distributions between 50 and 75% span are significantly different. In particular, the angle increases with radius for NGV 1, but decreases with radius for NGV 2. A comparison of the cross-flow profiles with those of the idealized shear layer study reveals that the exit flow angle distribution of NGV 1 will tend to *stabilize* the vortex sheet whereas that of NGV 2 will *encourage rollup*. This result is significant for two reasons. First, a clear difference between the NGV 1 and NGV 2 blades has been identified that has been qualitatively shown to promote vortex formation in NGV 2, but inhibit rollup in NGV 1. Second, the exit angle profile of a blade is a parameter well known to the turbomachine designer and may be manipulated, through changes to the blade geometry, so as to avoid the formation of a concentrated vortical feature.

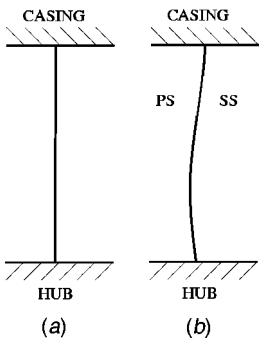

Fig. 11 Trailing edge shapes viewed along average exit camberline—(*a*) NGV 1, (*b*) NGV 2

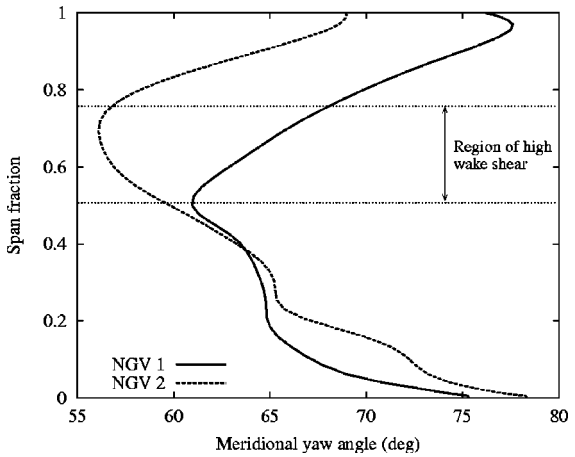

Fig. 12 Calculated pitchwise averaged meridional yaw angle, plane 2*a*

Conclusions

Two low-aspect ratio stator blades, designed to perform the same duty in a new low-speed research turbine at the Whittle Laboratory, generated very different exit flowfields. NGV 2 produced a strong streamwise vortex at 75% span while the companion geometry, NGV 1, did not.

Pneumatic probe traverses revealed that the vortex forms downstream of NGV 2 as a result of the rollup of the trailing shear layer. NGV 1 sheds a similar shear layer, but no such instability occurs.

Numerical simulations of an idealised nonuniform shear layer were used to investigate the influence of trailing edge shape and exit yaw angle distribution on wake stability. It was found that the spanwise yaw angle profile in the vicinity of the region of maximum streamwise vorticity has a significant effect on shear layer rollup. In NGV 1, the exit yaw angle distribution *inhibits* the formation of a vortex whereas it *encourages* the instability of the NGV 2 wake.

A sheet of streamwise vorticity shed from a blade will always tend to roll up into one or more vortices, but the length-scale over which this process takes place is strongly influenced by the trailing edge geometry and, in particular, the exit yaw angle distribution.

Acknowledgments

The authors would like to thank Eric Curtis and Nick Hooper of the Whittle Laboratory for their advice and technical expertise throughout this investigation. The assistance of David MacManus of Rolls-Royce plc is also gratefully acknowledged. The work was funded by Rolls-Royce plc, the Department of Trade and Industry (UK) and the Engineering and Physical Sciences Research Council (UK).

Nomenclature

p_0 = stagnation pressure
V_x = axial velocity
V_r = radial velocity
V_θ = tangential velocity
V_m = meridional velocity $= \sqrt{V_x^2 + V_r^2}$
$\mathbf{v}$ = velocity vector
$\boldsymbol{\omega}$ = vorticity vector
$\mathbf{e}_{prm}$ = unit vector in "primary" direction
α_m = meridional yaw angle $= \tan^{-1}(V_\theta / V_m)$
λ_v = distance between periodic boundaries
ρ = density
ω_{SW} = streamwise vorticity

References

[1] Horlock, J. H., and Lakshminarayana, B., 1973, ''Secondary Flows: Theory, Experiment, and Application in Turbomachinery Aerodynamics,'' Annu. Rev. Fluid Mech., **5**, pp. 247–280.

[2] Sieverding, C. H., 1985, ''Recent Progress in the Understanding of Basic Aspects of Secondary Flows in Turbine Blade Passages,'' ASME J. Eng. Power, **107**(2), pp. 248–257.

[3] Langston, L. S., 2001, ''Secondary Flows in Axial Turbines—A Review,'' Ann. N.Y. Acad. Sci., **934**, pp. 11–26.

[4] Dunkley, M. J., 1998, *The Aerodynamics of Intermediate Pressure Turbines*, Ph.D. thesis, University of Cambridge.

[5] Hawthorne, W. R., 1955, ''Rotational Flow Through Cascades Part 1—The Components of Vorticity,'' J. Mech App. Math., **8**.

[6] Langston, L. S., Nice, M. L., and Hooper, R. M., 1977, ''Three-Dimensional Flow Within a Turbine Cascade Passage,'' ASME J. Eng. Power, **99**, pp. 21–28.

[7] Goldstein, R. J., and Spores, R. A., 1988, ''Turbulent Transport on the Endwall in the Region Between Adjacent Turbine Blades,'' ASME J. Heat Transfer, **110**, pp. 862–869.

[8] Wang, H. P., Olson, S. J., Goldstein, R. J., and Eckert, E. R. G., 1997, ''Flow Visualisation in a Linear Turbine Cascade of High Performance Turbine Blades,'' ASME J. Turbomach., **119**, pp. 1–8.

[9] Binder, R., and Romey, A., 1983, ''Secondary Flow Effects and Mixing of the Wake Behind a Turbine Stator,'' ASME J. Eng. Power, **105**, pp. 40–46.

[10] Gregory-Smith, D. G., Graves, C. P., and Walsh, J. A., 1988, ''Growth of Secondary Losses and Vorticity in an Axial Turbine Cascade,'' ASME J. Turbomach., **110**, pp. 1–8.

[11] Zaccaria, M., and Lakshminarayana, B., 1995, ''Investigation of Three-Dimensional Flowfield at the Exit of a Turbine Nozzle,'' J. Propul. Power, **11**, pp. 55–63.

[12] Sherman, F. S., 1990, *Viscous Flow*, McGraw-Hill.

[13] Drazin, and Reid, 1981, *Hydrodynamic Stability*, Cambridge University Press.

[14] Thorpe, S. A., 1968, ''A Method of Producing a Shear Flow in a Stratified Fluid,'' J. Fluid Mech., **22**, pp. 693–704.

[15] Atsavapranee, P., and Gharib, M., 1997, ''Structures in Stratified Plane Mixing Layers and the Effects of Cross-Shear,'' J. Fluid Mech., **342**, pp. 53–86.

[16] Hackett, J. E., and Cox, D. K., 1970, ''The Three-Dimensional Mixing Layer Between Two Grazing Perpendicular Streams,'' J. Fluid Mech., **43**, pp. 77–96.

[17] Gründel, H., and Fiedler, H. E., 1993, ''The Mixing Layer Between Non-Parallel Streams,'' Appl. Sci. Res., **51**, pp. 167–171.

[18] Schröder, N., Hofmann, G., and Hourmouziadis, J., 2000, Trailing Edge 3D Free Shear Layers, *ASME 2000-GT-436*.

[19] Fric, T. F., 1995, Skewed Shear Layer Mixing Within a Duct, *AIAA 95-0869*.

[20] Lu, G., and Lele, S. K., 1994, Vortex Breakdown in Skewed Compressible Mixing Layers, *AIAA 94-0821*.

[21] Lanchester, F. W., 1907, *Aerodynamics*, Constable and Company.

[22] Denton, J. D., 2002, ''The Effects of Lean and Sweep on Transonic Fan Performance: A Computational Study,'' TASK Quarterly, **6**(1), pp. 1–17.

[23] Denton, J. D., 1992, ''The Calculation of Three Dimensional Viscous Flow Through Multistage Turbomachines,'' ASME J. Turbomach., **114**(1).

Turbine Blade Trailing Edge Flow Characteristics at High Subsonic Outlet Mach Number

Claus H. Sieverding
Turbomachinery & Propulsion Department,
von Karman Institute for Fluid Dynamics,
B-1640 Rhode Saint Genèse, Belgium
e-mail: sieverding@vki.ac.be

Hugues Richard
DLR,
Institut für Strömungsmechanik,
D-37073 Göttingen, Germany
e-mail: Hugues.Richard@dlr.de

Jean-Michel Desse
ONERA,
Institut de Mécanique des Fluides de Lille,
F-59045 Lille Cedex, France
e-mail: desse@onera.fr

The paper presents an experimental investigationof the effect of the trailing edge vortex shedding on the steady and unsteady trailing blade pressure distribution of a turbine blade at high subsonic Mach number ($M_{2,is}=0.79$) and high Reynolds number ($RE=2.8\times10^6$). The vortex formation and shedding process is visualized using a high-speed schlieren camera and a holographic interferometric density measuring technique. The blade is equipped with a rotatable trailing edge cylinder instrumented side-by-side with a pneumatic pressure tap and a fast response pressure sensor for detailed measurements of the trailing edge pressure distribution. The experiments demonstrate that contrary to the isobaric dead air region demonstrated at low subsonic Mach numbers the data reveal the existence of a highly nonuniform trailing edge pressure distribution with a strong pressure minimum at the center of the trailing edge. This finding is significant for the determination of the base pressure coefficient that is in general measured with a single pressure-sensing hole at the trailing edge center. The paper investigates further the effect of the vortex shedding on the blade rear suction side and discusses the superposition of unsteady effects emanating from the trailing edge and from the neighboring blade. The experimental data are a unique source for the validation of unsteady Navier-Stokes codes.
[DOI: 10.1115/1.1539057]

1 Introduction

The results presented in this paper are part of the European Research Project BRITE/EURAM CT96-0143 on ''Turbulence Modelling of Unsteady Flows in Axial Turbines,'' which was completed in 2000. The primary aim was to provide greater understanding of unsteady flow phenomena through a combination of computational and experimental work. The experimental work covered two types of unsteady flow aspects: (a) unsteadiness related to large coherent structures (von Karman vortices) in turbine blade wakes, and (b) unsteadiness related to the interference of wakes with downstream blade rows.

The experimental program on unsteady wakes was designed as an extension of a previous BRITE-EURAM project ''Time Varying Wake Characteristics behind Flat Plates and Turbine Blades,'' Sieverding et al. 1999. The requirement of high spatial and temporal resolution led to the choice of a very large-scale nozzle guide vane (280 mm chord length) with a relatively thick trailing edge. The blade was tested at the University of Genoa at low speed and at VKI at an outlet Mach number $M_2=0.4$. Results were reported by Ubaldi and Zunino [1], and by Cicatelli and Sieverding [2]. A particular feature of the VKI experiments was the instrumentation of the model with a rotatable trailing edge allowing the detailed measurement of the steady and unsteady pressure distribution around the trailing edge. Both the steady and time-averaged unsteady measurements confirmed the existence of an isobaric pressure region covering about 120 deg of the trailing edge circle, but also showed that prior to reaching this plateau the pressure and suction side flows underwent a strong overexpansion followed by a recompression to the plateau-pressure.

The knowledge of the trailing edge base pressure is important for the evaluation of the blade profile losses. Traupel [3] and Denton [4], approximate the contribution due to the trailing edge base pressure by

$$\Delta\varsigma(\text{resp.}\Delta Y)=C_p(D/o) \tag{1}$$

where C_p is the base pressure coefficient, D the trailing edge thickness, and o the throat. Systematic measurements of the base pressure in turbine blades are rather scarce. The base pressure correlation by Sieverding et al. [5] appears to be most widely used but interesting results were for example also reported by Xu and Denton [6] and most recently by Jouini et al. [7]. All experimental base pressure coefficients are derived from measurements obtained with a single pressure tapping at the trailing edge base covering typically 25–50% of the trailing edge thickness. In the light of the real trailing edge pressure distribution as measured by Cicatelli et Sieverding [2], the question arises of course whether under these circumstances the C_p-value in Eq. (1) reflects adequately the effect of the trailing edge base pressure on the profile losses.

The pressure distribution around the trailing edge is of course intimately linked to the vortex shedding process from the trailing edge. The presence of large coherent structures in turbine blade wakes, known as von Karman vortices, have experimentally been put into evidence by many authors using various types of techniques such as smoke visualizations [8], ultrashort schlieren photographs [9–12], or interferometric density measurements [12,13]. Carscallen et al. [14], were the first to measure the effect of the trailing edge vortices on the unsteady pressure and temperature distributions in the wake of a transonic turbine blade. The authors confirmed the existence of energy separation in the wake with cold spots in the wake center and hot spots at the edges of the wake, a phenomenon that so far had been investigated mostly in the context of vortex shedding from cylinders.

On the computational side several authors have attempted the prediction of the unsteady blade wake characteristics, e.g., [15–20]. Except for Magagnato [20] who uses a non-linear turbulence model, the authors make use of Baldwin-Lomax-type turbulence models or linear k-ε/k-ω-type two-equation models. The wake characteristics are presented in the form of instantaneous contour plots of velocity, total pressure, total temperature, or entropy. Arnone and Pacciani [15], Manna et al. [16] and Sondak [18] calculate also the trailing edge pressure distribution for the blade of Cicatelli and Sieverding [2]. Surprisingly these authors predict not only with fair to good accuracy the time-averaged trailing edge

Contributed by the International Gas Turbine Institute for publication in the JOURNAL OF TURBOMACHINERY. Manuscript received by the IGTI November 16, 2001; revised manuscript received September 25, 2002. Associate Editor: S. Sjolander.

Table 1 VKI cascade characteristics

Chord length c	140 mm
Axial chord length c_{ax}/c	0.656
Pitch to chord ratio g/c	0.696
Blade height h	100 mm
Aspect ratio h/c	0.714
Trailing edge thickness to chord ratio D/c	0.0531
Trailing edge wedge angle δ_{te}	7.5 deg
Stagger angle γ	−49.83 deg

Note: the blade coordinates can be obtained from VKI

pressure distribution but also the vortex shedding frequency. Manna attributes the quality of his results to the ''appropriate resolution of the separating turbulent shear layers;'' but he also insists on the fact that the simulation of the near and far wake development requires second moment closures to describe anisotropy, curvature and rotation effects.

Encouraged by the interesting results obtained at relatively low Mach number, $M_2 = 0.4$ it was decided to extend the experimental investigations into the high subsonic/transonic range. The reasons were manifold.

1. From the base correlation of Sieverding and al. [5], it was known that for blades with small rear suction side curvature like in the present case the base pressure undergoes a sharp drop in the high Mach number range. Why?
2. The higher density variations in the wake would allow a much better description of the wake vortices using interferometric density measuring techniques than at low Mach numbers.
3. Based on some unpublished experiences, it was expected that the pressure fluctuations at the trailing edge would be much larger than at low subsonic Mach numbers.
4. Vortex shedding would occur in a much more narrow frequency bandwidth facilitating thus the phase lock averaging procedure.

2 Experimental Setup

The extension into the high-subsonic/transonic Mach number region required a down-scaling of the blade dimensions by 50% with respect to those of the large-scale blade in Sieverding et al. [21] because of mass flow limitations and a slight increase of the number of blades to cope with the problems of periodicity at this Mach number level. The new test section has four blades of 140-mm chord length and 100-mm blade height. The cascade characteristics are summarized in Table 1.

Figure 1 shows a photograph of the test section setup.

Blade Instrumentation. All pressure measurements are taken on blade position no. 3 in the cascade (counted from the top). Two different blades had to be instrumented to satisfy all instrumentation needs.

Blade A (Fig. 2) is instrumented with 24 static pressure taps on the suction side and 18 on the pressure side. It is further instrumented with a rotating cylinder in the blade trailing edge carrying side-by-side a pneumatic pressure tap and a fast response pressure sensor (Kulite). The openings for the pressure sensing holes on the cylinder are 0.2×0.8 mm each with a corresponding angular extension of 3 deg of the trailing edge circle. The pressure sensor is mounted at a distance of 0.3 mm underneath the trailing edge surface. The rotating cylinder allows the measurement of the trailing edge pressure distribution with a very high spatial resolution. Several models were built to obtain a satisfactory smoothness of the transition from the solid blade to the cylinder. The final blade was equipped with a 10-mm-long cylinder. The thickness of the pressure and suction side lips was 0.02 mm and the width of the annular gap between blade and cylinder was 0.02 mm. Hence the relative height of the backwards-facing steps expressed in percentage of the trailing edge diameter is 0.5% only.

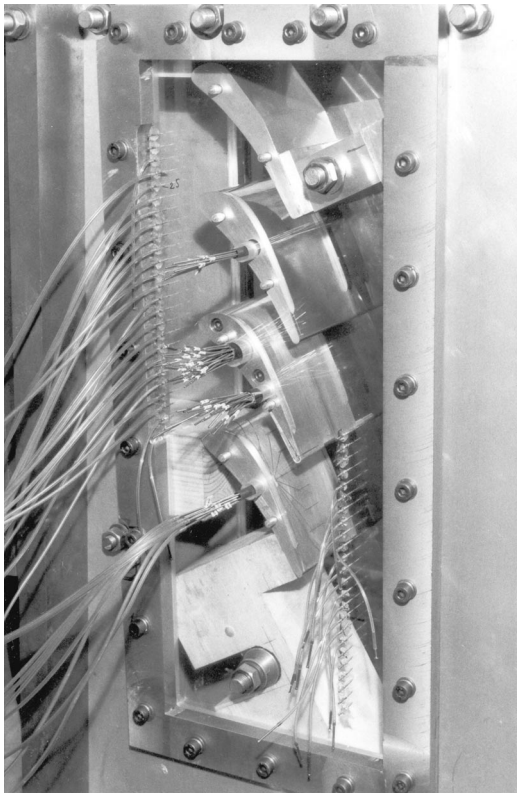

Fig. 1 Photograph of test section

Blade B with a normal trailing edge was instrumented rather coarsely with a total of 20 pressure taps (13 on suction and 9 on pressure side). In addition this blade was fitted with 10 fast pressure sensors. Eight sensors were implemented side-by-side with pneumatic pressure taps on the rear suction side between the throat region and the trailing edge. The other two sensors were positioned on the trailing edge circle on both the pressure and suction side.

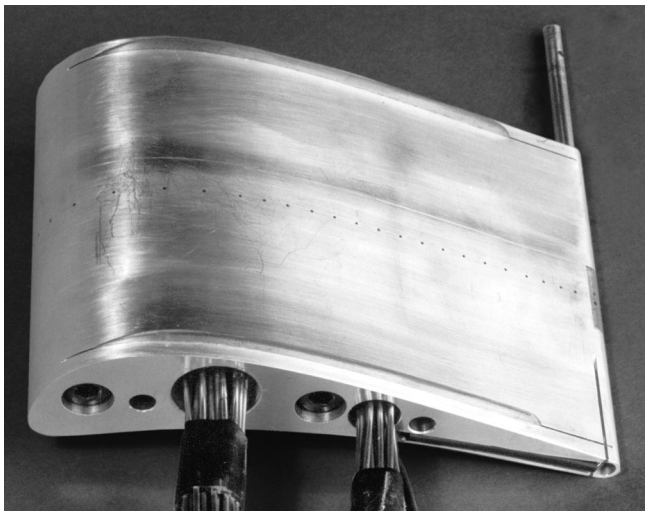

Fig. 2 Blade instrumented with pressure taps and equipped with rotatable trailing edge and boundary layer fences

Table 2 Overall flow conditions

Inlet total temperature T_{01}	280 K
Inlet total pressure P_{01}	1400 mbar
Inlet turbulent intensity TU	1%
Outlet isentropic Mach number $M_{2,is}$	0.79
Reynolds number RE (based on chord and outlet velocity)	2.8×10^6

3 General Flow Conditions

3.1 Inlet/Outlet Flow Conditions. The bulk of the experimental program was performed at the nominal isentropic outlet Mach number $M_{2,is}=0.79$ in a plane situated at a distance $x/c_{ax}=0.5$ from the trailing edge plane, but certain tests covered a wider Mach range. Table 2 presents the flow conditions at the nominal Mach number.

3.2 Two-Dimensionality. Because of the low aspect ratio of $h/c=0.714$, secondary flows may occupy a significant part of the blade span. To limit their influence the blade suction sides are fitted with boundary layer fences, see Fig. 1. The oil flow visualisations in Fig. 3 show the beneficial effect of the fences. The spanwise extension of the secondary flows is reduced by 50% and occupies only 5–7% of the blade height on each side.

3.3 Periodicity. The flow periodicity is controlled by either flexible tailboards attached to the trailing edges of the end blades or by changing the height of the backwards facing step behind these blades. The latter solution, see photograph in Fig. 1, provided the best results at high exit Mach numbers. The periodicity is evaluated also on the basis of the comparison of the blade surface Mach number distribution of blade no. 3 with that of the neighboring blades and from the downstream side-wall Mach number distribution.

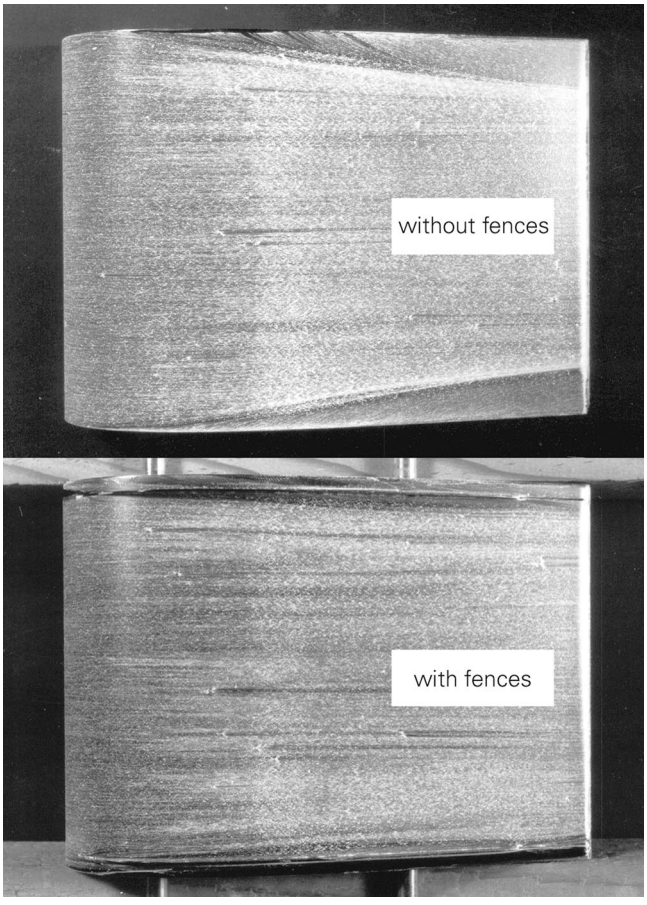

Fig. 3 Oil flow visualization demonstrating effectiveness of boundary layer fences—top: without fences; bottom: with fences

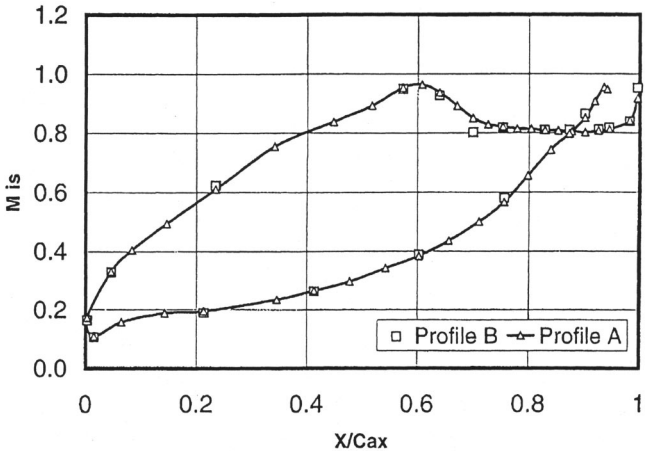

Fig. 4 Blade Mach number distribution at $M_{2,is}=0.79$

In the outlet Mach number range $M_2=0.8$ to 1.0 the downstream Mach number distribution varied over two pitches by less than $\pm2\%$. The mean blade-to-blade surface Mach variation of $\Delta M=0.027$ is judged satisfactory for such a small number of blades.

4 Steady-State Blade Velocity Distributions and Boundary Layer Characteristics

4.1 Blade Velocity Distribution. The blade surface velocity distribution at the nominal outlet Mach number $M_{2,is}=0.79$ is presented in Fig. 4 in the form of the local isentropic Mach number distribution in function of the axial chord x/c_{ax}. The figure contains data from both blades A and B. The agreement is overall excellent with the exception of one point at $x/c_{ax}\cong0.7$ on the blade suction side. The flow accelerates continuously along the suction side until it reaches its maximum value at $x/c_{ax}=0.60$ in the throat region, the geometric throat on the suction side being positioned at $x/c_{ax}=0.61$. The maximum blade velocity reaches with $M_l=0.97$ nearly sonic conditions. The maximum velocity is followed by a rather strong deceleration and a constant Mach number plateau of $M_l=0.8$ extending from $x/c_{ax}=0.75$ up to the beginning of the trailing edge circle where the flow re-accelerates before it separates from the trailing edge surface. The velocity plateau is explained by the fact that the blade is designed with a straight rear suction side from halfway down the throat to the trailing edge. On the pressure side the flow accelerates continuously from the leading edge to the trailing edge. The crossing of the pressure and suction side curves near the trailing edge is typical for blades with straight rear suction side.

4.2 Boundary Layer Characteristics. Boundary layer profiles were measured with a flattened pitot probe of 0.25 mm probe head thickness at a distance equal to one trailing edge diameter up-stream of the trailing edge circle. The uncertainty of the probe positioning is ±0.05 mm.

The boundary layer profiles for nominal outlet flow conditions are presented in Fig. 5. The physical boundary layer thickness is about 2.2 mm on the suction side and 0.7 mm on the pressure sides. The compressible shape factor is, respectively, $H=1.31$ and 1.53 for the suction side and pressure side. This is a clear indication for a turbulent state of the boundary layer on both sides before trailing edge separation.

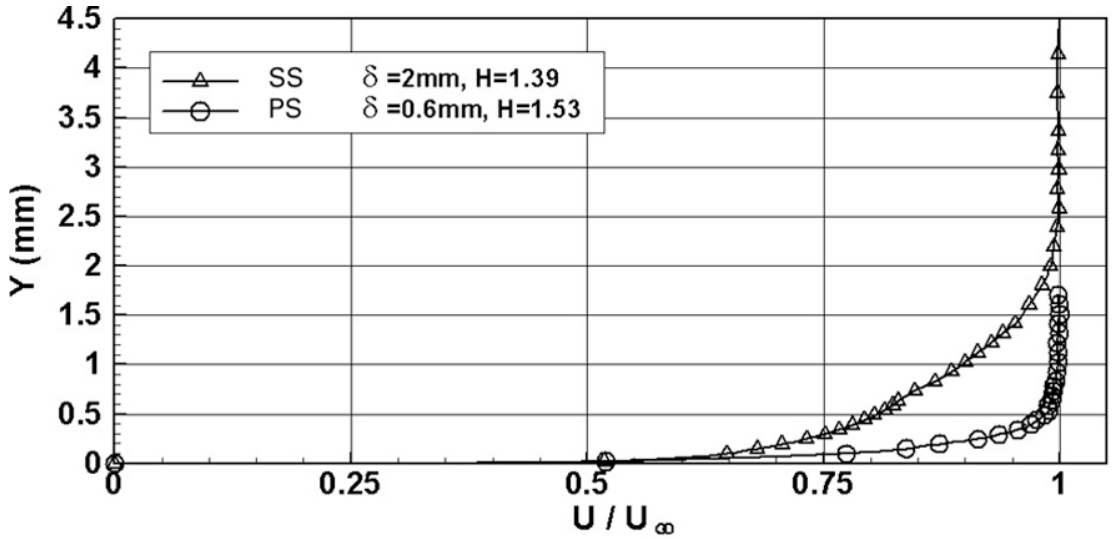

Fig. 5 Boundary layer profiles at trailing edge

5 Vortex Shedding Frequency

The vortex shedding frequency was measured with a fast response pressure sensor positioned at $x/c_{ax}=0.933$ at the beginning of the pressure side trailing edge circle. This position is in the area where the flow separates from the surface and where pressure fluctuations were expected to be particularly large. The sampling frequency for all unsteady tests was set at 300 kH and 65,536 samples were acquired. A typical FFT showing the dominant vortex shedding frequency and 4 harmonics is shown in Fig. 6. The evolution of the Strouhal number characterising the periodic vortex shedding is presented in Fig. 7 for the Mach range $M_{2,is}=0.38$ to 1.0. The Strouhal number is defined as

$$\mathrm{St}=(f\cdot D)/U \tag{2}$$

where U is derived from the pitch averaged downstream side wall pressure distribution taken at a trailing edge distance $x/c_{ax}=0.2$ and the upstream total pressure. The Strouhal number decreases linearly from $\mathrm{St}=0.27$ at $M_{2,is}=0.38$ to a plateau of $\mathrm{St}\cong 0.219$ between $M_{2,is}=0.7$ and 0.9 before rising again to a value of $\mathrm{St}=0.26$ at $M_{2,is}=1.0$. The decrease of St with Mach number in the subsonic range is likely due to a change of the blade boundary layer characteristics. Because of the suction side velocity peak in the throat region and the following strong deceleration the suction side boundary layer at the trailing edge may be assumed turbulent over a large subsonic Mach number range. The situation on the pressure side is different. Apart from a short nearly flat velocity distribution on the front pressure side the flow is constantly accelerated up to the trailing edge. At low Mach numbers, and therefore low Reynolds numbers, the pressure side boundary layer is likely to be in a laminar or transitional state while the boundary shape factor measured for the nominal outlet Mach number $M_{2,is}=0.79$ points clearly to a turbulent state. Previous research work by Sieverding and Heinemann [22] confirms the dependence of the Strouhal number on the state of the boundary layer. The value of $\mathrm{St}=0.219$ between $M_{2,is}=0.7$ and 0.9 are a clear indication of a turbulent boundary layer state on both the suction and pressure sides. From previous experience it also appeared that the periodicity of the vortex shedding process was particularly good in case of a turbulent boundary layer separation from both blade surfaces. Transitional boundary layers appear to deteriorate the periodicity of the vortex shedding. In such cases the narrow frequency spectrum with a strong dominant frequency, characteristic for fully turbulent boundary layers, gives way to a rather broad frequency spectrum which makes phase-lock averaging a rather hazardous undertaking. It is for this reason that it was decided to perform the bulk of the experiments at the outlet Mach number $M_{2,is}\cong 0.8$. The exact Mach number value turned out to be 0.79.

The increase of the Strouhal number in the transonic range in Fig. 7 is well known from the literature [12]. The explanation is that the characteristic distance is in reality not the trailing edge

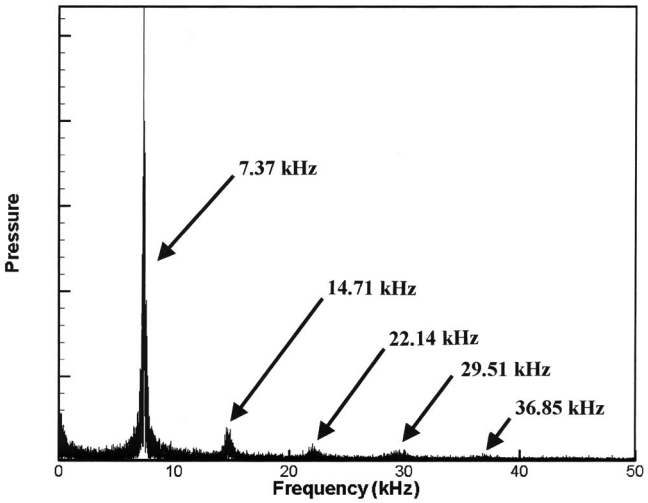

Fig. 6 Typical FFT of fast response pressure transducer near pressure side boundary layer separation point

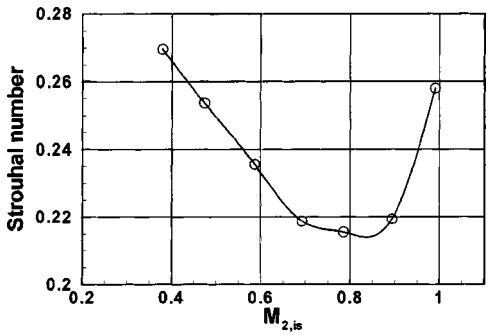

Fig. 7 Strouhal number in function of outlet Mach number

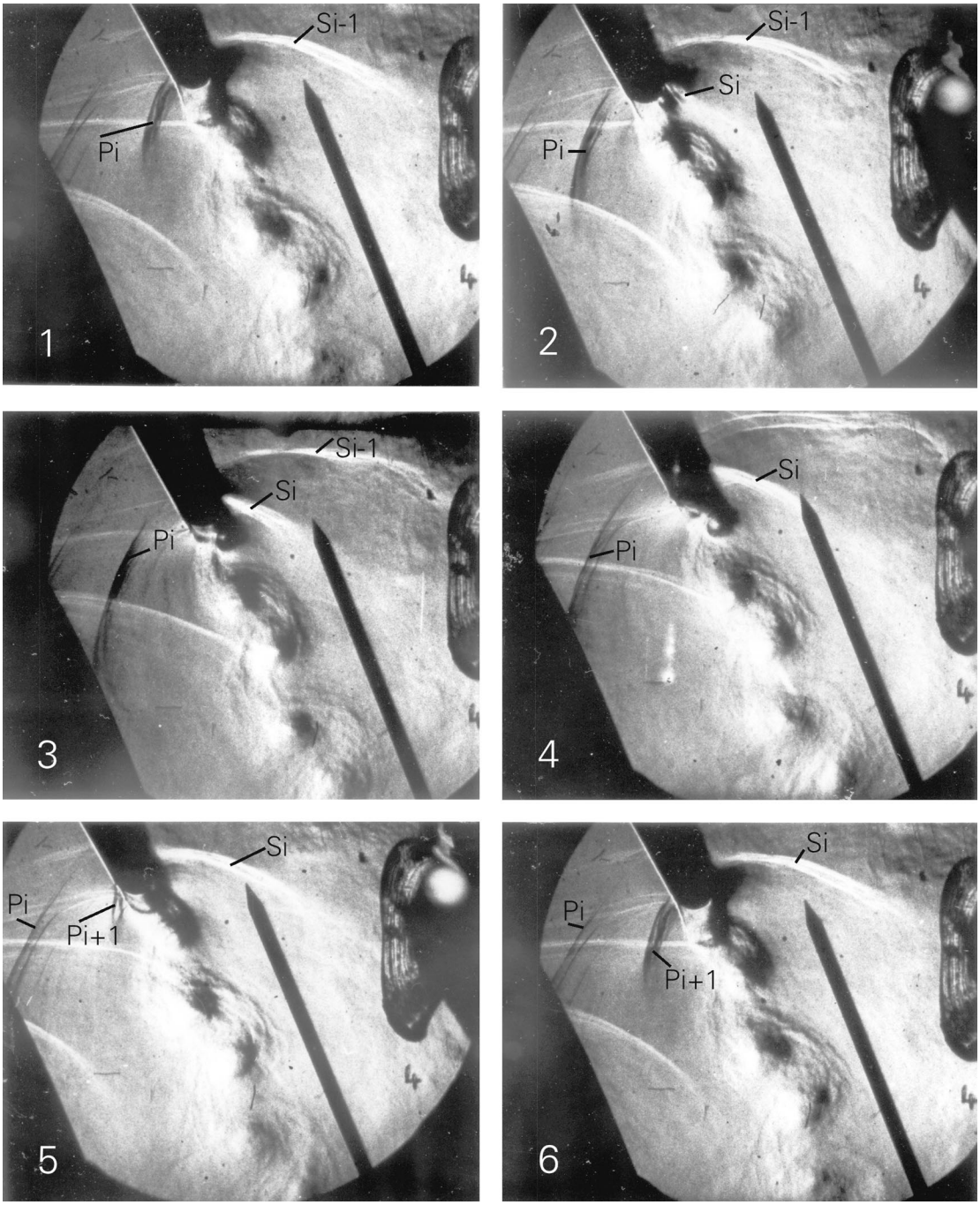

Fig. 8 Schlieren photographs for one vortex shedding cycle at $M_{2,is}=0.79$

distance, but the distance between the two boundary layer separation points on the trailing edge. For subsonic outlet flow conditions the position of the boundary layer separation point does not change significantly. However, at transonic outlet Mach numbers the trailing edge base region changes gradually from an open unstable base flow region with the appearance of strongly oscillating normal trailing edge shocks to a closed triangular region bordered by stable shear layers and oblique shocks originating from the region of confluence of the two shear layers. This gradual change is accompanied by a significant angular displacement of the boundary layer separation points around the trailing edge and therefore by a decrease of the characteristic dimension for the vortex shedding frequency. It is worthwhile mentioning that even with fully established supersonic flow conditions at the trailing edge, von Karman vortices may originate from the region of the confluence of the shear layers [11].

6 Wake Flow Visualizations

6.1 Schlieren Photographs. High-speed schlieren visualizations were taken using a continuous light source and a CORDIN 350 high-speed rotating drum and rotating prism camera with a maximum framing rate of 35,000 frames per second from ONERA. The time exposure is 750 ns with a time interval between two successive images close to 28.5 μs. Figure 8 shows a sequence of six schlieren photographs, taken at the nominal Mach

number of $M_{2,is}=0.79$. The sixth photograph repeats the first one. The figure shows the rear part of blade 3 and to the left of it the suction side of the neighboring blade 4. Hence the left side of blade 3 is the pressure side, the right side the suction side. A long needle probe is inserted into the flow on the right side of the wake to monitor the fluctuating pressure.

The schlieren pictures show impressively the formation and the evolution of vortical flow patterns in the blade wake. Besides the vortex structures the pictures show also the presence of acoustic pressure waves. The acoustic waves are directly linked to the oscillation of the separating shear layers. The waves are generated by the outward motion of the separating shear layers. The outward motion of the shear layer is in turn caused by a pressure rise in the separated zone next to the separating shear layer.

In image 1, the suction side shear layer has reached its farthest inward position and the local pressure just up-stream of the separation point has reached its minimum value. On the pressure side the separating shear layer has reached its most outward position. A pressure wave P_i originates from the point where the boundary layer separates from the trailing edge. In image 2, the suction side shear layer starts to move outward generating a weak pressure wave S_i that interferes with the needle probe stem a few millimetres downstream of the conical probe head. The pressure wave S_{i-1} up-stream of the probe head, generated during the preceding vortex shedding cycle, was already present in image 1 and has moved upstream. In image 3, the pressure wave S_i swings forward and interferes with the conical probe head, it reaches the probe nose in image 4 and is positioned upstream of it in image 5. As regards the position of the shear layers, the suction side shear layer is near its most outward position in image 4, while on the pressure side the shear layer is at its most inward position at this instant in time. From here on, the suction side shear layer moves inward and the pressure side shear layer outward.

The pressure wave generated by the outward motion of the pressure side shear layer appears the first time in image 5 (denoted as P_{i+1}). The same image shows also the presence of a pressure wave generated during the preceding vortex shedding cycle. This wave extends from the rear blade pressure side across the channel to the suction side of the neighboring blade from where it is reflected. Most images show in fact two reflected waves from two successive vortex-shedding cycles. It can therefore be expected that the suction side pressure distribution in the throat region is highly unsteady.

The observation of the pressure side shear layer shows very clearly the enrolment of the shear layer into a vortex, images 3 and 4, and the growing and shedding process of the vortex, images 5 and 1. A comparison with the schlieren visualisations obtained for the same profile at $M_{2,is}=0.4$ by Cicatelli and Sieverding [2], shows that the vortex formation in the present high subsonic test occurs at much closer distance from the trailing edge.

6.2 Holographic Interferometry. Holographic interferometry density measurements give further information on the formation and the shedding process of the von Karman vortices. A detailed description of the holographic interferometry technique used in these experiments is given in Sieverding et al. [21]. For the recording the laser light of a ruby laser is split into a reference beam passing outside the test section and an objective beam passing through the test section. The two beams are recombined on a photographic plate. Two exposures are recorded on the same plate: one exposure with the tunnel at rest, the other with the tunnel running. An He-Ne laser is used for reconstruction of the hologram after the development of the film.

Figure 9 presents a sequence of four interferograms taken with the double exposure holographic interferometry technique at four different phase angles of a vortex shedding cycle. Each image shows 4 to 5 density islands with closely spaced iso-density contours. The centers correspond to the vortex cores and coincide with a minimum in the static pressure. The pictures are taken randomly. To put them into the right sequence the most simple way is to follow the position of the suction side pressure wave, generated by the oscillating motion of the suction side separating shear layer (see also Fig. 8). The position of the pressure wave is taken with respect to the needle probe positioned on the right side of the wake. The exact value of the phase angle of each randomly taken hologram can be evaluated from a specific pressure signal acquired during the recording of the hologram. In general preference is given to the recording of the pressure variation with a sensor positioned at the beginning of the pressure side trailing edge circle (Kulite 8 at $x/c_{ax}=0.933$, Fig 14).

Image A is taken during the early formation of the pressure side trailing edge vortex; i.e., the local static pressure is dropping, the shear layer is moving inward and starts rolling up into a vortex. On the suction side the local trailing edge pressure is rising, the vortex is fully formed and starts to move away from the trailing edge. The supply of circulation in the upstream shear layer feeding the suction side vortex will be gradually cut off by the growing pressure side vortex that entrains fluid from the suction side shear layer. The suction side vortex enters the shedding phase of the vortex cycle (see Gerrard [23], for description of vortex formation mechanism).

In image B, the pressure on the pressure side continues to fall and the pressure side vortex continues to grow. At present it has entrained so much fluid from the opposite shear layer that the suction side vortex is nearly fully separated from the trailing edge, see pinch point of density lines.

In image C, the roles start to inverse. On the pressure side the vortex formation is completed, the iso-density lines show clearly the existence of a vortex center which is on the point of moving away from the trailing edge while on the suction side a new pressure minimum is forming announcing the formation of a new vortex. In image D, the separation of the pressure side vortex is nearly completed while on the suction side the vortex formation approaches the culminating point.

The density change between two successive density lines is $\Delta\rho/\rho_0=0.0185$. All holograms show a large number of iso-density lines ending on the trailing edge circle. This is an indication that under unsteady flow conditions there does not seem to exist any extended isobaric region, as one would expect for a large separated flow zone.

All interferograms show that the wake unsteadiness does not only influence the blade trailing edge region, but also the blade suction side. Pressure waves generated by the outward swing of the suction side shear layer propagate upstream along the suction side, while the corresponding waves generated on the pressure side reach the suction side of the neighboring blade across the throat.

Comparing the four interferograms in Fig. 9 reveals significant differences in shape and intensity of the vortices. To extract reliable phase-averaged quantitative information from interferometric density measurements requires a large amount of randomly taken photographs.

7 Steady and Unsteady Trailing Edge Pressure Distribution

Flow visualizations and interferometric measurements demonstrate very impressively the unsteady wake flow character, but their spatial resolution is still insufficient to give a full account of what happens right at the trailing edge. The rotating trailing edge cylinder device, Fig. 2, developed at VKI for detailed measurements of the trailing edge pressure distribution is therefore most valuable.

The angular displacement of the pressure sensor and the pneumatic pressure tap, implemented side-by-side on the trailing edge cylinder, from the suction side lip to the pressure side lip covers an angle range of 173.34 deg. This angle range is very close to the design value of 172.5 deg (trailing edge wedge angle $\delta_{te}=7.5$ deg). Data were taken both in a step-by-step procedure with

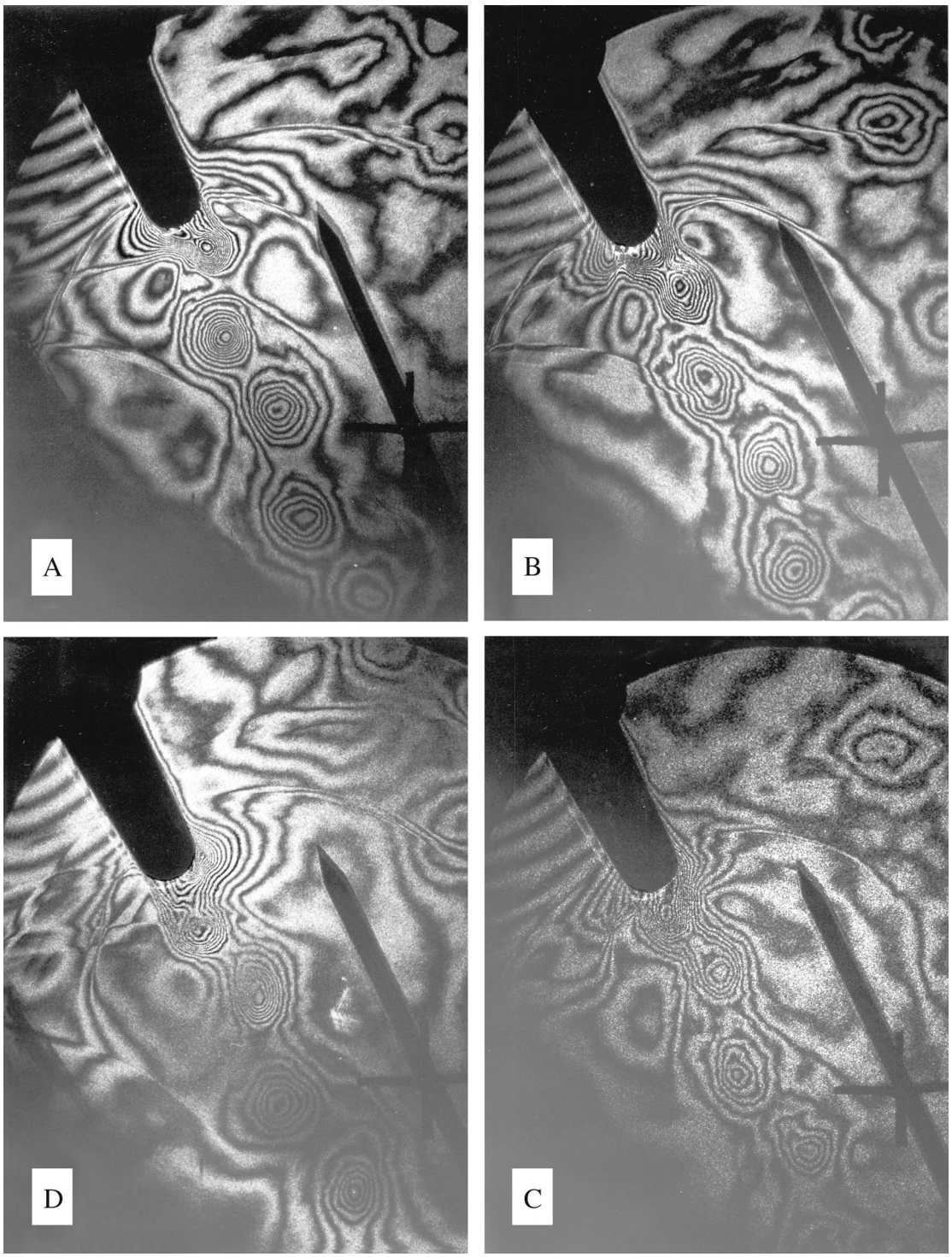

Fig. 9 Interferograms taken at four different phase angles of the vortex shedding cycle, $M_{2,is}=0.79$

fixed annular displacements and with a continuously slowly rotating trailing edge cylinder. For unsteady pressure measurements with the fast response pressure sensor the data were acquisitioned at a rate of 300 kHz.

7.1 Steady-State Pressure Distribution. Figure 10 shows a comparison of the trailing edge pressure distribution measured on one side with the pneumatic pressure tap in a step-by-step procedure and on the other side with the fast response pressure sensor during a continuous rotation of the TE cylinder through the entire angle range. The pressure sensor signal was low-pass filtered at 100 Hz. The data from the two measuring devices are overall in very good agreement. The pressure distribution is characterized by three pressure minima: the two pressure minima associated with the overexpansion of the suction and pressure side flow before separation from the trailing edge and an additional minimum around the center of the trailing edge circle. The pressure minima near the separation points are respectively $P/P_{01}=0.525$ at -73 deg for the pressure side and $P/P_{01}=0.52$ at $+85$ deg on the suction side, i.e., the local trailing edge surface Mach numbers before separation are close to 1. The separation region on the

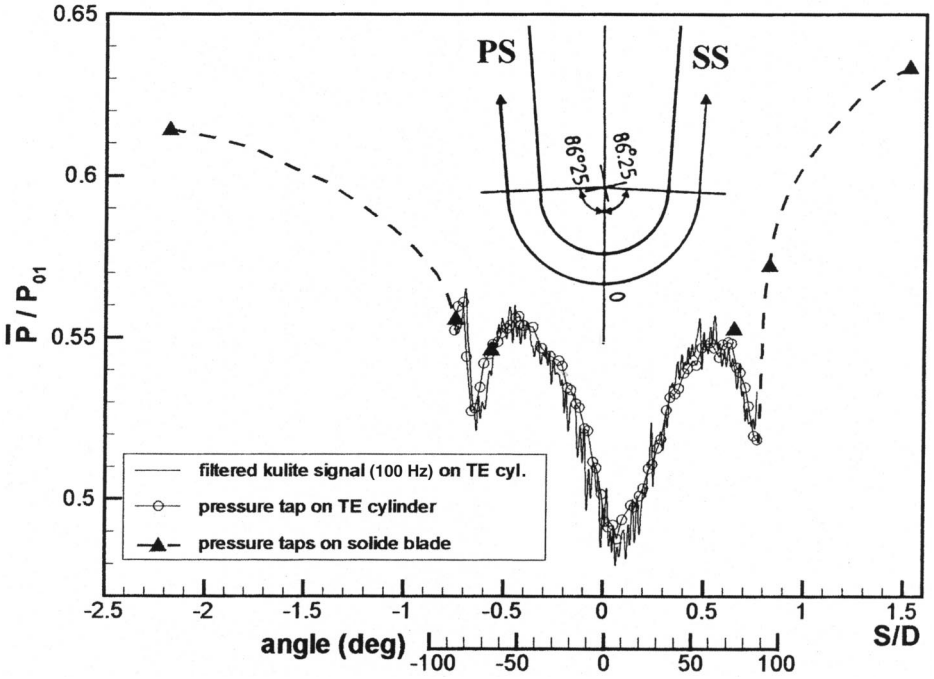

Fig. 10 Steady-state trailing edge pressure distribution

pressure side occurs later than on the suction side. This is possibly due to the blade circulation. In spite of a difference of 12 deg in the angular position of the pressure minima it is worth noting that the pressure minima are of the same order of magnitude. The reason is probably to look for in the upstream effect exerted by the trailing edge acceleration on the oncoming boundary layer causing its thinning and changing thus the effective flow turning angle. Because of the thicker suction side boundary layer this ''induced'' curvature effect is bigger on the suction side.

At low and medium subsonic outlet Mach numbers these overexpansions are followed by a pressure rise to a pressure plateau extending over the largest part of the trailing edge annular sector as, e.g., demonstrated by Cicatelli and Sieverding [2]. The existence of such a pressure plateau at the trailing edge is in line with the general assumption of an isobaric dead air region at the base of the trailing edge. The present tests show that the situation dramatically changes at high subsonic Mach numbers. As shown in the flow visualizations and interferograms the enrolment of the separating shear layers into a vortex occurs right at the trailing edge, the vortex core approaches the wake centerline and its distance to the trailing edge is less than half the trailing edge diameter. Consequently, the typical iso-baric region has given way to a zone characterized by a strong drop of the static pressure from values of respectively $P/P_{01}=0.551$ at -50 deg on the pressure side and $P/P_{01}=0.55$ at $+60$ deg on the suction side to a pressure minimum of $P/P_{01}=0.485$ at $+7$ deg. This departure from the generally assumed isobaric trailing edge base region explains possibly differences of base pressure data published by different authors at high subsonic/transonic Mach numbers. The base pressure measured with a single pressure tap at the trailing edge center depends obviously on the ratio of the sensing hole to the trailing edge diameter.

Figure 10 presents in addition to the trailing edge pressure distribution measured on the trailing edge cylinder some measurements taken on the solid blade (triangular symbols). On the pressure side the agreement is very good. The comparison also shows that the first two pressure side points on the cylinder should obviously be disregarded and is undoubtedly due to the small imperfection in the transition from the solid blade onto the cylinder. On the suction side the pressure measured at $+75$ deg on the solid blade is slightly higher than on the corresponding value on the cylinder but the difference is only 0.7% of the total pressure.

7.2 Unsteady Pressure Distribution. Figure 11 shows the non-dimensionlised raw pressure trace from the fast response pressure sensor on the trailing edge cylinder recorded at300 kHz and, superimposed to it, the same signal filtered at 100 Hz. The amplitudes of the pressure fluctuations are impressive. On the pressure side the fluctuations reach a maximum at around -50 to -60 deg of the trailing edge angle, on the suction side at around 60 to 70 deg. The positions of maximum fluctuations on each side correspond approximately to the position of a local maximum in the time averaged pressure distribution. Towards the trailing edge center the fluctuations decrease considerably.

The maximum peak-to-peak amplitudes ΔP derived from the phase lock averaged signal are of the order of 100% of the downstream dynamic head $(P_{01}-P_2)$, Fig. 12, and drop to 20% at the trailing edge center. The pressure oscillations are of course closely

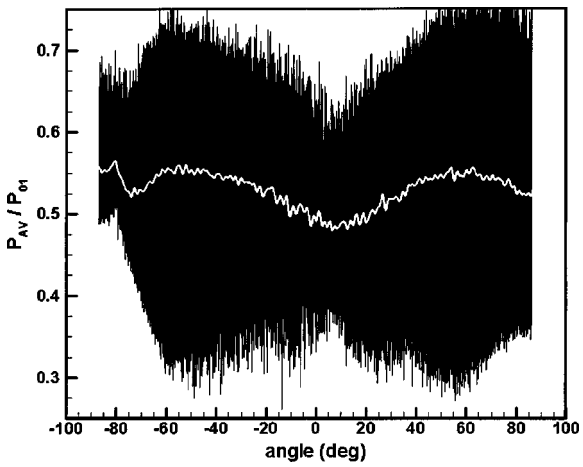

Fig. 11 Unsteady trailing edge pressure distribution recorded at 300 kHz

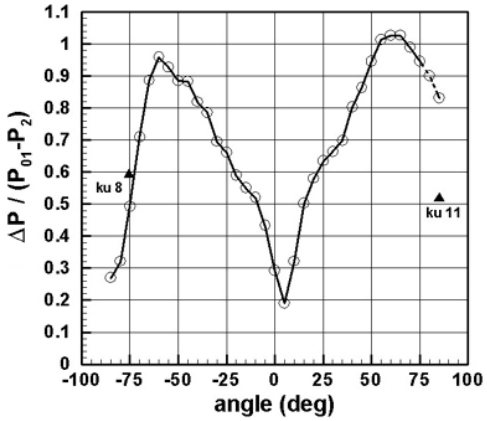

Fig. 12 Phase-lock-averaged pressure amplitudes around trailing edge

linked to the change of the boundary layer separation points between the positions reached for the farthest inward and the farthest outward motion of the free shear layer. The highest fluctuations occur just beyond the most downstream separation point. The minimum isentropic local Mach number for the farthest inward sweep of the free shear layer can be as high as $M_l = 1.25$. It may be assumed that the curvature-driven supersonic trailing edge expansion is the real cause for the formation of the vortex so close to the trailing edge, with entrainment of high-speed free-stream fluid into the trailing edge base region, which in turn changes the previous (i.e., at low and medium exit Mach numbers) iso-baric dead air region into a trailing edge base region with a strong nonuniform base pressure distribution characterized in particular by a pressure minima at the trailing edge center.

The pressure waves induced by the oscillating shear layers travel further upstream, but they are much weaker than the pressure changes related to the displacement of the boundary layer separation points.

The graph contains also two data points (triangles) from fast response pressure sensors on blade B with a solid trailing edge. On the pressure side the agreement from the two different models is very good, while a relative large discrepancy is observed on the suction side. By comparison with the pressure side one would have expected a much faster drop in the pressure amplitudes for the last points to the right. It is not excluded that the backwards-facing step and the small gap at the transition from the solid blade to the trailing edge cylinder could have a non-negligible effect on the pressure fluctuations in the last two points which are only 0.4 and 0.1 mm away from the lip, although this did not seem to be the case for the mean pressure.

Figure 13 shows the phase-lock averaged pressure signals for the angular positions -60 and $+40$ deg on the trailing edge circle. The signals were obtained using the wavelet analysis technique. A pressure drop indicates an acceleration of the flow around the trailing edge, i.e., the separating shear layer moves inwards, the vortex be in its formation phase. The following pressure rise causes the shear layer to sweep outwards; the vortex is in its shedding phase. Both curves indicate that the pressure variation over one cycle is not sinusoidal. In fact the pressure rise time is on both trailing edge sides shorter than the pressure fall time. Hence, the vortex formation time is longer than the vortex shedding time. This observation is also confirmed by the pressure signals from Kulites 8 and 11, positioned at the trailing edge angles -74.5 and $+85$ deg, respectively, on blade B with a solid trailing edge. The simultaneous recording of the pressures of Kulites 8 and 11 show that they are 180 deg out of phase.

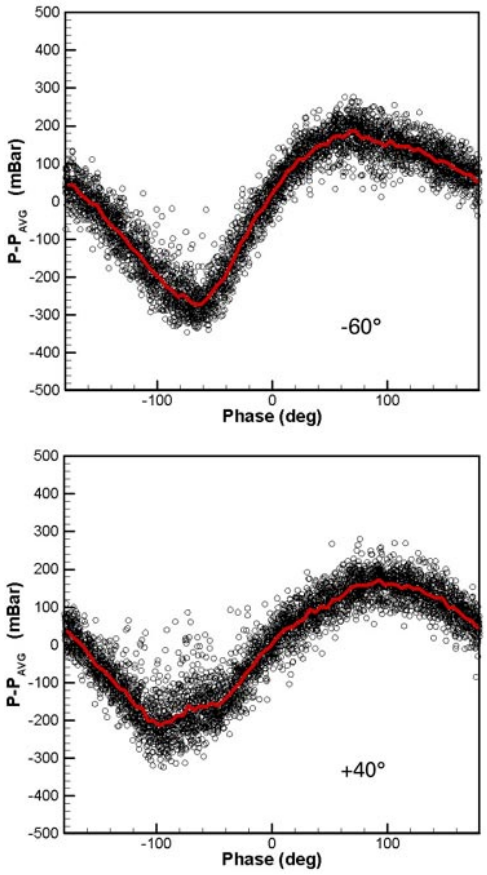

Fig. 13 Unsteady pressure variations along rear blade suction side

8 Effect of Wake Unsteadiness on Suction Side Pressure Distribution

In the discussion of the schlieren photographs and the interferograms it was pointed out that the wake unsteadiness is not limited to the blade trailing edge region, but also affects the blade suction side from the throat region down to the trailing edge. This unsteadiness was measured with fast response pressure sensors implemented on the suction side as shown in Fig. 14. An additional sensor is inserted on the pressure side trailing edge circle. Table 3 shows positions of transducers.

1. The throat on the blade suction side is positioned at $x/c_{ax} \cong 0.61$.
2. The transducers 11 on the suction side and 8 on the pressure side are situated at the trailing edge angle $+85$ and -74.5 deg, respectively, where the zero-angle is defined by the intersection of the tangent to the blade camberline with the trailing edge circle.

Details of the time varying pressure variations on the rear blade surface are presented in Fig. 14 for the case of the nominal outlet Mach number $M_{2,is} = 0.79$. Kulite 1 positioned slightly upstream of the throat and before the peak of the suction Mach number distribution (see Fig. 4) does not sense any pressure fluctuations induced by the trailing edge vortex shedding. At Kulite 2 in the throat area and at Kulite 3 slightly downstream of it, the fluctuations are not only important, but show a very distinct asymmetric behavior with a very fast pressure rise time followed by a slow pressure drop. This is particular the case for Kulite 3. (Note that the superimposed high-frequency small-pressure fluctuations of about 100 kHz correspond to the resonance frequency of the line-cavity-type implementation of the transducer.) The sharp pressure rise is due to the pressure wave P_i—see schlieren photograph in Fig. 8—that is caused by the oscillation of the separating shear

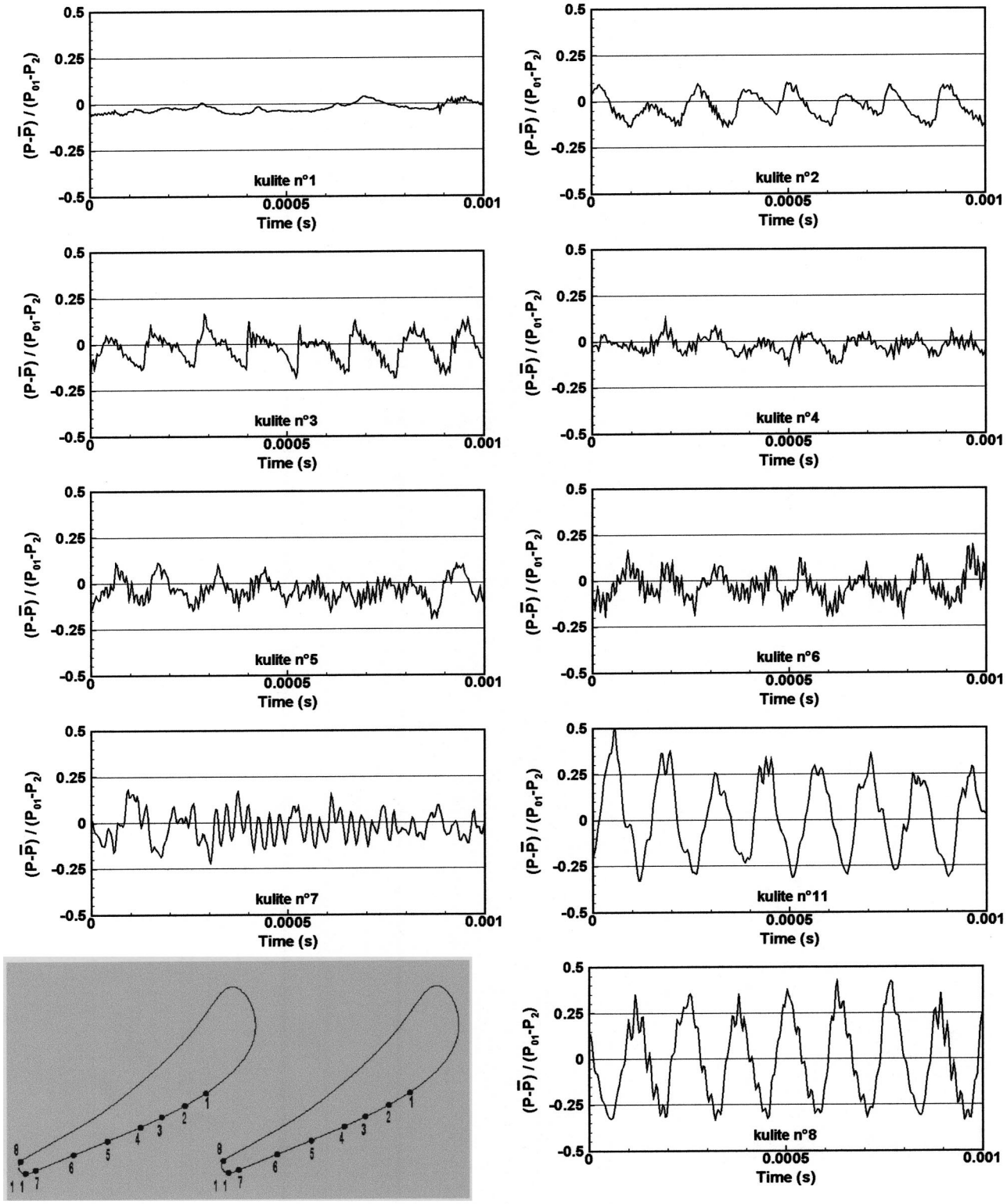

Fig. 14 Phase-locked average pressure variation at −60 and +40 deg trailing edge angle

layer from the neighboring blade pressure side and sweeps across the pressure sensor. This pressure wave appears first as a strongly backwards bent curve in the upper two schlieren photographs in Fig. 8. In pictures 3 and 4 of Fig. 8, the pressure wave starts to move upstream. Its rear part extends gradually to the suction side, straightens out and hits the suction side somewhere between the pressure sensors 3 and 4. After passing successively across the sensors 3 and 2 the pressure wave quickly looses intensity.

The pressure variations for the sensors 4, 5, and 6 are characterized by a more sinusoidal shape. This is also confirmed by the results of phase locked averaging data processing. These fluctuations are most likely caused by the downstream traveling wake

Table 3 Position of pressure sensors (Kulite) on blade surfaces

	Suction side								Pressure side
Kulite	1	2	3	4	5	6	7	11	8
x/c_{ax}	0.573	0.639	0.699	0.753	0.828	0.901	0.982	0.994	0.933
x/c	0.326	0.410	0.494	0.575	0.695	0.814	0.948	0.983	0.973

vortices of the neighboring blade. As regards sensor 7 situated slightly upstream of the trailing edge, the periodicity of the raw signal appears very poor and only a phase-lock averaging procedure provides useful information on its periodic character. The reason is most probably to look for in the interference of pressure waves induced by the wake vortices of the neighboring blade on one side and the pressure wave generated by the oscillating suction side shear layer of the blade under consideration on the other side. The situation then changes dramatically at the beginning of the trailing edge circle where the sensor 11 under the direct influence of the oscillating shear layer records a very strong and highly periodic pressure signal. Similar as in Fig. 13, the signal is slightly asymmetric. The pressure rise shows a steeper slope than the pressure fall. This is also the case for the sensor 8 on the trailing edge pressure side.

The pressure traces for both sensors 11 and 8 are characterized by nearly constant minima values. Their position on the trailing edge circle is such that the boundary layer separation points sweep across the sensing holes at Mach numbers higher than 0.7. Once the separation point has moved past the sensing hole, the pressure at the sensing hole has reached its lowest value. A further shift of the separation point around the trailing edge does not continue to affect the sensor.

9 Conclusions

The high-speed cascade program has produced some remarkable results concerning the significance of the trailing edge vortex shedding for both the steady and unsteady trailing edge and blade flow characteristics. The success of the program is partially due to the experience gained in a previous BRITE-EURAM project concerning the investigation of time varying wake characteristics behind turbine blades at moderate subsonic outlet Mach numbers. The previously developed technique of a rotatable trailing edge for a large-scale nozzle guide vane with a chord length of 280 mm was successfully applied to a 50% scaled-down version of the same profile.

In a certain sense the high Mach number tests proved to be easier than the previous low Mach number tests because of the remarkable periodicity of the vortex shedding process. The reason for the highly periodic character of the vortex shedding is most probably linked to the existence of fully turbulent boundary layers before separation at the trailing edge.

The most remarkable result is the observation that for the investigated blade profile the traditionally accepted isobaric trailing edge base flow region ceases to exist at high subsonic Mach numbers and gives way to a highly nonuniform time-averaged base pressure distribution with a pronounced pressure minimum at the trailing edge center. The reason is the formation of the vortices at such short distance from the trailing edge that they occupy alternatively the entire base region. It may be assumed that this flow feature will prevail until the formation of a closed near-wake region with the establishment of an oblique trailing edge shock system at the confluence of the pressure and suction side shear layers is completed. High-speed schlieren photographs and interferometric density measurements proved to be invaluable techniques for the interpretation of the results. The driving mechanism for the strong drop of the base pressure at high subsonic/transonic Mach numbers is the curvature driven supersonic trailing edge expansion of the unsteady trailing edge flow which exceeds by far that of the steady trailing edge flow.

The effect of the wake vortices is not limited to the trailing edge region, but affects the entire rear blade suction side. However, the shape of the time varying pressure distributions changes considerably between the throat and the trailing edge depending on whether they are dominated by the pressure wave induced by the oscillating separating pressure side shear layer or by the downstream traveling wake vortices.

In the introduction of the paper it was clearly stated that the purpose of this paper was to explain the sudden base pressure drop in the high subsonic/transonic range for blades designed with a low rear suction side curvature. Obviously, it would be wrong to conclude now that all blades exhibit a strong nonisobaric trailing edge dead air region at high subsonic/transonic flows as observed in the present case. To which degree the generally observed isobaric base pressure region at low Mach numbers gives gradually way to a nonisobaric region with increasing Mach number will depend on the rear suction side curvature of the blades. In fact, it is reasonable to assume that there exists a direct relation between the base pressure coefficient, the formation length of the trailing edge vortices and the deviation from an isobaric base flow region. Consequently, it can be expected that blades with high rear suction side curvature, and hence relatively high base pressure coefficients (as certified by base pressure correlations), are characterized by a rather long formation of the trailing edge vortex and hence a base flow region which differs only little from an isobaric one. It would be nevertheless desirable to confirm this through a similar experimental investigation on blades with a higher rear suction side curvature typical for optimum high subsonic blade design, and moreover to extend the present investigations to transonic/supersonic outlet Mach numbers.

Acknowledgments

This research was carried out under contract for the European Commission as part of the Industrial & Materials Technology Programme (BRITE EURAM III) project CT96-0143 on ''Turbulence Modelling of Unsteady Flows in Axial Turbines (TURMANS FLAT).'' The authors which to acknowledge their financial contribution.

Nomenclature

C_p = base pressure coefficient
c = chord length
D = trailing edge diameter
g = pitch
H = boundary layer shape factor
h = blade height
M = Mach no.
o = throat
P = static pressure
P_{01} = total pressure
RE = Reynolds no. based on chord and downstream velocity
s = streamline coordinate
St = Strouhal no. based on trailing edge diameter and downstream velocity
T_{01} = total temperature
TU = turbulent intensity
U = velocity
x = coordinate

Y = total pressure loss coefficient
δ = boundary layer thickness
δ_{te} = trailing edge wedge angle
ζ = kinetic energy loss coefficient
γ = stagger angle (resp. axial direction)

Subscripts

ax = axial
1 = upstream
2 = downstream
∞ = freestream

References

[1] Ubaldi, M., and Zunino, P., 1999, ''An Experimental Study of the Unsteady Characteristics of the Turbulent Wake of a Turbine Blade,'' *4th Int. Symp. Engineering Turbulence Modeling and Measurements*, Ajaccio.

[2] Cicatelli, G., and Sieverding, C. H., 1997, ''The Effect of Vortex Shedding on the Unsteady Pressure Distribution around the Trailing Edge of a Turbine Blade,'' ASME J. Turbomach., **119**(4), pp. 810–819.

[3] Traupel, W., 1997, *Thermische Turbomaschinen*, Erster Band, Springer.

[4] Denton, J. D., 1993, ''Loss Mechanisms in Turbomachines,'' ASME J. Turbomach., **115**(4), pp. 621–656.

[5] Sieverding, C. H., Stanislas, M., and Snoeck, J., 1980, ''The Base Pressure Problem in Transonic Turbine Blades,'' ASME J. Eng. Power, **102**(3), pp. 711–718.

[6] Xu, L., and Denton, J. D., 1988, ''The Base Pressure Loss of a Family of Four Turbine Blades,'' ASME J. Turbomach., **110**(1), pp. 9–17.

[7] Jouini, D. B. M., Sjolander, S. A., and Moustapha, S. H., 2000, ''Aerodynamic Performance of a Transonic Turbine Cascade at Off-Design Conditions,'' ASME Paper No. 2000-GT-0482

[8] Han, L. S., and Cox, W. R., 1983, ''A Visual Study of Turbine Blade Pressure Side Boundary Layer,'' ASME J. Eng. Power, **105**(1), pp. 47–52.

[9] Lawaczeck, O., and Heineman, J., 1975, ''von Karman Vortex Street in the Wake of Subsonic and Transonic Blades,'' AGARD-CP-177, *Unsteady Phenomena in Turbomachinery*, Paper 28.

[10] Heinemann, J., and Bütefisch, K. A., 1997, ''Determination of the Vortex Shedding Frequency of Cascades with Different Trailing Edge Thicknesses,'' AGARD-CP-227, *Unsteady Aerodynamics*, Paper 11.

[11] Carscallen, W. E., Feige, H. U., and Gostelow, J. P., 1996, ''Transonic Turbine Vane Wake Flows,'' ASME Paper No. 96-GT-419

[12] Cicatelli, G., and Sieverding, C. H., 1996, ''A Review of the Research on Unsteady Turbine Blade Wake Characteristics,'' AGARD-CP-571, *Loss Mechanisms and Unsteady Flows in Turbomchines*, Paper 6.

[13] Desse, J. M., 1998, ''Effect of Time Varying Wake Characteristics Behind Flat Plates,'' AIAA J., **36**(11), pp. 2036–2043.

[14] Carscallen, W. E., Currie, T. C., Hogg, S. I., and Gostelow, J. P., 1998, ''Measurement and Computation of Energy Separation in Vortical Wake Flow of a Turbine Blade,'' ASME J. Turbomach., **121**(4), pp. 703–708.

[15] Arnone, A., and Pacciani, R., 1997, ''Numerical Prediction of Trailing Edge Wake Shedding,'' ASME Paper No. 97-GT-89.

[16] Manna, M., Mulas, M., and Cicatelli, G., 1997, ''Vortex Shedding Behind a Blunt Trailing Edge Turbine Blade,'' Int. J. Turbo Jet Engines, **14**, pp. 145–157.

[17] Sondak, D. L., Dorney, D. J., 1998, ''Simulation of Vortex Shedding in a Turbine Stage,'' ASME J. Turbomach., **121**(3), pp. 428–435.

[18] Sondak, L. D., 1999, ''Vortex Shedding in a Turbine Cascade,'' Int. J. Turbo Jet Engines, **16**, pp. 107–126.

[19] Currie, T. C., and Carscallen, W. E., 1998, ''Simulation of Trailing Edge Vortex Shedding in a Transonic Turbine Cascade,'' ASME J. Turbomach., **120**(1), pp. 10–19.

[20] Magagnato, F., 1999, ''Unsteady Flow Past a Turbine Blade using Non-Linear Two-Equation Turbulence Models,'' *Proc., 3th European Turbomachinery Conference*, London, United Kingdom.

[21] Sieverding, C. H., Cicatelli, G., Desse, J. M., Meinke, M., and Zunino, P., 1999, *Experimental and Numerical Investigation of Time Varying Wakes behind Turbine Blades*, Notes on Numerical Fluid Mechanics Volume 67, Vieweg.

[22] Sieverding, C. H., and Heinemann, H., 1990, ''The Influence of Boundary Layer State on Vortex Shedding from Flat Plates and Turbine Cascades,'' ASME J. Turbomach., **112**(2), pp. 181–187.

[23] Gerrard, J. H., 1966, ''The Mechanism for the Formation Region of Vortices Behind Bluff Bodies,'' J. Fluid Mech., **25**(2), pp. 401–413.

A Novel Two-Dimensional Viscous Inverse Design Method for Turbomachinery Blading

L. de Vito[1]
e-mail: Laurent.deVito@muc.mtu.de

R. A. Van den Braembussche
Fellow ASME
e-mail: vdb@vki.ac.be

H. Deconinck
e-mail: deconinck@vki.ac.be

von Karman Institute for Fluid Dynamics,
Turbomachinery & Propulsion/Aerospace Departments,
Waterloose steenweg, 72,
1640 Sint-Genesius-Rode, Belgium

This paper presents a novel iterative viscous inverse design method for turbomachinery blading. It is made up of two steps: the first one consists of an analysis by means of a Navier-Stokes solver; the second one is an inverse design by means of an Euler solver. The inverse design resorts to the concept of permeable wall, and recycles the ingredients of Demeulenaere's inviscid inverse design method that was proven fast and robust. The re-design of the LS89 turbine nozzle blade, starting from different arbitrary profiles at subsonic and transonic flow regimes, demonstrates the merits of this approach. The method may result in more than one blade profile that meets the objective, i.e., that produces the viscous target pressure distribution. To select one particular solution among all candidates, a target mass flow is enforced by adjusting the outlet static pressure. The resulting profiles are smooth (oscillation-free). The design of turbine blades with arbitrary pressure distribution at transonic and supersonic outflow illustrates the correct behavior of the method for a large range of applications. The approach is flexible because only the pitch chord ratio is fixed and no limitations are imposed on the stagger angle.
[DOI: 10.1115/1.1545765]

Introduction

Inverse design methods, defining the blade geometry corresponding to a prescribed pressure distribution, have been the subject of many theoretical and computational studies and greatly matured over the last years. They are now reckoned to be a valuable alternative to the iterative use of direct methods. Although the latter ones allow an easier control of various geometrical parameters to meet the stress and cooling requirements, they demand a lot of physical insight of the designer in the flow mechanisms to foresee the changes required to reach a target pressure distribution. Compared to optimization methods, inverse design methods allow a more direct interaction with the blade pressure distribution and require much less computational effort.

Leonard and Van den Braembussche [1] and Demeulenaere and Van den Braembussche [2] devised an efficient inverse design method based on Euler solvers. Their method allows the definition of the 3-D geometry needed to obtain a prescribed pressure distribution on the whole blade surface. As it is based on the inviscid flow equations, it only provides ''inviscid'' geometries, from which the boundary layer displacement thickness must be subtracted to obtain the ''metal blade.'' The complexity to calculate a 3-D boundary layer makes this subtraction process quite cumbersome for 3-D flows and the precision of the whole design procedure may be compromised. In addition, the shock pattern at the trailing edge of a supersonic outflow turbine blade significantly differs between inviscid and viscous flows, which prevents correct results when using an inviscid technique for that application.

The method of Leonard and Demeulenaere cannot directly be transposed to a viscous flow solver because it is based on a time marching computation with permeable wall boundary conditions. The latter ones are not compatible with the Navier Stokes boundary conditions. Furthermore, the transpiration model, based on continuity, requires a nonzero tangential velocity on the surface, whereas the wall velocity is zero in viscous flow calculations.

Demeulenaere et al. [3] presented an extension of the method to viscous problems. The normal velocity distribution V_n, required by the transpiration model, is no longer obtained from a Navier Stokes calculation with modified boundary conditions, but defined by the following simplified expression:

$$V_n = -\frac{p^{\text{req}} - p^*}{\rho a} \tag{1}$$

where p^* is the pressure on the wall of the present geometry, calculated by a Navier Stokes solver, and p^{req} is the target pressure distribution. The geometry modification algorithm is again based on the transpiration principle, but it uses the tangential velocity estimated at the edge of the boundary layer.

The method has shown to converge, although slower than the original Euler version, for the redesign of subsonic blades. Extensive testing by Callot [4] for transonic and supersonic flows indicated serious convergence problems depending on the flow regime. They can be explained by considering Eq. (1) for the flow through a diverging Laval nozzle. If for instance the required static pressure is higher than the computed pressure, it will indicate a negative V_n (air is blown into the numerical domain), *whatever the flow regime*. However, air should be sucked out if the flow is subsonic and blown in at supersonic regime. The presence of a boundary layer does not invalidate this demonstration.

Equation (1) is in fact a simplified form of the following compatibility relation:

$$V_n = V^* - \frac{p^{\text{req}} - p^*}{\rho a} \tag{2}$$

in which V^*, the velocity extrapolated to the wall, is set to zero. By doing so, the modifications required by the flow field and the meaning of the compatibility relation are lost, which might explain the difficulty to handle a large variety of geometries with this approach.

The present paper describes and evaluates a novel viscous inverse design method that overcomes this defect. It combines the robustness of Demeulenaere's inviscid geometry modification method with the accuracy of a Navier-Stokes solver for the flow analysis. This approach somewhat slows down the convergence, because of a less accurate prediction of the required blade modification, but it is valid for both subsonic and supersonic flows.

[1]Presently at MTU Aero Engines, D-80995 München, Germany.

Contributed by the International Gas Turbine Institute and presented at the International Gas Turbine and Aeroengine Congress and Exhibition, Amsterdam, The Netherlands, June 3–6, 2002. Manuscript received by the IGTI November 27, 2002. Paper No. 2002-GT-30617. Review Chair: E. Benvenuti.

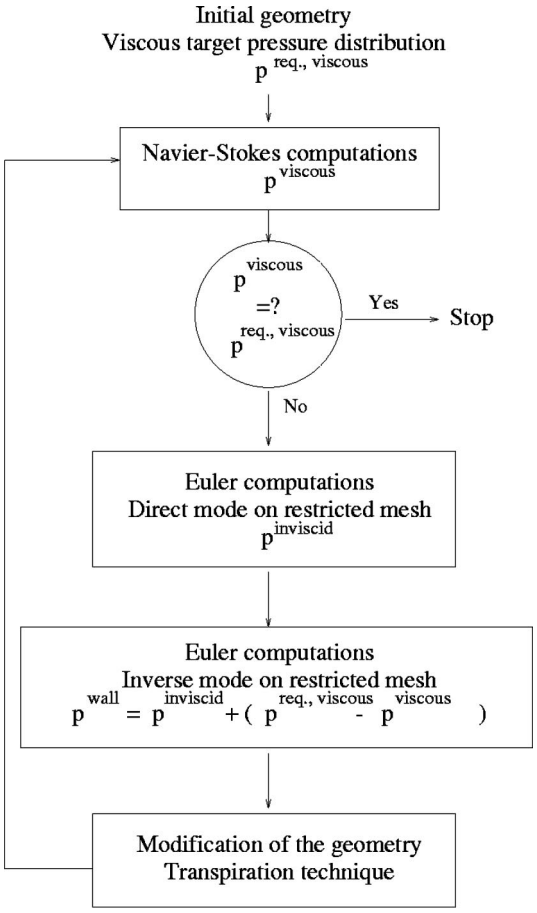

Fig. 1 Structure of the novel approach

Blade Design Method

The core of the new strategy consists in blending a Navier-Stokes solver, for the analysis, with an Euler solver for the inverse design. A similar approach was tested by Passrucker and Van den Braembussche [5] for the inverse-design of centrifugal impellers. Their method is a combination of a full 3-D and a quasi-3-D flow analysis program with a quasi-3-D geometry modification algorithm. The basic idea was to prescribe and obtain the desired velocity in the full 3-D flow, but to define the required modifications by a quasi-3-D model.

The underlying idea of both methods is to blend a ''higher level flow solver,'' for the analysis, with a ''lower level flow solver'' for the design. Other researchers [6] have shown that such an approach can cause oscillations in the profile because of the inconsistency between the numerical treatment in the direct and indirect method. They had to remove the oscillations by a smoothing algorithm once the inverse design process was completed. The present approach does not suffer from this drawback, as shown by a variety of calculations.

The detailed iterative procedure is set out on Fig. 1. It consists of:

Viscous Analysis: Computing the Navier-Stokes solution in direct mode; i.e., the airfoil is considered as solid and impermeable wall boundary conditions are used.

Inviscid Inverse Design—Part I: Computing the Euler flow field on a restricted mesh in direct mode *until convergence* with impermeable wall boundary conditions on the inner wall. The boundary conditions at the outer edges of the restricted mesh come from the viscous solution. This is very fast because a rather coarse mesh can be used.

Inviscid Inverse Design—Part II: Computing the Euler flow field on the restricted mesh, but in indirect mode: the blade is supposed to be permeable. The pressure p^{wall} enforced on the blade wall is $p^{\text{inviscid}}+(p^{\text{req. viscous}}-p^{\text{viscous}})$. It means that the driving pressure is the difference between the target pressure and the pressure obtained in the viscous analysis.

Transpiration Technique: Applying the transpiration technique to the previous Euler solution to define a new blade profile.

As the iterative process converges, the modifications to the blade geometry vanish. If $p^{\text{req. viscous}}\approx p^{\text{viscous}}$, the pressure imposed at the wall will be p^{inviscid}. As a consequence, the normal velocity component at the wall will be zero in the indirect mode, and the transpiration technique will not modify the profile.

Throughout the inverse design, the blade chord will be kept constant, along with the pitch. The first condition is required to keep the circulation, and hence the turning almost constant. The second condition is defined by the number of blades per row. Neither the axial chord nor the stagger angle are constrained.

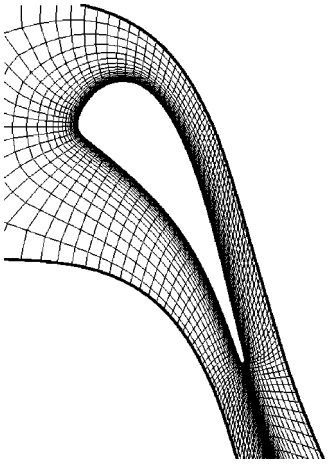

Fig. 2 Coarse 193×43 nonperiodic C-mesh around the LS89 blade for the viscous analysis

The Restricted Mesh. Figure 2 presents the coarse C-mesh around the LS89 turbine nozzle blade that will be used extensively in the numerical experiments. Figure 3 shows a restricted mesh that is extracted thereof and better suited for Euler computations. The outer boundary is a grid line of the Navier-Stokes grid at a location sufficiently far from the wall so that the viscous effects can be neglected. The inner wall is the present blade shape.

The restricted mesh does not include the trailing edge because it can not be defined by a viscous inverse method. Viscous flows separate from the thick trailing edges commonly used in turbine blades. An inverse-design of the blade shape is then not possible because the pressure depends on the shape of the separated flow

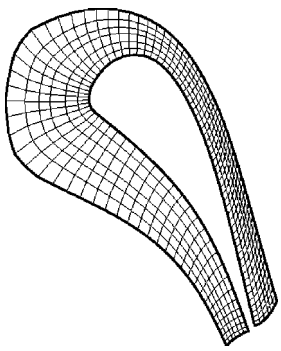

Fig. 3 Example of a restricted mesh around the LS89 blade for the (inviscid) inverse design

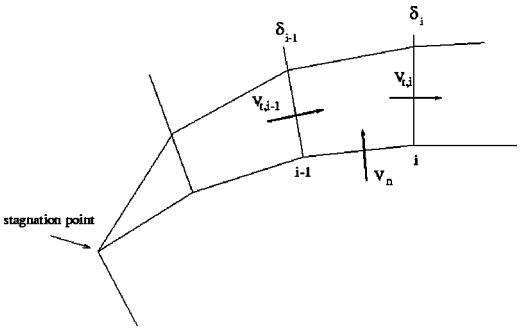

Fig. 4 The two-dimensional transpiration technique.

zone and not on the blade geometry. This is not the case when using an Euler solver where the flow remains attached to the wall and the pressure distribution (large peaks) is in direct relation to the local curvature.

This means that a reconstruction of the trailing edge is needed. It must respect the given chord length. The pressure and suction side near the restricted grid exit are extrapolated with a straight line and a circle is placed on the diagonal at the trailing edge position. The trailing edge, reconstructed in this way, is a symmetrical one but there is no problem if the designer wants to define an other trailing edge shape.

The Euler and Navier-Stokes Solver. The finite-volume cell-centered formulation is adopted for both the viscous and inviscid solvers.

The TRAF2D Navier-Stokes solver of Arnone [7] is used. It is a Jameson-Schmidt-Turkel-type two-dimensional second-order accurate viscous solver designed for cascade flow prediction. The Baldwin-Lomax model is used for the turbulence closure and all boundary layers are assumed to be fully turbulent. The grid is tailored for a y^+ of approximately 1. The inverse design method is not restricted to the present Navier Stokes solver. Using an other Navier Stokes solver can influence the accuracy of the result but not the convergence.

The Euler solver is an HLLC second-order accurate Riemann solver [8,9] developed at VKI by the first author. The scheme is second-order accurate through a multi-dimensional linear reconstruction [10]. Gradients are limited so that the scheme is local extremum diminishing using Venkatakrishnan's limiter [11]. The semi-discrete Euler equations are explicitly integrated in time with a four-stage Runge-Kutta algorithm. Convergence to steady state is accelerated by advancing the solution at each cell in time at a Courant number near the stability limit (local time-stepping)

Any Euler solver is suited for the inverse design since the validity of the results depends only on the accuracy of the viscous flow calculation.

The numerical boundary conditions for the inviscid inverse design deserve special attention. The approach formulated by Leonard [12], based on the compatibility relations, has the advantage to work in both direct (solid wall) and indirect (permeable wall) mode and was adopted.

The Transpiration Technique. If the blade is permeable, the flow can go in and out of the numerical domain through the wall. A new blade profile defined by streamlines of the inviscid flow field is recovered through the transpiration technique.

The discretized blade shape and control volumes are presented in Fig. 4. The mass conservation is applied to each cell, starting from the leading edge and marching downstream along the blade contour up to the trailing edge. The mass balance within each cell reads as follows:

$$d(\rho V_t \delta) = \rho V_n ds \tag{3}$$

or in discretized form

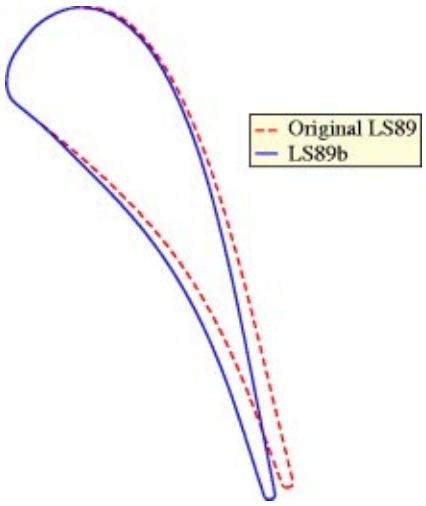

Fig. 5 Original LS89 blade and profile LS89b

$$\delta_i = \frac{1}{\rho_i V_{t,i}} (\delta_{i-1}\rho_{i-1}V_{t,i-1} + \Delta S \rho_n V_n) \tag{4}$$

where δ_i is the normal displacement at node i, and ΔS is the length of the edge $(i-1,i)$. This procedure is applied independently on the suction-and pressure side starting from the leading edge stagnation point.

Results

The method has been tested for turbine blades at different operating conditions. Two sets of tests have been performed to evaluate the performance and robustness of the new technique. The first one is the redesign of the nozzle blade LS89 starting from an arbitrary profile. The second set of investigations is stiffer and involves the design of new blades for given arbitrary pressure distributions with transonic and supersonic exit flow. The latter cases use the LS89 as initial profile.

Redesign of the LS89. In order to assess the robustness of the viscous inverse design method and its convergence to a unique solution, one has first tested the method by redesigning an existing blade. In this way one is sure that there will be no problems related to the existence of a solution.

The target geometry is the highly loaded transonic turbine nozzle vane LS89, experimentally investigated by Arts et al. [13]. The inlet flow angle is 0 deg. The outlet angle β_2 is close to -75 deg at subsonic outflows and decreases to -70 deg at supersonic outflow. The most important geometrical characteristics of the cascade are: $t/c=0.850$, $\gamma=55.0$ deg (from axial direction), throat/$c=0.2207$. The pressure distribution calculated by the Navier Stokes solver for an outlet Mach number of .97 is imposed as target for the design.

The initial geometry is the LS89b, which is the same profile as the LS89, but rotated over 2.5 deg in the clockwise direction, except close to the leading edge (Fig. 5).

The redesign has resulted in different profiles. Each of them satisfies the imposed pressure distribution (Fig. 6), but at different mass flow (Table 1). The different geometries were taken on-the-fly during the iterative inverse design process and the corresponding pressure distribution is obtained from a direct calculation. All pressure distributions coincide with the target pressure distribution (Fig. 6).

The exit Mach number M_2 and angle β_2 listed in Table 1 are mass-momentum- and energy averaged values and correspond to fully mixed-out conditions.

ζ is the loss coefficient based on the averaged outlet static and total pressure.

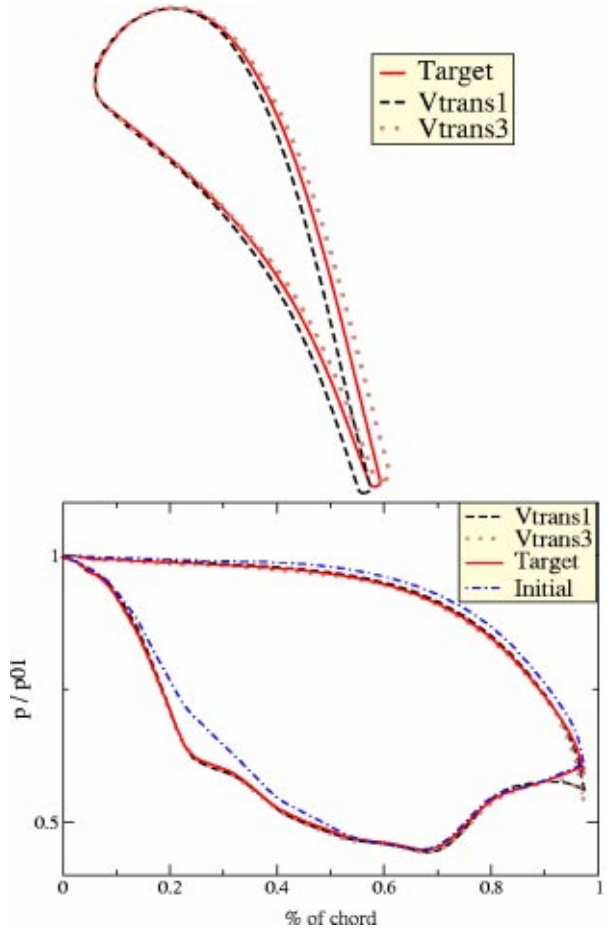

Fig. 6 Different blade profiles (top) and the corresponding pressure distributions (bottom); solutions with large mass flow errors

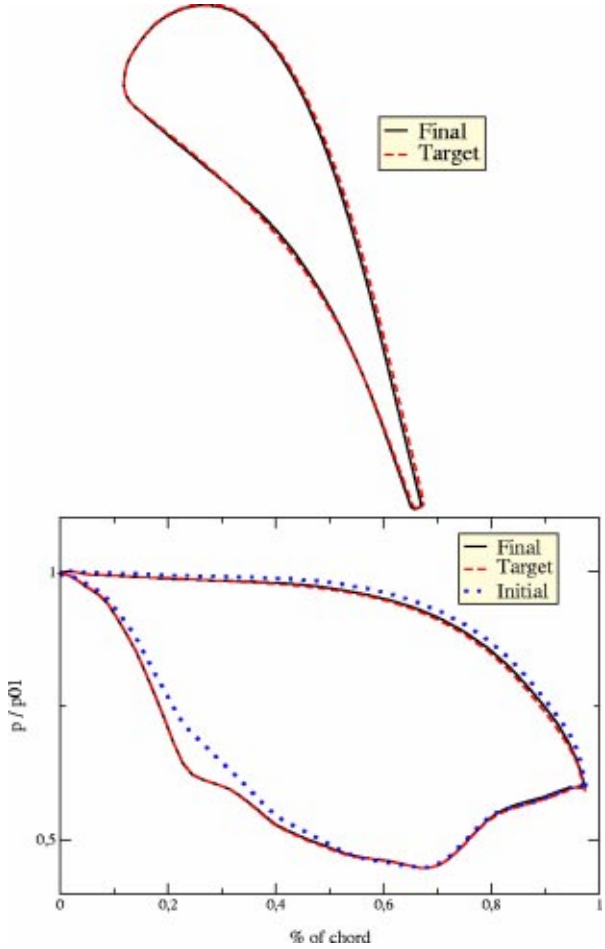

Fig. 7 Different blade profiles (top) and corresponding pressure distributions (bottom); a solution with small error on the mass flow

$$\zeta = 1 - \frac{1 - \left[\dfrac{\left(\dfrac{p}{p_{01}}\right)}{\left(\dfrac{p_{02}}{p_{01}}\right)}\right]^{\gamma-1/\gamma}}{1 - \left(\dfrac{p}{p_{01}}\right)^{\gamma-1/\gamma}} \tag{5}$$

$\Delta\dot{m}$ is the error on the mass flow, related to the mass flow through the original (target) LS89 cascade.

Obtaining different geometries for the same target pressure distribution means that the problem is ill posed when prescribing the outlet static pressure. This was theoretically demonstrated by Zannetti and Pandolfi [14]. Although their theory was made for the case with the suction- and pressure side pressure distribution prescribed along the axial length, it is likely that their conclusion also holds in our case where the pressure is prescribed along the blade contour. Similar problems have also been experienced by Demeulenaere [15].

The existence of more than one solution can be explained with the following relation:

$$\int Vds = V_{2x}(\tan\beta_2 - \tan\beta_1) \quad \text{pitch} \tag{6}$$

Strictly spoken this equation is valid only for isentropic irrotational flows, but it can also be used to get an insight for viscous flows. All previous solutions produce the target pressure distribution so that the circulation around the profile (the left-hand-side of (6)) is the same. The inlet angle β_1 is imposed at 0 deg, so that for a given target pressure distribution, Eq. (6) reduces to $V_{2x}.\tan\beta_2.\text{pitch} = \text{const}$.

A large number of combinations of mass flow ($\approx V_{2x}$ pitch) and exit angles can satisfy this relation. Except for some trivial values of the circulation, an infinite number of doublets are pos-

Table 1 Summary of redesign

	(Target) LS89	Vtrans1	Vtrans3
β_2	−74.6 deg	−75.4 deg	−73.9 deg
M_2	0.937	0.95	0.94
$M_{2,is}$	0.97	0.987	0.976
ζ	5.67%	6.31%	6.37%
$\Delta\dot{m}$		−5.5%	+3.3%

Table 2 Summary of design at constant mass flow

	(Target) LS89	Final
β_2	−74.6 deg	−74.6 deg
M_2	0.937	0.937
$M_{2,is}$	0.97	0.97
ζ	5.67%	5.64%
$\Delta\dot{m}$		−0.15%

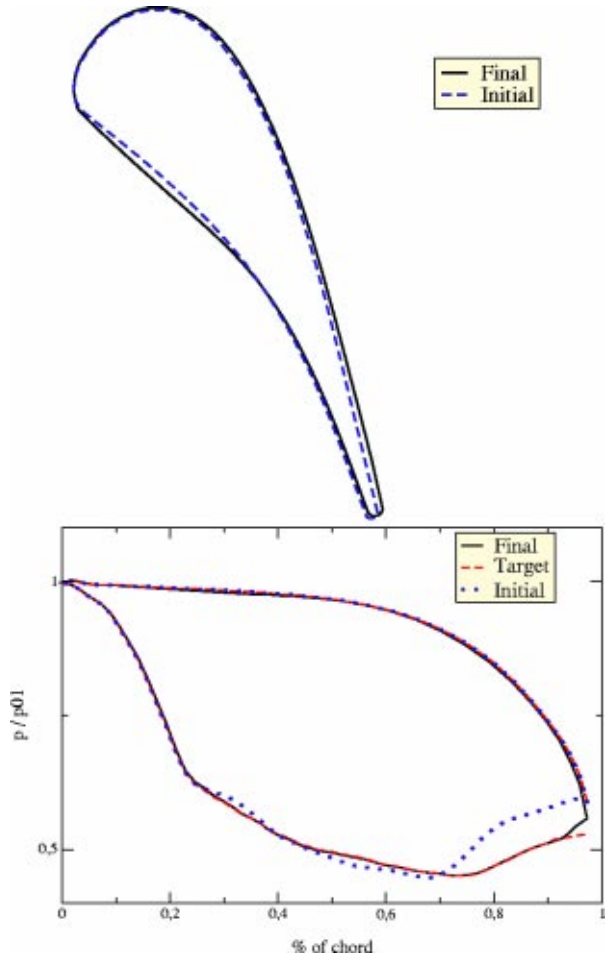

Fig. 8 Blade profiles (top) and pressure distributions (bottom); blind design in transonic regime

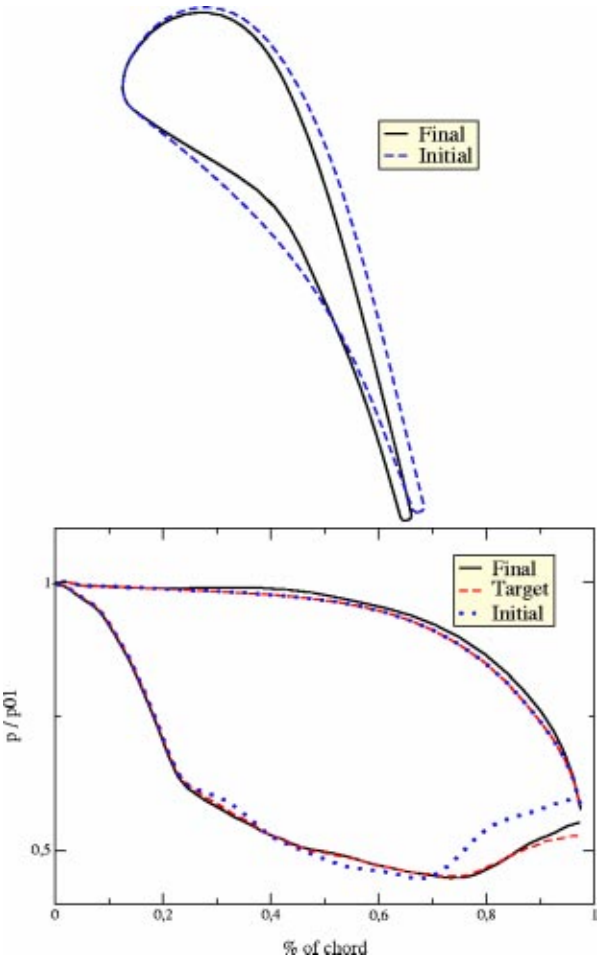

Fig. 9 Blade profiles (top) and pressure distributions (bottom), design at transonic regime; a solution with a large change in mass flow

sible. This does not guarantee that there will always exist a profile that produces the target pressure distribution, but our numerical experiments indicate that under some conditions a whole family of solutions is possible.

Equation (6) is verified for the solution Vtrans1 and Vtrans3 in Table 1. The mass flow for the Vtrans1 solution is smaller than the target, which according to (6) results in an exit angle β_2 with a larger absolute value. This is clearly visible on the geometry on Fig. 6. Conversely, the mass flow for the solution Vtrans3 is higher than the target, which according to (6) results into a more axial outlet flow than the target. This is also evidenced on Fig. 6.

An infinite number of solutions to the inverse problem are possible when the pressure distribution and pressure ratio are imposed. The latter one must be replaced by an other condition if one wants to pick up only one solution. This should either be the mass flow or the outlet flow angle. Zannetti and Pandolfi recommend to control the mass flow for highly negative exit angles (turbine nozzle, for instance). When designing for moderate negative exit angles (turbine rotor) and positive exit angles (compressor blades) the problem seems to be well posed when imposing a given back-pressure.

Imposing a back-pressure is by far more simple than assuring a constant mass flow. All other designs presented in the present paper are done at constant mass flow. The control is however indirect, since the back pressure is iteratively adjusted until the target mass flow is reached. Care has been taken in devising the algorithm to adjust the back-pressure as it could easily deteriorate the convergence rate by generating a self-sustained oscillatory system (over- and undershoots in the relative mass flow timelike evolution). In practice, the back-pressure is adjusted every three inverse iterations, and modifications are reduced when the mass flow is approaching the target. The result of such a calculation is shown on Fig. 7. The aerodynamic characteristics of the original and redesigned blade are listed in Table 2. The redesigned blade gives an almost perfect agreement between target and final pressure distributions (within plotting accuracy). The small discrepancies in the geometry have no impact on the pressure distribution

Table 3 Summary of blind design at transonic outflow

	Original LS89	Final
β_2	−74.6 deg	−74.5 deg
M_2	0.937	0.968
$M_{2,is}$	0.97	1.005
ζ	5.67%	6.03%
$\Delta\dot{m}$		+0.1%

Table 4 Summary of blind design at supersonic outflow

	Original LS89	Final
β_2	−70.49 deg	−70.94 deg
M_2	1.361	1.356
$M_{2,is}$	1.48	1.48
ζ	10.75%	11.55%
$\Delta\dot{m}$		−3.1%

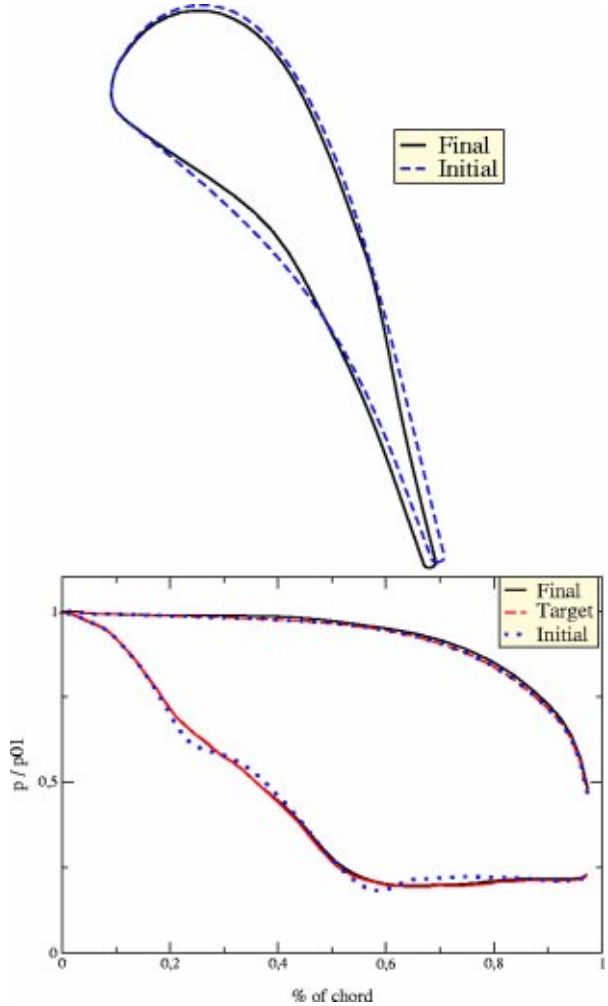

Fig. 10 Blade profiles (top) and pressure distributions (bottom); blind design at supersonic outflow

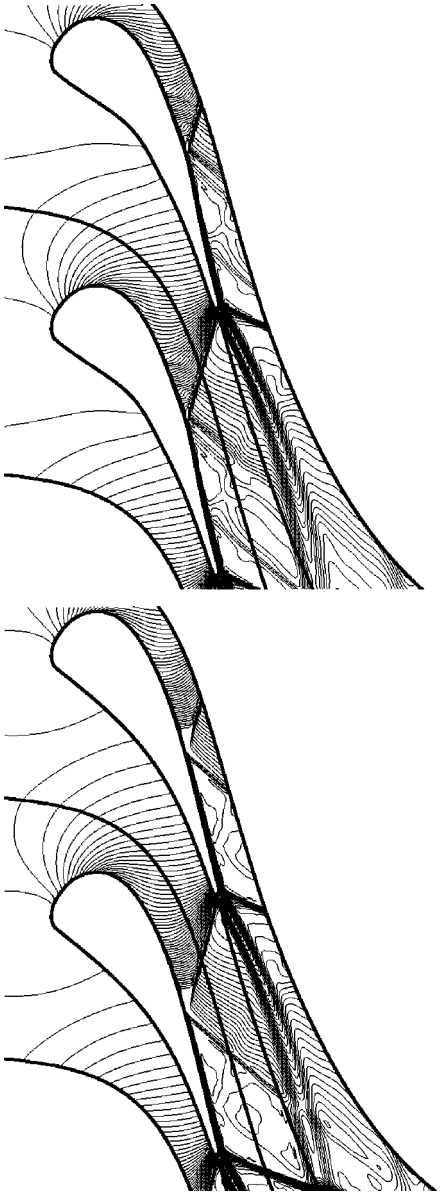

Fig. 11 Iso-Mach lines, solution (top) and initial profiles (bottom)

and might be due to the rather loose control of the mass flow (still .15% error) and to some extent to small differences between the original and reconstructed trailing edge shape.

Previous study was carried out in transonic regime, but similar observations have also been made at fully subsonic outflow. Because of lack of space those results will not be presented here.

New Blade Design at Transonic Outflow. When designing a new blade, for an arbitrary required pressure distribution (blind test) there is no guarantee that a solution to the inverse problem exists. The following viscous inverse design at transonic regime is therefore a more challenging problem. It starts from the original LS89 nozzle. The target pressure distribution is compared to the initial one on Fig. 8. The pressure distribution on the pressure side is unchanged, whereas from 20% of chord onwards the pressure distribution on the suction side is smoothed and the pressure rise due to the shock wave is erased. This shock-free distribution does not exclude the presence of a hanging shock in the flow field. This shock may eventually reappear at the wall when the incidence or back-pressure is modified. The target mass flow is the one of the starting geometry.

This design did not create any problems and an excellent agreement between the imposed and calculated pressure distribution is obtained (Fig. 8). The aerodynamic characteristics of the original and final profiles are listed in Table 3. A lower exit pressure (higher exit Mach number) is required to keep the mass flow constant. The shock wave was pushed downstream and stands very close to the trailing edge. This has resulted in a small increase of losses. The final design produces unexpectedly more losses than the base design. This does not invalidate the design method, but indicates that the imposed pressure distribution is not as optimum as was expected.

The profile shape corresponding to a given pressure distribution may change substantially if the mass flow is varied. Figure 9 shows the solution for a 2.5% lower mass flow. The blade shape is very different. The agreement in pressure distribution is satisfactory except for a small discrepancy on the pressure side. This illustrates an important advantage of the present method: to provide at least an approximate solution even when an exact solution is not possible.

New Design for Supersonic Outflow. The last test is a blade design for an outlet Mach number as high as 1.48. The starting geometry is again the original LS89 nozzle and the design is carried out at fixed isentropic exit Mach number ($M_{2,is}=1.48$, as shown in Table 4). The initial and target pressure distributions are compared on Fig. 10. The pressure distribution is unchanged on

the pressure side, whereas it is smoothed on the suction side to avoid the sequence of decelerations and accelerations.

The agreement between target and calculated pressure distribution is satisfactory, Fig. 10.

A particularity of this design is the kink on the suction side of the redesigned blade. It generates a Prantl-Meyer expansion that cancels the reflection of the shock wave originating from the trailing edge of the neighboring blade. This is visualized on Fig. 11.

This test case demonstrates the advantage of present method as compared to an inviscid design method. The latter one would give inaccurate results because of the very different shock patterns at the trailing edge. The right-running shock is not produced by an inviscid flow solver and the inviscid design procedure would therefore result in a different (incorrect) blade shape.

Conclusions

A viscous inverse design method based on the blending of a Navier-Stokes solver for the analysis with a Euler solver on a restricted mesh for the inverse design has been formulated.

The accuracy is verified by redesigning an existing blade (the LS89 nozzle blade) starting from a different arbitrary profile. The method is further validated at transonic and supersonic flow by redesigning new profiles with given arbitrary pressure distributions.

Though the target profile could never be exactly recovered, the validation has shown to be successful in terms of matching the pressure distribution.

The method performs also well at supersonic outflow and the trailing edge shocks are correctly modeled.

The approach is flexible as only the pitch-chord ratio is kept constant. In addition, the blending does not produce wiggles in the redesigned profile.

It has been shown how a unique solution can be obtained by setting the mass flow constant. This is done in an indirect way and causes the mass flow of the solution to be close to the target but not exact. This issue is benign as the error on the mass flow is very small.

The present design tool does not guarantee better performance as the optimum depends on the prescribed pressure distribution, which is an input for the method. It is still the task of the designer to find out how an optimum pressure distribution would look. Inverse boundary layer calculations and optimization techniques maybe useful for this purpose. When judging the impact of the redesign on the profile losses one should also keep in mind that the redesigns start from the LS89 blade which is an already optimized blade shape.

Nomenclature

a = speed of sound
β = relative flow angle
c = chord length
δ = displacement normal to blade contour
γ = stagger angle
i = node no.
M = Mach no.
$\dot{m}$ = mass flow
p = pressure
ρ = density
s = distance along contour
t = pitch
V = velocity
ζ = loss coefficient (Eq. (5))

Subscripts

n = normal to boundary
t = tangent to boundary
x = axial component
1 = inlet
2 = outlet
0 = stagnation value

Superscript

req = required
$*$ = extrapolated
wall = at the wall

References

[1] Leonard, O., and Van den Braembussche, R. A., 1992, ''Design Method for Subsonic and Transonic Cascades with Prescribed Mach Number Distribution,'' ASME J. Turbomach., **114**(3), pp. 553–560.

[2] Demeulenaere, A., and Van den Braembussche, R. A., 1996, ''Three-Dimensional Inverse Method for Turbomachinery Blading Design,'' ASME J. Turbomach., **120**(1), pp. 247–255.

[3] Demeulenaere, A., and Leonard, O., and Van den Braembussche, R. A., 1997, ''A Two-Dimensional Navier-Stokes Inverse Solver for Compressor and Turbine Blade Design,'' Proc. Second European Conference on ''Turbomachinery—Fluid Dynamics and Thermodynamics,'' Antwerp, Belgium, pp. 339–346.

[4] Callot, S., 1998, ''Inverse Blade Design by Means of a Navier-Stokes Solver,'' von Karman Institute, PR 1998-04.

[5] Passrucker, H., and Van den Braembussche, R. A., 2000, ''Inverse Design of Centrifugal Impellers by Simultaneous Modification of Blade Shape and Meridional Contour,'' ASME Paper No. 2000-GT-457.

[6] Bartelheimer, W., 1996, ''An Inverse Method for the Design of Transonic Airfoils and Wings,'' J. Inverse Problems Eng, **4**(1), pp. 21–51.

[7] Arnone, A., and Swanson, R. C., 1993, ''A Navier-Stokes Solver for Turbomachinery Applications,'' ASME J. Turbomach., **115**(2), pp. 305–313.

[8] Harten, A., Lax, P. D., and van Leer, B., 1983, ''On Upstream Differencing and Godunov-Type Schemes for Hyperbolic Conservation Laws,'' SIAM Rev., **25**(1), pp. 35–61.

[9] Toro, E. F., Spruce, M., and Speares, W., 1994, ''Restoration of the Contact Surface in the HLL-Riemann Solver,'' Shock Waves, **4**, pp. 25–34.

[10] Barth, T. J., and Jespersen, D. C., 1989, ''The Design and Application of Upwind Schemes on Unstructured Meshes,'' Paper AIAA-89-0366.

[11] Venkatakrishnan, V., 1993, ''On the Accuracy of Limiters and Convergence to Steady State Solutions,'' Paper AIAA 93-0880.

[12] Leonard, O., 1992, ''Conception et Développement d'une Méthode Inverse de Type Euler et Application à la Génération de Grilles d'Aubes Transsoniques,'' Ph.D. thesis, von Karman Institute and Faculté Polytechnique de Mons, Belgium.

[13] Arts, T., Lambert de Rouvroit, M., and Rutherford, A. W., 1990, ''Aero-Thermal Investigation of a Highly Loaded Transonic Linear Turbine Guide Vane Cascade,'' von Karman Institute, TN 174.

[14] Zannetti, L., and Pandolfi, M., 1984, ''Inverse Design Technique for Cascades,'' NASA CR 3836.

[15] Demeulenaere, A., 1997, ''Conception et Développement d'une Méthode Inverse pour la Génération d'Aubes de Turbomachines,'' Ph.D. thesis, von Karman Institute and Université de Liège, Belgium.

Improving the Aero-Thermal Characteristics of Turbomachinery Cascades

Marcello Manna

Raffaele Tuccillo

Dipartimento di Ingegneria, Meccanica per l'Energetica (D.I.M.E.), Università di Napoli "Federico II", Napoli, 80125 Italy

The paper presents the application of an optimization procedure to the aero-thermal design of high performance turbomachinery cascades. The blade profiles are parameterized with third-order Bezier polynomials for the pressure and suction sides, and quadratic functions for the leading and trailing edges, according to the composite curve approach. Evidence is given that fairly complicated blade shapes are well approximated by the present parameterization. The method is applied to an existing nozzle guide vane for which extensive and detailed experimental data are available, with the objective of decreasing in an integral sense the thermal load, maintaining or increasing the blade efficiency and the aerodynamic load. The results demonstrate that, despite the excellence of the initial design, there is room for improvements. [DOI: 10.1115/1.1544510]

Introduction

The main directions to follow in order to increase gas turbine performance are based on the possibility of achieving higher turbine inlet temperature and reducing profile losses, shock losses, trailing edge losses and cooling losses. This requires a thorough knowledge of both aerodynamic and heat transfer phenomena which have to be accounted for in the design process. However, most if not all of the existing blade design methods are based on the definition of a geometrical shape capable of providing a prescribed velocity distribution which is either specified locally on the suction and pressure sides, or globally through an overall flow turning [1–9]. In the former case the target distribution stems from the designer experience and heavily relies on existing experimental and computational data. When the design problem deals with high-pressure gas turbine nozzle guide vanes, there is an additional constraint to satisfy, i.e., the control of the blade surface heat transfer which is an issue of paramount importance in the last generation gas turbine concepts [10]. To our best knowledge, there are no examples of combined aero-thermal designs in the open literature, that is to say, the heat transfer properties of the aerodynamically designed blade are simply checked a posteriori. This work precisely addresses the issue of the definition of the optimal blade shape which both minimize the surface convective heat transfer distribution and maximize the blade load and efficiency.

To this aim we have envisaged a more general definition of the profile which could guarantee the adequate representation of very many different blade shapes with a reduced number of parameters. Following [11] we have used third-order Bezier polynomials for the pressure and suction sides, and quadratic functions (i.e., ellipses and circles) for the leading and trailing edges, according to the composite curve approach. As opposed to the single curve approach, which, however, guarantees global continuity, this technique allows for the direct control of key parameters, such as the leading and trailing edge thickness for which strict realizability conditions are often imposed by the manufacturers.

Based on the foregoing method for blade parameterization, the work attempts to improve the aero-thermodynamic characteristics of a highly loaded gas turbine nozzle for which extensive and detailed experimental data are available [12]. The objective of the design consists of decreasing (in an integral sense) the thermal load of the guide vane, while maintaining (or ultimately increasing) the blade efficiency and the aerodynamic load.

Preliminary encouraging results of a parametric analysis indicate that there is room for improvements, which have been then pursued by a gradient-based optimizer which drives a full Navier-Stokes solver according to a repeated analysis technique. A particular care was paid to find the best compromise between the requirements of satisfactory solution and reasonable computational times. The effectiveness of the optimizing procedure was improved by introducing proper selection criteria of the physically feasible solutions within the *n*-dimensional search space.

Strategies were also experienced for finding optimal solutions, based on different weights assigned to the cascade performance parameters, say the flow losses and the aerodynamic and thermal loads.

The Flow Solver

The flow fields are governed by the two-dimensional (i.e., $i=1, 2$) unsteady compressible Navier-Stokes equations, whose conservative form reads

$$\frac{\partial}{\partial t}\rho+\frac{\partial}{\partial x_j}(\rho u_j)=0$$

$$\frac{\partial}{\partial t}(\rho u_i)+\frac{\partial}{\partial x_j}(\rho u_i u_j+p\,\delta_{ij})=\frac{\partial}{\partial x_j}(\tau_{ij}) \tag{1}$$

$$\frac{\partial}{\partial t}(\rho e_o)+\frac{\partial}{\partial x_j}[(\rho e_o+p)u_j]=\frac{\partial}{\partial x_j}(\tau_{ij}u_i)-\frac{\partial}{\partial x_j}(q_j)$$

$$\tau_{ij}=\mu\left[2S_{ij}-\frac{2}{3}\frac{\partial u_k}{\partial x_k}\delta_{ij}\right];\quad S_{ij}=\frac{1}{2}\left(\frac{\partial u_i}{\partial x_j}+\frac{\partial u_j}{\partial x_i}\right) \tag{2}$$

$$q_j=-c_p\frac{\mu}{\mathrm{Pr}}\frac{\partial T}{\partial x_j} \tag{3}$$

where standard tensor notation has been employed. The gas is assumed to be calorically perfect, and the molecular viscosity μ is related to the temperature according to Sutherland's law.

Following the classical finite volume formulation, the integral form of Eqs. (1) is discretized on a set of nonoverlapping quadrangular elements. The flow solver enjoys the flexibility of a patching domain decomposition technique with conformal interfaces. The convective terms are evaluated by means of the approximated Riemann solver of Roe [13], whose interface values are obtained through a quadratic reconstruction procedure accord-

Contributed by the International Gas Turbine Institute and presented at the International Gas Turbine and Aeroengine Congress and Exhibition, Amsterdam, The Netherlands, June 3–6, 2002. Manuscript received by the IGTI February 6, 2002. Paper No. 2002-GT-30596. Review Chair: E. Benvenuti.

ing to the MUSCL approach [14]. The limiter function is applied to the characteristic variables. The diffusive terms are centrally discretized on a dual grid. Time advancement is carried out with an implicit scheme [15]. Additional details concerning the flow solver can be found in [16].

The flow solver has been inserted in a more general code consisting of a pre-processor, a post-processor and an optimizer. Unlike [17], the pre-processor does not include the grid generation procedure, which is based on the combined use of potential theory and an elliptic solver in a multi-domain formulation. Rather, the grid system for the initial blade geometry is built in a separate stage and then modified to accommodate for the new blade definition whose parameterization is detailed in the next section. A mapping procedure based on a nonconforming shearing transformation allows to avoid the use of the Poisson solver, whose forcing terms setting, ensuring the proper near boundary grid behavior, is delicate. For moderate geometrical changes considered herein (i.e., a 50% variation of the design variables with respect to the original values), the grid distortion does not influence the rate of the error decay.

The initial solution is taken to be the one pertaining to the previous cascade definition; this procedure proved to be more effective than any other starting procedure based on simplified first guess distributions. The main reasons for this favorable behavior are to be attributed both to the small step sizes of the optimizer updates, and to the advantage of retaining a very good estimate of the boundary layer distributions over the blade profile.

The flow solver carries over the analysis till the norm of the residuals is reduced by several orders of magnitude. A check on the maximum number of iterations is active when the flow exhibits massive separations; in these events, large-scale unsteadiness appear and the residuals drop no more than 2 or 3 orders of magnitude. When the convergence stalls this solution is not considered as first guess for the coming analysis, and the initial solution is taken to be the last one for which convergence could be attained.

Finally the data are processed as follows; the flow field is probed along a traverse carried out in the pitchwise direction at an axial distance of one pitch from the trailing edge. The data of the traverse are then numerically integrated with the trapezium rule to yield the pitchwise averaged values of the outlet flow angle β_{2f}, and of the cascade loss coefficient ξ.

Additional data processing provides the values of the blade load C_L and heat transfer coefficient C_H which are considered within the performance set for both the parametric analysis and the aerothermal optimization.

Blade Parameterization

One of the key ingredients necessary to efficiently carry over blade shape design or optimization consists of a powerful representation of the geometry. In this respect it is somehow compulsory that the adopted representation is allowed to span most, if not all, of the design space, and from this point of view orthogonal polynomial basis yielding best approximation in an inner product space, appear to be ideal candidates to fulfill this task. However, realizability and manufacturing constraints are so strict that the closeness of the approximation is often traded off with other properties, such as, for instance, bounding conditions of the approximant and its derivatives.

There is a considerable consensus on the capability of Bézier curves to represent arbitrarily complicated geometries with a small number or no inflection points at all [8]. This fact stems from several interesting features of the Bernstein polynomials, the weighting functions of the Bézier curves, the most important of which we wish to recall here: Bernstein polynomials provide *simultaneous* approximation of the function and its derivatives, and the approximant lies between the extreme values of the function itself, and its higher derivatives are bounded. This implies that monotonic and convex functions yield monotonic and convex approximations, respectively (see [18], p. 116). The main disadvantage of the Bernstein polynomials is their slow convergence rate and the absence of the permanence condition, a consequence of the minimum property theorem ([18], p. 171).

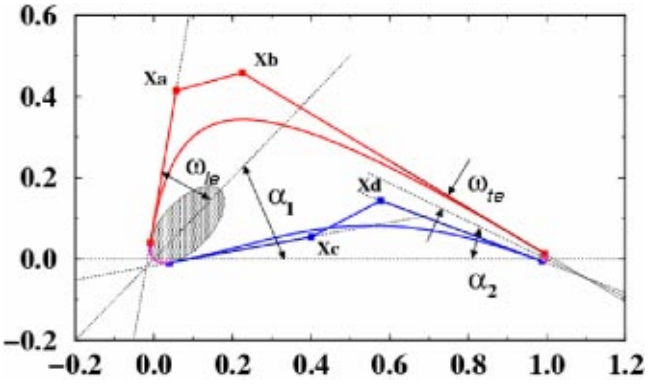

Fig. 1 Blade parameter definition

On the basis of manufacturing consideration we have preferred the composite curves approach over the single curve one; indeed global continuity over the whole profile is lost, but we claim that the direct control of key parameters (like the overall camber angle, or the leading and trailing edge thickness) is more important, especially in constrained optimization procedures.

Our blade parameterization is very similar to the one used by Anders and Haarmeyer [11], and is based on two independent third-order Bézier curves for the suction and pressure sides, connected with an elliptic leading edge and a circular trailing edge. The overall representation is only $\boldsymbol{C}_1$ (i.e., continuity is ensured up to the first derivative), and the global number of parameters adds up to 11, plus two for the cascade definition (i.e., solidity and stagger angle).

The blade (Fig. 1) is defined in the mechanical frame of reference so that the leading edge is at (0,0) and the trailing edge at (1,0); all coordinates are then scaled by the chord length.

The first two parameters define the inlet and outlet blade angles, with respect to the chord direction, so that their sum $(\alpha_1+\alpha_2)$ is representative of the overall geometrical turning.

Three additional parameters are necessary to complete the blade characterization, say the main diameter A and the diameter ratio (A/B) of the leading edge ellipse, and the trailing edge circle radius, r_{te}. Both diameter and circle radius are nondimensionalized by the chord length.

The Bézier polygons consist of four control points, two of which (beginning and ending) are determined from the tangency condition between the leading edge ellipse and the trailing edge circle and two straight lines. The latter are inclined of two angles, ω_{le} and ω_{te}, with respect to the inlet and outlet blade angle directions, α_1 and α_2, and are specified as part of the parameterization set. In the forthcoming, we shall refer to these angles as the leading and trailing edge *wedge angles*.

The other four control points, two for each side of the blade, are bound to belong to the straight lines which are inclined with respect to the unit vector $\bar{i}=(1,0)^T$ by $\alpha_1 \pm \omega_{le}$ and $\alpha_2 \pm \omega_{te}$ for the leading and trailing edges, respectively. The related nondimensional coordinates (X_a to X_d) are referred to the blade chord length; note that the $X_a - X_d$ coordinates are effectively distances computed in the aforementioned directions.

Figures 2 and 3 demonstrate the ability of the method to approximate both low turning decelerating (C4 series) and highly cambered accelerating profiles (the VKI LS89 blade is described in the next section); Table 1 shows the corresponding parameter values obtained through a minimization procedure aimed to reproduce the original profiles.

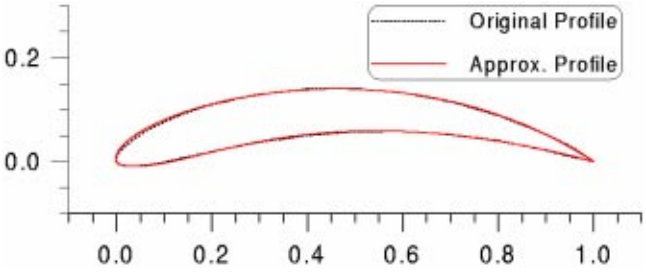

Fig. 2 Profile approximation for a circular arc airfoil of the C4 series

Cascade Definition and Parametric Study

As test bench we have selected the transonic linear turbine guide vane designed and tested by the turbomachinery department of the von Karman Institute [12], here and after referred to as the LS89 blade. The blade, designed for a downstream isentropic Mach number of 0.9 by means of an inverse method [5], is front loaded with an almost straight rear suction side. Accurate and detailed experimental data in terms of surface convective heat transfer coefficients, isentropic Mach number, loss coefficient and outlet flow angle are available for a set of Reynolds numbers, expansion ratios and free stream turbulence levels. Table 2 summarizes the main geometrical characteristics of the cascade and the flow conditions pertaining to the test case investigated herein.

Computations were carried out for the lowest Reynolds number case (viz., $\mathrm{Re}=5.6\times10^5$) and an isentropic outlet Mach number of 1.118; under these conditions the experimental data indicate that both the suction and pressure side boundary layers are in laminar conditions, as confirmed by the excellent agreement with the laminar computations reported in [12] and herein. Hence, uncertainties related to the turbulence closure are ruled out and the results reported in this work acquire a greater significance and generality.

To assess the resolution requirements we have carried out a grid convergence study, with a two level (refined in both streamwise and pitchwise directions) mesh systems. The surface grid point

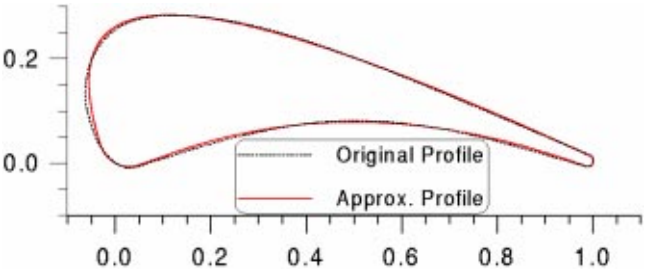

Fig. 3 Profile approximation for the LS89 turbine blade

Table 1 List of independent variables for blade design

Blade parameter			Blade type	
Name	Symbol	Units	LS89	C4
LE main ellipse diameter	A	(/)	0.065	0.013
LE diameter ratio	(A/B)	(/)	1.000	1.000
TE Circle radius	r_{te}	(/)	0.011	0.001
Blade inlet angle	α_1	deg	63.06	29.67
Blade outlet angle	α_2	deg	20.7	22.3
LE wedge angle	ω_{le}	deg	45.5	40.2
TE wedge angle	ω_{te}	deg	2.1	8.8
1st control point	X_a	(/)	0.331	0.101
2nd control point	X_b	(/)	0.968	0.486
3rd control point	X_c	(/)	0.129	0.143
4th control point	X_d	(/)	0.528	0.634

Table 2 Cascade and flow data

Blade stagger angle	$\gamma=-55.179$ deg
Cascade chord over pitch solidity	$\sigma=1.10875$
Isentropic Mach number	$\mathrm{M}_{2\mathrm{is}}=1.118$
Reynolds number	$\mathrm{Re}_2=5.6\times10^5$
Inlet flow angle	$\beta_{1f}=0$ deg
Inlet total pressure	$p_{01}=0.824$ bar
Inlet total temperature	$T_{01}=402.3$ K
Wall temperature	$T_w=304$ K

distribution has been obtained by means of potential theory, so that automatic clustering as a function of the local boundary curvature is achieved. The procedure is detailed elsewhere and will not be further discussed herein [19]. Two multi-domain grids consisting of $203\times37+67\times85$ and $405\times73+133\times169$ points have been employed to establish the convergence in the sense of the truncation error. The coarse mesh is obtained by the fine one deleting every other point in the two coordinate directions. The forcing terms in the Poisson equation for the mesh generation procedure were adjusted in such a way that the first point away from the wall results in an average $y^+=u_\tau y/\nu<0.5$, with $u_\tau=\sqrt{\tau_w/\rho}$. A typical convergence history is shown in Fig. 4. The same figures report the time history of the most relevant performance parameters (loss coefficient, blade load and heat transfer coefficient) normalized with their final value (N_{it} is the total number of iterations). The shadowed area denotes a 5% uncertainty band. The graph shows that thanks to the very rapid residual decay in the first stage of the time marching procedure (typical of implicit schemes), a few iterations are necessary to have the load coefficient within the 5% of its final value. Conversely, the loss coefficient needs almost 2500 iterations to enter the shaded area; after 2500 iterations the density residuals have dropped almost by five orders of magnitude!

Even more stringent are the convergence requirements in terms of heat load; in fact almost 5000 iterations (and seven orders of magnitudes residual drop) are needed to have C_H within 5% of its final value.

Thus, extreme attention has to be paid to the convergence level of the time marching process when the outcome of the computations concerns momentum and thermal layers.

Figure 5(*a*) shows the comparison of the measured and computed blade Mach number distributions for the $\mathrm{M}_{2\mathrm{is}}=0.85$ and $\mathrm{M}_{2\mathrm{is}}=1.02$ cases, with $\mathrm{Re}=1.0\times10^6$. The agreement is very good for the subsonic case and fair for the transonic one; the reason for discrepancies may be attributed to the laminar to turbulent transi-

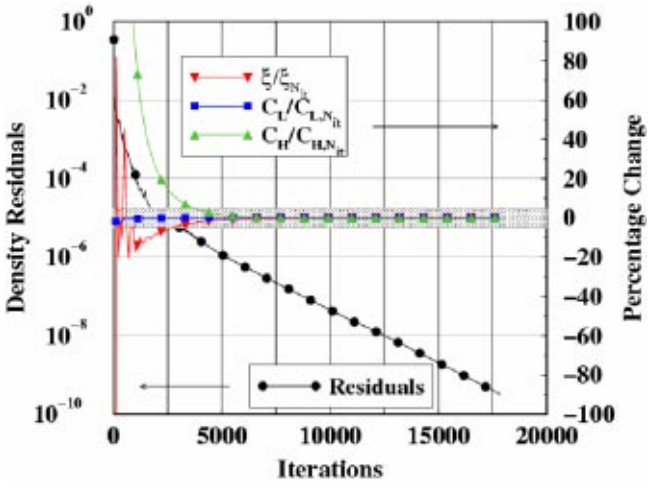

Fig. 4 A convergence history of the cascade flow calculation

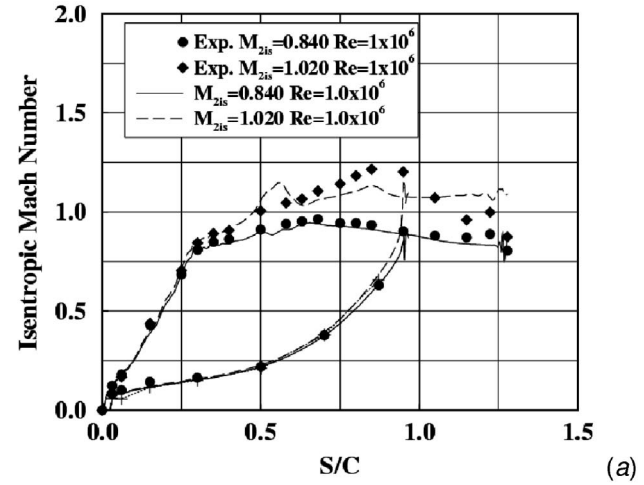

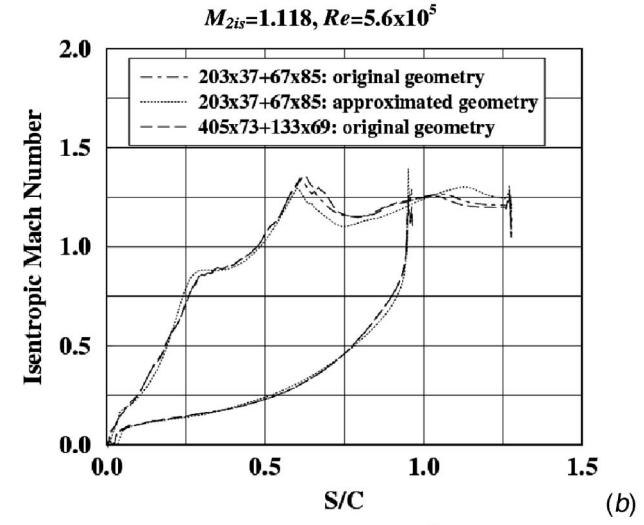

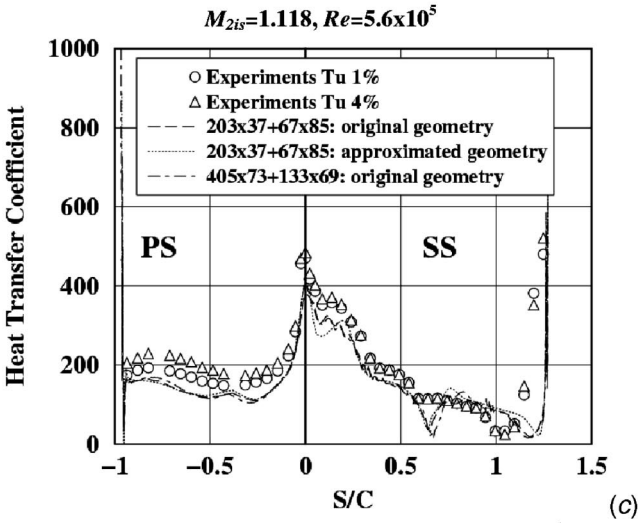

Fig. 5 Experimental data and computational results for different grid sizes and for the approximated blade geometry

tion occurring in the experiments at the rear part of the blade suction side, and to some related unsteady effects.

Figure 5(*b*) shows the computed isentropic blade Mach number distribution for the original and approximated geometries for the $M_{2is}=1.118$, $Re=5.6\times10^5$ case. No experimental data are available at these conditions in terms of blade velocity distribution. We first notice that the blade distribution of either computations on the coarse and fine grids are practically identical, thus proving that the coarse grid is definitely sufficient to guarantee grid independence. The comparison of the data referring to the original blade profile and to the approximated one, confirms that the adopted parameterization procedure is sufficiently accurate and general.

Figure 5(*c*) reports the convective heat transfer coefficient distributions, both for the original and approximated profiles, together with the experimental data for the $M_{2is}=1.118$, $Re=5.6\times10^5$ case. The grid refinement study confirms that the resolution is also adequate to properly capture the thin near wall thermal layer features, a definitely more demanding task. The experimental data are in good agreement with the grid converged computed data, although some discrepancies exists. Having assessed the quality of the computations we conjecture that the small differences should be attributed to the turbulence level of the incoming stream (assumed equal to zero in the computations), which is known to play a role on the surface heat transfer distribution [20]. No attempts were made to model these effects.

Prior to the true optimization of the blade profile we have carried out a parametric study to have a flavor of the cascade performance in a certain range of some blade parameters. The attention was naturally focused on the overall cascades aero-thermal characteristics which can be summarized by some integral results like the loss coefficient, ξ, and the blade load and heat coefficients, C_L and C_H. The related definitions are given as follows:

$$\text{Loss coefficient:} \qquad \xi=\frac{p_{o1}-p_{o2}}{p_{o1}-p_2} \tag{4}$$

$$\text{Load coefficient:} \qquad C_L=\frac{1}{C\cos(\gamma)}\oint \mathrm{M}_{\mathrm{is},w}dx \tag{5}$$

$$\text{Heat transfer coefficient:} \qquad C_H=\int_{-l_{ss}}^{+l_{ps}} C_h dl \tag{6}$$

l being a nondimensional curvilinear abscissa along the blade profile and C_h the local heat transfer coefficient

$$C_h=\frac{\dot{q}_w}{T_{01}-T_w} \tag{7}$$

The overall cascade performance is estimated in terms of a convex combination of the individual aero-thermodynamic coefficients defined above; in a first stage the weighting factors are simply taken so that the objective function is the arithmetic mean of the performance parameters, i.e.:

$$f=(\xi/\xi_{\mathrm{ref}}+C_{L\mathrm{ref}}/C_L+C_H/C_{H\mathrm{ref}})/3 \tag{8}$$

This definition was reconsidered when proceeding, in the following sections, with some multi-objective strategies, due to the nonlinearity associated with the load term. The reference values in Eq. (8) are obtained when the design variables are set to the values indicated in Table 1; viz.

Loss coefficient, $\xi_{\mathrm{ref}}=0.0673$

Load coefficient, $C_{L\mathrm{ref}}=0.818$

Heat coefficient, $C_{H\mathrm{ref}}=155.9\ \mathrm{W/(m^2K)}$

The parametric study was carried out through analyses in three connected two or three-dimensional spaces of independent variables, i.e., of some blade parameters, in accordance with the data given in Table 3.

The first analysis (referred to as PS1) employed variable fields centered around the reference values given in Table 1, viz. the LE ellipse diameter, A, the diameter ratio (A/B), and the LE wedge angle, ω_{le}.

The second analysis (PS2) examines an extended data range for (A/B) and ω_{le}, while the third one (PS3) introduces variations in the X_a and X_c parameters for given values of A, (A/B) and ω_{le}, which are fixed at their optimal levels detected in the previous analyses.

Table 3 Independent variables ranges and optimal cascade performance data in the parametric study

	Design variable					Performance			
Flow Analysis	A	(A/B)	ω_{le} [deg]	X_a	X_c	$f_{\min}$	$\xi_{\min}$	$C_{L\,\max}$	$C_{H\,\min}$
Reference case	0.065	1.	45.5	0.331	0.129	1.000	0.0673	0.818	155.96
PS1	0.035–0.095	0.7–1.3	30–60	0.331	0.129	0.936	0.0655	0.864	149.68
PS2	0.085	1–2	10–45	0.331	0.129	0.936	0.0655	0.867	151.75
PS3	0.085	1.3	30	0.13–0.53	0.03–0.43	0.917	0.0653	0.869	149.96

Table 3 also summarizes the best results obtained in terms of the individual performance parameters ξ, C_L and C_H, and of the function f given by Eq. (8). It is worth noting that, unlike the reference case, the best values in last four columns pertain to different blade shapes.

The PS2 and PS3 cases must be intended as two different attempts to improve the best results of the PS1 analysis. Indeed, some margins of improvement seem to exist, but the cascade performance in the two-dimensional spaces spanned by PS2 and PS3 (Figs. 6 and 7, respectively), show diverging trends. In particular, the search of minimum heat transfer conditions seems to conflict with that of minimum losses, while the latter is significantly far from the maximum in blade loading. These considerations mainly result from the second analysis (Fig. 6), which deals with parameters strongly affecting the leading edge shape, while the third one (Fig. 7) suggests only further marginal improvements, related to the modifications examined for the pressure and suction side shape in the blade inlet region (X_a and X_c parameters). In this case, the improvements in terms of heat coefficient reduction are more appreciable; but this condition can only be found for diminished blade loading levels and increased losses. The optimal region for the combined function is found for higher levels of the X_c coordinate which corresponds to an enlarged curvature of the blade pressure side.

Figure 8 compares the reference blade profile with those producing the best results in the second and third parametric analysis, in terms of the minimum combined function. The subsequent Fig. 9 presents the blade surface distribution of the isentropic Mach number and convective heat transfer coefficient. The optimal blade configurations resulting from the parametric study seem to present, in addition to the increased load level, a smoother accelerated flow towards the Mach number peak. Both analyses suggest the possibility of lower peaks in local heat transfer conditions, mainly along the blade suction side.

The parametric studies indicate that proper strategies must be set up for an integrated use of the Navier-Stokes based flow analysis with the optimization process. The purpose is to overcome some limits evidenced by the previous analysis, mainly in terms of conflicting results, but also with regard to the need of introducing further variables without increasing the computational costs.

The Objective Function and the Optimizer

The design problem is mathematically expressed as a constrained minimization problem, whose associated cost function minimizes a combination of the cascade performance parameters, say

$$f(\overline{X})=\left(W_{\xi}\frac{\xi}{\xi_{\text{ref}}}-W_L\frac{C_L}{C_{L\text{ref}}}+W_H\frac{C_H}{C_{H\text{ref}}}\right);\quad \overline{X}\in\mathbf{R}^n \tag{9}$$

where $\overline{X}$ is the set of independent variables listed in Table 1. The objective function formulation is similar to the one given by Eq. (8), except for the additional degrees of freedom associated with the definition of the W_{ξ}, W_L and W_H weights and for the linear dependence upon the load term. This more general definition of $f(\overline{X})$ allows for a more thorough control of the optimization process. A proper selection of the relative weights in Eq. (9) may guide the optimizer towards either minimal loss or minimal heat loaded profiles. In addition, a nonzero weight on the aerodynamic load term ensures preservation of an appropriate flow deviation, in accordance with the reference data specifications.

The optimizer further requires that n_e equality constraints and n_i inequality constraints have to be satisfied

$$C_j(\overline{X})=0 \quad (j=1,\ n_e)$$

$$D_k(\overline{X})\leqslant 0 \quad (k=1,\ n_i) \tag{10}$$

In previous applications [17] we have considered an equality constraint on the outlet flow angle (i.e., $n_e=1$, $C(\overline{X})=\beta_{2\,f}-\beta^*_{2\,f}=0$); but in this case a proper choice of the relative weights, Wj, renders the design problem properly defined without this assignment.

Inequality constraints control lower and upper bounds for the independent variables and limits (if any) imposed to both geometrical and flow parameters resulting from calculations (for instance: blade thickness, maximum Mach number level, etc.).

For the sake of generality, the complete formulation of the augmented Lagrangian function is hereby reported

$$F(\overline{X},\lambda,\pi_c,\pi_d)=f(\overline{X})-\lambda\cdot C(\overline{X})+\pi_c[C(\overline{X})]^2 + \pi_d\sum_k\ [D_k(\overline{X})]^2\equiv\min\ \ (\forall k:\ D_k>0) \tag{11}$$

where λ is the Lagrange multiplier or co-state vector, and π_c,π_d are quadratic penalty terms.

The augmented Lagrangian method [21] basically consists of the unconstrained minimization of a differentiable function involving Lagrange multipliers and one or more penalty terms. Since the shape of the search space is altered with respect to the original formulation (4) of the objective function, the optimizing process must be organized into a number of cycles with a progressive update of both Lagrange multipliers and penalty factors.

The basic structure of the iteration is outlined in the following.

Given an initial starting vector $\overline{X}^0$, an estimate of the Lagrange multiplier λ^0, a set of active constraints, penalty parameters π_c^0,π_d^0, and an upper-bound M for the number of unconstrained minimization to be performed, set:

1. *Outer loop* begin: $k\leftarrow 0$.
2. Convergence test: check the optimality condition and terminate with $\overline{X}^k$ as solution or exit if $k>\mathrm{M}$.
3. Begin *optimization cycle*: $\overline{X}_0=\overline{X}^k$ being the starting point, let $\overline{X}^{k+1}=\overline{X}_{p+1}$ be the best approximation after $p+1$ inner iterations of the optimization problem
$$\textit{minimize}\quad F(\overline{X},\lambda,\pi_c,\pi_d)\quad \overline{X}\in\mathbf{R}^n \tag{12}$$
4. Update the Lagrange multiplier: modify if necessary the specification of the active constraints set and compute a new estimate of the Lagrange multiplier according to the recursive formula
$$\lambda^{k+1}=\lambda^k-\pi_c^k\cdot C(\overline{X}^{k+1}) \tag{13}$$
5. Penalty update: increase the penalty parameters if the constraints violations at $\overline{X}^{k+1}$ have not reduced sufficiently. The

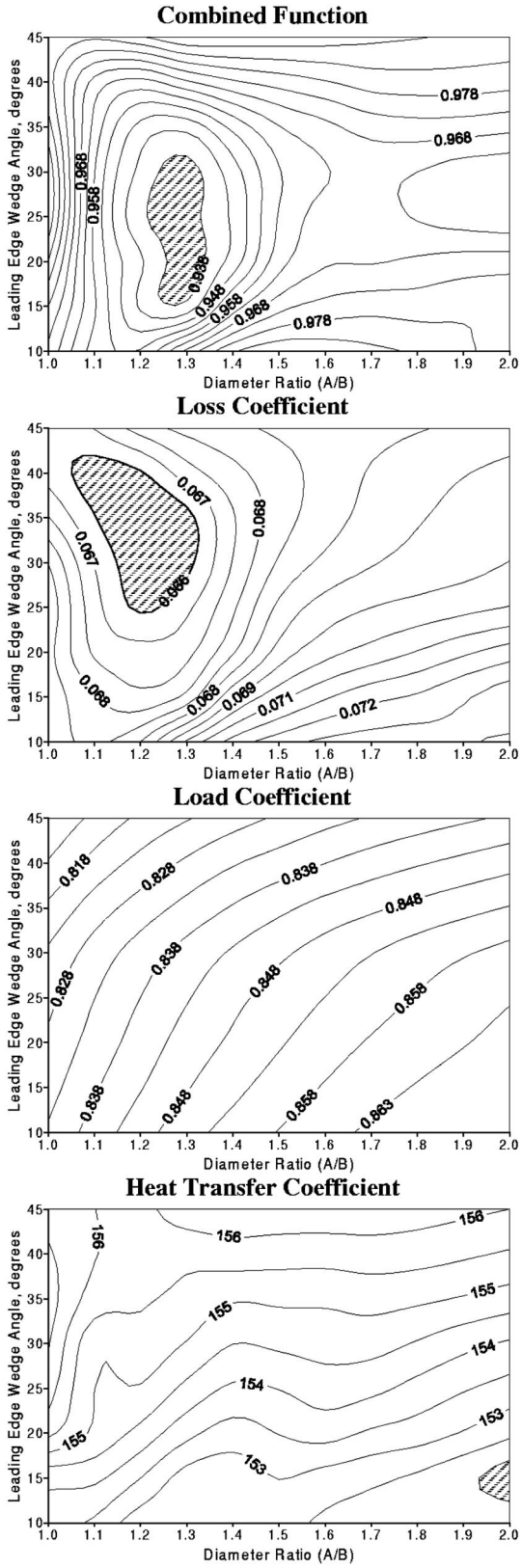

Fig. 6 Cascade performance behavior in the second parametric analysis

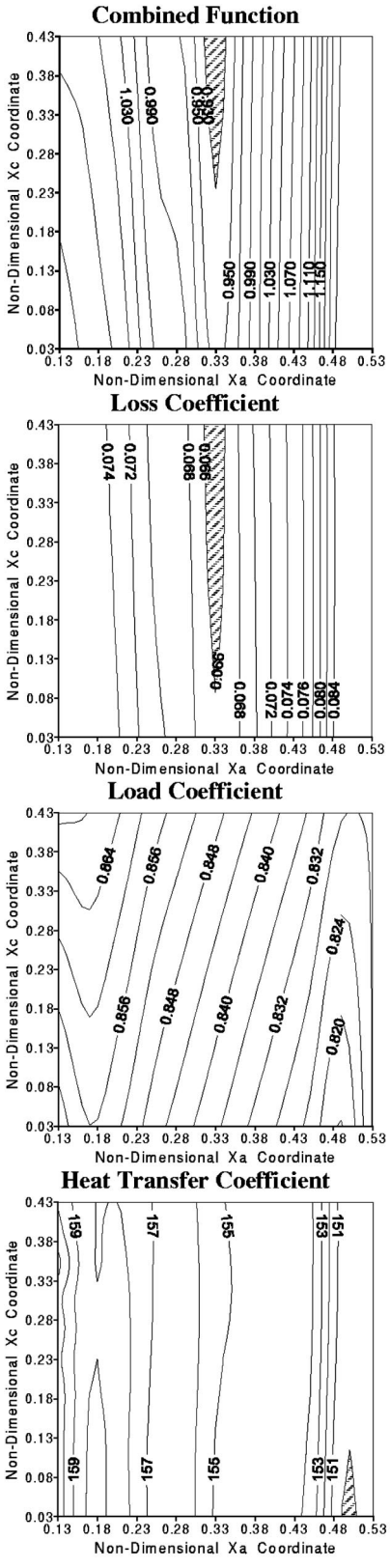

Fig. 7 Cascade performance behavior in the third parametric analysis

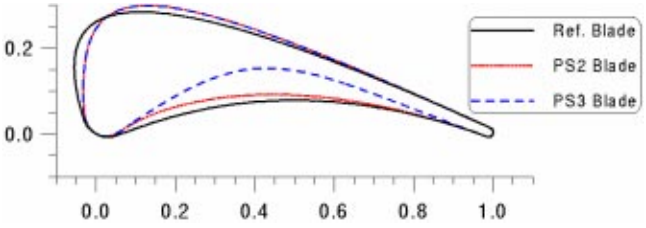

Fig. 8 Comparison of the original blade profile with the best results of PS2 and PS3

π_c, π_d increase is operated by

$$\pi_c^{k+1}=\frac{\lambda^{k+1}}{\varepsilon^k};\ \pi_d^{k+1}=\pi_d^k+\frac{\sum_k [D_k(\overline{X})]^2}{\varepsilon^k}\ (\forall k:\ D_k>0) \tag{14}$$

The error term, ε^k, is progressively decreased at each new cycle.

6. *Outer loop update*: set $k \leftarrow k+1$ for the new cycle and return to step 2.

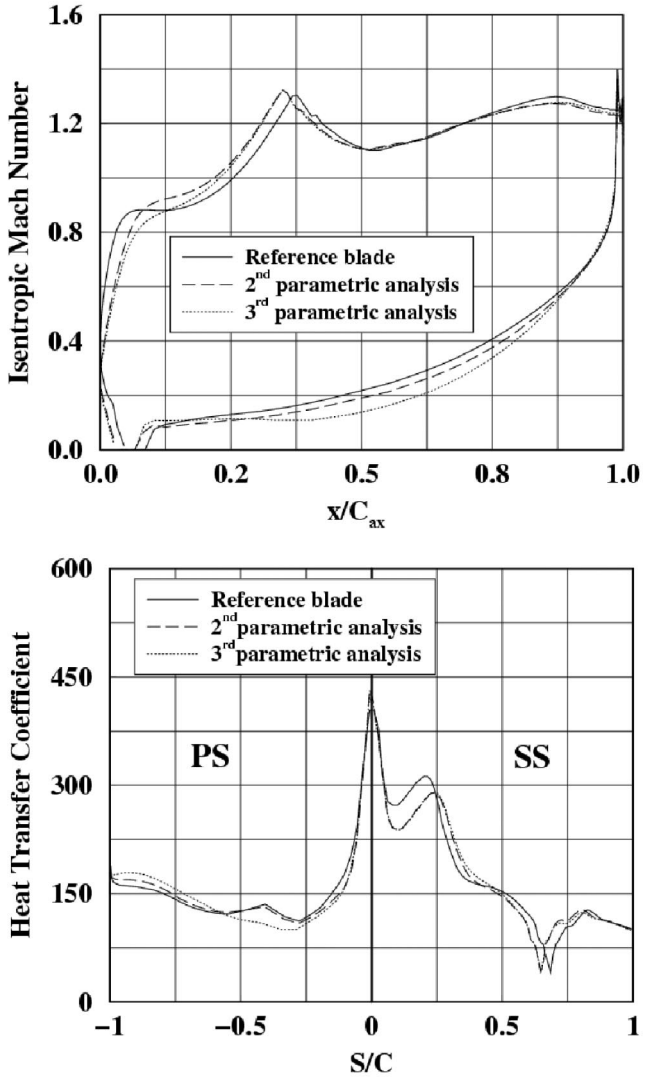

Fig. 9 Comparison of flow parameter distributions in the parametric study

In the case of absence of equality constraints, no Lagrange multiplier update is needed; but the foregoing sequence is still adopted to make more severe, at each new cycle, both the penalty factors and the convergence criteria.

Regarding to the optimizing algorithm, step 3 is carried out with a Newton-type method whose search directions are computed as:

$$\min[F(\overline{X})] \Rightarrow \overline{X}_{l+1}-\overline{X}_l=-\nabla[F(\overline{X}_l)]\cdot\bar{\bar{H}}^{-1}[F(\overline{X}_l)]\quad l=0,p \tag{15}$$

The computational cost of the method is therefore mainly due to the estimate of the Hessian matrix, $\bar{\bar{H}}$, and of the gradient. In addition, the algorithm implies the positive definiteness of $\bar{\bar{H}}$, in which case quadratic convergence is attained if the initial vector guess, $\overline{X}_0$, is sufficiently close to the final solution. When $\bar{\bar{H}}$ is indefinite the Newton method is replaced by a simpler steepest descent method of the following type:

$$\min[F(\overline{X})] \Rightarrow \overline{X}_{l+1}-\overline{X}_l=-\tau^*\nabla[F(\overline{X}_l)] \tag{16}$$

which requires an iterative search of the τ^* factor for establishing the optimal step along the gradient direction.

It has to be remarked that the optimization method of the Newton type has been chosen by the author after experiencing different methods, like those based on the genetic algorithm approach.

The Aero-Thermal Blade Optimization

The examples developed in this work aim to test the validity of the blade design procedure when trying to improve the overall cascade performance with different relative weights of the integral loss, load and heat coefficients.

Two optimizations were carried out: the first one (O1) balancing the importance of the foregoing performance parameters, the second one (O2) addressing a reduction of the blade heat load. These conditions are summarized in Table 4, together with the independent variable ranges. Note that the upper and lower design variables values indicated in Table 4 are essential to properly define the search space; as stated, this is controlled through the penalty term π_d. The choice of the blade parameters was confined to those most affecting the leading edge geometry and the blade shape in the inlet region. This is in accordance with the previously declared objective of improving the aero-thermal performance of the cascade, thus focusing the attention on the region involving the most intense heat transfer. The outcome of the optimization would produce significant benefit in terms of cooling flow rates reductions in the actual gas turbine operation.

It has to be remarked that some residual weight was assigned to the control of flow losses and aerodynamic load in the second optimization as well, in order to ensure a solution of practical interest. In other words, the optimized cascade configuration must preserve or increase the initial high level of flow turning and only a slight increase in loss coefficient may be accepted.

Table 4 Relative weights of performance parameters and variable data ranges in the optimization examples

Relative weight		Optim. no. 1	Optim. no. 2
W_ξ		1/3	1/5
W_L		1/3	1/5
W_H		1/3	3/5
Independent variable		**Lower value**	**Upper value**
LE main ellipse diameter	A	0.035	0.150
LE diameter ratio	(A/B)	0.7	1.7
Blade inlet angle	α_1	40 deg	80 deg
LE wedge angle	ω_{le}	10 deg	60 deg
1st control point	X_a	0.13	0.50
3rd control point	X_c	0.03	0.45

Table 5 Comparison of blade parameters and cascade performance data

	Cycle no.	Function evaluations	A	(A/B)	α_1 [deg]	ω_{le} [deg]	X_a	X_c	Obj. funct. decrease	β_{2f} [deg]	ξ	C_L	C_H [W/(m^2 K)]
Reference case	--	--	0.0650	1.000	63.06	45.50	0.331	0.129	--	−73.18	.0674	0.818	155.9
PS2	--		0.0850	1.300	63.06	20.00	0.331	0.129	−5.60%	−75.90	.0668	0.845	153.7
PS3	--		0.0850	1.300	63.06	30.00	0.220	0.430	−7.35%	−75.27	.0653	0.849	155.2
O1	8	600	0.0377	1.193	56.91	35.07	0.392	0.150	−7.90%	−75.92	.0672	0.855	152.5
O2	22	1197	0.0329	1.293	59.44	25.91	0.415	0.149	−5.17%	−76.59	.0690	0.863	149.6

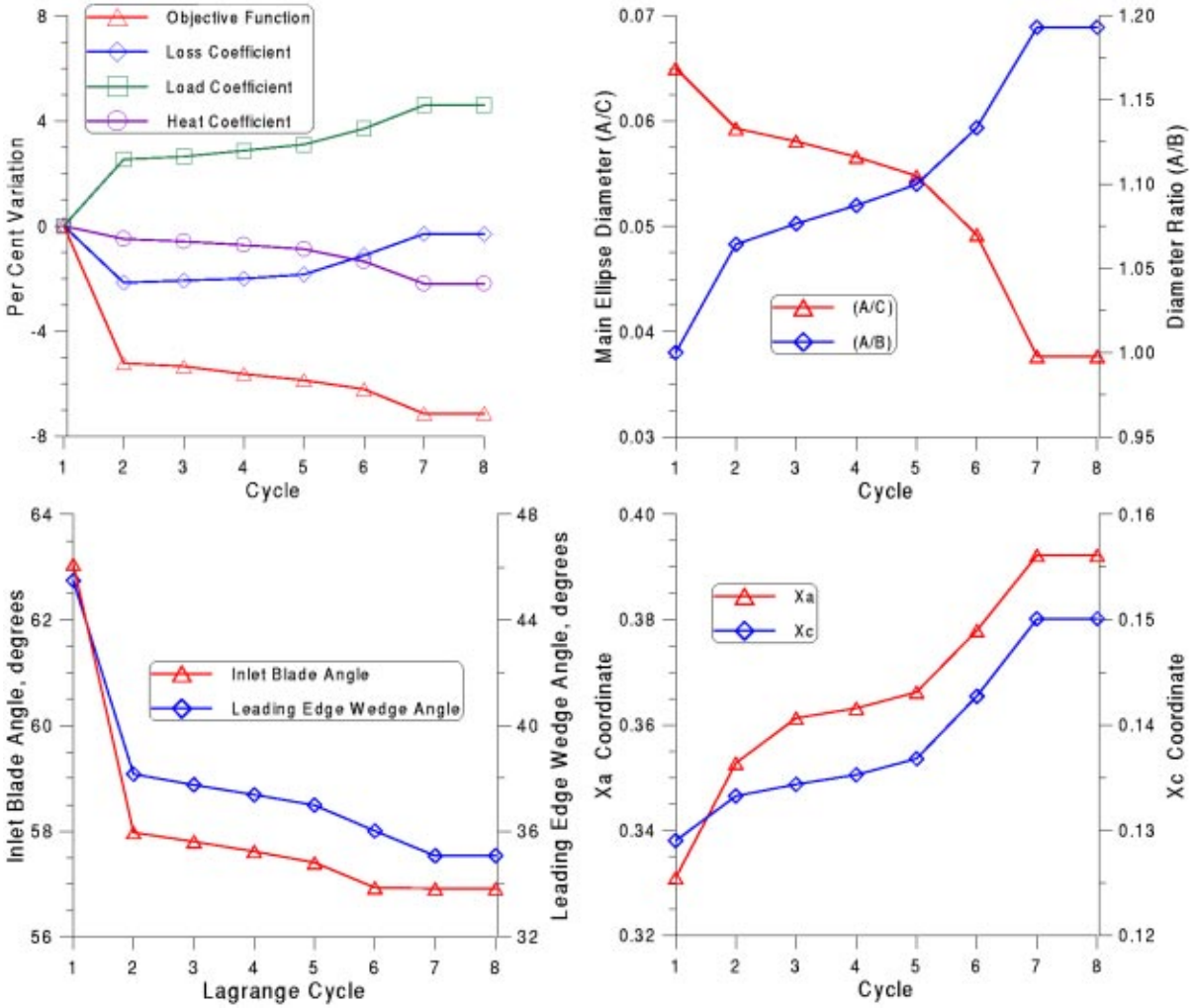

Fig. 10 Progress in the optimizing process O1

In all cases the optimization process was of the unconstrained type, except for the limitations imposed to the independent variable ranges detailed in Table 4. A number of optimizing cycles were however needed to reach the final solution with a fairly converging process.

Table 5 compares the results of the optimization tests with those obtained in the reference case and in the PS2 and PS3 parametric analyses. The objective function decrease is evaluated with respect to the value of the reference cascade configuration and by assuming, in all cases, the formulation given by Eq. (9). Both computations required, as predicted, several cycles to reach the convergence with a prescribed accuracy level. The rather high number of function evaluations can be explained by the fact that the starting point was set at the original values of the blade parameters, so neglecting the preliminary results of the parametric study. In the authors' opinion, this was the most challenging way

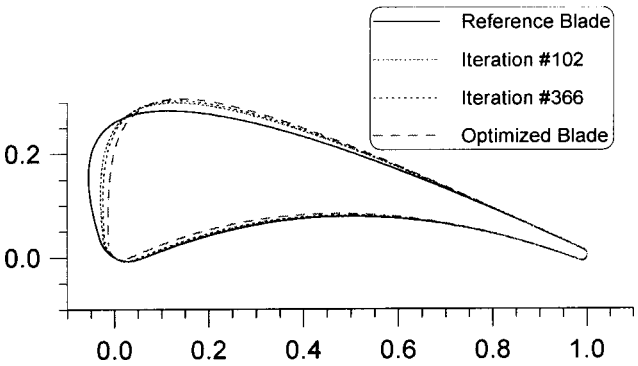

Fig. 11 Blade profile variation during the optimization O1

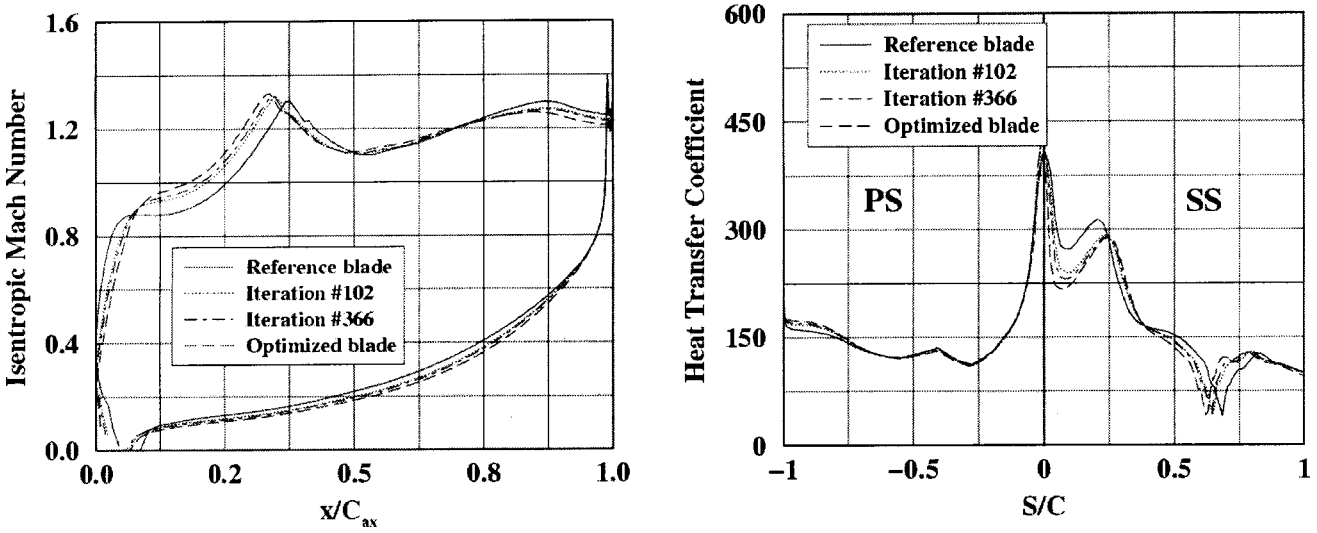

Fig. 12 Progress in flow parameter distribution during optimization O1

to test the effectiveness of the design methodology. Faster applications can be obtained by performing an appropriate preliminary *design of experiments*, in order to find by computational means a more feasible starting value for the optimizing procedure.

Referring to the first optimization, both Table 5 and Fig. 10 show that the final solution suggests modifications in all parameters affecting the leading edge shape, i.e., a more sharpened blade nose, due to the concurrent effect of the LE ellipse stretch-

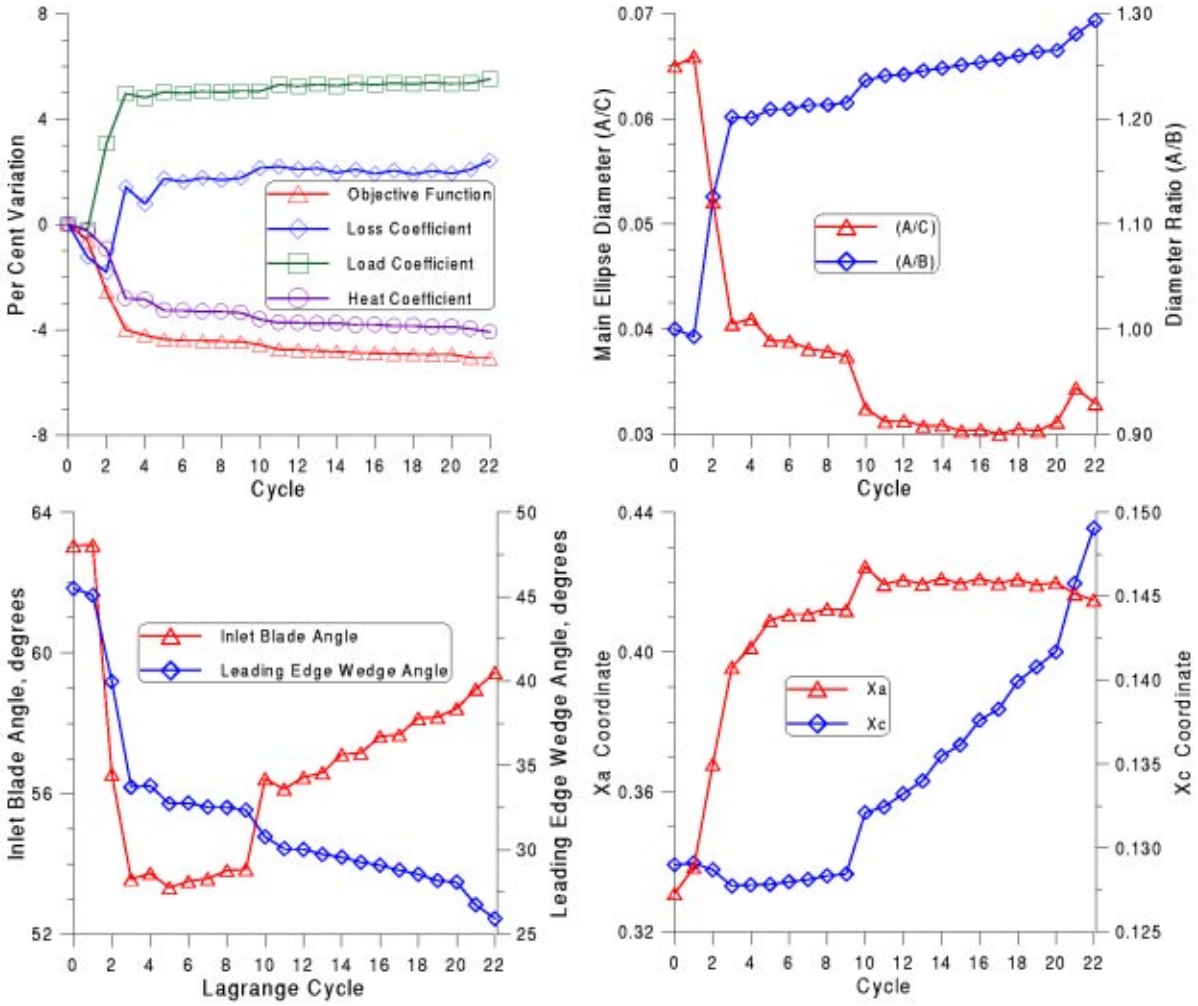

Fig. 13 Progress in the optimizing process O2

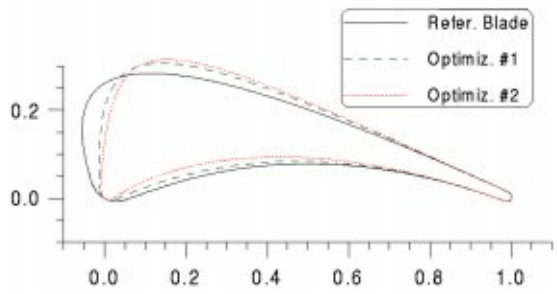

Fig. 14 Comparison of reference and optimized blade profiles

ing (increase in the A diameter and in the (A/B) ratio), and of the reduction in both inlet and wedge angles, α_1 and ω_{le}. Modifications are also produced in the blade suction side, due to the variation in the X_a parameter.

The resulting cascade performance parameters are slightly improved, if looking at both loss and heat coefficient, and more remarkably in terms of blade loading, as also confirmed by the increased flow turning represented by the β_{2f} value.

Figure 10 shows the progress in the optimizing process, while the following Figs. 11 and 12 highlight the variations produced in the blade shape and in flow distributions at several stages of the procedure. Figure 11 confirms that the most evident changes involve the blade leading edge and suction side, and in the same sense can be interpreted the wall distributions of both isentropic Mach number and heat transfer coefficient. The main progressive changes occur along the suction side, and this contributes to the aerodynamic load increase and to the limited decrease in the integral heat coefficient. Really, a certain reduction can be observed also in both heat flux peak, due to the leading edge modification. The latter also produces a smoother flow acceleration, as demonstrated by the suction side pattern of the M_{is} value.

Looking at the second optimization, a more appreciable reduction in the heat coefficient is achieved while preserving a high blade loading level and a limited loss increase, as demonstrated by the values in Table 4 and by the diagrams in Fig. 13. The latter figures also show the trend of variation of the independent variables which point towards more dramatic changes in the leading edge shape. These essentially consist of a decrease in both the ellipse size (i.e., the main diameter (A) reduces and the diameter ratio (A/B) increases), and in the wedge angle amplitude. Such new values also produce evident changes in the blade pressure side profile, although the *Xa* and *Xc* values remain practically the same as in the first optimization.

The whole change in blade profile and cascade arrangement is better evidenced by Figs. 14 and 16. The throat position is clearly anticipated when compared with the original configuration and with the one resulting from the first optimization. As a consequence the shock location is different for the three examined cases, as shown by the Mach number pattern in Fig. 15. The same figure highlights the considerable reduction which occurs, after

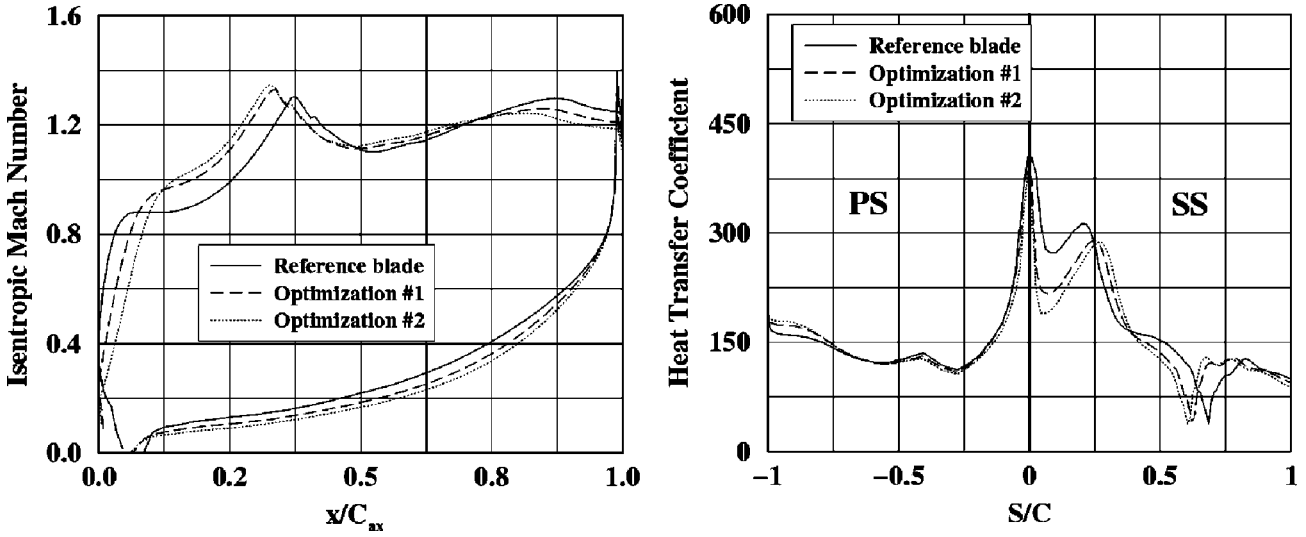

Fig. 15 Comparison of base and optimized flow parameter distributions

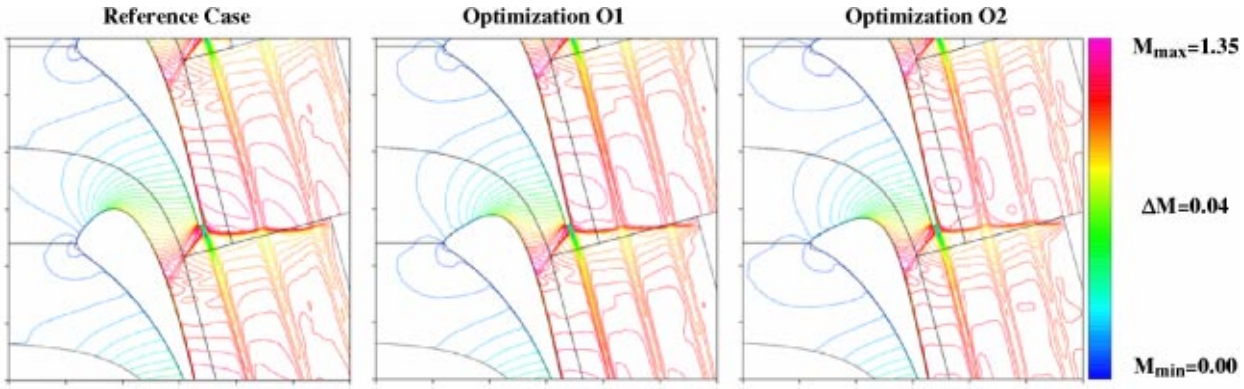

Fig. 16 Comparison of iso-Mach number lines

the second optimization, in the values of local heat transfer coefficient and, in particular, in the leading edge peak.

A detailed insight of the cascade flow distribution in the base and optimized cases is finally given in Fig. 16, in terms of Mach number iso-contours.

Conclusions

The authors have investigated the possibility of improving the performance of a well-designed existing turbine blade cascade, by addressing the issue of a direct control of the thermal load. The proposed parameterization of the blade shape is efficient and sufficiently general so that the initial geometry could be approximated within a few percent error.

A design procedure addressing the enhancement of the combined aero-thermal blade performance has been outlined; it makes use of a properly defined cost function consisting of a convex combination of the integral performance parameters with appropriate weights.

The results have shown that despite the excellence of the initial design, it is indeed possible to achieve a non-negligible improvement in the overall blade efficiency.

The associated reduction in the cooling flow rates may induce appreciable benefits to the whole gas turbine design process.

Nomenclature

C = blade chord
C_H = heat transfer coefficient
C_L = load coefficient
$C(\underline{X})$ = equality constraint
$D(\underline{X})$ = inequality constraint
e = internal energy
$f(\underline{X})$ = objective function
$F(\underline{X})$ = augmented Lagrangian function
$\bar{\bar{H}}$ = Hessian matrix
M_{is} = isentropic Mach no.
n = no. of independent variables
Pr = Prandtl no.
p = pressure
$\dot{q}$ = heat flux
Re = Reynolds no.
T = temperature
u_j = velocity component
u_τ = friction velocity
V = total velocity
x_j = coordinate
$\underline{X}$ = vector of independent variables
α = blade angle referred to chord direction
β_f = flow angle referred to axial direction
λ = Lagrange multiplier
μ = dynamic viscosity
π = penalty factor
ρ = density
σ = cascade solidity
τ = stress tensor
ξ = total-to-total pressure loss coefficient
ω = wedge angle

Subscripts

0 = total conditions
1, 2 = cascade inlet, outlet;
le = leading edge
ss = suction side
ps = pressure side
te = trailing edge
w = blade wall

References

[1] Baysal, O., et al., 1995, "CFD For Design and Optimization," ASME FED-Vol. 32.
[2] Borges, J., 1990, "A Three-Dimensional Inverse Method for Turbomachinery," ASME J. Turbomach., **112**, pp. 346–354.
[3] Demeulenaere, A., and Van den Braembussche, R., "Three-Dimensional Inverse Method for Turbomachinery Blading Design," ASME Paper No. 96-GT-39.
[4] Goel, S., et al., 1996, "Turbine Airfoil Design Optimization," ASME Paper No. 96-GT-158.
[5] Leonard, O., and Van den Braembussche, R., 1992, "Design Methods for Subsonic and Transonic Cascades with Prescribed Mach Number Distribution," Trans. ASME, **114**(3), pp. 553–560.
[6] Pierret, S., and Van den Braembussche, R. A., 1998, "Turbomachinery Blade Design Using a Navier Stokes Solver and Artificial Neural Network," ASME J. Turbomach., **121**, pp. 326–332.
[7] Shahpar, S., 2000, "A Comparative Study of Optimization Methods for Aerodynamic Design of Turbomachinery Blades," ASME Paper No. 2000-GT-523.
[8] "Turbomachinery Blade Design Systems," von Karman Institute *Lecture Series* 02, Rhode Saint Genese, 1999.
[9] Ashihara, K., and Goto, A., 2001, "Turbomachinery Blade Design Using 3-D Inverse Design Method: CFD Optimization Algorithm," ASME Paper No. 2001-GT-0358.
[10] Nomoto, H., Koga, A., Ito, S., Fukuyama, Y., Otomo, F., Shibuya, S., Sato, M., Kobayashi, Y., and Matsuzaki, H., 1997, "The Advanced Cooling Technology for the 1500C Class Gas Turbines: Steam-Cooled Vanes and Air-cooled Blades," ASME J. Eng. Gas Turbines Power, **113**, pp. 624–632.
[11] Anders, J. M., and Haarmeyer, J., 1999, "A Parametric Blade Design System," *Turbomachinery Blade Design Systems*, von Karman Institute Lecture Series 02.
[12] Arts, T., Lambert de Rouvroit, M., and Rutherford, A. W., 1990, "Aero-thermal Investigation of an Highly Loaded Transonic Linear Turbine Guide Vane Cascade," VKI TN174.
[13] Roe, P., 1981, "Approximate Riemann Solvers, Parameter Vectors, and Difference Schemes," J. Comp. Physics, **43**(2), pp. 357–372.
[14] Van Leer, B., 1981, "Towards the Ultimate Conservation Difference Scheme V: a Second Order Sequel to Godunov's Methods," J. Comp. Physics, **40**(2), pp. 101–136.
[15] Jameson, A., and Yoon, S., 1987, "Lower Upper Implicit Schemes with Multiple Grids for the Euler Equations," AIAA J., **25**(7).
[16] Manna, M., 1992, "A 3D High Resolution Compressible Flow Solver," Ph.D. thesis, Catholic University of Louvain/von Karman Institute for Fluid Dynamics.
[17] Manna, M., and Tuccillo, R., 2000, "The Combined Use of Navier-Stokes Solvers and Optimization Methods for Decelerating Cascade Design," ASME Paper No. 2000-GT-0524.
[18] P. Davis, 197, *Interpolation and Approximation*, Dover Publications Inc., New York.
[19] Manna, M., Mulas, M., and Cicatelli, G., 1997, "Vortex Shedding Behind a Blunt Trailing Edge Turbine Blade," Int. J. Turbo Jet Engines, **14**(3), pp. 145–157.
[20] Smith, M. C., and Kuethe, A. M., 1966, "Effects of Turbulence on Laminar Skin Friction and Heat Transfer," Phys. Fluids, **9**(12), pp. 2337–2347.
[21] Gill, P. H., Murray, W., and Wright, M. H., 1984, *Practical Optimization*, Academic Press, London, UK.
[22] "Inverse Design and Optimization Methods" 1997, *Lecture Series* 1997-05, von Karman Institute for Fluid Dynamics.
[23] "Optimum Design Methods for Aerodynamics" *AGARD FDP-VKI Special Course*, Apr. 1994.

Steven E. Gorrell
Mem. ASME,
Air Force Research Laboratory,
AFRL/PRTF,
Wright-Patterson AFB, OH 45433

Theodore H. Okiishi
Mem. ASME,
Fellow ASME,
College of Engineering,
Iowa State University,
Ames, IA 50011

William W. Copenhaver
Mem. ASME,
Fellow ASME,
Air Force Research Laboratory,
AFRL/PRTF,
Wright-Patterson AFB, OH 45433

Stator-Rotor Interactions in a Transonic Compressor—Part 1: Effect of Blade-Row Spacing on Performance

Usually less axial spacing between the blade rows of an axial flow compressor is associated with improved efficiency. However, mass flow rate, pressure ratio, and efficiency all decreased as the axial spacing between the stator and rotor was reduced in a transonic compressor rig. Reductions as great as 3.3% in pressure ratio, and 1.3 points of efficiency were observed as axial spacing between the blade rows was decreased from far apart to close together. The number of blades in the stator blade-row also affected stage performance. Higher stator blade-row solidity led to larger changes in pressure ratio efficiency, and mass flow rate with axial spacing variation. Analysis of the experimental data suggests that the drop in performance is a result of increased loss production due to blade-row interactions. Losses in addition to mixing loss are present when the blade-rows are spaced closer together. The extra losses are associated with the upstream stator wakes and are most significant in the midspan region of the flow. [DOI: 10.1115/1.1540119]

Introduction

A better understanding of the unsteady flow through a turbomachine is necessary to overcome many of the present-day technical challenges encountered during the design and operation of improved high-performance gas turbine engines. For example, unsteady flow phenomena play a primary role in setting gas turbine engine operating limits such as stall inception and in producing high-cycle fatigue and noise.

One area of current interest is the impact of blade-row interactions on turbomachine performance. Is the impact large enough to warrant the increased complexity of accounting for unsteady flow effects in the design process? What level of design tool is necessary to adequately account for these effects in the design process?

Many multistage axisymmetric flow models assume that the incoming flow to a blade row is a mixed-out average of the flow exiting the preceding blade row. Potential flow field effects between blade rows are generally not adequately considered. These models use empirical correlations based on an engine company's design experience to account for the effects of unsteady flow.

The average passage model developed by Adamczyk [1] accounts for the presence of neighboring blade rows through an average passage flow field representation. However, its accuracy is dependent on the models used to account for the effects of the unsteady flow environment on the average-passage flow field.

Unsteady Reynolds averaged Navier-Stokes equations provide a more accurate representation of the flow fields that exist in turbomachines. However, the computer resources required to obtain a solution of these equations make this option impractical for designers for the time being. For a good historical perspective of multistage turbomachine design models, see Adamczyk [2].

This paper contains some provocative ideas about the effects of blade-row interactions on compressor performance based on measured data. The test article and instrumentation used for the measurements are described. Compressor flow data that quantify the effects of closer axial spacing on the flow field and compressor performance are presented.

Contributed by the International Gas Turbine Institute and presented at the International Gas Turbine and Aeroengine Congress and Exhibition, Amsterdam, The Netherlands, June 3–6, 2002. Manuscript received by the IGTI November 7, 2001. Paper No. 2002-GT-30494. Review Chair: E. Benvenuti.

Reference [3] builds on the conclusions based on these measurements to introduce the notion of a previously unidentified loss producing mechanism resulting from the interaction of the transonic rotor bow shock with the trailing edge of the upstream stator. CFD simulations of the blade-row interaction and high-response stator blade static pressure measurements are used to develop this idea.

Subsonic Rotor-Stator Interactions. Experimental results from a four-stage compressor published by Smith [4] and another multistage compressor experiment discussed by Mikolajczak [5] demonstrate that reducing the axial gap between blade rows in multistage compressors increased the pressure ratio and efficiency for a given flow coefficient. In both cases efficiency was increased by one point when the blade rows were moved from far spacing to close spacing. Smith [6,7] proposed that the performance gains were partially a result of inviscid wake defect reduction through inviscid stretching and introduced the concept of wake recovery. Smith has described wake recovery as the process that occurs when a viscous wake is flattened (or stretched) reversibly while passing through a blade row, thus avoiding some of the entropy rise that occurs when a wake is flattened entirely by viscous dissipation. The end result is a reduction of wake mixing loss with small axial gaps between blade rows.

Since Smith's [7] description of wake recovery, Deregal and Tan [8], Adamczyk [9], Van Zante et al. [10], and van de Wall [11] have all advanced an understanding of the concept of wake recovery in rotor-stator interactions. From the results of their research it has been concluded that to reduce the amount of mixing loss between blade rows, it would be beneficial to minimize axial spacing. By reducing the blade-row axial spacing, the rotor wake is captured sooner which allows it to mix out more by means of inviscid wake stretching than by viscous dissipation. However, it was assumed that closer spacing would not increase losses due to potential flow field interactions.

Stator-Rotor Interactions. Stator-rotor interaction experiments in transonic compressors have focused on visualizing and quantifying the interaction mechanisms present in the flow field. Ottavy et al. [12,13] made laser two-focus anemometer measurements between an IGV and transonic rotor. The measurements and analysis concentrated on the interaction between the rotor bow

shock and the wake shed from the IGV. It was concluded that the shock wave had a much larger effect on the IGV wake than the remainder of the flow. Upstream of the shock wave the IGV wake depth was reduced and the wake was overturned as a result of an expansion zone in the flow due to the curvature of the rotor blade suction surface. Downstream of the shock wave the IGV wake deficit increased and the wake was underturned.

Stator-rotor interactions are known to play a major role in producing forcing functions that contribute to high-cycle fatigue. Sanders and Fleeter [14] have made both particle image velocimetry (PIV) and blade surface static pressure measurements in the IGV passage upstream of a transonic rotor. Their results show that the flow field was highly unsteady due to the reflection and diffraction of the rotor bow shock in the IGV passage. The shock interaction with the IGV trailing edge caused the trailing edge stagnation point to move periodically from the pressure to suction surfaces of the IGV. This interaction accounted for peak-to-peak fluctuations in static pressure as large as 60% of the inlet total pressure.

Focus of Research Effort. The research presented here continues the analysis of stator-rotor interactions by documenting for the first time the effect of stator-rotor axial spacing on mass flow rate, pressure ratio, and efficiency in a transonic compressor setting. The majority of research on blade-row spacing has focused on the effect of rotor-stator axial gap on compressor performance in subsonic flows. The focus of this research is to quantify the aerodynamic and thermodynamic changes that occur prior to the rotor entrance due to increased interaction between the upstream stator row and a downstream transonic rotor row. Although additional changes, beyond those considered in this study, appear at the exit to the rotor (primarily in the tip region) as a result of the interaction, it is believed that these are of lesser magnitude and therefore not important to the scope of this study.

Two specific issues are addressed, one being the influence of reduced stator-rotor axial spacing on the measured mass flow rate, pressure ratio and efficiency of a transonic compressor. Current results suggest that stator-rotor interactions impact the performance of a transonic compressor. The second issue addressed is the identification of primary blade-row interaction mechanisms that drive observed changes in overall performance. Steady measurements obtained at the rotor exit along with time-accurate computational analysis presented in reference [3] will be used for this.

Issue 1: Influence of Axial Spacing Between Blade Rows on Steady Performance

Documented here are the steady performance changes of a three-blade-row transonic compressor and a variation of the same compressor with the downstream stator blade row removed, as axial spacing is reduced between the upstream blade row and the rotor blade row. The experimental set up for both configurations of the test compressor will be described along with performance results for this phase of the research.

Stage Matching Investigation Rig (Three Blade Rows). All experimental and numerical research was performed on the U.S. Air Force's Stage Matching Investigation (SMI) rig. It is a high-speed, highly loaded compressor consisting of three blade rows: a wake generator, rotor, and stator as shown in Fig. 1. The rig was designed so that the wake generator to rotor axial spacing and the wake generator blade count could be varied. The axial spacings were denoted as ''close,'' ''mid,'' and ''far.'' The mid and far spacings represent typical axial gaps found in operational fans and compressors. However, the current generation of high-performance fans and compressors are being designed with the goal of minimizing blade-row spacing in order to reduce compressor length and thus weight and increase performance. The wake generator blade count could be set to 12, 24, or 40, or the rig could be run without any wake generators (identified as the ''clean inlet'' configuration). Table 1 gives the wake generator to rotor axial spacings normalized by the wake generator chord.

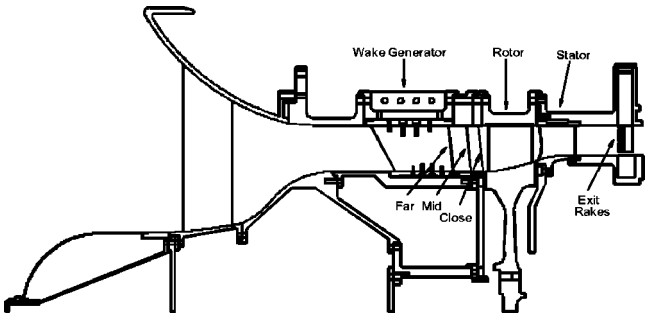

Fig. 1 Stage matching investigation rig layout

Compressor Stage. The rotor and stator were designed by Law and Wennerstrom [15]. A summary of the SMI stage aerodynamic design parameters is given in Table 2. The purpose of the wake generators was to create wakes typically found in modern-technology, highly loaded, low-aspect-ratio fan and compressor front stages. In general these wakes are turbulent and do not decay as rapidly as wakes from high-aspect-ratio stages with lower loading. The wake generators were designed with the intent of producing a two-dimensional representation of wakes measured at the exit of a high-pressure-ratio, low-aspect-ratio fan stage reported by Creason and Baghdadi [16]. A two-dimensional representation was desired in order to isolate the effect of different wake parameters during the experiment.

Details of the wake generator design were presented by Gorrell et al. [17]. In summary, the wake generators are uncambered symmetric airfoils that do not turn the flow. They have a small leading edge and a blunt trailing edge. This shape creates a large base drag and no swirl. Solidity is held constant from hub to tip by varying the chord, the intent being to hold spanwise loss and wake width constant.

Test Article Instrumentation. The SMI rig was tested in the Compressor Aero Research Lab (CARL) located at Wright-Patterson Air Force Base, OH. Exit conditions measured to compute compressor performance (pressure ratio and efficiency) were obtained from an array of total pressure and total temperature probes. The exit instrumentation consisted of ten pressure and ten temperature rakes with eight probes distributed spanwise on each rake (see reference [17]). Overall performance of the SMI rig was calculated by numerically averaging the 80 exit pressure and 80

Table 1 Wake generator-rotor axial spacing

Spacing	ax/c (mean)	ax/c (hub)	ax/c (tip)
Close	0.13	0.10	0.14
Mid	0.26	0.26	0.26
Far	0.55	0.60	0.52

ax=axial spacing
c=wake generator chord

Table 2 SMI aerodynamic design parameters

Parameter	Rotor	Stator
Number of airfoils	33	49
Aspect ratio—average	0.961	0.892
Inlet hub/tip ratio	0.750	0.816
Flow/annulus area, kg/s/m^2	195.30	—
Tip speed, corrected m/s	341.37	—
M_{REL} LE hub	0.963	0.820
M_{REL} LE tip	1.191	0.690
Max D factor	0.545	0.502
LE tip dia., m	0.4825	0.4825

exit temperatures. The rakes were positioned so that a pitchwise distribution in pressure and temperature could be established for a circumferentially periodic flow field. Placement was such that one stator pitch distribution (in 10% increments) was measured. Inlet conditions were determined from an array of 30 inlet thermocouples for temperature and inlet plenum static pressures for total pressure.

As discussed by Gorrell et al. [17] and Gorrell [18], if the exit rakes sense the influence of blade-rows upstream of the rotor, the upstream flow features will be aliased into the stator pitch results. For this experiment, with 12 and 24-wake generators in place upstream of the rotor, the influence of two wake generators was seen in the data measured for a single stator pitch. This phenomenon exists in any situation where fixed probes are used to quantify performance in embedded blade rows. Experiments by Cherret and Bryce [19] and Camp and Shin [20] have also shown that wakes from an upstream blade row may still be evident after passing through downstream blade rows. Therefore, the absolute value of the influence of wake generator spacing on performance will be influenced by aliasing, but the relative trends in measured performance between different configurations is still resolved.

Since this research includes a parametric study on the influence of small changes in axial blade-row spacing and wake generator solidity on compressor performance, it was necessary to determine what magnitude of performance changes should be considered significant. This was accomplished by establishing the repeatability (or precision error) of the experiment. The precision error of the measured mass flow rate, pressure ratio and efficiency was established through a series of repeat tests with the 24-wake-generator configuration and documented by Gorrell et al. [17]. It was concluded that at 100% Nc, performance differences greater than 0.068 Kg/s in mass flow rate, 0.008 pressure ratio, or 0.4 points in efficiency were a result of the configuration change and not within the uncertainty of the measurements.

Wake Generator/Rotor Only Configuration. To alleviate some of the concerns that were raised due to the effects of aliasing on the measured performance and to remove any effects the downstream stator may have had on performance with changes in blade-row axial spacing, the SMI rig was modified to run without the stator. This was accomplished by replacing the stator hardware with a circumferential traverse assembly (CTA) at the case and an inner ring at the hub that matched the flowpath geometry of the original stator. The wake generator/rotor only configuration allowed the isolation of the interaction between the wake generators and rotor as the primary experimental variable in producing performance changes.

A rake was designed and fabricated to measure the total pressure and temperature downstream of the rotor. The rake was positioned approximately 0.93 axial rotor chords downstream of the rotor trailing edge. The rake consisted of five kiel heads distributed spanwise. Within each kiel head total pressure and total temperature were measured. Due to the small flow area downstream of the rotor (approximately 39.4 mm) the number of kiel heads was limited. Guidelines were followed from reference [21] concerning the kiel head spacing and length to minimize the effect of the probe on the measured flow. Details of the rake are provided in reference [18]. For the 24-wake-generator configuration the CTA was traversed 30.75 deg circumferentially in increments of 0.375 deg (2.5% wake generator pitch). This corresponded to two wake generator pitches. For the 40 wake generator configuration the CTA was traversed 36 deg in increments of 0.225 deg (2.5% wake generator pitch) thus covering four wake generator pitches.

The angular placement of the CTA rake was chosen by varying the rake position in increments of 5 deg and evaluating the subsequent effect on mass flow rate, pressure ratio, and efficiency. The response time for the CTA rake to reach equilibrium was found to be 30 seconds. Therefore after positioning the CTA, the measurements were acquired after waiting 30 s. Data acquired from the CTA rake were then area-averaged. The area-averaged

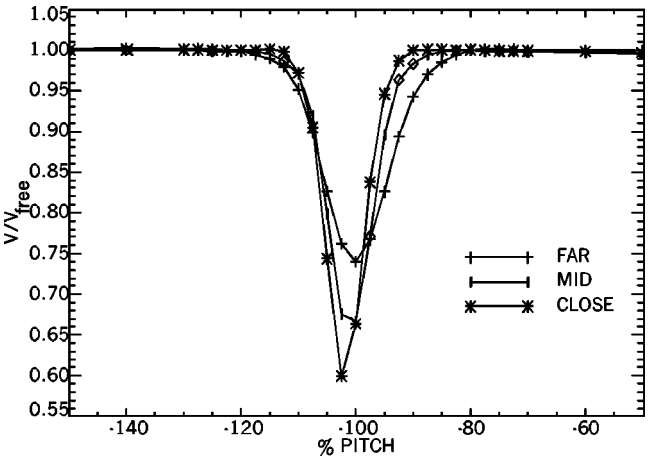

Fig. 2 Velocity profiles downstream of a wake generator at 42.4% span normalized by free stream velocity, $M_{in}=0.57$

total pressure and temperature were used with the measured inlet conditions described in the test article instrumentation section to determine the overall pressure ratio and isentropic efficiency for the wake generator/rotor only configuration.

The wake generator/rotor only configuration was run for the 24 and 40-wake-generator configurations since they showed the greatest changes of performance with axial gap.

Wake Calibration. The wake generators were calibrated for two purposes. One was to calculate the total pressure loss at various distances downstream of the wake generator blade-row. The loss was then used to correct the three-blade-row performance of the SMI rig at the rotor face to determine the effect of axial spacing on the flow capacity of an embedded compressor stage (two blade rows). Results of the flow capacity study were documented by Chriss et al. [22]. The second purpose was to evaluate the width and depth of the wakes interacting with the downstream rotor. Knowledge of the wake properties aided in analyzing the experimental and numerical results. It was desirable to understand the similarities and differences of the wake generator wakes and those produced by a typical stator found in a transonic compressor.

The wake generator loss coefficient, ω, is defined as

$$\omega = \frac{P_{\text{rake}} - P_{\text{inlet}}}{P_{\text{inlet}} - p_{\text{inlet}}}$$

where P_{rake} is the total pressure measured by the rake, P_{inlet} is the total pressure measured at the plenum, and p_{inlet} is a static pressure measurement located on the hub flowpath just upstream of the wake generator. This loss coefficient does not account for any losses other than that due to mixing.

Wake generator calibration was accomplished by using the SMI rig as a flow generating device, moving the wake generator blade row forward, and placing the CTA between the wake generator blade-row and the rotor blade row. The calibration procedure, instrumentation, and results are found in references [18] and [22]. From those results the widening of the wake from close to far spacing was clearly evident. Wake depth was deepest at close spacing and became shallower at mid and far spacing. Figure 2 shows the wake properties at 42.4% wake generator span for all spacings. The wake width was nearly constant from hub to case. This confirmed the intent of the wake generator design to produce a two-dimensional wake profile. The wake is constant in the circumferential and radial directions but not in the streamwise

Table 3 Wake generator loss coefficients (ω)

Spacing	24-wake generators	40-wake generators
Close	0.0822	0.1426
Mid	0.0917	0.1541
Far	0.1012	0.1845

$M_{in} \approx 0.57$

direction. Also, evident from rake measurements near the endwalls was the boundary layer growth as the spacing increased from close to far.

From calculated velocity profiles, it was observed that the wake depth was similar at the hub and case and deepest near midspan. Wake decay analyzed by Chriss et al. [22], showed that the SMI wake generator wakes demonstrated similar trends to that compared in the literature [23–25].

The overall mass-averaged loss coefficients are presented in Table 3. The flow Mach number during the calibration, M_{in}, was calculated based on measurements made upstream of the wake generator blade row. Loss coefficient uncertainty for a single wake generator was determined to be ± 0.001. However, due to wake-to-wake variability, the overall mass averaged loss coefficient uncertainty was established as ± 0.01.

Due to the blunt trailing edge of the wake generator, its wakes may be wider than what would be produced from a normally cambered stator airfoil, but wake measurements for comparison are not found in the open literature. Regardless of the wake thickness, the loss produced was very near the design intent and well within the range typically found in highly loaded stators.

SMI (Three Blade Rows) and Wake Generator/Rotor Only Performance. Performance characteristics for the SMI rig are shown for each configuration in Fig. 3. Figure 3 shows that for the 12-wake generator configuration the close and mid spacing performance were nearly identical. The far spacing pressure ratio and efficiency characteristics were consistently higher than that of close and mid spacing. The choking mass flow rate was higher for far spacing than close and mid. The difference in pressure ratio, efficiency, and mass flow rate between the far and close/mid configurations was greater than the determined repeatability. Therefore, it was concluded that the observed change in performance with axial blade-row spacing was real and not due to experimental measurement uncertainty.

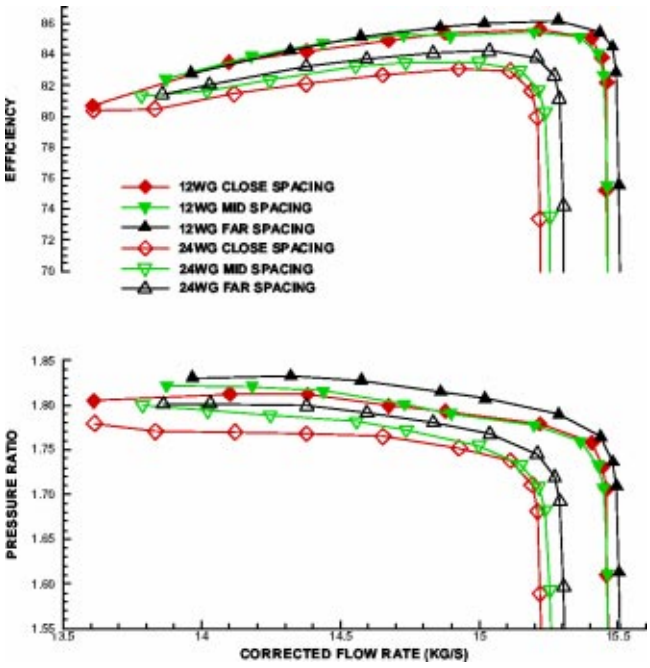

Fig. 3 SMI performance, 100% *Nc*

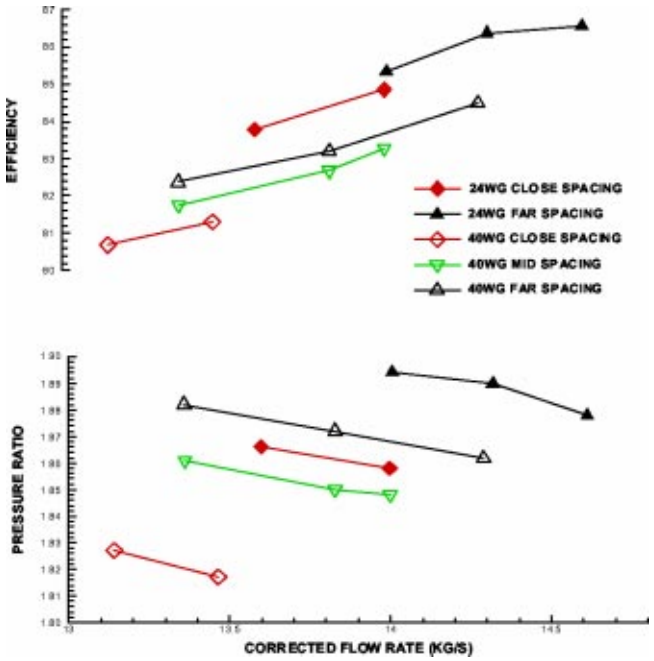

Fig. 4 Wake generator/rotor only performance, 100% *Nc*

For the 24-wake generator results shown there was a significant difference in performance between each of the three spacings tested. Both the pressure ratio and efficiency characteristics decreased significantly as the blade-row axial spacing was reduced from far to close. The choking mass flow rate decreased as the blade-row axial spacing was reduced. Performance characteristics at 70% *Nc* for the 24-wake generator configuration (see reference [18]) showed that there were no significant differences in performance between the three spacings.

Wake Generator/Rotor Only Results. Figure 4 shows the wake generator/rotor only performance results. A consequence of removing the SMI stator was a severe increase in backpressure in the facility flowpath downstream of the test article that limited the maximum mass flow rate attainable. For this reason the data shown in the wake generator/rotor only configuration was only attained for flows ranging from below peak efficiency to near-stall. Although the entire compressor map was not obtainable, the limited observations made are felt to be representative for the complete flow range. Removal of the downstream stator also eliminates upstream potential effects on the transonic rotor. Consequently, the wake generator/rotor only results are different than the SMI results. However, what does remain in common is the ability to measure the effect of blade-row axial spacing on the performance of each configuration.

Figure 4 shows that the pressure ratio and efficiency characteristics increased as the spacing was changed from close to far. The measured difference was greater than the experimental repeatability thus confirming its significance. For the 40-wake generator configuration the difference in efficiency between far and mid spacing was the same as the difference between mid and close spacing. The difference in pressure ratio between the close and mid spacing characteristics was greater than between mid and far spacing. Despite the limited control of mass flow rate during the wake generator/rotor only experiments, an attempt was made to acquire data at consistent mass flow rates for each of the three spacings.

The 24-wake generator/rotor only performance was only ob-

Table 4 SMI performance change near peak efficiency

	% decrease from far spacing PR	Change in η from far spacing
12 WG Mid	0.65	−0.707
12 WG Close	0.58	−0.540
24 WG Mid	0.72	−0.735
24 WG Close	0.88	−1.160

tained at far and close spacings. Consistent with the 40-wake generator results, both pressure ratio and efficiency increased significantly as the blade-row spacing was moved from close to far spacing.

Performance Summary. Both the SMI and wake generator/rotor only results show similar trends concerning the effect of blade-row axial spacing on the performance of a transonic compressor. For the 12-wake generator configuration there was a measurable decrease between far and close spacing in pressure ratio and efficiency. With 24-wake generators installed significant reductions in pressure ratio and efficiency were observed between far and close spacing.

The wake generator/rotor only performance at each spacing was compared at similar mass flow rates. For 40-wake generators this was approximately 13.38 Kg/s and for 24-wake generators it was 14.06 Kg/s. A significant reduction in pressure ratio and efficiency was observed for the 24-wake generator configuration as the spacing was reduced from far to close. For 40-wake generators there was a large decrease in pressure ratio and efficiency between mid and close spacing. A significant reduction in pressure ratio and efficiency was also observed in going from far to mid spacing. Tables 4 and 5 summarize the performance changes observed for both the SMI and the wake generator/rotor only experimental data. Two trends are observed. One is that pressure ratio and efficiency decreased with reduced blade-row axial spacing between the wake generator and transonic rotor. The other trend is that pressure ratio and efficiency decrease with increased solidity of the upstream blade row. The hypothesis that blade-row interactions are responsible for the decrease in performance is strengthened by these trends. The closer the spacing between blade rows, the stronger the interactions became. If these interactions are some type of wake-rotor, wake-shock, or blade-shock interaction, then obviously the more blades in a blade row, the more loss will be produced.

As the corrected speed was reduced the difference in performance with changes in blade-row spacing eventually became insignificant. This suggests that the interaction may be related to the shocks present in a transonic rotor.

Table 6 compares the choking mass flow rate for the 12, 24, and 40-wake generator configurations based on a percent reduction from the clean inlet value. The choking mass flow rate decreased as blade-row axial spacing was reduced and wake generator solidity was increased. This is a similar trend to that observed with pressure ratio and efficiency. The trend of decreased mass flow rate with increased solidity is expected because more wake generators produce more blockage, thus reducing the effective flow area. Since closer spacing between the wake generator blade-row and the transonic rotor blade row also decreased the mass flow rate it appears that the blade-row interactions may also produce more blockage. For this reason, rotor solidity should also have an effect on the severity of blade-row interactions because with more rotor blades there are more interactions with the upstream blade-row. Changes in mass flow rate with spacing were not significant at part speed. This suggests the increased blockage is not present at subsonic speeds.

Table 5 Wake generator/rotor only performance change at common mass flow rate

	% decrease from far spacing PR	Change in η from far spacing
24 WG Close	1.90	−0.494
40 WG Mid	1.12	−0.631
40 WG Close	3.29	−1.263

Table 6 SMI choking mass flow rate comparison at 100% *Nc*

Configuration	% reduction from clean inlet		
	Close	Mid	Far
12 WGs	0.92	0.90	0.57
24 WGs	2.39	2.26	1.88
40 WGs	4.09	3.51	3.24

Clean inlet=15.60 Kg/s

The experimental results presented in this section clearly show that a measurable difference in performance is observed when blade-row axial spacing is varied in a transonic compressor. The magnitude of performance changes observed would have a significant impact on the operation and mission capabilities of military aircraft gas turbine engines. From engine cycle analysis for a next generation Air Force fighter engine, drops in efficiency, pressure ratio, and mass flow rate at levels observed with the SMI experiment would result in a 2.5% increase in specific fuel consumption (SFC), a 1.7% reduction in net after burner thrust, and a 1.5% drop in thrust-to-weight ratio. In the current development of military compressors industry has often expended tremendous resources to overcome shortfalls in mass flow rate from the design goal. Understanding the affect of blade-row interactions on mass flow rate in transonic fans and compressors is of great interest to the military and industry.

Issue 2: Blade-Row Interaction Mechanisms (Experimental Analysis)

Having established that reduced blade-row axial spacing in the SMI compressor significantly decreased pressure ratio, efficiency, and mass flow rate, the challenge now becomes one of determining where in the compressor the performance decrease occurs most and then identifying the mechanisms responsible for the changes. This phase of the research study concentrated on identifying mechanisms that drive the performance changes found in the experimental results just presented.

Earlier, how wake mixing loss can be affected by blade-row axial spacing was explained. Additional loss sources exist in a compressor and can be generally grouped (see Cumpsty [26]) as 1) drag at solid surfaces; 2) mixing; 3) shock losses; and 4) shear work. Losses have an effect on blockage (an effective reduction in flow area), pressure rise, work input, and mass flow capacity.

Flow Capacity Experiment. Results from Chriss et al. [22] showed that losses in addition to wake mixing loss occur when the spacing was reduced from far to close. In their experiment the SMI rig was used to evaluate the effect of upstream blade-row wakes on the flow capacity of a downstream stage. This was accomplished by determining the wake generator total pressure loss measured from wake measurements at distances corresponding to each of the three spacings, and then correcting the three-blade-row performance for the total pressure deficit at the rotor inlet. The measured rotor-stator (or embedded stage) flow capacity at choke for each spacing was then compared. If all losses were accounted for, the corrected embedded stage should pass at least as much mass flow as the clean inlet configuration.

At some distance upstream of the rotor there will be minimal blade-row interactions and the loss generated between blade rows will be due to wake generator wake mixing. For the SMI rig this

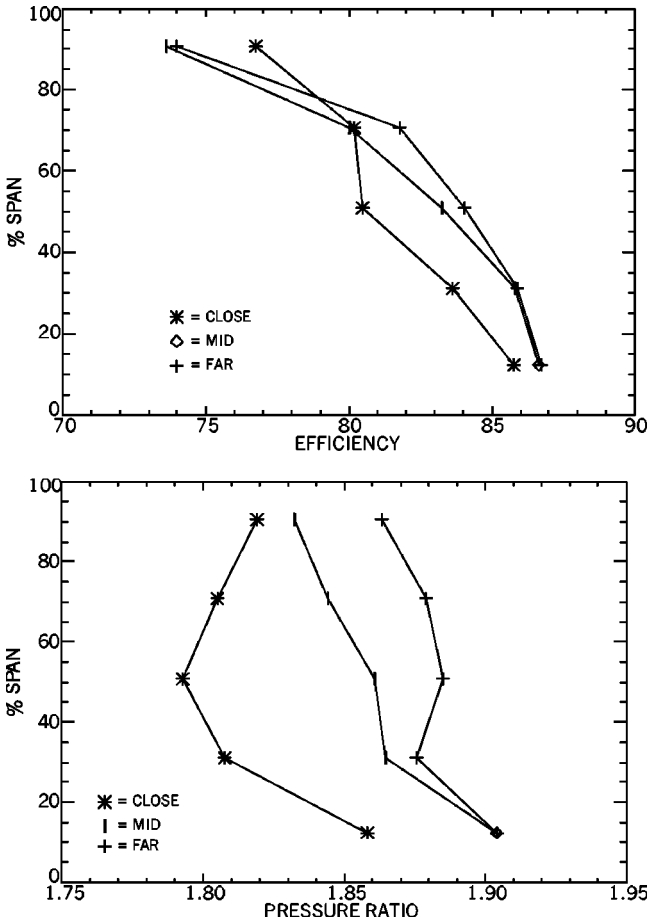

Fig. 5 40-wake generator profile comparison at 13.38 Kg/s

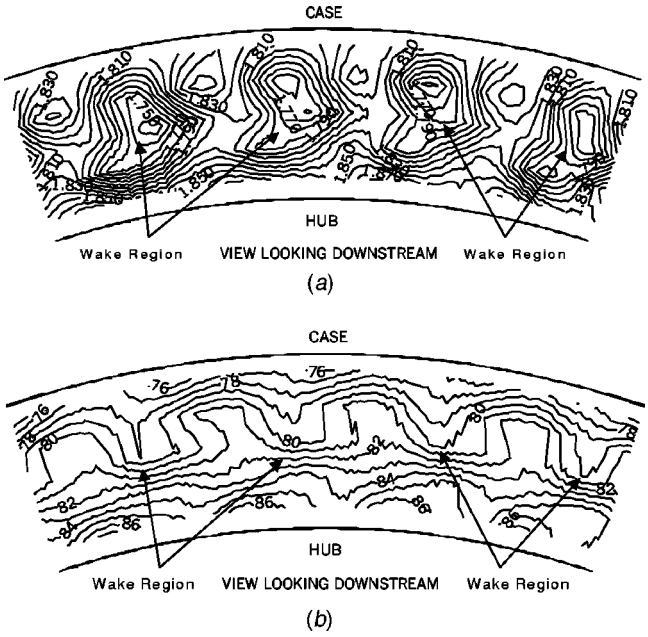

Fig. 6 40-wake generator performance contours at 13.38 Kg/s, close spacing—(*a*) pressure ratio, (*b*) efficiency

distance was very near far spacing. However at mid and close spacings, wake mixing alone did not account for the drop in flow capacity. Since blade-row axial spacing between the wake generators and rotor was the only variable, additional losses must have been a result of some blade-row interactions. Including these losses would increase the corrected embedded stage mass flow rate. The flow capacity study showed that at closer spacing more loss was unaccounted for that at midspacing.

Wake Generator/Rotor Only Analysis. Experimental data acquired during the wake generator/rotor only testing further aid in determining where in the compressor extra loss was produced. Measurements made by the traverse rake located 0.93 rotor chords downstream of the rotor were circumferentially averaged to produce radial profiles of pressure ratio and efficiency. Profiles for the 40-wake generator configuration are shown in Fig. 5. These profiles correspond to the data points presented in Fig. 4 at a mass flow rate near 13.38 Kg/s.

Inspection of Figure 5 shows that the close spacing pressure ratio profile is different in shape compared to the mid and far spacing profiles. There exists a major reduction between 10 and 75% span for close spacing compared to mid and far spacing. The mid spacing profile is similar in shape to the far spacing but of reduced magnitude. The efficiency profiles show a significant reduction in efficiency between 10 and 70% span compared to the far spacing values. Interestingly, the efficiency at the tip-most rake element shows a substantial increase at close spacing. Thus, even though the overall performance of the SMI rig suffers with reduced blade-row spacing, there is some benefit near the casing. This is the subject of another investigation.

Contour Plots of Pressure Ratio and Efficiency. Further insight into the effect of blade-row interactions with decreased blade-row axial spacing is gained by analyzing contour plots of pressure ratio and efficiency from the wake generator/rotor only steady-state traverse rake measurements. Since the greatest differences in performance were found between close and far spacing, results from those two data sets at a common mass flow rate of 13.38 Kg/s are presented. The 40-wake generator configuration is analyzed since more wake generator wakes are visible over the range traversed by the CTA rake. Figure 6 plots the contours of pressure ratio and efficiency at close spacing. The wake generator wakes are visible in Fig. 6(*a*) as four regions of high gradients leading to an area of low pressure ratio. The pressure ratio is lowest within the wakes between 25 and 75% span. In Fig. 6(*b*) the efficiency contours demonstrate a similar pattern in that the wakes are visible as pockets of reduced efficiency coincident with the regions of low pressure ratio.

Contours at the far spacing configuration are shown in Fig. 7. The wakes are still evident in Fig. 7(*a*) where regions of lower pressure ratio are visible. However, the steep gradients observed for close spacing are no longer present and the difference in pressure ratio between the free stream and wake is much less than for close spacing. In Fig. 7(*b*) the pockets of reduced efficiency are not visible. The efficiency contours have a radial profile decreasing from hub to tip. The only evidence of wakes is the sinusoidal-like wave pattern evident between 30 and 70% span.

At far spacing the wakes have nearly mixed out before entering the rotor and therefore are not very distinguishable downstream of the rotor. In the close spacing configuration the wakes have not mixed out very much before entering the rotor, and thus are clearly visible in the flow field downstream of the rotor.

It is possible to remove the steady-state rotor flow field common to both spacings and isolate the regions of increased loss as spacing is reduced from far to close. This is accomplished by subtracting point by point the far spacing data from the close spacing data and plotting the resulting difference contours. Figure 8 shows the result of subtracting Fig. 7 from Fig. 6. In Fig. 8(*a*) the entire flowfield has reduced (negative difference) pressure ratio, but the largest differences correspond to the four wake regions noted in Fig. 6. In Fig. 8(*b*) there are both gains (positive difference) and drops in efficiency. The greatest reductions once again

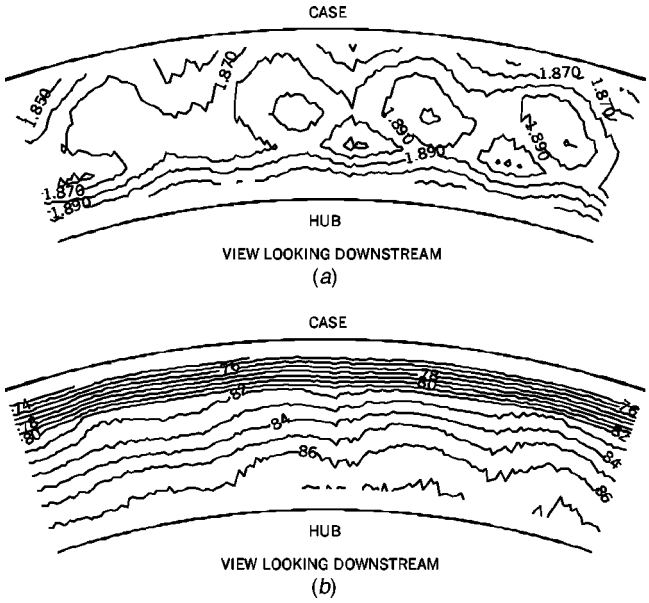

Fig. 7 40-Wake generator performance contours at 13.38 Kg/s, far spacing—(*a*) pressure ratio, (*b*) efficiency

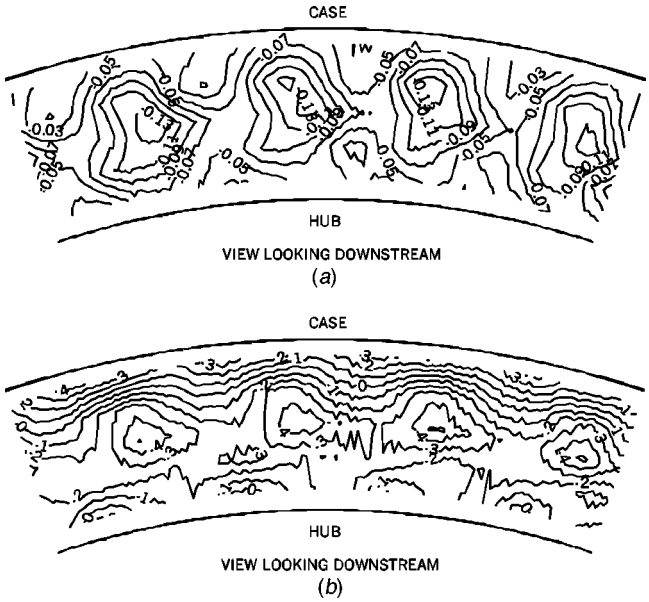

Fig. 8 40-wake generator performance differences, close-far spacing—(*a*) pressure ratio difference, (*b*) efficiency difference

correlate with the location of the wake generator wakes. The gains, although significant in magnitude, are only evident above 90% span.

Discussion of Experimental Results

Analysis of the wake generator/rotor only results shows the spanwise and circumferential extent of the increased loss production in the rotor exit flow field. The increased loss is apparent when the blade-row axial spacing is reduced from far to close and thus appears to be the result of blade-row interaction. Since these increased losses are observable only under transonic flow conditions, they are likely related to the presence of shocks in the rotor. This notion is further explored in reference [3].

The radial profiles and differencing contours suggest that at close spacing blade-row interactions produce additional loss between 20 and 70% span and are related in some manner to the wake generator blades and/or wakes. The two distinct regions of efficiency increase and decrease found in Fig. 8(*b*) suggest that multiple interactions are present. The pockets of reduced efficiency correspond to the wake generator wakes and the loss is therefore related to an interaction between the wake generator blade row and the transonic rotor blade row. The increase in efficiency is nearly constant circumferentially above 90% span, suggesting the gain is not related to the upstream blade row.

Various blade-row interaction mechanisms may exist simultaneously. Some interactions may be beneficial, while others may be detrimental. Each interaction may have a small or large effect on the overall compressor performance. The observation that performance decreased as the axial gap between blade rows was reduced is contrary to the concept of wake recovery and published low-speed experimental results. Using the model of Van Zante et al. [10], the potential for wake recovery in the SMI rotor was estimated at 50% span. Because of the 0-deg inlet angle of the wake generator wake, the model predicts no reduction in mixing loss as the wake generator wakes passes through the rotor.

To study in greater detail what unsteady fluid mechanics are responsible for the additional loss observed at close blade-row axial spacing, time-accurate numerical simulations of the SMI rig were carried out. In addition, high-response static pressure measurements acquired on the wake generator trailing edge blade surface were analyzed. Results of that study are presented in reference [3] with the main conclusion being that a previously unidentified loss producing mechanism resulting from the interaction of the transonic rotor bow shock with the trailing edge of the upstream wake generator resulted in increased loss production when the blade rows were drawn closer together axially.

Conclusions From Measured Results

The effect of blade-row axial spacing on the measured performance of a transonic compressor has been investigated. Measured data document that the axial spacing between an upstream stator and downstream transonic rotor has a significant effect on stage performance. Mass flow rate, pressure ratio, and efficiency all decreased as the axial spacing between the wake generator and transonic rotor was reduced. The number of blades in the wake generator blade-row also affected the stage performance. Higher wake generator blade-row solidity resulted in lower performance. Performance reduction with decreased spacing was most evident at design speed and nonexistent at lower speeds.

Analysis of the measured data suggests that loss in addition to mixing loss is present when the blade rows are close together. Extra loss production occurs as a result of interaction between the upstream wake generator and downstream transonic rotor. The extra loss is most significant between 20 and 70% span and coincides circumferentially in the vicinity of the wake generator wakes.

Relevant to these conclusions are those of reference [3] from which we get an idea of the flow mechanism responsible for much if not all of the observed increased loss. At close blade-row axial spacing the rotor bow shock is chopped by the wake generator trailing edge and is turned more normal to the free stream flow. A pressure wave forms on the upper surface of the wake generator that propagates forward. In the reference frame relative to this pressure wave, the flow is supersonic and a moving shock wave exists that produces an entropy rise and loss.

Acknowledgments

The wake generators, rotor, and stator were built by Pratt & Whitney. From the CARL group at Wright-Patterson AFB the authors would like to recognize Dr. Herb Law, Robert Wirrig, Ron Berger, Terry Norris, Bill Ullman, and Chris Blackwell for their assistance in gathering the data. Many of the ideas presented in the paper were influenced by discussions with other individuals.

The authors wish to acknowledge Dr. Steve Puterbaugh, Dr. Greg Bloch, and Dave Car from the CARL group and from NASA Glenn Research Center, Dr. John Adamczyk, Dr. Tony Strazisar, Dr. Randy Chriss, and Dr. Dale Van Zante. The authors thank the Propulsion Directorate management for supporting the research and allowing the presentation and publication of this paper.

References

[1] Adamczyk, J. J., 1985, ''Model Equation for Simulating Flows in Multistage Turbomachines,'' ASME Paper 85-GT-226.
[2] Adamczyk, J. J., 2000, ''Aerodynamic Analysis of Multistage Turbomachinery Flows in Support of Aerodynamic Design,'' ASME J. Turbomach., **122**, pp. 189–217.
[3] Gorrell, S. E., Okiishi, T. H., and Copenhaver, W. W., 2002, ''Stator-Rotor Interactions in a Transonic Compressor—Part 2: Description of a Loss Producing Mechanism,'' ASME Paper GT-2002-30495, ASME J. Turbomach. **125**(2), pp. 336–345.
[4] Smith, L. H., 1970, ''Casing Boundary Layers in Multistage Axial, Flow Compressors,'' *Flow Research in Blading*, ed. L. S. Dzung, Elsevier Publishing Company, Amsterdam.
[5] Mikolajczak, A. A., 1976, ''The Practical Importance of Unsteady Flow,'' AGARD CP 177, *Unsteady Flow Phenomena in Turbomachinery*.
[6] Smith, L. H., 1966, ''Wake Dispersion in Turbomachines,'' ASME J. Basic Eng., Series D, No. 3, pp. 688–690.
[7] Smith, L. H., 1993, ''Wake Ingestion Propulsion Benefit,'' J. Propul. Power, **9**(1), pp. 74–82.
[8] Deregal, P., and Tan, C. S., 1996, ''Impact of Rotor Wakes on Steady-State Axial Compressor Performance,'' ASME Paper 96-GT-253.
[9] Adamczyk, J. J., 1996, ''Wake Mixing in Axial Flow Compressors,'' ASME Paper 96-GT-29.
[10] Van Zante, D. E., Adamczyk, J. J., Strazisar, A. J., and Okiishi, T. H., 1997, ''Wake Recovery Performance Benefit in a High-Speed Axial Compressor,'' ASME Paper 97-GT-535, ASME J. Turbomach. **124**, pp. 275–284.
[11] van de Wall, A. G., Kadambi, J. R., and Adamczyk, J. J., 2000, ''A Transport Model for the Deterministic Stresses Associated With Turbomachinery Blade Row Interactions,'' ASME J. Turbomach., **122**, pp. 593–603.
[12] Ottavy, X., Trebinjac, I., and Vouillarmet, A., 2001, ''Analysis of the Interrow Flow Field Within a Transonic Axial Compressor—Part 1: Experimental Investigation,'' ASME J. Turbomach., **123**, pp. 49–56.
[13] Ottavy, X., Trebinjac, I., and Vouillarmet, A., 2001, ''Analysis of the Interrow Flow Field Within a Transonic Axial Compressor—Part 2: Unsteady Flow Analysis,'' ASME J. Turbomach., **123**, pp. 57–63.
[14] Sanders, A. J., and Fleeter, S., 1999, ''Transonic Rotor-IGV Interactions,'' Presented at the thirteenth International Symposium on Air Breathing Engines, Chattanooga, TN (ISABE 99-7029).
[15] Law, C. H., and Wennerstrom, A. J., 1989, ''Two Axial Compressor Designs for a Stage Matching Investigation,'' AFWAL-TR-89-2005.
[16] Creason, T., and Baghdadi, S., 1988, ''Design and Test of a Low Aspect Ratio Fan Stage,'' AIAA Paper, 88-2816.
[17] Gorrell, S. E., Copenhaver, W. W., and Chriss, R. M., 2001, ''Upstream Wake Influences on the Measured Performance of a Transonic Compressor Stage,'' J. Propul. Power, **17**, pp. 43–48.
[18] Gorrell, S. E., 2001, ''An Experimental and Numerical Investigation of Stator-Rotor Interactions in a Transonic Compressor,'' Ph.D. dissertation, Department of Mechanical Engineering, Iowa State University.
[19] Cherret, M. A., and Bryce, J. D., 1992, ''Unsteady Viscous Flow in a High-Speed Core Compressor,'' ASME J. Turbomach., **120**, pp. 287–294.
[20] Camp, T. R., and Shin, H. W., 1995, ''Turbulence Intensity and Length Scale Measurements in Multistage Compressors,'' ASME J. Turbomach., **117**, pp. 38–46.
[21] 1990, *Recommended Practices for Measurement of Gas Path Pressures and Temperatures for Performance Assessment of Aircraft Turbine Engines and Components*, AGARD Conf. Proc., AGARD-AR-245, ed. H. I. H Saravanamuttoo, North Atlantic Treaty Organization.
[22] Chriss, R. M., Copenhaver, W. W., and Gorrell, S. E., 1999, ''The Effects of Blade-Row Spacing on the Flow Capacity of a Transonic Rotor,'' ASME Paper 99-GT-209.
[23] Brookfield, J. M., Waitz, I. A., and Sell, J., 1996, ''Wake Decay: Effect of Freestream Swirl,'' ASME Paper 96-GT-495.
[24] Raj, R., and Lakshminarayana, B., 1973, ''Characteristics of the Wake Behind a Cascade of Airfoils,'' J. Fluid Mech., **61**, pp. 707–730.
[25] Stauter, R. C., Dring, R. P., and Carta, F. O., 1991, ''Temporally and Spatially Resolved Flow in a Two-Stage Axial Flow Compressor—Part 1: Experiment,'' ASME J. Turbomach., **113**, pp. 219–226.
[26] Cumpsty, N. A., 1989, *Compressor Aerodynamics*, Longman Scientific & Technical, England.

Stator-Rotor Interactions in a Transonic Compressor—Part 2: Description of a Loss-Producing Mechanism

Steven E. Gorrell
Mem. ASME,
Air Force Research Laboratory,
AFRL/PRTF,
Wright-Patterson AFB, OH 45433

Theodore H. Okiishi
Mem. ASME,
Fellow ASME,
College of Engineering,
Iowa State University,
Ames, IA 50011

William W. Copenhaver
Mem. ASME,
Fellow ASME,
Air Force Research Laboratory,
AFRL/PRTF,
Wright-Patterson AFB, OH 45433

A previously unidentified loss producing mechanism resulting from the interaction of a transonic rotor blade row with an upstream stator blade row is described. This additional loss occurs only when the two blade rows are spaced closer together axially. Time-accurate simulations of the flow and high-response static pressure measurements acquired on the stator blade surface reveal important aspects of the fluid dynamics of the production of this additional loss. At close spacing the rotor bow shock is chopped by the stator trailing edge. The chopped bow shock becomes a pressure wave on the upper surface of the stator that is nearly normal to the flow and that propagates upstream. In the reference frame relative to this pressure wave, the flow is supersonic and thus a moving shock wave that produces an entropy rise and loss is experienced. The effect of this outcome of blade-row interaction is to lower the efficiency, pressure ratio, and mass flow rate observed as blade-row axial spacing is reduced from far to close. The magnitude of loss production is affected by the strength of the bow shock and how much it turns as it interacts with the trailing edge of the stator. At far spacing the rotor bow shock degenerates into a bow wave before it interacts with the stator trailing edge and no significant pressure wave forms on the stator upper surface. For this condition, no additional loss is produced. [DOI: 10.1115/1.1540120]

Introduction

Measurements from a transonic compressor rig document how decreasing axial blade-row spacing and increasing stator solidity at close spacing degrades compressor performance (see reference [1]). The stage matching investigation (SMI) rig with and without a stator row downstream of the rotor was used for these measurements. It is a high-speed, highly loaded compressor consisting of three blade rows: a wake generator, rotor, and stator. The rig was designed to allow variations of wake generator to rotor axial spacing and wake generator blade count. Mass flow rate, pressure ratio, and efficiency all decreased significantly as the spacing between the wake generator and rotor was reduced. Reductions as great as 3.3% in pressure ratio and 1.3 points efficiency were observed as spacing between these blade-rows was decreased from far to close. The number of blades in the wake generator blade-row also affected the stage performance. The higher the solidity the lower the pressure ratio, efficiency, and mass flow rate.

The measurements suggest that losses in addition to wake mixing loss were experienced when the blade-rows were spaced close together. Analysis of the measured data acquired downstream of the rotor suggests this additional loss production was a result of an interaction between the wake generator blade row and the transonic rotor blade row.

This paper will focus on identifying a loss producing mechanism due to blade-row interaction. This additional loss is significant only when the blade rows are spaced close together axially. Numerical simulations of the interaction flow field and high-response static pressure measurements acquired on the wake generator blade surface were used for this purpose.

Contributed by the International Gas Turbine Institute and presented at the International Gas Turbine and Aeroengine Congress and Exhibition, Amsterdam, The Netherlands, June 3–6, 2002. Manuscript received by the IGTI November 7, 2001. Paper No. 2002-GT-30495. Review Chair: E. Benvenuti.

Numerical Approach

A limited number of numerical studies of transonic stator-rotor interactions have already been published. Liamis et al. [2] performed a simulation of an IGV-rotor combination with a quasi three-dimensional Navier-Stokes solver. Their results showed that the rotor bow shock interaction with the IGV wake had a large influence on the IGV instantaneous outlet angle and flow velocities. It was also noted that the detached rotor bow shock became weaker further upstream finally degenerating into a pressure wave in the IGV passage and reflected at the IGV blade surface.

Eulitz et al. [3] performed a simulation of a stator-rotor interaction solving both inviscid and viscous equations in a two-dimensional plane. The rotor shock interaction with the upstream stator and its subsequent reflections were visible in the Euler (inviscid) solution. However the viscous solution modeled additional features such as flow separation on the stator pressure surface due to the shock interaction with the stator blade boundary layer. The separation formed and disappeared in conjunction with the blade passing frequency.

The CFD program used for the current study was MSU-TURBO Version 4.1. MSU-TURBO [4–6] is a three-dimensional, viscous, time-accurate code that solves the Reynolds Averaged Navier-Stokes (RANS) equations in the rotating frame of reference. The solution algorithm is an implicit finite volume solver and turbulence modeling is accomplished with either the Baldwin-Lomax or k-ε model. Axial communication between blade rows is through a sliding interface that does not distort the grid.

Wave interactions between blade rows can only be accurately resolved if the exact blade counts are modeled. When this is done the effect of wakes convected downstream and the potential effects that propagate upstream and downstream will be accounted for. If phase-lag boundary conditions are applied at the circumferential and axial block interfaces only one blade passage from each blade row is required to model the unsteady blade-row interaction. Phase-lag boundary conditions assume that the unsteadiness of the blade-row interaction solely depends on the blade passing fre-

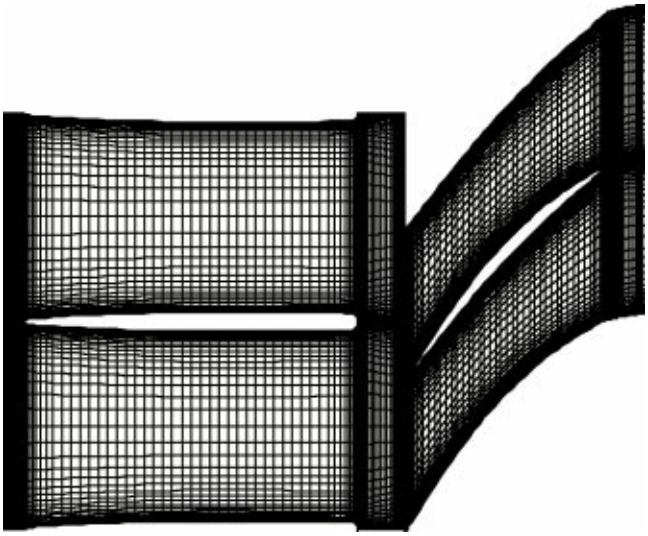

Fig. 1 Close spacing mesh at 75% span

quency of the adjacent blade row and its higher harmonics. Consequently, this method does not capture the details of unsteady flow features such as vortex shedding and flow separation. However, as shown by Chen and Barter [5], even if nondeterministic flows are present the phase-lag method produces overall numerical results similar to that of the periodic solution. Phase-lag boundary conditions are most useful when the blade-row interaction is dominated by the unsteadiness at the adjacent blade passing frequency. Flow visualization techniques applied by Estevadeordal et al. [7] confirm that this is indeed the case with the SMI rig at the operating conditions modeled with MSU-TURBO.

Initial Solution. The initial solution for the SMI rig was obtained using the method and computer programs of Van Zante [8]. This technique generates a starting flow field for MSU-TURBO from a converged APNASA [9,10] solution and mesh.

Both the APNASA and MSU-TURBO models used a sheared H-mesh grid. The number of nodes in the spanwise (or radial) and pitchwise (or tangential) directions were kept the same as the APNASA mesh. To help minimize computer resources required to run MSU-TURBO, the number of nodes in the axial direction was reduced from the APNASA mesh. The meshes were terminated shortly upstream of the wake generator and downstream of the rotor. Although flow gradients still exist at these axial locations, perturbation type [4,5] nonreflective boundary conditions are used at the upstream and downstream boundaries, which allows the MSU-TURBO mesh boundaries to be in areas of moderate to high gradients without adversely affecting the solution.

One variable in setting up the meshes used is the location of the sliding interface between blade rows. For these simulations the sliding interface was chosen to be close to the rotor leading edge in order to preserve the wake features of the wake generator. The aim was to keep the mesh density high in the wake region to reduce the numerical dissipation of the high gradient wake flow features. Figure 1 shows the close spacing mesh at 75% span. The ratio of grid points to spacing was kept constant between the meshes of the close and far models. The location of the sliding interface for the far mesh was chosen to be the same percent gap downstream of the wake generator (or upstream the rotor) as it was for the close mesh. The meshes used for each simulation are provided in Table 1. The mesh sizes are ordered in terms of the number of axial, radial, and tangential nodes.

Phase-lag boundary conditions, solving equations in the rotating frame of reference, and building the initial solution from an APNASA model reduce the required computational time by several orders of magnitude.

Table 1 MSU-TURBO mesh sizes

Simulation	Wake generator	Rotor
Close spacing	126×51×41	97×51×41
Far spacing	138×51×41	99×51×41

Wake Generator/Rotor Only Simulations. Simulations were run at operating points based on an APNASA solution near peak efficiency, at 100% corrected speed, for the close and far spacing 24-wake generator configurations. The time-accurate simulations used the k-ε turbulence model. MSU-TURBO Version 4.1 was designed to run most efficiently on a Cray supercomputer with a secondary storage device (SSD).

Convergence was determined by monitoring static surface pressures of each blade-row and the mass flow rates at the exit of the wake generator and entrance to the rotor. The solution was considered converged when the surface pressures were periodic and the difference in mass flows rates between blade-rows was less than 0.5%.

Numerical Results

Comparison of the far and close axial spacing MSU-TURBO simulations make it possible to study the fluid mechanics driving the increased loss production observed in reference [1].

The advantage of a three-dimensional time-accurate Navier-Stokes code is not just the accuracy of the solution, but its ability to visually present the rotation of the rotor and the resulting complex flow fields inherent to transonic compressors. Movies of the simulation have proven very useful in analyzing the flow fields. Unfortunately, the paper format limits the presentable material to select time-steps of each simulation.

Time-Average Results. The time-average results presented here are based on four rotor blade passes, each containing 20 time steps. The change in rotor mass flow rate, inlet and exit total pressure, and efficiency between an average of three rotor blade passes and four were less than 0.15%. The time-averaged MSU-TURBO performance of the close and far spacing simulations is shown in Table 2.

To check if the numerical simulations were capable of accounting for the loss observed experimentally due to an interaction between the wake generator blade-row and transonic rotor blade-row the time-average loss at the entrance to the rotor blade-row was compared. Denton [11] has suggested that the most informative measure of loss is entropy production. For the loss analyses presented in this section the entropy flux per unit area normalized by the specific heat at constant pressure ($\rho u \Delta s / C_p$) was chosen. This term will hereafter be used synonymously with loss.

Using the time-averaged solution, the loss was calculated at each node and then averaged to obtain a single value for the close and far spacing simulations. Taken from the exit of the wake generator grid the close spacing loss was 12.34% greater than far spacing loss. Using the method of Denton [11] the relationship between entropy change and adiabatic efficiency for the three blade row compressor can be defined as

$$\eta = 1 - \frac{T_{\text{exit}}(s_{\text{exit}} - s_{\text{inlet}})}{H_{\text{exit}} - H_{\text{inlet}}}$$

Table 2 Time-average MSU-TURBO results near peak efficiency

	Close spacing	Far spacing
Mass flow rate Kg/s	15.472	15.613
Pressure ratio	1.8373	1.8388
Efficiency %	88.506	89.323

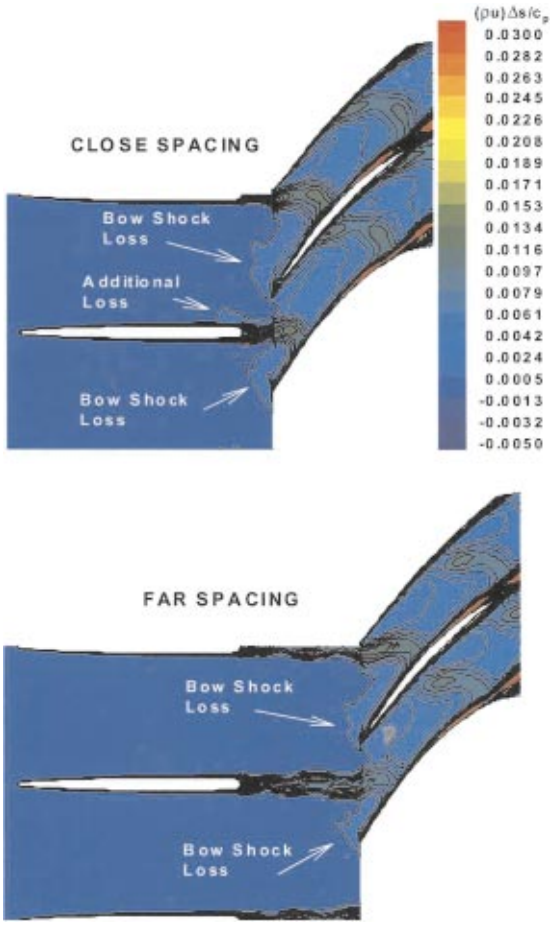

Fig. 2 MSU-TURBO flow field loss comparison, 75% span, time-step 5

A comparison can thus be made between the additional entropy predicted by MSU-TURBO and the decrease in efficiency measured from the experiment. Using temperature and enthalpy values measured at 50% span, an increase in entropy production of 12.34% corresponds to a decrease in efrficiency of 1.02. This is very close to the measured difference of 0.89 between far and close spacing near peak efficiency and confirms that the numerical model does capture an unsteady loss producing mechanism at close spacing that is not found at far spacing. It also suggests that the additional loss is produced upstream of the transonic rotor leading edge and accounts for the majority of performance difference measured experimentally [1].

Time-Accurate Results. The simulations were set up to output the flow field at 20 time-steps as the rotor blade moved one blade pass. A comparison of the close and far spacing simulation at time-step 5 is shown in Fig. 2. The figures are contour plots of loss ($\rho u \Delta s / C_p$) at 75% span. Plotting the loss highlights features such as shed vortices from the wake generator trailing edge, wake chopping and transport of the wake through the rotor, rotor bow shock, rotor passage shock, and boundary layers on the rotor blade surface. These features are seen on both the close and far spacing solutions.

In both simulations the wake appears to expand as it passes through the sliding interface between the blade-row meshes. This is a general feature of unsteady periodic or phase-lag boundary simulations using a sliding interface. At far spacing the wake has mixed out more before entering the rotor and is wider. As it passes through the sliding interface it does not expand as much through the interface as observed with the close spacing simulation.

A consequence of the wakes passing through the interface is the rotor performance may not be simulated as accurate as desired, thus affecting the ability to directly compare the simulations with the overall experimental results. An accurate representation of the wake generator wake entering the rotor is desirable to correctly model the flow through the rotor. The interface has more of an effect on the rotor flow field than on the upstream wake generator flow field. The majority of the bow shock is upstream of the interface, except very near the rotor leading edge. The simulations used in this research effort focus on the interactions between the rotor bow shock and the wake generator trailing edge. The effect of the sliding interface on the wake generator wake and its interaction with the rotor can be minimized with grid refinement. An effort to modify the grids to better model the rotor flow field is currently in progress.

The biggest difference between the close and far spacing contour plots presented in Fig. 2 is a region of additional loss found in the close spacing flow field not found in the far spacing flow field. This region is located near the trailing edge of the wake generator on the upper blade surface. From the close spacing simulation important insights are gained by analyzing the losses between the wake generator trailing edge and the rotor leading edge.

Flow fields at six equally spaced time steps from the close spacing simulation are shown in Fig. 3. The legend for Fig. 3 and all subsequent loss contour plots is the same as that presented in Fig. 2. During time-step 1 a loss associated with the rotor bow shock is observed upstream of the middle rotor blade. A similar loss region is evident from the lower rotor blade bow shock and extends up to the lower surface of the wake generator trailing edge. Examination of the wake generator trailing edge upper surface shows a region of additional loss. This loss region has a peak located near 95% wake generator chord and extends into the flowpath approximately 15% wake generator pitch for all time-steps. Loss from this peak convects downstream above the wake generator wake. As the rotor rotates the loss peak moves forward on the wake generator upper surface and the convected loss above the wake thickens. At time-step 5 the peak is centered at 92% wake generator chord. The bow shock loss from the lower rotor blade moves with the blade and no longer intersects the lower blade surface of the wake generator.

With rotor rotation the loss region on the wake generator upper surface continues to propagate forward and thicken. By time-step 9 it has reached 88% wake generator chord and has formed two peaks. The bow shock loss region of the middle rotor blade changes shape and forms two distinct branches. Between time-steps 9–13 the forward peak on the wake generator upper surface disappears leaving only one peak at 93% wake generator chord. By time-step 13 the wake generator wake and convected loss from the wake generator upper surface interacts with the bow shock branches which results in two additional peaks above the wake generator wake. From time-steps 13–17 the rotor chops the wake generator wake. The bow shock loss of the lower rotor splits into two branches as was observed previously for the middle rotor at time-step 9. By time-step 17 there is one peak on the wake generator upper surface and one just downstream of the wake generator trailing edge. The first peak is associated with the lower rotor blade and the second is associated with the middle rotor blade.

For time-steps 17–21 the upstream peak produced from the lower rotor blade reaches 91% wake generator chord before disappearing by time-step 21. The loss peak from the middle rotor propagates forward and interacts with the wake generator trailing edge. Time-step 21 is the same flow field as time-step 1 with the rotor blade at a different position. The magnitude of the additional loss or bow shock loss changes very little over time.

For comparison the same six time steps for the far spacing simulation are shown in Fig. 4. The simulation shows that the loss region associated with the rotor bow shock does not interact with the upstream wake generator at all and consequently there is no additional loss produced on the wake generator trailing edge up-

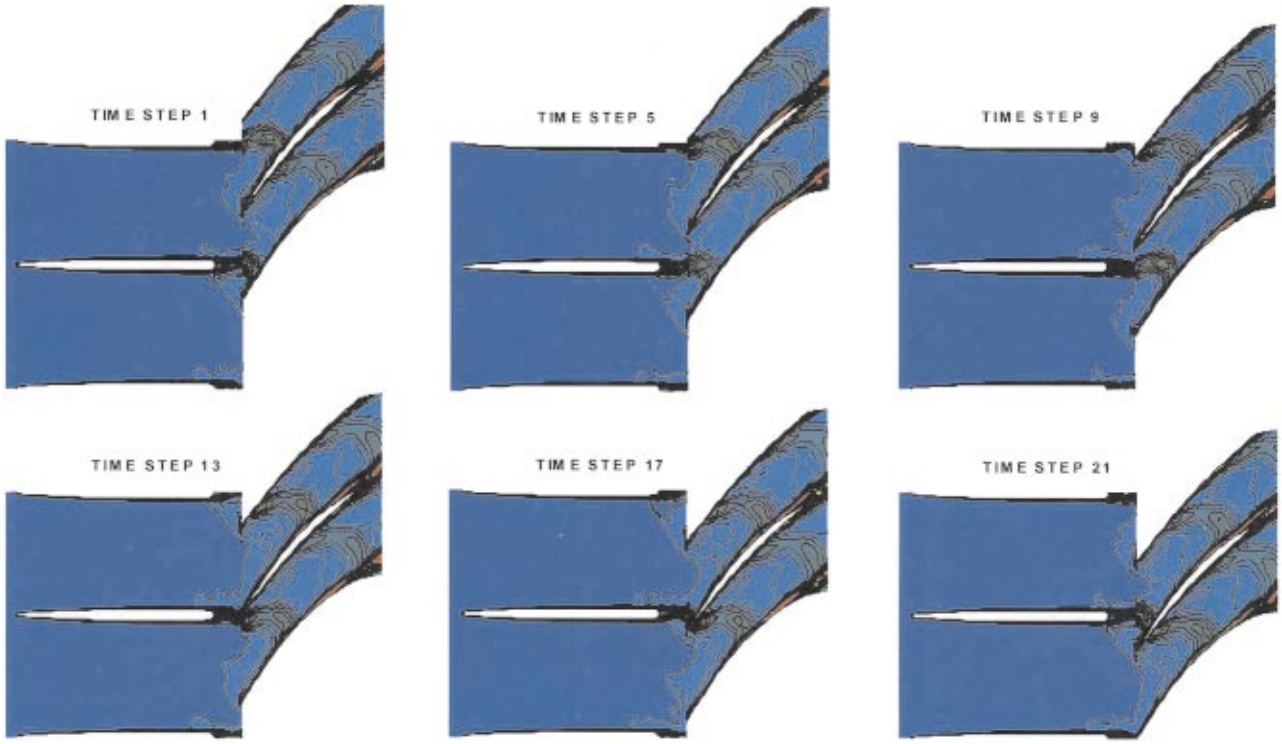

Fig. 3 MSU-TURBO close spacing loss contours, 75% span

per surface or above the wake boundary. Similarities to the close spacing simulation are observed at time-step 9 where the bow shock loss changes from one large area to two small branches. However, the branches are not as long as those observed at close spacing. Between time-steps 9–13 the two branches interact with the wake upper surface. The peaks are smaller than those observed at close spacing and they do not propagate upstream very far. The wake is chopped by the rotor between time steps 13–17. Similar to close spacing the loss magnitude of the bow shock is nearly constant.

Static Pressure Contours. Having established that the close

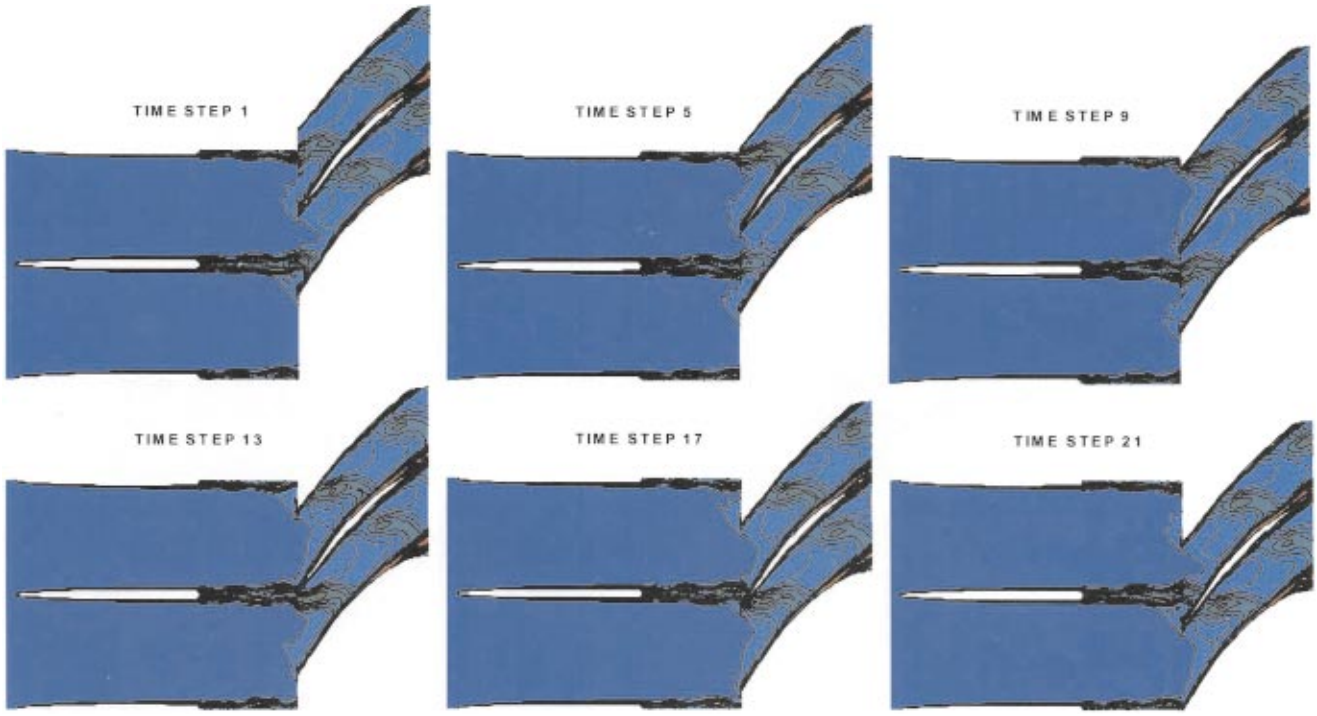

Fig. 4 MSU-TURBO far spacing loss contours, 75% span

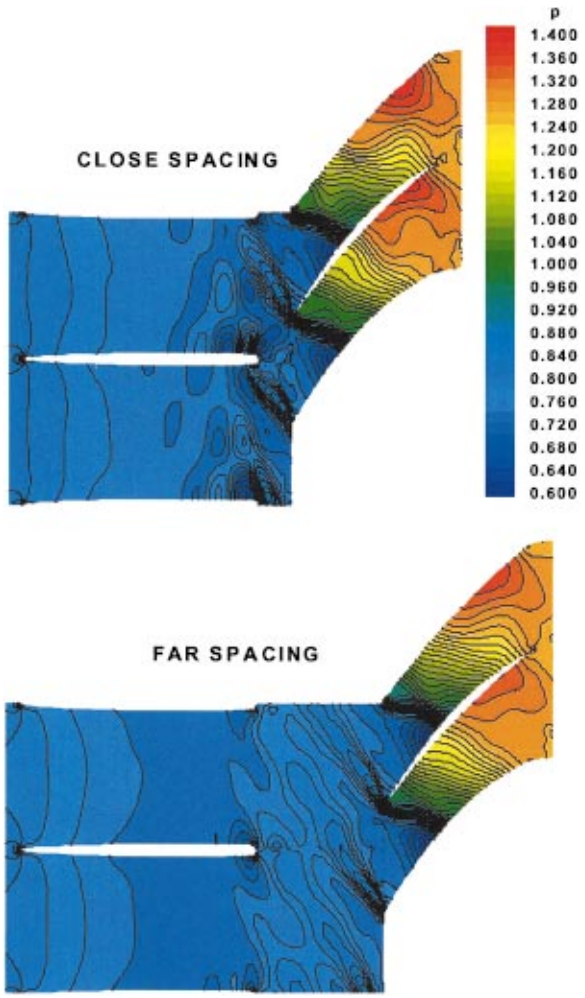

Fig. 5 MSU-TURBO flow field static pressure comparison, 75% span, time-step 5

spacing configuration produces additional loss on the upper surface of the wake generator trailing edge, the numerical model was used to further analyze the fluid mechanics associated with the loss production. Static pressure contours are especially helpful in gaining additional insight.

Figure 5 compares static pressure contours at 75% span for both close and far spacing simulations at time-step 5. The bow shock is oblique and detached from the rotor. The bow shock is strongest near the rotor leading edge and extends into the wake generator flow field. Farther away from the rotor leading edge the shock becomes weaker. A shock wave varies in strength depending on the flow properties upstream and downstream of the shock and the orientation of the shock wave to the flow. The changing strength of the bow shock is visible in Fig. 5 as the pressure contours are very close together near the rotor leading edge, but are fewer and farther apart as the bow shock approaches the lower surface of the wake generator. The passage shock is similar for close and far spacing, as is the bow shock near the rotor leading edge. However, at far spacing the bow shock dissipates in a shorter distance than at close spacing. Thus, closer spacing appears to affect the strength of the bow shock away from the rotor leading edge. Previous experimental research published by Koch et al. [12] confirms this observation.

Static pressure contours from the close spacing simulation are presented in Fig. 6. At time-step 1 a very high gradient region is observed at 96% chord where the bow shock from the lower rotor blade has been chopped by the wake generator trailing edge. This is similar to what happens when a rotor blade chops a wake. The remnants of the bow shock wave, hereafter referred to as the wake generator pressure wave, extend into the wake generator pitch about 25%. This is the amount the bow shock extended into the wake generator pitch at the time it was chopped by the wake generator.

At all time steps a low pressure region is observed near the wake generator trailing edge. This expansion zone is caused by the flow near the wake generator surface accelerating to negotiate the sharp turn around the blunt trailing edge.

From time-steps 1–5 the wake generator pressure wave moves from the wake generator trailing edge forward. The wake generator pressure wave passes through the expansion zone on the upper blade surface and the rotor bow shock passes through the expansion zone on the lower blade surface. Similar to the bow shock the static pressure increases across the pressure wave. As the oblique bow shock is chopped by the wake generator trailing edge the resulting wake generator pressure wave becomes oriented more normal to the wake generator surface. By time-step 13 the wake generator pressure wave is at 87% chord. The wake generator pressure wave moves with the rotor bow shock but is more normal to the wake generator blade surface. The pressure wave continues to weaken as it propagates forward.

By time-step 17 the weakened wake generator pressure wave has propagated upstream to 83% chord. The bow shock from the next rotor blade now approaches the wake generator trailing edge. During time-steps 17–21 the bow shock is chopped by the wake generator trailing edge and begins to pass through the low pressure expansion zone. The cycle then repeats itself with a new wake generator pressure wave forming on the wake generator upper surface.

The static pressure results for the far spacing simulation at 75% span are found in Fig. 7. It is immediately apparent that due to the larger axial gap between blade rows only weak remnants of the rotor bow shock, perhaps better described as a bow wave, interacts with the wake generator trailing edge. At no time does a pressure wave form on the upper surface of the wake generator. From time-steps 1–13 the bow wave extending to the upper passage sweeps past the wake generator trailing edge. As the wave makes contact with the wake generator it no longer protrudes into the passage. By time-step 13 the bow wave that existed in the upper wake generator passage has vanished. Between time-steps 13–21 the next bow wave proceeds to move toward and enter the upper wake generator passage.

A common feature observed in both the close and far spacing simulations is a low pressure expansion zone at the wake generator trailing edge. This low-pressure region is observed in both the close and far spacing simulations, and is uniquely associated with the wake generator trailing edge configuration.

The numerical simulations show the unsteady fluid mechanics that cause a difference in measured overall performance when blade-row spacing varies (see reference [1]). Blade-row interactions at close spacing produce increased loss on the wake generator trailing edge upper surface. The lower efficiency, pressure ratio, and mass flow rate measured in the close spacing configuration compared to the far spacing configuration is a result of this extra loss. As with any CFD model improvements can be made with finer meshes. A finer mesh would better resolve the bow shock, passage shock, and pressure wave.

Blade-Row Interaction Loss Production

Comparison of the loss and static pressure results for close spacing suggest that the wake generator pressure wave is directly related to the production of loss on the wake generator upper surface. The loss peaks on the blade surface coincide with the location of the wake generator pressure wave in time. As the pressure wave propagates forward it creates additional loss. The multiple loss peaks observed at time-step 13 of Fig. 3 are due to two pressure waves. One is from the lower rotor blade bow shock and the other from the middle rotor blade. At time-step 17 the

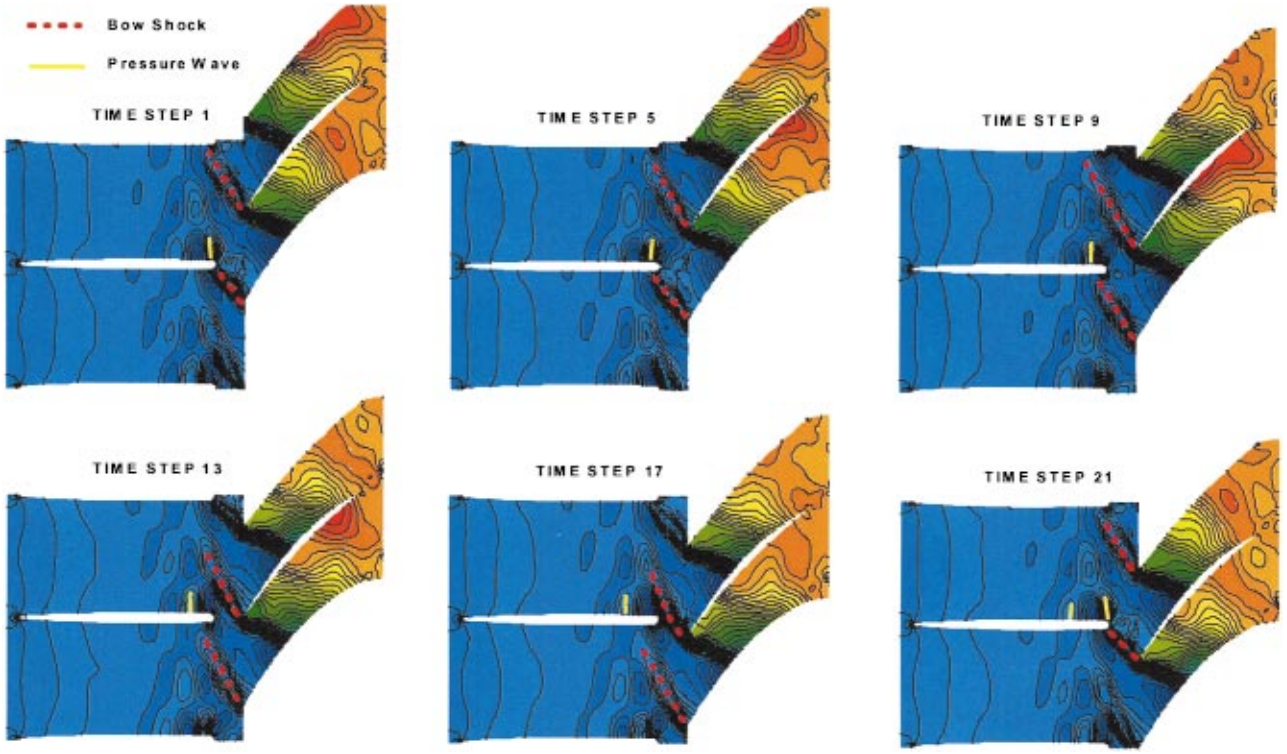

Fig. 6 MSU-TURBO close spacing static pressure contours, 75% span

forward peak is from the pressure wave produced when the lower rotor bow shock was chopped and the peak near the wake generator trailing edge is from the incoming rotor bow shock being chopped to form a new wake generator pressure wave. By time-step 21 the forward pressure wave has weakened sufficiently such that it no longer produces loss. It is proposed that in the reference frame relative to the wake generator pressure wave, the flow is supersonic and a moving shock wave almost normal to the freestream flow is formed that produces loss.

Wake Generator Unsteady Static Pressure Measurements. To validate this theory, unsteady static pressure measurements

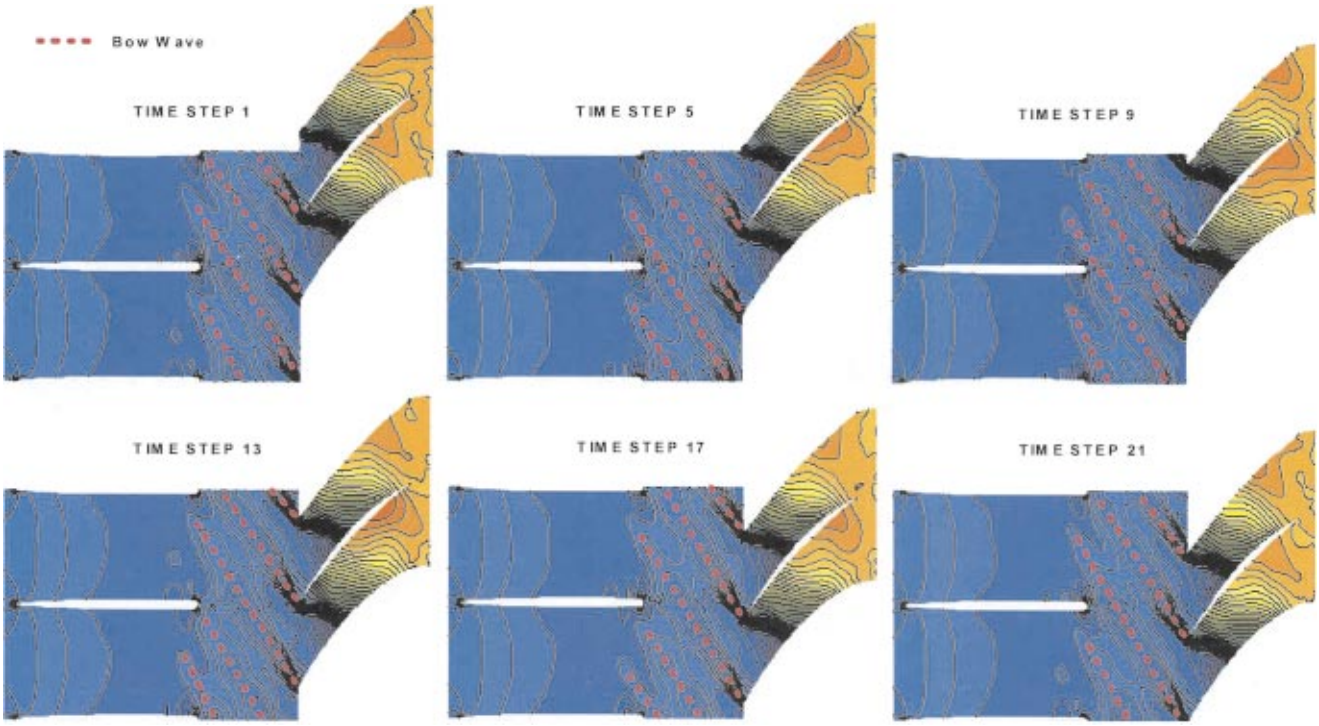

Fig. 7 MSU-TURBO far spacing static pressure contours, 75% span

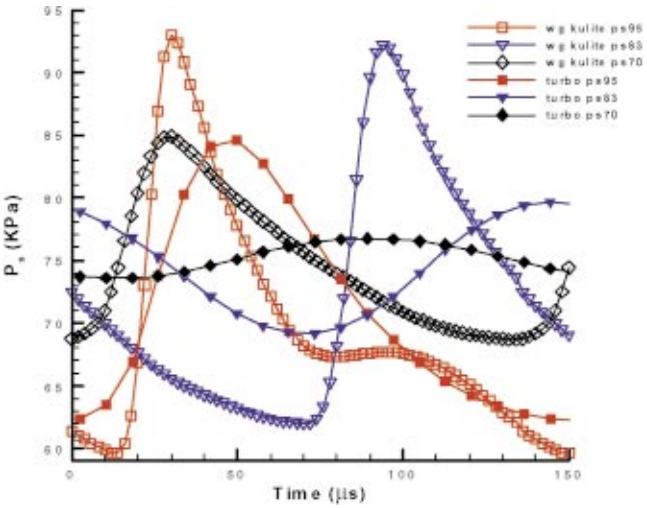

Fig. 8 Close spacing static pressure comparison, 75% span

made with Kulite high-response transducers were analyzed and compared with the MSU-TURBO results. Details of the static pressure measurements were reported by Probasco et al. [13]. Two wake generators were instrumented, one on the upper surface and the other on the lower surface. The transducers were located at 50 and 75% wake generator span at 95, 89, 83, 70, and 50% wake generator chord.

Figure 8 compares some of the measured and predicted static pressures for close spacing at 75% span. The peak-to-peak pressure measured by the Kulites was greater than that predicted by MSU- TURBO. The numerical results show a reduction in the peak-to-peak magnitude as the wave travels upstream. However, the experimental data suggest the weakening of the pressure wave is not so drastic as the wave does not begin to weaken until it has reached 70% chord. As expected the pressure wave measured experimentally is sharper than that predicted by the numerical model. The experimental and computational results at 95% chord show the upstream side of the wave is steeper than the downstream side. As the wave moves upstream it dissipates and widens.

At 95% chord the numerical results are nearly in phase with the Kulite measurements. At 89% chord the computation begins to lag the experiment and the phase lag increases further at 83 and 70% chord. This suggests the shock stagger angle of the simulation is not the same as that in the experiment thus resulting in a different wave propagation velocity.

The propagation velocity of the wake generator pressure wave, V_{wave}, was determined from the time it took the wave to travel the distance between two static pressure measurements. The Mach number of the pressure wave in its relative frame is defined as

$$\mathrm{M}_{\text{wave}} = \frac{V_{\text{wave}} + V_{\infty}}{a_{\infty}}$$

To estimate M_{wave} using experimental data, V_{∞} was estimated from downstream pressure measurements made during calibration of the wake generators [14]. With V_{wave} determined between 95% and 89% wake generator chord M_{wave} was calculated as 1.11. Calculating V_{wave} between 89% and 83% wake generator chord M_{wave} was slightly lower at 1.09. Additional details are presented in reference [14].

Based on the computational results at time-step 3 the wake generator pressure wave Mach number was 1.18. Comparing the experimental and numerical data used to determine M_{wave} two important observations were made. The propagation velocity of the wave, V_{wave}, was lower for the MSU-TURBO simulation and the low pressure region immediately upstream of the wave resulted in higher V_{∞} and lower a_{∞}. For the experimental calculation the conditions upstream of the wave were estimated from measurements made downstream of the wake generator during the wake calibration phase of the research program and thus would not account for any local changes in the flowfield due to neighboring blade rows.

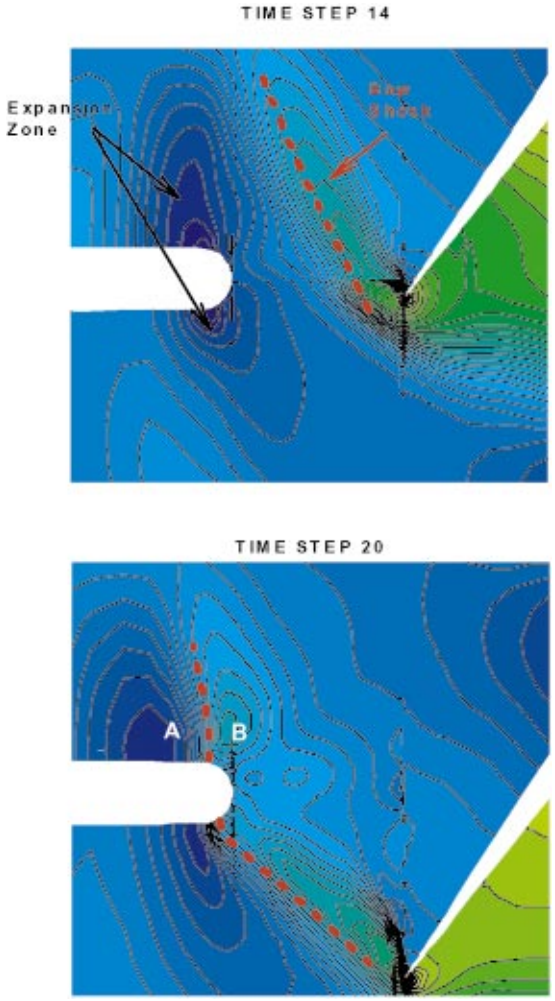

Fig. 9 Shock turning at close spacing

Shock Turning. The close spacing simulation shows that as the rotor bow shock comes in contact with the trailing edge of the wake generator the orientation of the shock becomes less oblique and the wake generator pressure wave that forms is nearly normal to the freestream flow. This change in orientation is due to an interaction with an expansion zone on the wake generator trailing edge upstream of the shock. Figure 9 shows that as the rotor bow shock approaches and passes through this low-pressure region, the shock geometry must change in order to satisfy conditions downstream of the shock. Because the expansion zone is at a significantly lower pressure, the bow shock turns more normal to the flow in order to increase the pressure rise across the shock. Because the chopped rotor shock turns more normal to the flow the entropy rise across the shock is greater than would have been experienced with the oblique orientation.

This shock turning is most noticeable on the wake generator upper surface, but it also occurs on the lower blade surface to a lesser extent (see time-step 1 in Figs. 3 and 5). The amount of turning depends on the conditions upstream and downstream of the shock wave. Once the shock wave passes through the expansion zone it dissipates and no longer produces additional loss. The expansion zone extends further upstream on the upper surface compared to the lower surface. The modeled relative Mach number upstream and downstream of the shock wave after turning

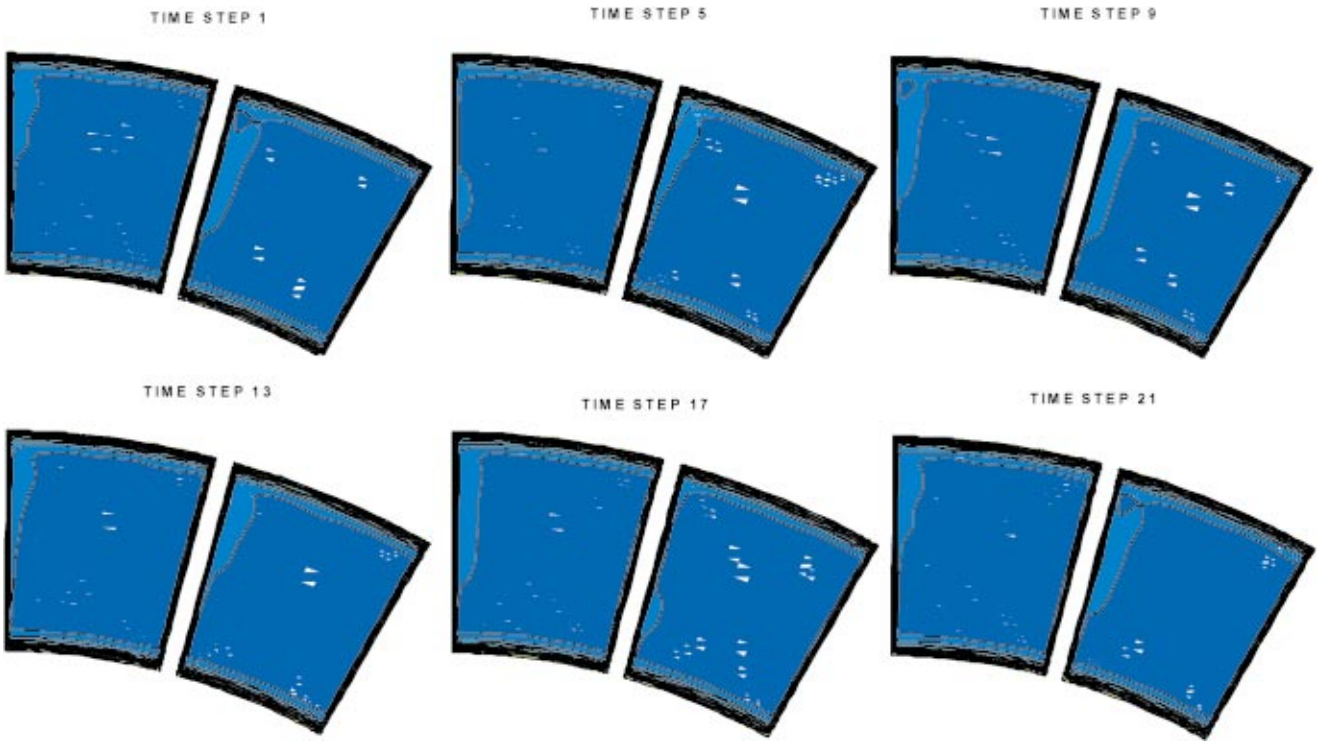

Fig. 10 MSU-TURBO close spacing loss contours, 93.74% wake generator chord

(time-step 20) are 1.26 at location A and 1.04 at location B. The simulation does not show a shock reflection from the wake generator upper surface because the incident shock is nearly normal and the conditions downstream of the rotor bow shock are nearly subsonic.

These calculations confirm that relative to the wake generator pressure wave a moving shock wave is formed that propagates upstream on the wake generator upper surface. The loss produced on the wake generator upper surface is a consequence of the entropy rise across the shock wave. The blade-row interaction loss predicted by MSU-TURBO is likely a conservative estimate because the pressure wave is weaker than that measured experimentally and does not propagate as far upstream as the Kulite measurements suggested. The wake generator pressure wave velocity, V_{wave}, was also higher in the experiment than predicted numerically.

Spanwise Extent of Loss Production. Having determined that the wake generator and rotor flow fields interact at 75% span to produce additional loss at close spacing, it is logical to investigate this phenomenon over the entire span. Since the extra loss produced is dependent on the presence of a shock wave at close spacing the majority of the span would be expected to produce the loss. From reference [15] the sonic radius of the SMI rotor is approximately 25% span.

Figure 10 presents six time-steps from the unsteady flow field in the pitchwise plane at 93.74% wake generator chord. The view is from downstream looking upstream and the analysis will focus on the right side of the middle wake generator. Additional loss is defined by a higher magnitude loss than the freestream that is not part of the endwall or tip clearance losses. At time-step 1 the loss is nearly two-dimensional and extends from 32 to 86% span and 12 to 18% wake generator pitch. Above 90% span and below 10% span the endwall losses exist and change very little with time. Below 3% pitch profile losses are always evident and are also independent of time. At this chord location additional loss is not observed on the left side of the wake generator.

From time-steps 1–5 the loss region moves up towards the case and increases in magnitude near the blade surface. At time-step 5 the loss is located between 39 and 87% span and from 5% to 14% pitch. During time-steps 5–9 the loss region thickens and is nearly constant in thickness from 28 to 95% span. At time-step 9 the loss extends from 29 to 88% span and 6% to 13% pitch. From time-steps 9–13 the loss region continues to thicken in the pitchwise direction and moves toward the case. At time-step 13 the loss region covers 48 to 88% span and 5 to 16% pitch. Between time-steps 13–17 the loss region narrows and its spanwise extent shrinks. At time-step 17 the loss region near the wake generator tip is no longer present but a new loss bubble has formed near 29% span. At time-step 17 the loss region covers 19 to 42% span and its width extends from 4 to 11% pitch. Between time-steps 17–21 the new loss region continues to grow in length and move up the span of the wake generator blade.

Figure 10 shows that additional loss from the blade-row interaction exists from as low as 19% span all the way to the blade tip. Depending on the position of the rotor blade in time, the loss region produced varies. Two observations explain this phenomenon. The first is that the relative Mach number of the flow changes with rotor span. Thus at lower spans the wake generator pressure wave formed when the rotor bow shock is chopped may not be as strong as at higher spans. The amount of shock turning near the wake generator trailing edge will also vary with span. Furthermore, the stagger angle of the rotor blade changes with span. At the lower spans the rotor blade is staggered less than at 75% span. A bow shock closer to the hub will therefore interact with the wake generator sooner than the bow shock at 75% span. Similarly, the pressure wave may not exist on the wake generator blade surface over all spans at the same time. In other words, since the wake generator will chop the bow shock at different times, the pressure wave formed at different spans will not be in phase with each other. Additional details of loss production at 29% span are found in reference [14].

Design Implications

It is difficult to establish specific design guidelines from this basic study. At best, some preliminary guidelines can be proposed for consideration. The influence of upstream stator contour, stagger angle, and trailing edge thickness on close spacing, interaction loss production must be studied prior to establishing more reliable design criteria.

As demonstrated in reference [1] at large enough axial spacing between blade rows, additional losses resulting from blade-row interaction effects are insignificant. Thus, it is possible to design for an axial gap large enough so that the rotor bow shock is not chopped at all or if chopped, with only a weak pressure wave forming.

Based on the equation defining the Mach number of the pressure wave in the relative frame, the local velocity and speed of sound upstream of the pressure wave along with the propagation velocity of the wave define the wave strength. Designing for lower local flow velocity near the trailing edge of the stator blade could reduce interaction loss for close spacing.

The strength of the pressure wave is also related to the strength of the rotor bow shock at the location it is chopped by the stator trailing edge. It may be possible to optimize the stator and rotor stagger angles so that the weaker part of the rotor bow shock interacts with the stator trailing edge. Also, the axial gap could be made intentionally larger further out in blade span where the bow shocks are strongest.

The angle of the moving wave affects the magnitude of the loss produced as an oblique shock generates less loss than a normal shock. For the SMI rig additional loss was produced due to the chopped rotor bow shock turning more normal to the free stream flow. This turning was directly related to the blunt trailing edge of the wake generator, but other stator designs may also have a local expansion zone at the blade trailing edge. Other flow phenomena may exist that produce a pressure wave due to close blade-row axial spacing. For example, Sanders and Fleeter [16] have shown that a pressure wave is formed when a rotor bow shock reflects off the trailing edge pressure surface of an upstream IGV.

The number of stator and rotor blades and the pitch ratio of both blade rows will determine how much loss is produced by the blade-row interaction. Obviously more interactions between blades result in greater overall loss due to this phenomenon. More interaction loss is produced when more blades are involved. In addition, as shown in the 24-wake generator, close spacing simulation, it is possible to have multiple pressure waves on the stator blade suction surface if the solidity of the rotor blade row is greater than the solidity of the stator blade row.

Conclusions

A previously unidentified loss producing mechanism due to blade-row interaction that has a significant effect on stage performance has been described. It should be considered when designing transonic fans and compressors because the consequent penalties in compressor performance can be significant. Numerical simulations of the blade-row interaction flow field, and static pressure measurements on the surface of the wake generator suggest that additional loss was produced on the stator surface with close axial spacing between the stator and rotor blade rows.

Analyses of the numerical simulations and high-response static pressure measurements acquired on the wake generator blade surface revealed some important details of the fluid dynamics of this additional loss producing mechanism. At close spacing the rotor bow shock is chopped by the wake generator trailing edge and forms a pressure wave on the upper surface of the wake generator that propagates upstream until it weakens. The bow shock is oblique as it interacts with the wake generator trailing edge, but the resulting pressure wave that forms is turned more normal to the wake generator blade surface. In the reference frame relative to the wake generator pressure wave, the flow is supersonic and a moving shock wave exists that produces an entropy rise and loss across the shock. At far spacing the rotor bow shock has degenerated into a pressure wave when it interacts with the wake generator. No pressure wave forms on the wake generator upper surface during this interaction. In this case the wake generator blocks the bow shock at the lower surface of the wake generator and it disappears.

Additional loss generation from the blade-row interaction for closely spaced blade rows exist from as low as 19% span all the way to the blade tip. The magnitude of loss production is affected by the strength of the bow shock at the location it interacts with the trailing edge of the wake generator. Additional loss is incurred if the rotor bow shock is turned more normal as it interacts with the wake generator trailing edge.

Before establishing too many specific design guidelines for this kind of blade-row interaction, further research involving more realistic hardware, e.g., a cambered stator, should be conducted. How having a more realistic stator affects the propagation and orientation of the pressure wave that results when the rotor bow shock is cut by the upstream stator blade, and how large the resultant loss produced is needs to be answered for different stator configurations spaced close axially to a transonic rotor before a reliable set of design rules can be specified.

Based on this limited study then, only preliminary guidelines are apparent. For close axial spacing between blade rows, factors affecting the strength of the moving pressure wave and resultant loss production are the local flow velocity near the stator surface upstream of the propagating wave and rotor bow shock strength. So, with close blade-row spacing, designing for lower local velocity upstream of the propagating wave would result in less loss across the moving pressure wave. For close axial spacing, setting the stator and rotor stagger angles so that only the weaker part of the rotor bow shock interacts with the stator trailing edge would also reduce loss production. Also, increasing the axial gap further up the span where the rotor bow shock is strongest may reduce interaction losses there. Finally, with close axial spacing of blade rows, paying appropriate attention to the number of stator and rotor blades and the pitch ratio of both blade rows could be an additional control of interaction loss.

Acknowledgments

The use of the MSU-TURBO code contributed immensely to the quality of this research. The authors would like to thank Dr. Dale Van Zante from NASA Glenn Research Center, Dr. J. P. Chen from Mississippi State University, and Dave Car from CARL for their help in getting MSU-TURBO running and in post-processing and interpreting the data. The support and assistance from the Naval Oceanographic Office Major Shared Resource Center (NAVO MSRC) where the code was run is also greatly appreciated. Many of the ideas presented in the paper were influenced by discussions with other individuals. The authors wish to acknowledge Dr. Steve Puterbaugh and Dr. Greg Bloch from the CARL group and from NASA Glenn Research Center Dr. John Adamczyk, Dr. Tony Strazisar, and Dr. Randy Chriss. The authors thank the Propulsion Directorate management for supporting the research and allowing the presentation and publication of this paper.

Nomenclature

a_∞ = speed of sound upstream of wake generator pressure wave $= \sqrt{\gamma R T_\infty}$

C_p = specific heat at constant pressure

H_{exit} = total enthalpy at compressor exit

H_{inlet} = total enthalpy at compressor inlet

M_{wave} = Mach no. of wake generator pressure wave in reference frame relative to wave

p = static pressure

R = gas constant

s = entropy

T_{exit} = total temperature at compressor exit
T_∞ = static temperature upstream of wake generator pressure wave
u = axial component of velocity
V_{wave} = velocity of wake generator pressure wave
V_∞ = velocity upstream of wake generator pressure wave
γ = ratio of specific heats
ρ = density
$\rho u \Delta s / C_p$ = loss parameter

References

[1] Gorrell, S. E., Okiishi, T. H., and Copenhaver, W. W., 2002, "Stator-Rotor Interactions in a Transonic Compressor—Part: 1: Effect of Blade-Row Spacing on Performance," ASME Paper GT-2002-30494, ASME J. Turbomach, **125**(2), pp. 328–335.

[2] Lamis, N., Bacha, J. L., and Burgand, F., 1996, "Numerical Simulations of Stator-Rotor Interactions on Compressor Blade Rows" *Loss Mechanisms and Unsteady Flows in Turbomachines*, AGARD CP-571, North Atlantic Treaty Organization.

[3] Eulitz, F., Engel, K., and Pokorny, S., 1996, "Numerical Investigation of Inviscid and Viscous Interaction in a Transonic Compressor" *Loss Mechanisms and Unsteady Flows in Turbomachines*, AGARD CP-571, North Atlantic Treaty Organization.

[4] Chen, J. P., Celestina, M. L., and Adamczyk, J. J., 1994, "A New Procedure for Simulating Unsteady Flows Through Turbomachinery Blade Passages," ASME Paper 94-GT-151.

[5] Chen, J. P., and Barter, J. W., 1998, "Comparison of Time-Accurate Calculations for the Unsteady Interaction in Turbomachinery Stage," AIAA Paper, 98-3292.

[6] Barter, J. W., Vitt, P. H., and Chen, J. P., 2000, "Interaction Effects in a Transonic Turbine Stage," ASME Paper 2000-GT-0376.

[7] Estevadeordal, J., Gogineni, S., Goss, L., Copenhaver, W., and Gorrell, S., 2001, "DPIV Study of Wake-Rotor Synchronization in a Transonic Compressor," AIAA Paper, 2001-3095.

[8] Van Zante, D. E., 2000, personal communication.

[9] Adamczyk, J. J., 1985, "Model Equation for Simulating Flows in Multistage Turbomachines," ASME Paper 85-GT-226.

[10] Adamczyk, J. J., 2000, "Aerodynamic Analysis of Multistage Turbomachinery Flows in Support of Aerodynamic Design," ASME J. Turbomach., **122**, pp. 189–217.

[11] Denton, J. D., 1993, "Loss Mechanisms in Turbomachines," ASME J. Turbomach., **115**, pp. 621–656.

[12] Koch, P. J., Probasco, D. P., Wolff, J. M., Copenhaver, W. W., and Chriss, R. M., 2001, "Transonic Compressor Influences on Upstream Surface Pressures with Axial Spacing," J. Propul. Power, **17**, pp. 474–476.

[13] Probasco, D. P., Leger, T. J., Wolff, J. M., Copenhaver, W. W., and Chriss, R. M., 2000, "Variations in Upstream Vane Loading With Changes in Back Pressure in a Transonic Compressor," ASME J. Turbomach., **122**, pp. 433–441.

[14] Gorrell, S. E., 2001, "An Experimental and Numerical Investigation of Stator-Rotor Interactions in a Transconic Compressor," Ph.D. dissertation, Department of Mechanical Engineering, Iowa State University.

[15] Law, C. H., and Wennerstrom, A. J., 1989, "Two Axial Compressor Designs for a Stage Matching Investigation," AFWAL-TR-89-2005.

[16] Sanders, A. J., and Fleeter, S., 1999, "Transonic Rotor-IGV Interactions," Presented at the thirteenth International Symposium on Air Breathing Engines, Chattanooga, TN, (ISABE 99-7029).

Aerodynamics of a Transonic Centrifugal Compressor Impeller

Seiichi Ibaraki
Tetsuya Matsuo
Hiroshi Kuma
Kunio Sumida
Toru Suita

Nagasaki R&D Center,
Mitsubishi Heavy Industries, Ltd.,
Nagasaki, 851-0392, Japan

High-pressure ratio centrifugal compressors are applied to turbochargers and turboshaft engines because of their small dimensions, high efficiency, and wide operating range. Such a high-pressure ratio centrifugal compressor has a transonic inlet condition accompanied with a shock wave in the inducer portion. It is generally said that extra losses are generated by interaction of the shock wave and the boundary layers on the blade surface. To improve the performance of high-pressure ratio centrifugal compressor, it is necessary to understand the flow phenomena. Although some research works on transonic impeller flow have been published, some unknown flow physics are still remaining. The authors designed a transonic impeller, with an inlet Mach number about 1.3, and conducted detailed flow measurements by using laser doppler velocimetry (LDV). In the result, the interaction between the shock wave and tip leakage vortex at the inducer and flow distortion at the downstream of inducer were observed. The interaction of the boundary layer and the shock wave was not observed. Also, computational flow analysis was conducted and compared with experimental results. [DOI: 10.1115/1.1540117]

Introduction

The use of large capacity and high pressure ratio is strongly required for the centrifugal compressor applied to turbochargers and turboshaft engines because of the recent trend of increased specific output power of engines. Furthermore, limitations of its outside diameter dimension necessitate the inlet blade height of the centrifugal compressor to increase, causing the relative Mach number at the inlet to be placed in a transonic inflow condition where the relative Mach number locally exceeds unity. It has been reported that performance of the centrifugal compressor depends on the relative Mach number at the inlet with its efficiency decrease being greater in the transonic region than in the subsonic region [1].

It is believed that in a transonic centrifugal compressor, an extra loss occurs because the shock waves, generated at the inducer, interfere with the blade surface boundary layer or leakage vortex.

With respect to internal flows of transonic centrifugal compressor, Krain et al. [2–4], conducted detailed L2F measurements of an experimental transonic impeller at a pressure ratio of 6.1:1 and calculation for verification of CFD. More recently, Krain et al. developed a three-dimensional laser measurement method to conduct internal flow measurements of the transonic centrifugal compressor for comparison with the two-dimensional flows, and pointed out that at the blade center where the flow changes from axial to radial direction, flow velocity greatly differs from the one obtained from the two-dimensional measurements [5]. Also, the authors conducted LDV measurements paying attention to the inducer portion of a transonic compressor with its inlet Mach number being about 1.3 and understood that a low flow region, probably due to interference by shock wave and leakage vortex from clearance, can be formed near the shroud [6]. However, there are only few other cases of such measurements, and the flow phenomena and loss generation mechanism of the transonic centrifugal compressor still remain to be fully elucidated.

For performance improvement of the transonic centrifugal compressor, design of the inducer blade causing shock waves is generally said to be important. It has also been reported that decreasing the turning angle of the inducer would improve efficiency, decrease blockage and enhance the operating range [1,7]. The boundary layer suction in the inducer and decreases of the tip blade thickness are also said to be effective [2,8].

Following a previous paper [6], the authors conducted further detailed flow measurements of the inducer portion up to the outlet of a high load and large capacity transonic impeller with a relatively small number of blades for turbochargers. Also, we attempted to understand the internal flow phenomena using CFD. For visualization of CFD, we used the vortex identification method based on the Critical Point theory capable of identifying vortexes even in a complicated three-dimensional flow field, recently applied to the internal flows of a transonic axial flow compressor rotor by Furukawa et al. [9]. In this paper, the authors verified the flow phenomena of the transonic centrifugal compressor from the LDV measurements and CFD.

Experimental Apparatus and Procedures

A cross section of the test compressor is shown in Fig. 1. A turbocharger was used as a compressor test rig for the present study. The test rig consists of a transonic impeller, a vaned diffuser and a volute. The test compressor was driven by the gas turbine equipped at the opposite rotor end. Figure 2 shows the test impeller. The test impeller is an open shroud impeller contains seven full blades and two rows of splitter blades with 25 deg of backswept from radial at exit. The tip diameter is 373 mm and the exit blade width is 23.5 mm. The inlet tip diameter is 261.3 mm, the inlet blade height is 83 mm, and the inlet tip angle is 29.8 deg from tangential. The tip clearance is 0.65 mm at the inlet and is 1.0 mm at the exit. The relative Mach number of the impeller leading edge tip is about 1.3.

A vaned diffuser, which consists of 19 blades and parallel walls, was installed at the downstream of the impeller to eliminate the influence of the flow asymmetry in peripheral direction due to the volute. The diameter of the blade leading edges is 429 mm, and the blade trailing edges are located at 590.1 mm in diameter. The blade height is equal to the impeller exit width. The blade inlet angle is 21 deg from tangential.

Figure 3 shows the meridional view of the test impeller and the LDV measurement locations. This paper presents results of the LDV measurements at cross section D, cross section E, and cross section F of the inducer portion, and cross section G of the impeller outlet and cross section H downstream of the impeller. Results of cross sections A through D can be found in a previous

Contributed by the International Gas Turbine Institute and presented at the International Gas Turbine and Aeroengine Congress and Exhibition, Amsterdam, The Netherlands, June 3–6, 2002. Manuscript received by the IGTI January 25, 2002. Paper No. 2002-GT-30374. Review Chair: E. Benvenuti.

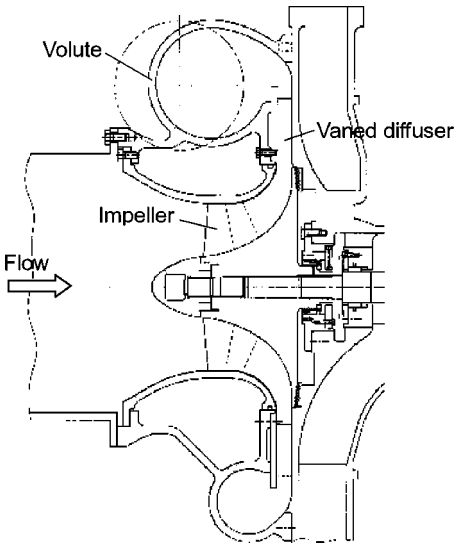

Fig. 1 Cross section of test compressor

paper [6]. For the space resolution of measurement, 0.5 deg/point along the blade pitch and 12 points along the blade height were used.

Figure 4 shows the pressure ratio-flow rate characteristics at the design rotation speed of the test compressor. The design rotation speed is 24,700 rpm (peripheral tip speed, 482 m/s), and the pressure ratio is 3.9. Internal flows were measured at three operating points, 6.3 m^3/s near surge, 6.8 m^3/s of the design flow and 7.3 m^3/s at the high flow side. This paper presents measurement results at the design flow rate. Also, static pressures on the shroud wall surface were measured, using 18 high-frequency response pressure sensors attached from upstream of the impeller to its outlet.

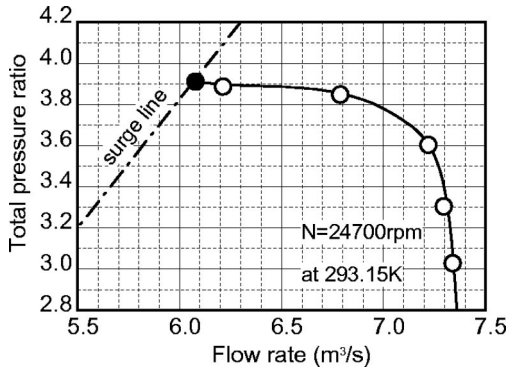

Fig. 4 Compressor stage characteristics

The LDV system is composed of an optical subsystem of fiber type using two colors and four beams, and a light source using argon ion laser. For signal processing, BSA was used. For data collection, a rotating speed detector was used to generate rotating pulses, and 10,000 points of data per blade pitch were acquired in synchronization of rotations to be used as averaged data. For the response frequency of the high frequency pressure sensor, 600 KHz was used for the inducer and 1 MHz for the downstream portion of the splitter blade.

Numerical Procedure

A three-dimensional Reynolds-averaged Navier-Stokes code developed by Dawes [10] was used to obtain the flow field of the test impeller. Dawes code use the turbulence model of Baldwin-Lomax [11]. The computational mesh is shown in Fig. 5. The H-type computational mesh is used and has 102 nodes pitchwise, 111 nodes streamwise, 41 nodes along the blade height and 10 nodes for clearance. The minimum grid spacing is about 0.5 percent of the blade pitch on the blade surface and is about 0.7 percent blade span on the hub and shroud wall.

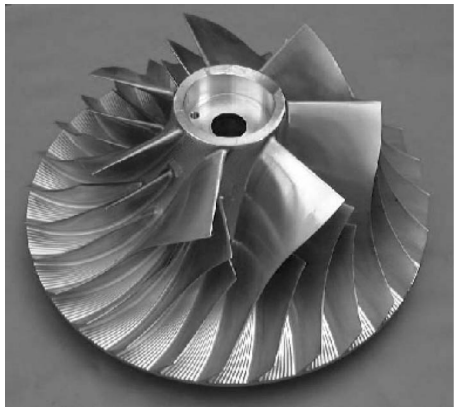

Fig. 2 Test impeller

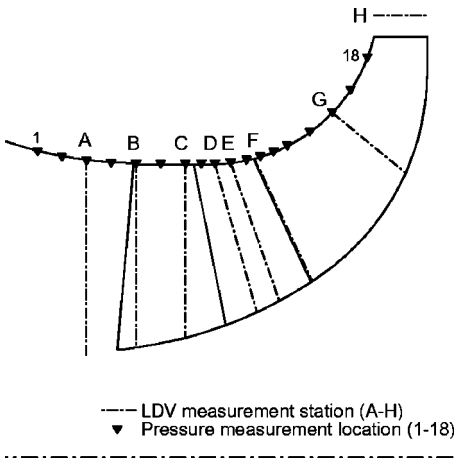

Fig. 3 Meridional view of test impeller showing measurement locations

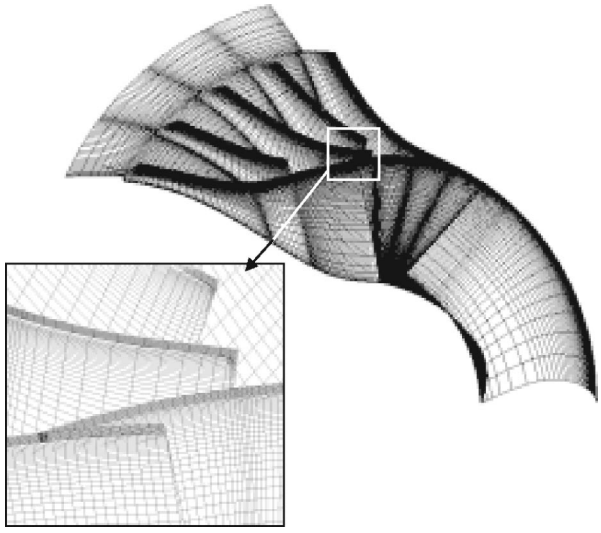

Fig. 5 Computational mesh

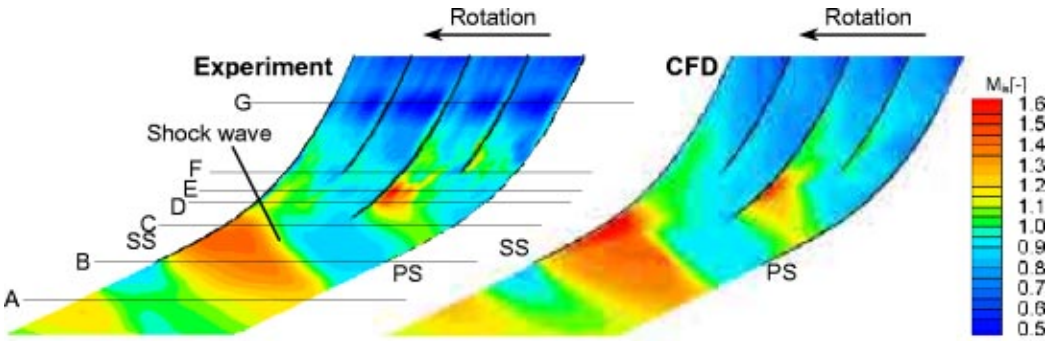

Fig. 6 Comparison of isentropic Mach number distribution of casing surface

Experimental Results and Discussions

Shroud Casing Pressure Measurements. Figure 6 shows isentropic Mach numbers obtained from the measurements of static pressures on the shroud casing wall surface at the design point. Figure 6 also shows isentropic Mach numbers obtained from CFD. Because the inlet pressure was not strictly in agreement between the measurement and CFD, the isentropic Mach numbers were computed from the wall surface static pressures for comparison. From the measured results, a large pressure change domain probably due to a shock wave could be captured in the inducer portion. The shock wave is generated from the suction surface of the full blade and extends upstream of the impeller. The root of the shock wave located on the suction surface of the full blade is approximately positioned in the leading edge of the first splitter blade. Also, a high-velocity region is formed on the suction surface of the first splitter blade, and the flow once decelerated by the shock wave from the full blade is re-accelerated to generate a weak shock wave on the suction surface of the 1st splitter blade.

From comparison between the measurements and the CFD results, it is known that a good agreement is seen in locations of the shock wave and in the patterns of the flow field. As the LDV measurement locations are shown in Fig. 6, the authors of the present study conducted detailed LDV measurements in cross sections E through H, the downstream of the cross section D corresponding to the root of the shock wave, referencing the shroud pressure measurement results.

LDV Measurements. Figure 7 compares meridional velocity distributions in cross sections D through H as obtained from LDV measurements with the CFD results. In cross section D, a high-velocity region, which appears to be the root of the shock wave, is generated near the shrouds of suction surfaces of the full blade and the splitter blade, and a low-velocity region is generated in the upper portion. This low-velocity region appears to be caused by interference by the shock wave and the shroud wall boundary layer or leakage vortex. Also, the flow velocity near the shroud of the first splitter blade suction surface was fast, and thus, the acceleration region obtained from the pressure measurements could also be confirmed in the LDV measurements. Meanwhile, CFD also showed formation of a low velocity region at the shroud side of the suction surface of the full blade, though smaller than in the measurements, and thus, this flow phenomenon could also be captured by CFD as well. However, the low-velocity region could not be confirmed at the suction surface side of the splitter blade.

In cross section E, the low-velocity region near the tip of the full blade suction surface has extended pitchwise, compared with cross section D upstream, and it appears that leakage vortex has been enhanced due to interference of the shock wave. Also, a local low-velocity region probably due to interference of the shock wave and the leakage vortex was confirmed at location about 20% pitchwise from the suction surface of the first splitter blade. This can be estimated from CFD results as described later.

Cross section F corresponds to the portion immediately after the leading edge of the second splitter blade, and it is seen that the low-velocity region measured in cross section E has diffused pitchwise. It has spread pitchwise near the shroud instead of spreading along the blade height direction.

In cross section G, it is seen that the accumulation of the low-velocity region is not remarkable. The low-flow regions are formed at the small part of the balde pitch near the shroud, compared with cross section F upstream. It is also seen that in the four flow passages divided by the first splitter blade and the second splitter blade, location of the low-velocity region near the tip differs from one another. Although there may be a quantitative difference between CFD and measurement results which are greater than the CFD results, patterns of the qualitative distributions are in a good agreement.

Cross section H corresponds to the downstream of the impeller and to the radius location about 1.05 times as large as the impeller diameter. A low-velocity region corresponding to the low-velocity region near the tip in cross section G and to the wake of the blade was observed.

Three-Dimensional Viscous Flow Analysis. Figure 8 compares pitchwise relative velocity distributions near the shroud (85–90% blade span), at the midspan, and near the hub (20–30% blade span) between blade pitches in the respective cross sections E through H.

From Fig. 8, it is known that CFD and measurements show qualitatively and quantitatively an agreement in midspan and near the hub in cross section E. Although in the experiment, a low velocity region probably due to interference of the shock wave and the leakage vortex was measured near the shroud, it is not so marked in analysis. Cross section F also shows a qualitative and quantitative agreement at midspan and near the hub. At near the shroud, the quantitative accuracy is somewhat lower than that at midspan and near the hub.

In cross section G, the measured velocities were greater than the CFD results, showing a quantitative discrepancy, but because the velocity patterns near the shroud exhibit an agreement for the four stream passages, it is expected that a general flow phenomenon could be evaluated. Although the effect of the centrifugal force acting on seeding particles used for experiment, etc., can be considered as the reason of different velocity levels between the measurements and the CFD results, its cause remains unknown and a future issue.

In cross section H, it is known that in the experimental results, mixing pitchwise is almost finished whereas the CFD results show that the pitchwise variation is greater.

Figure 9 shows visualization of the impeller internal flows using CFD. The figure shows the vortex cores identified on the basis

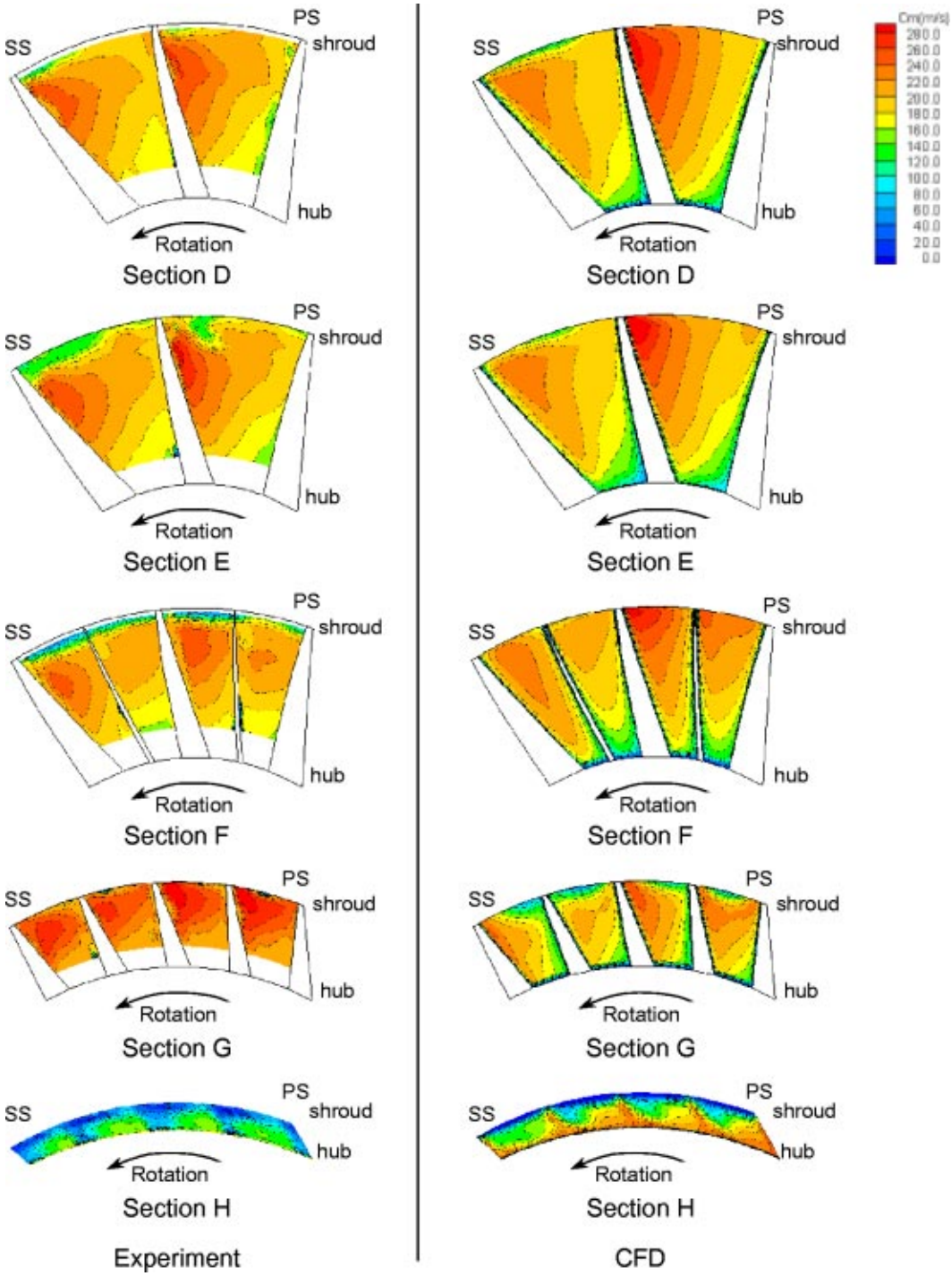

Fig. 7 Comparison of meridional velocity distribution at five sections

of the critical point analysis [9] and colored with normalized helicity. Normalized helicity is defined as cosine of the angle made between the vortex vector and the velocity vector, and the domain where its absolute value is one means the strong rolling-up of a streamwise vortex. The upper blade pitch of the impeller shown in Fig. 9 displays the relative Mach number distribution near the shroud and the relative velocity distribution of the cross section C, D and G together with the vortex cores. Also, the lower blade pitch displays limiting streamlines on blade suction surface and streamlines passing through the vortex cores.

From Fig. 9 it is seen that the rolling-up of a leakage vortex from clearance forms a vortex core at the leading edge of the full blade suction surface, and the core of the vortex increases and moves to the flow passage center when interacting with the shock wave. Also, the vortex core observed near the shroud of the full blade suction surface downstream is a vortex structure counterclockwise formed by the secondary flow which has run up from the hub side to the shroud side on blade surface.

Figure 10 shows the vortex cores and leakage flow with stagnation pressure at section D and G. From Fig. 10 tip leakage flow, jumping over that vortex core on the suction surface of full blade and splitter blade, flows toward the pressure surface of each blades and forms a vortex structure accompanied with complicated counterflows colored in red. The stream which has flowed

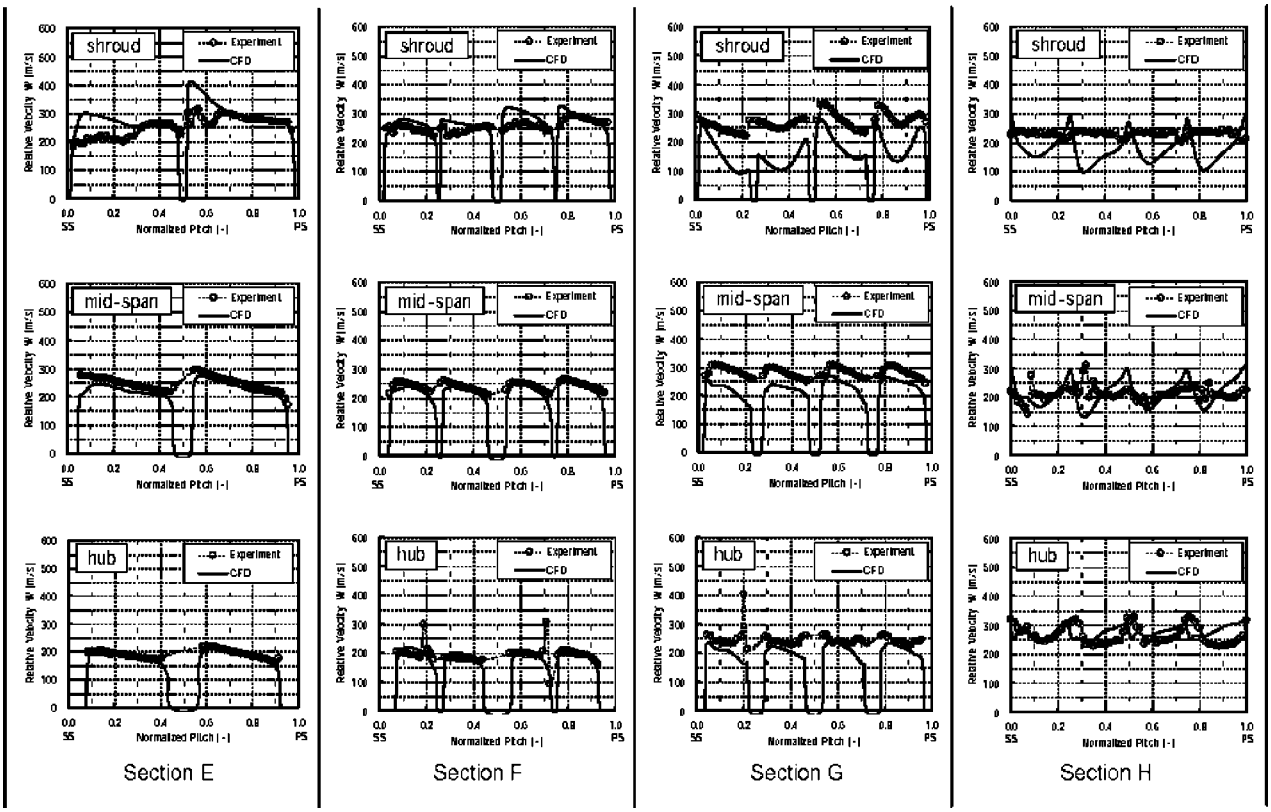

Fig. 8 Comparison of pitchwise relative velocity distribution at four stations

back from near the shroud downstream of the impeller due to pressure gradient is also drawn in here. This region agrees to the low-velocity region confirmed in the measurements at section G. As a result, it is inferred that the low-velocity region of section G measured by LDV is not an accumulation of low-energy fluids due to secondary flows as generally said but a low-velocity region formed by the leakage flow and counter flow from the impeller exit.

In Figs. 9 and 10 a vortex counterclockwise to the flow direction has been formed at the suction surface side of the second splitter blade ''b.'' This is not due to a leakage vortex but the vortex core which has developed from the full blade leading edge as already described and flowed in toward the suction surface of the second splitter blade. Also, a vortex core due to leakage vortex

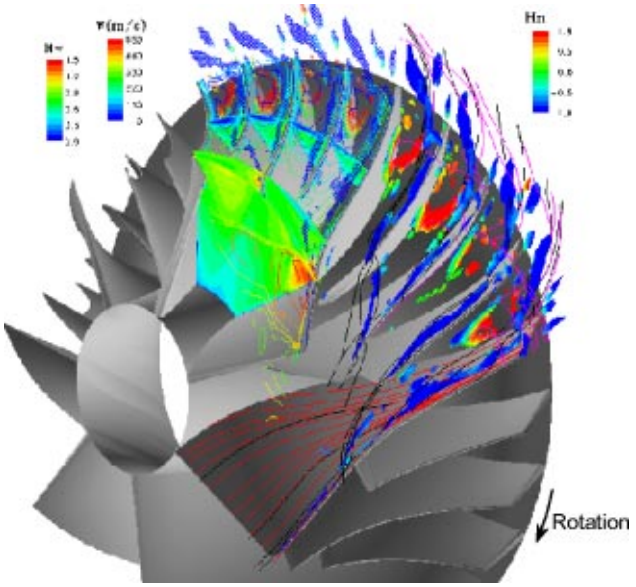

Fig. 9 Vortex cores colored with normalized helicity distribution

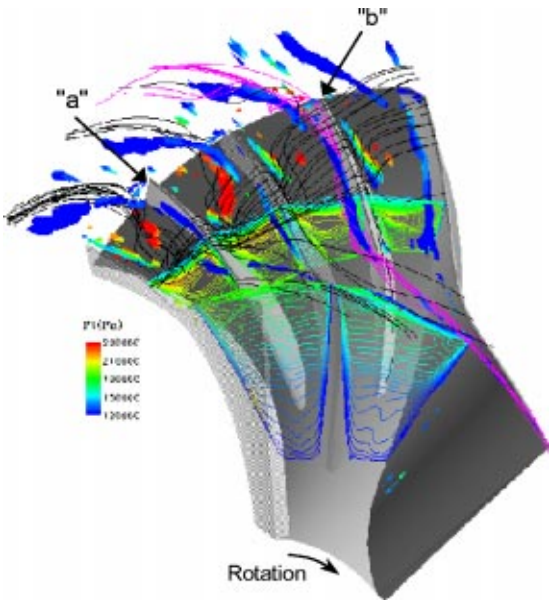

Fig. 10 Vortex cores and tip leakage flow with stagnation pressure distributions

from clearance is also observed at the leading edge of the first splitter blade and it flows into the pressure surface of the second splitter blade "a."

From Fig. 10 it has been found that the pressure loss is generated by interaction between tip leakage vortex and shock wave at section D. On the other hand, at section G the pressure loss is generated by the accumulation of tip leakage flow and back flow from impeller exit. This region which show large pressure loss is consistent with the low velocity region.

Conclusions

The authors conducted flow measurements using LDV and high frequency response pressure sensors as well as visualization of vortex structures utilizing CFD for a high-load and large-capacity transonic impeller. As a result, the following results could be obtained:

1. Low-velocity regions are formed near the suction surface tips of the full blade and the first splitter blade, downstream of the shock wave. From the shroud wall pressure measurements and CFD, it is judged that this is caused by interference of leakage flow and the shock wave.
2. Comparison between the measurements and CFD (Dawes Code) showed that the velocity distributions in the inducer portion exhibited a qualitative and quantitative agreement, except for location near the shroud. Because the qualitative distribution, though not quantitative, showed an agreement in the latter half of the impeller, it is believed that the flow phenomena could be simulated.
3. By the vortex identification of the CFD results it was found that in the inducer portion, the total pressure loss is increased by the leakage vortex rolling up from clearance. It was also found that interaction between the leakage vortex and the shock wave enhances the total pressure loss of the vortex core pitchwise, at downstream of the shock wave.
4. It seems that the low velocity region near the impeller exit is formed by the leakage vortex from clearance and counter flow from downstream of the impeller.

Nomenclature

C_m = absolute meridional velocity, m/s
C_p = specific heat at constant pressure
H_n = normalized helicity
I = rothalpy, J/kg
$\mathrm{M_{is}}$ = isentropic Mach no.
$\mathrm{M_{is}} = \sqrt{2\{\mathrm{I} - C_p T_s + 1/2(\omega r)^2\}}/\sqrt{\kappa R T_s}$
M_w = relative Mach no.
N = impeller rotational speed, rpm
P_t = relative total pressure, Pa
r = radius, m
R = gas constant, J/kg/K
T_s = static temperature, K
W = relative velocity, m/s
κ = ratio of specific heat
ω = angular velocity, radian/s
PS = pressure surface
SS = suction surface

References

[1] Rodger, C., 1998, "The Centrifugal Compressor Inducer," ASME Paper No. 98-GT-32.
[2] Pak, H., Krain, H., and Hoffman, B., 1993, "Flow Field Analysis in a High Pressure Ratio Centrifugal Compressor," AGARD Meeting.
[3] Krain, H., Hoffman, B., and Pak, H., 1995, "Aerodynamics of a Centrifugal Compressor Impeller with Transonic Inlet Conditions," ASME Paper No. 95-GT-97.
[4] Eisenlohr, G., Dalbert, P., Krain, H., Proll, H., Richter, F., and Rohne, K., 1998, "Analysis of the Transonic Flow at the Inlet of a High Pressure Ratio Centrifugal Impeller," ASME Paper No. 98-GT-24.
[5] Krain, H., Karpinski, G., and Beversdorff, M., 2001, "Flow Analysis in a Transonic Centrifugal Compressor Rotor Using 3-Component Laser Velocimetry," ASME Paper No. 2001-GT-0315.
[6] Ibaraki, S., Higashimori, H., and Matsuo, T., 2001, "Flow Investigation, of a Transonic Centrifugal Compressor for Turbocharger," 23rd CIMAC.
[7] Hayami, H., Umemoto, A., Itoh, K. and Kawaguchi, N., 1995, "Effects of Camber of Inducer on the Performance of a Transonic Centrifugal Compressor," ASME FED-Vol. 222, Fluid Machinery.
[8] Hah, C., and Krain, H., 1999, "Analysis of Transonic Flow Fields Inside a High Pressure Ratio Centrifugal Compressor at Design and Off Deign Conditions," ASME Paper No. 99-GT-446.
[9] Furukawa, M., Inoue, M., Saiki, K. and Yamada, K., 1998, "The Role of Tip Leakage Vortex Breakdown in Compressor Rotor Aerodynamics," ASME Paper No. 98-GT-239.
[10] Dawes, W. N., 1987, "Application of a Three-Dimensional Viscous Compressible Flow Solver to a High-Speed Centrifugal Compressor Rotor—Secondary Flow and Loss Generation," I Mech E Conf. Publ., No. C261/87.
[11] Baldwin, B., and Lomax, H., 1978, "Thin Layer Approximation and Algebratic Model for Separated Turbulent Flows," AIAA Pap., No. 78–257.

J. A. Kenyon
e-mail: james.kenyon@wpafb.af.mil
Propulsion Directorate,
Air Force Research Laboratory,
Wright-Patterson AFB, OH 45433

J. H. Griffin
e-mail: jg9h@andrew.cmu.edu

D. M. Feiner

Department of Mechanical Engineering,
Carnegie Mellon University,
Pittsburgh, PA 15213
e-mail: dfein@andrew.cmu.edu

Maximum Bladed Disk Forced Response From Distortion of a Structural Mode

A method is presented for obtaining maximum bladed disk forced response from distortion of a structural mode. It is shown that maximum response from mode distortion in a bladed disk occurs when the harmonic components of a distorted mode superimpose in a certain manner, causing localization of the mode and strong response in a particular blade. In addition, it is shown that the response of an intentionally mistuned system with maximum response does not change significantly when small random mistuning is added to the system. A method is described for calculating the structural mistuning necessary to obtain the distorted mode that gives maximum response. The theory is validated numerically.
[DOI: 10.1115/1.1540118]

Keywords: Mistuning, Blade Vibration, Maximum Response, Robust, Forced Response

1 Introduction and Background

Mistuning of bladed disks contributes to gas turbine high cycle fatigue by significantly increasing blade resonant vibration response. This in turn reduces the service life of blades and can lead to unexpected failures. Ideally, bladed disks are periodic structures that feature cyclic symmetry since each sector of the bladed disk is nominally identical. This leads to the existence of extended vibration modes in which vibrational energy is distributed throughout the bladed disk. In real bladed disks, however, minor variations in the structural properties of blades, referred to as mistuning, occur as a result of manufacturing variations or wear. Mistuning can lead to mode localization, which is characterized by strong vibration response in a small region of a bladed disk. Mode localization often results in a significant increase in the forced response amplitude of a few blades, resulting in premature fatigue of those blades. To exacerbate the problem, blade mistuning is random and can be difficult to measure accurately, making it difficult to predict when localization will occur and what blades will be affected.

Two important issues arise in determining the fatigue life for a bladed disk design. The first involves establishing the maximum response amplitude that a nominal design can experience when it is mistuned. Extremely high response amplitude can quickly lead to a fatigue failure. However, the maximum response of a system can be difficult to predict accurately. The second issue is determining the probability that a given bladed disk will have a response near the maximum. This is particularly difficult given the periodic nature of bladed disks. Because of the periodicity of bladed disks, they tend to have groups of modes with closely spaced natural frequencies. As a consequence, bladed disks tend to be sensitive to very small variations in system properties. Variations that may be too small to measure accurately can significantly affect the response of a bladed disk. Therefore, determining the forced response of a particular bladed disk and how this response amplitude compares to the maximum is difficult. Srinivasan [1] documents much of the pertinent literature dealing with the mistuning problem, both in terms of the effects that mistuning can have on forced response and the work that has been done to understand and mitigate the negative effects of mistuning.

Kenyon and Griffin [2] indicated that two primary physical mechanisms contribute to increased forced response in mistuned systems, frequency splitting and mode distortion. Frequency splitting refers to the separation of the nominally repeated natural frequencies that occur in tuned bladed disks into two distinct natural frequencies. Since the two modes in the pair no longer occur at the same natural frequency, they cannot combine into a pure traveling wave response, and instead superimpose in a manner that increases their forced response with respect to the tuned modes. In general, the net effect can be either an increase or a decrease in the forced response amplitudes, depending on the modes that are interacting and the amount of frequency separation between them. Mode distortion, also known as mode modulation, refers to harmonic content in the mode shape in addition to the fundamental waveform of the nominally tuned mode. Both of these phenomena are associated with the dynamics of many types of rotationally periodic systems (see Kim et al. [3]), though the study here is applied to bladed disks.

Frequency splitting was studied in detail by Ewins [4] and by MacBain and Whaley [5]. In particular, MacBain and Whaley analytically determined the maximum increase in forced response amplitude that can occur from frequency splitting when no distortion is present in the mode shapes. The goal of the present work is to isolate and study the effect of mode distortion on bladed disk forced response when the frequencies of the modes are sufficiently separated so that the effects of mode interaction through frequency splitting are small. In general, the effects of both frequency splitting and mode distortion will be present in mistuned forced response. However, it is useful to partition these effects and study them separately to systematically build a framework for understanding general mistuned forced response.

Kenyon and Griffin [2] argued that mode distortion is the primary cause of extremely high mistuned forced response amplitudes. Because of this, much of this paper is devoted to deriving an expression for the maximum forced response that can occur in a bladed disk due to mode distortion in an isolated family of modes. A previous solution of this type was derived by Whitehead [6]. A different solution was presented by Whitehead [7], though it was later recanted [8]. The solution for maximum forced response given here differs from that of Whitehead in several ways. First, the solution here is derived in terms of the structural modes of the system, rather than the aerodynamic modes presented in [6,8]. The model used for this analysis is the standard structural model that frequently appears in the literature (see for example Mignolet et al. [9]). For this type of model, the structural modes must be real, or in the case of repeated natural frequencies, must occur in

Contributed by the International Gas Turbine Institute and presented at the International Gas Turbine and Aeroengine Congress and Exhibition, Amsterdam, The Netherlands, June 3–6, 2002. Manuscript received by the IGTI January 30, 2002. Paper No. 2002-GT-30426. Review Chair: E. Benvenuti.

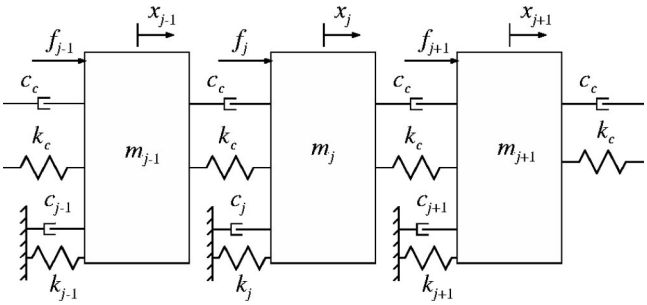

Fig. 1 Mass-spring-damper system

complex conjugate pairs. In the formulation given here, the distorted mode resulting in maximum response is a single real mode with a distinct natural frequency. The mode proposed by Whitehead for maximum response (see Eq. (6) of [6] with the proposed requirement that all of the z_r be equal except for one term) is complex, and thus can only occur in the standard structural model if there is a complex conjugate pair at the same frequency. As will be demonstrated later, this is not the case. The implication is that mode distortion given by Whitehead in [6,8] cannot be achieved through distortion of a single structural mode by mistuning the structural properties of a bladed disk. The result derived in this paper is relevant to the finite element-based mistuning models currently in use, particularly reduced-order models [10–15], since they are based on structural mistuning.

A second difference between the two approaches is that damping is included in the formulation given here. In deriving his expression for maximum response, Whitehead assumes that the damping is the same for all of the tuned modes [6,8]. This assumption is relaxed in the derivation here, and the effect of having variable damping is studied. When the damping is constant, the maximum response predicted using the structural mode approach is the same as that given by Whitehead [7] and is generally less than that given by Whitehead [8]. However, when the damping varies in the tuned modes it is shown here that the maximum response proposed by Whitehead [8] can be exceeded under certain conditions.

A practical aspect of any solution for maximum response is the amount of mistuning needed to achieve it and whether this mistuning can be practically expected to occur. By restricting the analysis to distortion of a single structural mode, the solution here is a local forced response maximum, though additional response maxima may be possible for a given system. The existence of multiple maxima has been documented in the literature [16,17]. The mistuning needed to achieve the particular maximum given here is relatively small, e.g. the variation in stiffness is often less than 10 percent (5 percent in frequency). Other maximum response solutions in the literature require much larger mistuning. For instance, one example provided by Whitehead requires stiffness mistuning of more than 250 percent in some of the blades (see Fig. 1 of [8]). In another example in the same paper, mistuning of approximately 50 percent is required for most of the blades on the disk, but one blade requires mistuning of -100 percent (see Fig. 2 of [8]). This implies that this blade has zero stiffness, which is not physically viable. There are several numerical optimizations in the literature in which maximum responses approaching the limit of Whitehead [8] are given. These either require large values of mistuning to combine frequency splitting and mode distortion effects [16], or involve interaction between multiple families of modes [17,18]. A more thorough discussion of the results reported in the literature will be given in Section 5.

One unique aspect of the solution for maximum response given here is the use of independent numerical forced response simulations to validate it. In fact, the work presented in this paper represents the first time that a direct solution for maximum response has been numerically demonstrated. Although Whitehead presents examples of solutions for maximum response in [8], there is no indication of numerical verification. Numerical simulations in [6] failed to achieve the predicted maximum response.

It is also demonstrated in this paper that the response of a system intentionally mistuned to obtain the maximum response is robust with respect to small random mistuning. The term robust is used in this paper to mean that small random mistuning added to the intentional mistuning will not significantly change the forced response experienced by the system. This has important practical applications in terms of real bladed disks. Small random mistuning cannot be controlled during the manufacture of bladed disks due to manufacturing tolerances. In addition, wear in service can cause small random mistuning in the bladed disk. Intentional mistuning can be added to a bladed disk so that the effects of small random mistuning are mitigated and the bladed disk responds as predicted. Here, the intentional mistuning results in maximum response. Although this may not be desirable in fielded systems, it provides a useful tool for developing test cases for high cycle fatigue experiments.

2 Theory of Robust Maximum Response

2.1 Derivation. Consider the mass-spring-damper system shown in Fig. 1. Similar models have been used extensively in the literature to examine the response of a single family of modes in a mistuned bladed disk, for example [9]. The equation of motion for the jth mass is

$$m_j\ddot{x}_j+(c_j+2c_c)\dot{x}_j-c_c(\dot{x}_{j-1}+\dot{x}_{j+1})+(k_j+2k_c)x_j -k_c(x_{j-1}+x_{j+1})=f_j(t),\quad j=0,\ldots,N-1 \tag{1}$$

where the "˙" superscript indicates differentiation with respect to time and N represents the number of blades on the disk. The system is cyclic such that $x_0=x_N$. The equations of motion for the entire system can be written in matrix form.

$$\mathbf{M}\ddot{\mathbf{x}}+\mathbf{C}\dot{\mathbf{x}}+\mathbf{K}\mathbf{x}=\mathbf{f}(t) \tag{2}$$

This formulation allows for mistuning in both mass and stiffness parameters. Thus, the mass matrix $\mathbf{M}=\mathbf{M}^\circ+\mathbf{\Delta M}$, where the superscript "$\circ$" indicates the tuned system matrix, and $\mathbf{\Delta M}$ is a diagonal matrix whose jth element represents a small perturbation in the mass of the jth sector, m_j. Similarly, the stiffness matrix $\mathbf{K}=\mathbf{K}^\circ+\mathbf{\Delta K}$, where $\mathbf{\Delta K}$ is a diagonal matrix containing small perturbations in the blade stiffnesses, k_j. Finally, it is assumed that the damping $\mathbf{C}$ is proportional to a linear combination of the tuned mass and stiffness matrices, $\mathbf{M}^\circ$ and $\mathbf{K}^\circ$.

The tuned modes are determined for $\mathbf{\Delta K}=\mathbf{\Delta M}=\mathbf{0}$ from the standard structural eigenvalue problem

$$\mathbf{K}^\circ\phi_m^\circ=\omega_m^2\mathbf{M}^\circ\phi_m^\circ \tag{3}$$

where ϕ_m° and ω_m are the mth tuned mode and its associated natural frequency. It is well known that the tuned system exhibits repeated natural frequencies for each m except $m=0$ and, in the case of N even, $m=N/2$. The modes corresponding to the repeated frequencies can be expressed as $\phi_{mj}^{\circ S}=b_m\sin m\theta_j$ and $\phi_{mj}^{\circ C}=b_m\cos m\theta_j$, where $\theta_j=2\pi j/N$. The modes for $m=0$ and $N/2$ have the form $b_m\cos m\theta_j$. The tuned modes are orthogonal with respect to the tuned mass, damping, and stiffness matrices, such that

$$\phi_m^\circ\mathbf{M}^\circ\phi_n^\circ=m_m\delta_{mn} \tag{4}$$

$$\phi_m^\circ\mathbf{C}\phi_n^\circ=c_m\delta_{mn} \tag{5}$$

$$\phi_m^\circ\mathbf{K}^\circ\phi_n^\circ=k_m\delta_{mn} \tag{6}$$

where δ_{mn} is the Kronecker delta.

The forced response of the tuned system to a traveling wave excitation is considered. The spatial distribution of the excitation is wave-like in form with an integer E number of harmonics

around the disk circumference, and moves in the disk reference frame at a rate of ω/E, where ω is the frequency of the excitation. This is known as an engine order excitation, where the engine order is E, and can be described mathematically by

$$f_j(t) = f_0 \cos(E\theta_j - \omega t) \tag{7}$$

Using standard modal analysis techniques, it can be shown that the amplitude of the steady-state response of each blade is the same, and at resonance ($\omega \approx \omega_{m=E}$ for small damping), this amplitude is

$$x_{\text{tuned}} = F_E b_E / c_E \omega_E \tag{8}$$

where F_E is the modal force in the mode corresponding to the engine order of the excitation, $F_E = b_E f_0 \eta_E$, and $\eta_E = N$ for $E = 0$ or $N/2$ and $\eta_E = N/2$ otherwise.

The tuned modes form a complete basis spanning the same displacement space as the mistuned modes. Therefore, the mistuned modes can be written as a linear combination of the tuned modes. Choosing as a starting point one of the tuned modes in which the wave number m is equal to the engine order E of the excitation, the corresponding mistuned mode becomes

$$\phi = \sum_{m=0}^{M} \alpha_m \phi_m^{\circ S} + \beta_m \phi_m^{\circ C} \tag{9}$$

with $M = (N-1)/2$ for N odd or $M = N/2$ for N even. Each α_m and β_m is a real constant signifying the contribution of the mth tuned modes to the mistuned mode. Physically, this represents distortion in the mode due to mistuning, since each tuned mode in the summation results in the superposition of an additional harmonic on the mode shape.

The blade that exhibits the highest response can be at any location on the disk. For mathematical convenience, this blade is assigned the reference coordinate $\theta = 0$ (i.e., $j = 0$), so that the contributions of the sine modes $\phi_m^{\circ S}$ at this blade location are zero. It should be noted that this practice is consistent with the results of Kenyon and Griffin [2], who maximized the response in the spatial coordinates of a continuous bladed disk model and found that the maximum response occurred at $\theta = 0$. The component of the mode (9) at $j = 0$, denoted ϕ_0, will be used for this discussion. It is assumed that damping is sufficiently small and that the frequencies are sufficiently separated so that only the response of a single mode can be considered. Noting that b_m are the arbitrary coefficients of the tuned modes and scaling the β_m in (9) such that $\beta_E = 1$,

$$\phi_0 = b_E + \sum_{m \neq E} \beta_m b_m \tag{10}$$

Examining the response in the mode (9) and using similar modal analysis techniques as in the tuned analysis, the maximum mistuned forced response occurs at blade $j = 0$ and can be shown to be

$$x_{\max} = F_E \phi_0 / c_E^* \omega_E^* \tag{11}$$

where the "*" superscript implies mistuned values and the modal force F_E remains the same as for the tuned case.[1]

In general, the frequency of a mode in a mistuned disk is only slightly different from the corresponding tuned natural frequency. Furthermore, significant changes in frequency cause artificial changes in forced response amplitude that are not generally associated with mistuning [19]. Therefore, it is assumed that $\omega_E = \omega_E^*$. The tuned modes are scaled so that $b_E = 1$, and the magnification in the response amplitude due to mistuning is defined, $g = x_{\max}/x_{\text{tuned}}$. Thus, from (8) and (11)

$$g = \phi_0 c_E / c_E^* \tag{12}$$

where the b_E in ϕ_0, (10), is unity. From (12), it can be seen that there are two primary factors that play a role in maximum forced response for small mistuning and damping, mode distortion represented by the harmonic components contributing to ϕ_0 and damping represented by c_E^*. Using orthogonality, the mistuned modal damping c_E^* is given by

$$c_E^* = c_E + \sum_{m \neq E} \beta_m^2 c_m \tag{13}$$

It is convenient to choose the mode scaling factors, b_m, so that all of the modes have the same modal damping c_m. Modes are commonly normalized so that the modal mass is unity. In this case, however, the tuned modes are normalized so that the modal damping equals c_E, i.e.,

$$\phi_m^{\circ} C \phi_m^{\circ} = c_E, \quad m = 0,1,\ldots,N-1 \tag{14}$$

Using (14) with (10) and (13), the amplitude magnification (12) becomes

$$g = \frac{1 + \Sigma_{m \neq E} b_m \beta_m}{1 + \Sigma_{m \neq E} \beta_m^2} \tag{15}$$

This expression (15) is significant because it captures the physical phenomena associated with maximum mistuned response due to mode distortion. The $b_m \beta_m$ terms in the numerator represent distortion in the mode. As the number of terms in the summation is increased, additional tuned modes or harmonics appear in the mistuned mode shape, causing the mode to become distorted from its original tuned counterpart. The size of each β_m determines the amount of distortion in the mode for a given harmonic component. Note that the distortion increases linearly in β_m. The denominator in (15) represents an increase in modal damping due to mistuning. The contribution of each harmonic to the modal damping is proportional to β_m^2. Since β_m^2 dominates this expression as β_m becomes large, the distortion leading to maximum response occurs for small values of β_m. It should be noted that the expression developed in (15) is based on the modes of any cyclic system without regard to its particular physical properties. Thus this result can be applied equally well to a simple system such as in Fig. 1 or to a single family of modes in a more complicated structure such as a bladed disk.

The maximum mistuned response of the bladed disk can be found by maximizing (15) with respect to all of the β_m simultaneously. Through extensive numerical simulations, it was consistently observed that a simple relationship exists between the β_m and the b_m at the maximum. Selecting one of the modes as a reference and labeling it the Rth mode, this relationship is expressed as

$$\beta_m^* / \beta_R^* = b_m / b_R \tag{16}$$

where the "*" superscript now indicates optimum values. Using this result and defining

$$\gamma = \sum_{m \neq E} b_m^2 / b_R^2 \tag{17}$$

(15) can be rewritten in terms of one variable, β_R^*. After some algebra, the maximum amplitude magnification factor is

$$g_{\max} = \frac{1 + \gamma b_R \beta_R^*}{1 + \gamma \beta_R^{*2}} \tag{18}$$

Since b_R and γ are defined by the tuned system properties, (18) represents an optimization problem in only one variable, β_R^*. A

[1]The contribution of a sine component in the optimum mode to the modal force was considered numerically. Although the contribution of the sine component increased the modal force, it also contributed to the modal damping in the response, as will be discussed in reference to (13). As a result, the maximum response was found to occur when there is no sine contribution to the mode. With no sine component in the mode, the modal force in the optimum mode is the same as that in the tuned system response.

simple expression for the optimum value of β_R^* can be found by setting the derivative of $g_{\max}$ equal to zero. One finds that

$$\beta_R^* = \frac{-1+\sqrt{1+\gamma b_R}}{\gamma b_R} \tag{19}$$

It should be noted that the amplitude magnification factor in (15) can be maximized either directly or by using the simpler expressions in (18) and (19). The direct maximization required a numerical solution that was uniformly consistent with results given by (16), (18), and (19). Clearly, (16), (18) and (19) provide a simple, convenient form for expressing the mistuned mode that gives maximum response.

It can be seen from (15) or (18) that the results depend directly on the damping in the system. Consider the system in Fig. 1. Suppose the system is tuned, so $c_j = c$, $m_j = m$, and $k_j = k$ for all j. Instead of normalizing the modes by (14), the modes are normalized so that $b_m = 1$ for all m. Then the modal damping in the mth tuned mode is given by

$$c_m = (\eta_m/N)(c + 4c_c \sin^2(\sigma_m/2)) \tag{20}$$

where $\sigma_m = 2\pi m/N$ is the interblade phase angle associated with the mth mode and η_m is defined as before. Two possible conditions will be considered. First, if all the coupling dampers are removed, $c_c = 0$, then $c_m = \eta_m c/N$. In this case, the analysis described in the foregoing simplifies when the modes are normalized by (14), since all of the b_m are equal except b_0 and $b_{N/2}$, which are different because $\eta_0 = \eta_{N/2} = 2\eta_m$ $(m \neq 0, N/2)$ in the formulation for (20). This case will be referred to as simple damping. In the more general damping case, e.g., $c_c \neq 0$, the modal damping varies as indicated by (20) when the modes are normalized for $b_m = 1$. This implies that the b_m will vary when the modes are normalized by (14). These two conditions will be considered more closely in the following subsections.

2.2 Simple Damping. For simple damping, the blade-to-blade dampers are removed, $c_c = 0$. With (14), all of the b_m in (15) become unity except for b_0 and $b_{N/2}$, which are $2(m \neq 0,\ N/2)$. The reference mode is selected so that $R \neq 0$ or $N/2$. Thus from (16), all of the β_m except β_0 and $\beta_{N/2}$ are equal to β_R^*, which will now just be denoted β for simplicity. The terms β_0 and $\beta_{N/2}$ are $\beta/2$. After maximizing (18) with respect to β and simplifying, it can be shown that for simple damping

$$g_{\max} = \frac{1}{2}\left(1+\sqrt{\frac{N}{2}}\right), \quad E \notin \{0, N/2\} \tag{21}$$

$$g_{\max} = \frac{1}{2}(1+\sqrt{N}), \quad E \in \{0, N/2\} \tag{22}$$

The results given in (21) and (22) are identical to those of Whitehead in 1976 [7], but differ from Whitehead's results in 1966 and 1998 [6,8]. A thorough discussion of Whitehead's results and how they are related to this work will be provided later in the paper. The results in (21) and (22) are corroborated by numerical simulations, which will also be discussed later.

The results described here also differ from those of Kenyon and Griffin [2] in several respects. First, the method presented here is based on the number of tuned modes that participate in the mistuned response, while the theory presented in [2] was based on the number of harmonics present in the mistuning pattern. As a result, no contribution from the zero-nodal diameter mistuning component was included in [2], though that component is present in the modal formulation here. Second, the modal mass in the $m = N/2$ tuned mode differs from that of the other modes for the discrete system model when the modes are normalized for $b_m = 1$, resulting in the different value of β for that mode. This effect was not included in [2] because it does not appear in the continuous system formulation. However, it appears in the theory presented here through the modal damping calculation of (20). Finally, truncation in the expressions for the modes was required in the formulation of Kenyon and Griffin [2], which leads to some truncation error in the response. No truncation was required in the modal formulation here, so truncation error does not occur.

2.3 Variable Damping. In the case of variable damping, i.e. $c_c \neq 0$ for the system in Fig. 1, the b_m vary according to the amount of damping in each tuned mode when the modes are normalized by (14). Recall (15). If the damping in the mth tuned mode is larger than the damping in the Eth tuned mode, then $b_m < b_E$ when the modes are normalized by (14), and the contribution of this term in (15) is less than for simple damping. Physically, this means that the energy associated with this tuned mode is more difficult to draw into the response of the mistuned mode, and the maximum forced response is less than predicted by (21) or (22) and by Whitehead [7]. If the damping in the mth tuned mode is smaller than the damping in the Eth tuned mode, then $b_m > b_E$ when the modes are normalized by (14), and the contribution of this term in (15) is greater than for simple damping. The energy associated with this tuned mode is easier to draw into the response of the mistuned mode, and the maximum response can exceed that predicted by (21) or (22) and by Whitehead [6–8].

2.4 Localization. Mode localization, in which the energy of a mode is concentrated in a small region of a bladed disk, has long been associated with mistuning and high forced response amplitudes (see, for example, [16]). The theory presented here offers an explanation of localization in the context of maximum response. The mode described in (10) for the single blade at $\theta_j = 0$ can be written for the entire disk.

$$\phi_j = b_E \cos E\theta_j + \sum_{m \neq E} \beta_m b_m \cos m\theta_j \tag{23}$$

The sine terms in (9) are not included here since it was shown that they do not contribute to the mode that yields maximum response. In the case of simple damping, in which all of the $b_m = 1$ and $\beta_m = \beta$ except as noted in Section 2.2, the mode that yields maximum response can be rewritten.

$$\phi_j = (1-\beta)\cos E\theta_j - 1/2\beta(1+\cos N\theta_j/2) + \sum_{m=0}^{M} \beta \cos m\theta_j \tag{24}$$

The first term of this expression represents a fundamental wave corresponding to the engine order of the excitation. The contribution of the second term is relatively small compared to the other terms. The summation in the third term mathematically represents a discrete Fourier series approximation of the Dirac delta function at $\theta_j = 0$, $\delta(0)$. The presence of the Dirac delta function in the mode shape indicates localization. It should be noted that the mode shape described by (23) and (24) is independent of the physical properties of the bladed disk, and depends only on the engine order of the excitation and the number of blades on the disk.

The mode described by (24) for a third engine order excitation is shown in Fig. 2 for different numbers of blades. The modes are normalized so that their lengths are unity. The fundamental wave and the large response at $\theta_j = 0$ are evident in the mode shapes for all numbers of blades. As seen in the figure, the relative amplitude of the fundamental wave with respect to the localized response decreases as the number of blades increases. The characteristics of the mode shape and the change in the relative amplitude of the fundamental wave can be interpreted in terms of maximum response as follows. In order to obtain maximum response in a bladed disk, one of the system's modes must have two characteristics. First, it must contain a significant wave component corresponding to the engine order of the excitation. This wave constitutes the fundamental wave and results in a large generalized force in that mode. Second, the energy of the excited mode must be concentrated in a small region of the disk or a single blade, which

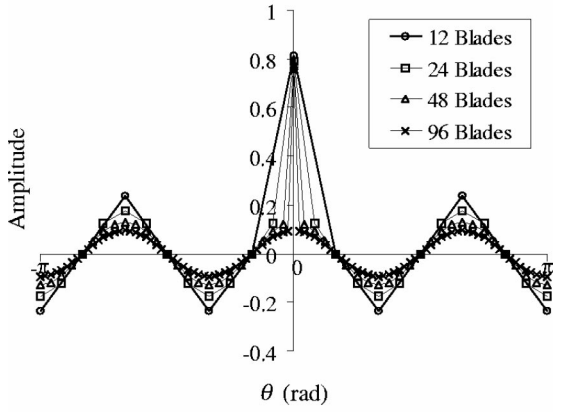

Fig. 2 Localization of mode for maximum response

is done through the Dirac delta function. The harmonic content of the mode described by (19) represents a tradeoff between the size of the generalized force and the amount of localization in the mode. The maximum response is achieved for a certain combination of these two components. As more blades are introduced in the system, the magnitude of the localized response grows, and a smaller generalized force is needed to achieve maximum response. Thus, the relative size of the fundamental wave with respect to the localized response decreases as the number of blades on the disk increases.

It is useful to consider the behavior of the mode in the limiting case as N becomes large. For the simple damping case, the expression for β^* which gives maximum response, (19), simplifies to

$$\beta^* = \frac{-2+\sqrt{2N}}{N-2} \tag{25}$$

As the number of blades on the disk increases, this value slowly converges to zero at a rate of approximately $\sqrt{2/N}$. Examining (24), the amplitude of the fundamental wave goes to unity in this limit. The summation grows at a rate of approximately $\sqrt{N/2}$, though this term applies only at the blade $j=0$. The length of the mode in the limiting case of N large is $\sqrt{N}$, so when the mode is normalized for unit length, it approaches

$$\phi(\theta_j) \approx (1/\sqrt{N})\cos E\theta_j + (1/\sqrt{2})\,\delta_{j0} \tag{26}$$

where δ_{j0} represents the Kronecker delta. The amplitude of the fundamental wave slowly goes to zero, and the amplitude of the blade at $\theta=0$ converges to $1/\sqrt{2}$. This behavior is consistent with the behavior of the modes in Fig. 2. The results given in (26) can be viewed in straightforward terms. For simple damping and N large, the length of the mode that results in maximum response contains equal contributions from the fundamental wave and the delta function.

2.5 Robustness of Maximum Response. The maximum forced response is robust with respect to small random variations in the system properties. In other words, if a system is intentionally mistuned for maximum response, additional small random mistuning will not significantly change the forced response. The predicted maximum response will occur in the bladed disk despite the presence of small random mistuning. The robustness of the system response is a direct consequence of the process used to obtain the maximum response. The amplitude magnification factor (15) can be thought of as a continuous function whose domain is an N-dimensional space spanned by the elements of the modal content vector $\{\beta_m\}$. The maximum of this function is found by setting the gradient of the function to zero and solving for the $\{\beta_m\}$ that satisfies this condition. As will be shown in Section 3 for the simple system considered here, the mapping of $\{\beta_m\}$ onto the mistuning space spanned by the elements of $\mathbf{\Delta K}$, $\{\delta k_j\}$, is a bijection except for an arbitrary rotation around the disk due to the periodicity of the system. As a consequence, the maximum in the forced response with respect to β_m implies a maximum with respect to δk_j. The gradient of the forced response function in the N-dimensional $\{\delta k_j\}$ space is zero and small variations in δk_j will have minimal impact on the forced response amplitude. This interpretation of robustness is the same as that adopted by Petrov and Ewins [17]. Therefore, by maximizing the forced response in the manner described here, a robust system with predictable forced response characteristics is obtained.

3 Mistuning to Obtain Desired Mode Shape

The formulation presented in Section 2 provides a theoretical basis for determining a system with the maximum amplitude increase due to mode distortion. In order to implement this theory, it is necessary to develop a method to determine the actual system property variations that would produce a system with the desired mode shape. Therefore, the following problem is considered: given the tuned system $\{\mathbf{M}^\circ, \mathbf{K}^\circ\}$, find a set of mistuning, $\mathbf{\Delta K}$, such that the resulting mistuned system contains the mode $\phi = \Phi^\circ \beta$. Here Φ° is a matrix whose columns are the tuned system mode shapes, and β is a vector of the set $\{\beta_m\}$ which maximizes (15). For simplicity, only stiffness mistuning is considered; however, mass mistuning can easily be incorporated.

Thus far in the development, the tuned system modes have been considered discretized $\sin m\theta_j$ and $\cos m\theta_j$ modes. At this point it is useful to consider the exponential forms of the modes, which are obtained by combining the sine and cosine modes through Euler's formulas. In this form, two linearly independent functions, $e^{im\theta}$ and $e^{-im\theta}$, are required to describe all of the system modes. Making use of the periodicity of the system, the modes can be conveniently written

$$\tilde{\phi}^\circ_{mj} = A_m e^{i2\pi mj/N} \tag{27}$$

where $m=0,1,\ldots,N-1$, and the complex coefficients A_m depend on how the modes are normalized. Since the modal coefficients, β, which define the mode with maximum response are based on the real representations of the tuned modes, it is necessary to define an equivalent β, denoted β^c, which describes the maximum responding mode as a sum of the complex tuned modes given by (27). The elements of β^c are given by

$$\beta^c_m = \begin{cases} \beta_m & \text{for } m=0 \\ \frac{1}{2}(\beta_{2m-1} - i\beta_{2m}) & \text{for } m<N/2,\ m\neq 0 \\ \beta_m & \text{for } m=N/2 \\ \frac{1}{2}(\beta_{2(N-m)-1} + i\beta_{2(N-m)}) & \text{for } m>N/2 \end{cases} \tag{28}$$

The eigenvalue problem for the mistuned system mode with no mass mistuning is

$$[\mathbf{K}^\circ + \Delta\mathbf{K}]\phi = \omega^2 \mathbf{M}^\circ \phi \tag{29}$$

The mistuned mode ϕ can be written as a sum of the tuned modes,

$$\phi = \tilde{\Phi}^\circ \beta^c \tag{30}$$

where $\tilde{\Phi}^\circ$ is a matrix of the complex modes of the tuned system given by (27), with the modes normalized for unit modal mass. The frequency ω of the mistuned mode can be selected arbitrarily provided that the choice of frequency does not require zero or negative stiffness to obtain. To be consistent with the earlier derivation of maximum response, the frequency is selected to be the same as the frequency of the tuned mode(s) of interest. Substituting (30) into (29) and pre-multiplying by $\tilde{\Phi}^{\circ H}$ yields

Table 1 Nominal properties of 10-bladed example, simple damping

Parameter	Value
k	1
k_c	0.03
m	1
c	0.00025

$$\Delta\hat{\mathbf{K}}\underline{\beta}^c=[\omega^2\mathbf{I}-\Omega^{\circ 2}]\underline{\beta}^c \tag{31}$$

where

$$\Delta\hat{\mathbf{K}}=\tilde{\Phi}^{\circ H}\Delta\mathbf{K}\tilde{\Phi}^{\circ} \tag{32}$$

and $\Omega^{\circ 2}=\tilde{\Phi}^{\circ H}\mathbf{K}^{\circ}\tilde{\Phi}^{\circ}$ is a diagonal matrix whose elements are the natural frequencies of the tuned system. The operator H denotes Hermitian. Since $\Delta\mathbf{K}$ is a diagonal matrix and $\tilde{\Phi}^{\circ}$ is derived from (27), the elements of $\Delta\hat{\mathbf{K}}$ are given by

$$\Delta\hat{\mathbf{K}}_{pq}=A_p^*A_q\sum_{j=0}^{N-1}(\delta k_j)e^{i2\pi j(q-p)/N} \tag{33}$$

where $\{p,q\}\in\{0,1,\ldots,N-1\}$, and the "*" superscript indicates the complex conjugate.

Due to the periodicity of the exponential term in (33), the summation in (33) has only N distinct values. Each distinct value is denoted $\delta\hat{k}_r$, where $r=0,1,\ldots,N-1$, and

$$r=\begin{cases} q-p & \text{for } q\geqslant p \\ q-p+N & \text{for } q<p \end{cases} \tag{34}$$

Thus

$$\delta\hat{k}_r=\sum_{j=0}^{N-1}(\delta k_j)e^{i2\pi rj/N}. \tag{35}$$

The left side of (31) can be recast in terms of $\delta\hat{k}_r$

$$\Delta\hat{\mathbf{K}}\underline{\beta}^c=\mathbf{B}\delta\underline{\hat{k}} \tag{36}$$

where

$$\mathbf{B}=\begin{bmatrix} A_0^*A_0\beta_0^c & A_0^*A_1\beta_1^c & \cdots & A_0^*A_{N-1}\beta_{N-1}^c \\ A_1^*A_1\beta_1^c & A_1^*A_2\beta_2^c & \cdots & A_1^*A_0\beta_0^c \\ \vdots & \vdots & \ddots & \vdots \\ A_{N-1}^*A_{N-1}\beta_{N-1}^c & A_{N-1}^*A_0\beta_0^c & \cdots & A_{N-1}^*A_{N-2}\beta_{N-2}^c \end{bmatrix} \tag{37}$$

and $\delta\underline{\hat{k}}=\{\delta\hat{k}_r\}$. Substituting (36) into (31) and pre-multiplying by $\mathbf{B}^{-1}$ yields an expression for $\delta\underline{\hat{k}}$ in terms of known quantities.

$$\delta\underline{\hat{k}}=\mathbf{B}^{-1}[\omega^2\mathbf{I}-\Omega^{\circ 2}]\underline{\beta}^c \tag{38}$$

It can be seen from (35) that $\delta\hat{k}$ is the discrete Fourier transform of the physical stiffness variations $\delta\underline{k}$. Thus, the physical stiffness variations can be obtained from the inverse Fourier transform of $\delta\underline{\hat{k}}$.

$$\delta k_j=\frac{1}{N}\sum_{r=0}^{N-1}(\delta\hat{k}_r)e^{-i2\pi rj/N} \tag{39}$$

Table 2 Mistuning for maximum response, simple damping, $N=10$, $E=2$

Blade	10	1	2
δk	0.2171	−0.0128	0.2171

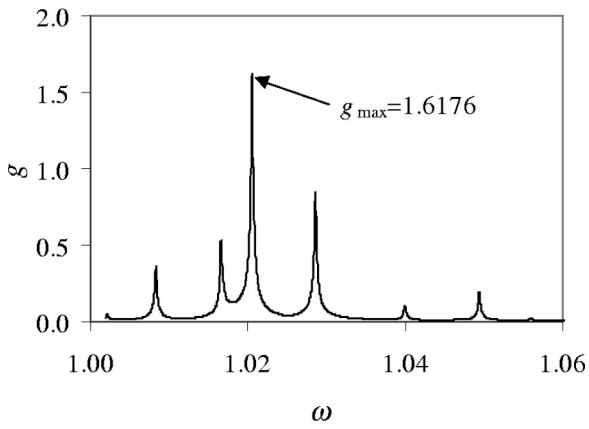

Fig. 3 Forced response simulation of intentionally mistuned system

This process can now be used to explicitly determine the physical stiffness variations δk_j that result in a mistuned mode exhibiting maximum forced response.

4 Numerical Validation

4.1 Simple Damping. As an example, consider the system shown in Fig. 1 with $N=10$ subject to an $E=2$ traveling wave excitation. The properties of the nominal tuned system are shown in Table 1. No units are given, though any system of units can be used provided that a consistent scaling is used for all properties and their relative values are the same. The dampers between the masses have their constants set to zero, i.e. $c_c=0$. The theoretical maximum response of this system is given by (21) with $N=10$, $g_{\max}=1.6180$.

The modal content of the mistuned mode corresponding to the $m=2$ tuned cosine mode was calculated by (19), and the mistuning required to obtain this mode was calculated using (38) and (39). Table 2 shows the mistuning required to obtain the maximum response. Blades not shown in the table had zero mistuning. The maximum mistuning required in any single blade for this modal content was 22%. The forced response of the mistuned system was calculated and divided by the tuned response, Fig. 3. The maximum amplification factor of the mistuned system was calculated to be $g_{\max}=1.6176$, in agreement with the theoretical result.

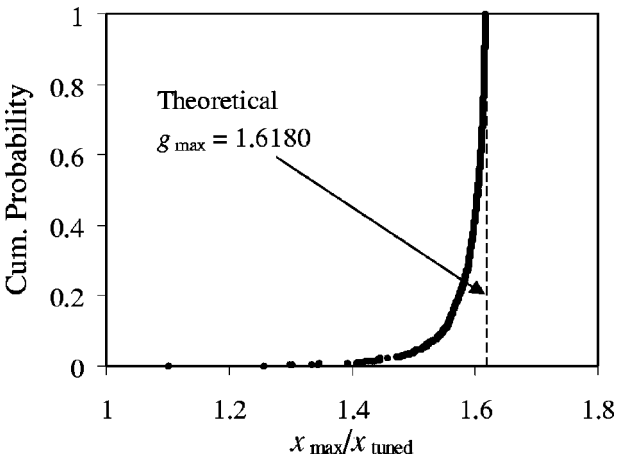

Fig. 4 Probability distribution of response for intentionally mistuned system

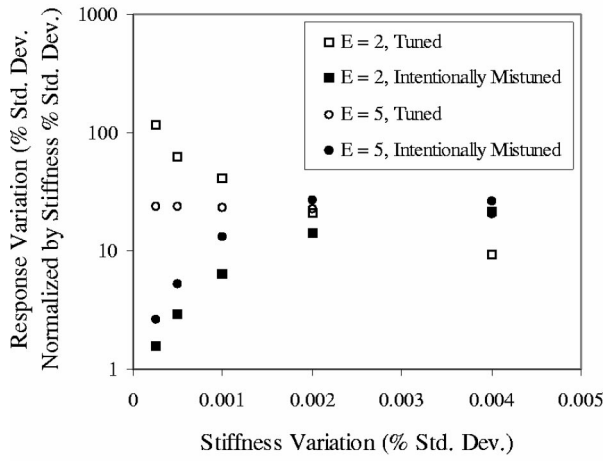

Fig. 5 Reduction in sensitivity for intentionally mistuned systems with simple damping

The robustness of the intentionally mistuned system was demonstrated through Monte Carlo simulations. A set of 1000 disk models with the nominal system parameters given in Table 1 was intentionally mistuned to yield maximum response to an $E=2$ excitation. Next, normally distributed random stiffness variations with a standard deviation of $\overline{\sigma_k}=0.2\%$ were superimposed on the base stiffnesses of the intentionally mistuned system. These small random variations simulate the variations that may occur in a real system as a result of manufacturing tolerances or wear. The maximum forced response of each disk was calculated. From this data, the cumulative probability distribution of the responses in the Monte Carlo simulations was obtained, Fig. 4. The probability distribution indicates the probability (ordinate) that the response will be at or below the indicated value (abscissa). The response amplitudes have been normalized by the tuned value to give the amplitude magnification. The theoretically predicted maximum response is shown for reference.

Two important observations can be made from Fig. 4. First, the response of the system has a high probability of being near that predicted from the theory. In particular, the probability that the system response will be within 10% of the predicted response is 97%. The variation observed in the response is small because the gradient of the maximized response is zero with respect to the mistuning parameters for each blade, as previously discussed. Thus, intentionally mistuning the system for maximum response makes the response predictable. Secondly, it can be seen that no response exceeds the theoretically predicted maximum. Since the response was maximized by requiring zero gradient with respect to the mistuning parameters, any small mistuning must cause a decrease in the response. The response cannot exceed the maximum value predicted by the theory when the random mistuning is small.

The robustness of the intentionally mistuned system can be measured by examining how the variation in the response changes with the amount of variation in the stiffness. To do this, Monte Carlo simulations were performed for the intentionally mistuned system using different standard deviations in the random stiffness mistuning, ranging from 0.4 percent down to 0.025%. The standard deviation of the response for 1000 simulations was determined for each value of $\overline{\sigma_k}$ and normalized by the theoretically predicted value to obtain a percent standard deviation in the response. Finally, this result was normalized by the standard deviation of mistuning to obtain the relative variation of the response. The relative variation is essentially the slope of the response variation with respect to the amount of random mistuning in the system. The results are shown in Fig. 5. In addition, the results for the same nominal system with no intentional mistuning are shown for comparison.

Table 3 Mistuning for maximum response, simple damping, $N=10$, $E=5$

Blade	10	1	2
δk	−0.0949	0.0456	−0.0949

Table 4 Nominal properties of 20-bladed system, variable modal damping

Parameter	Value
k	1
k_c	0.03
m	1
c	0.000025
c_c	0.00005

It can be seen in Fig. 5 ($E=2$) that the relative variation in the response decreases significantly for the intentionally mistuned system as the random variation in the stiffness is reduced. Since the system becomes increasingly insensitive as the size of the random perturbations is decreased, the system is robust according to the definition previously discussed. Moreover, the intentionally mistuned system is much less sensitive than its tuned counterpart, for which the sensitivity actually increases as the stiffness variations are decreased over the range of $\overline{\sigma_k}$ considered. This increase in sensitivity for the tuned system is a result of the relationship between frequency splitting and damping for small damping (for example, consider the parameter S/ζ described in [5]).

It should be noted that this solution for maximum response caused by distortion of a structural mode does not involve numerical optimization. The maximum response and the mistuning necessary to realize it are calculated explicitly and can be verified with a single forced response simulation. Moreover, the forced response from numerical simulations converge to the theoretical solution in the limit as damping goes to zero. For this example, as the damping is reduced in the forced response calculations, the numerical solution converges to $g_{\max}=1.618033982$, while the theoretical solution is $g_{\max}=1.618033989$. The difference is within the working precision of the computer.

An additional case study with simple damping was considered. For this study, $N=10$ and $E=5$, corresponding to the $E=N/2$ case where the response is given by (22). The nominal properties

Table 5 Mistuning for maximum response, variable damping, $N=20$, $E=1$

Blade	1	2	3	4	5
δk	−0.018	0.0092	0.0068	0.0053	0.0052
Blade	6	7	8	9	10
δk	0.0179	−0.002	−0.0005	−0.0002	−0.0001
Blade	11	12	13	14	15
δk	−0.0001	−0.0001	−0.0002	−0.0005	−0.002
Blade	16	17	18	19	20
δk	0.0179	0.0052	0.0053	0.0068	0.0092

Table 6 Nominal properties of 10-bladed system, variable modal damping

Parameter	Value
k	1
k_c	0.01
m	1
c	0.000025
c_c	0.0000125

of the system were the same as for the previous example, Table 1. The maximum predicted by the theory was $g_{max}=2.0811$. The maximum obtained from numerical simulation was $g_{max}=2.0798$, in agreement with the theory. Table 3 gives the mistuning in each blade that was required for maximum response; blades not shown had zero mistuning. The maximum mistuning in any single blade to achieve this response was 9.5 percent. The relative sensitivity of the intentionally mistuned system response was calculated for various amounts of random mistuning and compared to the sensitivity of the tuned system. The results are shown in Fig. 5 ($E=5$). As before, the sensitivity of the intentionally mistuned system decreases significantly for small mistuning, indicating that the system is robust. The sensitivity of the tuned system remains approximately constant. Unlike the previous case study, the tuned sensitivity does not increase since the primary mode in the response has a distinct frequency, and no frequency splitting is involved.

4.2 Variable Modal Damping. Two additional numerical examples were studied in which the modal damping was varied systematically. The damper between blades, c_c in Fig. 1, was given a non-zero value so that the modal damping is given by (20) if the modes are normalized for $b_m=1$. The first example examines a case where the maximum response of the system is less than predicted for simple damping. In this example, a system with $N=20$ subject to an $E=1$ traveling wave excitation is considered. The system properties are given in Table 4. The modal damping of each tuned mode was calculated using (20) with the modes normalized for $b_m=1$, resulting in the lowest modal damping in the $m=1$ mode. The maximum response predicted by optimizing (18) was $g_{max}=1.4982$. This represents a significant increase over the tuned response, but is also much less than the maximum response for this system with simple damping, $g_{max}=2.0811$. A forced response simulation was performed, and the maximum response from the simulation was determined to be $g_{max}=1.4982$, in agreement with the theoretical prediction. The mistuning for each blade is shown in Table 5. The maximum mistuning in any blade to achieve this response was 1.8 percent.

The second case study investigates maximum response which exceeds that predicted for simple damping and by Whitehead [6–8]. For this study, a system with $N=10$ and $E=5$ was considered, with system properties as shown in Table 6. With the tuned modal damping calculated using (20) when the modes are normalized for $b_m=1$, the largest modal damping occurs in the $m=5$ mode, which is the tuned mode responding to the $E=5$ excitation. The maximum response was calculated according to the theory, $g_{max}=2.5809$. This is significantly greater than the maximum response predicted by (22) and previously by Whitehead [6–8], $g_{max}=2.0811$. This result was again verified using a forced response simulation. From the simulation, the maximum response was determined to be $g_{max}=2.5601$, in reasonable agreement with the theoretical prediction. As before, the solution converged to the theoretical value as damping was decreased. The mistuning needed to achieve this result is shown in Table 7. The maximum mistuning in a single blade to achieve this result was 58 percent. From a practical standpoint, this indicates that realization of such an extreme case is difficult. However, this example demonstrates that variable damping can result in mistuned response larger than previously predicted with simple damping.

4.3 Practical Implications of Small Damping. The goal of this paper is to investigate the maximum response that can occur in a bladed disk from distortion of a structural mode. The effects of mode interaction via frequency splitting are not considered. In the derivation of the maximum response, the frequency of the mistuned mode is assumed to be sufficiently separated from the other system frequencies so that it does not interact with other modes. To accomplish this in the numerical simulations, the damping in the system was reduced so that the modes were separated. This resulted in damping which is unrealistically small in the systems studied numerically. From a phenomenological standpoint, this is not an issue, since the goal of this work is to systematically separate the effects of the different mistuning phenomena and study them individually. From a practical standpoint, however, the applicability of the results presented here to systems with more realistic damping must be investigated.

Table 7 Mistuning for maximum response, variable damping, $N=10$, $E=5$

Blade	1	2	3	4	5
δk	0.0204	0.581	0.0138	−0.0053	0.0013
Blade	6	7	8	9	10
δk	−0.0007	0.0013	−0.0053	0.0138	0.581

As an illustrative example, the simple damping case with $N=10$ and $E=2$ described previously is considered. With the system properties described in Table 1, particularly the damping $c=0.00025$, the modal damping ratio in the tuned and mistuned modes was $\zeta=0.00012$. The magnification factor from the numerical simulation was $g_{max}=1.6176$, which is approximately 0.02 percent less than the theoretical magnification of 1.6180. The damping c in the system was increased in numerical simulations to investigate how the response changes with more realistic damping values. With damping $c=0.005$, the modal damping ratio was $\zeta=0.0024$ in both the tuned and the mistuned modes. This level of damping is comparable to damping that has appeared in the literature, both in numerical studies [4,20] and experiments [21]. The amplitude magnification factor from the numerical simulation was $g_{max}=1.4908$, which is approximately 7.9 percent less than the predicted magnification factor. The decrease in the response is attributed to interaction of the mistuned mode that exhibits maximum response with the neighboring mode that nominally occurs at the same frequency in the tuned system. However, the theoretically predicted maximum gives a reasonable estimate of the actual forced response amplitude.

In many cases, it may also be feasible to separate the frequency of the mistuned mode from its closest neighbor using small harmonic mistuning in addition to the mistuning for the maximum response. The wave number of the harmonic mistuning pattern is equal to twice the engine order of the excitation (see Kenyon and Griffin [2]). Such mistuning does not significantly change the mode shape in the mistuned mode that exhibits maximum response, but sufficiently separates its frequency from that of its neighbor to obtain response in a single mode. Although not discussed in detail here, this technique was used by Kenyon [22], who experimentally demonstrated the maximum response due to distortion of a structural mode using a simple bladed disk with 18 blades. Thus, it may be possible to achieve the maximum response described here without resorting to small damping assumptions.

5 Discussion—Mistuning Mechanisms and Maximum Response

As pointed out in Kenyon and Griffin [2], there are two primary physical phenomena associated with mistuned forced vibration response in isolated families of bladed disk modes, frequency splitting and mode distortion. Frequency splitting refers to the separation of the repeated natural frequencies that occur in tuned bladed disks into two distinct natural frequencies. Since the two modes in the pair no longer occur at the same natural frequency, they cannot combine into a pure traveling wave response but, instead, superimpose in a manner that increases the forced response of the two modes with respect to the tuned response. Mode distortion refers to harmonic content in the mode shape of a mistuned system in addition to the fundamental waveform of the nominally tuned mode. These two phenomena, individually or in combination, are responsible for the magnification of forced response amplitudes in bladed disks. It has been noted in the literature (see, for example,

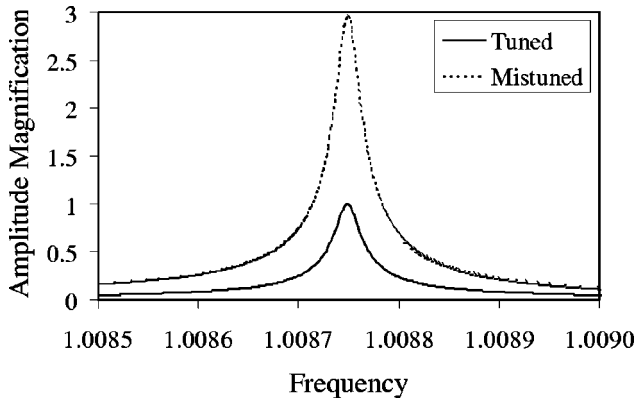

Fig. 6 Forced response using Whitehead formulation

[23]) that frequency veering, or interaction between multiple families of modes, can also lead to increased forced response, but the current discussion is limited to an isolated family of modes.

Frequency splitting of undistorted modes was studied by Ewins [4] and MacBain and Whaley [5]. In particular, MacBain and Whaley derived an analytical solution for the maximum response due to frequency splitting. They found that frequency splitting could lead to a 21 percent increase in the response. The amount of the increase depends on the degree to which the frequencies in a pair are separated and the amount of damping in the system. Their result agreed with the numerical result of Ewins and was corroborated by Kenyon and Griffin [2]. This result is useful in that it isolates the effects of one of the physical phenomena associated with mistuning. However, the maximum response due to frequency splitting is typically less than the maximum response from distortion of a structural mode. For instance, with simple damping the maximum response from frequency splitting is less than the maximum from mode distortion for bladed disks with more than three blades. Thus, a larger maximum than that from frequency splitting alone is a concern for most bladed disks.

This paper gives a direct analytical solution for the maximum amplitude magnification due to mode distortion in a distinct structural mode. The magnifying effects of frequency splitting are not present in this solution. Although it is recognized that the effects of both frequency splitting and mode distortion will be present in most practical systems, the current analysis is useful in that it permits isolation of one of the phenomena associated with mistuning so that its effects may be studied in detail and provide a framework for understanding the general mistuning problem.

A number of researchers have investigated how to either predict or numerically obtain the maximum response that can occur in an isolated family of bladed disk modes. Therefore, it is useful to place the theory presented here in the context of other solutions for maximum response that appear in the literature. Among the most notable of these are the solutions of Whitehead [6–8], who proposed a direct solution for the maximum response based on the number of blades on the disk. The solution for maximum response given here for simple damping agrees with the result of Whitehead in 1976 [7], in which Whitehead states that the maximum response for a system with only structural coupling between the blades is given by (21) and (22). In 1998, Whitehead asserted that

Table 8 Mistuning for Whitehead maximum response, $N=24$, $E=3$

Blade	24	1	2
δk	$0.1039-i0.1039$	-0.0352	$0.1039+i0.1039$

Table 9 Natural frequencies for Whitehead maximum response, $N=24$, $E=3$

Mode	1	2	3	4
ω	1.0003	1.0012	1.0026	1.0047
Mode	5	6	7	8
ω	1.0067	1.0087	1.0097	1.0136
Mode	9	10	11	12
ω	1.017	1.0211	1.0249	1.0293
Mode	13	14	15	16
ω	1.0333	1.0374	1.0412	1.045
Mode	17	18	19	20
ω	1.0482	1.0512	1.0537	1.0557
Mode	21	22	23	24
ω	1.0571	1.058	1.0837	1.0837

the result in 1976 was incorrect, and that the correct maximum response was given in the 1966 paper, $g_{\max}=1/2(1+\sqrt{N})$, for all engine orders [6,8].

To fully evaluate the Whitehead result [6,8] in the context of the results offered here, it is necessary to first examine his approach in more detail. Whitehead formulated the mistuned mode as a linear combination of the tuned system modes (see Eq. (6) of [6]), an idea that has been followed here. The tuned modes are given in complex form, so that each mode pair corresponding to repeated frequencies consists of a pair of complex conjugate modes. For maximum response, he found that the tuned modes must combine in phase, again consistent with the findings of the present work. This occurs in the complex notation when $\theta=0$ so that each exponential term is unity. The mistuned mode at $\theta=0$ can then be described as a sum of the contributions of each tuned mode, similar to the sum given here in (10). Assuming system damping equivalent to the simple damping case described here, Whitehead found that the maximum response occurs at $\theta=0$ when a single term in this summation corresponding to the excitation is $(1+1/\sqrt{N})/2$, while all the other terms are equal to $1/2\sqrt{N}$. In the cases of $E=0$ or $E=N/2$ (for an even number of blades), the conjugate pairs in the summation of the tuned modes add together to form real components in the mistuned mode, and the results are the same as those given in the current paper. When $E\neq 0$ or $N/2$, however, some of the coefficients of the conjugate pairs do not have the same magnitude. Specifically, the coefficient corresponding to the excitation in exponential form has a larger magnitude than the coefficient of its conjugate mode. When these modes are summed in the linear combination, the mistuned mode is real at $\theta=0$, but in general is complex at other locations. Mathematically, it can be shown that the structural modes of a bladed disk system that is subjected to structural mistuning cannot be complex unless they correspond to repeated natural frequencies. In this case, the

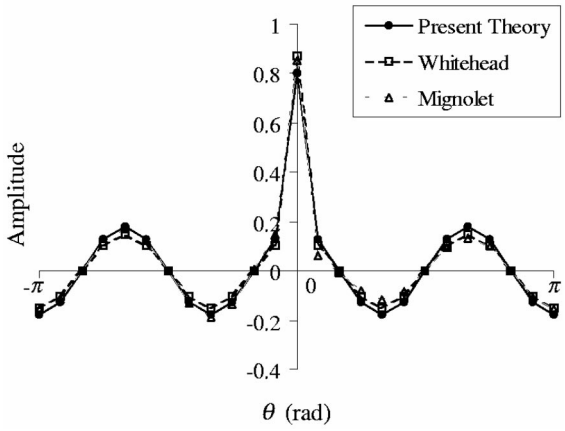

Fig. 7 Comparison of mode shapes for maximum response

Table 10 Mignolet seven-blade partial mistuning, base k = 430,000 N/m, N=24, E=3

Blade	22	23	24	⋯
δk	2299.8	−13291.3	236179.9	⋯
Blade	1	2	3	4
δk	−23328.3	88457.5	−10297.2	−802

complex conjugate of each mode is also a mode of the system. It will be shown that this is not the case for the Whitehead [6,8] mode and, consequently, that the Whitehead mode specified in [6,8] as giving maximum response cannot be achieved through structural mistuning and distortion of a structural mode.

Consider the following example. The structural bladed disk model of Fig. 1 is examined. The bladed disk has 24 blades and the physical parameters given in Table 1. The mode that exhibits maximum response was calculated using Whitehead's approach, i.e., utilizing Eq. (6) of [6], and maximized according to the development leading to Eq. (7) in [6]. The mistuning needed to obtain this mode in a structural model was calculated using the method presented in Section 3, and a numerical forced response simulation was performed with an $E=3$ traveling wave excitation. The forced response amplitudes of blade 1 ($\theta=0$) for the tuned and mistuned systems are shown as a function of excitation frequency in Fig. 6. Both response curves in the figure have been normalized by the maximum tuned amplitude, so that the response shown for the mistuned system is the magnification factor. It can be seen in the figure that the maximum amplitude magnification in the mistuned forced response is $g_{\max}=2.95$, which is the result predicted by Whitehead for 24 blades [6,8]. Thus, it is clear that Whitehead's results have been applied correctly since the mistuned system that was constructed gave his higher magnification factor. However, this mode is not achievable through structural mistuning of the commonly used mistuning model of Fig. 1.

The mistuning needed to achieve Whitehead's mode for maximum response using the structural model of Fig. 1 is given in Table 8. Only the mistuning in three blades is shown; zero mistuning was required in the other blades. As shown in the table, the necessary mistuning is complex, with the imaginary parts of blades 2 and 24 equal to the real parts. This implies that the stiffness matrix must be complex, which is not viable in a structural model. Furthermore, the mode resulting in maximum response must be complex, as described in the previous paragraphs. In a structural model, this is only possible if the mode is part of a repeated frequency pair. The natural frequencies of the mistuned system are shown in Table 9. It is clear from the table that the frequencies are not repeated, particularly not the value $\omega=1.0087$ corresponding to the mode with maximum response. Thus, the Whitehead maximum [6,8] for bladed disk forced response cannot be achieved through structural mistuning and distortion of a single structural mode in the system considered.

An alternative interpretation of the 1966 Whitehead [6] result can be considered. The mode described by Whitehead can be considered two separate modes, consisting of the real and imaginary parts of the complex mode. The real part of the Whitehead mode for a disk with $N=24$ blades is shown in Fig. 7. The figure also shows the mode derived by optimizing (18) for maximum response. Both modes are normalized to have unit length. As can be seen in the figure, the real part of the Whitehead mode is essentially the same as the mode derived using the theory given here. However, the Whitehead result also involves a second mode, given by the imaginary part of the complex Whitehead mode, that superimposes on the first mode. This superposition is similar to what occurs when two frequencies are very close, as discussed for the frequency splitting phenomenon. However, the mode shapes described by the real and the imaginary parts of the Whitehead mode are distinct, so that this superposition at the same frequency is mathematically a degeneracy that cannot be obtained using a structural mistuning model.

Although the Whitehead maximum cannot be obtained from structural mistuning, it can be approximated by combining the effects of mode distortion and frequency splitting. If a system contains the mode that results in maximum response (Fig. 7), a maximum response that approaches the Whitehead result can be achieved by causing a second mode to superimpose on the mode for maximum response. This is done by bringing the natural frequency of the second mode close to the natural frequency of the original mode. As an example, consider the case described by Rivas-Guerra and Mignolet [16], where they use a numerical optimization technique to achieve $g_{\max}=2.69$ for a bladed disk with $N=24$ subject to a third engine order excitation. Their result exceeds the maximum given by (21), $g_{\max}=2.23$, and approaches the Whitehead maximum of 2.95. System parameters and mistuning for a related study were provided by Mignolet, and are the same as reported in [16], except that the coupling stiffness $kC=20{,}000$ N/m, and the damping $c=0.1443$ Ns/m. The mistuning required for maximum response is shown in Table 10, and corresponds to a seven-blade partial mistuning case (see [16] for details on partial mistuning). Blades not shown in the table were tuned. The maximum mistuning in a blade is approximately 55 percent of the tuned value. The amplitude magnification observed for this system was 2.87, approaching the Whitehead maximum, and the maximum response occurred at a frequency of 6225 rad/s. The natural frequencies and modes of the system were calculated. A pair of modes with natural frequencies near the frequency where the maximum response occurred was found. One mode had a natural frequency of 6222 rad/s and one had a natural frequency of 6228 rad/s. These natural frequencies differ by 6 rad/s, while the half-power bandwidth of the response based on the given damping was 124 rad/s. Thus, equivalent modes could be formulated from linear combinations of the original modes. A pair of orthogonal modes was determined which spanned the same space as the original pair of modes. One of these modes is shown in Fig. 7 and is similar to the mode determined from the present theory and the real part of the Whitehead mode.

The sensitivity of the forced response to the amount of damping in this system was examined. The damping in the system was incrementally reduced, and the amplitude magnification was determined for each damping value. When the damping was reduced to $c=0.08$ Ns/m, two distinct peaks with equal amplitudes became evident in the frequency response. Qualitatively, the effect of reducing the damping was similar to increasing the parameter S/ζ in MacBain and Whaley [5]. When the damping was reduced below $c=0.03$ Ns/m, the amplitude magnification factor fell below the maximum predicted in Section 2. Based on this observation, the high-amplitude magnification observed in [16] was achieved by bringing the natural frequencies of two distinct modes into close proximity to approximate the superposition of modes implied by the Whitehead result. This is a different maximum than that examined by the present theory since it combines the effects of frequency splitting and mode distortion. In addition, this result requires large mistuning, as reported by Rivas-Guerra and Mignolet [16], in another numerical study by Sinha [20], and as shown in Table 10.

As a final note, an additional result has been reported in the literature in which the response approaches the Whitehead maximum. Petrov and Ewins [17] reported a method for optimizing the mistuning in bladed disks with realistic geometry. One example reported was a turbine disk with 92 blades. The amplitude magnification observed for this disk in its first bending family of modes subject to an $E=6$ excitation was 5.0, while the Whitehead result for this disk is 5.30. The maximum mistuning in any blade was 5 percent. Further investigation showed that the reported response occurs near a frequency-veering region, where the first bending family of modes interacts with another mode family (see

Fig. 4 of [18]). It has been observed in the literature (see, for example, [15]) that such frequency veerings can substantially increase forced response amplitudes with relatively small amounts of mistuning. Thus, the analysis here and in Whitehead [6,8] for an isolated family of bladed disk modes cannot be applied to this model.

6 Conclusions

A theory has been developed for predicting the maximum forced vibration response of a mistuned bladed disk from distortion of a structural mode. In this approach, the mistuned mode is represented as a sum of the tuned modes, where the coefficients of the tuned modes in the modal summation represent the amount of distortion present in the mode. It was shown that for small damping and mistuning, the primary mechanisms involved in extreme mistuned forced response are mode distortion, which leads to localization, and damping in the mistuned mode. The theory results in a closed-form expression for the maximum response of the system in terms of the participation of the tuned modes in the mistuned response. If this expression is maximized, the amplitude magnification factor can be cast in terms of a single variable that completely describes the mistuned mode that results in maximum response. For simple damping in which there is no blade-to-blade damping and blade-to-ground damping is the same for each blade, the maximum response predicted by the theory is the same as that of Whitehead in 1976 [7]. However, if the damping is more complicated, then the maximum response is different than that previously predicted by Whitehead. In some cases, the maximum response may be lower, but in other cases the maximum response may exceed that previously predicted in [6,8].

Mode localization is described in the context of this theory. For simple damping, the mode that yields maximum response consists of a Dirac delta function superimposed on a fundamental wave whose wave number corresponds to the engine order of the excitation. The fundamental wave results in a generalized force that excites the mode, while the Dirac delta function concentrates the vibrational energy of the response in a single blade, resulting in localization and high forced response amplitude. The forced response of the system is maximized when a certain balance between the generalized force and localization is achieved. In addition, the theory predicts that when a system is intentionally mistuned to achieve maximum response, the response is insensitive to small random mistuning. The actual forced response of the system with small random mistuning will be close to that predicted by the theory.

A method for assessing the mistuning needed to obtain the mode with maximum response has been developed. Once the mistuned mode resulting in maximum response is determined, the mistuning in the system that will produce this mode can be explicitly calculated. The system is transformed into the complex domain, where the discrete Fourier transform of the stiffness variations is calculated from known quantities including the tuned system frequencies and a complex representation of the modal content of the maximum responding mode. The inverse Fourier transform is then computed, giving the physical mistuning that results in maximum forced response.

The methods developed here were demonstrated numerically. Two examples were described for the simple damping case. Forced response simulations with these models agreed very well with theoretical predictions. In addition, Monte Carlo simulations were used to demonstrate that the forced responses of the intentionally mistuned systems were insensitive to small random mistuning. Two additional examples were described in which the modal damping was varied systematically. In the first example, the maximum response that the system could realize was less than that predicted for constant modal damping. In the second example, the forced response of the system exceeded that for simple damping and predicted by Whitehead [6–8]. Again, forced response simulations agreed well with predictions.

The results derived here were compared to the previous development by Whitehead [6,8]. For simple damping, the maximum response predicted here is less than that predicted by Whitehead except in the special cases of $E=0$ or $E=N/2$. However, it was shown that the maximum response predicted by Whitehead cannot be achieved with a structural model of a bladed disk, such as the finite element-based models currently used in practice. The Whitehead maximum can be approximated by combining the effects of mode distortion and frequency splitting, though this approach requires large mistuning.

The techniques demonstrated in this paper can be used to make turbine engine high cycle fatigue testing more reliable. In the case of mistuned bladed disks, forced response testing is prohibitively expensive and time consuming. Because of this, only a limited number of bladed disks can be tested. The likelihood that a particular disk selected for testing will exhibit extremely high forced response amplitudes is small, so that a high cycle fatigue problem from mistuning may go unnoticed. The method described here can potentially be applied to bladed disks to develop test cases with high forced response amplitudes so that high cycle fatigue problems can be identified and mitigated earlier in the development process.

Acknowledgments

The authors wish to thank Professor M. Mignolet of Arizona State University for providing the data necessary to compare his result to the result given here. The authors also wish to express appreciation to Prof. Mignolet for his candid discussion and insight with regard to the maximum response problem. Professor Mignolet has ongoing research in the area of modeling and predicting maximum mistuned forced response, though the approach taken by Prof. Mignolet is generally different from that described here. At the time of the discussion in March 2001, both approaches had been extensively and independently formalized. In addition, the authors wish to thank Dr. E. Petrov of the Imperial College of Science at the University of London for his assistance in identifying the turbine disk reported in his work.

References

[1] Srinivasan, A. V., 1997, "Flutter and Resonant Vibration Characteristics of Engine Blades," ASME J. Eng. Gas Turbines Power, **119**(4), pp. 742–775.
[2] Kenyon, J. A., and Griffin, J. H., 2001, "Harmonic Mistuning of Turbine Engine Bladed Disks and Implications on Sensitivity to Forced Response," ASME Paper 2001-GT-0274, International Gas Turbine Institute Turbo Expo, New Orleans, LA.
[3] Kim, M., Moon, J., and Wickert, J. A., 2000, "Spatial Modulation of Repeated Vibration Modes in Rotationally Periodic Structures," J. Vibr. Acoust., **122**, pp. 62–68.
[4] Ewins, D. J., 1969, "The Effects of Detuning Upon the Forced Vibrations of Bladed Disks," J. Sound Vib., **9**(1), pp. 65–79.
[5] MacBain, J. C., and Whaley, P. W., 1984, "Maximum Resonant Response of Mistuned Bladed Disks," ASME J. Vib., Acoust., Stress, Reliab. Des., **106**, pp. 218–223.
[6] Whitehead, D. S., 1966, "Effect of Mistuning on the Vibration of Turbomachine Blades Induced by Wakes," J. Mech. Eng. Sci., **8**(1), pp. 15–21.
[7] Whitehead, D. S., 1976, "Research Note: Effect of Mistuning on Forced Vibration of Blades with Mechanical Coupling," J. Mech. Eng. Sci., **18**, 6, pp. 306–307.
[8] Whitehead, D. S., 1998, "The Maximum Factor by Which Forced Vibration of Blades Can Increase Due to Mistuning," ASME J. Eng. Gas Turbines Power, **120**(1), pp. 115–119.
[9] Mignolet, M. P., Hu, W., and Jadic, I., 2000, "On the Forced Response of Harmonically and Partially Mistuned Bladed Disks. Part II: Partial Mistuning, and Applications" Int. J. Rotating Mach., **6**(1), pp. 43–56.
[10] Castanier, M. P., Ottarsson, G., and Pierre, C., 1997, "A Reduced Order Modeling Technique for Mistuned Bladed Disks," J. Vibr. Acoust., **119**(3), pp. 439–447.
[11] Kruse, M. J., and Pierre, C., 1996, "Forced Response of Mistuned Bladed Disks Using Reduced-Order Modeling," Proc. 37th AIAA/ASME/ASCE/AHS/ASC Structures, Structural Dynamics, and Materials Conference, Salt Lake City, UT, **4**, pp. 1938–1950.
[12] Yang, M.-T., and Griffin, J. H., 1997, "A Reduced Order Approach for the Vibration of Mistuned Bladed Disk Assemblies," ASME J. Eng. Gas Turbines Power, **119**(1), pp. 161–167.
[13] Yang, M.-T., and Griffin, J. H., 1999, "A Reduced Order Model of Mistuning Using a Subset of Nominal System Modes," ASME Paper 99-GT-288, Inter-

national Gas Turbine Institute Turbo Expo, Indianapolis, IN.
[14] Bladh, R., Castanier, M. P., and Pierre, C., 2000a, ''Component-Mode-Based Reduced Order Modeling Techniques for Mistuned Bladed Disks, Part I: Theoretical Models,'' ASME Paper 2000-GT-0360, International Gas Turbine Institute Turbo Expo, Munich, Germany.
[15] Bladh, R., Castanier, M. P., and Pierre, C., 2000b, ''Component-Mode-Based Reduced Order Modeling Techniques for Mistuned Bladed Disks, Part II: Application,'' ASME Paper 2000-GT-0361, International Gas Turbine Institute Turbo Expo, Munich, Germany.
[16] Rivas-Guerra, A. J., and Mignolet, M. P., 2001, ''Local/Global Effects of Mistuning on the Forced Response of Bladed Disks,'' ASME Paper 2001-GT-0289, International Gas Turbine Institute Turbo Expo, New Orleans, LA.
[17] Petrov, E. P., and Ewins, D. J., 2001, ''Analysis of the Worst Mistuning Patterns in Bladed Disc Assemblies,'' ASME Paper 2001-GT-0292, International Gas Turbine Institute Turbo Expo, New Orleans, LA.
[18] Petrov, E., Sanliturk, K., Ewins, D., and Elliot, R., 2000, ''Quantitative Prediction of the Effects of Mistuning Arrangement on Resonant Response of a Practical Turbine Bladed Disk,'' Proc., 5th National Turbine Engine High Cycle Fatigue Conference, Chandler, AZ.
[19] Rivas-Guerra, A. J., and Mignolet, M. P., 2001, ''Maximum Amplification of Blade Response Due to Mistuning: a Localization-Based Optimization,'' Proc., 6th National Turbine Engine High Cycle Fatigue Conference, Jacksonville, FL.
[20] Sinha, A., 1997, ''Computation of the Maximum Amplitude of a Mistuned Bladed Disk Assembly via Infinity Norm,'' Proc., 1997 ASME International Mechanical Engineering Congress and Exposition, Dallas, TX, **AD-55**, pp. 427–432.
[21] Stange, W. A., and MacBain, J. C., 1983, ''An Investigation of Dual Mode Phenomena in a Mistuned Bladed Disk,'' ASME J. Vib., Acoust., Stress, Reliab. Des., **105**, pp. 402–407.
[22] Kenyon, J. A., 2002, ''Robust Maximum Forced Response in Mistuned Turbine Engine Bladed Disks,'' Ph.D. dissertation, Carnegie Mellon University.
[23] Kruse, M. J., and Pierre, C., 1996, ''Dynamic Response of an Industrial Turbomachinery Rotor,'' AIAA Pap., 96-2820, 32nd AIAA/ASME/SAE/ASEE Joint Propulsion Conference and Exhibit, Lake Buena Vista, FL.

Analytical Formulation of Friction Interface Elements for Analysis of Nonlinear Multi-Harmonic Vibrations of Bladed Disks

E. P. Petrov
e-mail: y.petrov@ic.ac.uk

D. J. Ewins

Imperial College of Science,
Technology and Medicine,
Center of Vibration Engineering,
Mechanical Engineering Department,
London SW7 2BX, UK

An analytical formulation for the vectors of contact forces and the stiffness matrix of the nonlinear friction contact interface is developed for the analysis of multi-harmonic vibrations in the frequency domain. The contact interface elements provided here an exact description of friction and unilateral contact forces at the interacting surfaces, taking into account the influence of the variable normal load on the friction forces, including the extreme cases of separation of the two surfaces. Initial gaps and interferences at the contact nodes, which affect the normal force, as well as the unilateral action of the normal force at the contact surface, are all included in the model. The accurate calculation of the force vector and the tangent stiffness matrix provides a very reliable and fast convergence of the iteration process used in the search for the amplitudes of nonlinear vibrations of bladed disks. Numerical investigations demonstrate excellent performance with respect to speed, accuracy and stability of computation. [DOI: 10.1115/1.1539868]

Introduction

One of the most important sources of nonlinear behavior in turbomachinery structures is the dynamics of the contact surfaces between different parts of assembled structures. In some cases, these effects are advantageous, are exploited by designers (as in underplatform or impact dampers of bladed dises), but in other cases the effect of the resulting forces is problematic and has to be reduced.

The problem of effective modeling the friction contact effects, and of developing reliable methods for analysis of systems with friction, have attracted attention of many scientists and engineers. A modern insight in the friction phenomenon from the point of view of contact mechanics can be found in (Tworzydlo et al. [1]), together with a good list of publications on the topic. A review of research on the analysis and use of friction damping in blade vibration is given in paper (Griffin [2]).

Analysis of the vibrations of bladed disks with friction dampers is usually performed in the frequency domain owing to the high computational efficiency of this approach. Transformation of the formulation of the problem into the frequency domain can be carried out by representing each steady-state displacement as a sum of harmonic components, or even as one harmonic only. Then, a set of nonlinear equations with respect to the amplitudes of the harmonics is obtained using a refinement of the harmonic balance method, the so-called ''multi-harmonic balance method.'' The latter term is used to highlight the use of many harmonics in the displacement expansion. The general scheme of solution for non-linear problems using the multi-harmonic balance method is described in (Cardona et al. [3]). The analysis of monoharmonic vibrations with friction damping effects in turbomachines can be found in papers by Griffin [4]; Sanliturk et al. [5]; Sextro [6] and Csaba [7], whereas multi-harmonic vibrations are studied in papers by Pierre et al. [8]; Cameron and Griffin [9]; Berthillier et al. [10]. In these papers, friction interface nodes are assumed to be in contact continuously and the normal load at the friction interfaces is assumed to be invariable.

Contributed by the International Gas Turbine Institute and presented at the International Gas Turbine and Aeroengine Congress and Exhibition, Amsterdam, The Netherlands, June 3–6, 2002. Manuscript received by the IGTI January 22, 2002. Paper No. 2002-GT-30325. Review Chair: E. Benvenuti.

In practical bladed disks, due to vibration, the relative displacements along both directions (normal as well as tangential to the contact surface) are inevitably nonconstant. The magnitude of the normal displacement variation can be large, which can even result in temporary separation of the contact surfaces and moreover in changes of the time instants of the slip-to stick and back transitions in tangential motion. Interaction forces, as well as stiffness properties due to abrupt changes of the contact conditions during vibrations stiffness values, can change discontinuously. The robustness and accuracy of calculations of the nonlinear vibrations are completely determined by the accuracy of the determination of the friction forces and the stiffness matrix of the interface contact model.

The problems of accurately determining the stiffness matrix of the friction element, as well as the harmonic components of friction forces and the force of unilateral interaction along the normal, for consistent friction models with variable normal load have not been solved in the literature to date. In some papers [3,8,10], the stiffness matrices are derived for simple, Coulomb-type friction models with constant normal load and a friction contact model for the case of variable normal load has been developed in Yang et al. [11] and Chen and Mend [12]. However, in the latter papers the stiffness matrix of the interface has not been determined. For the cases of mono-harmonic vibrations considered in [5–7], a ratio of the amplitude of the interaction force to the amplitude of the relative displacement is usually used instead of the stiffness matrix. Such a rough approximation cannot substitute for the proper stiffness matrix in an iterative solution of the nonlinear equations and is likely to cause difficulty, or even failure, in solution convergence, especially for cases when strongly nonlinear effects are revealed.

In this paper an approach is proposed for the analysis of multi-harmonic vibrations for systems with friction and gaps based on analytically derived contact interface elements.

A friction model and an interface friction element are developed that describe friction forces under the variable normal load and unilateral interaction along the normal of a contact surface. To guarantee both high accuracy and a rapid convergence rate of the iterative solution process, the friction interface elements are derived analytically including their stiffness matrices. This analytical derivation has allowed us to overcome difficulties in the nu-

merical analysis of structures having abrupt changes of contact conditions (such as contact-absence of contact; slip—stick, etc.). Such difficulties have been common in the past, often leading to loss of the convergence and failure in the search for steady-state solutions.

The friction model and element proposed here are equally accurate for constant and for variable normal loads and even for cases of interfaces with contact-to-separation transitions. Because of that, they can be applied to the analysis of a wide variety of systems with friction and friction-impact interfaces, such as occur in bladed disks (underplatform dampers, root damping in bladed disk assemblies; intershroud contacts in shrouded bladed disks, etc.) or in other mechanical structures. The friction interface element proposed describes the interaction of the contacting surfaces at one node and the application of such elements over many nodes of the prospective contact can be used for modeling contact interaction over complex areas.

Multi-Harmonic Balance/Newton-Raphson Method for Analysing Vibration of Nonlinear Systems

The equation for vibration of a bladed disk consisting of a linear part (which is independent on vibration amplitudes) and nonlinear friction interfaces can be written in the following form:

$$\mathbf{K}\mathbf{q}(t)+\mathbf{C}\dot{\mathbf{q}}(t)+\mathbf{M}\ddot{\mathbf{q}}(t)+\mathbf{f}(\mathbf{q}(t),\dot{\mathbf{q}}(t))-\mathbf{p}(t)=0 \tag{1}$$

where $\mathbf{q}(t)$ is a vector of displacements for all degrees of freedom (DOFs) in the considered bladed disc; **K**, **C**, and **M** are accordingly stiffness, viscous damping and mass matrices of its linear part; $\mathbf{f}(\mathbf{q}(t))$ is a vector of nonlinear, friction interface forces, which are dependent on displacements and velocities of the interacting nodes and $\boldsymbol{p}(\boldsymbol{t})$ is a vector of external excitation forces.

In cases where the excitation forces are periodic, it is usually desirable to find steady, periodic regimes of response variation. For a search of the periodic vibration response the variation of all DOFs of the system in time can be represented as a restricted Fourier series, which can contain as many and such harmonic components as are necessary to approximate the sought solution, i.e.

$$\mathbf{q}(t)=\mathbf{Q}_0+\sum_{j=1}^{n}\mathbf{Q}_{2j-1}\cos m_j\omega t+\mathbf{Q}_{2j}\sin m_j\omega t \tag{2}$$

where Q_j $(j=0...2n)$ are vectors of harmonic coefficients for system DOFs; m_j $(j=1...2n)$ are specific harmonics that are kept in the displacement expansion in addition to the constant component; ω is a principal vibration frequency which is expressed by the vibration periodicity, T, as follows: $\omega=2\pi/T$.

In accordance with the multi-harmonic balance method, the expansion from Eq. (2) is substituted into the motion Eq. (1), after which a Galerkin-type procedure is applied to the equation obtained using each of the harmonic functions. Equation (1) is sequentially multiplied by $(\cos m_j\omega)$ and $(\sin m_j\omega)$ for all harmonics from the expansion and integrals over the vibration period, T, are calculated. As a result, equations for determination of the all unknown harmonic components are obtained in the form:

$$\mathbf{R}(\mathbf{Q})=\mathbf{Z}(\omega)\mathbf{Q}+\mathbf{F}(\mathbf{Q})-\mathbf{P}=\mathbf{0} \tag{3}$$

where $\boldsymbol{Q}=\{\boldsymbol{Q}_0,\boldsymbol{Q}_1,\boldsymbol{Q}_2,\ldots,\boldsymbol{Q}_{2n-1},\boldsymbol{Q}_{2n}\}^T$ is a vector of harmonic coefficients for system DOFs; $\boldsymbol{F}(\boldsymbol{Q})$ is a vector of nonlinear forces; $\boldsymbol{P}$ is a vector of harmonic components of exciting forces, and $\boldsymbol{Z}(\omega)$ is the dynamic stiffness matrix of the linear

$$\mathbf{Z}=\begin{bmatrix}
\mathbf{K} & \mathbf{0} & \mathbf{0} & \cdots & \mathbf{0} & \mathbf{0}\\
\mathbf{0} & \mathbf{K}-(m_1\omega)^2\mathbf{M} & m_1\omega\mathbf{C} & \cdots & \mathbf{0} & \mathbf{0}\\
\mathbf{0} & -m_1\omega\mathbf{C} & \mathbf{K}-(m_1\omega)^2\mathbf{M} & \cdots & \mathbf{0} & \mathbf{0}\\
\cdots & \cdots & \cdots & \cdots & \cdots & \cdots\\
\mathbf{0} & \mathbf{0} & \mathbf{0} & \cdots & \mathbf{K}-(m_n\omega)^2\mathbf{M} & m_n\omega\mathbf{C}\\
\mathbf{0} & \mathbf{0} & \mathbf{0} & \cdots & -m_n\omega\mathbf{C} & \mathbf{K}-(m_n\omega)^2\mathbf{M}
\end{bmatrix} \tag{4}$$

Equation (3) represents a nonlinear set of equations with respect to **Q**. One of the most efficient methods for solution of the nonlinear equations is the Newton-Raphson method which possesses quadratic convergence when an approximation is close enough to the solution. An iterative solution process is expressed by the following formula:

$$\mathbf{Q}^{(k+1)}=\mathbf{Q}^{(k)}-\left(\frac{\partial\mathbf{R}^{(k)}}{\partial\mathbf{Q}}\right)^{-1}\mathbf{R}(\mathbf{Q}^{(k)}) \tag{5}$$

where superscript $^{(k)}$ indicates the number of the current iteration. Performing differentiation of Eq. (3) with respect to **Q**, the recurrence formula can be rewritten in the form

$$\mathbf{Q}^{(k+1)}=\mathbf{Q}^{(k)}-\left[\mathbf{Z}(\omega)+\frac{\partial\mathbf{F}(\mathbf{Q}^{(k)})}{\partial\mathbf{Q}}\right]^{-1}\mathbf{R}(\mathbf{Q}^{(k)}) \tag{6}$$

When derivatives $\partial\mathbf{F}(\mathbf{Q}^{(k)})/\partial\mathbf{Q}$ are calculated using finite-difference formulas, this results in a very large computational effort, difficulty with the choice of the step for the numerical evaluation of the derivatives and—very often—to a loss of accuracy and robustness of the solution. In further sections we derive analytical expressions for a nonlinear force vector of the friction interface, $\mathbf{F}(\mathbf{Q}^{(k)})$, and for its tangent stiffness matrix, $\partial\mathbf{F}(\mathbf{Q}^{(k)})/\partial\mathbf{Q}$, which provide exact and extremely fast calculations.

Derivation of Nonlinear Friction Interface Elements

In order to derive expressions for friction interface matrices, we consider the relative motion of the contacting nodes in terms of tangential, x, and normal, y, motion components (Fig. 1).

Contact surface mechanical properties are described by a friction coefficient, μ, and stiffness coefficients k_x and k_y, which characterize elastic deformation of the asperities of the contacting surfaces in the tangential and normal directions, respectively. Moreover, an initial static preload normal force, N_0, can also be prescribed. The general case is considered here, when the preload normal force can take a negative value (corresponding to an initial gap between contacting surfaces which is determined as follows: $g=-N_0/k_y$).

The periodic motion of each degree of freedom can be represented by a sum of all harmonic components analyzed, i.e.,

$$x(\tau)=\mathbf{H}_-^T(\tau)\mathbf{X};\quad y(\tau)=\mathbf{H}_-^T(\tau)\mathbf{Y} \tag{7}$$

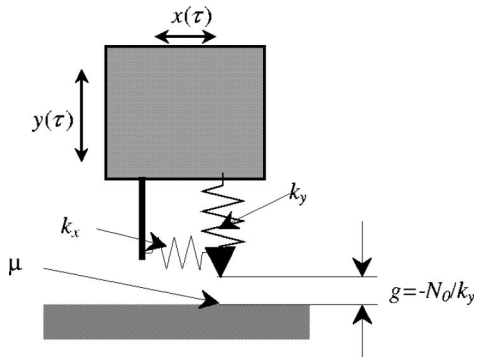

Fig. 1 Friction interface element

where **X**, and **Y** are vectors of harmonic coefficients of relative motion in the tangential and normal directions, respectively, which are selected from vector, **Q**, of harmonic coefficients for the whole system; $\mathbf{H}_{-}=\{1,\cos m_1\tau,\sin m_1\tau,\ldots,\cos m_n\tau,\sin m_n\tau\}^T$ is a vector consisting of harmonic functions, which is used for transition from frequency domain to time domain, and $\tau=\omega t$ is nondimensional time.

Modeling of the Nonlinear Interface Forces. During relative motion of the contacting surfaces several different states are possible.

The motion along the normal direction, $y(\tau)$, determines whether the interacting surfaces are in contact or separated.

During contact two other different states are possible: slip or stick. In slip, the tangential force, f_x, is a dry friction force and in the stick state, this force is a force due to elastic asperity deformations. Taking into account the influence of the variable normal force occurring during motion along normal direction, expressions for nonlinear interaction forces can be derived for all possible states in the following form:

- Tangential force

$$f_x=\begin{cases} f_x^0+k_x(x-x_0) & \text{for stick} \\ \xi\mu f_y & \text{for slip} \\ 0 & \text{for separation} \end{cases} \tag{8}$$

- Normal force

$$f_y=\begin{cases} N_0+k_y y & \text{for contact} \\ 0 & \text{for separation} \end{cases} \tag{9}$$

where $\xi=\pm 1$ is a sign function of the tangential force at the time instant of slip state initiation, τ_{slip}. For the conventional case of constant normal force, the value of the sign is determined by that of the tangential velocity: $\xi=\text{sgn}(\dot{x}(\tau_{\text{slip}}))$. However, for the case of variable normal load, the sign is determined by that of the tangential force at the end of the preceding stick phase, i.e., $\xi=\text{sgn}(f_x(\tau_{\text{slip}}))$, which guarantees time continuity of the tangential force. The other constants in Eqs. (8) and (9), $x_0=x(\tau_{\text{stick}})$ and $f_x^0=f(\tau_{\text{stick}})$, are values of the relative tangential displacement and the interaction force at the beginning of the stick-state, τ_{stick}, respectively. The force value, f_x^0, has to be equal to the value of the interaction force at the end of preceding slip in order to be continuous over the vibration period, i.e.

$$f_x^0=-\xi\mu f_y(\tau_{\text{stick}}) \tag{10}$$

Determination of the State Transition Times

Stick to Slip Transition. The stick state lasts during the contact phase, while the tangential interaction force, $f_x(\tau)$, is less than the limiting value due to dry friction

$$|f_x(\tau)|<\mu f_y(\tau) \tag{11}$$

So, stick to slip transition occurs when the tangential interaction force of the stick state, f_x, reaches this limiting value, i.e., when

$$f_x^0+k_x(x(\tau)-x_0)=\pm\mu(N_0+k_y y(\tau)) \tag{12}$$

Equation (12) is solved with respect to time for both values of the sign on the limiting friction force. Lower value of τ gives the time of the stick-to-slip transition and the sign used in the equation gives the magnitude of the sign function, $\xi=\text{sgn}(f_x(\tau_{\text{slip}}))$.

Slip to Stick Transition. For the conventional case of constant normal load, the stick state begins when the relative velocity is equal to zero, i.e., when $\dot{x}(\tau)=0$. For a case of variable normal load, the slip-to-stick transition has to be determined from a general stick state condition given by Eq. (11). Such transition occurs only when this condition can be satisfied during at least an infinitesimal time interval, $\Delta\tau$, i.e.

$$|f_x(\tau+\Delta\tau)|=\xi f_x(\tau+\Delta\tau)<\mu f_y(\tau+\Delta\tau) \tag{13}$$

Linearization of Eq. (13) in the vicinity of the slip-to-stick transition time gives another, differential, form for the condition of stick-state existence

$$\xi\dot{f}_x(\tau)<\mu\dot{f}_y(\tau) \tag{14}$$

Equality of rates of stick and slip tangential force variation in time then allows us to write out an equation for slip-to-stick transition in the form

$$\xi k_x\dot{x}(\tau)=\mu k_y\dot{y}(\tau) \tag{15}$$

To select from all possible solutions of Eq. (15) only those instants satisfying conditions (13) and (14), the following condition is also imposed:

$$\xi k_x\ddot{x}(\tau)<\mu k_y\ddot{y}(\tau) \tag{16}$$

This condition guarantees larger rate of increase for a limiting value for the friction force determined by the normal load than that of friction force at the found time instant.

Contact-Separation Transitions. Contact to separation (and back) transitions occur when the normal force, f_y, is equal to zero, and because of that, the corresponding time instants are determined from the equation

$$N_0+k_y y(\tau)=0 \tag{17}$$

When at the transition time instant $\dot{y}(\tau)>0$, this is a time of transition from separation to contact; otherwise, it is time of transition from contact to separation.

Periodic Set of State Transition Times. Since periodic steady-state vibrations are analyzed here, the periodic set of instants for state transitions has to be calculated which provides periodic variation of nonlinear interface forces. Because the tangential force expressions given by Eq. (8) are history-dependent, and include a-priori unknown parameters x_0, f_x^0, ξ, this represents a nontrivial problem and an efficient algorithm can be proposed to determine such set of transition times. Two cases should be distinguished here.

The first case is that when there is no separation during the vibration cycle. For this case, a simple way to find the periodic set of transition times is to start the search of the transition times from time instant, τ^*, when the tangential displacement is zero. This time is calculated from equation $x(\tau^*)=0$ and at this instant the following parameters for the stick case are assumed: $x_0=f_x^0=0$. Then, the first stick-to-slip transition after τ^* is determined from Eq. (12) and the time of the next slip-to-stick transition, τ^{**}, is calculated from Eq. (15). Values $x_0(\tau^{**})$, $f_x^0(\tau^{**})$, $\xi(\tau^{**})$ can be now determined and all transition times can easily be calculated

over the interval $[\tau^{**},\tau^{**}+2\pi]$ using Eqs. (12) and (15) and the set of transition times obtained provides the periodic interaction force variation.

The second case relates to a separation of the contacting surfaces during vibration. For this case, all times of the contact-separation transitions are first calculated from Eq. (17) and then slip-stick transition times are calculated using Eqs. (12) and (15) for each jth contact interval $[\tau^{(j)}_{\text{contact}},\tau^{(j)}_{\text{separation}}]$, separately. To determine whether the contact interval starts from a stick or a slip condition, Eq. (14) is used with the sign function value, ξ, determined as $\xi=\text{sgn}(\dot{x}(\tau^{(j)}_{\text{contact}}))$. If the contact interval starts from the stick state, initial parameters of this state are $x_0=x(\tau^{(j)}_{\text{contact}})$ and $f^0_x=0$, otherwise the expression for tangential force is determined simply by $\xi\mu f_y$ of Eq. (8).

Force Vector and Stiffness Matrix. Vectors of Fourier expansion coefficients for tangential, $\mathbf{F}_x$, and normal, $\mathbf{F}_y$, forces can be expressed in the form

$$\begin{Bmatrix}\mathbf{F}_x\\ \mathbf{F}_y\end{Bmatrix}=\frac{1}{\pi}\sum_{j=1}^{n_\tau}\int_{\tau_j}^{\tau_{j+1}}\begin{Bmatrix}\mathbf{H}_+(\tau)f_x\\ \mathbf{H}_+(\tau)f_y\end{Bmatrix}d\tau=\sum_{j=1}^{n_\tau}\begin{Bmatrix}\mathbf{J}_x^{(j)}\\ \mathbf{J}_y^{(j)}\end{Bmatrix} \tag{18}$$

where $\mathbf{H}_+=\{\frac{1}{2},\cos m_1\tau,\sin m_1\tau,\ldots,\cos m_n\tau,\sin m_n\tau\}^T$ and τ_j are instants of contact-separation or slip-stick transitions. Substituting the expressions for the interaction forces given by Eqs. (8) and (9) into Eq. (18) and taking into account Eq. (7), gives an expression for the force vector. Introduced here are vectors of integrals $\mathbf{J}_x^{(j)}$ and $\mathbf{J}_y^{(j)}$ over each interval of stick, slip, or separation which are expressed in the form

$$\mathbf{J}_x^{(j)}=\begin{cases}k_x\mathbf{W}_j\mathbf{X}+c_j\mathbf{w}_j & \text{stick}\\ \xi\mu(N_0\mathbf{w}_j+k_y\mathbf{W}_j\mathbf{Y}) & \text{slip}\\ \mathbf{0} & \text{separation}\end{cases} \tag{19}$$

$$\mathbf{J}_y^{(j)}=\begin{cases}N_0\mathbf{w}_j+k_y\mathbf{W}_j\mathbf{Y} & \text{contact}\\ \mathbf{0} & \text{separation}\end{cases} \tag{20}$$

where

$$\underset{(n\times n)}{\mathbf{W}_j}=\frac{1}{\pi}\int_{\tau_j}^{\tau_{j+1}}\mathbf{H}_+(\tau)\mathbf{H}_-^T(\tau)d\tau;\qquad \underset{(n\times 1)}{\mathbf{w}_j}=\frac{1}{\pi}\int_{\tau_j}^{\tau_{j+1}}\mathbf{H}_+(\tau)d\tau \tag{21}$$

$$c_j=f_x^0(\tau_j)-k_xx(\tau_j)=-\xi\mu(N_0+k_yy(\tau_j))-k_xx(\tau_j) \tag{22}$$

Since the vector used for transformation from time domain into frequency domain, $\mathbf{H}_+$, and that for transformation backward, $\mathbf{H}_-$, consist of sine and cosine functions of different orders then components of matrix $\mathbf{W}$ and vector $\mathbf{w}$ are simple integrals of sine and cosine functions and integrals of products of these functions. These integrals can be calculated analytically, which provides an exact and very fast calculation for the vectors of Fourier expansion coefficients of the interface forces.

The stiffness matrix of the friction interface element is determined as a matrix of derivatives of the Fourier coefficients for the friction interface forces with respect to the Fourier coefficients for relative displacements. An exact expression for the stiffness matrix is also derived analytically. This matrix is obtained by differentiating Eq. (18) with respect to vectors $\mathbf{X}$ and $\mathbf{Y}$. Because of the independence of the normal force to the tangential displacement, the stiffness matrix has the following inherently unsymmetrical structure:

$$\mathbf{K}_f=\begin{bmatrix}\dfrac{\partial\mathbf{F}_x}{\partial\mathbf{X}} & \dfrac{\partial\mathbf{F}_x}{\partial\mathbf{Y}}\\ \mathbf{0} & \dfrac{\partial\mathbf{F}_y}{\partial\mathbf{Y}}\end{bmatrix}=\sum_{j=1}^{n_\tau}\begin{bmatrix}\dfrac{\partial\mathbf{J}_x^{(j)}}{\partial\mathbf{X}} & \dfrac{\partial\mathbf{J}_x^{(j)}}{\partial\mathbf{Y}}\\ \mathbf{0} & \dfrac{\partial\mathbf{J}_y^{(j)}}{\partial\mathbf{Y}}\end{bmatrix} \tag{23}$$

where

$$\frac{\partial\mathbf{J}_x^{(j)}}{\partial\mathbf{X}}=\begin{cases}k_x\mathbf{W}_j+\mathbf{w}_j\left(\dfrac{\partial c_j}{\partial\mathbf{X}}\right)^T & \text{stick}\\ \mathbf{0} & \text{slip}\\ \mathbf{0} & \text{separation}\end{cases} \tag{24}$$

$$\frac{\partial\mathbf{J}_x^{(j)}}{\partial\mathbf{Y}}=\begin{cases}\mathbf{w}_j\left(\dfrac{\partial c_j}{\partial\mathbf{Y}}\right)^T & \text{stick}\\ \xi\mu k_y\mathbf{W}_j & \text{slip}\\ \mathbf{0} & \text{separation}\end{cases} \tag{25}$$

$$\frac{\partial\mathbf{J}_y^{(j)}}{\partial\mathbf{Y}}=\begin{cases}k_y\mathbf{W}_j & \text{contact}\\ \mathbf{0} & \text{separation}\end{cases} \tag{26}$$

Contained in Eqs. (24) and (25), derivatives of the constant term of the tangential force with respect to $\mathbf{X}$ and $\mathbf{Y}$ are determined in the following form:

$$\frac{\partial c_j}{\partial\mathbf{X}}=-\xi\mu k_y\dot{y}(\tau_j)\frac{\partial\tau_j}{\partial\mathbf{X}}-k_x\left(\mathbf{H}_-(\tau_j)+\dot{x}(\tau_j)\frac{\partial\tau_j}{\partial\mathbf{X}}\right) \tag{27}$$

$$\frac{\partial c_j}{\partial\mathbf{Y}}=-\xi\mu k_y\left(\mathbf{H}_-(\tau_j)+\dot{y}(\tau_j)\frac{\partial\tau_j}{\partial\mathbf{Y}}\right) \tag{28}$$

During the differentiation, dependence of the values of tangential force, $f_x^{(0)}$, tangential displacement, x_0, at the beginning of stick-state and time of the transition from slip to stick, τ_{stick}, on the harmonic coefficients of relative displacements is taken into account.

The expressions for derivatives of the slip-to-stick transition time with respect to $\mathbf{X}$ and $\mathbf{Y}$, are derived by differentiation of the slip-to-stick condition given in Eq. (15). Dependence of $\dot{x}$ and $\dot{y}$ on $\mathbf{X}$ and $\mathbf{Y}$ as well as dependence of the stick times, i.e. $\tau_{\text{stick}}=\tau_{\text{stick}}(\mathbf{X},\mathbf{Y})$, is accounted for here, and results into the following expressions:

$$\frac{\partial\tau_{\text{stick}}}{\partial\mathbf{X}}=\frac{-k_x}{k_x\ddot{x}(\tau_{\text{stick}})-\mu k_y\ddot{y}(\tau_{\text{stick}})}\dot{\mathbf{H}}_-(\tau_{\text{stick}}) \tag{29}$$

$$\frac{\partial\tau_{stick}}{\partial\mathbf{Y}}=\frac{\mu k_y}{k_x\ddot{x}(\tau_{\text{stick}})-\mu k_y\ddot{y}(\tau_{\text{stick}})}\dot{\mathbf{H}}_-(\tau_{\text{stick}}) \tag{30}$$

For the special case when stick occurs immediately after full separation, the time of the stick beginning coincides with the time of contact beginning. Because of that it is independent on $\mathbf{X}$, i.e.,

$$\frac{\partial\tau_{\text{stick}}}{\partial\mathbf{X}}=\mathbf{0} \tag{31}$$

and derivatives with respect to vector $\mathbf{Y}$ are obtained by differentiation of the contact condition given by Eq. (17)

$$\frac{\partial\tau_{\text{stick}}}{\partial\mathbf{Y}}=-\frac{1}{\dot{y}(\tau_{\text{stick}})}\mathbf{H}_-(\tau_{\text{stick}}) \tag{32}$$

Thus-derived analytical expressions for the vector of harmonic components of interface forces (Eqs. (18)–(20)) and for the stiffness matrix (Eqs. (23) and (24)–(26)) allow exact calculation of all components of the friction contact interface element.

It should be noted that, in the proposed analytical formulation for the interface element, computational efforts for calculation of the stiffness matrix are negligible compared with the expense of calculation of the force vector. This is achieved owing to the fact that obtained expressions for tangent matrix are based on simple matrix operations with matrix, $\mathbf{W}$, and vector $\mathbf{w}$, which are already calculated for the determination of the forces. The expressions derived for the vectors of harmonic components of friction interface forces given by Eq. (18), and the expression for the tangent stiffness matrix given by Eq. (23), are nonlinearly dependent on the vectors of harmonic components for tangential, $\mathbf{X}$, and

normal, **Y**, displacements since the times of slip-to-stick and contact-separation transitions, $\tau_j = \tau_j(\mathbf{X},\mathbf{Y})$, are, in general, dependent on these vectors.

For two special cases the expressions for the vector and the stiffness matrix can be written down immediately. These cases are: (i) the case of full separation and (ii) the case when contact is permanent and slip does not occur.

For the full separation case the interface forces and tangent matrix are equal to zero, i.e.

$$\mathbf{F}_x = \mathbf{F}_y = \mathbf{0} \quad \text{and} \quad \mathbf{K}_f = \mathbf{0} \tag{33}$$

For the case of permanent contact without slip, contact forces are linear and the expressions for vector of forces and tangent matrix take the form

$$\begin{Bmatrix} \mathbf{F}_x \\ \mathbf{F}_y \end{Bmatrix} = \begin{Bmatrix} k_x\mathbf{X} \\ k_y\mathbf{Y} \end{Bmatrix}; \quad \mathbf{K}_f = \begin{bmatrix} k_x\mathbf{I} & \mathbf{0} \\ \mathbf{0} & k_y\mathbf{I} \end{bmatrix} \tag{34}$$

where **I** is the identity matrix.

Numerical Results

The developed method for calculation of the force vector and tangent matrix for the interface element has been applied to the analysis of forced response of different systems described in the forthcoming.

System 1. For initial exploration of the approach, a single-degree-of-freedom oscillator was considered. The equation of motion of the oscillator has the following form:

$$\ddot{x} + 0.4\dot{x} + 40x + f(x,\dot{x}) = 100 \sin \omega t \tag{35}$$

where $f(x,\dot{x})$ is a nonlinear force. To study both major parts (for friction force and normal force determination) of the developed friction interface element two cases were included: (i) when the non-linear force, $f(x,\dot{x})$, is assumed to be a force of unilateral contact, f_y, as determined in Eq. (9), and (ii) when the non-linear force is a friction force, f_x, as determined in Eq. (8), with prescribed variation of the normal load, f_y. The first ten harmonics are kept in the multiharmonic solution.

Results of the forced response calculations obtained for the first case are presented in Figs. 2 and 3, where the maximum displacement over the period of vibration is plotted. The influence of gap value is shown in Fig. 2, where the gap is varied from negative values (corresponding to an initial interferences) to positive values and the stiffness coefficient value is: $k_y = 120$. It is assumed that the parameters of the system that are used in Eq. (35), and the friction interface parameters are all given in a consistent system of units. Since their particular choice does not affect the results, they are not specified here.

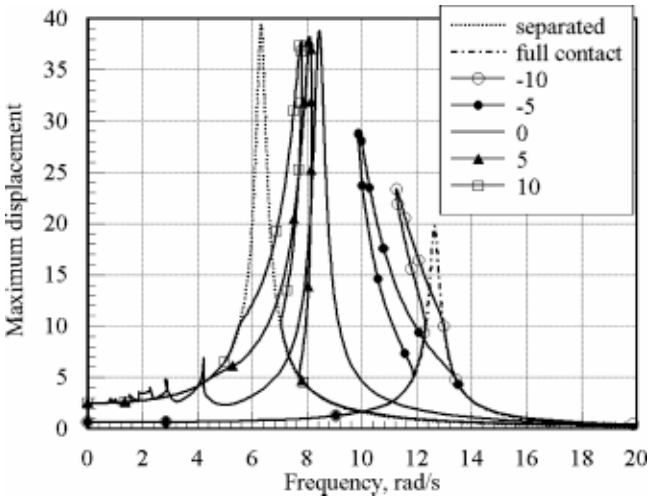

Fig. 2 Forced response for different gap values

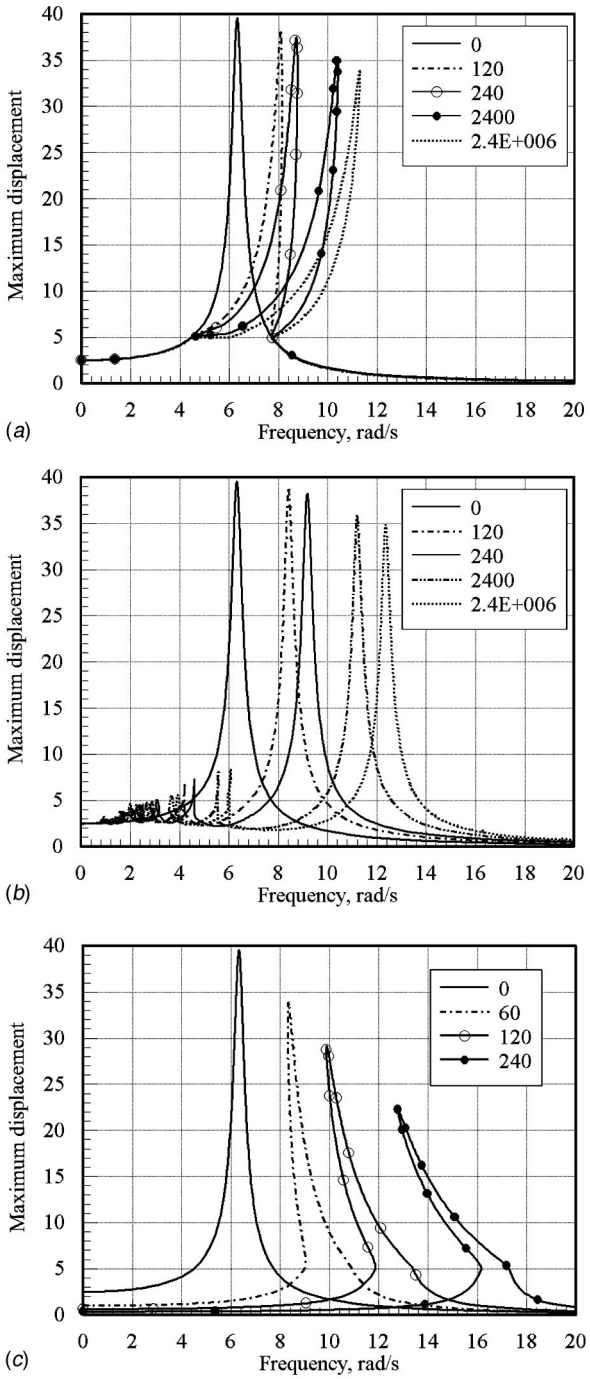

Fig. 3 Influence of stiffness coefficient, k_y, on forced response for different gap values: (*a*) g=5; (*b*) g=0; (*c*) g=−5

Forced responses for the two linear vibration cases are plotted here by dotted curves: (i) for the case when the gap is never closed ($g = \infty$, and the resonance frequency is equal to $\sqrt{40}$ rad/s), and (ii) for the case when full contact exists throughout ($g = -\infty$, and the resonance frequency is $2\sqrt{40}$ rad/s). Forced responses corresponding to different gap values specified in Fig. 2 are plotted by solid lines. One can see large variations in the resonance frequencies of the nonlinear vibration under the gap variation. Moreover, for the case of a zero gap value many superharmonic resonances occur in the range of low excitation frequencies.

In Fig. 3, the variation of forced response under stiffness coef-

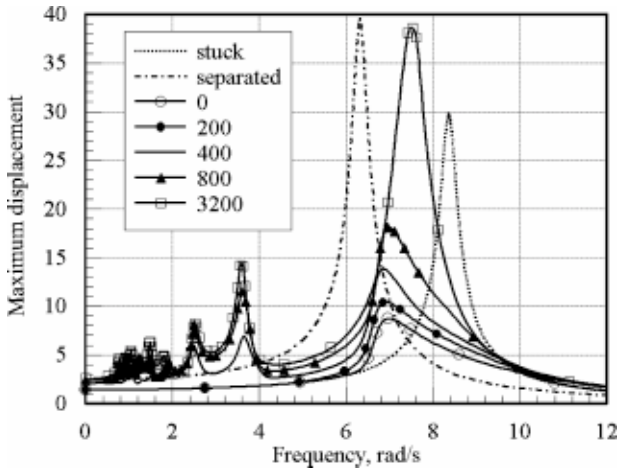

Fig. 4 Forced response for different values of static component in the variable normal load

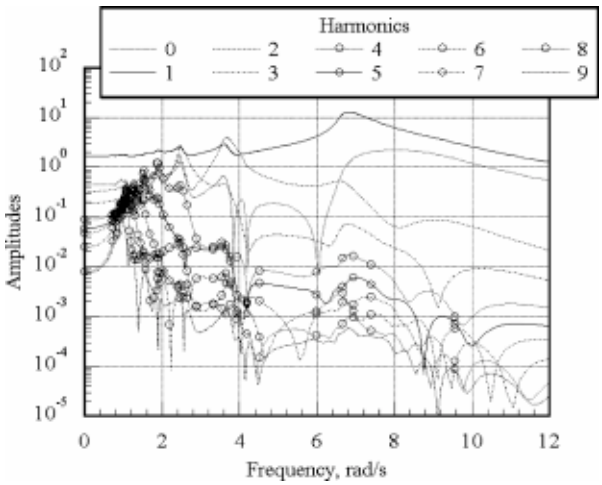

Fig. 6 Amplitudes of harmonic components of the multiharmonic motion (case of $f_y = 300 + 400 \cos \tau$)

ficient, k_y, variation is presented. For a positive gap value, the FRF exhibits a stiffening characteristic, i.e., with an increase of vibration amplitude, the natural frequency is increased. For a negative gap value, the FRF takes a softening characteristic and for zero gap, neither stiffening nor softening effects occur. When the gap is not negative, the possibility of increasing the resonance frequency is rather restricted: as seen, even $k_y = 2.4*10^6$ does not induce an increase of the resonance frequency of more than two times.

In Figs. 4–6, forced vibration response of the oscillator is shown when a friction damper is applied as the nonlinear force, $f(x,\dot{x})$. The following parameters of the contacting surfaces were accepted in the calculations: $k_x = 30$; $\mu = 0.3$. The effect of normal load variation, $f_y = N_0 + a \sin \tau$, is demonstrated in Fig. 4 when the constant component of the normal load, N_0, is varied and the amplitude of the load variation is fixed ($a = 200$).

In Fig. 5, forced response curves are plotted for different values of the amplitude variation, a, with fixed $N_0 = 300$. For comparison, FRFs of linear systems are plotted in both the figures: namely, the response of the system when there is a full separation of the damper during vibrations (resonance frequency $\sqrt{40}$ rad/s) and of the system with fully stuck state of the damper vibrations (resonance frequency $\sqrt{70}$ rad/s).

The existence of superharmonic resonances, for the cases when partial separation occurs, should be noted. Superharmonic resonances are found for all harmonics that are used in the mutltiharmonic analysis. The displacements at these superharmonic resonances are significant, which differs from their much smaller levels noticed also in [12] for the case of three harmonics used there. For the fixed level of the normal load variation, $a = 200$, there is an optimal value of N_0 (for the considered case $N_0 = 600$) which provides the minimum response level. When the constant component of the normal load is fixed higher levels of normal load variation lead to higher vibration levels.

The harmonic spectrum of the multiharmonic vibration shown in Fig. 6 (for the case where $f_y = 300 + 400 \sin \tau$) demonstrates the importance of keeping many harmonics in the solution. It is interesting to note that even the zero harmonic, which reflects a constant component in the vibration displacement induced by the harmonic excitation, is not negligible and has significant values in some excitation frequency ranges.

In all calculations, the condition $\|\mathbf{R}(\mathbf{Q})\| < 10^{-8}$ was used to check the convergence of the iteration process (see Eq. (6)). This high accuracy was successfully achieved in all the cases considered. An example of the number of iterations required, and the distribution of the solution points over the plotted FRFs, are shown in Fig. 7 for both the aforementioned cases: (i) a unilat-

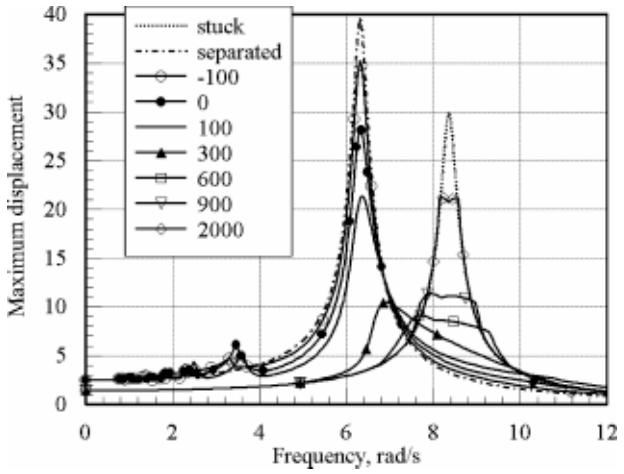

Fig. 5 Forced response of the system with friction damper for different amplitudes of the normal load variation

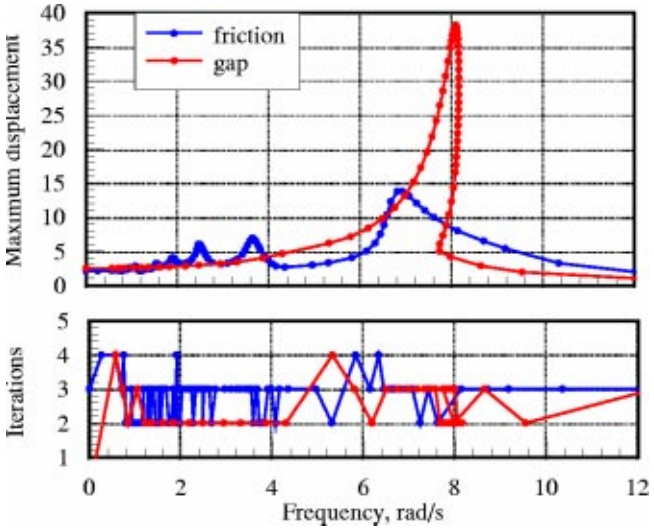

Fig. 7 Illustration of the computational efficiency

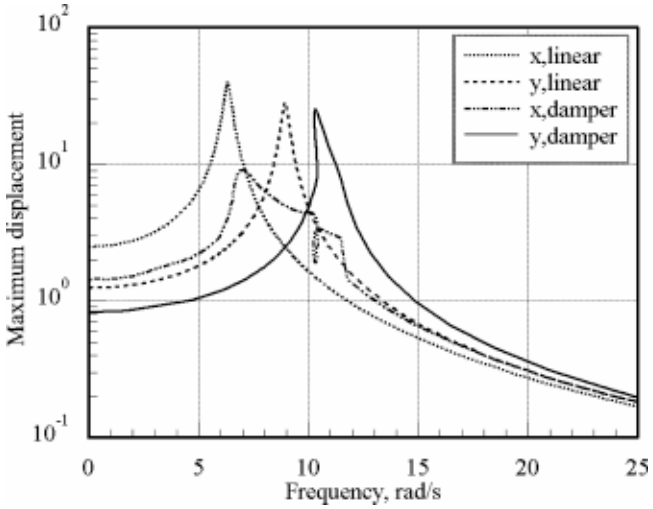

Fig. 8 Forced response of 2DOF system with the friction damper

eral force with a gap (for values $k_y=120$ and $g=5$), and (ii) friction force with prescribed normal load variation $f_y=300+400\sin\tau$.

System 2. Interaction of the normal and tangential vibration at contact interface is illustrated on an example of two-degree-of-freedom system, where vibrations along both axes are coupled only by the friction damper

$$\ddot{x}+0.4\dot{x}+40x+f_x(x,\dot{x},y)=100\sin\omega t$$
$$\ddot{y}+0.4\dot{y}+80y+f_y(y)=100\sin\omega t \tag{36}$$

The parameters of the friction element in this case are: $k_x=30$; $k_y=40$; $\mu=0.3$; $N_0=300$. Calculated amplitudes of the vibration response are shown in Fig. 8 together with the amplitudes of the system without the friction damper. As can be seen from Eq. (36), the system without the friction element vibrates independently in two directions, x and y, and it has two natural frequencies $\sqrt{40}$ and $\sqrt{80}$ rad/s. The introduction of the friction element causes an increase of the resonance frequencies to values 6.98 and 10.31 rad/s, respectively. Moreover, coupling between tangential displacement, x, and normal displacement, y, occurs in the system. One can see that high amplitudes of normal displacement are attained in the vicinity of second resonance $\omega=10.31$ rad/s and can there cause a decrease in amplitude of the tangential displacement.

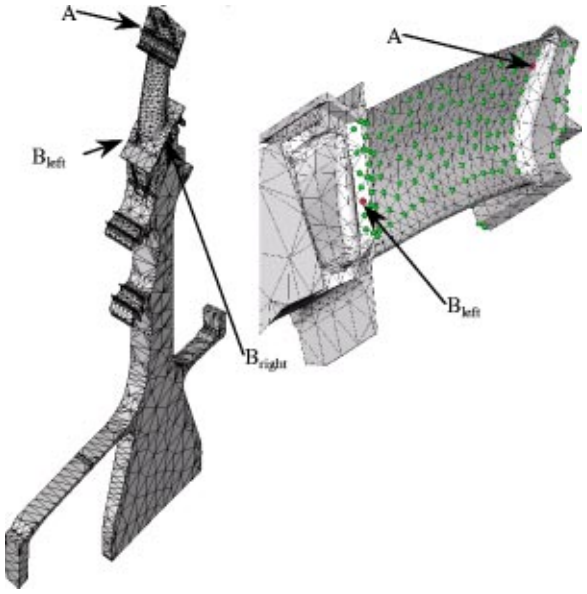

Fig. 9 Finite element model of a sector of a high-pressure turbine-bladed disk and nodes of friction contact

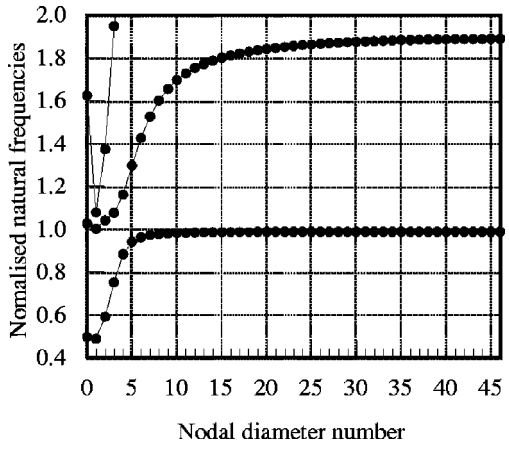

Fig. 10 Natural frequencies of the bladed disk analyzed

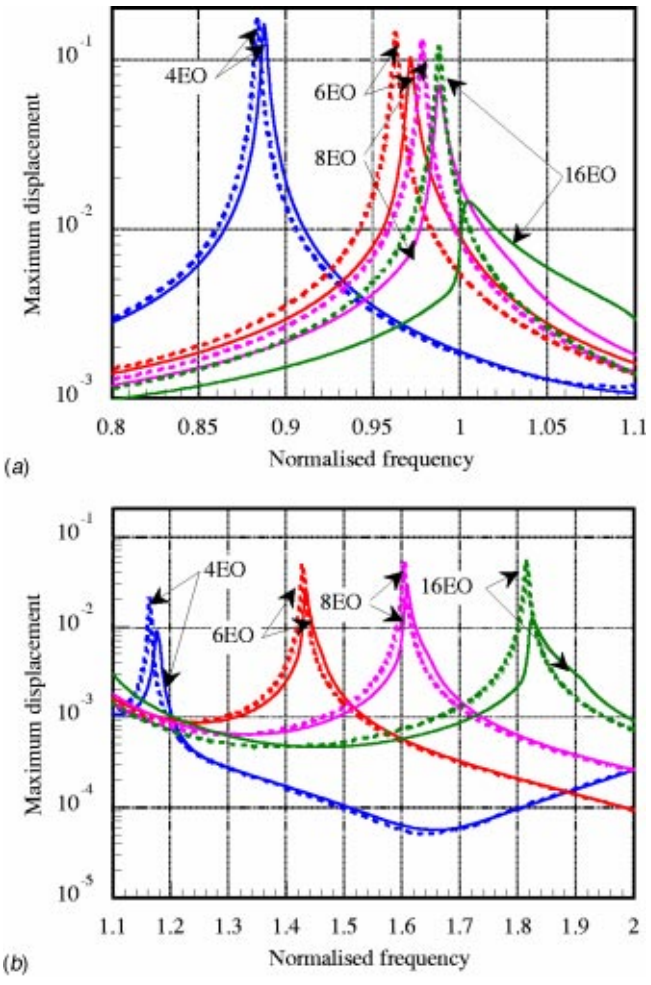

Fig. 11 Forced response of the high-pressure turbine-bladed disk with a friction damper (solid line) and without a friction damper (dashed line) for different numbers of engine orders

System 3. The developed friction interface element has been also applied for the analysis of vibration response of a practical high-pressure bladed turbine disc comprising 92 blades with friction dampers. A finite element model of a sector of the bladed disk is shown in Fig. 9.

Nodes where each of the bladed-disk sectors has the friction contact, B_{left} and B_{right}, are located at the blade platform and another node, where displacements were calculated, A, is selected near tip of the blade. The nodes are marked in Fig. 9 by red circles. For each sector node B interacts through the friction element with the corresponding node of the following sector of the bladed disk and, moreover, its counterpart on the other, left side of the considered sector interacts with the preceding sector. As an example, forcing by 4th, 6th, 8th, and 16th engine-order excitations are considered in the frequency range corresponding to a family of first predominantly flapwise blade modes, and in the frequency range of second family of natural frequencies. In order to compare the damping effect produced by the friction elements, the amplitudes of the excitation loads are assumed to be the same for all engine orders studied. Natural frequencies of the high-pressure turbine disk normalized with respect to the first blade-alone frequency are shown in Fig. 10 for all possible nodal diameter numbers.

Examples of FRFs of maximum displacement at a node A are shown in Fig. 11 where, for comparison, FRFs for the bladed disk without the friction damper are also plotted. Damping produced by the friction damper decreases the response amplitudes significantly and, moreover, the friction damper can increase the resonance frequency significantly. For both the considered families of modes (first flapwise modes and first edge-wise modes with different numbers of nodal diameters), higher damping effects appear for the higher engine orders when relative displacements of neighboring blades are larger.

Conclusions

A method for the analytical derivation of the force vector and stiffness matrix of a friction interface element has been derived for the case of multi-harmonic vibration analysis.

Normal and tangential forces in the developed analytical formulation of the friction element are coupled, as occurs in most practical cases. The method provides for exact and extremely fast calculation of the interface element characteristics.

The numerical efficiency of the developed friction interface element is proved, and the effect of normal load variation has been studied, using representative test cases. A phenomenon of significant levels of superharmonic resonances due to friction under partial separation of contact surfaces has been found.

High robustness and efficiency of the developed analytical formulation have allowed to perform forced response analysis of practical turbine bladed disks with detailed finite element models.

Acknowledgments

The authors grateful to Rolls-Royce plc. for providing the financial support for this project and for giving permission to publish this work.

References

[1] Tworzydlo, W. W., Cecot, W., Oden, J. T., and Yew, C. H., 1998, ''Computational Micro- and Macroscopic Models of Contact and Friction: Formulation, Approach and Applications,'' Wear, **220**, pp. 113–140.
[2] Griffin, J. H., 1990, ''A Review of Friction Damping of Turbine Blade Vibration,'' Int. J. Turbo and Jet Engines, No. **7**, pp. 297–307.
[3] Cardona, A., Coune, T., Lerusse, A., and Geradin, M., 1994, ''A Multiharmonic Method for Non-Linear Vibration Analysis,'' Int. J. Numer. Methods Eng., **37**, pp. 1593–1608.
[4] Griffin, J. H., 1980, ''Friction Damping of Resonant Stresses in Gas Turbine Engine Airfoils,'' ASME J. Eng. Power, **102**, pp. 329–333.
[5] Sanliturk, K. Y., Imregun, M., and Ewins, D. J., 1997, ''Harmonic Balance Vibration Analysis of Turbine Blades With Friction Dampers,'' ASME J. Vibr. Acoust., **119**, pp. 96–103.
[6] Sextro, W., 1996, ''The Calculation of the Forced Response of Shrouded Blades with Friction Contacts and Its Experimental Verification,'' Proc., 2nd European Nonlinear Oscillation Conference, Prague, September pp. 9–13.
[7] Csaba, Gabor, ''Modelling of a Microslip Friction Damper Subjected to Translation and Rotation,'' ASME Paper No. 99-GT-149.
[8] Pierre, C., Ferri, A. A., and Dowell, E. H., 1985, ''Multi-Harmonic Analysis of Dry Friction Damped Systems Using an Incremental Harmonic Balance Method,'' ASME J. Appl. Mech., **52**, pp. 958–964.
[9] Cameron, T. M., and Griffin, J. H., 1989, ''An Alternating Frequency/Time Domain Method for Calculating Steady Response of Nonlinear Dynamic Systems,'' ASME J. Appl. Mech., **56**, pp. 149–154.
[10] Berthillier, M., Dupont, C., Mondal, R., and Barrau, R. R., 1998, ''Blades Forced Response Analysis With Friction Dampers,'' ASME J. Vibr. Acoust., **120**, pp. 468–474.
[11] Yang, B. D., Chu, M. I., and Menq, C. H., 1998, ''Stick-Slip-Separation Analysis and Non-Linear Stiffness and Damping Characterization of Friction Contacts Having Variable Normal Load,'' J. Sound Vib., **210**(4), pp. 461–481.
[12] Chen, J. J., and Menq, C. H., 1999, ''Prediction of Periodic Response of Blades Having 3-D Nonlinear Shroud Constraints,'' ASME Paper 99-GT-289, pp. 1–9.

On the Three-Dimensional Finite Element Analysis of Dovetail Attachments

J. R. Beisheim
Development Group,
ANSYS, Inc.,
Canonsburg, PA

G. B. Sinclair
Department of Mechanical Engineering,
Louisiana State University,
Baton Rouge, LA 70803

The stress analysis of dovetail attachments presents some challenges. These stem from the high stress gradients at the edges of contact. They also stem from the nonlinearities accompanying conforming contact. Even with two-dimensional analysis, obtaining converged peak stresses is not trivial. With three-dimensional analysis, convergence can be expected to be more difficult to achieve because of the added computational costs of refinement in three dimensions. To meet these challenges, this paper describes a submodeling procedure with finite elements. The submodeling approach features bicubic surface fits to displacements for submodel boundary conditions. The approach also features a means of verifying these boundary conditions have converged; this is crucial to obtaining accurate converged peak stresses. The approach is applied to a three-dimensional test piece used to simulate a dovetail attachment. This application leads to converged three-dimensional stresses. These stresses serve to quantify the sort of increases in contact stresses in attachments due to three-dimensional effects. [DOI: 10.1115/1.1539867]

1 Introduction

1.1 Background and Motivation. Figure 1(*a*) shows half of a section through a typical dovetail blade attachment (this figure also includes a finite element grid). The disk is essentially held fixed in place while the centripetal acceleration of the spinning blade causes a force pulling the blade upward (indicated with an arrow in Fig. 1(*a*)). The blade is restrained by contact with the disk along the flat portion shown more clearly in Fig. 1(*b*). At the edges of this contact region, high stresses occur. Oscillations in these high stresses during operation can be expected to be a significant contributor to the fretting fatigue of attachments near the edges of contact. Accordingly, accurately resolving edge of contact stresses in dovetail attachments is a problem of some engineering importance.

The first difficulty in resolving these stresses stems from their magnitudes and gradients. The second difficulty in resolving these stresses stems from the nonlinearities that accompany conforming contact problems. The expanding contact regions on the blade and disk induce a geometric nonlinearity. These expanding contact regions must be carefully tracked to obtain accurate converged peak stresses. Both of these difficulties are compounded in going from a two-dimensional analysis to a three-dimensional one. In the first instance, this is because there can be higher stresses located in the ''corners'' of contact in three-dimensional analysis than those at the edges of contact in two dimensions. In the second instance, this is because determining the contact region involves the computation of an area in three-dimensional analysis rather than just the line involved in two-dimensional analysis.

On reviewing the literature that specifically addresses the stress analysis of dovetail attachments, we focus on those using finite element analysis. This is because the complexity of such configurations dictates the use of numerical methods, and because, of the numerical methods available, the finite element method is arguably the most adaptable and the most widely used in industry.

There are several papers that describe finite element analysis (FEA) of dovetail attachments. An early contribution is Boddington et al. [1], which considers two-dimensional elastic analysis. This paper explores the feasibility of implementing Amonton's law with finite elements and is successful in devising an approach for doing this. Such a capability is now available in standard codes (e.g., ANSYS [2]). Other papers that include two-dimensional elastic FEA are Kenny et al. [3], Papanikos and Meguid [4], and Meguid et al. [5]. A more recent two-dimensional elastic FEA paper is that of Sinclair et al. [6]. Even with just two-dimensional analysis, only the last paper appears to have achieved converged edge-of-contact stresses (typically to within five percent in Sinclair et al. [6]).

The ambitious task of a three-dimensional elastic analysis is included in Papanikos et al. [7]. However, no explicit convergence check is reported therein. Thus it remains an open issue to achieve converged three-dimensional stresses in dovetail attachments and thereby accurately quantify any increases in stress concentration occurring as a result of three-dimensionality.

1.2 Objective and Scope. Here then we seek to provide an approach for obtaining converged results for the three-dimensional elastic stresses occurring near the edges of contact in dovetail blade attachments. These stresses are shown to be nonsingular in [6]. However, because of the steep stress gradients present, a highly refined mesh is required at the edges of contact. One means of achieving converged peak stresses with this level of refinement using modest computing resources is *submodeling* with finite element analysis.

Submodeling involves running an initial global analysis that includes the local region with the stress concentration of interest. A subregion, or submodel, around this region of interest is broken out and analyzed separately. An example is illustrated in Fig. 1. Figure 1(*a*) shows the initial global finite element grid and Fig. 1(*b*) is a close-up of the contact region. At the edge of contact, where the peak stress occurs, the small darkened areas represent the submodel region. Figure 1(*c*) shows the coarse grid for this submodel region. ''Boundary'' conditions taken from the FEA with the initial global grid are then applied to the refined submodel grid.

In what follows, in Section 2 we outline our submodeling procedure for two-dimensional finite element analysis, and then describe how the procedure is extended to three-dimensional analysis. Key, here, is the choice of the submodel extents so that ''boundary'' condition errors are controlled, and having a means for knowing they are in fact controlled. In Section 3 we demonstrate our submodeling procedure with a three-dimensional finite

Contributed by the International Gas Turbine Institute and presented at the International Gas Turbine and Aeroengine Congress and Exhibition, Amsterdam, The Netherlands, June 3–6, 2002. Manuscript received by the IGTI October 10, 2001. Paper No. 2002-GT-30305. Review Chair: E. Benvenuti.

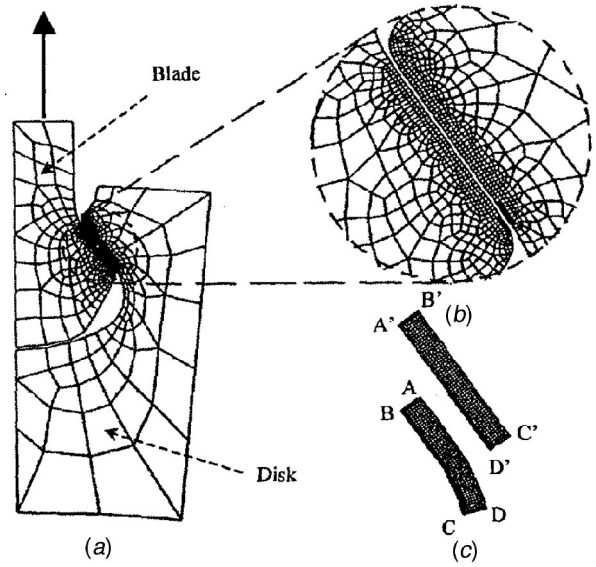

Fig. 1 Dovetail blade attachment from a gas turbine engine: (*a*) global grid, (*b*) close-up of contact region in global grid, (*c*) submodel grid

element analysis of a test piece that simulates a dovetail attachment. This application demonstrates how converged peak stresses can be obtained using our procedure. In Section 4 we close by offering some concluding remarks based on these results.

2 Submodeling Procedure

2.1 Global Analysis. To check convergence, we begin with a global analysis that is run using three systematically refined grids labeled coarse, medium, and fine. Typically elements in successive grids are formed by halving element sides.[1] In two-dimensional analysis halving element sides results in the number of elements increasing by a factor of four, while in three dimensions it results in an increase by a factor of eight. Also, in three-dimensional analysis there is usually an extra degree of freedom at each node. Consequently, it is not difficult to attempt an FEA in three dimensions wherein computational capabilities become taxed as grid refinement proceeds, even to the point of it not being possible to compute results on a fine grid. To avoid this we proceed as follows. We first estimate the maximum number of degrees of freedom that the computational facilities available can handle. Then we design a fine grid with about this number of degrees of freedom, or somewhat fewer. Thereafter, we successively coarsen this grid by combining sets of typically eight elements to furnish a medium grid, then a coarse grid. In this way we arrive at a computationally tractable set of global grids on which convergence can be checked.

Upon running the three global grids, we apply convergence checks to the desired peak stress component. The first such convergence check determines whether the peak stress is *converging*. The peak stress is judged converging if

$$|\sigma^m_{\max} - \sigma^c_{\max}| > |\sigma^f_{\max} - \sigma^m_{\max}| \tag{1}$$

where the superscripts identify the coarse, medium, and fine global grids on which the peak stress, $\sigma_{\max}$, is calculated. The second convergence check determines whether the peak stress is *converged*. The peak stress is judged converged if

$$\left|\frac{\sigma^f_{\max} - \sigma^m_{\max}}{\sigma^f_{\max}}\right| < \varepsilon_s \tag{2}$$

where ε_s is the error level sought in the analysis. For peak stress results, we view an $\varepsilon_s = 0.01$ as leading to excellent accuracy, $\varepsilon_s = 0.05$ as good, and $\varepsilon_s = 0.10$ as satisfactory. Of course, if the peak stress is judged to be converging and to have converged to within ε_s, the analysis is complete. Otherwise, we proceed with the submodeling procedure.

2.2 Two-Dimensional Submodeling. Here we first explain the submodeling procedure as used in two-dimensional analysis. This procedure largely follows that of Cormier et al. [9]. This is because the procedure in [9] has demonstrated markedly greater efficiency than other procedures reported in the literature to date.

The first step of the submodeling procedure in two dimensions is locating the boundaries of the submodel region and, as a result, establishing the size of the submodel region. Clearly, the maximum sought-after stress component has not converged; otherwise there would be no need to submodel. Away from this maximum stress location, however, it can converge. We choose distances away from the peak stress location and check that the sought-after stress component is converging in accordance with (1), and has converged as in (2). The positions closest to the maximum stress location where the sought-after stress component has converged set the extents of the submodel region.

Next, we discretize the submodel region with its own coarse, medium, and fine grids. Typically, these grids are uniform, thereby enabling completely systematic refinement. The size of the elements in the coarsest of these grids corresponds to that of the next grid in the global sequence if one were to continue to refine this sequence, and thus is smaller than the fine global grid. These submodel grids require conditions on parts of their boundaries to be taken from the global FEA. We choose to use displacements in these conditions in what follows.

After selecting and discretizing the submodel region, we check for converging displacements from the global FEA along those parts of the boundaries of the submodel interior to the global region; that is, in the example of Fig. 1, on the boundaries AB, BC, CD, and their primed counterparts. Knowing that the sought-after stress is converging at this distance away from the peak stress location and that displacements converge more rapidly than stresses,[2] it is likely that the displacements are also converging. Indeed, this more rapid convergence is the reason for choosing displacements over stresses as boundary conditions in our submodel.[3] Analogous to (1), the boundary displacements are judged *converging* if

$$|u^c_i - u^m_i| > |u^m_i - u^f_i| \tag{3}$$

at practically every boundary node. In (3), u_i represents the displacements at a given node and the superscripts continue to identify the particular grid used in their evaluation. Given the boundary displacements are judged to be converging, we continue with the submodeling procedure.

Next, we need to interpolate the converging nodal displacements. This interpolation is necessary to obtain intervening values between the nodes of the global fine grid, even for the coarsest of submodel grids. One choice of this regard is displacement shape functions, and this is the choice implemented in some standard codes (e.g., ABAQUS, ANSYS). However, while displacement shape functions are continuous at element edges, they are not continuously differentiable there. This at variance with the elastic displacement fields we are trying to replicate on the boundary. Accordingly, it is a less than ideal choice. Indeed, the use of shape functions can be shown to introduce spurious logarithmic stress singularities all along the submodel boundaries; see Sinclair and

[1]Some justification for this approach to convergence checks in stress analysis with FEA is given in Sinclair [8].

[2]See, e.g., Strang and Fix [10].

[3]Some numerical evidence of the superiority of displacements over stresses in submodel boundary conditions is given in Sinclair et al. [11].

Epps [12]. Hence, instead we use cubic splines because they are continuous and continuously differentiable throughout. This choice is thus in accord with the elastic displacements being interpolated, and also avoids log singularities (ibid.).

Using the fitted boundary displacements, we run our three submodel grids and check whether the applied submodel boundary conditions have *converged*. To determine if the displacements in the boundary conditions are converged, we must recognize and separate the two sources of error that accompany submodeling. The first source of error is *boundary condition error*. We define ε_{bc} as our estimate of this source of error by

$$\varepsilon_{bc}=\frac{\sigma_{\max}^{fbc}-\sigma_{\max}^{mbc}}{\sigma_{\max}^{fbc}} \tag{4}$$

where $\sigma_{\max}^{fbc}$ and $\sigma_{\max}^{mbc}$ are evaluated on the fine submodel grid using boundary conditions taken from the fine global grid and medium global grid, respectively. The other source of error is the *discretization error* that is inherent with FEA. We define ε_d as our estimate of this source of error by

$$\varepsilon_d=\frac{\sigma_{\max}^{fs}-\sigma_{\max}^{ms}}{\sigma_{\max}^{fs}} \tag{5}$$

where $\sigma_{\max}^{fs}$ and $\sigma_{\max}^{ms}$ are evaluated on the fine submodel grid and medium submodel grid, respectively, using boundary conditions taken from the fine global grid. With these definitions, our estimate of the total error, ε, results from simply adding both the boundary condition error and discretization error. Thus

$$\varepsilon=\varepsilon_{bc}+\varepsilon_d \tag{6}$$

With this means, two different situations arise: one when ε_{bc} and ε_d are of opposite signs and cancel each other to a degree, the other when they are of the same sign and accumulate. To ensure the magnitude of the actual total error is less than the error level sought in our analysis, we therefore take

$$\begin{aligned} &|\varepsilon_{bc}|<\varepsilon_s \quad \text{and} \quad |\varepsilon_d|<\varepsilon_s \quad \text{if } \varepsilon_{bc}\varepsilon_d<0 \\ &|\varepsilon_{bc}|<\alpha\varepsilon_s \quad \text{and} \quad |\varepsilon_d|<(1-\alpha)\varepsilon_s \quad \text{if } \varepsilon_{bc}\varepsilon_d>0 \end{aligned} \tag{7}$$

In the second of (7), α is a number between 0 and 1. Consequently, the second of (7) is a more stringent criterion than the first. In lieu of anything obviously superior, taking $\alpha=1/2$ would seem to be reasonable.

Further justification for the means of estimating the errors that accompany submodeling and details for an improved means for estimating the discretization error can be found in Beisheim and Sinclair [13].

2.3 Three-Dimensional Submodeling. In this section we explain how to implement the foregoing submodeling procedure for three-dimensional analyses. The key distinctions between using this procedure in two-dimensional and three-dimensional FEA involve the sizing of the submodel region and the interpolation of the submodel boundary conditions.

As mentioned in the previous section, choosing the submodel boundaries in two-dimensional analysis involves finding the locations where the sought-after stress component has converged. In three-dimensional analysis, these locations can result in a submodel region that is too large. That is, a submodel region that, with the computational facilities available, does not permit computation on the three grids needed for convergence checks. If this is the case, we in effect revert to the grid refinement approach described for the global region. That is, we size the submodel region so that we can in fact compute results with a discretized grid with elements of the size of the fine submodel grid (element sides 1/8 of the element sides in the fine global grid). Then we coarsen this grid by successively combining sets of eight elements to realize medium and coarse submodel grids. This is a grid sequence that is computationally tractable. Moreover, while the global analysis of the sought-after stress component has not converged at all submodel boundary locations under these circumstances, it is nonetheless quite possible that the global displacements there have converged sufficiently. This is a consequence of the more rapid convergence of displacements over stresses noted earlier.

The interpolation of the submodel boundary conditions in two dimensions involves fitting displacements on lines. In three dimensions, it involves fitting displacements across surfaces. We choose a bicubic surface because it matches the function, its first derivatives, and its cross derivative at the corner points of each interpolation region. As a consequence, it can be shown to result in a surface that is continuous with continuous first derivatives in passing from one interpolation region to the next. Thus, our bicubic surface, like the cubic spline, is continuous and continuously differentiable, as is any displacement it is trying to replicate.

One form of this bicubic interpolation is given in the Appendix, and this is the approach used here. Alternatively, a code for implementing bicubic interpolation can be found in Press et al. [14].[4] These two methods have been found to give exactly the same results with similar computational effort. Ransom and Knight [15] provide an alternative smooth interpolation scheme. In essence, they fit an elastic plate through each of the respective sets of nodal displacements. This shares with the aforementioned procedures C^1 continuity throughout the submodel boundary surfaces. It does, however, result in large matrix systems as the number of elements increases. The procedure used here has no such matrix system because the individual interpolation regions have closed-form expressions for the constants involved (see Appendix). This is thought to possibly offer some computational advantage over the approach of Ransom and Knight [15].

Irrespective of the means chosen to interpolate, it is important to preserve C^1 continuity throughout submodel boundaries. This is not only because this property is in accord with the elasticity displacements that we are attempting to replicate, but also because the absence of C^1 continuity leads to spurious logarithmic stress singularities on the submodel boundaries. For the three-dimensional case of concern here, the log singularities for in-plane extension [12] and anti-plane shear (Sinclair [16]) are both active. This is shown in Aksentian [17]. It is also possible to induce additional log singularities in the corners of surfaces that are peculiar to three-dimensional analyses (this can be shown by an analysis along the lines of Sinclair and Epps [12]).

3 Application

3.1 Description of Dovetail Attachment Test Piece. Figure 2 shows the geometry of a test piece used to simulate a dovetail attachment. Herein the blade base simulates the bottom of an actual blade including its contacting flats with a disk, while the disk segment simulates that portion of an actual disk to which a blade is attached. At the edges of contact, there are blend radii that are of the order of 5% of the blade base thickness. The applied stress, σ_0, then simulates the effects of rotation of the remainder of the blade. After this load is transferred to the disk segment, this segment must be further restrained. In practice, this is achieved by attaching the segment to the center of the disk. In this test piece, the segment is restrained by two pieces that are held fixed: an outer restraining ring shown in Fig. 2, and a platform not shown in Fig. 2. The platform is attached to the top surface of the portion of the disk segment shown in Fig. 2.

Contact is assumed to be frictionless in this initial study. Numerically this circumvents the contact elements having to iterate to police friction inequalities and thereby reduces computation time somewhat (the contact elements still have to police contact

[4]Both of these methods are well suited for the submodel boundary surfaces when eight-node brick elements are used. The use of higher-order elements can result in the need to perform some extra interpolation at the middle of element surface areas (e.g., the 20-node brick). Consistent with the use of the bicubic surface, the average of one-dimensional cubic spline interpolation in each direction should be used for these additional midsurface points.

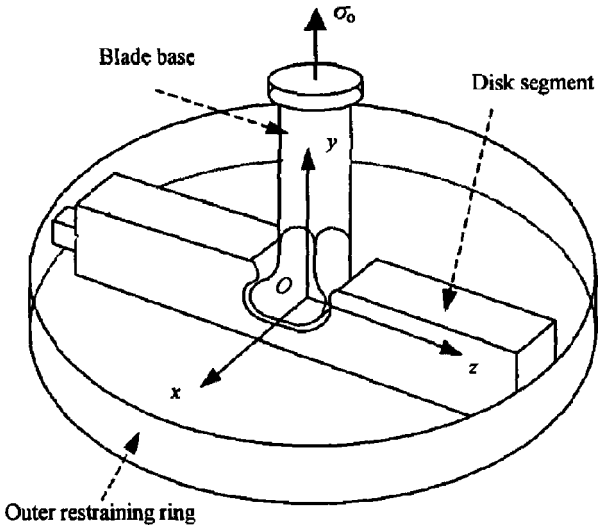

Fig. 2 Dovetail attachment test piece

inequalities to determine the extent of contact and so are still iterating to some degree). Without friction, normal contact stresses are higher because there are no shear tractions to carry some of the load (see [6]). Thus, stress gradients are higher without friction. It follows that, if our grid sequence can achieve spatial convergence without friction, the same sequence should suffice to achieve spatial convergence with friction. Ultimately, the latter case needs to be run to obtain more physically representative stresses.

To describe the geometry of the test piece more precisely, we use a rectangular Cartesian coordinate system with coordinates (x,y,z). The origin, O, of this coordinate system is located at the bottom of the blade beneath the center of the circular cross section. The y-axis is aligned with the center of the blade base, while the x and z-axes are also central. Thus the planes $x=0$ and $z=0$ are planes of symmetry with the present axial loading σ_0. This enables us to focus attention on just the quadrant of the blade base and the disk segment confined within $x \geqslant 0$ and $z \geqslant 0$. We further simplify the problem by excluding the geometry of the platform by modeling this as a rigid contact surface. Thus it only enters as a boundary condition on the top of the disk segment. We also simplify the analysis by replacing the outer ring by an effective stiffness in the z direction.

In general, then, we seek the stresses σ_x, σ_y, σ_z, τ_{xy}, τ_{xz}, τ_{yz}, and their associated displacements u, v, w, throughout the blade and disk, satisfying: the stress equations of equilibrium in the absence of body forces; the stress-displacement relations for a homogeneous and isotropic, linear elastic solid; and the following boundary conditions. Symmetry boundary conditions are applied to the surfaces at $x=0$ and $z=0$ for our quarter-symmetry model. A tensile normal traction, σ_0, is applied to the top surface of the blade base, while the shear tractions there are taken to be zero (see Fig. 2). On the surface of the disk segment where the outer ring is connected, $\sigma_z = kw$, while the shear tractions are taken to be zero. We describe how the outer ring stiffness, k, is determined in Section 3.2. With the exception of the contact surfaces to be described next, stress-free boundary conditions are applied on all other surfaces.

The contacting surfaces between the platform and the disk, and the contacting surfaces between the blade and the disk, must each comply with the following frictionless contact conditions and constraints. First, the contact conditions require that the normal stresses on the contacting surfaces be equal and the normal displacements on the contacting surfaces be equal. Second, the shear stresses must be everywhere zero in the contact region consistent with the assumed frictionless contact. Third, the contact constraints require that the normal stress be nowhere tensile inside the contact region and that there be no interpenetration outside the contact region.

In particular we seek the normalized peak contact stress normal to the contact surfaces of the blade and disk. We define the normalized peak contact stress as

$$\overline{\sigma}_{\max} = \sigma_{\max} / \sigma_0 \tag{8}$$

where $\sigma_{\max}$ is the peak contact stress normal to the contact surfaces inside the contact region.

3.2 Finite Element Analysis. Eight-node hexahedral (brick) elements are used to discretize most of the blade and disk (SOLID45, ANSYS [2]). We use low-order brick elements to facilitate interpolation with the bicubic surface when submodeling. Away from the submodel region, some higher-order tetrahedral elements are used to discretize the curved neck of the blade as they provide a better fit to the geometry (SOLID92, ANSYS [2]). We place a boundary layer of elements around the region of interest on both the blade and disk. This boundary layer has a depth of three-eighths the smallest radius of curvature of the blade, a depth that is somewhat more conservative than the value previously tested in the numerical analysis of conforming contact problems (see [6]). Inside this boundary layer, we create uniform grids of elements and systematically refine these grids by halving element sides. Outside this boundary layer we only approximately systematically refine the global grids. We do this by specifying the number of elements along the edges of the blade and disk away from the region of interest. We then use the VMESH command in ANSYS [2] to automatically mesh the rest of the region. The resulting global coarse grid is shown in Fig. 3(*a*).

To police the aforementioned contact constraints between the blade and the disk we use surface-to-surface contact elements (TARGE170 and CONTA173, ANSYS [2]). These surface elements overlay the spatial elements on the contact surfaces within the boundary layer. An important input parameter for these contact elements in ANSYS is the normal contact stiffness factor (FKN). This factor controls the stiffness of the contacting surfaces, which affects the amount of penetration of the contact surface into the target surface. We override the default value of one with a value of ten in order to help limit penetration while still maintaining good convergence of the contact algorithm in ANSYS. The total number of spatial and contact elements for each of the global grids is given in Table 1 (the number of contact elements in each global grid includes the small number of spring elements used to represent the stiffness of the outer restraining ring).

As mentioned in the previous section, we simplify our global grids by excluding the geometry of the platform and outer restraining ring. To model the restrained platform we use the same contact elements used for the contact surfaces between the blade and disk. However, we define the target surface of the platform to be rigid and use the default value for FKN. To model the outer restraining ring we use one-dimensional equivalent springs (COMBIN14, ANSYS [2]).

To calculate the stiffness of the equivalent springs, we first analyze the outer restraining ring separately. We apply a uniform traction, $\overline{\sigma_z}$, to the surface where the outer ring connects to the disk and measure the average displacement, $\overline{w}$. We then use three systematically refined grids to calculate our estimate of the stiffness, k, via $k = \overline{\sigma_z}/\overline{w}$. The coarse grid in this sequence is shown in Fig. 3(*c*). The total numbers of elements used for the outer ring analysis are given in Table 1 (no contact elements are used in this analysis). Effectively, we therefore have an outer submodel that seeks to furnish the k required for the outer-ring boundary conditions in our global analysis.

We find that the stiffness determined from our outer ring analysis is converging and does converge, so that no further analysis of the outer ring is needed. On the other hand, we find that the

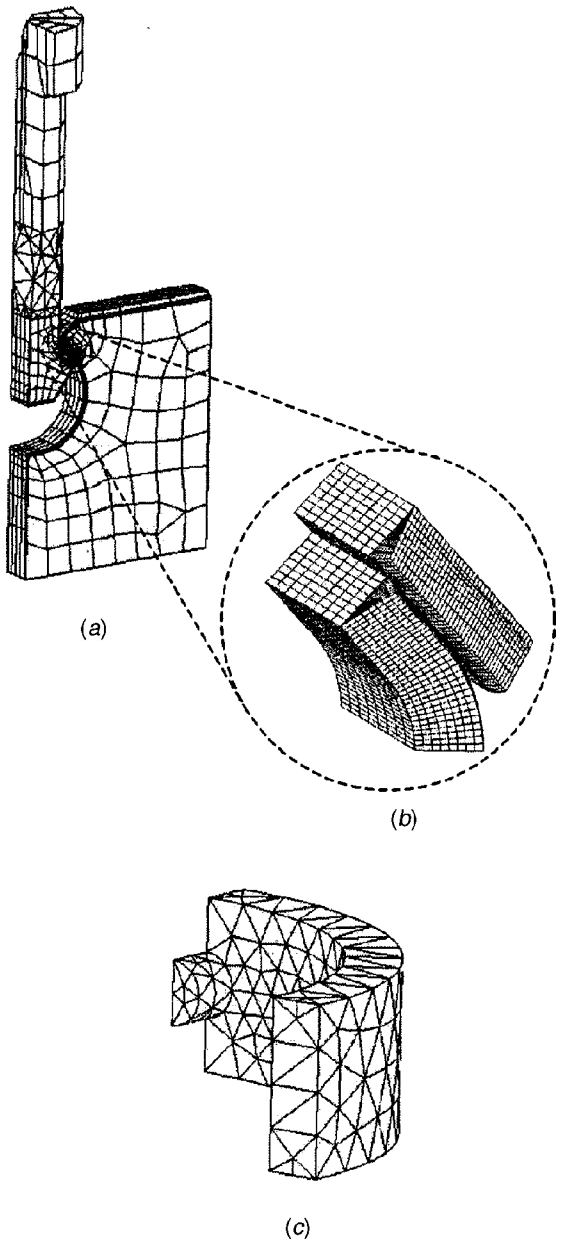

Fig. 3 Finite element grids for dovetail attachment test piece: (*a*) global coarse grid, (*b*) submodel coarse grid, (*c*) outer restraining ring coarse grid

normalized peak contact stress, while converging, has not yet converged. Therefore, we continue by using the submodeling procedure described in Sections 2.2 and 2.3.

To start the submodeling procedure we must first choose the boundaries of the submodel region. We need to choose boundaries far enough from the location of the peak contact stress to have converged displacement boundary conditions, but close enough to keep the number of degrees of freedom within the limits of our available computational resources. Plotting some contact stresses from each global grid along lines in three directions from the peak stress gives us an idea of where the boundary displacements are likely to be converged. We then break out our submodel along the uniform grid lines and check that we can obtain three refined grids inside this submodel region that are computationally tractable. Again, our submodel coarse grid (see Fig. 3(*b*)) has element sizes that would correspond to a global superfine grid had we refined the global fine grid. Also, as with the global grids inside the boundary layer, we systematically refine the submodel grids by halving element sides. Thus, we have three submodel grids that contain the number of spatial and contact elements shown in the bottom of Table 1. By way of comparison, a global grid with the same degree of refinement as the fine submodel grid could be expected to have about forty million elements. Such a grid would certainly be beyond our present computational capabilities.

Table 1 Number of elements for each finite element grid

Grid	Spatial	Contact	Total
Global Coarse	2,127	487	2,614
Medium	14,990	1,943	16,933
Fine	108,870	7,765	116,635
Outer Ring Coarse	540	0	540
Medium	4,140	0	4,140
Fine	34,147	0	34,147
Submodel Coarse	9,216	1,152	10,368
Medium	73,728	4,608	78,336
Fine	589,824	18,432	608,256

Table 2 Normalized stiffness results for outer restraining ring

Grid	Stiffness, $\bar{k}$	Difference	Error (%)
Outer Ring Coarse	1.1874E-2		
Medium	1.1631E-2	−2.43E-4	−2.1
Fine	1.1602E-2	−2.90E-5	−0.2

3.3 Results. We first examine the results of the analysis involving the outer restraining ring to check for convergence. We define a normalized stiffness as

$$\bar{k} = \frac{kL}{E} \tag{9}$$

where L is the length of the cylindrical segment that connects the outer restraining ring to the disk segment and E is the Young's modulus of the outer restraining ring. The results from the analysis of the outer restraining ring for the normalized stiffness values are listed in Table 2.

Error estimates computed in Table 2 are made by taking differences between successive grid values for $\bar{k}$, then dividing by the value for the latter $\bar{k}$ in the difference (the analog of (5)). Clearly results are consistent with converging estimates because differences are decreasing (cf. (1)). Results are also consistent with an estimate that has converged to within 1% (see error estimates in Table 2). This level of accuracy is judged to be sufficient for present purposes.

After finding the stiffness of the outer restraining ring to be converged, we run our three global grids and proceed to check the stress results for convergence. We find that the normalized peak contact stress is converging on our sequence of global grids. This is reflected in the decreasing magnitudes of differences shown in Table 3, and the consequent compliance with (1). However, discretization errors given in Table 3 show that they have not yet converged sufficiently on the global grids to be even satisfactory (these estimates are for successive pairs of grids using the analog of (5)). Thus we proceed with a submodel.

Table 3 Normalized peak contact stress results

Grid	$\bar{\sigma}_{\max}$	Difference	ε_d(percent)
Global Coarse	−16.2		
Medium	−25.7	−9.5	37.0
Fine	−30.7	−5.0	16.3
Submodel Coarse	−37.9		
Medium	−47.9	−10.0	20.9
Fine	−51.3	−3.4	6.6

Table 4 Boundary condition errors

Grid	$\bar{\sigma}^{mbc}_{\max}$	$\bar{\sigma}^{fbc}_{\max}$	ε_{bc}
Submodel Coarse	−39.9	−37.9	−5.3
Medium	−50.7	−47.9	−5.8
Fine	−53.3	−51.3	−3.9

The normalized peak contact stress results are also checked for convergence on our sequence of three submodel grids with boundary conditions taken from the global fine grid. We see in Table 3 that differences are decreasing on the submodel grid sequence so that we have convergence in the sense of (1). Note, though, that (1) is not complied with between the global and submodel grids. This sort of somewhat erratic convergence is not uncommon in contact problems as the contact extent is located more precisely with each successive grid. Table 3 shows the discretization error to have converged with an estimated error of 6.6%. This is satisfactory in itself: It remains to determine the boundary condition error to conclude whether our total estimate of (6) is satisfactory.

In completing our submodeling procedure, we must check for convergence in the boundary conditions applied to the submodel. We perform this check by running the sequence of three submodel grids using boundary conditions taken from the global medium

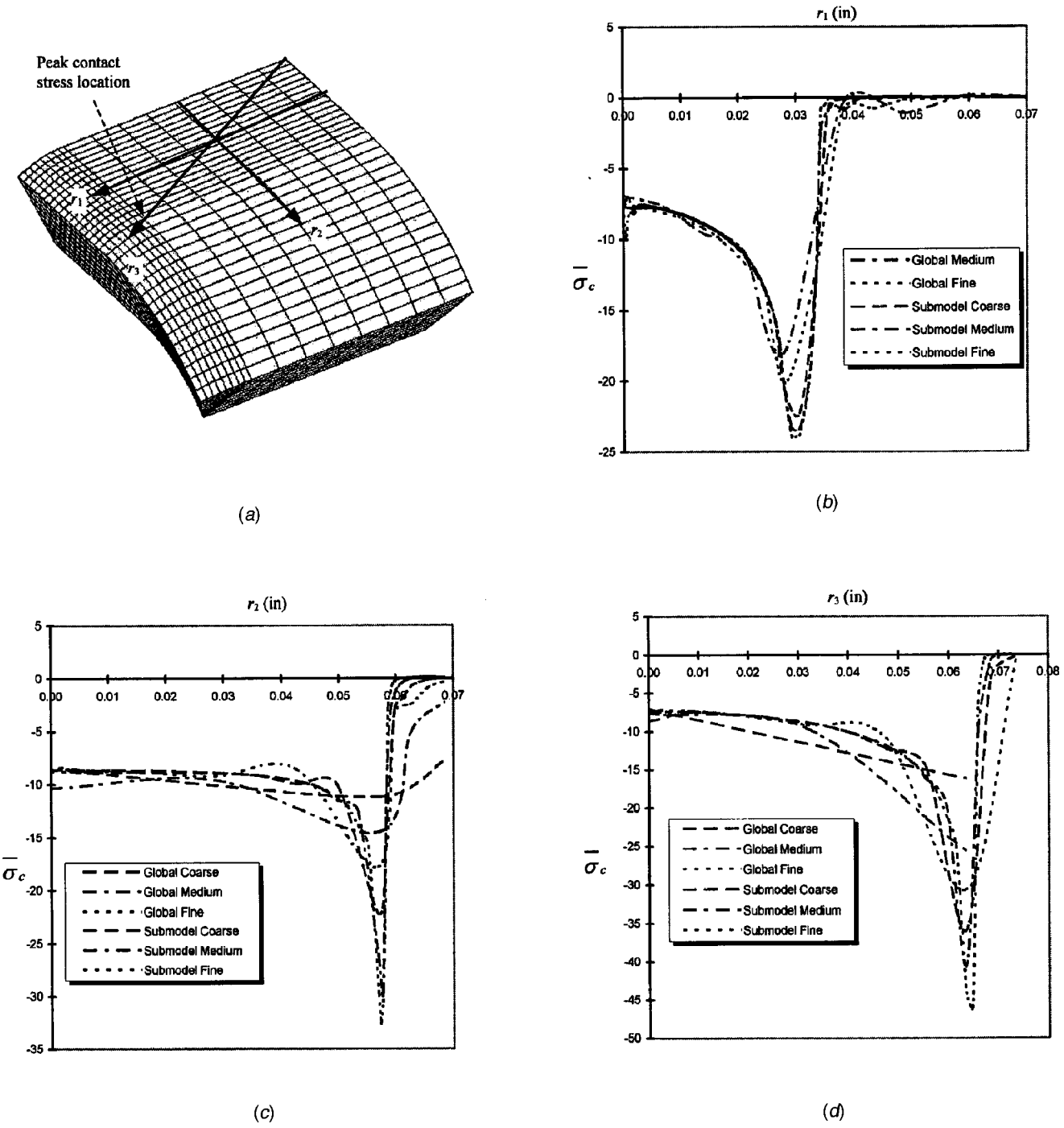

Fig. 4 Normalized contact stress results: (*a*) blade segment with lines along which stresses are taken, (*b*) contact stresses straight across the blade (r_1), (*c*) contact stresses down the blade (r_2), (*d*) contact stresses diagonally across the blade (r_3)

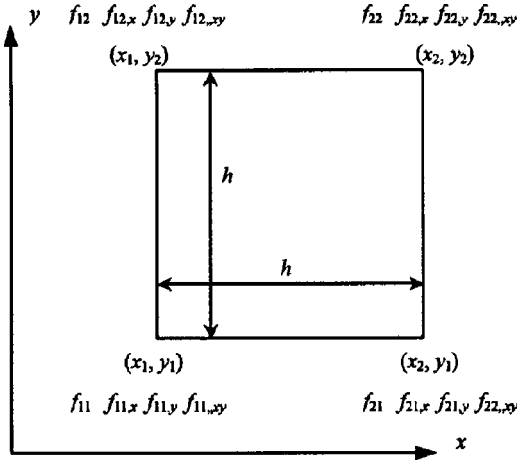

Fig. 5 Representative region for interpolation with bicubic surface

grid and comparing these results with those found using boundary conditions taken from the global fine grid. The results for peak normalized contact stress for each case are given in Table 4. We can see in Table 4 that the boundary condition error has converged to −3.9%. Thus the results for the discretization error and the boundary condition error offset each other, as in the first of (7). Our estimate for the total error in this problem is then 2.7%, which is actually within our good level of accuracy of 5%.

To demonstrate the significance of three-dimensional effects on the normalized peak contact stress, we provide the following plots in Fig. 4. Figure 4(*a*) shows the lines along which the normalized contact stresses, $\overline{\sigma_c}$, are plotted in Figs. 4(*b*), (*c*), and (*d*), and their associated radial coordinates r_1, r_2, and r_3, which have units of inches. We define the normalized contact stress as

$$\overline{\sigma_c} = \sigma_c / \sigma_0 \tag{10}$$

where σ_c is the contact stress at the contact surfaces along the lines shown in Fig. 4(*a*). Figures 4(*b*) and (*c*) represent plots of stresses that might be judged two-dimensional in nature. Figure 4(*d*) represents a plot of stresses that are truly three-dimensional in nature. The results for the normalized peak contact stress in three-dimensions are approximately 1.6 times the results for the normalized peak contact stress in two dimensions. These higher stresses demonstrate why three-dimensional analysis is important if the true peak contact stress is to be found.

This sort of increase in contact stress in corners can be found in other contact problems. For example, a frictionless, flat, square, rigid punch acting on an elastic half-space. Herein, if the stress is averaged over the last fourteen percent near the edge away from the corner, the stress concentration factor over the stress in the middle is 3.6, whereas if the same average is performed in the corner the corresponding factor is 7.6 (see Brothers [18]). Thus, three-dimensional effects increase stresses here by a factor of 2.1. These sorts of increases can be expected to persist to a degree when the punch is no longer rigid nor has a sharp corner, as here. Moreover, introducing friction does not remove these effects (see, e.g., [18]). Hence, the increase in stresses due to three-dimensional effects found here can be expected to persist when friction is ultimately introduced.

4 Concluding Remarks

Three-dimensional analysis is necessary to obtain true edge-of-contact stresses in dovetail blade attachments because two-dimensional analysis can significantly underestimate the true peak stress at the edge of contact. Three-dimensional contact analyses are generally too difficult to solve analytically. Finite element analysis is then a natural recourse. However, even with FEA, obtaining accurate 3-D stresses in dovetail attachments is not a trivial task. This is because the application of the requisite convergence checks can be computationally prohibitive. With the submodeling approach described here, these computational difficulties can be overcome, and good converged estimates of contact stresses obtained in return for reasonable levels of computational effort.

Acknowledgments

We are most grateful to General Electric Aircraft Engines of Cincinnati for providing the funding for this research. We also appreciate being furnished specifications for the dovetail test piece application by Pratt & Whitney. In addition, we are grateful to ANSYS for providing access to their software which is used exclusively throughout.

Appendix

Here we provide details on the bicubic interpolation used to interpolate the displacements on the boundaries of the submodel. The function f for interpolating on the square region in Fig. 5 is given by

$$\begin{aligned} f = {} & \frac{f_{11}}{h^2}(x_2-x)(y_2-y) + \frac{f_{21}}{h^2}(x-x_1)(y_2-y) + \frac{f_{12}}{h^2}(x_2-x)(y \\ & -y_1) + \frac{f_{22}}{h^2}(x-x_1)(y-y_1) + c_1(x-x_1)(x_2-x)^2(y_2-y) \\ & + c_2(x-x_1)^2(x_2-x)(y_2-y) + c_3(x-x_1)(x_2-x)^2(y-y_1) \\ & + c_4(x-x_1)^2(x_2-x)(y-y_1) + c_5(x_2-x)(y-y_1)(y_2-y)^2 \\ & + c_6(x_2-x)(y-y_1)^2(y_2-y) + c_7(x-x_1)(y-y_1)(y_2-y)^2 \\ & + c_8(x-x_1)(y-y_1)^2(y_2-y) + c_9(x_2-x)^2(y_2-y)^2(x-x_1) \\ & \times (y-y_1) + c_{10}(x-x_1)^2(y_2-y)^2(x_2-x)(y-y_1) \\ & + c_{11}(x_2-x)^2(y-y_1)^2(x-x_1)(y_2-y) + c_{12}(x-x_1)^2(y-y_1)^2 \\ & \times (x_2-x)(y_2-y) \end{aligned}$$

Here

$$c_1 = \frac{1}{h^3}\left[f_{11,x} + \frac{1}{h}(f_{11} - f_{21}) \right]$$

$$c_2 = \frac{-1}{h^3}\left[f_{21,x} + \frac{1}{h}(f_{11} - f_{21}) \right]$$

$$c_3 = \frac{1}{h^3}\left[f_{12,x} + \frac{1}{h}(f_{12} - f_{22}) \right]$$

$$c_4 = \frac{-1}{h^3}\left[f_{22,x} + \frac{1}{h}(f_{12} - f_{22}) \right]$$

$$c_5 = \frac{1}{h^3}\left[f_{11,y} + \frac{1}{h}(f_{11} - f_{12}) \right]$$

$$c_6 = \frac{-1}{h^3}\left[f_{12,y} + \frac{1}{h}(f_{11} - f_{12}) \right]$$

$$c_7 = \frac{1}{h^3}\left[f_{21,y} + \frac{1}{h}(f_{21} - f_{22}) \right]$$

$$c_8 = \frac{-1}{h^3}\left[f_{22,y} + \frac{1}{h}(f_{21} - f_{22}) \right]$$

$$c_9=\frac{1}{h^4}\left[f_{11,,xy}+\frac{1}{h}(f_{11,x}-f_{12,x}-f_{21,y}+f_{11,y})+\frac{1}{h^2}(f_{11}-f_{12}-f_{21}+f_{22})\right]$$

$$c_{10}=\frac{-1}{h^4}\left[f_{21,,xy}+\frac{1}{h}(f_{21,x}-f_{22,x}+f_{11,y}-f_{21,y})+\frac{1}{h^2}(f_{11}-f_{12}-f_{21}+f_{22})\right]$$

$$c_{11}=\frac{-1}{h^4}\left[f_{12,,xy}+\frac{1}{h}(-f_{12,x}+f_{11,x}-f_{22,y}+f_{12,y})+\frac{1}{h^2}(f_{11}-f_{12}-f_{21}+f_{22})\right]$$

$$c_{12}=\frac{1}{h^4}\left[f_{22,,xy}+\frac{1}{h}(-f_{22,x}+f_{21,x}+f_{12,y}-f_{22,y})+\frac{1}{h^2}(f_{11}-f_{12}-f_{21}+f_{22})\right]$$

and a comma preceding a subscript denotes differentiation with respect to that subscript, e.g., $f_{11,x}=\partial f/\partial x|_{x_1,y_1}$.

References

[1] Boddington, P. H. B., Chen, K., and Ruiz, C., 1985, ''The Numerical Analysis of Dovetail Joints,'' Comput. Struct., **20**, pp. 731–735.

[2] ANSYS personnel, 1998, *ANSYS Advanced Analysis Techniques*, Revision 5.5, ANSYS Inc., Canonsburg, PA.

[3] Kenny, B., Patterson, E. A., Said, M., and Aradhya, K. S. S., 1991, ''Contact Stress Distributions in a Turbine Disk Dovetail Type Joint—A Comparison of Photoelastic and Finite Element Results,'' Strain, **27**, pp. 21–24.

[4] Papanikos, P., and Meguid, S. A., 1994, ''Theoretical and Experimental Studies of Fretting-Initiated Fatigue Failure of Aeroengine Compressor Discs,'' Fatigue Fract. Eng. Mater. Struct., **17**, pp. 539–550.

[5] Meguid, S. A., Refaat, M. H., and Papanikos, P., 1996, ''Theoretical and Experimental Studies of Structural Integrity of Dovetail Joints in Aeroengine Discs,'' J. Mater. Process. Technol., **56**, pp. 668–677.

[6] Sinclair, G. B., Cormier, N. G., Griffin, J. H., and Meda, G., 2002, ''Contact Stresses in Dovetail Attachments: Finite Element Modeling,'' ASME J. Eng. Gas Turbines Power, **124**, pp. 182–189.

[7] Papanikos, P., Meguid, S. A., and Stjepanovic, Z., 1998, ''Three-Dimensional Nonlinear Finite Element Analysis of Dovetail Joints in Aeroengine Discs,'' Finite Elem. Anal. Design, **29**, pp. 173–186.

[8] Sinclair, G. B., 1998, ''FEA of Singular Elasticity Problems,'' *Proc., Eighth International ANSYS Conference*, Pittsburgh, PA, **1**, pp. 225–236.

[9] Cormier, N. G., Smallwood, B. S., Sinclair, G. B., and Meda, G., 1999, ''Aggressive Submodelling of Stress Concentrations,'' Int. J. Numer. Methods Eng., **46**, pp. 889–909.

[10] Strang, W. G., and Fix, G. J., 1973, *An Analysis of the Finite Element Method*, Prentice-Hall, Inc., Englewood Cliffs, NJ.

[11] Sinclair, G. B., Beisheim, J. R., Epps, B. P., and Pollice, S. L., 2000, ''Towards Improved Submodeling of Stress Concentrations,'' *Proc., Ninth International ANSYS Conference*, Pittsburgh, PA, CD-ROM.

[12] Sinclair, G. B., and Epps, B. P., 2002, ''On the Logarithmic Stress Singularities Induced by the Use of Displacement Shape Functions in Boundary Conditions in Submodelling,'' Commun. Numer. Methods. Eng., **18**, pp. 121–130.

[13] Beisheim, J. R., and Sinclair, G. B., 2001, ''Improved Control of Boundary Condition Error in Submodeling,'' Report SM 1.01, Dept. of Mechanical Engineering, Louisiana State University, Baton Rouge, LA.

[14] Press, W. H., Teukolsky, S. A., Vetterling, W. T., and Flannery, B. P., 1992, *Numerical Recipes in C*, Cambridge University Press, New York, NY.

[15] Ransom, J. B., and Knight, Jr., N. F., 1990, ''Global/Local Stress Analysis of Composite Panels,'' Comput. Struct., **37**, pp. 375–395.

[16] Sinclair, G. B., 2000, ''Logarithmic Stress Singularities in Two-Dimensional and Three-Dimensional Elasticity,'' *Proc., Twentieth Southeastern Conference of Theoretical and Applied Mechanics*, Callaway Gardens, GA, pp. SM94.1–8.

[17] Aksentian, O. K., 1967, ''Singularities of the Stress-Strain State of a Plate in the Neighborhood of an Edge,'' J. Applied Mathematics, **37**, pp. 193–202.

[18] Brothers, P. W., 1976, ''The Rigid Rectangular Punch on the Elastic Half-Space,'' Master's thesis, University of Auckland, Auckland, New Zealand.

CFD Optimization of Cooling Air Offtake Passages Within Rotor Cavities

Colin Young

Guy D. Snowsill

Rolls-Royce plc,
Derby, DE24 8BJ England

In modern gas turbine engines, up to 20% of the core airflow is bled off from various compressor stages to facilitate internal cooling, bearing chamber, and rim sealing, as well as axial load management. As this secondary airflow makes no direct contribution to engine thrust, there are strong economic incentives to reduce the quantity and quality of offtake air and maximize its effective use. Secondary airflows are commonly bled off via circular drillings in the compressor rotor, thereby augmenting their swirl velocity. This results in the creation of vortices within the rotor cavity and strong radial pressure gradients opposing inflow. In the present work the relative performance of a series of noncircular offtake passages has been assessed using CFD techniques. The results of this work demonstrate the degree of control that may be exercized over swirl uptake, which can be used to suppress the creation of vortices in rotor cavities.
[DOI: 10.1115/1.1556405]

Keywords: CFD, Modeling, Offtake Passages, Optimization

Introduction and Background

It is a common requirement in secondary air systems to bleed air from part way through a compressor. Such bleeds are required to provide ventilation flows for the rotor and are often a dominant element in defining rotor end load. The difficulty with any inward flow is that conservation of angular momentum causes any initial swirl to increase as the air flows inwards, with a resulting high-pressure loss.

The primary aim of previous investigations into this area of gas turbine technology has focused on evaluating the flow losses that occur in rotating passages and cavities, e.g., reference [1]. However, it is clear that an appreciation of the mechanisms underlying swirl uptake is fundamental to the understanding of this flow behavior, which is an area that to the authors' knowledge appears to have attracted little attention to date.

Figure 1 shows a typical offtake arrangement on an aero engine IP compressor, in which the air from the main annulus passes into the rotor cavity via a set of drillings provided around the circumference of the stator well. In passing through the offtake passage, swirl is imparted to the bleed air resulting in the creation of a vortex in the rotor cavity. The presence of this vortex has the undesired effect of opposing, and therefore substantially reducing, the flow of secondary air through the system. In addition, the system pressure drop associated with the vortex flow limits the scope for exercizing end-load management and may necessitate the use of higher-pressure compressor bleed.

It is clear from the foregoing discussion that considerable benefit would accrue from the use of offtake passages that are shaped in such a way as to reduce the level of swirl uptake experienced by the bleed air. For reasons of economy and manufacturing convenience, these offtake passages tend to be circular in cross section; however, to date little consideration has been given to whether this represents the most appropriate geometry when considered in terms of overall engine cost and performance.

In the present work, computational fluid dynamics (CFD) techniques have been used to assess the degree of swirl uptake that occurs in air bled off from a typical IP compressor stage via a passage of circular cross section. In addition, the flow through two alternative offtake passage cross sections has been simulated, in which the predicted swirl uptake is substantially reduced. While it is recognized that there would be a cost penalty associated with the adoption of noncircular offtake passage cross sections, there is strong evidence to suggest that these costs can be more than offset by the improvements to secondary air system and end load management effectiveness.

Contributed by the International Gas Turbine Institute and presented at the International Gas Turbine and Aeroengine Congress and Exhibition, Amsterdam, The Netherlands, June 3–6, 2002. Manuscript received by the IGTI January 23, 2002. Paper No. 2002-GT-30480. Review Chair: E. Benvenuti.

CFD Model Setup—Current Offtake Design

It can be seen from Fig. 1 that the complete IP compressor offtake flow path is quite extensive, whereas for the purposes of this investigation only the region in the vicinity of the offtake cavity is of direct interest. In recognition of this, a CFD model of the IP compressor offtake flow path was set up which was bounded by the stator well and the IP shaft in the radial direction and the offtake cavity as well as the adjacent neighboring cavities in the axial direction. In the tangential direction, a single $\sim$2.4 deg pitch of the 152 offtake passages was represented, thereby allowing cyclic boundary conditions to be imposed to simulate the influence of the remainder of the physical domain.

Using the approximations described in the foregoing section, the model geometry was created and meshed using the ICEM DDN CAD [2] and Hexa mesh generation packages [3], which are shown in Figs. 2 and 3, respectively.

The thickness of the Ekman layers within the rotor cavity were estimated using a momentum-integral method [4–6] and were found to be about $\sim$1 mm thick. This approach allowed a suitable near-wall mesh spacing to be established, as defined in reference [7], before embarking on the mesh generation activity. By adopting this approach the need for remeshing/adaption to achieve acceptable nondimensional near-wall distances ($y+$) was significantly reduced. The resulting calculational mesh is illustrated in Fig. 3 and consisted of 576,318 hexahedral cells.

It will be noted that with the exception of the stator surface, all of the solid boundaries represented in the model rotate at the IP rotor speed of 884 rad/s. In order to account for this, the flow was solved relative to a reference frame attached to the IP rotor. Based on the cavity outer radius of 0.330 m, the rotational Reynolds number for this flow was evaluated to be $\sim 1\times 10^7$.

The flow within the cavity model was simulated using the Fluent flow modelling software suite [8]. The boundary conditions

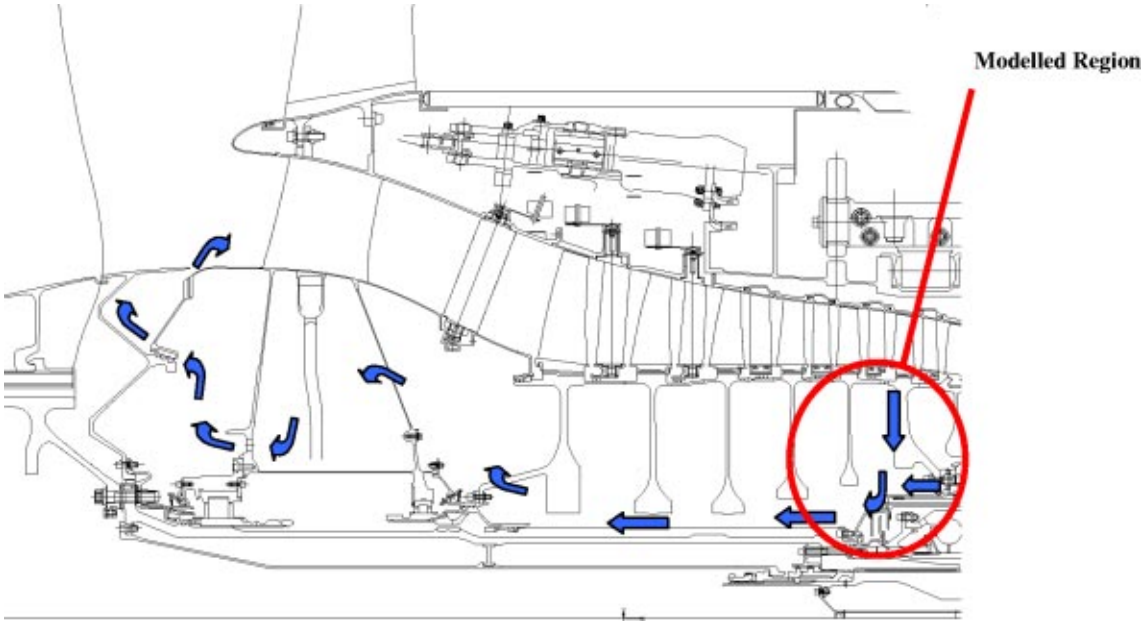

Fig. 1 Schematic diagram of a typical IP compressor offtake flow path

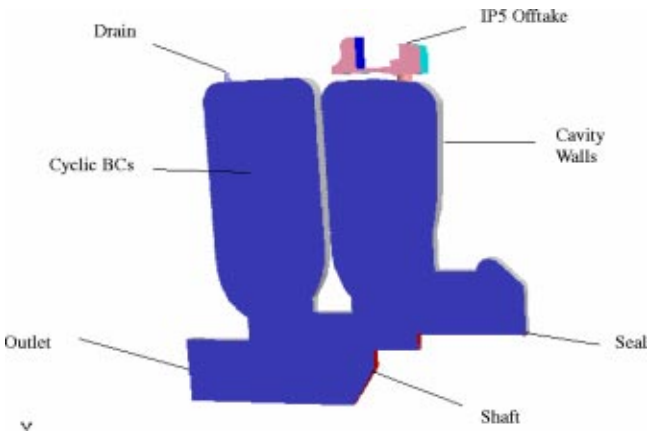

Fig. 2 Modeled region of the IP5 offtake

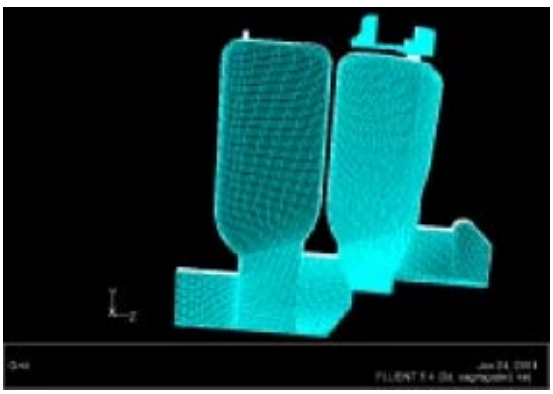

Fig. 3 Basic calculational mesh

applied to the model were based on data obtained from main annulus CFD and air system network models and are summarized in Table 1.

Although the actual model boundaries were assumed to be adiabatic, thermal effects within the flow due to viscous heating were included via solution of the energy equation. In addition, compressibility effects were included by representing the offtake air as an ideal gas, thereby providing a coupling between the energy, momentum and continuity equations through the local fluid properties (ρ, μ, C_p, and K). The effects of turbulence in the flow were represented in this application using the k-ε model [9] and the logarithmic law of the wall [10].

Results of Offtake Simulation

The basic IP compressor offtake model described above was solved using the segregated implicit solution procedure, during which the moment coefficient history was monitored as shown in Fig. 4.

The slow convergence behavior exhibited by strongly rotating flows of this type is evident from Fig. 4. The abrupt change in moment coefficient at around 5000 iterations corresponds to the changeover from the constant density to ideal gas representation. In particular, it can be seen from this convergence history that the moment coefficient increases in a near-linear manner from iteration 2000 for approximately 18,000 iterations before finally leveling off after a total of ~35,000 iterations.

It is informative to investigate the rate at which swirl uptake occurs within the offtake passage. In particular, were it to be found that the offtake flow had already attained a high degree of swirl prior to entering the offtake passages, there could be little expectation of reducing this swirl by simply changing the passage

Table 1 CFD model boundary condition data

Boundary	Boundary condition definition	Value
Inlet	Mass flow and total temperature	$m_{in}=0.003$ kg/s, $T_{tot}=506.9$ K
Interstage recirc.	Gage static pressure	$P_{static}=417.37$ kPa
Seal	Velocity vector and total temperature	$V_{in}=5.25$ m/s, $T_{tot}=620$ K
Drain	Gage static pressure	$P_{static}=329.42$ kPa
Outlet	Gage static pressure	$P_{static}=0$ kPa
Operating pressure	Pressure	460.0 kPa

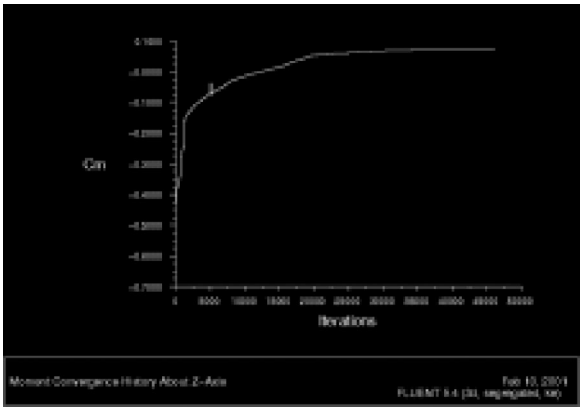

Fig. 4 Typical moment coefficient history

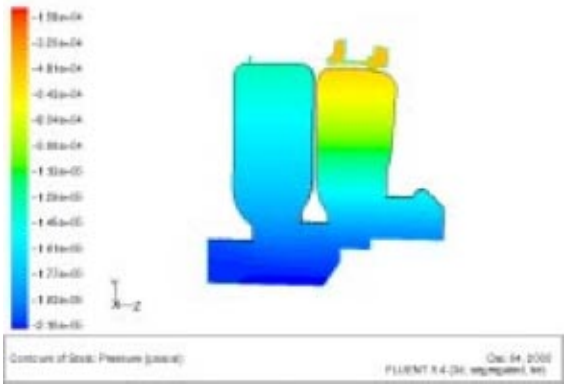

Fig. 6 Static pressure contour plot

cross section. The model predictions of mass averaged swirl coefficient (C_s) at a series of planes down the ~3 mm length of the passage are presented in Fig. 5.

As can be seen from Fig. 5, the change in swirl coefficient within the offtake passage is indeed significant, ranging from 0.41 to 0.93 in the vicinity of the inlet and outlet planes, respectively. Because the degree of swirl uptake within the passage itself is significant, these results suggest that there is some potential to design out swirl uptake. The results presented in Fig. 5 are also of interest as they provide insight into the rate of swirl uptake that takes place as the flow passes through the offtake passage. In particular, these results indicate that 70% of the total increase in swirl experienced by the fluid within the passage is taken up in the first millimetre of the passage length. Similarly the model predictions indicate that 94% of the total swirl uptake occurs within the first 2 mm of passage length.

Based on these results, it would be necessary to halve the length of the offtake passage (or rotor wall thickness) in order to achieve an appreciable reduction in swirl uptake with the current offtake cross section. However, it is clear that the introduction of a feature of this sort would have serious structural implications. On the other hand, the model predictions suggest that less radical reductions in offtake passage length/rotor wall thickness, e.g., 0.5 mm, would be totally ineffective.

The static pressure and velocity magnitude field predictions obtained using the model are presented, for a plane coincident with the offtake centreline, in the form of contour plots in Figs. 6 and 7.

As one might have expected for the case of a strongly rotating flow of this sort, the only significant pressure gradients occur in the radial direction over most of the solution domain. The only area in which axial pressure gradients are appreciable is in the vicinity of the modelled outlet plane, which is largely attributable to the presence of inflow across part of this boundary. Clearly this feature of the modelled flow is undesirable, however subsequent investigations have been carried out to confirm that this feature has minimal influence on the offtake cavity flow behavior.

In the velocity magnitude contour plot presented in Fig. 7, the jet emanating from the offtake passage is visible. It can be seen that the fluid velocity increases as it spirals inwards within the offtake cavity, and then decelerates as it encounters the lower velocity fluid emanating from the seal and in the region of the shaft surface.

It is also informative to consider the velocity predictions within the actual offtake passage itself. Tangential and radial velocity contours are presented on an axial slice through the model in Figs. 8 and 9, respectively. The model predictions again exhibit the aforementioned extremely rapid uptake of swirl within the passage. It can also be seen from Fig. 8 that the tangential velocity tends to be somewhat larger at the leading edge of the offtake passage than at the trailing edge. The reason for the increased tangential velocity in the region of the leading edge of the passage becomes clearer when this result is considered in conjunction with the corresponding radial velocity contours. As can be seen from Fig. 9, the model predicts the presence of positive, i.e., radially outward, velocity at the leading edge of the offtake passage, whereas the corresponding velocity predictions are negative, i.e., inward, at the trailing edge of the passage.

Thus, at the trailing edge of the offtake, the passage wall rotation forces the offtake flow onto its surface, locally thinning the boundary layer. The largest radially inward velocities occur in this region which result in correspondingly low residence time and hence swirl uptake in the passage. Conversely, at the leading edge of the passage, relative rotation tends to make the fluid separate from the wall, giving rise to the positive, radially outward velocity

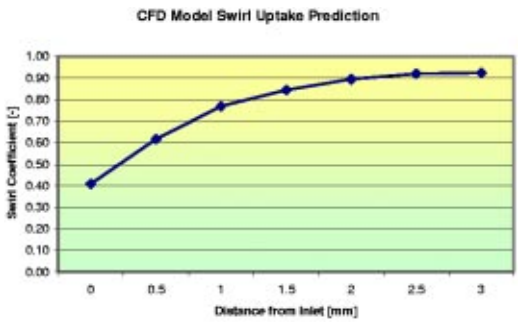

Fig. 5 Variation of offtake swirl coefficient

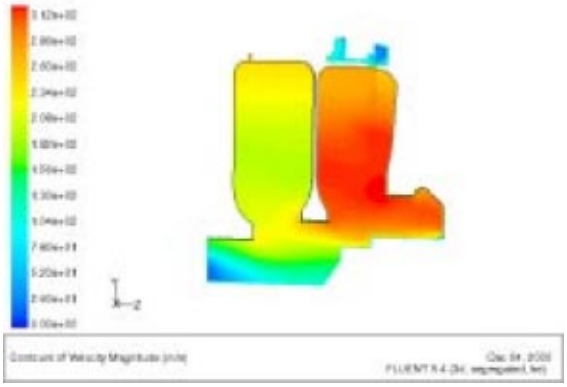

Fig. 7 Velocity magnitude contour plot

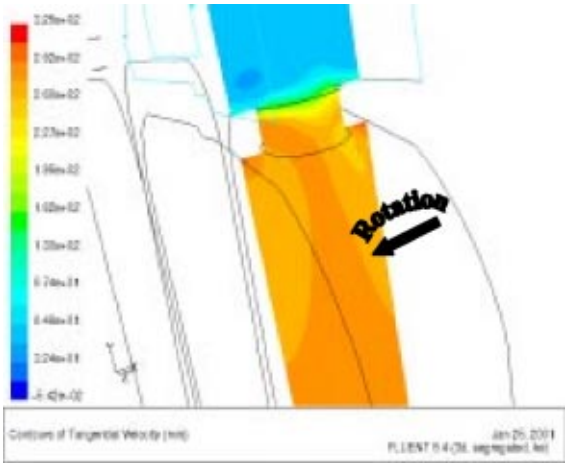

Fig. 8 Tangential velocity contours

components. This tends to transport swirling fluid from the outlet end of the offtake passage—and from within the cavity itself—outwards towards the passage inlet.

It is clear from this that the presence of this recirculation within the offtake passage is quite influential in terms of determining the level of swirl that exists in the vicinity of the offtake passage inlet. Indeed this effect will also tend to decouple the state of the flow within the passage from the more slowly swirling fluid within the stator well region.

In an attempt to verify/corroborate these results, the aforementioned integral momentum cavity mode [4–6] was used to simulate the flow within a cavity with the leading dimensions of the offtake cavity. Using this model, the offtake cavity pressure difference was estimated for a range of values of inlet swirl coefficient. The results obtained are presented graphically in Fig. 10, with the CFD model result superimposed on the graph.

The graphical data presented in Fig. 10 are of interest for two reasons. Firstly, the results exhibit good agreement between the two models, providing confidence that these two independent solutions are capturing the physics of this complex flow. Secondly, these results quantify the reduction in the rotor cavity pressure difference that could be achieved by reducing the swirl coefficient of the offtake flow at inlet to the cavity. For example, it can be seen from these data that the current level of the cavity pressure difference (~138 kPa) could be halved by reducing the inlet swirl coefficient from the current value of 0.93 to ~0.6.

A posteriori checks of near-wall cell distances confirmed that the near-wall $y+$ values lay within a range having a minimum of ~40 and a maximum of 90. In addition mesh sensitivity studies

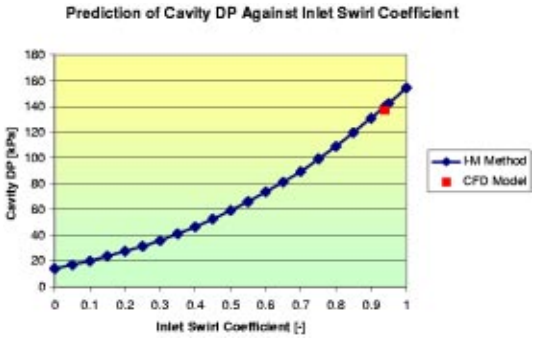

Fig. 10 Comparison of cavity pressure difference predictions

were undertaken using meshes consisting of approximately 250,000 and 850,000 hexahedral cells. Comparison of the results on the base and fine meshes exhibited good agreement (P,V,T), while the coarse and base mesh comparison was less good, exhibiting differences typically in the range 8–12 percent.

Offtake Passage Optimization Studies

On the basis of these results two alternative offtake passage cross sections were represented using variants of the CFD model used to investigate the circular offtake flow. The offtake passages considered in these assessments were essentially slot-shaped, consisting of a rectangular section of varying length at 8.5 mm wide and with semi-circular ends, as shown in Fig. 11.

The length of the rectangular section, X, was chosen to make the cross-sectional area of the slot an integer multiple (2 or 4) of the area of the current 8.5-mm-dia offtake holes, as defined in Table 2, where D was taken as 8.5 mm.

For each of the alternative offtake designs considered, the total offtake area was conserved at its original value. Hence, whereas the current offtake arrangement consists of 152 holes of ϕ 8.5, the number of offtake slots was reduced in the 2A and 4A offtake simulations to 76 and 38, respectively. As a consequence of this, it was also necessary to successively double the angular extent of the model for each of these simulations, resulting in a series of larger models. The results of these alternative offtake simulations are presented in the following subsections.

2A Offtake Passage Simulation. As already noted, the 2A offtake passage is essentially a slot with semi-circular ends of 4.25 mm radius, joined by a rectangular central section of a length chosen to give a slot area equal to twice that of a ϕ 8.5 hole. A calculational mesh representing this geometry was set up, following the same general approach that was previously adopted, re-

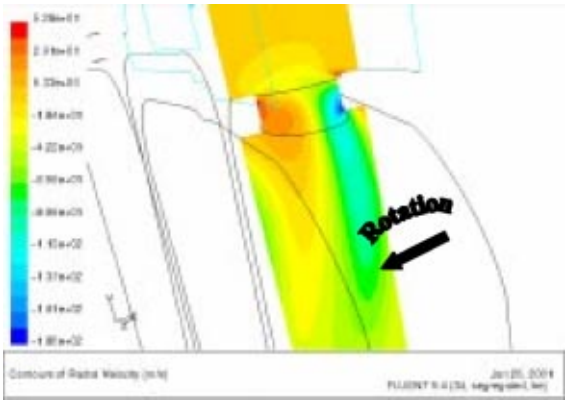

Fig. 9 Radial velocity contours

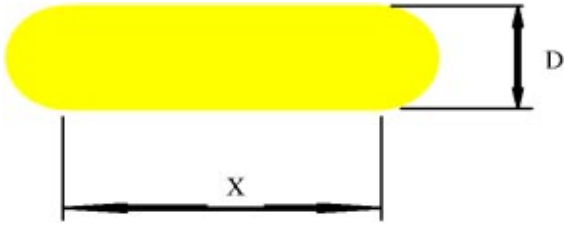

Fig. 11 Typical slotted offtake cross section

Table 2 Length of rectangular section of offtake slot

Slot	Slot area	X
2A	$2\times\pi D^2/4$	$\pi D/4$
4A	$4\times\pi D^2/4$	$3\pi D/4$

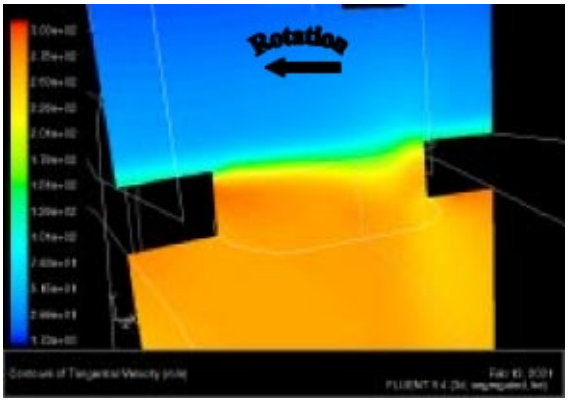

Fig. 12 2A tangential velocity contours

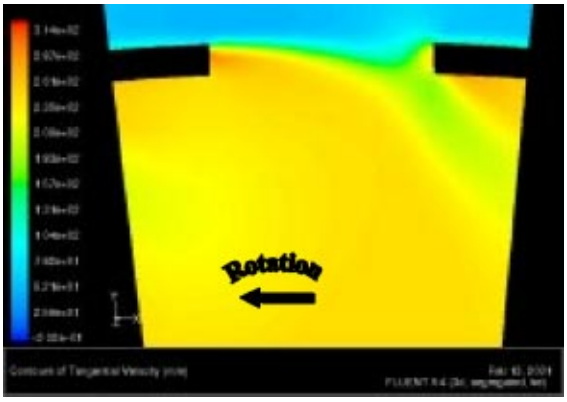

Fig. 14 4A tangential velocity contours

sulting in a mesh which consisted of 658,329 hexahedral cells. This reduction in mesh density, relative to the original simulation, was achieved by accepting some diminution in mesh density in the regions of secondary interest, e.g., the outlet section and the cavities adjacent to the offtake cavity.

The boundary conditions applied in this simulation were identical to those previously described in Table 1, with the exception of mass flow rate definitions, which were doubled to take account of the increased angular extent of the modelled region.

The pressure field prediction obtained using the model was very similar to that obtained for the current design. However, as the main outlet, the stator well recirculation and drain outlet boundary conditions were all defined pressure boundaries, that result was to be expected. In addition, the predicted velocity field in the vicinity of the offtake, exhibits similar behavior to that of the cylindrical offtake, with the offtake flow being forced onto the trailing edge of the passage, while there is evidence of recirculation at the leading edge. Contour plots of the tangential and radial velocity contours in this region are presented for the 2A offtake geometry in Figs. 12 and 13, respectively.

Again, it can be seen from Figs. 12 and 13 that the fluid passing close to the trailing edge of the offtake passage exhibits the largest radially inward velocity, and therefore has the smallest residence time. It is also interesting to note that these radial velocity contours extend diagonally into the cavity, opposing the direction of rotation. As in the original simulation, there is also evidence of a positive radial velocity at the leading edge of the passage, indicating the presence of a recirculation. This results in the fluid experiencing a longer residence time in the offtake passage, and consequently increased swirl velocities.

4A Offtake Passage Simulation. The 4A offtake passage simulation was set up in an identical manner to that previously described, except that the area of the offtake slots was again doubled, being equal to that of four ϕ 8.5 holes. The angular extent of the model was also correspondingly increased, which resulted in a mesh that consisted of 915,349 cells.

Contour plots of the tangential and radial velocity in the vicinity of the 4A slotted offtake passage are presented in Figs. 14 and 15, respectively.

Once again, the model predictions exhibit similar trends to those observed in previous simulations. However, it is clear that the tangential velocity imparted to the offtake air as it passes through the slotted passage is considerably reduced. In addition, it can be seen that the negative radial velocity contours, corresponding to high velocity fluid entering the cavity, extend even further in the direction opposing rotation. The positive radial velocity region still persists within the offtake passage, which serves to transport relatively highly swirling fluid from within the cavity and offtake passage back to the inlet plane.

Assessment of Alternative Offtake Design Performance

The predictions of swirl uptake within the offtake passage are presented in Fig. 16, in the form of a graph of local swirl coefficient (C_s) against distance from the passage inlet. Data are presented for the current $152\times\phi 8.5$ (A) offtake arrangement, together with corresponding data for the 2A and 4A slotted offtakes.

Using the swirl uptake data presented in Fig. 16, in conjunction with the cavity pressure drop data shown in Fig. 10, one may infer a cavity pressure differential for the respective offtake designs. These data are presented in Table 3.

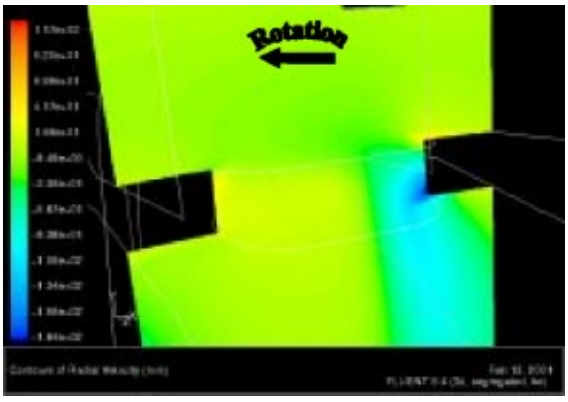

Fig. 13 2A radial velocity contours

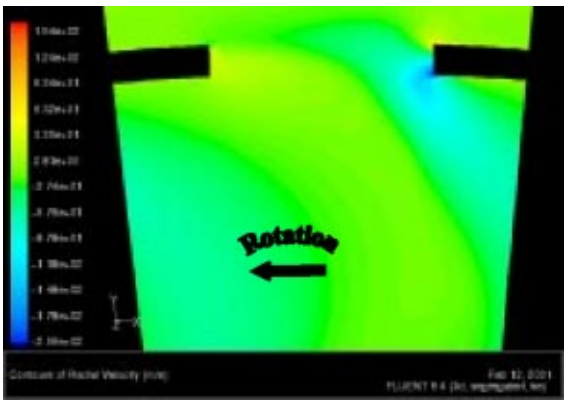

Fig. 15 4A radial velocity contours

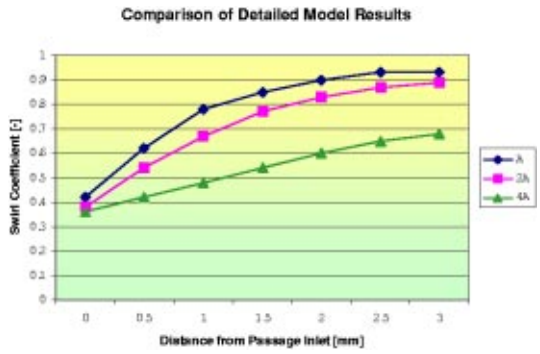

Fig. 16 Comparison of offtake swirl uptake

Table 3 Predicted cavity pressure difference comparison (using data presented in Fig. 16)

Offtake design	Cavity inlet swirl coefficient [-]	Cavity pressure difference [kPa]
A	0.93	137.8
2A	0.89	128.4
4A	0.68	86.6

It can be seen from the data presented in Table 3 that the introduction of the 2A and 4A slotted offtakes is predicted to result in approximately 4 and 26% reductions in the inlet swirl coefficient. These reductions in swirl uptake would in turn be translated into reductions in the offtake cavity pressure difference of about 4% (9 kPa) and 37% (64 kPa), respectively.

Conclusions and Recommendations for Further Work

The foregoing results indicate that the uptake of swirl within the various offtake passages that have been considered—including the current design—is extremely rapid. As a consequence of this, there appears to be relatively little scope for suppressing swirl uptake by reducing the offtake length—and hence the rotor thickness—unless fairly radical changes could be accommodated.

However, if the local stress fields remained acceptable, it may be possible to introduce localized thinning of the rotor wall in the vicinity of the offtake orifices, by countersinking for example. Such an arrangement would reduce the tendency of the bluff faces of the offtake passage to impart swirl to the air and would also diminish the degree of recirculation that has been predicted at the leading edge of the rotating passage. While it is likely that such an approach would prove beneficial, this alternative was not considered in this work as it was felt that the major benefits, in terms of swirl reduction, would be realised by increasing the circumferential length of the offtake passages.

In the scoping studies that were undertaken in this work, the model predictions indicated that the adoption of slot-shaped offtakes would be beneficial in reducing swirl uptake. In the case of a slot having an area four times that of the current 8.5 mm diameter holes, it was predicted that the cavity inlet swirl coefficient would reduce from 0.93 to 0.68. For the particular configuration investigated in this work, it is estimated that this would manifest itself as an increase in cavity pressure in the region of ~51 kPa. These results indicate that the offtake flow swirl coefficient on entry to the IP compressor cavity can be suppressed through the adoption of slotted offtakes that are elongated in the direction of rotor rotation.

Based on these results, it seems highly likely that further increases in IP compressor cavity pressure could be achieved by other modifications to the offtake geometry. In particular, the following options may be worthy of further consideration:

- Simply extending the scope of the present study, by investigating the adoption of fewer, longer offtake slots. A good starting point for such an analysis would be a 8.5 mm wide slot with an area of about ten times that of a ϕ8.5 hole.
- Modifying slot width (a constant slot width of 8.5 mm was assumed in this work). Reducing offtake width for a given area would allow the adoption of an equal or greater number of longer offtake slots.
- Local thinning of the offtake passage (and hence rotor) wall to reduce residence time within the offtake passage.

The model predictions presented in this work have shown that the conditions prevailing within the offtake passage are relatively insensitive to conditions within the stator well. Furthermore, the static pressure predictions have shown that there is a virtual absence of either axial or circumferential pressure gradients within the cavity. Based on these findings there may be some value in undertaking a more rigorous assessment to clarify whether there is a need to include complete and detailed representations of the upstream stator well and the downstream offtake cavity.

The suggestion from this work is that the offtake passage flow is largely decoupled from conditions within the stator well, due to the presence of the recirculation region at the leading edge of the passage. It is therefore likely that a less detailed representation of the stator well region may be sufficient for all but the most exacting flow analyses. In addition, the absence of axial and circumferential pressure gradients within the offtake cavity would suggest that it may be possible to apply a constant pressure outlet boundary condition over a plane of constant radius, without serious loss of accuracy.

If the modeling simplifications suggested above can be implemented without serious loss of accuracy—which could be established by comparisons with the present work—model size (in terms of calculational cells) could be reduced to about a quarter of that considered in this work. This would then reduce model execution times to the order of one day, which would allow a far more comprehensive assessment of alternative offtake designs to be undertaken.

Acknowledgments

The authors would like to thank Rolls-Royce plc for giving permission to publish this work.

Nomenclature

C_m = moment coefficient ($=M/\frac{1}{2}2\rho\Omega^2R_o^5$)
C_p = specific heat capacity at constant pressure
C_s = swirl coefficient ($=V_\theta/\Omega r$)
D_h = hydraulic diameter
k = turbulent kinetic energy
K = thermal conductivity
l = offtake passage length
M = moment
r = local radius
Re_θ = rotational Reynolds no. ($=\rho\Omega R_o^2/\mu$)
R_o = cavity outer radius
V_θ = tangential velocity
δ_{Ek} = Ekman layer thickness
ΔP = pressure difference
ε = dissipation rate of turbulent kinetic energy
μ = dynamic viscosity
ρ = density
Ω = angular velocity

References

[1] Brillert, Reichert, and Simon, 1999, ''Calculation of Flow Losses in Rotating Passages of Gas Turbine Cooling Systems,'' ASME Paper 99-GT-251.

[2] ICEM CFD Tutorial Manual, 2000, Direct CAD Interfaces, Version 4.0, ICEM CFD, Mar.

[3] ICEM CFD Tutorial Manual, 1999, Meshing Modules, Version 4.0, ICEM CFD, Feb.

[4] Chew, and Snell, 1988, ''Prediction of Pressure Distribution for Radial Inflow between Co-Rotating Discs,'' ASME Paper 88-GT-127.

[5] Chew, and Owen, 1989, ''The Use of De-Swirl Nozzles to Reduce the Pressure Drop in a Rotating Cavity with Radial Inflow, Farthing,'' ASME Paper 89-GT-184.

[6] Chew, 1989, ''A Theoretical Study of Ingress for Shrouded Rotating Disc Systems with Radial Outflow,'' ASME Paper 89-GT-187.

[7] Casey and Wintergerste, eds., 2000, European Research Community On Flow, Turbulence and Combustion (ERCOFTAC): CFD Best Practice Guidelines, Version 1.0, Jan.

[8] Fluent 5 User's Guide, 1998, Volumes 1–4, Fluent Inc.

[9] Launder and Spalding, 1972, *Lectures in Mathematical Modelling of Turbulence*, Academic Press, London, England.

[10] Launder, and Spalding, 1974, The Numeric Computation of Turbulent Flows, Comput. Methods Appl. Mech. Eng., **3**, pp. 269–289.

Influence of Rub-Grooves on Labyrinth Seal Leakage

J. Denecke
e-mail: Jens.Denecke@its.uni-karlsruhe.de

V. Schramm

S. Kim

S. Wittig

Lehrstuhl und Institut für Thermische Strömungsmaschinen, Universität Karlsruhe (TH), 76128 Karlsruhe, Germany

An experimental investigation on the influence of stator rub-grooves on labyrinth seal leakage is presented in the present paper. In current labyrinth seal designs, abradable lands allow the rotor labyrinth teeth to rub grooves into the stator. These rub-grooves have a large influence on the seal leakage characteristic and impair the overall engine efficiency. To improve the understanding of rub-groove effects, discharge coefficients were determined using a plain nonrotating labyrinth seal model of scale 4:1 considering a wide variation of rub-groove geometries at different seal clearances. Three labyrinth seal types were covered in this investigation that are generally used in gas turbines, namely 1) straight-through labyrinth seals, 2) stepped labyrinth seals with forward facing steps, and 3) stepped labyrinth seals with backward facing steps. To attain a deeper insight into the flow mechanisms, water-channel visualizations were performed. The large data set generated in this study, provides the basis to analyze and quantify the influence of rub-grooves on the seal leakage for the three aforementioned labyrinth seal types. Current results were in agreement with previous studies on worn labyrinth seals for several seal geometries. [DOI: 10.1115/1.1539516]

Introduction

Labyrinth seal leakage has often been the subject of investigations in the past because it influences the overall engine efficiency and heat balance. During transient operation of gas turbines, the rotor and stator expand differently. Hence, in labyrinth seals the radial clearance and axial position of the knifes change, which was quantified by Steward and Brasnett [1] using an X-ray visualization technique. These seal movements cause leakage changes. Rubbing of the knifes on the stator occurs and therefore abradable lands or honeycomb structures are deployed to prevent the danger of a seal failure. During the first engine cycles rub-grooves form on these stator lands (Fig. 1) and due to the new stator geometry, the leakage characteristic of the labyrinth seals with rub-grooves changes significantly compared to plain configurations (e.g., Zimmermann and Wolff [2]). The results from [1] showed that the knife tips of some seals even reside inside these rub-grooves during engine operation. However, the seal discharge behavior at negative nominal clearances has not been investigated in the past.

The objective of the present study is to analyze and quantify the influence of rub-grooves on labyrinth seal leakage for a wide range of configurations and operating conditions. To gain such a broad picture, the three labyrinth seal types commonly used in gas turbines are considered. For each seal type, a parametric study was conducted varying the clearance, the rub-groove geometry and the pressure ratio. In this parameter range negative nominal radial clearances are included, that correspond to engine conditions measured by Steward and Brasnett [1]. To identify the flow mechanisms responsible for the altered sealing performance, flow visualizations were performed in a water-channel.

Following the introduction, the theoretical aspects needed to analyze labyrinth seal leakage are discussed. Then, the test facility and the seal geometry are described. Finally, the results of the present study are presented and compared with those found in the literature.

Theoretical Aspects and Previous Work

There are three basic types of labyrinth seals that are generally used in gas turbines: straight-through labyrinth seals, stepped labyrinth seals with forward facing steps and stepped labyrinth seals with backward facing steps. These seals show distinctly different leakage characteristics, based on the different seal geometries. A number of semi-empirical models have been developed to predict the seal leakage rates. In these models, the leakage mass flow is commonly described by a discharge coefficient as defined in Eq. (1).

$$C_D = \frac{\dot{m}_{\text{real}}}{\dot{m}_{\text{ideal}}} \tag{1}$$

The definition of the ideal mass flow in Eq. (2) follows from the simplifications for a series of ideal throttles by Martin [3].

$$\dot{m}_{\text{ideal}} = \frac{A p_{t,0}}{\sqrt{R T_{t,0}}} \sqrt{\frac{1-\pi^{-2}}{n+\ln(\pi)}} \tag{2}$$

In the literature, the throttling area A has always been defined with the nominal clearance s (Rhode and Allen [4]). In contrast to the configurations investigated in the past, negative nominal clearances $s<0$ mm are considered in the present study. The following examples demonstrate, that the conventional definition of the discharge coefficient is not suited for the present study. For a given clearance, doubling the rub-groove depth results in a significant change of the nominal discharge coefficient due to the enlargement of the throttling area and a change in the flow field. These two effects cannot be separated, if the nominal clearance is used to define the discharge coefficient. Furthermore, the discharge coefficient approaches infinity for nominal clearances close to $s=0$ mm, because the nominal throttling area A stands in the denominator of Eq. (1). Therefore, throughout this work the throttling area A is defined using the smallest distance $s_{\min}$ between the knife tip and the stator as defined in Eq. (3). Figure 2 shows the three possible configurations, named ''Case 1,'' ''Case 1b,'' and ''Case 2.'' ''Case 1b'' is special and only occurs rarely.

$$A_{\text{Case 1}} = B_{\text{Seal}} \cdot (s + t_N)$$

$$A_{\text{Case 1b}} = B_{\text{Seal}} \cdot \left[\left(\frac{b_N}{2} - \frac{b}{2} \right) \cos\frac{\alpha}{2} + s \cdot \sin\frac{\alpha}{2} \right]$$

$$A_{\text{Case 2}} = B_{\text{Seal}} \cdot \sqrt{\left(\frac{b_N}{2} - \frac{b}{2} \right)^2 + s^2} \tag{3}$$

Contributed by the International Gas Turbine Institute and presented at the International Gas Turbine and Aeroengine Congress and Exhibition, Amsterdam, The Netherlands, June 3–6, 2002. Manuscript received by the IGTI October 15, 2001. Paper No. 2002-GT-30244. Review Chair: E. Benvenuti.

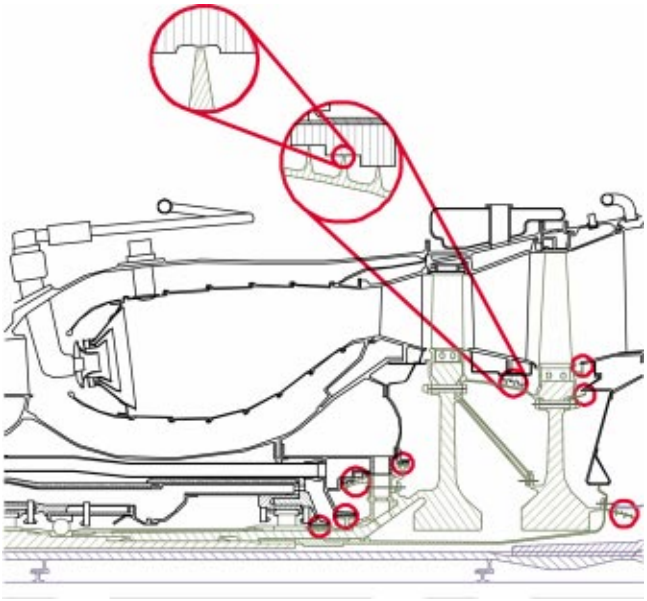

Fig. 1 Rub-grooves in engine labyrinth seals

Discharge coefficients $C_{D,\mathrm{nom}}$ from the cited literature, that are based on the nominal clearance, can be converted using a geometric factor ξ as defined in Eq. (4), similar to the factor defined by Schramm et al. [5].

$$C_{D,\mathrm{nom}} = \xi \cdot C_D \qquad \xi = \frac{s_{\min}}{s} \tag{4}$$

There are numerous effects that influence the measured leakage mass flow $\dot{m}_{\mathrm{real}}$ and that are not reflected by the thermodynamic considerations $\dot{m}_{\mathrm{ideal}}$ is based on. For example the Reynolds number Re determines the shape of the vena contracta in throttles and hence changes $\dot{m}_{\mathrm{real}}$ (Weißenberger [6]). The Reynolds number is defined in Eq. (5) given the assumption, that the seal clearance s is much smaller than the seal radius r_{Seal}.

$$\mathrm{Re} = \frac{2\dot{m}}{\mu B_{\mathrm{Seal}}} \tag{5}$$

Regarding the leakage characteristics of straight-through labyrinth seals, another effect can be observed. The accelerated fluid behind the throttling area does not lose its velocity before it enters the next throttle. This so called ''kinetic carryover effect'' significantly impairs the sealing efficiency of straight-through labyrinth seals in comparison to the stepped seal type (Vermes [7]). In stepped labyrinth seals, the direct flow path to the next throttle is obstructed by the step as long as the clearance is smaller than the step height. However, for clearances larger than the step height, the kinetic carryover effect also reduces the sealing efficiency of stepped labyrinth seals.

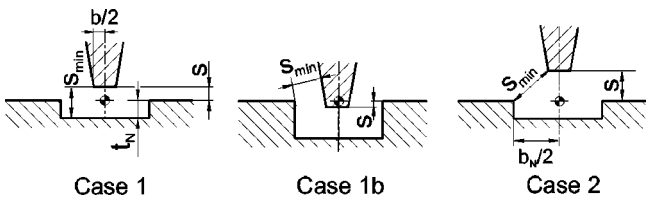

Fig. 2 Geometry definition of rectangular grooves

For small clearances, which are in the focus of interest in the present study, the sealing efficiency is strongly influenced by the geometry of the throttling area, i.e., the knife tip geometry and the composition of the stator surface above the knife [7,2]. Several aspects of the influence of the throttling geometry on the seal leakage were investigated in the past: Weißenberger [6] described the influence of Reynolds number Re and of the knife width to clearance ratio b/s on the shape of the streamlines behind contractions. The influence of rounded knife tips on the leakage rate was analyzed by Zimmermann et al. [8] and Rhode and Allen [4]. Stocker et al. [9] investigated the impact of porous stator lands on the sealing efficiency. The way honeycomb structures on the stator alter the flow and thereby the sealing performance due to geometry changes in the throttle was discussed by Schramm et al. [5].

The first author to investigate basic effects of rub-grooves on labyrinth seal leakage was Keller [10]. Their leakage measurements and visualizations showed that the leakage increases due to rub-grooves. Later, Stocker et al., [9] found that rub-grooves in porous abradable lands reduced the leakage, because the rub-grooves blocked the flow through the porous stator material. While Stocker et al. [9] investigated a special rub-groove geometry, all subsequent authors approached the rub-groove shape by a rectangular cut as defined in Fig. 2. Because a rectagular shape is well suited for a parametric study, it was also used in the present work. A typical rub-groove geometry as it was found in an engine surface roughness measurement was published by Zimmermann et al. [8], who addressed the topic of worn labyrinth seals using numerical simulations. Later, Zimmermann and Wolff [2] developed a correlation on the basis of experiments to assess the influence of rub-grooves on the leakage of straight-through labyrinth seals. Rhode and Allen [4,11] investigated leakage effects of rub-grooves in straight-through and stepped labyrinth seals with forward facing steps. They derived leakage resistance coefficients from measurements in a water-channel test facility and visualized the corresponding flow field. In a recent study, Rhode and Adams [12] used numerical methods to investigate forward facing stepped labyrinth seals with rub-grooves.

From the analysis of the cited publications, it follows that an experimental data basis of leakage measurements for the three basic labyrinth seal types with rub-grooves does not yet exist. Especially seal configurations with backward facing steps and configurations with negative nominal clearances, where the knife has moved inside the rub-groove, have not yet been targeted by previous investigators. Therefore, the main objective of the present study is to provide such a data base for a wide range of configurations and to identify and describe the main flow mechanisms influencing the seal leakage.

Table 1 Labyrinth seal geometry

h/t	b/t	H/t	s/t	α	t
0.46	0.047	0.143	−0.029 . . . 0.171	20 deg	28 mm

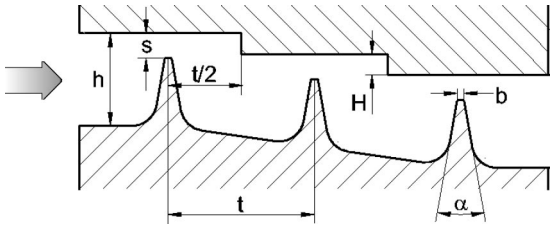

Fig. 3 Labyrinth seal geometry definition (forward-facing steps)

Seal Geometry

The labyrinth seal geometry investigated in the present study is defined in Table 1 and Fig. 3. The basic seal geometry is identical to that of the previous studies by Schramm et al. [5] and Willenborg et al. [13,14]. The corresponding dimensions of the straight-through labyrinth seal are identical to the stepped seal type. In a plain nonrotating model as used in the present study there is no convergent or divergent seal flow, because the throttling areas are equal above each knife. Therefore, these cases are named stepped labyrinth seal with forward facing steps and backward facing steps. The model setup is symmetric, so it can be used for both flow directions. The results of a plain nonrotating model can be applied to rotating seals, provided that in the rotating seal, the mean axial velocity is larger than the circumferential velocity in the seal (Waschka et al. [15]). The scale of 4:1 was chosen, because it offers the advantage of reduced machining tolerances. As Wittig et al. [16] discussed, the scale-up of the seal model leads to increased Reynolds numbers. The Reynolds number range investigated in this study corresponds to engine Reynolds numbers at take-off conditions [8], where the seal leakage is maximum.

Test Facility and Rig Instrumentation

The experiments were conducted at the labyrinth seal test facility of the Institut für Thermische Strömungsmaschinen, Universität Karlsruhe (TH), which has been used in a number of previous studies to investigate leakage and heat transfer characteristics of labyrinth seals (e.g. Wittig et al. [16,17], Waschka et al. [15], Schramm et al. [5], Willenborg et al. [13,14]). This facility has the capability to provide air at variable temperatures and pressures through the test section (Fig. 4).

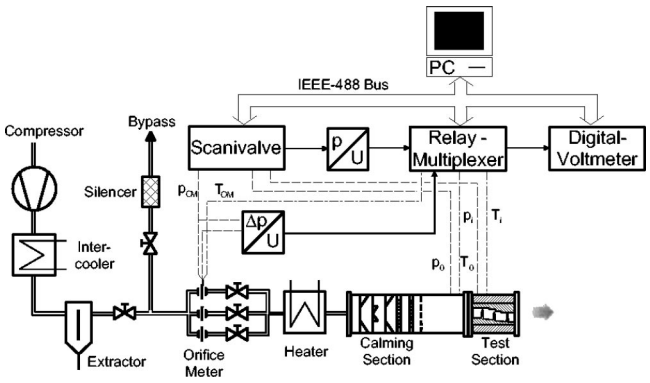

Fig. 4 Labyrinth seal test facility

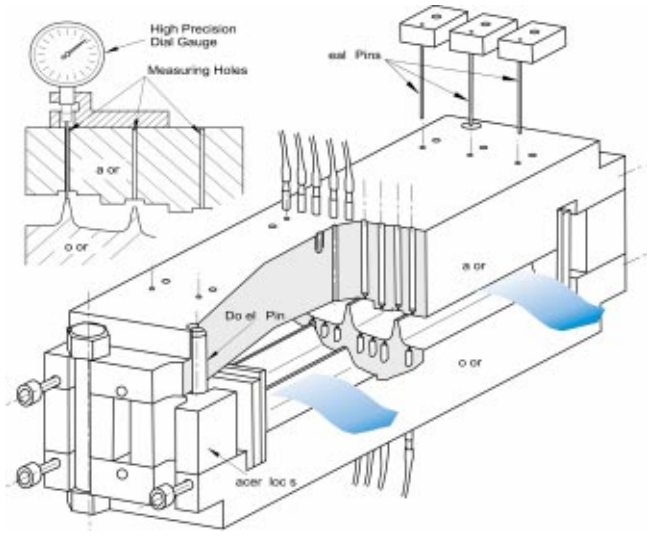

Fig. 5 Labyrinth seal model

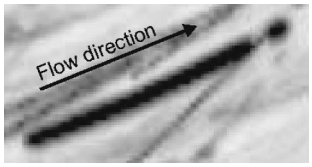

Fig. 6 Multi-exposure of tracking particles yields streamlines and flow direction

The compressor supplies the air to the test section. After cooling and drying, the air mass flow is measured by orifice meters. Three orifice meters of different diameters allow a measuring range from 5 to 500 g/s and were designed according to DIN EN ISO 5167. The pressure ratio over the labyrinth seal model was adjusted from $\pi=1.05$ to $\pi=1.8$ with valves downstream of the orifice meters. A uniform velocity and temperature profile at the inlet of the seal test section was ensured by several meshes in the calming section. In the plenum of this calming section, the total air temperature $T_{t,0}$ and total pressure $p_{t,0}$ were measured. Pressures were measured by a pressure transducer and a Scanivalve system as shown in Fig. 4. The heater was not used in this investigation and the air entered the test section at a temperature of $T_{t,0}=17°C$. All electrical signals were measured by a digital voltmeter, that was part of the computer controlled data acquisition system. Figure 5 shows the setup of a labyrinth seal model, that was used in the present study. The model consists of a bottom part with knifes representing the rotor and a top part with rub-grooves representing the stator. Two dowel pins ensure the relative position of both parts, while the seal clearance was adjusted by massive spacer blocks located at the side walls of the seal. The model width corresponds to the seal circumference B_{Seal} from Eq. (3) and was chosen such that the influence of the side walls is negligible. A high precision dial gage (± 0.008 mm) was used to measure the actual clearance at three positions over each knife after the model had been assembled to the test rig. The holes were closed during the measurements by seal pins as shown in Fig. 5. The massive design of the model prevents the clearance from changing measurably when pressurized. These design details allowed an estimated mean uncertainty of $\pm 3.7\%$ for all measurements of discharge coefficients, including the small distances.

The flow visualizations were conducted with a seal model of the same scale. The stator part of the seal model was manufactured from Perspex for optical access. A 10 kHz copper-vapor-laser with appropriate optics provided a light sheet to illuminate air bubbles, generated by the circulating pump, as tracking particles in the water. This laser light sheet was placed at a distance of about 50 mm from one side wall of the model. A larger distance would have reduced visible regions due to the camera perspective. At a smaller distance, the side wall would have influenced the flow field in the seal. A high-speed digital camera was used to take multi-exposure pictures as shown in Fig. 6. The colors were inverted so that the illuminated bubbles appear in black. The air bubbles from thirty exposures form the streamline in Fig. 6. After a break of 0.3 ms, another three exposures shape a dot that indicates the flow direction. In order to investigate transient phenomena, this recording procedure was repeated 20 times at constant time intervals. To increase the number of tracking particles in the images shown here, these 20 multi-exposure images were added up to a single image, showing an average flow field. The water-channel allowed maximum Reynolds numbers of about Re $=10{,}000$. Since the discharge coefficients are independent of the Reynolds number in this range as shown in Fig. 10 (see also Wittig et al. [16]), the influence of the Reynolds number on the flow field can be considered negligible.

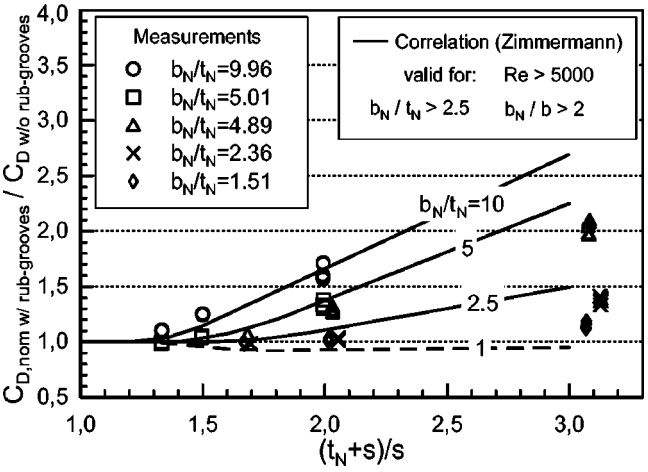

Fig. 7 Comparison to literature correlation

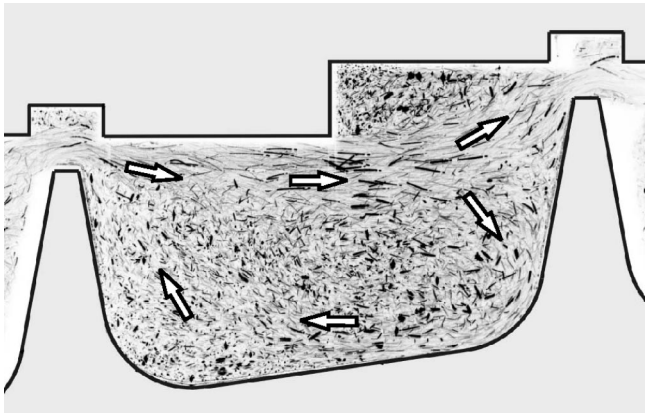

Fig. 8 Visualization of flow through a labyrinth seal with backward-facing steps, (s/t=0.057, b_N/b=3.01, b_N/t_N=4.89)

Results and Discussion

As a first step to analyze the rub-groove influence on labyrinth seal leakage, the results of the present study are compared to the correlation for straight-through labyrinth seals given by Zimmermann and Wolff [2]. This correlation is based on leakage data for a labyrinth seal of scale 2.5:1 with five knifes. In Fig. 7 the ratio of the nominal discharge coefficients with rub-grooves to the discharge coefficients without rub-grooves, is plotted over $(t_N+s)/s$. The nondimensional geometric parameter $(t_N+s)/s$ characterizes the relative clearance and rub-groove dimensions. Due to these definitions, the correlation can only be applied to positive nominal clearances. As an additional parameter, the rub-groove shape b_N/t_N is used. In general, the correlation predicts increasing leakages for deeper rub-grooves at a constant width as well as for wider rub-groove shapes at a constant depth. The results of the present study are fairly well predicted by the correlation, even though it is based on a different seal geometry. The results for rub-groove shapes of $b_N/t_N=2.36$ and $b_N/t_N=1.51$ suggest, that the correlation from [2] can be extended below the original limits.

The data of the stepped labyrinth seals cannot be correlated as described for the straight-through seal type, because their geometry causes flow effects that change the leakage behavior. To attain a deeper understanding of the flow mechanisms governing the sealing performance, water-channel visualizations were conducted and will be presented in the following section.

Water-Channel Visualization. Visualizations of flow structures in labyrinth seals with rub-grooves have been published by Rhode and Allen [11] for the straight-through type and by Rhode and Allen [4] for labyrinth seals with forward facing steps. To complete this series, two exemplary visualizations of the backward facing step seal type are presented here. The discharge coefficients measured for these configurations are provided in Fig. 11.

As a first example a configuration with a positive nominal seal clearance of $s/t=0.057$ is shown in Fig. 8. The overall flow direction is from the left to the right side of the image. A jet is visible, that is widened behind the contraction by the rub-groove, but still follows the stator wall. Behind the seal step, a recirculation zone forms and part of the jet gradually bends towards the downstream throttling area. On the downstream knife a stagnation point can be seen. A smaller part of the jet is redirected from the stagnation point towards the chamber ground and propels a large chamber vortex. The series of images showed, that this vortex is moving back and forth in the seal chamber. Generally, the flow field for configurations with larger clearances and also for ungrooved seals was found to be similar. Only the position of the stagnation point changed slightly, depending on the configuration. A large part of the jet directly enters the downstream seal chamber and thereby reduces the sealing efficiency. From straight-through labyrinth seals this is known as the kinetic carryover effect. With decreasing step height the influence of the kinetic carryover would increase until the geometry and the flow field equal the straight-through seal type. Labyrinth seals with forward facing steps show a distinctly different flow field at a comparable clearance, as can be seen in the visualizations of from Rhode and Allen [4]. As long, as the rub-groove does not dominate the flow field, the seal step redirects the jet towards the chamber ground and thereby prevents the kinetic carryover effect.

If the rotor expands and the clearance reduces to $s/t=0.0$ as shown in Fig. 9, the flow field changes significantly. The jet is completely redirected by the rub-groove and follows the rotor surface, before it enters the next chamber through the downstream throttling area. The chamber vortex has changed its sense of rotation, compared to the configuration with a larger positive nominal clearance in Fig. 8. The significant change of the flow field affects the loss mechanisms responsible for the leakage behavior. The extent of the jet redirection into the chamber volume dominates the seal leakage in the range of small clearances, while the seal step and the kinetic carry-over effect have a minor influence. Since the chamber geometry of the three seal types is similar the leakage resistance should only depend on the rub-groove geometry and the clearance. These assumptions were confirmed by the measurements of the discharge coefficients.

Discharge Coefficients. As a reference, ungrooved labyrinth seal geometries were investigated first. Figure 10 shows the discharge coefficients for a medium clearance of $s/t=0.057$ plotted

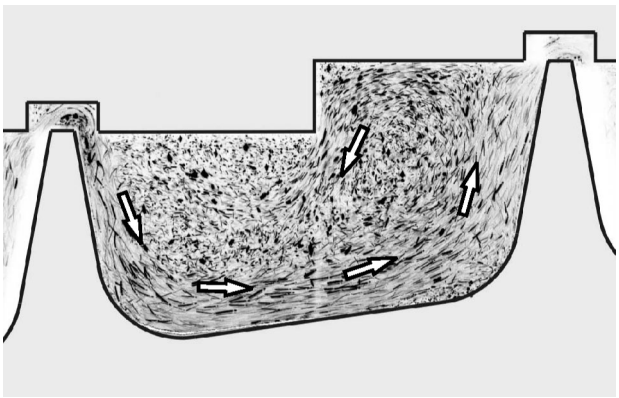

Fig. 9 Visualization of flow through a labyrinth seal with backward-facing steps (s/t=0.0, b_N/b=3.01, b_N/t_N=4.89)

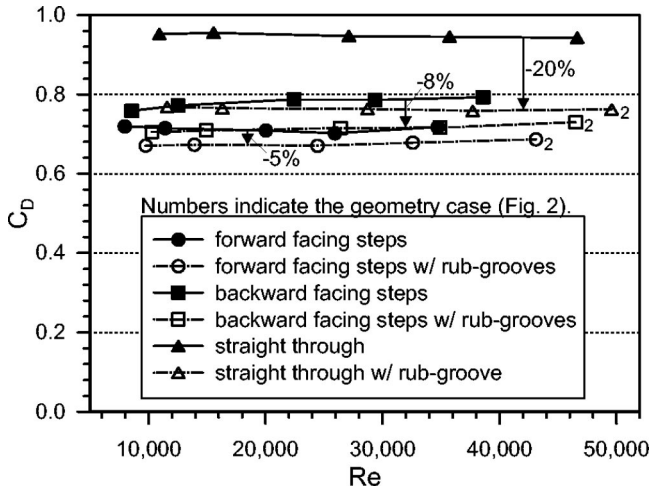

Fig. 10 Discharge coefficients of straight through, backward-facing stepped and forward-facing stepped labyrinth seals with smooth stator or rub-grooves ($b_N/b=3$, $b_N/t_N=5$, $s/t=0.057$)

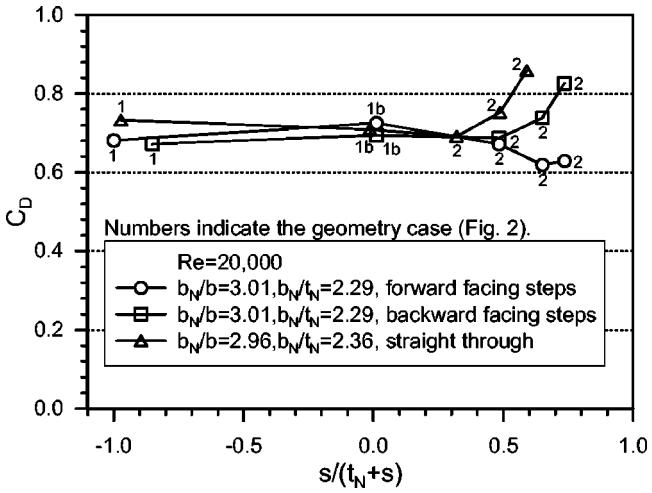

Fig. 11 Influence of glearance on seal discharge coefficient C_D

against the Reynolds number. The number at the markers indicates the case applied in Eq. (3). For all geometry variations, pressure ratios of $\pi=1.05$, 1.1, 1.3, 1.5, 1.8 were adjusted for the measurements and are indicated by markers in Fig. 10, where the lowest pressure ratio yields the lowest Reynolds number. In agreement with the literature (e.g., [7]) it was found, that straight-through labyrinth seals are the least efficient labyrinth seal type. Stepped labyrinth seals with backward facing steps show lower leakage rates at similar pressure ratios and labyrinth seals with forward facing steps provide the best sealing efficiency of these basic labyrinth seal types.

If a rub-groove is added to the stator of a labyrinth seal, the nominal discharge coefficient $C_{D,\mathrm{nom}}$ as defined in the literature increases [12], due to the increase of the throttling area. However, as marked in Fig. 10, the discharge coefficient defined in the present paper is reduced by about 20% for the straight-through labyrinth seal, for the seal with backward facing steps by 8% and for the seal with forward facing steps by 5%. These losses caused by the rub-grooves are not represented by the conventional nominal discharge coefficient. The increased mass flow at the same pressure ratios due to the area increase is also indicated in Fig. 10. The markers for configurations with rub-grooves shift to larger Reynolds numbers compared to the configuration without rub-groove, which means that rub-grooves increase the mass flow.

These losses induced by the rub-grooves can be explained by the flow visualizations. For positive nominal seal clearances, the dominating influence on the leakage is the kinetic carryover effect [7]. The rub-groove widens the jet at the exit of the throttle, and thereby reduces the kinetic carryover for the straight-through and backward facing stepped seal type. Also, additional vortices in the rub-groove contribute to the reduction of the discharge coefficient. It can be seen in Fig. 10, that in the measured range the discharge coefficients are generally little dependent on the Reynolds number. To eliminate even small deviations due to Reynolds number effects, the discharge coefficients of the following discussions are all interpolated to a constant Reynolds number. The value of Re $=20{,}000$ was chosen, because it corresponds to engine take-off conditions as discussed earlier. Since one intention of the present investigation is to analyze the leakage at different clearances, the discharge coefficients are plotted against a dimensionless number describing the clearance. The nominal discharge coefficient and the ratio $(t_N+s)/s$ are obviously not suited for clearances close to zero. To describe the leakage in the complete clearance range the reciprocal ratio $s/(s+t_N)$ from Fig. 7 is used here. A value of $s/(s+t_N)=-1.0$ means that the knife tip is positioned halfway into the rub-groove. A value of $s/(s+t_N)=0.5$ means that the clearance equals the rub-groove depth, and if the value approaches $s/(s+t_N)=1$, the clearance is infinitely larger than the rub-groove depth.

Figure 11 shows such a plot for a rub-groove width of $b_N/b \approx 3$. It can be seen, that at clearances larger than $s/(t_N+s)>0.3$, distinct differences between the leakage rates occur and the labyrinth seal type dominates the underlying loss mechanisms. The discharge coefficients of the straight-through labyrinth seal and the seal with backward facing steps increase with $s/(s+t_N)$, because the kinetic carryover effect gains influence with increasing clearance. The shift of the curve of the seal with backward facing steps compared to the straight-through seal indicates, that the beginning of the carryover effect depends on the step height. Because of this shift, the correlation of Zimmermann and Wolff [2] cannot be applied to seals with backward facing steps. The discharge coefficient for the seal with forward facing steps decreases with increasing clearance, because the direct flow path is blocked by the step. However, if the seal clearance s grows larger than the step height H, the kinetic carryover effect also sets in for the labyrinth seal with forward facing steps. This can be seen in Fig. 11 at the largest clearance $s/(t_N+s)=0.74$ measured.

In the range of small clearances $s/(t_N+s)<0.3$, there are only minor differences between the discharge coefficients of the different seal types. If this observation holds true for all measurements, it confirms the assumptions made from the flow visualizations. In this clearance range, the jet redirection prevents the kinetic carryover effect and the rub-groove and overall chamber geometry dominate the leakage behavior. The seal type (straight-through or stepped labyrinth seal) is reduced to a second order effect.

To analyze the influence of the rub-groove shape b_N/t_N, results are plotted in Fig. 12 where the rub-groove width b_N is held constant at $b_N/b=6.06$ and the depth is doubled. The discharge coefficients of the seals with deeper rub-grooves ($b_N/t_N=4.62$ and $b_N/t_N=4.89$) are smaller than the coefficients of the shallow form ($b_N/t_N=9.86$ and $b_N/t_N=9.96$). The cause can be found in the change of the flow field due to the rub-groove. Rhode and Allen [11] described that the rub-groove shape and the clearance determine at which angle the jet behind the contraction area enters the labyrinth chamber, and thereby influences the leakage resistance. The jet of the deeper rub-groove is redirected into the chamber at a larger angle to the rotor axis, and thereby the leakage resistance is increased. This jet redirection by the rub-groove leads to an interesting detail for the forward facing step seal type in Fig. 12. The curve for $b_N/t_N=4.62$ shows an increase of the

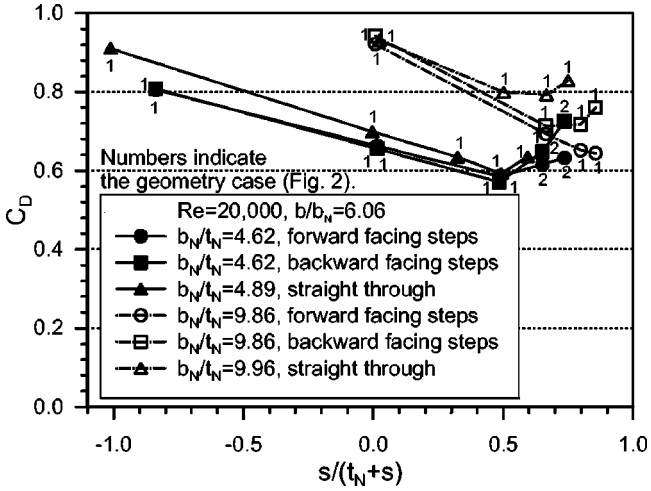

Fig. 12 Influence of the rub-groove depth t_N at a constant width b_N

discharge coefficient C_D for $s/(t_N+s)>0.5$, while for $b_N/t_N=9.86$ there is a continuous decrease. The cause was described by Rhode and Adams [12]: the flow field of seals with forward facing steps is changed by certain rub-grooves in a way that a kinetic carryover effect appears. The redirected jet does not form a stagnation point on the step front anymore, but can enter the next throttling area directly, and thereby reduces the sealing efficiency. Because of this additional effect, the correlation from [2] is not applicable to labyrinth seals with forward facing steps.

In Fig. 13 different rub-groove sizes, characterized by b_N/b, are compared keeping the rub-groove shape constant at a value of $b_N/t_N \approx 5$. The discharge coefficients of the seals with larger rub-grooves of $b_N/b=6.06$ are smaller than the discharge coefficients for seals with small rub-grooves ($b_N/b=2.95$ and $b_N/b=3.03$). Besides the throttling area change this difference of the leakage resistance of the two rub-groove sizes defines the gradient of the correlation curves in Fig. 7.

In Figs. 12 and 13 all measured discharge coefficients show a minimum in the interval $0.3<s/(t_N+s)<0.7$, and again, there is only a minor influence of the labyrinth seal type on the discharge coefficients for small clearances $s/(t_N+s)<0.3$. Therefore, in this range the jet redirection into the seal chamber dominates the flow field and the leakage characteristics, while the seal type is of minor importance. In contrast, for values of $s/(t_N+s)$ larger than at the minimum, the seal type and the extent of the carryover effect dominate the leakage behavior. From these results it is concluded, that the parameter $s/(t_N+s)$ defined in the present study serves to determine the dominating loss mechanisms influencing the leakage.

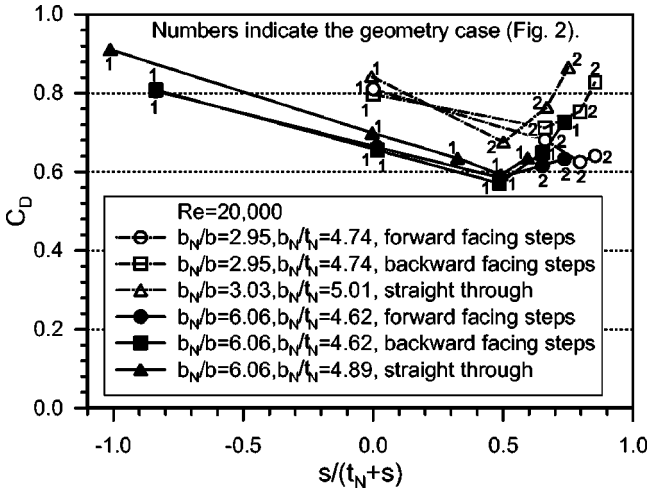

Fig. 13 Influence of the rub-groove size b_N/b at a constant shape $b_N/t_N \approx 5$

Summary

During engine operation, rub-grooves form on the stator of labyrinth seals. In the present study the discharge behavior of labyrinth seals with rub-grooves has been investigated. Leakage measurements for the straight-through, backward and forward facing step seal type were conducted for a wide range of geometry configurations, including negative nominal clearances. Additionally, laser light-sheet visualizations were conducted in a water-channel. The visualizations provided additional information to interpret the discharge behavior.

In the present study the main flow mechanisms induced by rub-grooves were identified and described for all configurations usually occurring during engine operation. A modified discharge coefficient was introduced, which allowed to analyze configurations with rub-grooves at clearances around and below zero. A minimum of the discharge coefficient was found at clearances in the range of $0.3<s/(s+t_N)<0.7$ for all configurations. The parameter $s/(s+t_N)$ serves to distinguish between typical changes of the flow field and the resulting leakage behavior.

For values below $s/(s+t_N)<0.3$, the present study shows that the influence of the seal type is negligible and the rub-groove geometry, the clearance, and the overall seal dimensions dominate the leakage characteristics.

For values $s/(s+t_N)>0.7$ above the minimum the three labyrinth seal types investigated show a distinct leakage behavior. In this parameter range it was found that for straight-through labyrinth seals, the correlation from [2] is capable to predict the influence of rub-grooves for the seal geometry used here. However, the correlation is not suited for stepped labyrinth seals. Labyrinth seals with backward facing steps in principle show a similar behavior to straight-though seals, but the kinetic carryover effect is reduced by the seal step, which leads to a reduction of the discharge coefficient. Labyrinth seals with forward facing steps show the smallest discharge coefficients in this comparison. A leakage increase induced by some rub-groove configurations for seals with forward-facing steps that was reported by Rhode and Allen [4] was confirmed by the present measurements.

Acknowledgment

These investigations were financed by the German Luft- und Raumfahrtforschungsprogramm Engine 3E/II and supported by Rolls-Royce Deutschland GmbH.

Nomenclature

A = area, [m²]
B_{Seal} = seal circumference, [m]
b = Knife tip thickness, [m]
b_N = Rub-groove width, [m]
C_D = Discharge coefficient, [-]
H = Seal step height, [m]
h = seal knife height, [m]
$\dot{m}$ = mass flow rate [kg/s]
n = no. of seal knifes, [-]
p = pressure, [kg/(m s²)]
R = specific gas constant, [kJ/kg K]
r_{Seal} = seal radius, [m]
$\mathrm{Re}=2\dot{m}/\mu B_{Seal}$ = Reynolds no. [-]
s = seal clearance [m]
T = temperature, [K]
t = seal knife pitch, [m]
t_N = rub-groove depth, [m]

α = knife taper angle, [deg]
ξ = geometric factor, [-]
$\pi = p_{t,0}/p_{s,1}$ = pressure ratio, [-]
μ = dynamic viscosity, [kg/m s]

Subscripts

0 = seal inlet
1 = seal exit
ideal = ideal
min = minimum
nom = nominal
N = rub-groove
real = real\measured
s = static
t = total

References

[1] Steward, P. A. E., and Brasnett, K. A., 1978, ''The Contribution of X-Ray to Gas Turbine Air Sealing Technology,'' AGARD Conf. Proc., **237**, pp. 10.1–10.13.
[2] Zimmermann, H., and Wolff, K. H., 1998, ''Air System Correlations: Part 1—Labyrinth Seals,'' ASME Paper 98-GT-206.
[3] Martin, H. M., 1908, ''Labyrinth Packings,'' Eng. J., **85**, pp. 33–36.
[4] Rhode, D. L., and Allen, B. F., 1999, ''Measurement and Visualization of Leakage Effects of Rounded Teeth Tips and Rub-Grooves on Stepped Labyrinths,'' ASME Paper 99-GT-377.
[5] Schramm, V., Willenborg, K., Kim, S., and Wittig, S., 2000, ''Influence of a Honeycomb-Facing on the Flow Through a Stepped Labyrinth Seal,'' ASME Paper 2000-GT-0291, ASME J. Eng. Gas Turbines Power, **124**, pp. 140–146.
[6] Weißenberger, E., 1952, ''Strömung durch Spaltdichtungen,'' Ph.D. thesis, Fakultät für Maschinenwesen, Universität Karlsruhe (TH).
[7] Vermes, G., 1961, ''A Fluid Mechanics Approach to the Labyrinth Seal Leakage Problem,'' ASME J. Eng. Power, **83**, pp. 161–169.
[8] Zimmermann, H., Kammerer, A., and Wolff, K. H., 1994, ''Performance of Worn Labyrinth Seals,'' ASME Paper 94-GT-131.
[9] Stocker, H. L., Cox, D. M., and Holle, G. F., 1977, ''Aerodynamic Performance of Conventional and Advanced Design Labyrinth Seals with Solid-Smooth, Abradable and Honeycomb Lands,'' NASA-CR-135307.
[10] Keller, C., 1934, Strömungsversuche an Labyrinthdichtungen für Dampfturbinen, Escher Wyss. Mitteilungen, Vol. 7, pp. 9–13.
[11] Rhode, D. L., and Allen, B. F., 1998, ''Visualization and Measurements of Rub-Groove Leakage Effects on Straight-Through Labyrinth Seals,'' ASME Paper 98-GT-506.
[12] Rhode, D. L., and Adams, R. G., 2000, ''Computed Effect of Rub-Groove Size on Stepped Labyrinth Seal Performance,'' ASME Paper 2000-GT-0292.
[13] Willenborg, K., Kim, S., and Wittig, S., 2001, ''Effect of Reynolds Number and Pressure Ratio on Leakage Loss and Heat Transfer in a Stepped Labyrinth Seal,'' ASME Paper 2001-GT-0123, ASME J. Turbomach. **123**, pp. 815–822.
[14] Willenborg, K., Schramm, V., Kim, S., and Wittig, S., 2000, ''Influence of a Honeycomb Facing on the Heat Transfer in a Stepped Labyrinth Seal,'' ASME Paper 2000-GT-0290, ASME J. Eng. Gas Turbines Power, **124**, pp. 133–139.
[15] Waschka, W., Wittig, S., and Kim, S., 1992, ''Influence of High Rotational Speeds on the Heat Transfer and Discharge Coefficients in Labyrinth Seals,'' ASME J. Turbomach., **114**, pp. 462–468.
[16] Wittig, S., Dörr, L., and Kim, S., 1983, ''Scaling Effects on Leakage Losses in Labyrinth Seals,'' ASME J. Eng. Power, **105**, pp. 305–309.
[17] Wittig, S., Jacobsen, K., Schelling, U., and Kim, S., 1988, ''Heat Transfer in Stepped Labyrinth Seals,'' ASME J. Eng. Gas Turbines Power, **110**, pp. 63–69.

Computation of Flow Between Two Disks Rotating at Different Speeds

Muhsin Kilic
Department of Mechanical Engineering,
Uludag University,
Bursa, Turkey

J. Michael Owen
Department of Mechanical Engineering,
University of Bath,
Bath BA2 7AY, UK

Disks rotating at different speeds are found in the internal cooling-air systems of most gas turbines. Defining Γ *as the ratio of the rotational speed of the slower disk to that of the faster one then* $\Gamma=-1$, *0 and* $+1$ *represents the three important cases of contra-rotating disks, rotor-stator systems and co-rotating disks, respectively. A finite-volume, axisymmetric, elliptic, multigrid solver, employing a low-Reynolds-number* k-ε *turbulence model, is used for the fluid-dynamics computations in these systems. The complete* Γ *region,* $-1\leqslant\Gamma\leqslant+1$, *is considered for rotational Reynolds numbers of up to* $\mathrm{Re}_\phi=1.25\times10^6$, *and the effect of a radial outflow of cooling air is also included for nondimensional flow rates of up to* $C_w=9720$. *As* $\Gamma\rightarrow-1$, *Stewartson-flow occurs with radial outflow in boundary layers on both disks and between which is a core of nonrotating fluid. For* $\Gamma\approx0$, *Batchelor-flow occurs, with radial outflow in the boundary layer on the faster disk, inflow on the slower one, and between which is a core of rotating fluid. As* $\Gamma\rightarrow+1$, *Ekman-layer flow dominates with nonentraining boundary layers on both disks and a rotating core between. Where available, measured velocity distributions are in good agreement with the computed values.* [DOI: 10.1115/1.1539515]

Keywords: Rotating Disks, Fluid Dynamics

1 Introduction

In the internal cooling-air systems of gas turbines, the air often flows over one or more rotating turbine disks. In some cases the disk rotates close to a stationary casing, and in others it rotates close to another disk which may be co-rotating or, more rarely, contra-rotating. Such configurations can be modelled by so-called rotating-disk systems in which two plane disks are used to represent the more complex geometries found in engines [1,2].

It is convenient to classify these systems using the parameter Γ, where $\Gamma=\Omega_2/\Omega_1$, Ω_2 being the rotational speed of the slower disk and Ω_1 the faster one. Three important cases are: the rotating cavity in which both disks co-rotate, where $\Omega_1=\Omega_2$ and $\Gamma=1$; the rotor-stator system, where $\Omega_2=0$ and $\Gamma=0$; contra-rotating disks, where $\Omega_1=-\Omega_2$ and $\Gamma=-1$. Schematic diagrams of the flow in these three systems are shown in Fig. 1 for the case where there is a superposed radial outflow of cooling air. In all cases there is a source region near the inlet, where inertial forces are dominant, with boundary-layer flow at larger radii. For $\Gamma=-1$, there is radial outflow in the (entraining) boundary layer on each disk; for $\Gamma=0$, there is radial outflow in the boundary layer on the rotating disk (on the LHS of the figure) and inflow on the stationary disk; for $\Gamma=1$, there is radial outflow in each of the (nonentraining) boundary layers: the latter are referred to as Ekman layers, after Ekman [3]. For $\Gamma=0$ or 1, there is a core of inviscid fluid that rotates at a speed intermediate between that of the two disks; for $\Gamma=-1$, the inviscid core is virtually stationary.

These three cases, which are often referred to as source-sink flows, have been studied extensively: the current authors [4–8] have mapped out the region from $-1\leqslant\Gamma\leqslant0$, but relatively little experimental or computational work has been conducted for the region $0<\Gamma<1$. This paper sets out to explore the entire region $-1\leqslant\Gamma\leqslant+1$ computationally and, where available, experimental velocity measurements are compared with computed values. An appreciation of the fluid dynamics, and of how the flow structures change with Γ, should be useful to the designer of internal cooling-air systems.

In Section 2, the computational method is outlined. Section 3 uses computed streamlines to illustrate the transition of flow structures between $\Gamma=-1$ and $\Gamma=+1$. Section 4 shows the effect of Γ on the distributions of computed radial and tangential components of velocity, comparing them with available measurements, and Section 5 shows the effect of Γ on the computed moment coefficients. Conclusions are summarized in Section 6.

2 Computational Method

The computer code used was a finite-volume, steady, axisymmetric, elliptic, multigrid solver, employing a low Reynolds number k-ε turbulence model [9–11]. The code has been used successfully to compute the flow in rotating-disk systems, and details can be found in references [4–8]. In a cylindrical-polar coordinate system, the time-averaged, axisymmetric, steady-state conservation equations for mass, momentum, energy, and the turbulence quantities turbulence kinetic energy, k, and its dissipation rate, ε, together with the low-Reynolds number k-ε turbulence model, were solved to compute the flow in the cavity. A finite-difference mesh of 113×137 (axial$\times$radial) nodes was employed, with a combination of geometrically expanding/contracting grid spacings to cluster nodes near the solid boundaries. For all the cases considered, the grid point closest to each disk was set to ensure that $y^+<0.5$ (which corresponded to a distance of around 1.5-μm from the surface), and the geometric expansion/contraction factors did not exceed 1.2. (Computations carried out with a coarser grid of 67×67 nodes showed no significant differences in the graphical results but there were differences in the computed moment coefficients; computations with a finer mesh showed no significant difference to the computed results but required a large increase in computing time and memory.)

The computational geometry (see Fig. 1) matched the experimental one described in [7]: $a/b=0.13$, $G=s/b=0.12$, $G_c=s_c/b=0.01$. For the solid boundaries (i.e., disks and shrouds), no-slip boundary conditions were used. For the inlet, the air was assumed to enter the system radially with uniform radial velocity

Contributed by the International Gas Turbine Institute and presented at the International Gas Turbine and Aeroengine Congress and Exhibition, Amsterdam, The Netherlands, June 3–6, 2002. Manuscript received by the IGTI January 16, 2002. Paper No. 2002-GT-30242. Review Chair: E. Benvenuti.

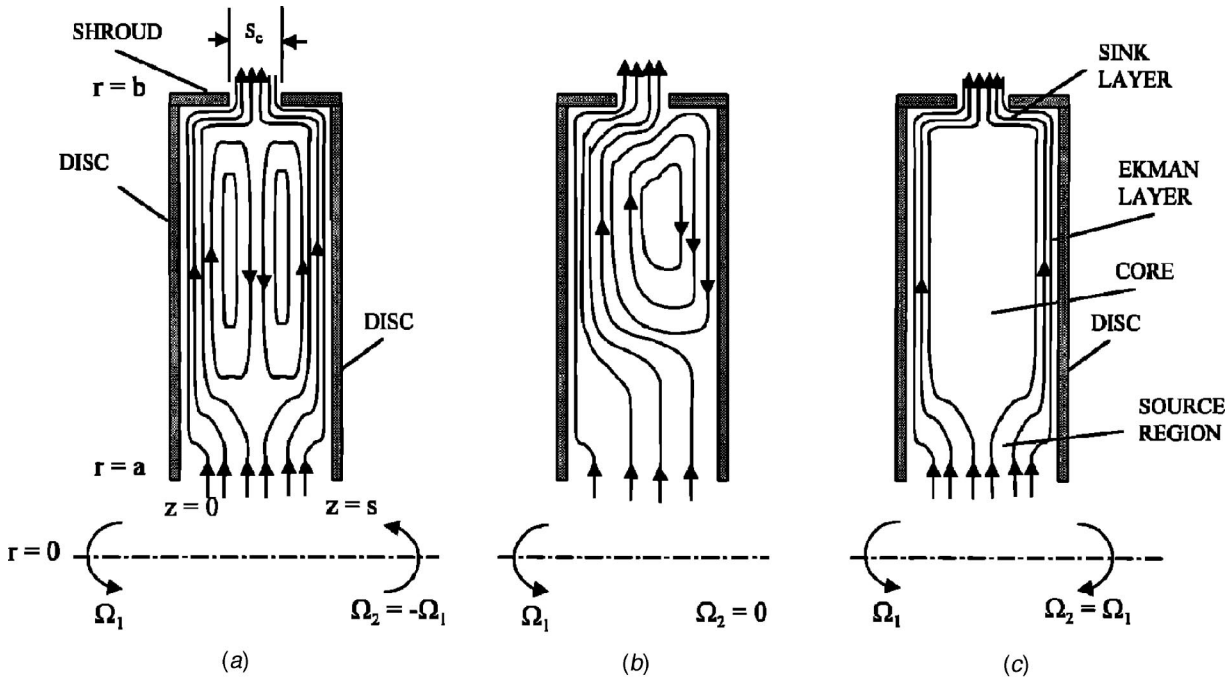

Fig. 1 Schematic diagram of flow structure for $\Gamma=-1$, 0, +1 ($C_w>0$)

and zero swirl at $r=a$, so that $V_r=\dot{m}/(2\pi\rho as)$, $V_\phi=0$, $V_z=0$. For the outlet region at $r=b$, a uniform radial velocity was imposed to ensure the mass balance between the inlet and outlet, and zero normal-derivative conditions were applied for the other variables.

3 Effect of Γ on Flow Structure

Figure 2 shows the computed streamlines in the r-z plane for $\mathrm{Re}_{\phi,1}=1.25\times10^6$, $C_w=6100(\lambda_{T,1}=C_w\,\mathrm{Re}_{\phi,1}^{-0.8}=0.0809)$, and $G=0.12$, and for $\Gamma=-1$, -0.4, 0, $+0.4$, and $+1$. When $\Omega_1\neq\Omega_2$, the left-hand disk (at $z=0$) represents the faster one. In all cases, the air enters the system as a uniform source, without swirl, at $r=a$ and leaves through the small clearance, s_c (not shown) between the two shrouds at $z/s=0.5$ and $r=b$. Figure 1 should help to determine the direction of the flow in the streamlines in Fig. 2.

As shown by Owen and Rogers [2], for a given value of Γ the flow structure depends principally on the turbulent flow parameter, λ_T, and the inlet swirl ratio, which is zero here. A value of $\lambda_{T,fd}=0.219$ corresponds to the nondimensional flow rate, $C_{w,fd}$, entrained by a free disk with a rotational Reynolds number Re_ϕ.

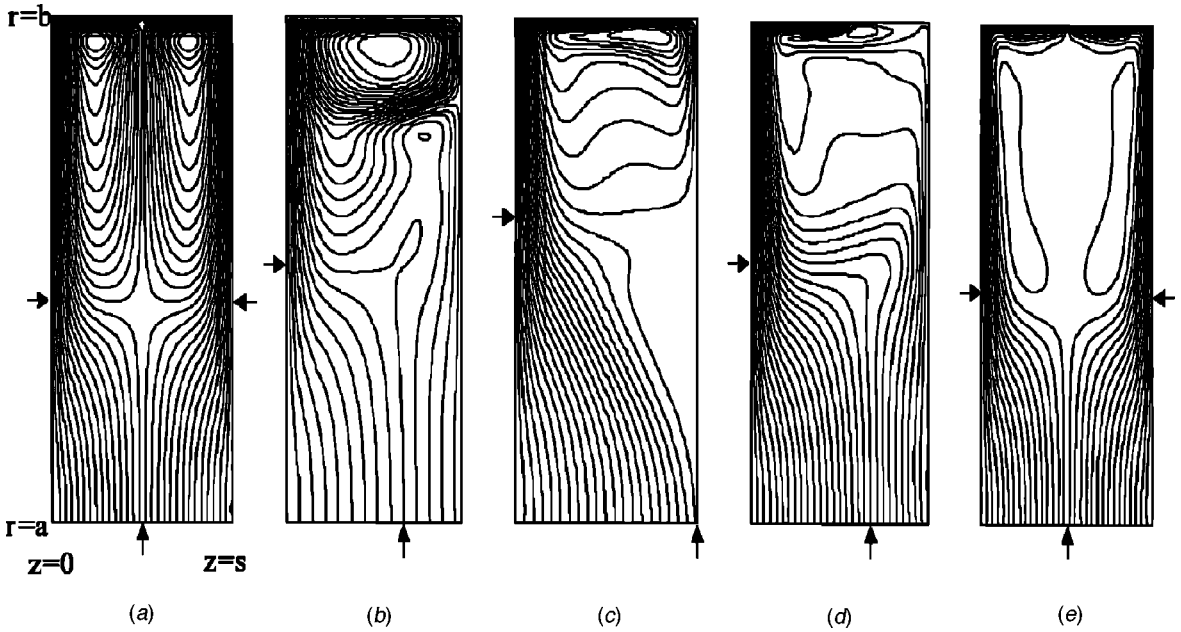

Fig. 2 Effect of Γ on computed streamlines for $\mathrm{Re}_{\phi,1}=1.25\times10^6$, $C_w=6100$, $\lambda_{T,1}=0.0809$, $G=0.12$; $\rightarrow x_e$ (Eq. (4)) $\uparrow z_d/s$ (Eq. (7))—(*a*) $\Gamma=-1$, (*b*) $\Gamma=-0.4$, (*c*) $\Gamma=0$, (*d*) $\Gamma=0.4$, (*e*) $\Gamma=1$

In most engines, when the air is used to cool the disks and seal the wheel-space, $\lambda_T < \lambda_{T,fd}$, which is the case considered here. Although $\mathrm{Re}_\phi = 1.25 \times 10^6$ is lower than that found in typical engines (where values around 10^7 are common), the turbulent flow structures shown in Fig. 2 are believed to be representative of those found in engines. (Computations conducted for $\mathrm{Re}_\phi = 10'$ and $\lambda_{T,1} = 0.0809$ produced results very similar to those shown in Fig. 2.)

3.1 Flow in Inviscid Core. If the inviscid core, between the boundary layers downstream of the source region, is in near-solid-body rotation such that Coriolis accelerations dominate (which is the case for $\Gamma = +1$ and small values of λ_T) then the Taylor-Proudman theorem [12] is valid. For axisymmetric flow, this requires that

$$V_{r,\infty} = \frac{\partial V_{z,\infty}}{\partial z} = \frac{\partial V_{\phi,\infty}}{\partial z} = 0 \tag{1}$$

where the subscript ∞ denotes flow in the core. In the special case where $\Gamma = +1$ and where the flow is symmetrical about the midplane ($z/s = 0.5$), it follows that

$$V_{z,\infty} = 0 \tag{2}$$

Under these conditions, there can be no radial or axial flow in the core, and the boundary layers are therefore nonentraining.

For such rotating flows, where Coriolis accelerations dominate, the nonlinear inertial accelerations can be neglected and the Navier-Stokes equations reduce to the so-called *linear equations*. Ekman's discovery and solution of these linear equations give rise to what are now referred to as Ekman layers. Owen et al. [13] obtained solutions of the integral linear and nonlinear equations for laminar and turbulent flow. They used the term ''Ekman-type layers'' for the nonlinear case, but that distinction is not made here.

3.2 Size of Source Region. For all Γ in Fig. 2, the source region downstream of the inlet can be clearly seen. In this region, air is entrained into the boundary layer on each (rotating) disk, and the source region ends (at $x = x_e$, say) when all the superposed flow has been entrained. The radial extent of the source region can be estimated using the method of Owen and Rogers [2] who considered the case of $\Gamma = +1$ for laminar and turbulent flow with and without inlet swirl. It is assumed here that, for zero swirl at inlet, each boundary layer entrains fluid at the same rate as a free disk such that, for turbulent flow,

$$\frac{\dot{m}_i}{\mu b} = 0.219 x (x^2 \, \mathrm{Re}_{\phi,\mathrm{i}})^{0.8} \tag{3}$$

where $i = 1,2$ corresponds to the left-hand and right-hand disk, respectively. The source region ends when $\dot{m}_1 + \dot{m}_2 = \dot{m}$ (the superposed flow rate) and $x = x_e$; hence, using Eq. (3)

$$x_e = 1.79 \left(\frac{\lambda_{T,1}}{1 + |\Gamma|^{0.8}} \right)^{0.385} \tag{4}$$

and

$$\frac{\dot{m}_2}{\dot{m}_1} = |\Gamma|^{0.8} \tag{5}$$

It is implicitly assumed that the entrainment rate is unaffected by the direction of rotation of the disk.

Equation (5) determines how the inlet flow is divided between the two boundary layers, and there is a streamline at $z = z_d$, say, that marks the division between the flow that is entrained by each disk. Thus, for a uniform flow at the inlet

$$\frac{z_d}{s} = \frac{\dot{m}_1}{\dot{m}} \tag{6}$$

and from Eqs. (5) and (6)

$$\frac{z_d}{s} = \frac{1}{1 + |\Gamma|^{0.8}} \tag{7}$$

The edge of the source region and the location of the dividing streamline according to Eqs. (4) and (7), respectively, are shown in Fig. 2. It can be seen that, in the source region for all cases, the computed streamlines show that the flow to the left of z_d/s is entrained by the boundary layer on the left-hand disk; for $\Gamma = 0$, all the flow is entrained by the left-hand disk. The size of the source region shown by the streamlines for $\Gamma = -1$ is virtually the same as for $\Gamma = +1$, and x_e provides a good estimate; this is consistent with the assumption that entrainment is not affected by the direction of rotation. For $\Gamma = +0.4$, the axial flow shown by the streamlines for $x > x_e$ occurs in the inviscid core *after* that flow has been entrained into the boundary layer on the right-hand disk. For $\Gamma = -0.4$, for $x > x_e$ there is evidence of the Batchelor flow and Stewartson flow discussed in the forthcoming. (Reasonable agreement between theoretical and computational values of x_e was also found at other values of $\lambda_{T,1}$.)

The source-sink flow structure described in the foregoing can only occur if $\lambda_{T,1}$ is small enough to ensure that the source region does not fill the entire cavity (that is, $x_e < 1$). If $\lambda_{T,\max}$ is the value of $\lambda_{T,1}$ when $x_e = 1$ then, from Eq. (4),

$$\lambda_{T,\max} = 0.219(1 + |\Gamma|^{0.8}) \tag{8}$$

When $\Gamma = 0$, $\lambda_{T,\max} = \lambda_{T,\mathrm{fd}}$, the free-disk value. For turbine-disk cooling and sealing systems, $\lambda_{T,1} < \lambda_{T,\max}$ and source-sink flow occurs for all Γ. However, for pre-swirl cooling systems with $\Gamma = +1$ [14], where the swirling air is used to cool the turbine blades, $\lambda_{T,1} > \lambda_{T,\max}$. The behavior of the flow in these pre-swirl systems is very different from that described in the foregoing.

3.3 Transitional Flow Structures. For $\Gamma = +1$ in Fig. 2, the nonentraining Ekman layers and inviscid core, where $V_{r,\infty} = V_{z,\infty} = 0$, can be clearly seen. (The kidney-shaped recirculations adjacent to the Ekman layers are similar to those found in laminar flow as a result of the spatially-oscillatory form of the axial distribution of velocity inside the Ekman layers.) As shown by Eq. (1), $V_{\phi,\infty}$ is invariant with z in the core.

Consider next the other limiting case of $\Gamma = -1$ where, outside the source region, the flow is significantly different from that for $\Gamma = +1$. In particular, there are large axial variations of $V_{r,\infty}$ and $V_{z,\infty}$ in the core, with radial inflow near the midplane, and the boundary layers entrain air which flows radially outward. Although not apparent from the streamlines, $V_{\phi,\infty} \approx 0$ in the core: Coriolis accelerations are weak and the Taylor-Proudman theorem is invalid. This flow structure is often referred to as Stewartson flow, after Stewartson [15].

The case of $\Gamma = 0$ is different from the other two. There is radial outflow in the boundary layer on the rotating disk and inflow on the stationary one. Air flows axially across the core from the stationary disk to be entrained by the boundary layer on the rotating disk. At larger radii, where the core rotates sufficiently fast, the Taylor-Proudman theorem comes into play and Eq. (1) applies. This flow structure is often referred to as Batchelor flow, after Batchelor [16].

Kilic et al. [5,6] showed that as Γ increases from -1 to 0, a two-cell structure occurs with Stewartson-flow at the smaller radii (where $V_{\phi,\infty} \approx 0$) and Batchelor-flow at the larger radii (where $0 < V_{\phi,\infty}/\Omega_1 r < 1$). Such a flow can be seen at $\Gamma = -0.4$ in Fig. 2.

The structural transition between Batchelor flow at $\Gamma = 0$ and Ekman-layer flow at $\Gamma = +1$ is less spectacular, and an intermediate case is shown for $\Gamma = +0.4$. Unlike $\Gamma = 0$, there is radial outflow in the boundary layers on both disks with axial migration of air from the slower to the faster disk. Computations at $\Gamma = +0.2$ (not shown here) show that radial inflow only occurs for $x \gtrsim 0.85$, and as $\Gamma \to 1$ the flow structure changes progressively to Ekman-layer flow.

Details of the velocity distributions in these different flow structures are given in the following.

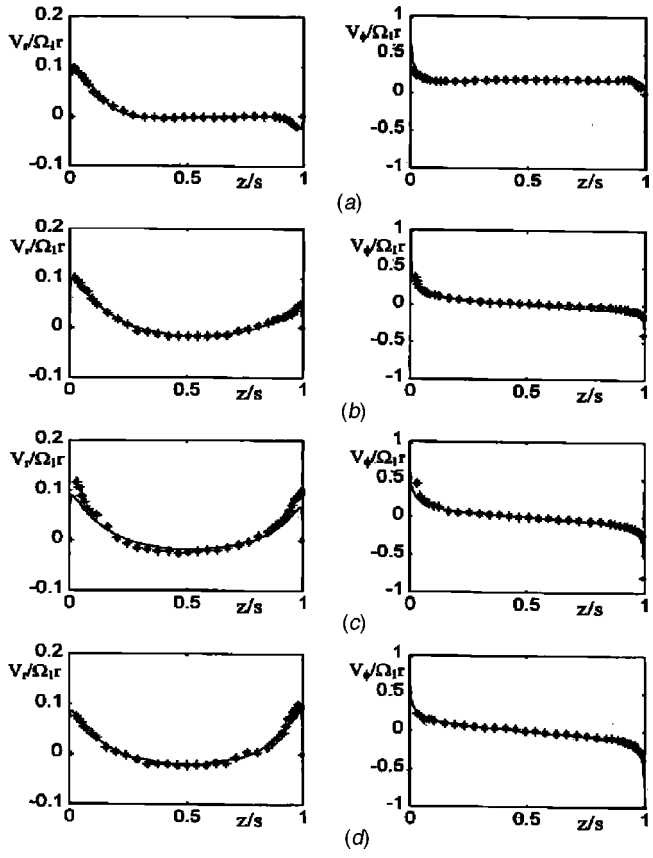

Fig. 3 Effect of Γ (for Γ≤0) on axial distributions of $V_r/\Omega_1 r$ and $V_\phi/\Omega_1 r$ at x=0.8 for $Re_{\phi,1}=1.25\times10^6$, $C_w=6100$, $\lambda_{T,1}=0.0809$, $G=0.12$; ——computations; * measurements of Gan et al. [7]—(*a*) Γ=0.0, (*b*) Γ=−0.4, (*c*) Γ=−0.8, (*d*) Γ=−1.0

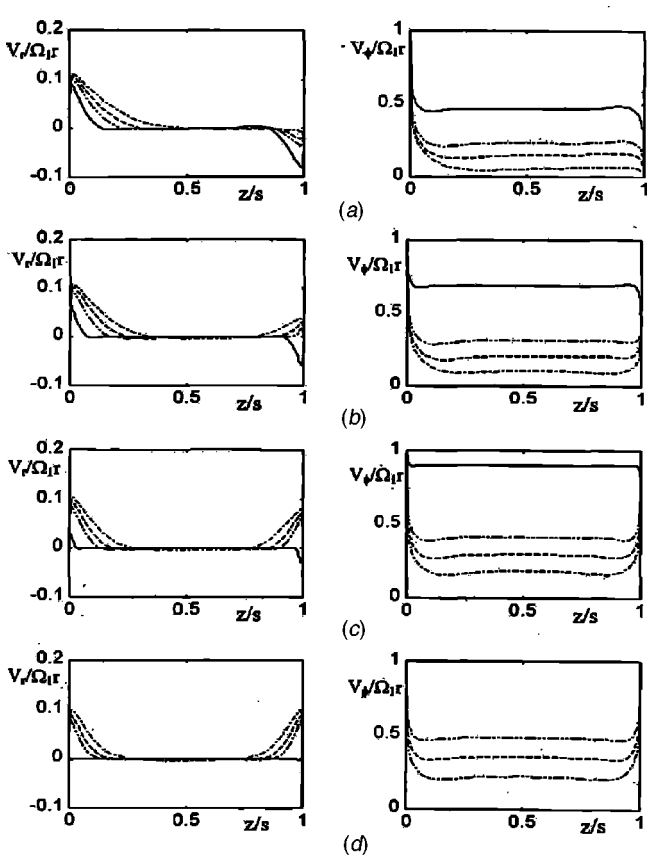

Fig. 4 Effect of Γ (for Γ≥0) on computed axial distributions of $V_r/\Omega_1 r$ and $V_\phi/\Omega_1 r$ at $x=0.8$ for $Re_{\phi,1}=1.11\times10^6$, $G=0.12$; ——$C_w=0$, $\lambda_{T,1}=0$; — — — — $C_w=3926$, $\lambda_{T,1}=0.0572$ – – – – $C_w=6100$, $\lambda_{T,1}=0.0889$; — — — $C_w=9720$, $\lambda_{T,1}=0.142$—(*a*) Γ=0.0, (*b*) Γ=0.4, (*c*) Γ=0.8, (*d*) Γ=1.0

4 Velocity Distributions

It is convenient to consider separately the cases of $-1\leq\Gamma\leq0$ and $0\leq\Gamma\leq+1$. Contra-rotating disks ($\Gamma<0$) have received considerable attention whereas, apart from $\Gamma=+1$, co-rotating disks ($\Gamma>0$) have received little attention.

4.1 Contra-Rotating Disks (Γ≤0). Figure 3 shows the axial distributions of $V_r/\Omega_1 r$ and $V_\phi/\Omega_1 r$, at $x=0.8$, for the same conditions as those used in Fig. 2. The experimental results were obtained by Gan et al. [7] using laser-Doppler anemometry (LDA).

For $\Gamma=0$, where $V_{\phi,\infty}/\Omega_1 r\approx0.2$, Batchelor flow occurs, at this value of *x*, with radial inflow in the boundary layer on the stationary disk. For $\Gamma=-0.4$, -0.8, -1, where $V_{\phi,\infty}/\Omega_1 r\approx0$, Stewartson flow occurs with radial outflow on both disks.

The computed and measured values of $V_r/\Omega_1 r$ are consistent with the streamlines shown in Fig. 2: at $x=0.8$, there is radial outflow on the slower disk for $\Gamma=-0.4$ and -1, and inflow at $\Gamma=0$. The mainly good agreement between computations and measurements for those cases where experimental data are available gives confidence in the computations.

4.2 Co-Rotating Disks (Γ≥0). Figure 4 shows the computed axial distributions of $V_r/\Omega_1 r$ and $V_\phi/\Omega_1 r$, at $x=0.8$, for $Re_{\phi,1}=1.11\times10^6$, G=0.12, Γ=0, 0.4, 0.8 and 1, and $C_w=0$, 3926, 6100, and 9720, corresponding to $\lambda_{T,1}=0$, 0.0572, 0.0889, 0.142. (A value of $Re_{\phi,1}=1.11\times10^6$, rather than 1.25×10^6, was chosen as experimental data are available at Γ=1 for this Reynolds number.)

For all values of Γ and C_w in Fig. 4, $V_{\phi,\infty}/\Omega r>0$ and "Taylor-Proudman effects" can be seen in the core: $V_{r,\infty}=0$ and $\partial V_{\phi,\infty}/\partial z=0$. It can also be seen that $V_{\phi,\infty}/\Omega r$ increases as Γ increases and as C_w and $\lambda_{T,1}$ decrease. Also, the radial inflow ($V_r<0$) in the boundary layer on the slower disk reduces, and eventually reverses, as Γ increases. These computed values of $V_r/\Omega_1 r$ are consistent with the streamlines shown in Fig. 2 where there is radial outflow everywhere on the right-hand disk for $\Gamma\geq0.4$.

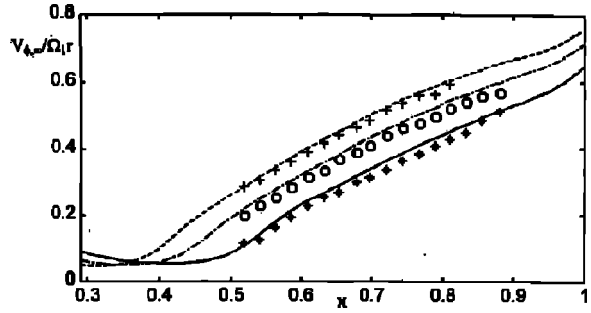

Fig. 5 Effect of $Re_{\phi,1}$ on radial distribution of $V_{\phi,\infty}/\Omega_1 r$ for Γ=+1, $C_w=2500$, $G=0.10$

$Re_{\phi,1}/10^6$	Computations	Measurements of Owen et al.[13]
0.55	——	*
0.82	— — —	0
1.10	– – – –	+

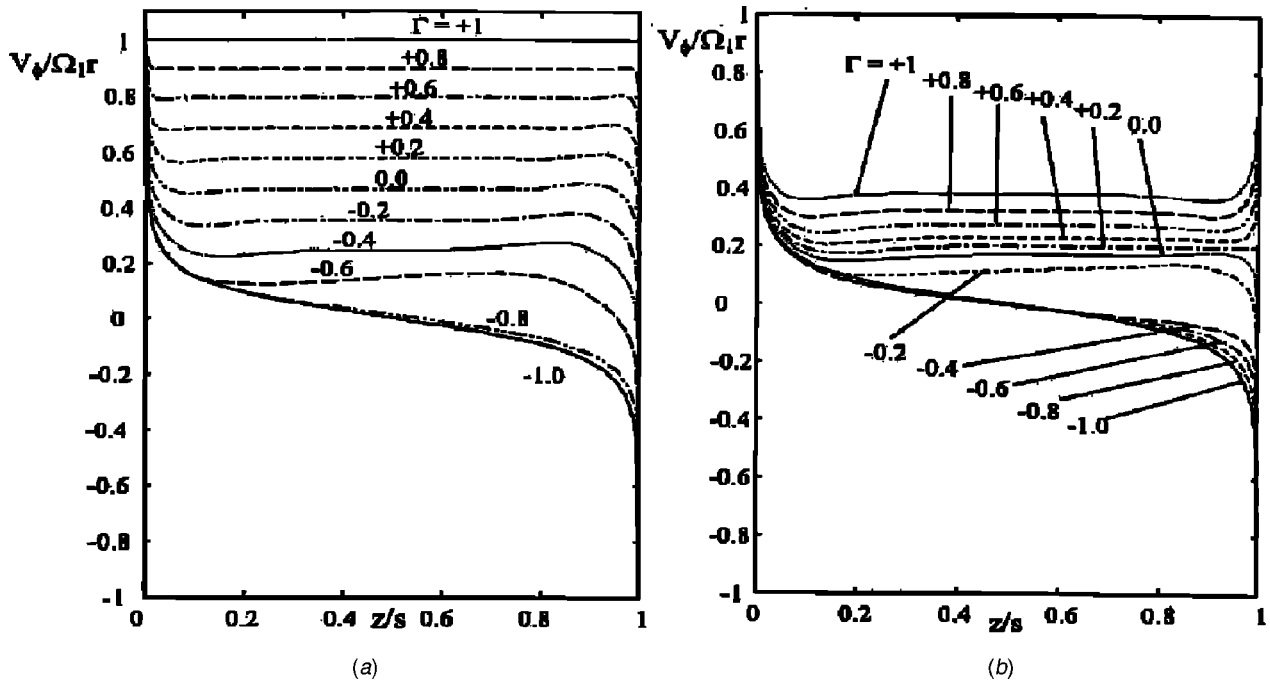

Fig. 6 Effect of Γ (for $-1 \leq \Gamma \leq +1$) on computed axial distributions of $V_\phi/\Omega_1 r$ at $x=0.8$ for $Re_{\phi,1}=1.25\times10^6$, $G=0.12$—(*a*) $C_w=\lambda_{T,1}=0$; (*b*) $C_w=6100$, $\lambda_{T,1}=0.0809$

There are no experimental data, except for $\Gamma=1$, to corroborate the above computations in Fig. 4, but Fig. 5 shows a comparison between computed and measured radial distributions of $V_{\phi,\infty}/\Omega_1 r$ (at $z/s=0.5$) for $\Gamma=1$. The LDA measurements were obtained by Owen et al. [13] in a rig, with $a/b=0.1$ and $G=0.1$, for $C_w=2500$, and $Re_\phi/10^6=0.55$, 0.82, and 1.10 ($\lambda_{T,1}=0.0639$, 0.0464, 0.0367). It can be seen that $V_{\phi,\infty}/\Omega_1 r$ increases as x increases and as C_w (and $\lambda_{T,1}$) decreases. Again, the mainly good agreement between the computations and measurements provides confidence in the accuracy of those computations where no experimental data are available for corroboration.

4.3 Contra-Rotating and Co-Rotating Disks ($-1 \leq \Gamma \leq +1$). Figures 6 and 7, respectively, show the computed axial and radial distributions of $V_\phi/\Omega_1 r$.

Figure 6(*a*) shows the effect of Γ on the axial distribution of

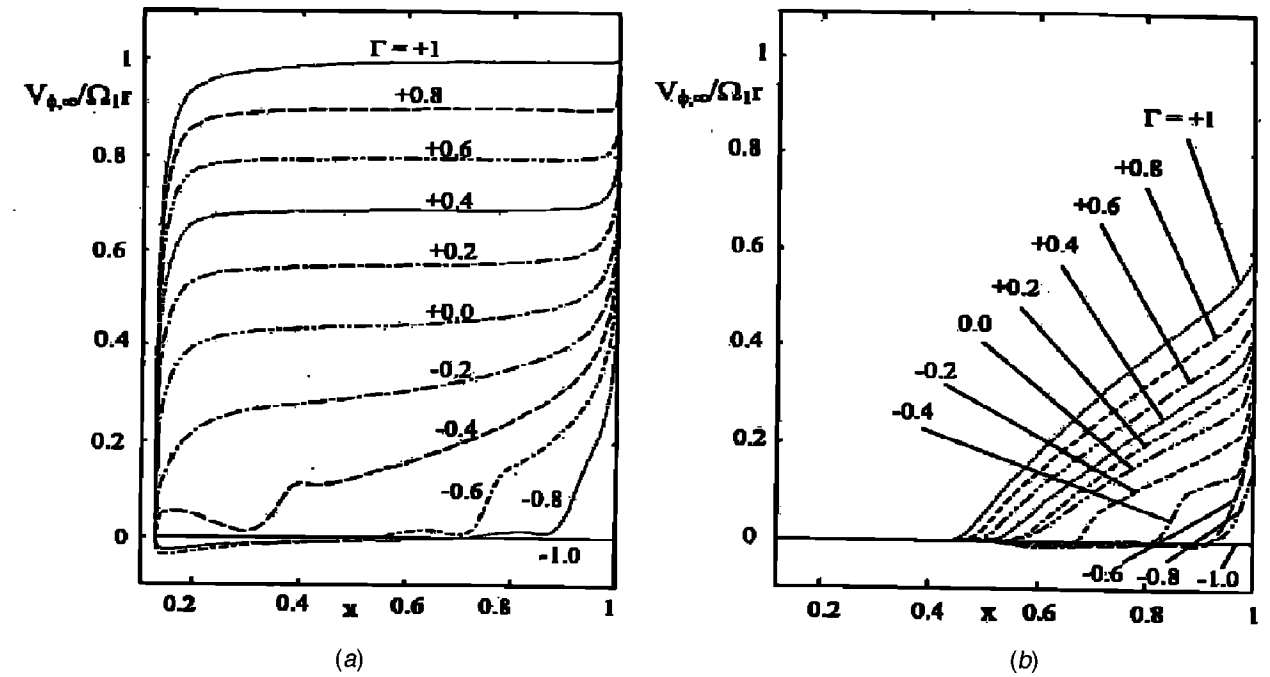

Fig. 7 Effect of Γ (for $-1 \leq \Gamma \leq +1$) on computed radial distributions of $V_{\phi,\infty}/\Omega_1 r$ at $z/s=0.5$ for $Re_{\phi,1}=1.25\times10^6$, $G=0.12$—(*a*) $C_w=\lambda_{T,1}=0$; (*b*) $C_w=6100$, $\lambda_{T,1}=0.0809$

Table 1 Computed moment coefficients for $Re_{\phi,1}=1.25\times10^6$, $-1\leq\Gamma\leq1$, $G=0.12$, $C_w=0$ and 6100

	$C_w=0$					$C_w=6100$			
Γ	$C_{m,1}\times10^3$ (LHS)	$C_{m,2}\times10^3$ (RHS)	M_2/M_1	$Re_{\phi,2}\div10^5$	$C_{m,fd,2}\times10^3$	$C_{m,1}\times10^3$ (LHS)	$C_{m,2}\times10^3$ (RHS)	M_2/M_1	$\lambda_{T,2}$
−1	4.28	4.28	−1.00	12.50	4.63	4.28	4.28	−1.00	0.08087
−0.8	4.20	5.31	−0.81	10.00	4.82	4.32	4.50	−0.67	0.09668
−0.6	3.91	8.86	−0.82	7.50	5.09	4.35	5.00	−0.41	0.12170
−0.4	3.43	17.75	−0.83	5.00	5.51	4.27	8.50	−0.32	0.16833
−0.2	2.79	58.75	−0.84	2.50	6.34	4.10	23.00	−0.22	0.29307
0	2.17	⋯	⋯	0.00	⋯	3.90	⋯	⋯	⋯
0.2	1.60	−34.50	−0.86	2.50	6.34	3.73	−1.00	−0.01	0.29307
0.4	1.08	−5.94	−0.88	5.00	5.51	3.57	2.25	0.10	0.16833
0.6	0.64	−1.58	−0.89	7.50	5.09	3.35	2.69	0.29	0.12170
0.8	0.29	−0.41	−0.90	10.00	4.82	3.08	2.78	0.58	0.09668
1	0.01	0.01	1.00	12.50	4.63	2.75	2.75	1.00	0.08087

$V_\phi/\Omega_1 r$ at $x=0.8$ for $Re_{\phi,1}=1.25\times10^6$, $C_w=0$, and $G=0.12$; Fig. 6(*b*) shows the computations for $C_w=6100$ ($\lambda_{T,1}=0.0809$), corresponding to the conditions in Fig. 2.

Figure 6(*a*) shows that, as Γ increases, $V_{\phi,\infty}/\Omega_1 r$ at $z/s=0.5$ increases monotonically from $V_{\phi,\infty}/\Omega_1 r=0$ at $\Gamma=-1$ to $V_{\phi,\infty}/\Omega_1 r=1$ at $\Gamma=+1$. It can also be seen that, as Γ increases, the boundary-layer thickness decreases and $V_{\phi,\infty}/\Omega_1 r$ in the core becomes invariant with z/s. For $\Gamma\leqslant-0.8$, $\partial V_{\phi,\infty}/\partial z<0$; for $\Gamma\geqslant-0.4$ (where $V_{\phi,\infty}/\Omega_1 r\gtrsim0.25$), $\partial V_{\phi,\infty}/\partial z\approx0$.

Figure 6(*b*) shows that $V_{\phi,\infty}/\Omega_1 r$ increases as Γ increases and, by comparison with Fig. 6(*a*), decreases as C_w (and $\lambda_{T,1}$) increases. Stewartson flow (in which $V_{\phi,\infty}/\Omega_1 r\approx0$) occurs for $\Gamma\leqslant-0.4$; Batchelor flow (in which $V_{\phi,\infty}/\Omega_1 r>0$) occurs for $\Gamma>-0.2$. The invariance of $V_{\phi,\infty}$ with z (which is consistent with the Taylor-Proudman theorem) occurs when $V_{\phi,\infty}/\Omega_1 r\gtrsim0.2$ ($\Gamma\gtrsim0$).

Figure 7(*a*) shows the radial distributions of $V_{\phi,\infty}/\Omega_1 r$ at $z/s=0.5$ for $Re_{\phi,1}=1.25\times10^6$ and $C_w=0$ ($\lambda_{T,1}=0$), corresponding to the axial distributions shown in Fig. 6(*a*). For the co-rotating cases ($\Gamma>0$), it can be seen that $V_{\phi,\infty}/\Omega_1 r$ increases as Γ increases and, away from the inner and outer radii, $V_{\phi,\infty}/\Omega_1 r$ is virtually invariant with x. For the contra-rotating cases ($\Gamma<0$), the picture is more complicated: the regions where $V_{\phi,\infty}/\Omega_1 r\approx0$ correspond to Stewartson flow, and those where $V_{\phi,\infty}/\Omega_1 r>0$ correspond to Batchelor flow; the latter regions increase in size as Γ increases.

Figure 7(*b*) shows the radial distributions for $C_w=6100$ ($\lambda_{T,1}=0.0809$), corresponding to the axial distributions shown in Fig. 6(*b*). For $\Gamma\geqslant0$, the smaller values of x, where $V_{\phi,\infty}=0$, are in the source region; the edge, at $x=x_e$, is the point where $V_{\phi,\infty}/\Omega_1 r>0$. For $\Gamma\geqslant0$, x_e increases as Γ decreases; Eq. (4) shows the same qualitative effect but overestimates the value of x_e determined from Fig. 7(*b*). Compared with Fig. 7(*a*), for $\Gamma<0$, the effect of increasing $\lambda_{T,1}$ is to increase the radial extent of Stewartson flow.

5 Computed Moment Coefficients

5.1 Definition of C_m. It is customary to define the moment coefficient, C_m, so that it is positive when the adjacent fluid creates drag on the rotating disk: that is, $C_m>0$ when the fluid tends to *brake* the disk; conversely, $C_m<0$ when the fluid tends to *drive* the disk. To ensure that this convention holds for both disks, the moment coefficient is defined here as

$$C_{m,i}=\mathrm{sgn}(M\Omega)_i\,\frac{|M_i|}{\frac{1}{2}\rho\Omega_i^2 b^5} \tag{9}$$

The moment, M, on one surface of the disk, is given by

$$M_1=-2\pi\int_a^b r^2\tau_{\phi,o}dr \tag{10a}$$

and

$$M_2=+2\pi\int_a^b r^2\tau_{\phi,s}dr \tag{10b}$$

where $\tau_{\phi,o}$ and $\tau_{\phi,s}$ are the tangential shear stresses at $z=0$ and $z=s$, respectively.

It is useful to compare the computed moment coefficients with the turbulent free-disk values of Dorfman [17], where

$$C_{m,fd}=0.491[\log_{10}(Re_\phi)]^{-2.58} \tag{11}$$

5.2 Effect of Γ on $C_{m,1}$. Table 1 shows the effect of Γ on the computed moment coefficients for $Re_{\phi,1}=1.25\times10^6$, $G=0.12$ and for $C_w=0$ and $C_w=6100$, $\lambda_{T,1}=0$ and 0.809).

The free-disk moment coefficient is a useful datum for comparison; in Table 1, $C_{m,fd,1}=C_{m,fd,2}=4.63\times10^{-3}$ at $\Gamma=\pm1$. It can be seen that, for $C_w=0$, $C_{m,1}$ decreases monotonically as Γ increases: $C_{m,1}$ is approximately 92% of $C_{m,fd,1}$ at $\Gamma=-1$, and is approximately 47% of $C_{m,fd,1}$ at $\Gamma=0$. (The small value of $C_{m,1}$ at $\Gamma=+1$ is caused by the fact that $V_{\phi,\infty}=0$ at $r=a$ in the computation; if $V_{\phi,\infty}=\Omega a$ at $r=0$ then there would be solid-body rotation throughout the cavity and $C_{m,1}$ would be zero.)

For $C_w=6100$ ($\lambda_{T,1}=0.0809$), $C_{m,1}$ has the same value at $\Gamma=-1$ as that for $C_w=0$. (For additional computations at $\Gamma=-1$ and $3.7\times10^5\leqslant Re_{\phi,1}\leqslant1.1\times10^6$, it was found that $C_{m,1}$ increases slightly as C_w increases, but the increase is negligible for $Re_{\phi,1}>1.1\times10^6$.) The value of $C_{m,1}$ for $C_w=6100$ changes little for $-1\leqslant\Gamma\leqslant-0.4$ where, as discussed in Section 4, Stewartson flow occurs over most of the disk surface. For $\Gamma>-0.4$, $C_{m,1}$ decreases monotonically as Γ increases, but, unlike the results for $C_w=0$, $C_{m,1}$ is still significant at $\Gamma=+1$, where it is around 59% of $C_{m,fd,1}$.

It can be concluded that $C_{m,1}$ tends to increase as C_w increases but the magnitude of the increase depends on Γ: for $\Gamma=-1$, the increase in $C_{m,1}$ is very small; for $\Gamma=+1$, it is large.

5.3 Effect of Γ on $C_{m,2}$. Table 1 shows that, for $\Gamma<0$ and $C_w=0$, $C_{m,2}$ increases as Γ increases, which contrasts with the behavior of $C_{m,1}$. (This increase is caused by the definition given in Eq. (9), where $C_{m,2}\propto M_2\Omega_2^{-2}$.) For $0<\Gamma<1$ and $C_w=0$, $C_{m,2}<0$; the reason for these negative values can be deduced from Fig. 6(*a*) where, for $\Gamma>0$, the core rotates *faster* than the right-hand disk, tending to drive rather than brake it. It is interesting to note that, for $-0.8\leqslant\Gamma\leqslant+0.8$, $M_2/M_1\approx0.85\pm0.05$; the reason for the relatively small variation of M_2/M_1 with Γ is not known.

For $C_w=6100$, a negative value of $C_{m,2}$ occurs only at $\Gamma=0.2$ in Table 1. Figure 6(*b*) shows that, for $\Gamma\leqslant0.2$, the core rotates faster than the right-hand disk; for $\Gamma>0.2$, it rotates slower, creating drag. That is, for $\Gamma>0$ as C_w increases, the core rotation decreases and $C_{m,2}$ consequently increases.

6 Conclusions

Computations have been conducted for steady, axisymmetric, turbulent flow in a rotating-disk system, with and without a radial outflow of air, for $-1 \leqslant \Gamma \leqslant +1$. The following conclusions have been drawn from studying the computed streamlines, velocity distributions and moment coefficients.

For $C_w > 0$ (and $\lambda_{T,1} < \lambda_{T,\max}$), for all values of Γ there is a source region downstream of the inlet, sink layers on the outer shrouds, boundary layers on both disks, and an inviscid core. An approximate method has been used to estimate x_e, the nondimensional radius of the source region, z_d/s, the location of the dividing streamline between the two disks, and $\lambda_{T,\max}$, the maximum value of $\lambda_{T,1}$ for which source-sink flow occurs. For $\Gamma = -1$, where $V_{\phi,\infty} \approx 0$ in the core, there is Stewartson flow with radial outflow in both boundary layers. For $\Gamma = 0$, where $V_{\phi,\infty} > 0$, there is Batchelor flow with radial outflow on the rotating disk and inflow on the stationary one. For $\Gamma = +1$, there is Ekman-layer flow with nonentraining boundary layers on both disks.

For contra-rotating disks, $-1 < \Gamma < 0$, a two-cell structure can develop, with Batchelor-flow at the larger radii and Stewartson flow at the smaller radii; as $\Gamma \to 0$, single-cell Batchelor flow dominates. For co-rotating disks, as Γ increases from 0 to +1, Batchelor flow is converted progressively to Ekman-layer flow in a single-cell structure. In general, $V_{\phi,\infty}/\Omega_1 r$ increases as x increases, as Γ increases and as $\lambda_{T,1}$ decreases. As $V_{\phi,\infty}/\Omega_1 r$ increases, Coriolis accelerations dominate over inertial accelerations: the equations of motion became increasingly linear, and "Taylor-Proudman effects" can be seen in the rotating core. Under these conditions (which appear to occur for $V_{\phi,\infty}/\Omega_1 r \gtrsim 0.2$) $V_{r,\infty} = 0$, $\partial V_{z,\infty}/\partial z = 0$, and $\partial V_{\phi,\infty}/\partial z = 0$. This can be seen in many of the co-rotating cases and in some of the contra-rotating ones.

For $\Gamma < 1$, the moment coefficient on the faster disk, $C_{m,1}$, is always positive. For $C_w = 0$, $C_{m,1}$ decreases monotonically as Γ increases from a maximum value (close to the free-disk value) at $\Gamma = -1$ to effectively zero at $\Gamma = +1$. For $C_w > 0$, $C_{m,1}$ tends to increase as C_w increases: for $\Gamma = -1$, the increase in $C_{m,1}$ is very small; for $\Gamma = +1$, the increase is large.

The moment coefficient on the slower disk, $C_{m,2}$, is negative for $C_w = 0$ and $0 < \Gamma < 1$; this is caused by the core rotating faster than the disk. For $C_w > 0$ and $\Gamma > 0$, $C_{m,2}$ increases as C_w increases, reducing the range of Γ in which $C_{m,2} < 0$.

Although the computed axisymmetric flows considered here are in good agreement with available experimental evidence, in the physical world it is quite possible for rotating flows to become nonaxisymmetric and unsteady; that possibility is beyond the scope of this paper.

Nomenclature

a = inner radius of cavity
b = outer radius of cavity
C_m = moment coefficient $(= \mathrm{sgn}(M\Omega)_{1,2}(|M|/\frac{1}{2}\rho\Omega^2 b^5)_{1,2})$
C_w = nondimensional flow rate $(= \dot{m}/\mu b)$
G = gap ratio $(= s/b)$
G_c = shroud-clearance ratio $(= s_c/b)$
$\dot{m}$ = superposed mass flow rate
M = moment on rotating disk
r = radius
Re_ϕ = rotational Reynolds no. $(= \rho\Omega b^2/\mu)$
s = axial gap between disks
s_c = axial clearance between shrouds
V_r, V_ϕ, V_z = radial, tangential, axial components of velocity
x = nondimensional radius $(= r/b)$
x_e = nondimensional radius of source region
z = axial distance from left-hand disk
z_d = axial location of dividing streamline
Γ = ratio of speed of slower disk to faster one $(= \Omega_2/\Omega_1)$
λ_T = turbulent flow parameter $(= C_w\,\mathrm{Re}_\phi^{-0.8})$
μ = dynamic viscosity of air
ρ = density of air
τ_ϕ = tangential shear stress
Ω = angular speed of disk

Subscripts

1,2 = relating to faster, slower disk
fd = free-disk value
max = maximum value
0 = value at $z = 0$
s = value at $z = s$
∞ = value in inviscid core or at z/s=0.5

References

[1] Owen, J. M., and Rogers, R. H., 1989, *Flow and Heat Transfer in Rotating Systems*, Vol. 1: *Rotor-Stator Systems*, Research Studies Press, Taunton, UK, John Wiley, New York, NY.
[2] Owen, J. M., and Rogers, R. H., 1995, *Flow and Heat Transfer in Rotating Systems*, Vol. 2: *Rotating Cavities*, Research Studies Press, Taunton, UK, John Wiley, New York, NY.
[3] Ekman, V. W., 1905, "On the Influence of the Earth's Rotation on Ocean-Currents," Ark. Mat., Astron. Fys., **2**, pp. 1–52.
[4] Kilic, M. 1993. "Flow Between Contra-Rotating Discs," Ph.D. thesis, University of Bath, Bath, UK.
[5] Kilic, M., Gan, X., and Owen, J. M., 1994, "Transitional Flow Between Contra-Rotating discs," J. Fluid Mech., **281**, pp. 119–135.
[6] Kilic, M., Gan, X., and Owen, J. M., 1996, "Turbulent Flow Between Two Discs Contrarotating at Differential Speeds," ASME J. Turbomach., **118**, pp. 408–413.
[7] Gan, X., Kilic, M., and Owen, J. M., 1994, "Superposed Flow Between Two Discs Contrarotating at Differential Speeds," Int. J. Heat Fluid Flow, **15**, pp. 438–446.
[8] Gan, X., Kilic, M., and Owen, J. M., 1995, "Flow Between Contra-Rotating Discs," ASME J. Turbomach., **117**, pp. 298–305.
[9] Morse, A. P., 1988, "Numerical Predictions of Turbulent Flow in Rotating Cavities," ASME J. Turbomach., **110**, pp. 202–214.
[10] Morse, A. P., 1991, "Assessment of Laminar-Turbulent Transition in Closed Disc Geometries," ASME J. Turbomach., **113**, pp. 131–138.
[11] Morse, A. P., 1991, "Application of a Low Reynolds Number k-ε Turbulence Model to High Speed Rotating Cavity Flows," ASME J. Turbomach., **113**, pp. 98–105.
[12] Batchelor, G. K., 1967, *An Introduction to Fluid Dynamics* Cambridge University Press, London, UK.
[13] Owen, J. M., Pincombe, J. R., and Rogers, R. H., 1985, "Source-Sink Flow Inside a Rotating Cylindrical Cavity," J. Fluid Mech., **155**, pp. 233–265.
[14] Karabay, H., Wilson, M., and Owen, J. M., 2001, "Predictions of Effect of Swirl on Flow and Heat Transfer in a Rotating Cavity," Int. J. Heat Fluid Flow, **22**, pp. 143–155.
[15] Stewartson, K., 1953, "On the Flow Between Two Rotating Coaxial Discs," Prog. Cambridge, Philos. Soc., **49**, pp. 333–341.
[16] Batchelor, G. K., 1951, "Note on a Class of Solutions of the Navier-Stokes Equations Representing Steady Rotationally-Symmetric Flow," Q. J. Mech. Appl. Math., **4**, pp. 29–41.
[17] Dorfman, L. A., 1963, *Hydrodynamic Resistance and the Heat Loss of Rotating Solids*, Oliver and Boyd, Edinburgh, Scotland.